

Lecture Notes in Civil Engineering

Madhavi Latha Gali
P. Raghuvver Rao *Editors*

Construction in Geotechnical Engineering

Proceedings of IGC 2018

 Springer

Lecture Notes in Civil Engineering

Volume 84

Series Editors

Marco di Prisco, Politecnico di Milano, Milano, Italy

Sheng-Hong Chen, School of Water Resources and Hydropower Engineering,
Wuhan University, Wuhan, China

Ioannis Vayas, Institute of Steel Structures, National Technical University of
Athens, Athens, Greece

Sanjay Kumar Shukla, School of Engineering, Edith Cowan University, Joondalup,
WA, Australia

Anuj Sharma, Iowa State University, Ames, IA, USA

Nagesh Kumar, Department of Civil Engineering, Indian Institute of Science
Bangalore, Bengaluru, Karnataka, India

Chien Ming Wang, School of Civil Engineering, The University of Queensland,
Brisbane, QLD, Australia

Lecture Notes in Civil Engineering (LNCE) publishes the latest developments in Civil Engineering - quickly, informally and in top quality. Though original research reported in proceedings and post-proceedings represents the core of LNCE, edited volumes of exceptionally high quality and interest may also be considered for publication. Volumes published in LNCE embrace all aspects and subfields of, as well as new challenges in, Civil Engineering. Topics in the series include:

- Construction and Structural Mechanics
- Building Materials
- Concrete, Steel and Timber Structures
- Geotechnical Engineering
- Earthquake Engineering
- Coastal Engineering
- Ocean and Offshore Engineering; Ships and Floating Structures
- Hydraulics, Hydrology and Water Resources Engineering
- Environmental Engineering and Sustainability
- Structural Health and Monitoring
- Surveying and Geographical Information Systems
- Indoor Environments
- Transportation and Traffic
- Risk Analysis
- Safety and Security

To submit a proposal or request further information, please contact the appropriate Springer Editor:

- Mr. Pierpaolo Riva at pierpaolo.riva@springer.com (Europe and Americas);
- Ms. Swati Meherishi at swati.meherishi@springer.com (Asia - except China, and Australia, New Zealand);
- Dr. Mengchu Huang at mengchu.huang@springer.com (China).

All books in the series now indexed by Scopus and EI Compendex database!

More information about this series at <http://www.springer.com/series/15087>

Madhavi Latha Gali · P. Raghuv​eer Rao
Editors

Construction in Geotechnical Engineering

Proceedings of IGC 2018

 Springer

Editors

Madhavi Latha Gali
Department of Civil Engineering
Indian Institute of Science
Bangalore, Karnataka, India

P. Raghuvveer Rao
Department of Civil Engineering
Indian Institute of Science
Bangalore, Karnataka, India

ISSN 2366-2557 ISSN 2366-2565 (electronic)
Lecture Notes in Civil Engineering
ISBN 978-981-15-6089-7 ISBN 978-981-15-6090-3 (eBook)
<https://doi.org/10.1007/978-981-15-6090-3>

© Springer Nature Singapore Pte Ltd. 2020

This work is subject to copyright. All rights are reserved by the Publisher, whether the whole or part of the material is concerned, specifically the rights of translation, reprinting, reuse of illustrations, recitation, broadcasting, reproduction on microfilms or in any other physical way, and transmission or information storage and retrieval, electronic adaptation, computer software, or by similar or dissimilar methodology now known or hereafter developed.

The use of general descriptive names, registered names, trademarks, service marks, etc. in this publication does not imply, even in the absence of a specific statement, that such names are exempt from the relevant protective laws and regulations and therefore free for general use.

The publisher, the authors and the editors are safe to assume that the advice and information in this book are believed to be true and accurate at the date of publication. Neither the publisher nor the authors or the editors give a warranty, expressed or implied, with respect to the material contained herein or for any errors or omissions that may have been made. The publisher remains neutral with regard to jurisdictional claims in published maps and institutional affiliations.

This Springer imprint is published by the registered company Springer Nature Singapore Pte Ltd. The registered company address is: 152 Beach Road, #21-01/04 Gateway East, Singapore 189721, Singapore

Preface

Indian Geotechnical Conference IGC-2018 was held at the National Science Complex of the Indian Institute of Science, Bangalore, during 13–15 December 2018. This is the annual conference of the Indian Geotechnical Society (IGS), which was established in the year 1948 with the aim to promote cooperation among engineers, scientists and practitioners for the advancement and dissemination of knowledge in the field of Geotechnical Engineering. IGC-2018 was a special event since it coincided with the 70 years Celebrations of IGS.

The conference was a grand event with about 700 participants. The conference was inaugurated on 13th December in the presence of the President of IGS Prof. G. L. Sivakumar Babu and the Chief Guest, Prof. E. C. Shin, Vice-president Asia, International Society of Soil Mechanics and Geotechnical Engineering (ISSMGE). The conference had 14 keynote lectures and 12 theme lectures presented by eminent academicians and practitioners from different parts of the world. A total of 313 technical papers under 12 different themes of the conference were presented during the conference in 19 oral presentation sessions and 10 digital display sessions. All the participants of the conference had a common vision of deliberating on current geotechnical engineering research and practice and to strengthen the relationship between scientists, researchers and practicing engineers within the fields of geotechnical engineering and to focus on problems that are relevant to society's needs and develop solutions. The conference acted as a platform to academicians and field engineers to interact, share knowledge and experiences and identify potential collaborations. The conference also provided opportunity to many young students, researchers and engineers and helped them to get connected to people involved in geotechnical engineering research and practice and national and international groups and technical committees.

All papers submitted to IGC-2018 had undergone a peer-review process and subsequently revised before being accepted. To publish conference proceedings through Springer, selected papers from the conference were grouped into four different volumes, namely, Geotechnical Characterization and Modelling, Construction in Geotechnical Engineering, Geohazards and Problematic Soils and Ground Improvement. This book on *Construction in Geotechnical Engineering*

contains 56 chapters written on various technical aspects, challenges, testing methods and case studies related to geotechnical engineering constructions including foundations, retaining walls, dams, roads, waste disposal facilities, stone columns and underground structures.

We sincerely thank the Indian Geotechnical Society, especially Prof. G. L. Sivakumar Babu, President, IGS and Prof. J. T. Shahu, Honorary Secretary, IGS for their great support in organizing the conference. We also thank the Organizing committee of IGC-2018, Prof. P. V. Sivapullaiah, Conference chair, Prof. H. N. Ramesh, Conference Vice-chair, Dr. C. R. Parthasarathy, Prof. P. Anbazhagan and Prof. K. V. Vijayendra, Organizing Secretaries, Prof. K. Vijaya Bhaskar Raju, Treasurer, for all their hard work, long working hours spent and responsibility shared in planning and executing various tasks of this outstanding event. The unconditional support extended by the Conference advisory committee, Technical committee, Sponsors of the conference, Keynote Speakers, Theme speakers, Session chairs, Session coordinators, Student volunteers, participants, presenters and authors of the technical papers in making the conference a grand success is sincerely appreciated. We thank the entire Springer Team, in particular Swati Meherishi, Rini Christy Xavier Rajasekaran, Muskan Jaiswal and Ashok Kumar for their hard work and support in bringing out the proceedings of IGC-2018.

Bangalore, India

Madhavi Latha Gali
P. Raghuv eer Rao

Contents

Increasing the Yield of Ring Wells by User Friendly Method	1
H. S. Prasanna, S. C. Harshavardhan, A. R. Chaitra, P. K. Pooja, and P. Beerasha	
Study on the Effect of Soil as a Filler in Foamed Concrete	17
K. S. Kavya, K. K. Jithiya, N. Athulya Vijay, Jiji L. Jayan, M. Karthik, Y. Sheela Evangeline, and Sajan K. Jose	
Effect of Variation of In Situ Moisture Content on Pullout Capacity of Grouted Soil Nail	27
Avishek Ghosh, Sayantan Chakraborty, and Ashish Juneja	
Behavior of Instrumented Piles Under Different Loading and Soil Conditions	41
Anshul Gautam and Satyendra Mittal	
Effect of Piles on the Design of Raft Foundation	57
L. M. Malavika, V. Balakumar, and S. S. Chandrasekaran	
Interaction Effect on Laterally Loaded Piles in Cohesionless Deposit	81
Sachchidanand Kushwaha and Ashok Kumar Khan	
Review of Load Test Performance of Base Grouted Concrete Piles	99
D. Nagarajan, K. Raja Rajan, and T. Vijayakumar	
Uplift Capacity of Single-Belled Anchor in Cohesionless Foundation Media	119
Tanaya Deb and Sujit Kumar Pal	
Effect of Footing Shapes and Reinforcement on Bearing Capacity of Three Adjacent Footings	135
S. S. Saraf and S. S. Pusadkar	

Analysis of Torpedo Anchors for Mooring Operations	149
S. Keerthi Raaj, R. Sundaravadivelu, and Nilanjan Saha	
Ground Improvement for Foundations of Structures Using Stone Column—Case Study on Road Connectivity to ICTT, Vallarpadam Port in Cochin, Kerala, India	161
Avik Kumar Mandal, S. Sailesh, and Pradyot Biswas	
Combined Piled Raft Foundation (CPRF) System for Polymerization Loop Reactor Structure	185
P. Jayarajan and K. M. Kouzer	
Bearing Capacity Estimation of Shallow Foundations on Dense Sand Underlain by Loose Sand Strata Using Finite Elements Limit Analysis	203
Pragyan Paramita Das and Vishwas N. Khatri	
Lateral and Uplift Capacities of Barrette Pile in Sandy Soil	215
Anju Kumari, S. W. Thakare, and A. I. Dhattrak	
Analyses of Footing Resting on Confined Layered Sandy Soil	237
Apoorva M. Kulkarni, S. W. Thakare, and A. I. Dhattrak	
Analyses of Shell Footing in Layered Sandy Soil	255
A. I. Dhattrak, P. S. Yaldarkar, and S. W. Thakare	
Performance of Suction Pile Anchor for Floating Offshore Structures	271
S. W. Thakare, Aparna H. Chavan, and A. I. Dhattrak	
Image-Based Measurements to Estimate Bearing Capacity of Hollow Driven Piles Under Impact Loading	285
G. Sreelakshmi, Asha M. N., Divya Viswanath, Y. N. Yogesh kumar, and S. Vinodini	
Experimental Analysis and Validation Techniques of Piled-Raft Foundation System	299
R. Vignesh and M. Muttharam	
Prediction of Ultimate Uplift Capacity of Short Piles in Sandy Soils	315
R. M. Thejaswini, L. Govindaraju, and V. Devaraj	
Experimental Investigation of Piled Raft Foundation Under Combined Vertical, Lateral and Moment Loads	325
Diptesh Chanda, Rajib Saha, and Sumanta Haldar	
Study on Cyclic Pile Load Test of Pile Socketed in Rock	339
A. P. Sumisha and Arvee Sujil Johnson	

Uplift Capacities of Inclined Double-Plate Circular Anchors at Shallow Depths in Sand 353
 B. Vidya Tilak and N. K. Samadhiya

Analysis and Design of Pile Foundations for a Sewage Treatment Plant 363
 S. Samarth, S. Nethravathi, M. S. Nagakumar, and G. Venugopal

Analytical and Numerical Analysis of Piled-Raft Foundation of Storage Tank 373
 Mahdi O. Karkush and Ala N. Aljorany

Comparative Study of Methods for Analysis of Laterally Loaded Well Foundation 385
 Ramyasri Rachamadugu and Gyan Vikash

Influence of Shape of Footing on Coefficient of Elastic Uniform Compression of Soils 399
 C. N. V. Satyanarayana Reddy and S. Swetha

Effective Cut Slope of Rock Slope Along NH-44 405
 Promit Kumar Bhaumik, Rituraj Devrani, Apurba Das, S Sreedeeep, and S. B. Prasath

Raising of Ash Pond for Augmented Storage 417
 B. V. Sushma

Possible Use of High Draining Material in Core of Earth Dam with Admixtures 433
 Saroj Kundu, Pritam Dhar, and B. C. Chattopadhyay

Experimental Study on Cantilever Sheet Pile Wall 445
 Aparna and N. K. Samadhiya

Effects of Geogrid and Floating Piles on Performance of Highway Embankment Constructed Over Clayey Soil 455
 Dinesh Kumar Verma and Baleshwar Singh

Dynamic Behavior of Retaining Wall Back Paneled by Waste Tire Shredded Rubber Fiber—An Experimental Study 465
 Upendra Modalavalasa, Shyam A. Hatiwala, Brijesh K. Agarwal, Swapnali Pawar, and Jignesh B. Patel

Suitability of Fly ash in Raising the Embankments 483
 Teja Munaga, Pothula Sai Charan, Mathew Sai Kiran Raju, Lahir Yerra, Bilal Kothakota, and Gonavaram Kalyan Kumar

Displacement-Based Analysis of Retaining Wall with Constrained Backfill 493
 Godas Srikar, Satyendra Mittal, Sumit Bisht, and Ankarapu Sindhuja

Behaviour of Strip Footing Resting on Pretensioned Geogrid-Reinforced Ferrochrome Slag Subgrade	503
Atul Kumar, Anil Kumar Choudhary, and Sanjay Kumar Shukla	
Dynamic Response of Tall Chimneys on Pile–Raft Foundation Subjected to Wind Load	521
L. Lakshmi, Monu Lal Burnwal, Samit Ray Chaudhuri, and Prishati Raychowdhury	
Construction Dewatering for Underground Station in Urban Environment	537
K. Raja Rajan, D. Nagarajan, and T. Vijayakumar	
Investigations On the Impact of Sub-Structures on Groundwater Flow	557
Rohitha P. Kamath and N. Unnikrishnan	
Application of Jet Grouting for Geotechnical Challenges	565
Akhila Manne, P. V. S. R. Prasad, and Madan Kumar Annam	
Optimal Foundation Solution for Residential Projects	579
B. Vani and Madan Kumar Annam	
Reanalysis of Failure of Soil-Nailed Shoring System and Remedial Measures	589
S. Vibha, S. P. Srinivas, and G. L. Sivakumar Babu	
Determination of Compacted Dense Sand Layer Thickness on Loose Sand Using Odemark’s Method for Design of Shallow Foundation	599
Partha Pratim Biswas, Manoj Kumar Sahis, and Agnimitra Sengupta	
Reliability Analysis on Fatigue and Rutting Failures of Flexible Pavement with the Variation of Surrounding Atmospheric Condition and Mix Design of Bitumen	607
Sourav Mitra, Saurav Pal, and Pritam Aitch	
Application of Under Sleeper Pads to Enhance the Sleeper-Ballast Interface Behaviors	619
Sinniah K. Navaratnarajah and Buddhima Indraratna	
Strengthening of Weak Subgrade Using Geocell	637
G. Sridevi, G. Sudarshan, and A. Shivaraj	
Stresses Induced on Existing Pipeline Due to Laying of New Pipeline	645
Seema Gurnani, Altaf Usmani, and Charanjit Singh	
Some Studies on Pavements on Flyash-Stabilized Expansive Subgrades	655
D. Nigade-Saha Sanjivani and B. V. S. Viswanadham	

Comparison of Geostatistical Technique to Assess the Safe Zones of Water Storage 677
 Sunayana, Vikas Kumar, and Komal Kalawapudi

Pullout Capacity of Ground Anchors in Non-homogeneous Cohesive–Frictional Soil 691
 Soumya Sadhukhan and Paramita Bhattacharya

Settlement Analysis of Single Circular Hollow Pile 703
 Ravikant S. Sathe, Jitendra Kumar Sharma, and Bharat P. Suneja

Effect of Excavation on the Settlement of Adjacent Structures 713
 M. S. Aswathy, Achal Mittal, and Sidharth Behera

Full-Scale Load Test on Bored Cast in situ Piles—A Case Study 723
 B. V. S. Viswanadham and Pankaj Kumar

Review of Historic Forensic Geotechnical Engineering 733
 Leonardo Souza and Purnanand Savoikar

Machine-Induced Vibration Isolation Using Geocell Reinforcement 755
 K. N. Ujjawal and A. Hegde

About the Editors

Dr. Madhavi Latha Gali is a Professor in the Department of Civil Engineering, Indian Institute of Science (IISc) Bangalore, India. She completed her Ph.D. from Indian Institute of Technology Madras, and has previously worked as a post-doctoral fellow and assistant professor at IISc and IIT Guwahati respectively. Professor Latha is a member of various professional bodies including IGS, ISSMGE and ISRM, and is the Editor-in-Chief of the Indian Geotechnical Journal, and an Editorial board member in many reputed journals. Her research work focuses on fundamental aspects of soil and ground reinforcement, and she has authored 70 journal articles, 4 book chapters and has developed a web-course on Geotechnical Earthquake Engineering on the NPTEL platform, sponsored by the Ministry of Human Resources Development, Government of India.

Dr. P. Raghuvver Rao is Principal Research Scientist at Department of Civil Engineering and involved in teaching, research and consultancy in the broad area of geotechnical engineering. He has been working with the department since 1989 and has been teaching courses related to subsurface exploration and soil testing, Earth retaining structures, behavior and testing of unsaturated soils, and fundamental of soil behavior for Masters and Doctoral students. His research interests are geotechnical instrumentation, slope stability analysis, numerical modelling, mechanics of unsaturated soils, contaminant transport through soil and reinforced earth structures. He has conducted several field and laboratory tests for design of foundations of different structures like buildings, turbo-generator and water tanks. He has analyzed stability of several embankments, tailing dams and stability of large size surge shafts for a hydropower project through numerical modelling and trial wedge method. He has 21 publications in journals and conference proceedings.

Increasing the Yield of Ring Wells by User Friendly Method



H. S. Prasanna, S. C. Harshavardhan, A. R. Chaitra, P. K. Pooja,
and P. Beerasha

Abstract Inadequacy of water for the irrigation purposes is being reported as the remarkable problem from the farmers. The groundwater and well systems have to be promoted where the construction of dams, reservoirs, canals, etc. alone can't serve the farmers. In this study, an attempt has been made to develop to draw water efficiently, to the ring wells situated along the bank of a river. A ring well was selected as the prototype along the river bank and the physical properties of the soil along the periphery of the well were determined to know the soil profile around the well. A model was simulated accordingly and the yield of the model was determined by conducting recuperation tests. Further, perforated laterals of two different lengths were inserted in eight radial directions alternatively at the bottom of the well, and yield was measured for various combinations of the laterals. Similarly, the recuperation tests are conducted even for the slotted laterals and compared with that of the perforated ones. The yield of the model without laterals and with laterals has been compared to know the efficiency of the model. The combination of laterals which gives the optimum yield in the model was selected and provided in the prototype. From the present study, it can be concluded that usage of laterals increases the permeability of the system and thereby increases the yield of the well without the need for increasing the cross section of the well and thus saving valuable time and money.

H. S. Prasanna (✉) · S. C. Harshavardhan · A. R. Chaitra · P. K. Pooja · P. Beerasha
Department of Civil Engineering, NIE, Mysuru, Karnataka, India
e-mail: hsprasanna62@gmail.com

S. C. Harshavardhan
e-mail: harsharx100@gmail.com

A. R. Chaitra
e-mail: chaitrarajmys@gmail.com

P. K. Pooja
e-mail: poojapk2425@gmail.com

P. Beerasha
e-mail: beerasha4121993@gmail.com

Keywords Ring wells · Yield of the well · Perforated lateral · Slotted lateral · Regression analysis

1 Introduction

Agriculture sector occupies a vital portion in the overall economy of the country. About 80% of the population directly or indirectly depends on income derived from agriculture. Although agriculture is the backbone of India, it is observed, that it is extremely low in terms of annual yield of crops per acre, in relative comparison to other developing countries. Employment of scientific techniques especially in developed countries such as USA and Russia has achieved tremendous progress. Initially, machines have superseded manual labor, i.e., a larger average is brought under cultivation in more efficient manner.

In many developing countries the major contribution to the economic development, this can be supplemented through irrigation network systems. It is observed that the consumption of agricultural products is on a rising demand in many developing countries due to the magnitude of population increase, in order to meet this rising demand the respective governments made several attempts to keep the supply and demand chain in an economical order. Demand for agricultural products is generally met by rain-fed agriculture/through cultivating techniques by means of irrigation or by means of imports. Out of these, the magnitude of agricultural product output is through irrigated agricultural methods.

Irrigation increases the stability and efficiency of cropping systems and diminishes the risks of drought and desertification. An irrigation system serves as an important economic resource to provide a basis for settlements and related social amenities in areas that otherwise support sparse populations. However, the history of irrigated agriculture has not always recorded success. Some past schemes—and some very recent ones—suffered severe setbacks through silting, waterlogging, and salinization as well as social and political challenges. Some schemes proved excessively expensive. The development of irrigation can be justified from the point of view of economic necessity. Irrigation is often costly, technically complex and requires skill and experience to realize full benefits.

Supply of bulk water for irrigation is under pressure from the demands of other water-using sectors, constraints on further water resource development, and is compounded by poor maintenance of existing irrigation infrastructure. The principal sources of irrigation can be divided into Canals, Wells, Tanks, etc. The large volumes of water required for irrigation usually have to be transported over some distance to the field. For surface water, canals, and pipes can enable conveyance; in the case of groundwater, extraction is provided via tube wells. Water from rivers is extracted by constructing ring wells along the river beds. When the permeability of the soil along the river bed is more, it fetches more yield of the well. But excessive extraction of water from these ring wells also results in the subsidence of soils along the periphery of the soil, giving rise to dredging problems which is costlier for the

marginal farmers who can't even afford, the increase in the size of the wells in order to get more discharge. Hence, there is a need to find a feasible solution for these problems.

In the present experimental study, an attempt has been made to solve the above-stated problems by using slotted laterals in the ring wells which gives maximum discharge from the well without increasing the diameter of the well and decreasing the problem of soil subsidence around the wells.

2 Literature Review

As it is necessary to determine the performance of each method of application of water and crop performance in each system, various methodologies have to be overviewed to develop a new one.

Al-Zuhairi et al. (2002) investigated the efficiency of using sand columns in improving soft clayey soils. Variables such as reinforcement ratio (number and cross section of sand column) and relative density of column material and their effect on the new soil system were studied. They concluded that the undrained shear strength of reinforced sample was found to be depended on both reinforcement ratio, and relative density of the sand in the column. The improvement gained was highly affected by the number of sand columns used rather than the relative density of soil in the column.

Many methods were developed in the past to recharge the existing bore-wells to supplement the magnitude of water deficit during summer seasons, i.e., Sikandar et al. (2008), Raphael (2009). Increasing the efficiency of bore-wells by Hydro-fracturing technique, Thangasala et al. (2010), Bank filtration, etc.

Patel et al. (2011) made an attempt to evaluate the hydraulic performance of porous pipe used as micro-irrigation lateral in sub-surface irrigation system and measured the discharge from the lateral tube and concluded that the porous pipe tested did not possess the qualities of good micro-irrigation lateral.

Sandhu et al. (2011) studied on Potential for Riverbank filtration in India and examined selected operating bank filtration sites. He elucidated additional potential RBF sites based on water problems and hydrogeologic suitability.

Mayilswami et al. (2013) studied on Guidelines for augmentation of groundwater resources under climate change in Tamil Nadu. Earlier, the ring wells were used to fetch water, now it was used to increase the water level. An age-old practice is receiving a modern twist to improve the water table in Kaniyambadi block of Vellore district. Recharge wells also known as ring wells are being built in 21 panchayats of Kaniyambadi block to improve the water table. The aim of constructing the recharge wells is to conserve rainwater and increase the water table. It is being carried out on a pilot basis in Kaniyambadi block. Water from the stream will flow into these wells. An impact study was carried out to see how this helped in improving water table for one to two years. It was found that water does not flow into the river directly. Once

the groundwater level increases, water reaches the lakes in the second year and then flows into the river in the third year following three monsoons.

No studies have been reported in the documented literature regarding the increase in yield of wells using laterals.

3 Materials and Methods

A ring well located (at 12.1487400E, 76.7761970 N) along the bank of river Kabini, situated in Nagarle village, Nanjangud taluk, Mysuru district, Karnataka state, India, was selected as prototype for the present experimental study. Cylindrical galvanized pipes with threaded collars were fabricated as core cutter for sampling. In situ undisturbed and disturbed representative soil samples were brought from the site for the laboratory investigation to know the soil profile along the periphery of the well. The various laboratory tests were conducted as per relevant IS codes of practice to know the physical properties of the soils.

In situ density test [IS: 2720 (part-29)-1975] was carried out to know the field density of the fine-grained soil in four radial directions around the well. Table 1 shows the average values of In situ density of the fine-grained soil up to a depth of 1.2 m.

Specific gravity test [IS: 2720 (part-3 sec-1)-1980] was determined for both the types of soils. Free swell ratio test [IS: 2911 (part-3)-1980] was determined to the dominant clay mineralogy in the soil. Grain size analysis [IS: 3104-1965] was done as per IS code. Atterberg limits [IS: 2720 (part-5)-1985] were determined and liquid limit of the soil sample was found by both Casagrande method. Table 2 shows the characteristics of the soil that was found up to a depth of 1.2 m.

Uniformly graded sandy soil (Poorly graded soil—SP) was found to a further depth of 5.2 m and there on. The soil samples collected at different depths from the core cutter were directly transferred to the permeameter and kept for saturation. Then, the permeability test [IS: 2720 (part-17)-1986] by variable head for fine-grained soil was carried out to determine the permeability characteristics of the soil along the soil profile. Table 3 shows the values of coefficient of permeability for the soils.

Results obtained were used for the simulation of the model to estimate the yield of the prototype. The model was simulated to the field density and along with laterals of two different lengths (0.152 and 0.305 m) inserted to the well in eight radial directions in an alternative manner. Fabrication of perforated laterals for field is

Table 1 Average values of In situ density of the fine-grained soil up to a depth of 1.2 m

Soil sample	In situ density (kN/m ³)
Sample 1	17.66
Sample 2	19.75
Sample 3	20.11
Sample 4	19.52

Table 2 Characteristics of soil up to a depth of 1.2 m

Characteristics	Soil
Specific gravity	2.54
Free swell ratio	1.27
Liquid limit (%)	28
Plastic limit (%)	20
Shrinkage index (%)	18
Sand (%)	61
Silt (%)	32
Clay (%)	7
IS classification	SM

Table 3 Values of Coefficient of permeability for both the soils

Sample	Coefficient of permeability (mm/s)	
	Fine-grained soil	Sandy soil
1	1.83×10^{-5}	4.01×10^{-2}
2	4.65×10^{-6}	3.98×10^{-2}
3	7.12×10^{-6}	4.04×10^{-2}
4	9.01×10^{-7}	4.00×10^{-2}
Avg. Value	7.74×10^{-6}	4.00×10^{-2}

difficult than making slots in the laterals. Hence, the slotted laterals were preferred for field installation. Figure 1 represents the schematic diagram of the model.

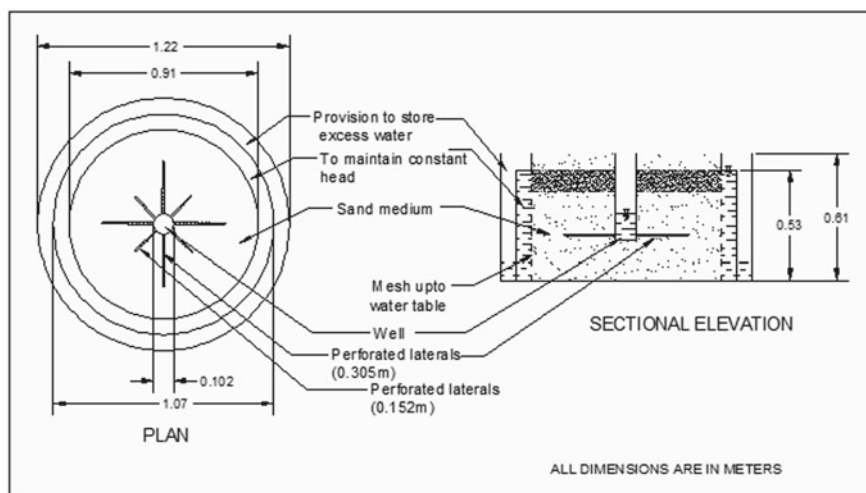


Fig. 1 Schematic diagram of model

Constant head was maintained, to measure the yield of the well by conducting recuperation test, for both the conditions. The yield was measured for the different combinations of laterals and the variation of discharge with perforated and slotted laterals were studied, respectively, and results were compared accordingly. Multi-linear regression analysis was carried out to know the correlation between the discharges obtained from the slotted and perforated laterals.

Soil subsidence was found along the periphery of the well in the model during excessive discharge from the well with no laterals. When the site was investigated regarding this, the soil subsidence around the prototype was also observed. From the farmers, it was reported that during excessive discharge from the well; the soil subsidence takes place along the periphery of the well which is the major problems faced by them. Figures 2 and 3 show the subsidence in the model and prototype, respectively.

During the experimental study, the soil subsidence was reduced after the usage of laterals. Thus, providing laterals being an effective solution to reduce the soil subsidence.

Fig. 2 Subsidence in model



Fig. 3 Subsidence in prototype



4 Results and Discussions

4.1 Results of the Perforated Laterals

For the first combination of laterals, inlets of the laterals of length 0.305 m were opened and others were closed using rubber cork. For the second combination of the laterals, only the inlets of laterals of length 0.152 m were opened. For the third combination of laterals, inlets of all the 0.305 m length laterals were opened and inlets of the 0.152 m length laterals were opened one by one for different trials. For the fourth combination of laterals, inlets of all the 0.152 m length laterals were opened and inlets of the 0.305 m length laterals were opened one by one for different trials.

Tables 4, 5, 6 and 7 present the values of discharge for different no. of perforated laterals along with different combinations of laterals. Figures 4, 5, 6 and 7 represent the variation of discharge with different number of laterals.

Table 4 Values of discharge for different number of perforated laterals of length 0.305 m

Nos and length of laterals	Discharge (cm^3/s)
0	27.30
1 (0.305 m)	37.17
2 (0.305 m)	47.05
3 (0.305 m)	63.98
4 (0.305 m)	79.33

Table 5 Values of discharge for different number of perforated laterals of length 0.152 m

Nos and length of laterals	Discharge (cm^3/s)
0	27.30
1 (0.152 m)	33.08
2 (0.152 m)	37.63
3 (0.152 m)	43.04
4 (0.152 m)	48.45

Table 6 Values of discharge for different number of perforated laterals (both the lengths 0.305 m and 0.152 m)

Nos and length of laterals	Discharge (cm^3/s)
4 (0.305 m) + 1 (0.152 m)	68.35
4 (0.305 m) + 2 (0.152 m)	73.43
4 (0.305 m) + 3 (0.152 m)	65.05
4 (0.305 m) + 4 (0.152 m)	72.18

Table 7 Values of discharge for different number of perforated laterals (both the lengths 0.152 m and 0.305 m)

Nos and length of laterals	Discharge (cm^3/s)
4 (0.152 m) + 1 (0.305 m)	57.80
4 (0.152 m) + 2 (0.305 m)	69.04
4 (0.152 m) + 3 (0.305 m)	64.44
4 (0.152 m) + 4 (0.305 m)	71.43

Fig. 4 Discharge curve w.r.t. number of perforated laterals (for 0.305 m laterals)

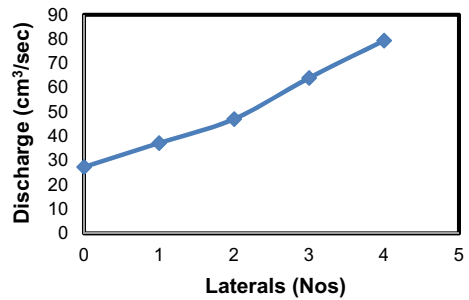


Fig. 5 Discharge curve w.r.t. number of perforated laterals (for 0.152 m laterals)

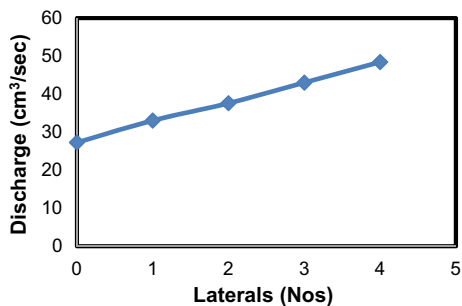


Fig. 6 Discharge curve w.r.t. number of perforated laterals (for both 0.305 m Laterals + 0.152 m Laterals)

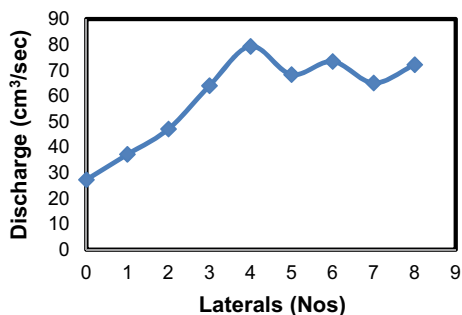


Fig. 7 Discharge curve w.r.t. number of perforated laterals (for both 0.152 m Laterals + 0.305 m Laterals)

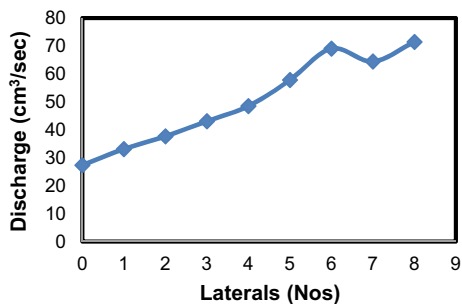


Table 8 Values of discharge for different number of slotted laterals of length 0.305 m

Nos and length of laterals	Discharge (cm ³ /s)
4 (0.305 m) + 1 (0.152 m)	70.94
4 (0.305 m) + 2 (0.152 m)	77.62
4 (0.305 m) + 3 (0.152 m)	68.68
4 (0.305 m) + 4 (0.152 m)	76.63
0	27.71
1 (0.305 m)	38.02
2 (0.305 m)	48.85
3 (0.305 m)	67.14
4 (0.305 m)	81.35

4.2 Results of the Slotted Laterals

Tables 8, 9, 10 and 11 present the values of discharge for different no. of slotted laterals along with different combinations of laterals. Figures 8, 9, 10 and 11 represent the variation of discharge with different number of laterals.

From Figs. 4 and 8, it can be observed that the discharge from the well increases with the increase in the no. of perforated and slotted laterals, respectively. Similarly

Table 9 Values of discharge for different number of slotted laterals of length 0.152 m

Nos and length of laterals	Discharge (cm ³ /s)
0	27.71
1 (0.152 m)	33.83
2 (0.152 m)	38.74
3 (0.152 m)	44.78
4 (0.152 m)	49.95

Table 10 Values of discharge for different number of slotted laterals (both the lengths 0.305 and 0.152 m)

Nos and length of laterals	Discharge (cm ³ /s)
4 (0.305 m) + 1 (0.152 m)	70.94
4 (0.305 m) + 2 (0.152 m)	77.62
4 (0.305 m) + 3 (0.152 m)	68.68
4 (0.305 m) + 4 (0.152 m)	76.63

Table 11 Values of discharge for different number of slotted laterals (both the lengths 0.152 and 0.305 m)

Nos and length of laterals	Discharge (cm ³ /s)
4 (0.152 m) + 1 (0.305 m)	60.14
4 (0.305 m) + 2 (0.305 m)	72.69
4 (0.305 m) + 3 (0.305 m)	68.41
4 (0.305 m) + 4 (0.305 m)	80.04

Fig. 8 Discharge curve w.r.t. number of slotted laterals (for 0.305 m laterals)

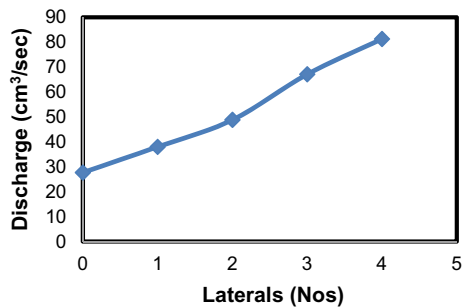


Fig. 9 Discharge curve w.r.t. number of slotted laterals (for 0.152 m laterals)

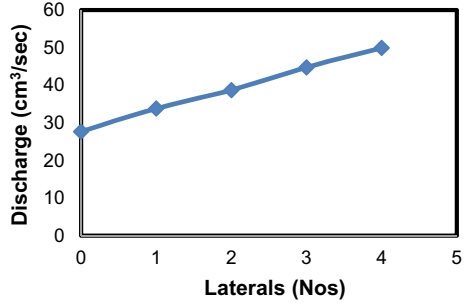


Fig. 10 Discharge curve w.r.t. number of slotted laterals (for both 0.305 m Laterals + 0.152 m Laterals)

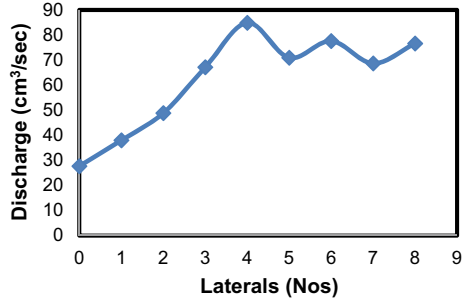
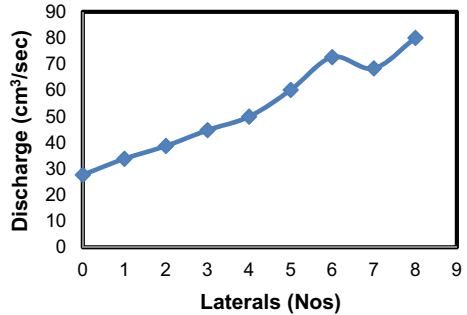


Fig. 11 Discharge curve w.r.t. number of slotted laterals (for both 0.152 m Laterals + 0.305 m Laterals)



from Figs. 5 and 9, it can be observed that there is an increase in the discharge from the well with the increase in the no. of perforated and slotted laterals, respectively.

From Figs. 6 and 10, it can be observed that discharge for the laterals of 0.305 m length is maximum (with 4 no. of laterals) than for the laterals of 0.152 m length.

From Figs. 7 and 11, representing the combination of 0.305 m laterals and 0.152 m laterals, it is observed that discharge is maximum for four large laterals and usage of 8 laterals would be uneconomical. It is observed that discharge is maximum for the combination of 4 no. of 0.152 m & 2 no. of 0.305 m laterals.

Even though 6 laterals gives the maximum discharge but it is less than the discharge obtained by providing 4 laterals (Figs. 7 and 11).

Thus, the yield obtained by the maximum discharge from 4 no. of 0.305 m laterals is considered to be the optimum one in both perforated and slotted laterals. From the yield comparison between optimum no. of laterals and no laterals, it is observed that the yield of the well is increased by 190.57% for perforated laterals and 193.58% for slotted laterals.

4.3 Correlation of Discharge Slotted with Discharge Perforated

Making perforations in the laterals used for installing in the field were found to be difficult than making slots. Hence, slotted laterals were preferred for both model and field installation and experiments are conducted on both perforated and slotted laterals in the model to know the correlation between them and their efficiency is checked.

Figure 12 represents the correlation of discharge obtained for slotted and perforated laterals (for the combination of 0.305 m laterals). Figure 13 represents the

Fig. 12 Correlation of Discharge obtained for slotted and perforated laterals (for the combination of 0.305 m laterals)

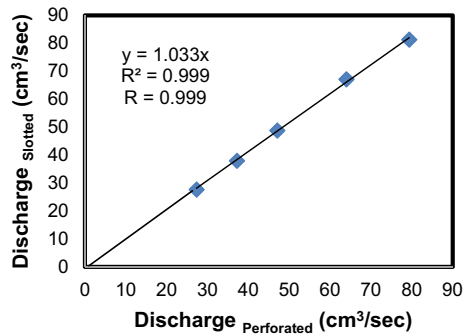
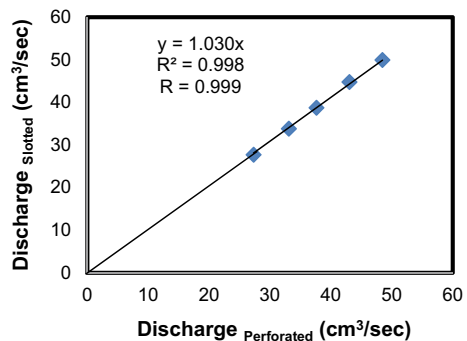


Fig. 13 Correlation of Discharge obtained for slotted and perforated laterals (for the combination of 0.152 m laterals)



correlation of discharge obtained for slotted and perforated laterals (for the combination of 0.152 m laterals). Figure 14 represents the correlation of discharge obtained for slotted and perforated laterals (for the combination of 0.305 m + 0.152 m laterals). Figure 15 represents the correlation of discharge obtained for slotted and perforated laterals (for the combination of 0.152 m + 0.305 m laterals). Figure 16 represents the correlation of discharge obtained for slotted and perforated laterals irrespective of the combination of laterals.

Fig. 14 Correlation of Discharge obtained for slotted and perforated laterals (for the combination of 0.305 m + 0.152 m laterals)

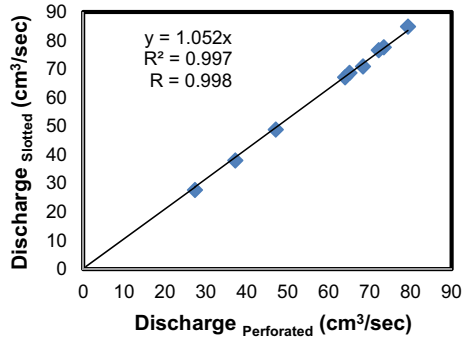


Fig. 15 Correlation of Discharge obtained for slotted and perforated laterals (for the combination of 0.152 m + 0.305 m laterals)

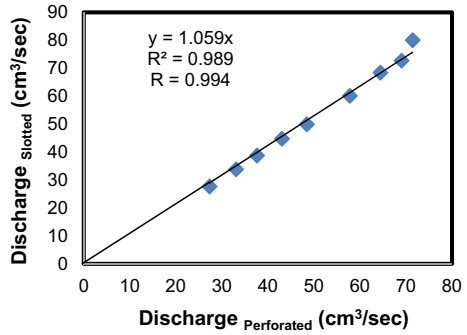
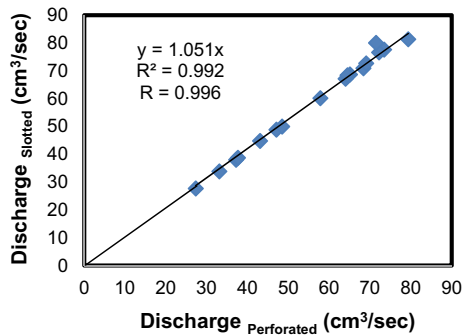


Fig. 16 Correlation of Discharge obtained for slotted and perforated laterals irrespective of the combination of laterals



From the above figures, it can be observed that the discharge obtained from the slotted laterals can be effectively correlated with the discharge obtained from the perforated laterals with coefficient of correlation of 0.99.

5 Conclusions

In the present experimental study on increasing the yield of the well-using laterals, following are the important conclusions made from the results and observations:

- It can be concluded that the discharge from the well can be increased by providing the laterals which influences the permeability of the soil. Thus, the yield of the well can be increased without increasing the cross-sectional area of the well.
- Even though, all the combinations of laterals result in the increase in the yield of well, the combination of 4 no. of 0.305 m laterals gives the maximum yield of the well in both slotted and perforated laterals.
- From the regression analysis, it can be concluded that the discharge obtained from the slotted laterals can be effectively correlated with the discharge obtained from the perforated laterals with coefficient of correlation of 0.99.
- It is also observed that the provision of laterals also prevents subsidence of the soil mass around the periphery of the well, thus, reducing the problems of dredging of soil from the well.
- As the usage of laterals is more economical than increasing the size of the well to increase the yield, this method greatly helps the marginal farmers and hence to the society at large.
- Due to its simplicity and maximum efficiency, this technology can be considered as user friendly.

References

- Al-Zuhairi AH et al (2002) The use of sand columns to improve soft soil. 2nd Minia international conference for advanced trends in engineering, Egypt, Mar 2002, pp 16–18
- IS: 2720-Part 3/Sec-1 (1980) Indian standard methods of test for soils: determination of Specific gravity. Bureau of Indian Standards, New Delhi, India
- IS: 2720-Part 4 (1985) Indian standard methods of test for soils: grain size analysis. Bureau of Indian Standards, New Delhi, India
- IS: 2720-Part 5 (1985) Indian standard methods of test for soils: determination of liquid limit and plastic limit (second revision). Bureau of Indian Standards, New Delhi, India
- Mayilswami C et al (2013) Guidelines for augmentation of groundwater resources under climate change in Tamil Nadu. ICAR collaborative network project, NICRA, Water technology center, Tamil Nadu Agricultural University, Coimbatore, India
- Patel GR et al (2011) Hydraulics performance evaluation of porous pipe (Sub surface) irrigation system. IJAE 4(2):156–159

- Raphael J (2009) Mazhapolima wells in kerala for rain harvesting, Kerala, India. Raghunath HM (2007) Ground water. New Age International (P) Limited, New Delhi, India
- Sandhu et al (2011) Potential for rainwater filtration in India. Clean Techn Environ Policy 13:295–316
- Sikandar M (2008) Sankalpa rural development society, Karnataka, India
- Thangasal SR et al (2010) Hydrofracturing, article: January 2010. Research gate, Tamil Nadu, India

Study on the Effect of Soil as a Filler in Foamed Concrete



K. S. Kavya, K. K. Jithiya, N. Athulya Vijay, Jiji L. Jayan, M. Karthik, Y. Sheela Evangeline, and Sajan K. Jose

Abstract The problem of concrete waste disposal poses a major challenge to the engineers working in the construction industry. In this scenario, soil can be envisaged as an eco-friendly building material. Soil-based foamed concrete is a novel lightweight construction material consisting of cement, soil, water, and foaming agent. The form of concrete with random air-voids created within the volume by the action of foaming agents is known as foamed concrete. It is characterized by its high flowability, low cement content, low aggregate usage, and excellent thermal insulation. It also possesses characteristics such as high strength-to-weight ratio and low density. Foamed concrete is considered as an economical solution in the fabrication of large-scale lightweight construction materials and components such as structural members, partitions, filling grades, and road embankment infills mainly due to its easy production process from manufacturing plants to final position of the applications. In this paper, the effect of partially replacing conventional cement with two different types of clayey soil is explored and reported. The results indicate that the strength of soil-based foamed concrete satisfies the minimal strength requirement for a building block as per Indian Standards (IS) specifications along with significant improvement of thermal characteristics. Water absorption and density properties are also reported.

Keywords Soil · Foamed concrete · Compressive strength · Thermal conductivity

K. S. Kavya (✉) · K. K. Jithiya · N. Athulya Vijay · J. L. Jayan · M. Karthik · Y. Sheela Evangeline · S. K. Jose
Department of Civil Engineering, College of Engineering Trivandrum, Trivandrum 695016, Kerala, India
e-mail: kavyasidharan07@gmail.com

© Springer Nature Singapore Pte Ltd. 2020
M. Latha Gali and P. Raghuvier Rao (eds.), *Construction in Geotechnical Engineering*, Lecture Notes in Civil Engineering 84,
https://doi.org/10.1007/978-981-15-6090-3_2

1 Introduction

A right building material promises a healthy living environment. Building materials strongly influence the indoor climate as well as the quality of living. It is being widely accepted that the use of concrete as a building material is no more a sustainable method. Hence, researchers have started exploring the feasibility of soil-based concrete in modern buildings. Soil-based building materials for construction purpose have been in use for centuries. Soil can be molded into any shape or size with least effort.

Clay has been selected as the material for study owing to various factors including the commercial considerations, its natural availability and recyclable nature. Clay has a porous structure filled with air in the voids in dried state. Hence, it possesses great thermal insulation properties which is largely useful to regulate the temperature inside the living space. Bing and Cong (2014) discuss the effects of foam content and silica fume on the physical properties of soil-based foamed concrete. Soft clay and protein-based foaming agent were used in their study. Their experimental results show that the properties such as thermal conductivity, water absorption, density, and compressive strength decrease with increase in volume of foam; but are improved by silica fume content.

In this paper, the properties of foamed concrete blocks prepared using two types of clay soil are evaluated.

2 Experimental Details

2.1 Materials and Mix Proportion

Two types of clay were blended with cement for the experiment; swelling clay (bentonite), and non-swelling clay (kaolinite). Synthetic foaming agent under the commercial name Ebassoc and Portland Pozzalana cement was used. Throughout this experimental study, tap water was used to produce all foamed concrete specimens. The properties of bentonite and kaolinite found out as per IS are presented in Table 1.

Table 1 Properties of soil

Sl. no.	Properties (%)	Swelling clay (Bentonite)	Non-swelling clay (Kaolinite)
1	Free swell index	1900	14.28
2	Plastic limit	54.5	30
3	Liquid limit	291	64
4	Plasticity index	236.5	34
5	Specific gravity	2.67	2.68

2.2 Specimen Preparation

Nandi et al. (2016) discuss the procedures for preparing foamed concrete specimens. Cement and soil were mixed in dry state. Foam is prepared by adding 30 ml foaming agent in 1000 ml of water and the mix is then agitated mechanically. 0.4 m^3 of foam was added for every 1 m^3 of concrete. Photograph of foam is shown in Fig. 1. The water-cement ratio was fixed as 0.55 for obtaining a good consistency for the concrete. Foam is added during the wet mixing of concrete. Cube specimens of size $15 \times 15 \times 15 \text{ cm}$ were prepared and water cured for 7 and 28 days. Photograph of samples prepared is shown in Fig. 2. Seven different mixes were used by varying the type and proportion of clay used as mentioned in Table 2. The cured specimens were tested for density, compressive strength, water absorption, and thermal conductivity.

Fig. 1 Foam



Fig. 2 Cube specimens prepared for the study



Table 2 Mix ratio

Soil type	Mix no.	Proportion by weight (%)	
		Cement	Soil
Bentonite	C	100	0
	B1	80	20
	B2	60	40
	B3	40	60
Kaolinite	C	100	0
	K1	80	20
	K2	60	40
	K3	40	60

3 Results and Discussions

3.1 Compressive Strength

Compressive strength of different specimens at 7 days and 28 days is presented in Table 3 and the graphical variation of 28 day compressive strength of specimens with varying soil proportion is shown in Fig. 3. It is clear that the compressive strength decreases with the increase in proportion of soil. Also kaolinite-based foamed concrete exhibits more strength than that of bentonite-based foamed concrete. All the specimens satisfy the minimal strength requirement for a building block as per IS 1077 (2007) that is 3.5 N/mm².

Table 3 Compressive strength of soil-based foamed concrete

Proportion by weight (%) (Cement: Soil)	7 days strength (N/mm ²)		28 days strength (N/mm ²)	
	Kaolinite	Bentonite	Kaolinite	Bentonite
100: 0	12	12	14.6	14.6
80: 20	8.6	6	13.5	11.8
60: 40	5.9	2.7	12.9	5.5
40: 60	2.7	2.4	5.6	3.8

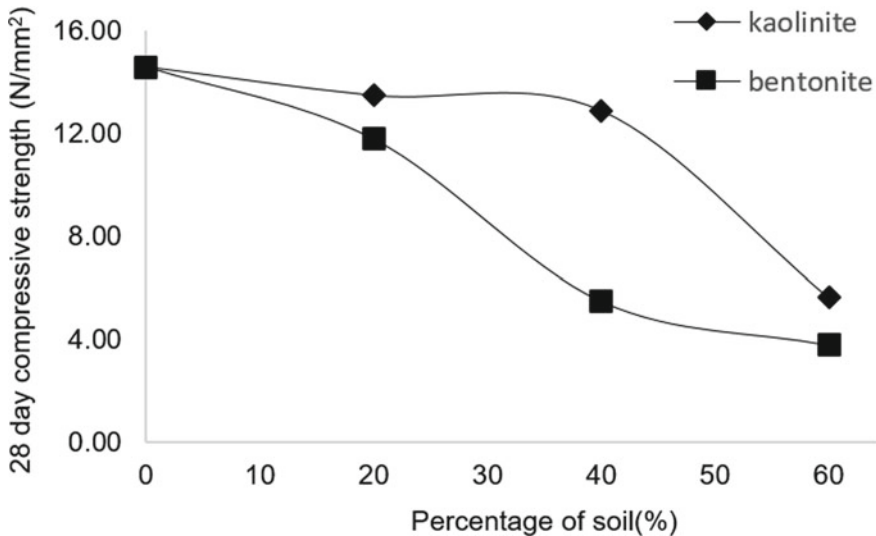


Fig. 3 Variation of compressive strength of specimens with percentage of soil added

3.2 Density

The bulk density of foamed concrete specimens is shown in Table 4 and the graphical variation of density of specimens with varying soil proportion is shown in Fig. 4. The density decreases with the increase in proportion of soil. Kaolinite-based specimens are more denser than bentonite-based specimens. This may be due to the high swelling characteristics of bentonite.

Table 4 Bulk density of soil-based foamed concrete

Proportion by weight (%) (Cement: Soil)	Density (kg/m ³)		Percentage increase of Kaolinite Specimens over Bentonite Specimens (%)
	Kaolinite	Bentonite	
100: 0	1840	1840	0.00
80: 20	1805	1731	4.27
60: 40	1767	1598	10.58
40: 60	1681	1455	15.53

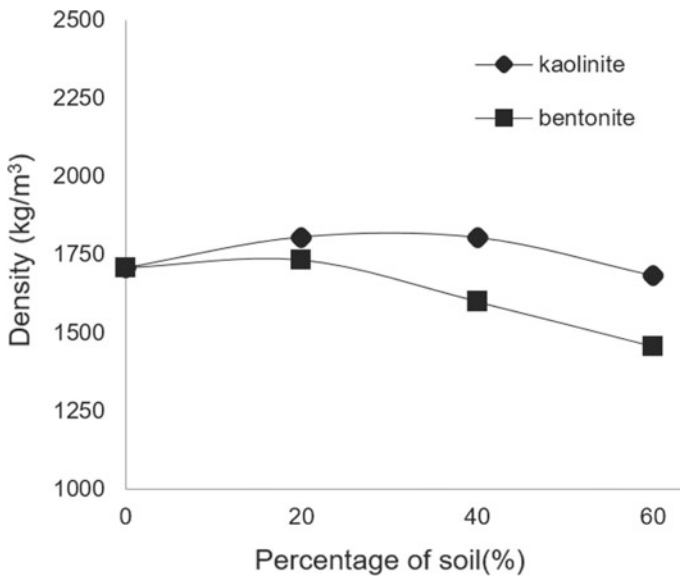


Fig. 4 Variation of density of specimens with percentage of soil added

3.3 Thermal Conductivity

Thermal conductivity of specimens is measured as per ASTM D5334 using portable thermal resistivity meter. Photograph of thermal resistivity meter is shown in Fig. 5. The thermal conductivity values of specimens are shown in Table 5. Thermal conductivity decreases with the increase in proportion of soil and this is due to the thermal insulation characteristics of clay in its dry state. However for both the soils specimens with 20% soil exhibits higher thermal conductivity than that of ordinary foamed concrete specimen. As per IS 3346 (2004), thermal conductivity of foamed concrete varies from 0.53 to 0.63 W/mK as the density ranges from 1400 to 1800 kg/m³. However for the same density of soil-based foamed concrete the thermal conductivity values are much lesser.

Fig. 5 Thermal resistivity meter



Table 5 Thermal conductivity

Proportion by weight (%) (Cement: Soil)	Thermal resistivity (W/mK)	
	Kaolinite	Bentonite
100: 0	0.038	0.038
80: 20	0.043	0.049
60: 40	0.040	0.037
40: 60	0.034	0.033

Table 6 Percentage of water absorption

Proportion by weight (%) (Cement: Soil)	Water absorption (%)	
	Kaolinite	Bentonite
100: 0	2.24	2.24
80: 20	2.42	5.20
60: 40	3.68	11.04
40: 60	14.45	14.49

3.4 Water Absorption

The water absorption values of different specimens are enlisted in Table 6. The water absorption values increases with increase in soil proportion for specimens prepared out of both clays. As per IS 2185 (Part IV) (2008) the water absorption values for preformed foam cellular concrete blocks shall not be more than 10% by mass. The specimens C, K1, K2, and B1 exhibit water absorption values within the limit as per IS.

4 Conclusions

The study was carried out to look into the scope of usage of soil as a filler in foamed concrete for which two clays, say kaolinite and bentonite were selected. The following conclusions were drawn from the study conducted:

1. Compressive strength decreases with increase in soil content. However, all the specimens satisfy the minimal strength requirement for a building block as per IS.
2. Thermal insulation property increases with increase in soil content. Both the clays exhibit almost similar thermal properties.
3. Water absorption of foamed concrete increases whereas density decreases with increase in soil content for both clays. Kaolinite-based foamed concrete exhibits lesser water absorption than bentonite-based foamed concrete.

4. Kaolinite-based foamed concrete exhibits better strength characteristics than the other and hence it can be used for making building blocks, pavement base, etc.
5. Bentonite-based foamed concrete is light in weight and hence can be used for low-density applications like construction of non-load bearing walls, backfill for retaining walls, etc.

References

- ASTM D5334-14-Standard test method for determination of thermal conductivity of soil and soft rock by thermal needle probe procedure
- Bing C, Cong M (2014) Properties of a foamed concrete with soil as filler. *Constr Build Mater* 76:61–69
- IS 1077 (2007) Common burnt clay building bricks-specifications
- IS 3346 (2004) Method for the determination of thermal conductivity of thermal insulation materials
- IS 2185 (2008) Concrete masonry units, Part 4: preformed foam cellular concrete blocks
- Nandi S, Chatterjee A, Samanta P, Hansda T (2016) Cellular concrete and its facets of application in civil engineering. *Int J Eng Res* 5:37–43

Effect of Variation of In Situ Moisture Content on Pullout Capacity of Grouted Soil Nail



Avishek Ghosh, Sayantan Chakraborty, and Ashish Juneja

Abstract Soil nailing has traditionally been used as a method to retain soil excavation and to stabilise soil slopes. The effectiveness of this method depends on the pullout resistance of the nail, amongst other factors. There have been instances when the shear resistance between the soil and the nail has deteriorated when the soil volume reduces or when the soil shrinks with the decrease in moisture content. This can happen during the curing period of the cement used in the grouted nails. In the present study, a number of laboratory model tests were conducted in cemented grouted nails installed within silty soils. The variation of pullout resistance with curing period of the cement grout was determined. Spatial variation of the moisture content with depth and distance away from the nail was determined after each pullout test. To support the findings, direct shear tests were performed between the cement grout and the soil at the same moisture content at which pullout tests were conducted. The results indicate a reverse behaviour of the interface friction angle due to the change in moisture content.

Keywords Cement grouting · Pullout capacity · Soil nailing

1 Introduction

Soil nailing technique has been widely used for soil excavation during the construction period of the highway, underground metro lines, widening the purpose road under existing bridge ends, stabilising the slope and reconstruction of the existing soil nailing structure, e.g. (Hong et al. 2003). The interlocking between the nail and the soil is enhanced with the use of grout (Cheng and et al. 2013). Determination of pull out force is an important parameter for designing purpose of soil nailing during earthwork. When sliding of huge soil mass occurs due to the natural or manmade cause, a critical slip surface develops which pulls out the grouted soil nails. The skin

A. Ghosh (✉) · S. Chakraborty · A. Juneja
Department of Civil Engineering, Indian Institute of Technology Bombay, Bombay,
Maharashtra, India
e-mail: avishekg90@gmail.com

© Springer Nature Singapore Pte Ltd. 2020
M. Latha Gali and P. Raghuvver Rao (eds.), *Construction in Geotechnical Engineering*, Lecture Notes in Civil Engineering 84,
https://doi.org/10.1007/978-981-15-6090-3_3

friction between the grouted soil nails and the surrounding soil resists that outward pull movement and correspondingly stabilises the soil mass (Schlosser 1982).

The pullout capacity of grouted nail depends upon many parameters such as the type of soil, soil–nail interface strength, installation procedure, nail geometry and method of grouting (Gurpersaud et al. 2011). The soil–nail interface strength is influenced by the moisture content of the soil surrounded by the nail. Though the infiltration of the cement grouting increases the bond between soil and nail and the hydration effect of the cement hardening can reduce the moisture content of the surrounding soil. Aytekin and Nas (1998) stated that hydrated cement fetched up to 20% of its own weight of water from the surrounding soil. Cheng-Yu et al. (2013) stated that the moisture content of soil samples decreases closer to grouted body soil when compared to the distant soil sample. So change in the moisture content in the soil is an important factor to be considered during design which will ultimately affect the final strength of the soil.

In the present study, the effect of moisture content of soil on the pullout capacity of grouted soil nail was experimented. Extensive laboratory tests were performed for this experimental study. Due to the limitation of providing proper vertical confining stress and difficulties of drilling to the horizontal face of the soil for grouted soil nail in the 1-g model test, the pullout tests were carried out on the vertically inserted soil nails. Franzen (2001) proposed that vertical pullout test is an alternative method to determine the effect of different parameters on the pullout capacity of the soil nails. A series of direct shear tests were also performed between grout cement and soil to examine the change in interface strength with curing period. It helps to predict the cement grouted soil nail behaviour with time and correspondingly determine the soil model parameters for the numerical studies.

2 Experimental Setup for Pullout Test

2.1 Soil Property

Fine grained soil was used in the tests. The soil property is given below (Table 1) (IS 2720(IV) 1985).

2.2 Pullout Procedure

The tank dimension was 690 mm × 340 mm × 555 mm. Soil bed was prepared at optimum moisture content. The soil was compacted in layers up to a height of 450 mm. A hammer of 0.025 kN was used for compaction and each layer was compacted 30 times.

Table 1 Characteristics of tested soils

Parameters	Powai soil
Moisture content (OMC)	18%
Degree of saturation (OMC)	90.47%
Liquid limit	50.2%
Plastic limit	33.4%
Shrinkage limit	15.5%
Cohesion (kN/m ²)	22
Angle of internal friction(Φ)	27°
Sand	44%
Silt	38%
Clay	18%

After preparing the soil bed, a borehole of 60 mm in diameter and 300 mm in height was prepared. The grout with a w/c ratio of 0.45 was then poured into the hole at a constant rate and allowed to settle for about 5–10 min. Nail of 280 mm length and 16 mm diameter was then pushed into the grouting cement. With this arrangement, nails were installed in the vertical direction. This is not the usual orientation at which the nails are installed in the field, wherein the inclination is only 10–20° to the horizontal. Since the overburden was small, the nail orientation was unlikely to significantly affect its pullout capacity. This was the case as the pullout capacity was investigated only due to the effect of moisture changes. This arrangement also enabled the use of the existing setup without any significant changes.

Dial gauges were then installed to measure the displacement of the nail. To minimise the influence of the front wall, the front wall was lubricated by glycerin (Palmeira and Milligan 1989). Three nails at a distance of 225 mm and 175 mm from each were inserted and pullout tests were carried out after 7, 14 and 21 days (see Fig. 1). According to Nicholson (1986), the nail spacing should be around 6–10 times its diameter. In this experiment, the spacing was kept above 10 times its diameter, as the diameter of the nail was 16 mm. The nail head was firmly connected to a load cell of 50 kN capacity during the time of tests. Figure 2 shows the complete setup of the experimental setup.

3 Results

Total 2 sets of pullout tests were done at 7, 14 and 21 days. The first pullout was done on the middle nail after 7 days and then following the other two nails were done at 14 and 21 days. Stress-controlled pullout test was performed using a hydraulic jack.

To measure the change in moisture content due to cement grouting, the soil from the surrounding grouting and at a radial distance of 45, 60 and 90 mm from the centre

Fig. 1 Nail setup

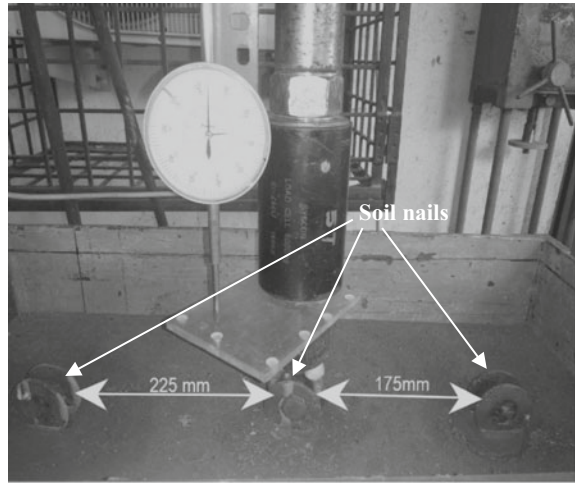
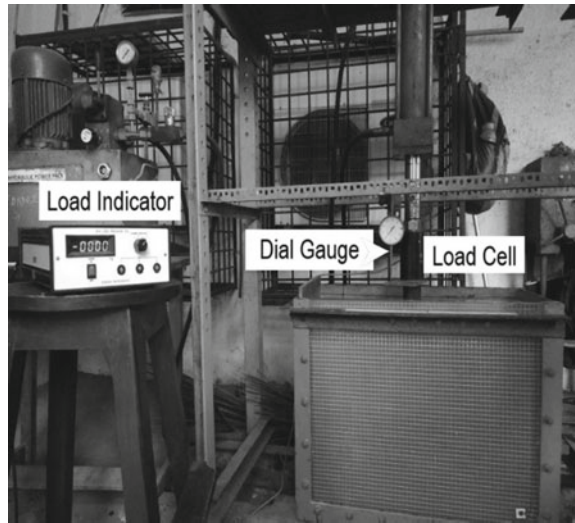


Fig. 2 Complete setup



of the grouted nail were taken. The moisture content measurement zone is presented in Fig. 3.

Figure 4 shows the vertical pullout test results after 7, 14 and 21 days. The peak pullout force after 7 days was approximately 5.8 kN whereas it was decreased to 2.5–2.7 kN after 14 days and 2.05–2.3 kN after 21 days.

It can be seen that the pullout strength decreased significantly between 7 and 14 days but became almost constant after 14 days. The test results showed almost repeatable behaviour in both trials. In those tests, moisture content was the only parameter which varies with time due to evaporation. This evaporation can be

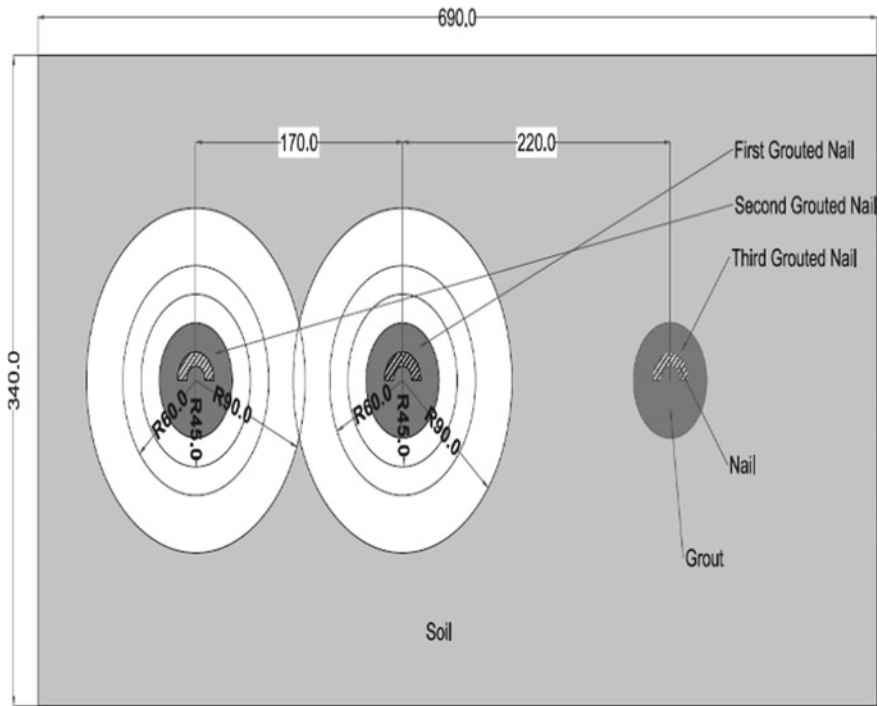


Fig. 3 Moisture content measurement zone (top view) (all dims. are in mm)

Fig. 4 Pullout test results of soil nails after different curing periods

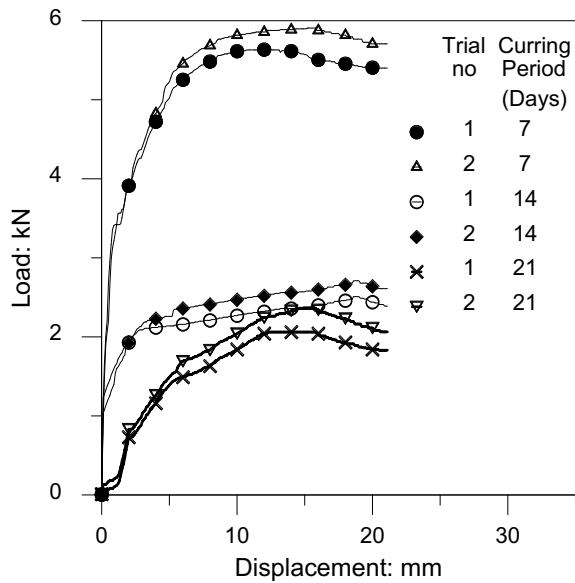
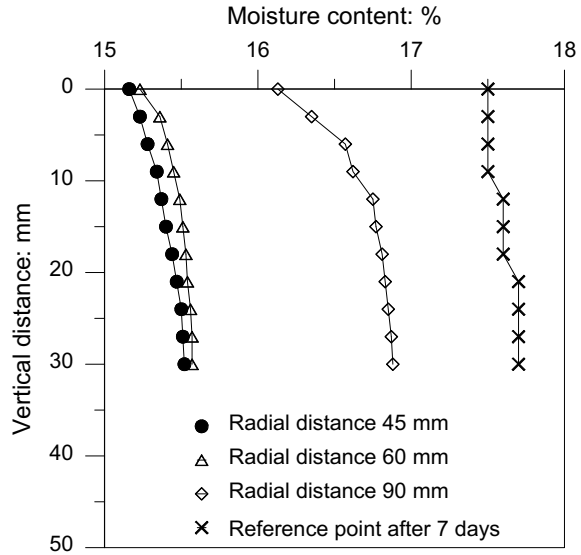


Fig. 5 Moisture content in between 1st and 2nd nail after 7 days



happened due to temperature variation in the atmosphere and temperature variation due to curing of the grouted cement. So an experimental study was carried on to check the variation in the moisture content of the soil with time. Then those results were compared with the pull out strengths to derive the reason behind the decrease in strength. In the experiments, the soil nails, which were pulled out after 7 and 14 days, were pushed back again into the soil to observe the moisture content variation along those nails up to 21 days.

Figures 5, 6, 7, 8, 9 and 10 show the change in moisture content between 1st and 2nd nail and 2nd and 3rd nail after 7, 14 and 21 days. The moisture content was measured up to a depth of 30 mm using a spiral screw of 40 mm length. Moisture content was measured only in the top 30 mm of the soil so as to not to disturb the structure and cause the soil to flow around the remaining nails.

As there is evaporation happening due to atmospheric temperature, a polyethene sheet was used to cover the soil from the above. Still, there was evaporation. So a reference point on the soil was chosen which is far away from the soil nails. The moisture content variation on that point was considered only due to evaporation by atmospheric temperature. When the moisture content variations near the soil nails were compared with the reference point results, it will give a clear idea about the effect of curing of cement grout on the moisture content of the soil.

Figures 5, 6, 7, 8, 9 and 10 show that moisture content reduction is more near to the soil nails up to a radial distance of 60 mm and beyond that this reduction decreases with the radial distance from the nails. If the moisture content near the soil nails is compared with the moisture content at a reference point, a significant variation can be observed. It implies the effect of curing period on the moisture content of the surrounding soils of the soil nails. This reduction in the moisture content of the soil

Fig. 6 Moisture content in between 2nd and 3rd nail after 7 days

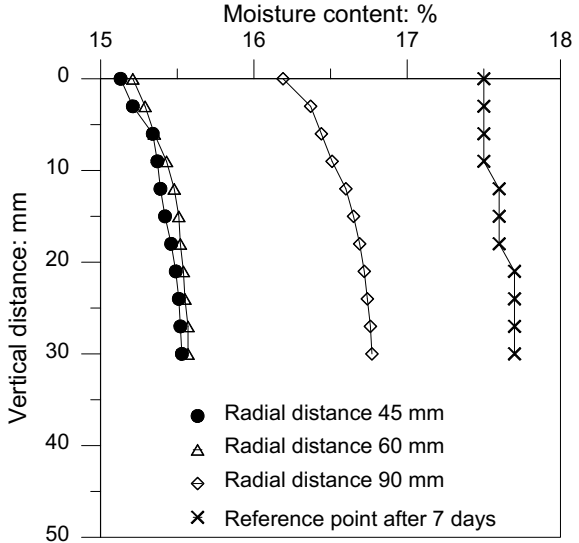
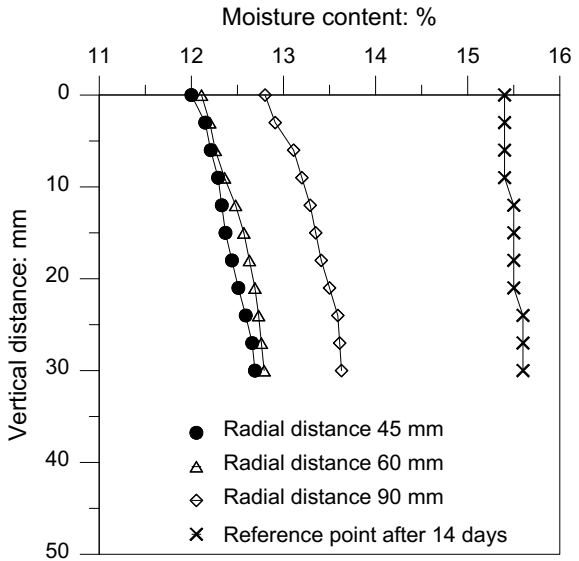


Fig. 7 Moisture content in between 2nd and 3rd nail after 14 days



sample may be responsible for shrinkage of the soils near the soil–nail interface. So a gap created between soil and nail was the reason for the reduction in pullout strength with time.

It can also be seen from the figures that the moisture content near the soil nails reduced below the shrinkage limit after 14 days. Therefore, the variation in the pullout strength after 14 days becomes almost constant as shown in Fig. 4. Figure 11 shows

Fig. 8 Moisture content in between 2nd and 1st nail after 14 days

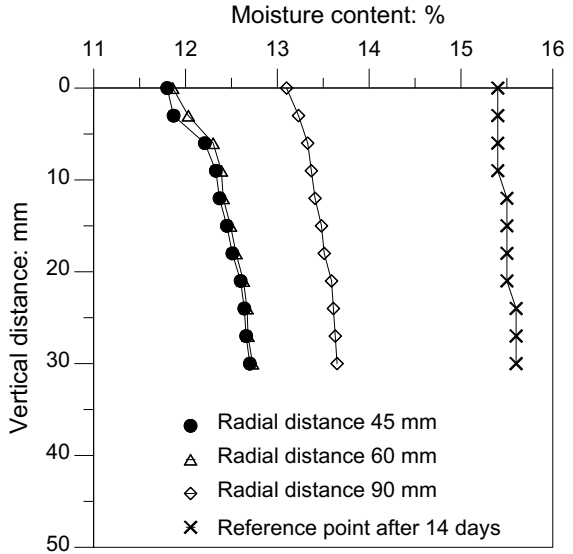
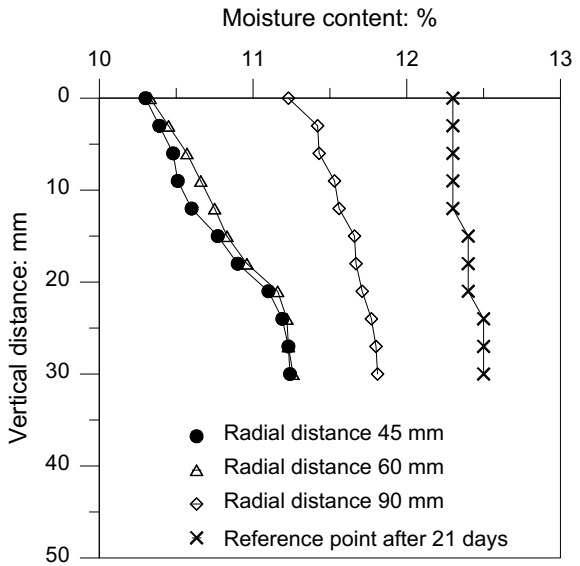


Fig. 9 Moisture content in between 2nd and 1st nail after 21 days



the average moisture content variation with time. It can be seen that the average value of the moisture content of the soil reduces almost linearly up to 21 days.

Fig. 10 Moisture content in between 3rd and 2nd nail after 21 days

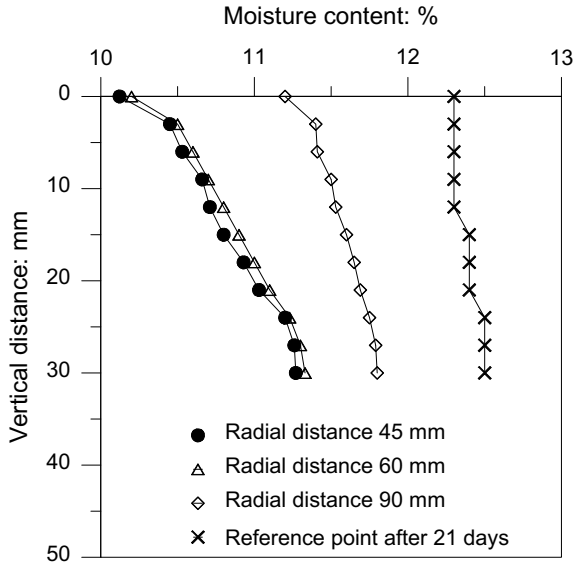
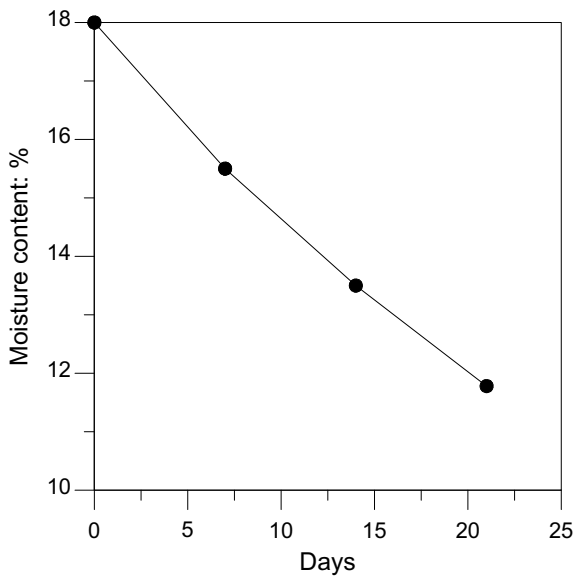


Fig. 11 Average variation of moisture content after 7, 14 and 21 days



4 Skin Friction Between Soil and Grouting Materials

In the present experiment of vertical pullout tests, the results showed that the pullout capacity of grouted nails reduced with time. The reduction of pullout capacity may be attributed due to the reduction of skin resistance between soil and grouting material.

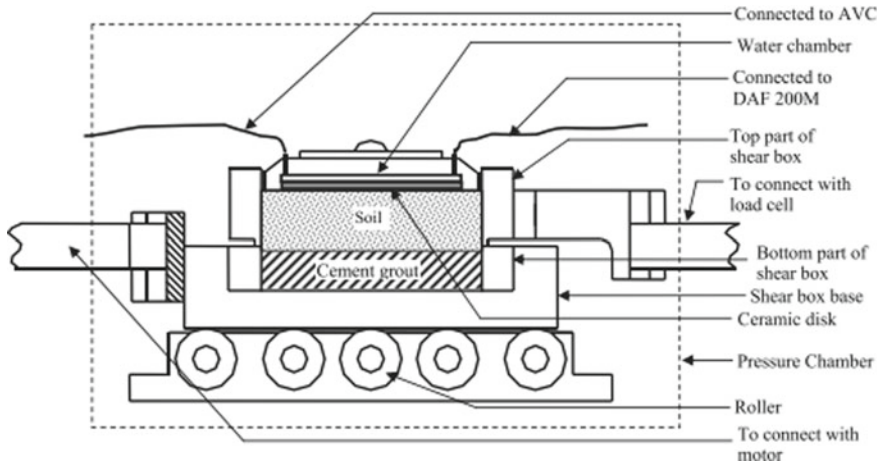


Fig. 12 Direct shear test setup (from Hossain and Yin 2014)

To determine the effect of moisture content reduction on the skin resistance between grout and soil, a series of direct shear tests on the same soil and grout were performed. The method of preparing the soil sample had to be representative and the same water–cement ratio was employed during the nailing tests.

Following ASTM D5321, (ASTM D5321/D5321M 2014) the soil–cement interface skin friction angle and adhesion between the soil–cement were determined under various normal stresses. After the grouting mixture was prepared at the bottom layer of the direct shear box, the top layer of the box had been filled up with soil. A total number of nine samples were prepared and sets of three samples were taken. The first set was kept for 7 days curing and other two were kept for 14 and 21 days, respectively. The strain rate was kept at 1.2 mm/min throughout the test. After the tests were done, the moisture content of the soils was measured. Though the interface thickness between soil–cement can't be completely identified for moisture content measurement (Hossain and Yin 2014), the moisture content of the soil was taken 2 mm distance from the soil grout interface.

The soil–cement was sheared in the direct shear box of 72,000 mm³. The arrangement of the setup is shown in Fig. 12. The soil was also sheared at the optimum moisture content of 18%. The top surface of cement paste had kept rough to simulate the result similar to the pullout test.

5 Skin Friction Results

The moisture contents were found around 16, 13 and 11% after 7, 14 and 21 days at the interface, which was almost same when the moisture content was measured at the interface after the vertical pullout tests were done. Figure 12 shows the direct

shear test results of soil–cement interface for different curing periods and those were compared with test result performed only on the soil. To perform the direct shear test on the soil only, soil was compacted at OMC value of 18% and tested immediately after preparation. It can be seen that soil–cement interface strength is less than soil shear strength after 7 days of curing but it is more after 14 days of curing. It can also be seen from the figure that the soil–cement interface strength increases with curing period which is an opposite phenomenon compared to the pullout tests of the soil nails. Two possible reasons could be there. First of all, it was not known the thickness of the soil cement interface in the cement grouted soil nails. In the direct shear tests, the interface strength was measured exactly at the soil–cement joint which may be few grains thick in the actual case. The soil grains exactly in contact with cement can change their fabric orientation and can go for higher strength. Also reduction in the moisture content with curing period may also be the reason behind that. The second reason is that the normal stress upon the soil restricts the soil particles to lose its contact with cement after shrinkage due to a reduction in water content. Another observation can be drawn from Fig. 13 that the variation in the shear strength is minimal after 14 and 21 days of curing though there is a reduction in 2% of moisture content. It may be due to the reduction in moisture content reaches a value less than shrinkage limit of the soil after 14 days of curing. So fabric orientation due to change in moisture content after 14 days would be minimum and corresponding change in strength is also insignificant. The adhesion and skin friction values determined from direct shear test results are listed in Table 2.

Fig. 13 Shear strength variation of the soil–cement interface with curing period compared with only soil

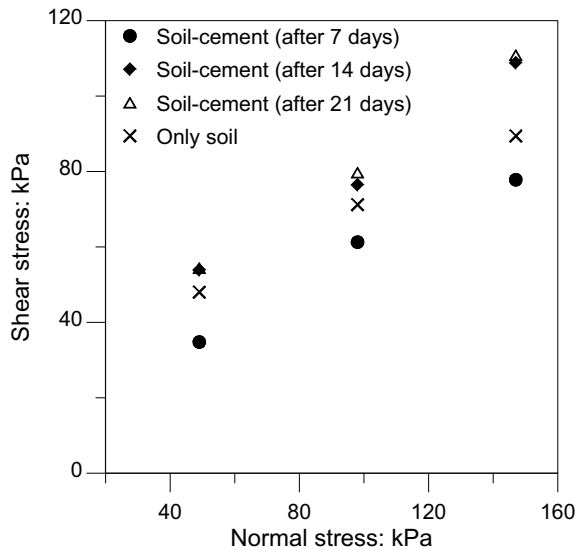


Table 2 Skin friction test results

Curing period (day)	M/C (%)	Adhesion c_a (kN/m ²)	Skin friction angle, δ
7	16	14.9	24°
14	13	24.8	29°
21	11	25.2	30°
Only soil	18	28.1	23°

6 Conclusions

This paper discussed the effect of the heat generated during curing of the cement grouted soil nails on the moisture content of the surrounding soils and the corresponding effect on the pullout strength. A significant reduction in moisture content was observed within a radial distance of the 4 times the diameter of the soil nails with curing period. This reduction became minimal beyond that distance. In vertical pullout tests, the strength was reduced with time. This was due to loosening of the contact between the soil and nail as the soil shrank with a reduction in moisture content. This reduction in strength became minimal after 14 days of curing as the moisture content reduced below the shrinkage limit of the soil. So there would be no further gap created between soil and nails. Therefore, it can be concluded that the pullout strength after 14 days could be considered for the design purpose. On the contrary, the direct shear test results showed an increase in the soil–cement interface strength with the curing period. This may be due to the unknown of the thickness of the soil–cement interface on the soil nails above which interface friction has to be considered. Another reason is the normal stress upon the soil in the direct shear test which restricts the creation of the gap between the soil and cement due to reduction in the moisture content. A thorough study can be possible to carry out in the future on those aspects. It was also observed that the increment of the interface strength with time was minimum after 14 days of curing period as the moisture content reduced below the shrinkage limit of the soil.

References

- ASTM D5321/D5321M (2014) Standard test method for determining the shear strength of soil-geosynthetic and geosynthetic-geosynthetic interfaces by direct shear, vol 17. American, Society for Testing and Materials International, pp 1–11
- Aytekin M, Nas E (1998) Soil stabilization with lime and cement. *Tech J Turkish Chamber Civ Eng* 9(1):471–477
- Cheng YH, Jian-hua YIN, Hua-fu PEI (2013) Comparative study on pullout behaviour of pressure grouted soil nails from field and laboratory tests. *J Cent South Univ* 13(20):2285–2292
- Franzén G (2001) Prediction of pullout capacity of soil nails. *Int Soc Soil Mech Geotech Eng* 3:1743–1747

- Gurpersaud N, Vanapalli SK, Sivathayalan S (2011) Pull out capacity of soil nails in unsaturated soils. Pan Am CGS geotechnical conference, Toronto, Canada, pp 1–8
- Hossain M, Yin J (2014) Dilatancy and strength of an unsaturated soil-cement interface in direct shear tests. *Int J Geomech* 15(5):1–10
- Hong YS, Wu CS, Yang SH (2003) Pullout resistance of single and double nails in a model sandbox. *Can Geotech J* 40(5):1039–1047
- IS 2720(IV) (1985) Grain size analysis
- Nicholson PJ (1986) Soil nailing a wall. *Civ Eng* 56(12):37–39
- Palmeira EM, Milligan GW (1989) Scale and other factors affecting the results of pull-out tests of grids buried in sand. *ICE* 3:511–524
- Schlosser F (1982) Behaviour and design of soil nailing. In: Proceedings of the international symposium. Asia Institute of Technology, Bangkok, Thailand, pp 399–419

Behavior of Instrumented Piles Under Different Loading and Soil Conditions



Anshul Gautam and Satyendra Mittal

Abstract A pile is primarily a long container of cylindrical shape having small diameter which is made up of a strong material such as concrete, steel, wood, etc. and is placed or driven into the ground to support the structures or buildings built upon it. With increase in infrastructure development in today's world, a lot of advanced structures are being constructed globally. But the assurance of success of these structures after construction is still hard to determine. However, nowadays with the advancement in technology in the field of instrumentation, it is possible to validate the performance of the structures periodically. It has been seen several times that the superstructures may need some changes in its architectural or structural patterns. These changes will bring some extra load over the structure, which is not considered by the developers. Hence, to study these changes, instrumentation of the piles is to be done. In the present study, a test pile of 7 cm diameter and 50 cm height was casted and was monitored while carrying out series of compression, uplift, and lateral load tests on different soil conditions. The "load versus settlement curves" as well as "load versus strain curves" were plotted and were compared for different loading and soil conditions. Finally, the amount of the load that would be taken by pile reinforcement and pile material was calculated separately and load transferred through skin friction was obtained.

Keywords Pile foundation · Instrumentation · Compression test · Uplift · Lateral load test

1 Introduction

In the context of pile foundation, the most important role of a geotechnical engineer would be design, installation, and the future safety of them. But whenever it comes to future safety, a lot of probability and undulations are to be dealt with. However, instrumentation methods in the field of foundations, has become simpler to calculate

A. Gautam · S. Mittal (✉)
Department of Civil Engineering, IIT Roorkee, Roorkee, Uttarakhand, India
e-mail: satyendramittal@gmail.com

© Springer Nature Singapore Pte Ltd. 2020
M. Latha Gali and P. Raghuvver Rao (eds.), *Construction in Geotechnical Engineering*, Lecture Notes in Civil Engineering 84,
https://doi.org/10.1007/978-981-15-6090-3_4

risk or reliability. With the advent of instrumentation of the piles, it is possible to calculate strains along the length of the pile around the various cross sections; deformations in the pile as a result of loading at top; load applied at various cross sections; and rebound after loading.

Literature review available in this field is very limited. Muthukkumaran et al. (2004) carried out research work on behavior of instrumented piles under vertical loading. Brown et al. (2006) carried out analysis of a rapid load test on an instrumented bored pile in clay. The maximum load and its duration are regulated by controlling the quantity of fuel and the venting of the gas. Krasinski and Kusio (Krasinski and Kusio 2015) focused on some aspects of the application of strain gauge sensors for model pile tests. Bica et al. (2013) carried out their work on instrumentation and axial load testing of displacement piles.

The present study deals with the behavior of instrumented test pile for different loading and soil conditions. For this purpose, an M25 grade concrete pile of 7 cm diameter and 50 cm height was casted with a single reinforcement bar of 12 cm. Six electrical resisting type strain gauges FLK-2-11 manufactured by Tokyo Sokki Kenkyujo Co. Ltd were attached along the reinforcement at a height of 1, 25, and 49 cm from one end, so that strain distribution could be obtained at top, bottom, and mid-depth of the pile along the reinforcement. Waterproofing seal was applied over the strain gauges to avoid their damage during the casting process. One no. vibrating resisting type strain gauge (model 4200 manufactured by Geokon, USA) was attached at mid-depth of the pile inside concrete during the process of casting of pile. The placement of strain gauges was carried out under expert guidance with great precision and accuracy. Reinforcement bar after mounting of strain gauges has been shown in Fig. 1, while the pile after casting has been shown in Fig. 2.

The test pile was monitored under a series of nine tests, i.e.

- (a) Compression load test in dry sand.
- (b) Compression load test in saturated sand.
- (c) Compression load test in layered soil.

Fig. 1 Reinforcement after attaching strain gauges



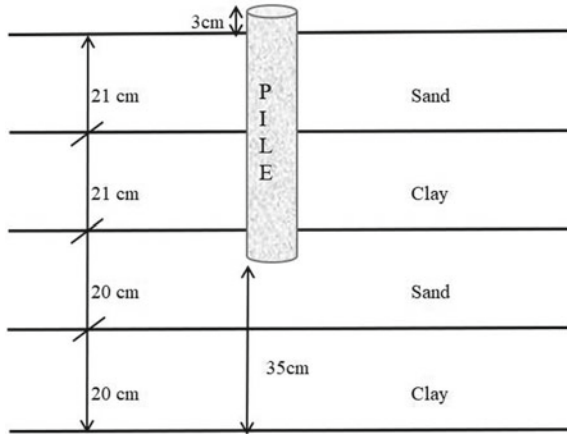
Fig. 2 Piles after casting

- (d) Uplift load test in dry sand.
- (e) Uplift load test in saturated sand.
- (f) Uplift load test in layered soil.
- (g) Lateral load test in dry sand.
- (h) Lateral load test in saturated sand.
- (i) Lateral load test in layered soil.

2 Experimental Setups

A cylindrical drum of diameter 60 cm and height 90 cm was used as a tank inside which tests were carried out. Markings were made inside the tank at regular interval of 10 cm each from the bottom. Basic properties of the soil were already determined in the laboratory as per IS 2720-1985. The soil was filled according to its field density layer by layer. Tamping rod was used for the compaction of sand. The tank was filled with soil till the depth of 35 cm from bottom, after then pile was placed over it at the center of drum and then soil was filled further until only 3 cm of pile was left

Fig. 3 Line diagram for layered soils



for exposure. A circular weight weighing 1 kg and having an opening on a side from center to circumference was used as a pile cap, so that wires could escape out from that opening.

For the case of layered soils, layering was done such that bottom 20 cm was clay, followed by 20 cm sand, 21 cm clay, and 21 cm sand, respectively. Hence, the end bearing resistance was neglected only skin friction was considered in all the nine cases. Line diagram for the layered soil has been shown in Fig. 3.

Saturated soil conditions were created by drilling four small holes diametrically opposite at the bottom side of the tank. These holes were covered by a geotextile membrane from inside. After filling the soil in the tank, water was made to flow from the upper end of the tank. When the water started coming out from the holes that were drilled at the bottom, the holes were sealed off and the water supply was cut off from above.

Reaction beams were used as loading mechanism for compression load test and load was applied with the help of a hydraulic jack and measured by a proving ring.

While for lateral and uplift load test, pulley system was used for application of load. Settlement was observed using two dial gauges whereas strains were measured with the help of a data logger and vibrating wire readout.

The basic properties of soil were calculated in the laboratory and have been mentioned in Tables 1 and 2 for sand and clay, respectively. The classification of the soil has been done as per Indian standard soil classification system (ISSCS). The sand has been classified as SP (Poorly graded sand) while the clay has been classified as CI (Clay with intermediate compressibility).

Table 1 Properties of sand

Property	Values
Maximum dry density	15.18 kN/m ³
Minimum dry density	13.045 kN/m ³
Maximum void ratio	0.79
Minimum void ratio	0.545
Relative density	50%
D_{60}	0.2 mm
D_{30}	0.18 mm
D_{10}	0.09 mm
C_u	2.22
C_c	1.8
Soil classification (as per ISSCS)	SP

Table 2 Basic properties of clay

Properties	Values
Specific gravity	2.52
Liquid limit	45.25%
Plastic limit	19.25%
Plasticity index	26%
Maximum dry density	17.62 kN/m ³
Optimum moisture content	16.1%
UCS	120 kPa
Soil classification (as per ISSCS)	CI

3 Tests Conducted

All the tests were conducted as per IS-2911 Part 4 (1985). The wires of the strain gauges were attached to the data logger and vibrating wire readout so as to monitor strain. The test setup has been shown in Figs. 4 and 5, respectively. A minimum of two dial gauges was used to measure settlement of the pile.

The safe load was taken according to IS-2911 Part 4 (1985). For compression load test safe load was taken as 50% of the final load at which the total displacement equals 10% of pile diameter in case of uniform diameter pile, i.e. corresponding to settlement of 7 mm in current study. For uplift load test, safe load was taken as the minimum of two-thirds of the load at which the total displacement is 12 mm or half of the load at which the load-displacement curve shows a clear break (downward trend). For lateral load test, safe load was taken as the minimum of 50% of the final load at which the total displacement is observed to be 12 mm or the final load at which the total displacement corresponds to 5 mm.

Fig. 4 Test setup for lateral load test



Young's modulus of steel was taken as $2 \times 10^5 \text{ N/mm}^2$ while the Young's modulus of concrete was taken as $5000\sqrt{f_{ck}}$, i.e. 2500 N/mm^2 . Cross-sectional area of steel was calculated as

$$\frac{\pi}{4} \times 12^2 = 113.09 \text{ mm}^2$$

Here, 12 mm is the diameter of reinforcement bar. While for the concrete it was calculated as-

$$\frac{\pi}{4} \times (70^2 - 12^2) = 3660.35 \text{ mm}^2$$

Here, 70 mm and 12 mm are the diameters of pile and reinforcement, respectively.

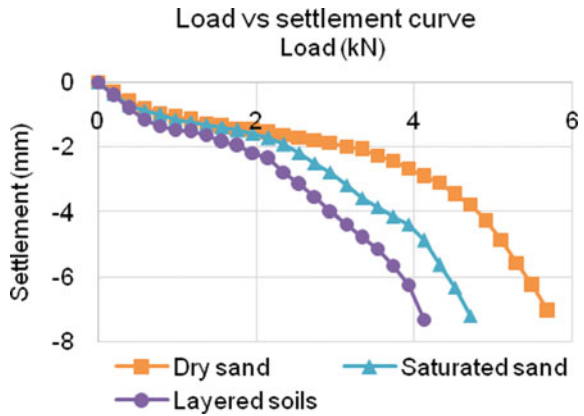
The load settlement curve obtained for compression, lateral, uplift and load test has been shown in Figs. 6, 7 and 8, respectively.

Strains with respect to particular load were also monitored simultaneously and hence a series of load versus strain curves were also plotted for different locations of pile segment and subsequently for different soil conditions. Load versus strain curves for concrete portion of the pile has been shown in Figs. 9, 10 and 11 respectively,

Fig. 5 Test setup for compression load test



Fig. 6 Load versus settlement curve for compression load test



strains of which were measured with the help of vibrating resisting type strain gauge embedded in concrete portion of the pile.

It is observed from Figs. 9, 10 and 11 that strain in concrete portion of pile almost increases linearly as per increase in load and it differs only in magnitude for

Fig. 7 Load versus settlement curve for lateral load test

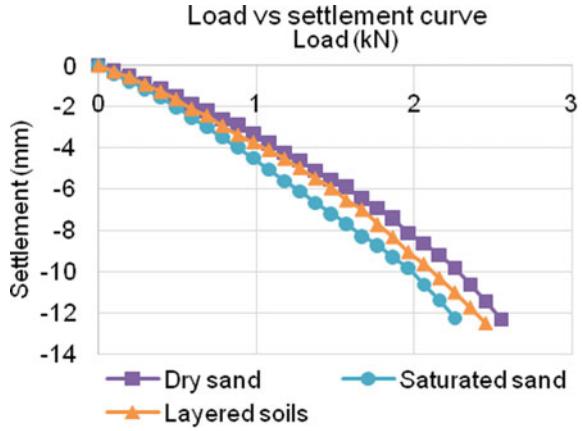


Fig. 8 Load versus settlement curve for uplift load test

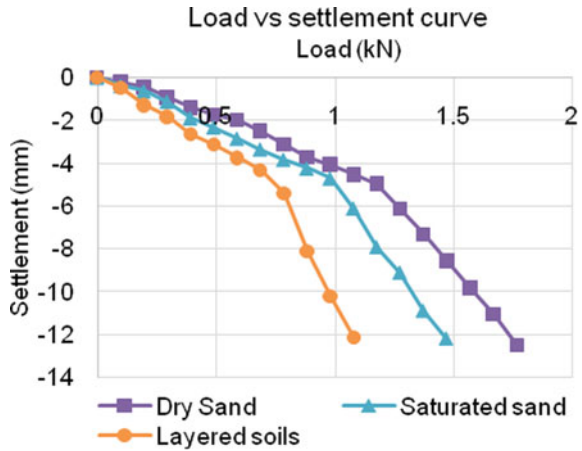


Fig. 9 Load versus strain curve for compression load test for concrete portion of pile

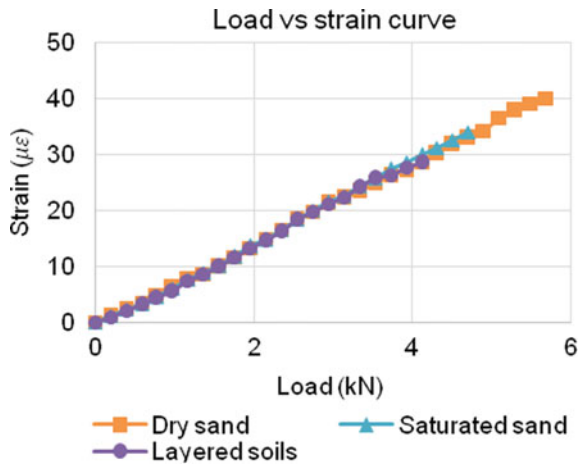


Fig. 10 Load versus strain curve for lateral load test for concrete portion of pile

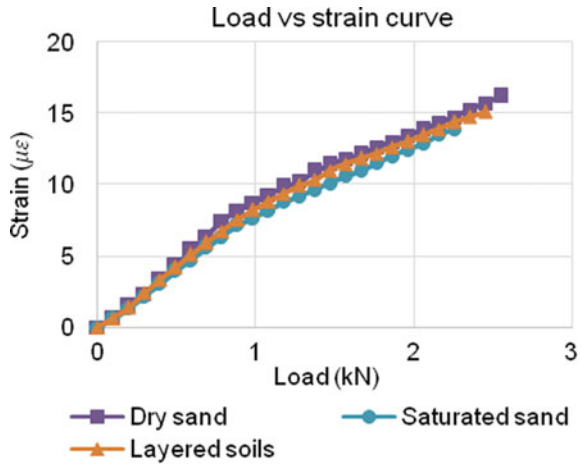
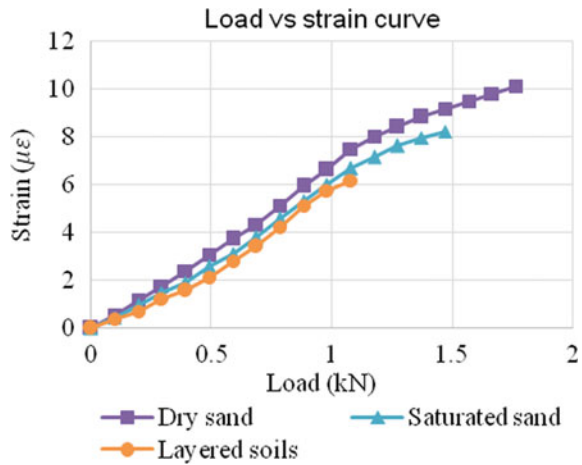


Fig. 11 Load versus strain curve for uplift load test for concrete portion of pile

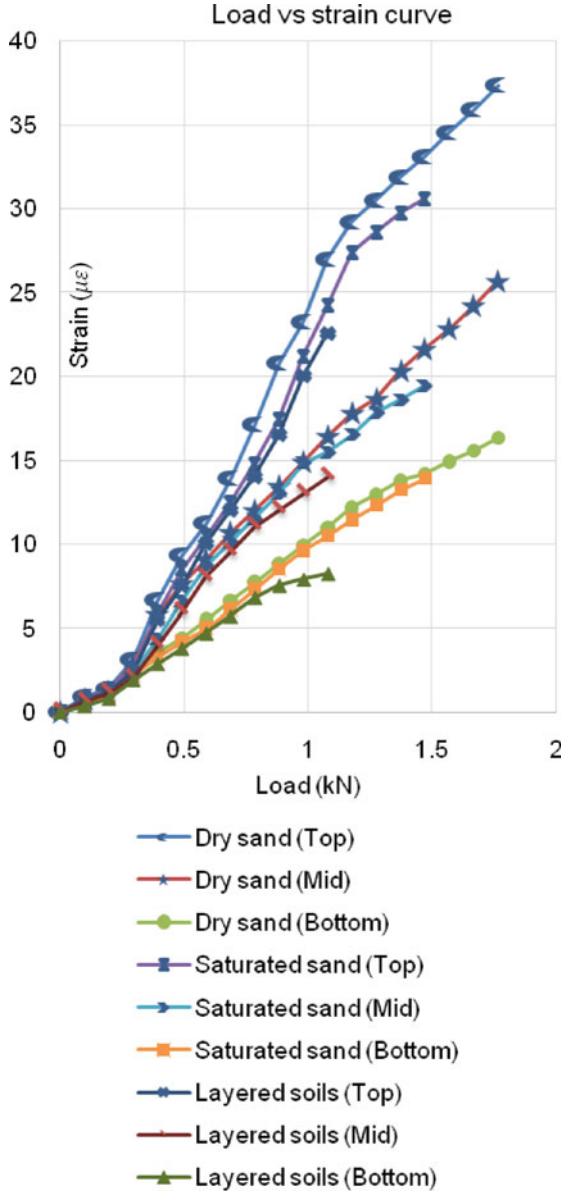


different types of soil conditions. Similarly, load versus strain curves were plotted and compared for different locations of pile ,i.e. at top portion, mid-depth, and bottom with the help of electrical resisting type strain gauges which were installed at different locations of pile segments and the results of which has been shown in Figs. 12, 13 and 14.

It is observed from Figs. 12, 13 and 14 that strain was maximum at the top portion of the pile’s reinforcement followed by mid-depth and bottom portion of the pile.

Strain values were further used to plot bending moment and shear force diagrams. However, this paper is confined to determination of load shared by reinforcement bar and pile materials and load transferred through skin friction.

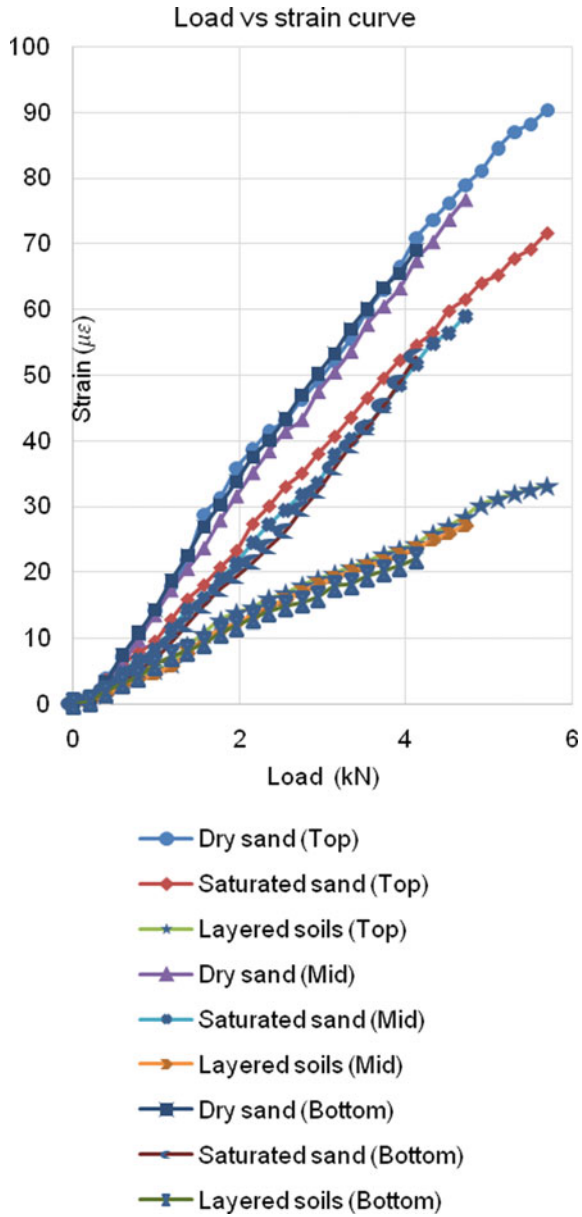
Fig. 12 Load versus strain curve for compression load test at different locations of pile segments for reinforcement bar



4 Calculations

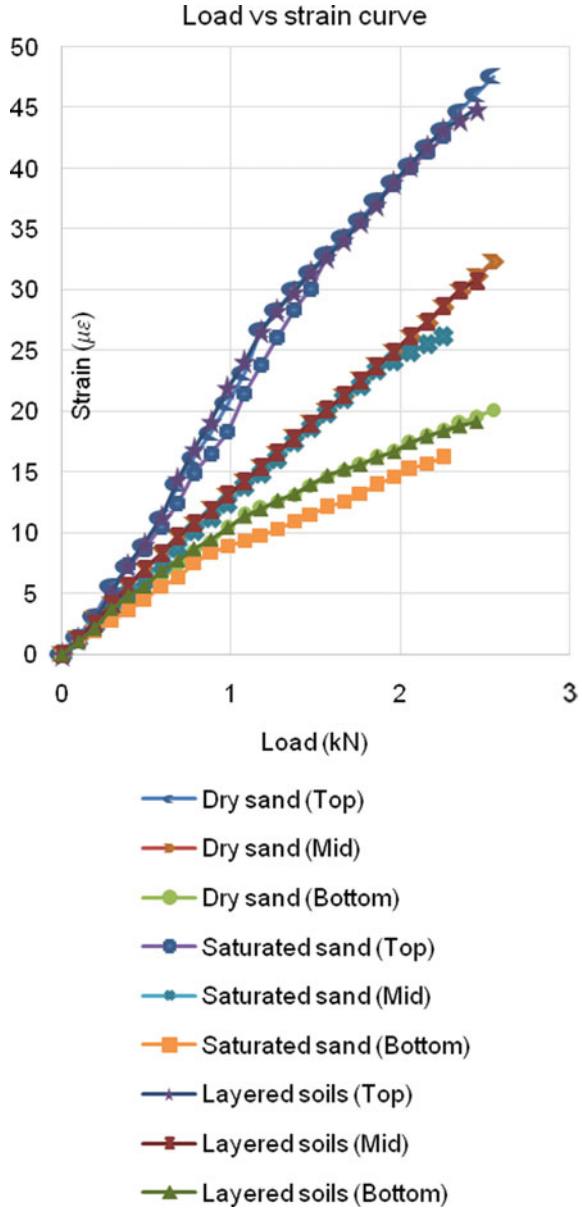
The main aim of the study was to calculate the load taken by the concrete and reinforcement separately as well as load transferred through skin friction. Hence, for this purpose, first of all stresses for concrete as well as reinforcement were

Fig. 13 Load versus strain curve for compression load test at different locations of pile segments for reinforcement bar



calculated at various cross sections by multiplying strain at that section with their respective Young’s modulus. Finally, the load was obtained by multiplying stress by the respective cross-sectional areas, the final result of which has been shown in as “Load on concrete” and “Load on rebar” in Tables 3, 4 and 5. Load taken by soil was obtained by subtracting the load taken by reinforcement bar and load taken

Fig. 14 Load versus strain curve for compression load test at different locations of pile segments for reinforcement bar



by concrete from the total failure load and it has been shown as “Load on soil” in Tables 3, 4 and 5. The test results were validated by calculation of failure load by static ultimate resistance formulas, and the results were found out to be in acceptable limits. The load taken by reinforcement bar and concrete as a whole were validated

Table 3 Test results for compression load test

	Dry sand (kN)	Saturated sand (kN)	Layered soil (kN)
Failure load	5.88	4.91	4.12
Load on Concrete	3.66	3.11	2.61
Load on rebar	1.47	1.23	1.08
Load on soil	0.75	0.57	0.42

Table 4 Test results for lateral load test

	Dry sand (kN)	Saturated sand (kN)	Layered soil (kN)
Failure load	2.65	2.26	2.45
Load on concrete	1.48	1.27	1.38
Load on rebar	0.75	0.64	0.72
Load on soil	0.41	0.34	0.35

Table 5 Test results for uplift load test

	Dry sand (kN)	Saturated sand (kN)	Layered soil (kN)
Failure load	1.77	1.47	1.08
Load on concrete	0.93	0.75	0.57
Load on rebar	0.61	0.48	0.28
Load on soil	0.23	0.21	0.19

by assuming pile to be a cantilever beam and following design steps as per IS 456-2000. The results obtained have been shown in Tables 3, 4 and 5 for compression, lateral, and uplift load test, respectively.

5 Results and Discussions

It can be seen from Tables 3, 4 and 5 that the failure load corresponding to dry sand is more than saturated sand which is further more than layered soil. It is true as in case of sands more skin friction resistance is available and since hard stratum was

not available at the end of pile in layered soils, end bearing resistance was neglected and hence failure load obtained was quite less as compared to dry and saturated sand. Also, it can be seen that the value of failure load obtained is more in case of compression load test than lateral load test which is further more than uplift load test which is how it should be.

6 Conclusions

In actual pile foundation situations, it is not possible to determine the proportions of the load that would be shared by the reinforcement, pile material, and the load that would be transferred to the soil. But, as per present study, with the instrumentation of piles these parameters could be determined which are very beneficial, as with the increase in load over superstructure, its effect over pile foundation could be monitored.

It has been seen from the results that the failure load was maximum for dry sands followed by saturated sands and layered soils in compression load test and uplift load test while for the lateral load test, failure load was maximum for dry sands followed by layered soils and saturated sands.

It has also been seen that strains in concrete portion of the pile almost varied linearly with loading and is not much dependent on the soil conditions. Different soil conditions deflected changes only in the magnitudes of strains, for example, in case of dry sands magnitude of strains were observed to be more than saturated sands and layered soils.

It has also been observed that strain variations in the latter stages of uplift test and lateral load is quite less, which shows that lesser constraints were available at the time of failure of pile. While in the case of compression load test, strain variations were more in the latter stages, which showed much higher constraints were available at failure.

It has been noted that amount of the load taken by concrete was maximum for the case of compression load test followed by lateral load and uplift load test while for pile reinforcement amount of load taken by rebar was maximum for the uplift load test followed by lateral load.

With the mounting of strain gauges inside the pile foundations, the designer has an extra eye which keeps focus on the behavior of the structure. Any unusual strain variation will give enough warning before the failure of the structure. Therefore, it will be possible to save many valuable lives in case of the structure failure.

Hence, the practicing consultant should employ instrumentation in the piles for more accuracy and reliability to observe the actual load transfer rates, particularly where significant economic benefit may result.

Acknowledgments This work was supported by Mr. Vijay Kumar, CEO, Record tech electronics, Roorkee by providing his valuable assistance in the field of strain gauges.

References

- Bica AV, Prezzi M, Seo H, Salgado R, Kim D (2013) Instrumentation and axial load testing of displacement piles. In: Proceedings of the ICE-Geotechnical engineering
- Brown MJ, Hyde AFL, Anderson WF (2006) Analysis of a rapid load test on an instrumented bored pile in clay. *Geotechnique* 56(9):627–638
- Code, IS 1498–1970 Classification and identification of soils for general engineering purposes (first revision). Bureau of Indian Standards
- Code, IS 2720–1985 Methods of test for soils: Grain size analysis-Part 4. Bureau of Indian Standards
- Code, IS 2911–1985 Code of practice for design and construction of pile foundations-Part 4. Bureau of Indian Standards
- Code, IS 456 (2000) Code of practice for plain and reinforced concrete. Bureau of Indian Standards
- Geokon Inc (1986) Instruction manual for model 4200/4202/4210 vibrating wire strain gages. Geokon Inc, Lebanon, New Hampshire 24
- Kraśiński A, Kusio T (2015) Pile model tests using strain gauge technology. *Studia Geotechnica et Mechanica* 37(3):49–52
- Muthukkumaran K, Sundaravadivelu R, Gandhi SR (2004) Behaviour of instrumented pile under vertical loading. IGC
- Mittal S (2017) Pile foundation design and construction. CBS Publishers & Distributors Pvt Ltd, New Delhi, India

Effect of Piles on the Design of Raft Foundation



L. M. Malavika, V. Balakumar, and S. S. Chandrasekaran

Abstract The combined raft, soil and pile foundation system has reached a high level of familiarity and is now being used to support a large number of structures. When the bearing capacity of the raft foundation is acceptable but the settlement value exceeds the permissible limit, raft-soil system is reinforced with piles to reduce settlement. Here, piles act as settlement reducers to the raft-soil foundation system. Different researchers have studied the effect of varying pile, raft and soil parameters on the settlement response and load-sharing behaviour of the raft and piles in a combined raft, soil and pile foundation system but less attention has been paid to the stress response behaviour of the raft. As this aspect is considered to be important from economics of raft design, a study has been performed to understand the stress response of the raft on the introduction of piles. The stress response of the raft for varying load conditions, E_c/E_s ratios, thicknesses of raft and diameters of pile have been studied by performing numerical analyses on the foundation system supporting a moderately loaded 12-storeyed real-time commercial structure located in Chennai, India. An attempt has been made to study the applicability of Equivalent Pier concept. The above analyses were performed for two different layouts of piles. The behaviour of the stress and settlement responses of the raft reinforced with piles was compared with unpiled raft. Staad-Pro V8i and Ansys 16.0 have been used for the study and this paper presents observations and discussions from the study.

Keywords Raft reinforced with piles · Raft stress response · Raft settlement response · Equivalent pier

L. M. Malavika (✉)
VIT, Vellore, Tamil Nadu, India
e-mail: lingashetty.malavika@gmail.com

V. Balakumar
Simplex Infrastructures Limited, Chennai, Tamil Nadu, India

S. S. Chandrasekaran
Department of Structural & Geotechnical Engineering, VIT, Vellore, Tamil Nadu, India

1 Introduction

Exponential growth in infrastructure development has forced the designers to accept any ground condition irrespective of its nature. The foundation system must satisfy the serviceability and ultimate limit state conditions and also be viable economically in spite of the ground conditions. The economics of the raft design lies in designing the foundation such that the factor of safety against bearing capacity failure is at the minimum specified value and the total settlement is less than the permanent settlement.

Rafts are designed for the required bearing capacity, however, when the bearing capacity of the raft foundation is acceptable but the settlement values exceed beyond the permissible limits, the raft-soil system is reinforced with piles to reduce settlement (Zeevaert 1957). Here, piles act as settlement reducers to the raft-soil foundation system.

Extensive research had been performed by various researchers to understand the settlement reduction in raft on the introduction of piles (Poulos 1994a, b). Various raft, soil and pile parameters that affect the settlement response and the load-sharing behaviour of the raft and piles in a combined raft, soil and pile foundation system had been also studied extensively. However, very little research has been performed to study the effect of introducing piles on the raft stress response and bending moment. Therefore, it becomes a necessity to study the behaviour of raft stresses on the introduction of piles in a raft-soil foundation system for an effective and economical design since the economy of a foundation lies in both optimum pile layout and provisions in raft.

2 Objective

The main objective of this study is to determine the effect of reinforcing the raft-soil system with piles on the raft stresses and bending moment.

3 Methodology

In the present study, a twelve-storied commercial building resting on a raft-soil foundation system reinforced with piles has been adopted. The structure was analysed in Staad-Pro to obtain the column reactions. These column reactions act at the base of the structure. The linear soil-structure interaction analysis of the combined raft-soil and pile foundation system was performed using Ansys Workbench 16.0.

The behaviour of the raft stress and settlement response was studied by plotting graphs and contours for four different conditions obtained by varying parameters like Young's modulus of soil (E_s), Pile diameter (D), Raft thickness (t) and type of

loading. The above analyses were performed for two different pile layouts. The stress response for the pile reinforced raft was compared with unpiled raft. An attempt was made to study the applicability of Equivalent Pier concept (Balakumar et al. 2013a, b). Effort was made to know if there was any variation in the raft stress response.

3.1 Structural Analysis

The shape of the twelve-storied commercial building is irregular with a width of 27.38 m and a length of 41.2 m along the largest span. The building lies on a raft—soil foundation system reinforced with piles. The dimensions of the raft are same as the shape of the building. Figures 1 and 2 shown below represent the floor plan and

Fig. 1 Floor plan

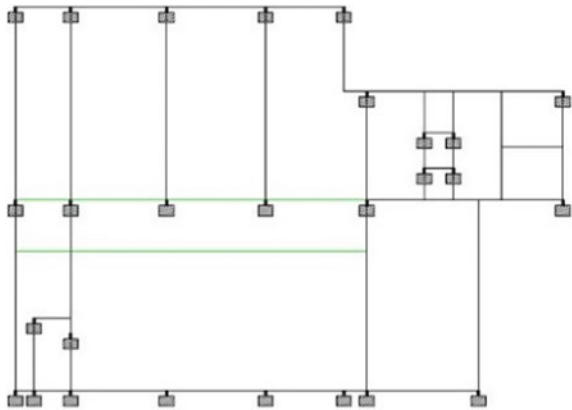


Fig. 2 Structural frame

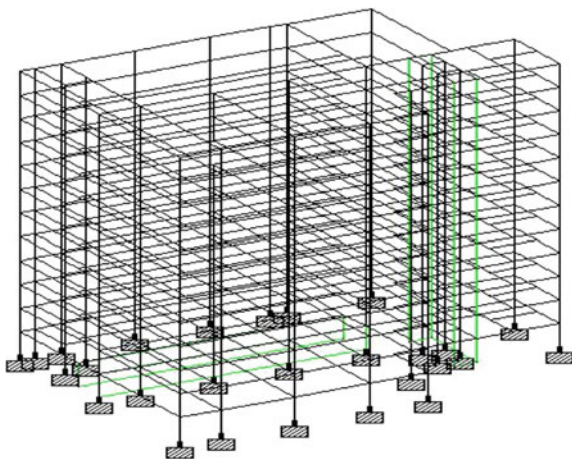


Table 1 Physical properties of model

Specification	Value (mm)
Slab thickness	200
Size of beams along lateral direction	800 × 750
Size of beams along transverse direction	450 × 600
Size of columns	800 × 800
Outer wall thickness	230
Inner wall thickness	230
Storey height	3750
Number of storeys	12

the structural frame of the twelve-storied building respectively. Table 1 presents the dimensions of the physical components of the twelve-storied building.

The framed model is subjected to a combination of Dead load (D.L.) and Live load (L.L.). Three-dimensional analysis has been performed to obtain the support reactions. These reactions obtained at the base of the structure act as the structural load on the foundation.

3.2 Numerical Analysis

In the case of Staad-Pro, it is a known fact that geotechnical problems cannot be handled. Although some approximations can be done, the applications are very limited like preliminary analysis of retaining walls which is conforming to beam elements. Since the soil cannot be modelled, Ansys was chosen to do the soil–structure interaction studies. The physical and material properties of the combined foundation system are mentioned in Tables 2 and 3, respectively.

The pile length of 0.8 times the least dimension of the raft (B) was chosen since it is the optimum limit beyond which the piles do not possess additional bearing capacity (Cooke 1986; Balakumar 2008). Figures 3 and 4 show the individual raft and pile models, respectively.

In the case of unpiled raft, shown in Fig. 5, the depth of the soil block is taken as 2.5 times the least dimension of the raft (B) and both the length and width of the soil block as 3 times the least dimension of the raft (B). This is due to the reason that the impact

Table 2 Physical properties of raft, piles and soil

Property	Raft	Piles	Soil
Material	M25 concrete	M25 concrete	Medium dense sand
Shape	Irregular	Circular	Cube
Depth	1 m	24 m	68.45 m
Width	27.38 m	0.9 m	82.14 m

Table 3 Material properties of raft, piles and soil

Property	Raft	Piles	Soil
Material	Concrete	Concrete	Sand
Compressive strength (kN/m ²)	27579	27579	–
Elastic modulus (Pa)	3×10^{10}	3×10^{10}	3×10^6
Density (kN/m ³)	22.54	22.54	15.5
Poisson ratio	0.18	0.18	0.3
Shear angle	–	–	33^0

Fig. 3 Raft

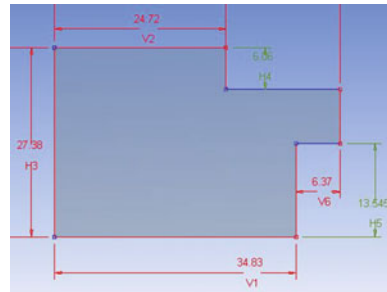
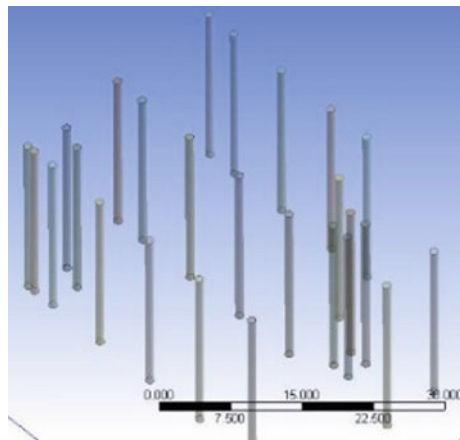
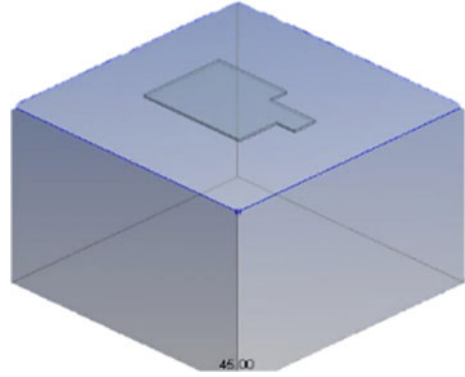
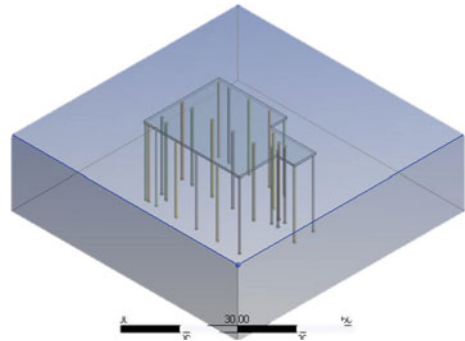


Fig. 4 Piles



of the raft does not exceed these limits in the surrounding soil (Balakumar 2008). Figure 6 represents the raft reinforced with piles in the raft-soil system wherein the depth of the soil is taken equal to the length of the piles to provide contact between the tip of the piles and the bottom of the soil surface.

Perfect contact is provided between raft—soil, raft—piles and piles—soil (Balakumar 2008). The accuracy of the analysis depends upon meshing and continuity of the elements in the nodes. Hence, in generation of mesh, extreme care was

Fig. 5 Unpiled raft in soil**Fig. 6** Raft with piles in soil

taken to ensure identical mesh refinement patterns for different analytical cases under comparison. A 2-m uniform quadrilateral mesh was provided throughout the entire foundation system.

Fixed boundary conditions are provided at the bottom surface and along the four edges of the soil block (Balakumar 2008). The fixity conditions act as bounding limits to the soil. The loads are imposed on the raft and the settlement and stress values are obtained after the analysis. The values thus obtained at each node along the orthogonal directions of the raft at the centre and the edge are used in plotting the graphs.

Type of loading. The column loads at the base of the structure were given as two different types of input for soil–structure interaction analysis in Ansys Workbench. They are as follows:

- Concentrated loads
- Equivalent uniformly distributed load of 157.766 kN/m²

Figures 7 and 8 show the type of loading imposed on raft. Initially, the unpiled raft (Case–A) was subjected to concentrated load as well as equivalent UDL for E_c/E_s ratios of 10,000, 2,000, 1,500, 1,200, 1,000 and 100.

Fig. 7 Point load on raft

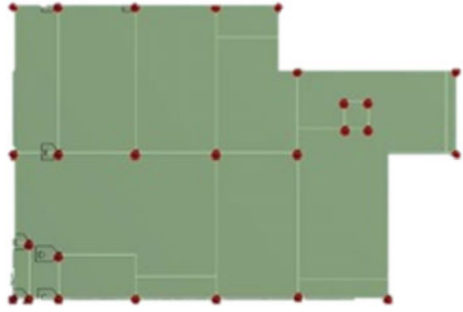


Fig. 8 Uniformly distributed load on raft



Later, the piles were introduced below the raft in two different layouts, one layout with piles located below the position of the columns under the raft (Case–B) and the other layout with piles located in between the position of the columns under the raft (Case–C). Figures 9 and 10 represent the different pile layouts.

Table 4 presents a comparison for the maximum settlement between cases A, B and C subjected to PL and UDL, respectively. It can be seen that the total settlement exceeds the permissible limits in all cases except for one case where there is an extreme reduction in the maximum settlement in the unpiled raft when the E_c/E_s ratio is equal 100. This is because the E_c/E_s ratio equal to 100 indicates a very dense and stiffer soil condition. Such a stiffer and denser soil possesses a very high

Fig. 9 Case B

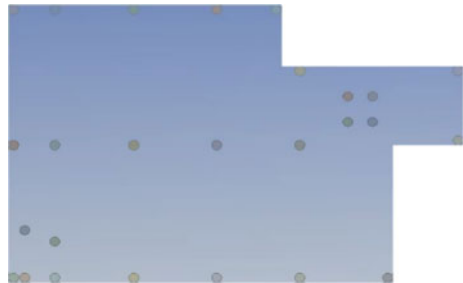
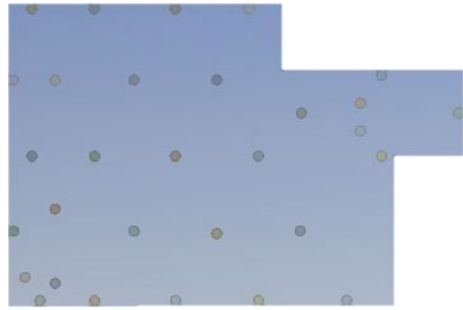


Fig. 10 Case C**Table 4** Comparison of settlement in cases A, B and C

Ec/Es	Max. settlement under PL (mm)			Max. settlement under UDL (mm)		
	Case A	Case B	Case C	Case A	Case B	Case C
10,000	1347.0	1079.3	1028.7	1160.8	694.0	694.4
2,000	309.0	356.1	356.7	255.0	166.3	167.1
1,500	297.0	294.0	266.7	194.2	132.7	132.3
1,200	192.9	253.9	228.0	158.0	111.9	111.4
1,000	300.7	225.6	200.6	131.9	97.3	96.7
100	20.3	50.8	49.8	138	13.6	5.9

bearing capacity and hence the raft-soil foundation system in such dense soil shows less settlement. Designing the raft for such maximum settlement values will make the design uneconomical. This necessitates the introduction of settlement-reducing piles.

It was also observed from Table 4 that the introduction of piles in the raft-soil system has reduced the total settlement to about 25–45% on an average. This validates the purpose of the addition of piles as settlement reducers to the raft-soil foundation system.

It can be seen from Table 4 that the settlement reduction is maximum for Ec/Es equal to 10,000 and it decreases with an increase in Ec/Es ratio. This is because piles are fully frictionized when Ec/Es is equal to 10,000 but as the Ec/Es ratio decreases, the soil becomes denser and the capacity of the piles to turn into friction piles reduces (Cooke 1986).

A considerable difference was observed in the settlement contour pattern under PL and UDL conditions for all the three cases. This is because of the variation in the type of loading. In the case of raft-soil foundation system subjected to PL, the contact pressure varies due to variation in loads and hence the settlement profile also varies accordingly as seen in Fig. 11.

In the case of UDL, there is uniform contact pressure distribution throughout the area of the raft due to the uniformity in loading. This resulted in a more uniform settlement contour as seen in Fig. 12. Figure 13 indicates that the effect of raft

Fig. 11 Settlement contour under point load

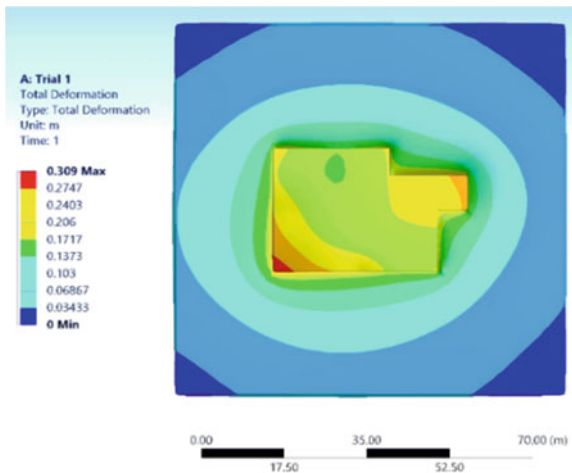


Fig. 12 Settlement contour under UDL

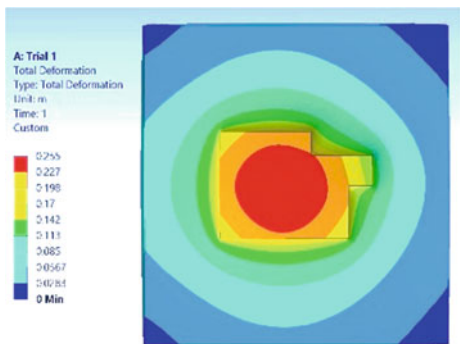


Fig. 13 3D view—Settlement contour

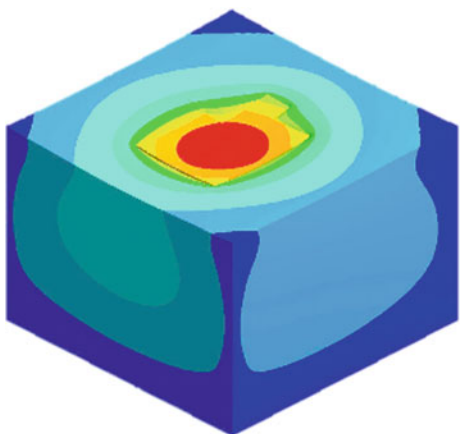


Fig. 14 Settlement under UDL for Case B

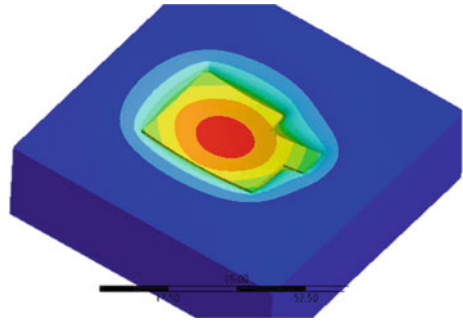
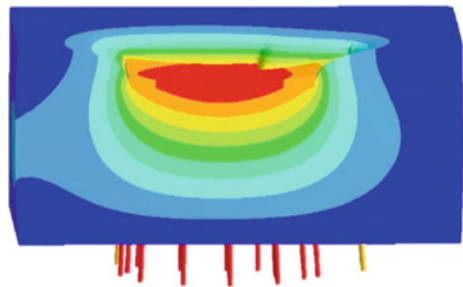


Fig. 15 Section view of contour



settlement is negligible at the bottom and at the edge of the soil which justifies that the impact of the raft is limiting in the soil as discussed in Sect. 3.2.

Figures 14 and 15 represent the settlement contours for complete and section views of a combined raft, soil and pile foundation system under UDL for case B, respectively. It can be seen from Figs. 12 and 14 that the settlement pattern remains identical but vary in magnitude.

Figure 15 shows the settlement contour along the depth of the foundation. The maximum settlement occurs at the centre as well as the tip of the piles. This denotes the transfer of the load to the surrounding soil through the tip of the piles from the centre portion of the raft.

The settlement of the raft along the orthogonal grids was obtained and graphs have been plotted to present a comparison for the settlement in Cases A, B and C when subjected to PL and UDL. Figures 16 and 17 present a comparison between cases A and B for the raft settlement along the transverse grid when subjected to PL and UDL for a ratio of E_c/E_s equal to 2,000.

It can be observed from Figs. 16 and 17 that the settlement pattern for unpiled raft and piled raft subjected to PL and UDL are similar, respectively, but the raft reinforced with piles exhibited much lesser settlement compared to unpiled raft. This validates that the piles act as settlement reducers in raft-soil system.

It can be seen from the above settlement graphs that the settlement trend curve for foundation system subjected to UDL showed a concave profile with maximum settlement at the centre reflecting the nature of the raft mainly flexible raft. But under

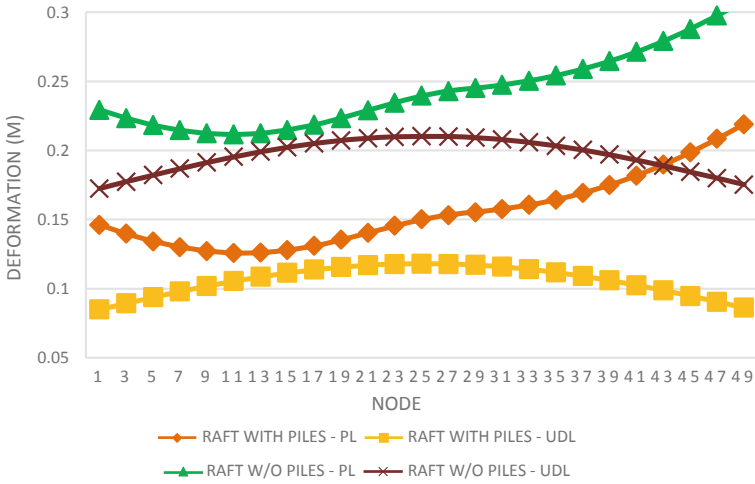


Fig. 16 Settlement graph for cases A and B—Outer Grid

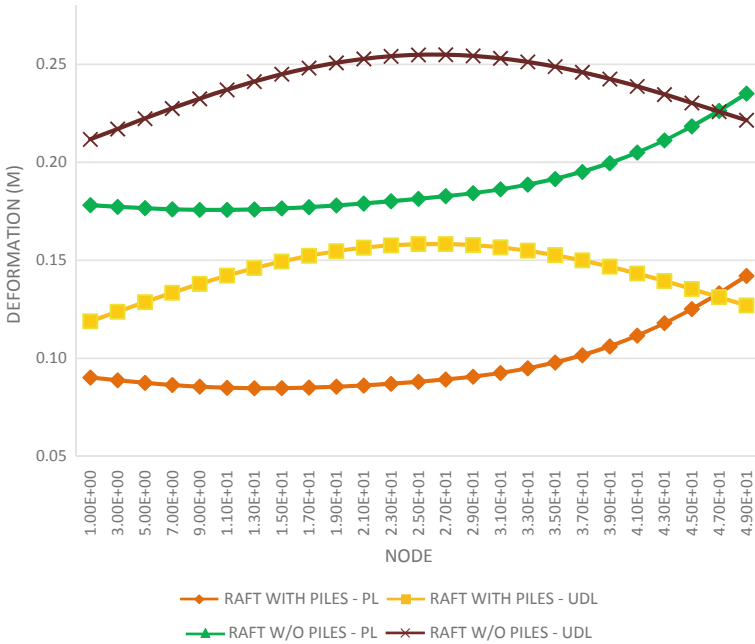


Fig. 17 Settlement graph for cases A and B—Central Grid

the same condition, when the load is considered as PL, the outer and central grids show a reversal in shape due to their dependence on the individual column load. Similar graphs were plotted for all other cases for different E_c/E_s ratios and it was observed that the raft settlement response remained same but varied in magnitude. It was observed that the deformation reduced from 45–55% at the edges and 40–45% at the centre of the raft on introduction of piles.

Similar to settlement profile, Table 5 presents a comparison between the maximum stress values of the combined foundation system subjected to PL and UDL for different E_c/E_s ratios. It can be seen from Tables 5 and 6 that the maximum stress value remained same for unpiled rafts subjected to PL for all the E_c/E_s ratios whereas the maximum stress value varied for unpiled rafts subjected to UDL. In the case of foundation system subjected to PL, the stresses were concentrated in the raft area subjected to high concentrated loads whereas under UDL, the stresses were redistributed throughout the entire area of the raft due to uniformity in the distribution of loads. It can also be seen that the maximum stress value decreased with a decrease in the E_c/E_s ratio. As the E_c/E_s ratio decreases, the soil becomes denser leading to less deformation and eventually lesser stresses in the raft.

Similar to the raft settlement response, a variation in the stress contours of unpiled rafts subjected to PL was observed. Figures 18 and 19 represent the stress contours in the unpiled raft-soil foundation subjected to UDL for E_c/E_s ratio equal to 2,000.

From Fig. 18, it can be observed that the raft stresses are concentrated more at the centre portion of the raft and are negligible at the edges. Since the settlement is

Table 5 Maximum stress under point load (Pa)

Ec/Es	Maximum stress under point load (Pa)		
	Case A	Case B	Case C
10,000	11.28×10^7	11.24×10^7	11.28×10^7
2,000	11.29×10^7	11.21×10^7	11.29×10^7
1,500	11.29×10^7	11.25×10^7	11.29×10^7
1,200	11.29×10^7	11.25×10^7	11.29×10^7
1,000	11.28×10^7	11.25×10^7	11.29×10^7
100	11.29×10^7	11.25×10^7	11.29×10^7

Table 6 Maximum stress under uniformly distributed load (Pa)

Ec/Es	Maximum stress uniformly distributed load (Pa)		
	Case A	Case B	Case C
10,000	2.91×10^7	3.39×10^7	2.65×10^7
2,000	1.21×10^7	1.43×10^7	1.28×10^7
1,500	0.99×10^7	1.05×10^7	1.06×10^7
1,200	0.85×10^7	0.89×10^7	0.90×10^7
1,000	0.74×10^7	0.77×10^7	0.77×10^7
100	0.12×10^7	0.13×10^7	0.12×10^7

Fig. 18 Stress contour in unpiled raft under point load

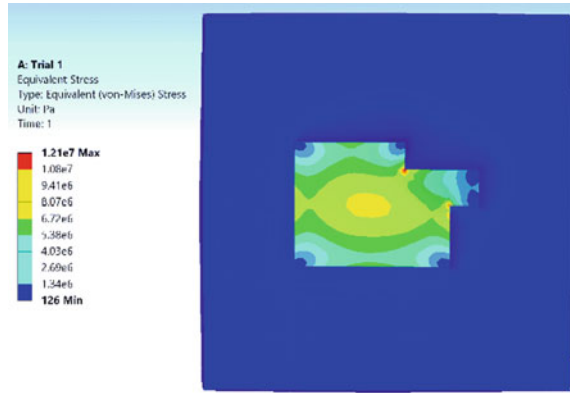
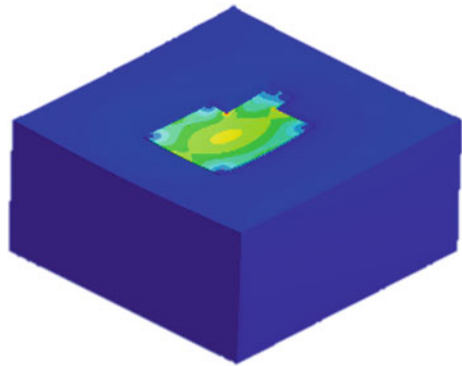


Fig. 19 Stress contour in soil



more at the centre of the raft, the stresses are highly concentrated at the centre. This trend in stress variation is similar to the settlement response of the unpiled raft when subjected to UDL as seen in Fig. 14. It can be seen from Fig. 19 that the stresses in the soil are negligible.

The stress contours at the section of the unpiled raft were obtained to study the stress pattern along the depth of the foundation. The stresses in the soil were negligible for all the three cases as discussed previously.

It can be seen from Fig. 20 that the raft stress is minimum at the centre and maximum at the top and bottom of the unpiled raft under UDL. The raft design can therefore be optimized accordingly with respect to raft stress and settlement behaviour.

The variation in stresses means that the Bending Moment (B.M.) and Shear Force (S.F.) will also vary along the raft area. Hence it becomes important to study the stress response behaviour of the raft from the view of the economics of the raft.

Figure 21 represents the stress variation at the bottom surface of the piled raft. It can be observed that the stress varies uniformly along both the orthogonal directions of the surface of the raft. Similar stress trend was observed in Cases B and C but with

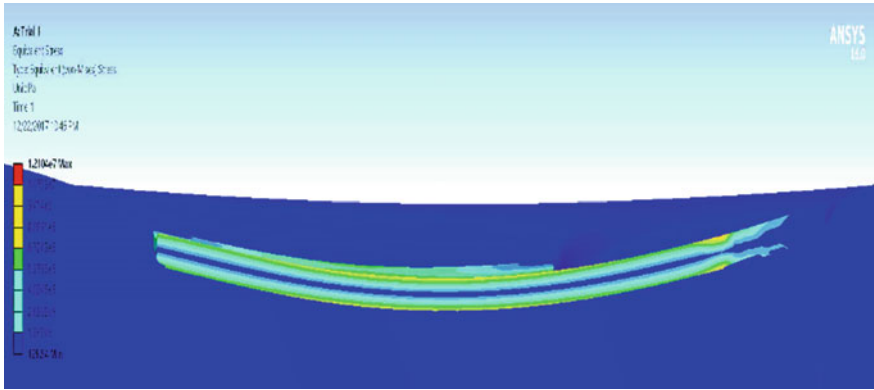


Fig. 20 Section contour for stresses in case A under UDL

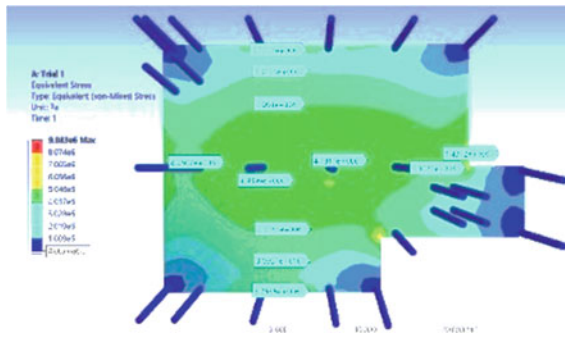


Fig. 21 Stress contour at the bottom of raft

a variation in magnitude under PL and UDL for different E_c/E_s ratios. The stress in piles was observed to be minimum in all cases as seen in Fig. 22.

Figures 23, 24 and 25 represent the stress in piles. It can be observed that stress in the area of raft-pile contact is maximum. This is due to the transfer of raft stress to the piles. The stress in the piles is maximum at the head and it reduces with an increasing depth in the piles as indicated in Figs. 22 and 23. Variation of stress indicates a variation in the B.M. and shear forces. Hence, the reinforcement in the raft can be optimized by designing it in areas of higher stresses leading to an economical design.

Graphs have been plotted for raft stresses at the bottom surface in cases A, B and C and a comparison has been made between them to study the raft stress behaviour. Figures 26 and 27 present a comparison between the unpiled and piled raft stresses at the bottom surface area of the raft for E_c/E_s equal to 2,000.

It was observed from the stress response graphs of the raft that the stress response pattern although remains similar in trend under UDL, it has a pronounced variation particularly in the case of outer grids. This is mainly due to the varying magnitude

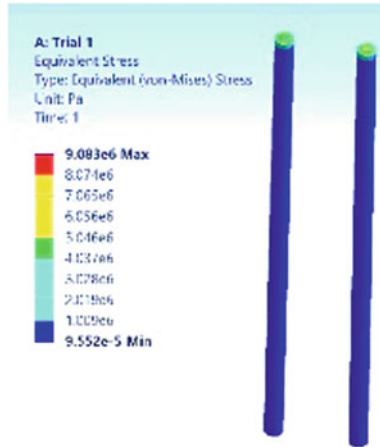


Fig. 22 Stress contour in piles

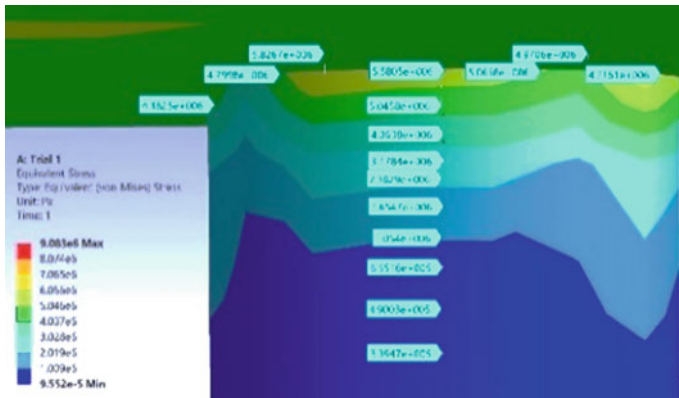


Fig. 23 Stress contour at raft-pile contact area

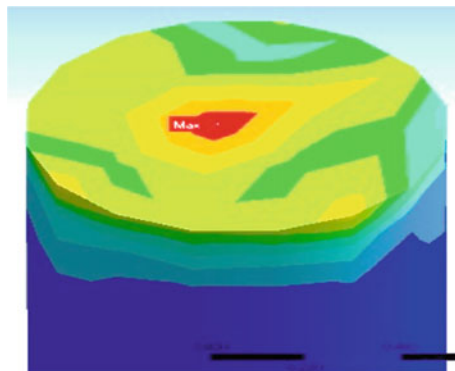


Fig. 24 Stress contour at head of the pile

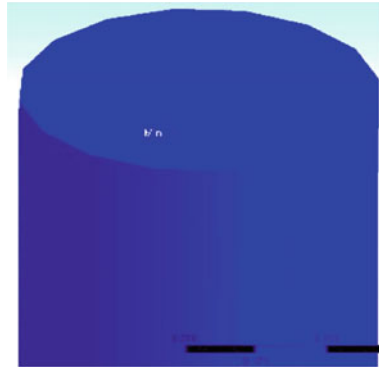


Fig. 25 Stress contour at pile tip

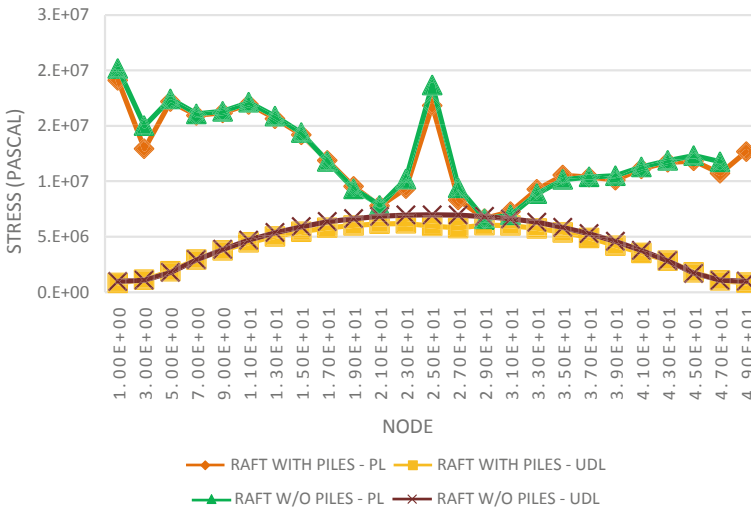


Fig. 26 Stress graph along the outer grid of the raft in transverse direction

of the column load. The upper peaks in the stress trend curves under PL reflect the concentration of raft stresses at the pile locations. The transfer of stresses from the raft to the piles occurs here as mentioned previously. The lower peaks reflect the raft between the piles. In the present structure, columns are very widely spaced, therefore, the stress pattern under the PL follows the same pattern.

Similar graphs were plotted for all other cases for different E_c/E_s ratios and it was observed that the stress pattern remained same but with a variation in magnitude. It was observed that the stress value reduced from 7–15% at the edges and 10–20% at the centre of the raft due to the introduction of piles in the raft.

Thus, it can be concluded that the method of applying loads influences the displacement and stress patterns. It was observed that the displacement and stress

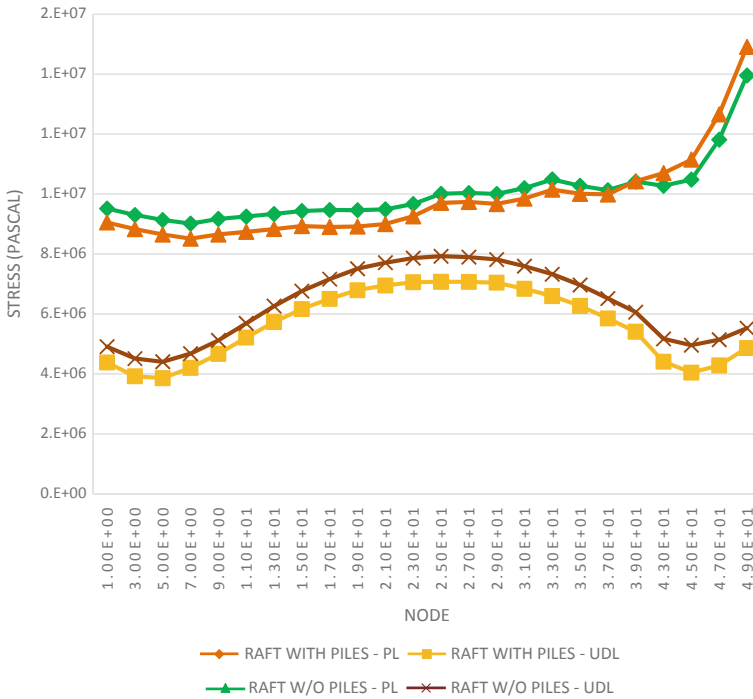


Fig. 27 Stress graph along the central grid of the raft in transverse direction

patterns were identical for all the three cases with a pronounced reduction in magnitude in raft reinforced with piles, i.e. cases B and C. The raft and pile design can be optimized efficiently by studying the settlement and stress responses of the raft and the piles.

Variation in E_c/E_s . In the present case, numerical analyses were performed on an unpiled raft of thickness 1 m located at a depth of 3 m from the ground surface. Retaining wall was considered around the raft. A pressure of 111276 Pa was obtained by deducting the surcharge pressure at 3 m depth. Numerical analyses were repeated for cases B and C and the results were compared to study the raft behaviour. In the analysis, the E_c value was kept constant as 3×10^7 kN/m² whereas the E_s value was varied. The raft, pile and soil properties mentioned in Tables 2 and 3 were adopted. Table 7 presents a comparison of the stresses in cases A, B and C for varying E_c/E_s ratios.

From the above table, it can be seen that the stress reduces on the introduction of piles for both the pile layouts. It was observed that the stress contour trend remained similar to unpiled and piled rafts under UDL in previous sections but with a slight variation in magnitude. For the present case, the settlement value for E_c/E_s ratio equal to 2,000 satisfies the permissible limits. Hence, the ratio of E_c/E_s equal to 2,000 had been adopted in the further studies.

Table 7 Comparison of stresses in cases A, B and C

Ec/Es	Maximum stress (in Pa) under a load of 111276 Pa		
	Case A	Case B	Case C
10,000	2.45×10^7	2.39×10^7	1.80×10^7
2,000	0.95×10^7	0.90×10^7	0.90×10^7
1,500	0.80×10^7	0.74×10^7	0.74×10^7
1,200	0.69×10^7	0.63×10^7	0.63×10^7
1,000	0.57×10^7	0.54×10^7	0.54×10^7
100	0.08×10^7	0.09×10^7	0.08×10^7

Graphs were plotted similar to previous section and comparison was made. It was observed that the trend for the settlement and stress responses of the raft varied along a concave profile which was similar to the previous observations but with a variation in magnitude. It was observed that the settlement reduced from 45–55% at the edges and 40–45% at the centre of the raft on the introduction of piles. Similar results were observed for all the other grids under all cases.

Figures 28 and 29 represent the stress response of the raft for cases A and B when Ec/Es is equal to 2,000. The raft stresses were obtained at the raft-soil contact surface but on the raft surface. The pattern of stress distribution with piles obtained after analysis was similar to the results published by Balakumar (2008). The slight variation in the stress trend curves as seen in Figs. 28 and 29 is due to the non-uniform spacing of piles.

It was observed from the calculations that the stress value reduced about 7–15% at the edges and 10–20% at the centre of the raft due to the introduction of the piles for both the layouts. At the raft edges, the variation in stress was marginally less compared to the centre. This variation is mainly due to the edge being free and not restrained by retaining walls in actual analysis.

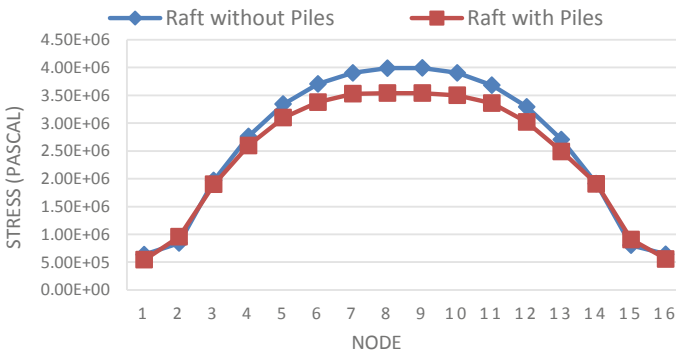


Fig. 28 Stress graph along outer grid of raft in transverse direction

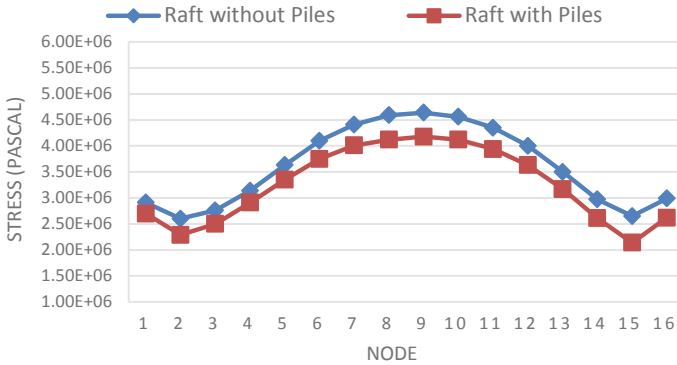


Fig. 29 Stress graph along central grid of raft in transverse direction

Variation of D/t when pile diameter (D) is kept constant. In the present case, the numerical analyses were performed on the combined raft, soil and pile foundation system for four D/t ratios, where D is the diameter of the pile and t is the thickness of the raft. The diameter of the piles was kept constant as 0.9 m and the raft thickness was varied. The raft was located at a depth of 3 m from the ground surface and the piles of length 24 m were modelled under the raft beneath the location of the columns. The soil was modelled as a block of medium dense sand condition. A constant E_c/E_s ratio of 2,000 was adopted to perform all the analyses under the present case, where E_c was equal to $3 \times 10^{10} \text{ N/m}^2$ and E_s equal to $1.5 \times 10^7 \text{ N/m}^2$. The results obtained from various analyses of conditions A, B and C were compared with each other.

It was observed that the introduction of piles reduced the settlement for about 23–37%. It was also observed that the reduction in the overall settlement increased with an increase in the raft thickness (Poulos 1998, 2001) for a constant pile diameter.

Table 8 presents a comparison between the maximum stresses for cases A, B and C for varying D/t ratios when D was kept constant. It was observed that there was no much variation between the maximum stress values for cases B and C when the pile diameter was kept constant. It was observed that the settlement and stress trend was similar to previous sections for all the D/t ratios but with a variation in magnitude.

Table 8 Comparison of stresses in cases A, B and C when D is constant

D/t	D (mm)	t (mm)	Maximum stress (Pa)		
			Case A	Case B	Case C
1.2	900	750	0.90×10^7	0.89×10^7	0.89×10^7
1.0	900	900	0.94×10^7	0.92×10^7	0.92×10^7
0.9	900	1000	0.95×10^7	0.90×10^7	0.90×10^7
0.8	900	1125	0.94×10^7	0.86×10^7	0.86×10^7

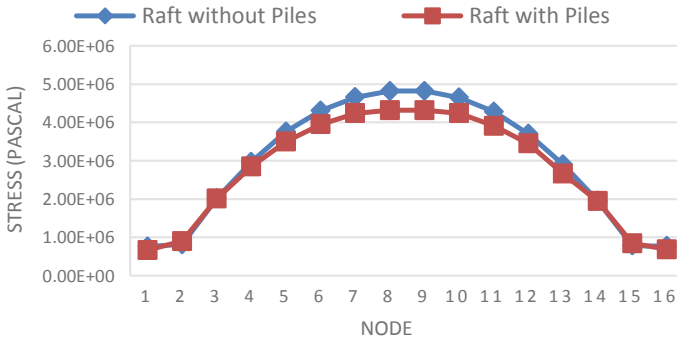


Fig. 30 Stress graph along outer grid of raft in transverse direction

It was observed that the deformation reduced for about 45–55% at the edges and 40–45% at the centre of the raft on introduction of piles.

Graphs were plotted to compare the raft stress response for cases A, B and C for varying D/t ratios when D was kept constant. Figure 30 represents the stress response behaviour of the raft for a D/t ratio of 1.2. The stress value reduced from 7–15% at the edges and 10–20% at the centre of the raft due to the introduction of piles. Similar trend was observed in all the other cases.

Variation of D/t when raft thickness (t) is kept constant. In the present case, the numerical analyses were performed similar to the above section but here, raft thickness of 1 m was adopted and kept constant whereas the pile diameter was varied. Table 9 presents a comparison of stresses between cases A, B and C for varying D/t ratios when t was kept constant.

It can be observed from the table that the stresses in the raft under cases B and C increases as the pile diameter decreases for a constant raft thickness. For D/t ratios less than 1.2, i.e. when the pile diameter is less than the raft thickness, there is an increase in the raft stresses. It was observed that the settlement and stress trend was similar to previous sections for all the D/t ratios but with a variation in magnitude.

Table 9 Comparison of stresses in cases A, B and C when t is constant

D/t	D (mm)	t (mm)	Maximum stress (Pa)		
			Case A	Case B	Case C
2.00	2000	1000	0.85×10^7	0.76×10^7	1.42×10^7
1.75	1750	1000	0.85×10^7	0.81×10^7	0.72×10^7
1.5	1500	1000	0.85×10^7	0.83×10^7	0.79×10^7
1.2	1200	1000	0.85×10^7	0.85×10^7	0.86×10^7
1.0	1000	1000	0.85×10^7	0.90×10^7	0.90×10^7
0.8	800	1000	0.85×10^7	0.91×10^7	0.93×10^7

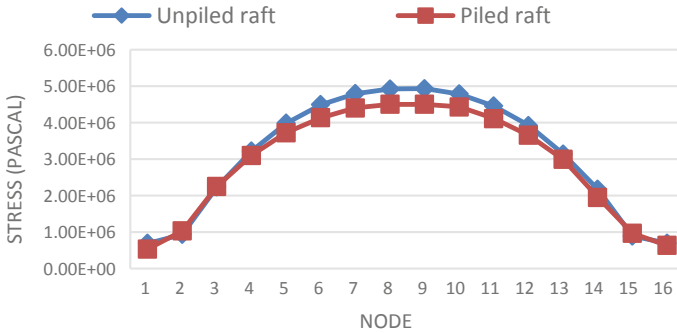


Fig. 31 Stress graph along central grid of raft in transverse direction

The graph representing the stress response behaviour of the raft was also similar in pattern but varied in magnitude as seen in Fig. 31.

Figure 31 represents the stress response behaviour of the raft for a D/t ratio equal to 1.2. The stress value reduced from 7–15% at the edges and 10–20% at the centre of the raft due to the introduction of piles. Similar trend was observed in all the other cases.

Equivalent Pier Analysis. A special case of equivalent pier system has been analysed to study its applicability and influence on the behaviour of raft deformation and stresses. Three equivalent pier analyses have been performed by adopting a raft of thickness 1 m located at a depth of 3 m from the ground surface. Equivalent piles of length 24 m were modelled under the raft surrounded by medium dense sandy soil. E_c/E_s ratio of 2,000 has been adopted for the analyses. Equivalent pier diameter (Dequ) was calculated. The equivalent piles of 24 m length are shown in Fig. 32.

Tables 10 and 11 present a comparison for the maximum settlement and stresses in a raft between the cases of unpile raft (Case A), raft reinforced with piles below the position of columns (Case B) and raft reinforced with equivalent piles below the

Fig. 32 Equivalent Piles

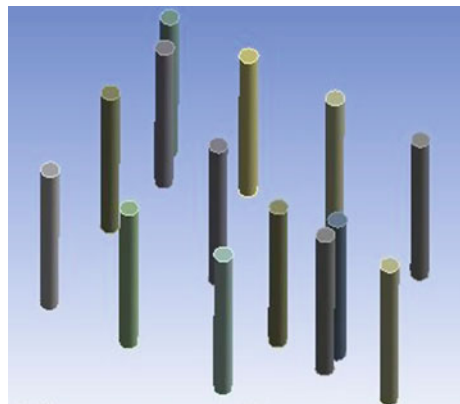


Table 10 Comparison of maximum deformation

D (m)	t (m)	Dequ (m)	Maximum deformation (mm)				
			Case A	Case B	Case Bequ	Case C	Case Cequ
1.5	1	2.1	135.29	119.13	118.48	117.95	119.19
1.2	1	1.8	134.95	118.97	118.20	118.01	119.08
1.0	1	1.4	119.25	118.81	118.81	117.93	118.87

Table 11 Comparison of maximum stresses

D (m)	t (m)	Dequ (m)	Maximum stress (Pa)				
			Case A	Case B	Case Bequ	Case C	Case Cequ
1.5	1	2.1	0.99×10^7	0.83×10^7	0.83×10^7	0.79×10^7	0.77×10^7
1.2	1	1.8	0.94×10^7	0.85×10^7	0.84×10^7	0.86×10^7	0.86×10^7
1.0	1	1.4	0.92×10^7	0.90×10^7	0.90×10^7	0.90×10^7	0.89×10^7

columns (Case Bequ). Similar comparison was performed for Case C and equivalent piles located in between the position of columns (Case Cequ).

It was observed from Tables 10 and 11 that the maximum settlement and stress values reduced on the introduction of equivalent piles in the raft when compared to unpiled raft. Also, the settlement and stress values showed a very negligible variation in the cases between raft reinforced with regular piles and raft reinforced with equivalent pier for the two different pile layouts. The settlement and stress trend contours and magnitude also remained similar for the above two cases.

From Figs. 33 and 34, it was observed that the settlement and stress response pattern of the raft remained similar to other cases. It was observed that the variation in stresses and deformation between equivalent pier and piles was only about 2–5%. Thus, it can be concluded that equivalent piles can be used in the combined raft, pile and soil foundation system based on their availability.

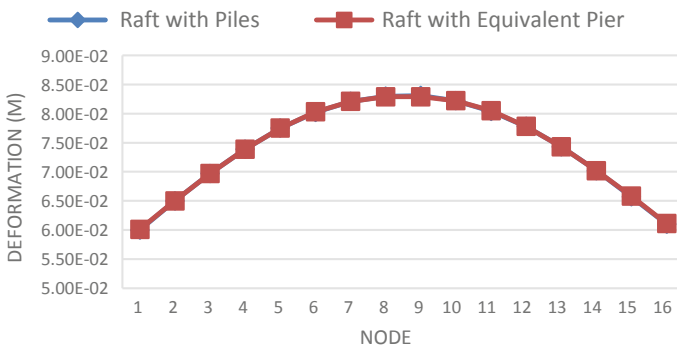


Fig. 33 Comparison of raft deformation

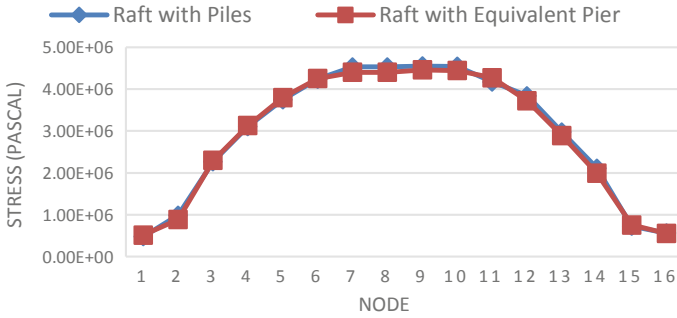


Fig. 34 Comparison of raft stresses

4 Conclusion

It was observed that the trend of settlement and stress variation in unpiled raft and piled raft for different layouts of piles was identical but with a variation in magnitude. The deformation reduced from 45–55% at the edges and 40–45% at the centre of the raft and the stress value reduced from 7–15% at the edges and 10–20% at the centre of the raft on an average due to the introduction of piles.

The load on the piles located at the centre of the raft was much higher than the piles positioned at other locations in the raft. The raft contact stresses obtained from the numerical analyses show uniform distribution except at the edges and pile locations. The stress distribution obtained from the numerical analysis indicated that the shaft stress is higher near the pile head and reduces towards the pile tip. The high stress at pile head was due to the transfer of raft stresses to the piles. It was also observed from the analyses that the tip stresses in piles were lesser than the head stresses indicating that the shaft friction was fully mobilized and the piles were dominantly friction piles. Also the mobilization of higher raft stress as the load increased and low pile tip stress at the final settlement confirms the behaviour of the pile group as settlement reducer (Cooke 1986, Fran 1991).

It was observed from the present study that the introduction of the piles not only reduced the raft settlement but also the stress level. Consequent to the reduction in stresses, the bending moment and the shear forces also get reduced. Thus, the study of raft stresses and bending moment along with the raft settlement leads to a better and effective design of the raft.

The variation in stresses and deformation between equivalent pier and general piles was only about 2–5%. Hence, equivalent pier system can also be used effectively based on requirement.

References

- Balakumar V (2008) Experimental studies of model piled raft on sand and field study of proto type behaviour. Doctoral dissertation, PhD thesis, Anna University, Chennai
- Balakumar V, Huang M, Oh E, Balasubramaniam AS (2013a) Equivalent pier theory for piled raft design. In: Proceedings of the 18th international conference on soil mechanics and geotechnical engineering
- Balakumar V, Huang M, Oh E, Balasubramaniam AS (2013b) A design method for piled raft foundations. In: Proceedings of the 18th international conference on soil mechanics and geotechnical engineering, Paris, pp 2671–2674
- Cooke RW (1986) Piled raft foundation on stiff clays—a contribution to design philosophy. *Geotechnique* 36(2):169–203
- Fran E (1991) In: Measurements beneath piled rafts. Keynote lecture. ENPC conference Paris, pp 1–21
- Poulos HG (2001) Piled raft foundations: design and applications. *Geotechnique* 51(2):95–113
- Poulos HG (1994a) Alternative design strategies for piled raft foundations. In: Proceedings of the 3rd international conference deep foundations, Singapore, pp 239–244
- Poulos HG (1994b) An approximate numerical analysis of pile–raft interaction. *Int J Numer Anal Methods Geomech* 18(2):73–92
- Poulos HG (1998) The pile-enhanced raft—an economical foundation system. In: Proceedings, XI Brazilian conference on soil mechanics and geotechnical engineering, Brasília, vol 4, pp 27–43
- Zeevaert L (1957) Compensated friction pile foundation to reduce the settlement of buildings on highly compressible volcanic clay of Mexico city', In: Proceedings of the 14th international conference on soil mechanics and foundation engineering, London (1957)

Interaction Effect on Laterally Loaded Piles in Cohesionless Deposit



Sachchidanand Kushwaha and Ashok Kumar Khan

Abstract Pile is the only solution to transfer the vertical and lateral loads to deeper strata in high-rise buildings. Here, an attempt has been made on laboratory model single pile and pile groups to investigate lateral resistance of the piles. However, this paper puts up the results of lateral static load tests executed on model steel and wooden single pile and pile groups, in cohesion-less deposit about 1 m deep at varying sand density and length to diameter ratio keeping the spacing constant. Load is applied using turn-buckle and measured by a spring balance. Dial gauges are installed to investigate the average displacement. The effects of embedded length to diameter ratio, sand density, configuration of piles, material of piles and group efficiency are studied and explored. The test results are substantiated theoretically by GEO5 software for both single pile and pile groups considering the properties in aligned with that of experimental studies.

Keywords Efficiency · Pile–soil–pile interaction · Lateral load · Pile groups · Load settlement · Turn-buckle

1 Introduction

In general, pile foundations are subjected to lateral loads due to earth pressure, wind action, wave action, earthquake, impact of ships and so on, which are claimed to be found in the range of 10–15% of the vertical loads in case of onshore structures and 25–30% in case of coastal and offshore structures (Gandhi and Selvam 1997). In many situations, piles are constructed in groups to support the structure which differs in behaviour substantially as compared to that in single pile. The pile–soil–pile interactions as observed cause pile groups to deflect more in significant to the single

S. Kushwaha (✉)

Department of Civil Engineering, Indian Institute of Technology, Ropar 140001, India
e-mail: Sachchidanand1295@gmail.com

A. K. Khan

Department of Civil Engineering, National Institute of Technology, Jamshedpur 831014, India
e-mail: akk.nitjsr@gmail.com

© Springer Nature Singapore Pte Ltd. 2020
M. Latha Gali and P. Raghuvver Rao (eds.), *Construction in Geotechnical Engineering*, Lecture Notes in Civil Engineering 84,
https://doi.org/10.1007/978-981-15-6090-3_7

pile for the same average load applied on both. The bending moment, also, in case of group of piles is significantly more than that in single pile due to weakening of soil resistance (Brown et al. 1988). It is because of the ability to represent the nonlinear behaviour of soil, versatility and simplicity, the p - y curve method is broadly used in the design among the different methods available for analysis of lateral loaded piles. In 1988, Brown et al. proposed the concept of p -multipliers to reduce p - y curve of a single pile to obtain p - y curves for piles in group for incorporating group interaction effects. Previous research studies on group of piles in sand include full field tests and centrifuge model tests (Brown et al. 1988; Poulos and Davis 1980; Rollins et al. 2005).

Piles are seldom isolated but are usually arranged in a manner of pile groups in order to strengthen the load resistance. Although a pile group strengthens the overall lateral load resistance, the soil-structure interaction effect weakens the individual pile response of the piles in the group (Poulos 1971b). The overall lateral load is divided among each of the piles in the group. Each pile pushes against the soil behind it creating a shear zone in the soil (Phanikanth et al. 2010). These shear zones begin to enlarge and overlap as the lateral load increases (Broms 1964; Poulos 1971a). More overlapping occurs as the piles are spaced very closely together in the group arrangement. The overlapping occurring in between two piles along the same row is referred as “edge effects” and that in different rows is referred as “shadowing effects” (Rollins et al. 1998). All of these “group interaction effects” result in less lateral resistance per pile in the pile group.

However, the majority of the reported field tests on groups have been carried out at different spacing and single to two, three L/D ratios. Lateral load tests on pile groups with most efficient spacing of $3.5D$ diameters and of two materials are insufficient (Walsh 2005). Effects of pile group configuration and pile spacing in the direction perpendicular to loading were not comprehensively investigated. In this study, an extensive experimental procedure has been opted to perform tests on the model pile group embedded in sand subjected to lateral loads. The density of sand that has been used is obtained at two heights, that is, 45 and 65 cm by rainfall method technique. Also, the mechanism of providing the load and measuring it has never been used in the past to provide the smooth lateral loading. The effects of number of piles, arrangement of piles and different materials of the piles have been studied effectively.

2 Materials Used

2.1 Sand

The sand collected from Kharkai River, located near Jamshedpur city (India), is used in the present study. The direct shear test was performed on the sample of air dried sand. Relative density test was performed at three heights 25, 45 and 65 cm at which

Table 1 Index properties of soil

S. no.	Description	Value
1	Uniformity coefficient, C_u	2.7
2	Coefficient of curvature C_c	1.0
3	Fineness modulus of sand	3.34
4	Modulus of elasticity of sand	1.7 kg/cm ²
5	Specific gravity	2.76
6	Maximum dry density	1.71 g/cc
7	Minimum dry density	g/cc

the densities obtained were 58, 72 and 85%, respectively. The present study is done on 45 and 65 cm height of rainfall. The sand is classified as course sand in zone II by performing fineness modulus test depicting a value of 3.34, which lies in the range of 2.9–3.7 for coarser sand. Dry sieve analysis is also done to ensure the particle size distribution of the sand used (Table 1).

2.2 Pile

In this study, the scaling law is used to select the model pile material and its dimensions (Walsh 2005). Steel and wooden piles have been selected using the scale law. The length of the pile is 65 cm and diameter 4.4 cm. In case of steel pipe pile the wall thickness has been chosen as 0.25 cm. For wooden piles, solid wooden material of diameter and length same as that of steel is chosen. Pile cap in case of steel pile has been used of same material of thickness 4 mm having holes at required spacing so that the piles can be easily fixed by nut and screw mechanism. In case of wooden pile arrangement with the pile cap, two separate wooden plywood of thickness 15 mm are used, and the bottom plywood is having the hole while the top plywood has the head rest for the pile head. Fixity of the wooden pile cap to the wooden pile is done by the nut and bolt mechanism.

$$\frac{E_m I_m}{E_p I_p} = \frac{1}{n^5} \quad (1)$$

where E_m = modulus of elasticity of model pile; E_p = modulus of elasticity of prototype pile; I_m = moment of inertia of model pile; I_p = moment of inertia of prototype pile; and $1/n$ = scale factor for length. This is used to simulate the prototype pile in software GEO5, of 1000 mm diameter of steel pipe pile in case of steel piles and wooden pile of same diameter for wooden case study. The other scaling factors used in the study are presented in the table. The pile cap was attached to the piles leaving 150 mm above the sand surface as a free standing length for the group. Screwing of top of the piles and providing a hole in pile cap for threading the bolts in the piles to fix them was done to ensure partial fixity (Table 2).

Table 2 Scaling factors used in the study

Variable	Scaling factor
Length	1/10
Density	1
Stiffness	1/10
Stress	1/10
Strain	1
Pile flexural rigidity	1/10 ⁵
Pore fluid density	1/10 ³

2.3 Turn-Buckle and Spring Balance

Turn-buckle is used to provide lateral load by rotating the central shaft of the turn-buckle. It is connected from one side to the pile cap and from another side to the spring balance which measures the load applied by the turn-buckle at any instant. Dial gauges have been installed on both sides of the turn-buckle to measure the average deflection of the pile cap.

3 Experimental Programme

3.1 Experimental Setup and Instrumentation

The schematic diagram of the test setup is shown in Fig. 1. Tests were conducted on model piles group embedded in the sand in rectangular steel testing chamber of 1.3 m × 1.3 m area and 0.90 m depth. Piles were placed at suitable depth from top of the tank to maintain the L/D ratios of 12 and 15, where L denotes the embedded length of the pile into the sand and D being the diameter of the pile. Rectangular plate of thickness 4 mm has been used as the pile cap.

Turn-buckle has been used to apply the load and a spring balance is attached to the turn-buckle for noting down the pull generated by the turn-buckle. Two dial gauges have been set on both sides of the turn-buckle to obtain the average displacement of the pile cap in the direction of the load.

3.2 Soil Bed Preparation and Pile Installation

In the present study, the sand bed was prepared similar to the procedure that was adopted by Rollins et al. (2005) in layers maintaining the uniformity throughout the tank. The collected sand from Kharkai River was air dried and sieved through 4.5 mm sieve to obtain a range of particle size less than 4.5 mm. Sand sample were placed at a

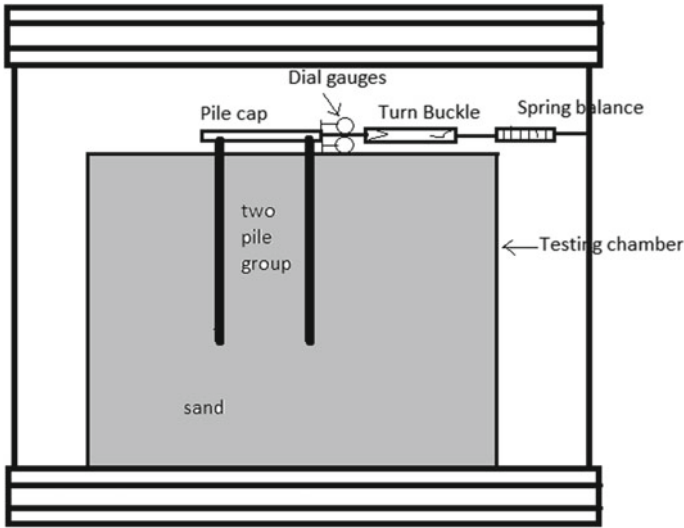


Fig. 1 Schematic diagram of the experimental setup

location where no moisture was entrapped into the sand. The pile has been placed at the desired depth, then sand was placed from a desired height uniformly throughout the tank with the help of aluminium box by rainfall method which was ensured to allow specific amount of sand uniformly through the hole provided for pouring the sand into the tank.

The uniformity of the sand was maintained by placing cans in each layer and calculating the density at the end of each test. In case the density did not simulate the required density of the sand, the test was repeated. The verticality of the pile has been done by placing spirit level on the head of the pile. In this case, the installation process simulates the bored pile condition. Model penetrometer test was conducted at each layer to ensure the uniform density all along. The density and un-drained shear strength were determined as per Bureau of Indian Standards BIS 2002. The un-drained shear strength of sand was measured by conducting tri-axial tests on the samples of 38-mm diameter and 76-mm height.

3.3 Test Procedure

Static lateral load was applied on the model piles by turn-buckle which was connected to the pile cap by nut and bolt mechanism at one end, the other being attached to the spring balance which was mounted on the horizontal rod parallel to the tank width movable at different heights. The loads were applied in increments and were maintained for a period of 30 min to allow the deflection to stabilize as per the Bureau of Indian Standards BIS 006b. During the application of static loads, the load



Fig. 2 Actual setup of dial gauges; turn-buckle, spring balance and pile attached with pile cap

transferred to the pile group was measured through the weighing balance and the deflection was measured by two dial gauges placed on the pile cap as shown in the schematic diagram (Fig. 2).

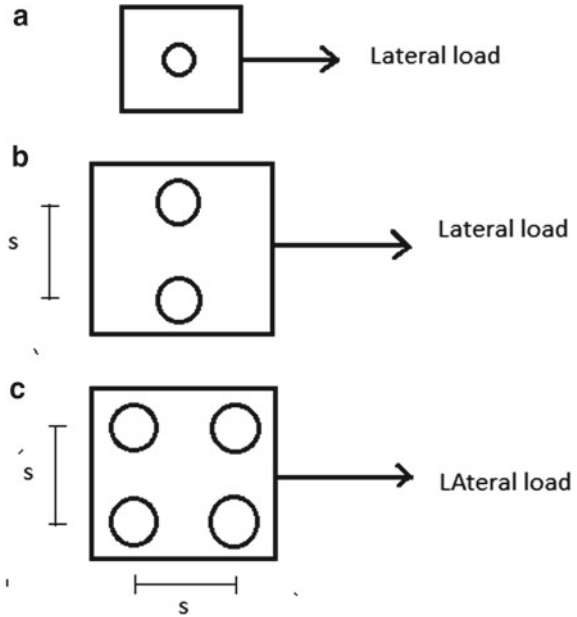
3.4 Testing Phases

Static lateral load tests were conducted on model single piles and pile groups embedded in sand. Experimental loading test was done at first and then the software analysis was done to substantiate the test results obtained experimentally. Tests were conducted in the following sequence:

1. Single steel and single wooden pile with embedment length to diameter L/D ratios of 12;
2. 1*2 and 2*2 steel and wooden pile groups with L/D ratio of 12 and 15 keeping S/D ratio 3.4.
3. Single steel and wooden pile in GEO5 software following the scaling factor and keeping the L/D ratio of 12 and 15 and S/D ratio 3.4.
4. 1*2 and 2*2 steel and wooden pile groups in GEO5 software following the same scaling factor and keeping L/D ratio of 12 and 15 and S/D ratio of 3.4.

The spacing in the direction perpendicular to the direction of loading S_T was kept constant as $3.4D$ for 1×2 and 2×2 pile groups. The deflection in the GEO5 software is calculated and compared with the deflection observed in experimental results. The configurations of pile groups are shown in Fig. 3.

Fig. 3 Configuration of pile groups used in the study: **a** 1 × 1, **b** 1 × 2, **c** 2 × 2



The piles are classified as rigid or flexible based on the relative stiffness factor K_{rc} (Poulos and Davis 1980).

$$K_{rc} = \frac{E_p I_p}{E_s L^4} \tag{2}$$

where E_p = modulus of elasticity of model pile material; I_p = moment of inertia of pile section; E_s = secant modulus of soil; and L = embedded length of pile. The pile is said to be rigid if K_{rc} is greater than 10^{-2} and flexible if K_{rc} is less than 10^{-2} (Poulos and Davis 1980).

4 Results and Discussion

4.1 Group Efficiency

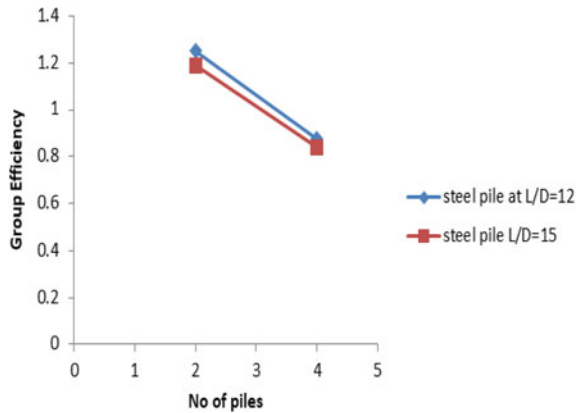
Pile group interaction effect is also studied by calculating the group efficiency and is given as

$$\eta = \frac{Q_G}{\eta_s Q_s} \tag{3}$$

Table 3 Group efficiency of steel pile experimental

Length/diameter (L/D)	Pile group	Spacing/diameter S/D	Group efficiency
12	1 × 2	3.4	1.25
	2 × 2	3.4	0.875
15	1 × 2	3.4	1.19
	2 × 2	3.4	0.84

Fig. 4 Group efficiency versus number of piles



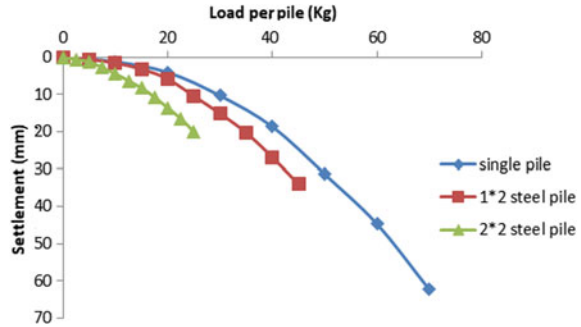
where Q_G = lateral load capacity of the group corresponding to a deflection of 0.2D; Q_S = lateral load capacity of the single pile corresponding to a deflection of 2.2D; and n_g = number of piles in the group. Group efficiencies of the single pile and group of piles have been shown in Table 3 corresponding to a deflection of 0.23 D (Fig. 4).

4.2 Effect of Number of Piles

To evaluate the effect of number of piles on the behaviour of pile groups at 3.4D spacing with L/D ratios of 12 and 15, the average load-pile head deflection curves for groups with varying number of piles are presented in Fig. 5. At larger pile head deflections, the average pile group response shows softer curve than that obtained in the case of single pile.

This points it out the reduction in stiffness of piles in the group. It can now be interpreted from Fig. 5 that the degree of nonlinearity in the response of piles in the group tends to increase with the size of the pile group. This happening of increase in the nonlinearity occurs due to the interaction effect of the piles in the group. Also their combined load bearing zone into the sand strata comes out as a reason for such nonlinearity.

Fig. 5 Load settlement behaviour of steel piles with $L/D = 12$ and $RD = 70\%$



This interaction zone under the soil of the pile in the pile group is solely responsible for the increase in the nonlinearity and reduction in the stiffness of the pile group. The percentage reduction in lateral capacity, corresponding to a deflection of $0.23D$, has been computed and been presented in graphs.

This provides a route to the conclusion that there is an increase in the percentage reduction of the lateral capacity of the pile groups as compared to that is single pile with increase in the number of piles in the group. Also, the fact that a single pile shows less deflection at the applied load as compared to that applied to the pile group is considered as another reason for reduction in lateral capacity. There occurs an increase in overlapping of stress zone due to increased number of piles in the group which leads to a sharp reduction in the lateral capacity.

4.3 Effect of Embedment Length

The lateral capacity of 1×2 groups at $3.4D$ spacing increases with embedment length, as shown in Table 2, due to the additional passive resistance developed along the increased embedment length (Figs. 6 and 7).

4.4 Effect of Sand Density

Sand density affects the load capacity of piles in sand. With more dense sand, the load capacity of the pile decreases. Two densities of sand have been obtained at 45 cm rainfall and 65 cm rainfall. At these two, the settlement behaviour of piles has been studied. Owing to increase in density, the load carrying capacity increases due to more firm soil strata to withhold the piles. Corresponding to same settlement value of $0.23D$, the load carrying capacity of pile shows the inverse pattern with the increase in number of piles (Figs. 8 and 9).

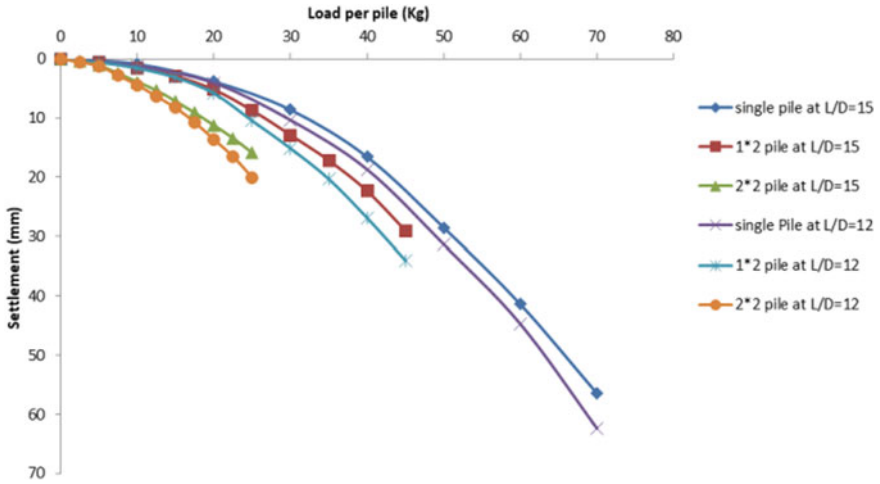


Fig. 6 Load settlement behaviour of steel pile at RD = 70%

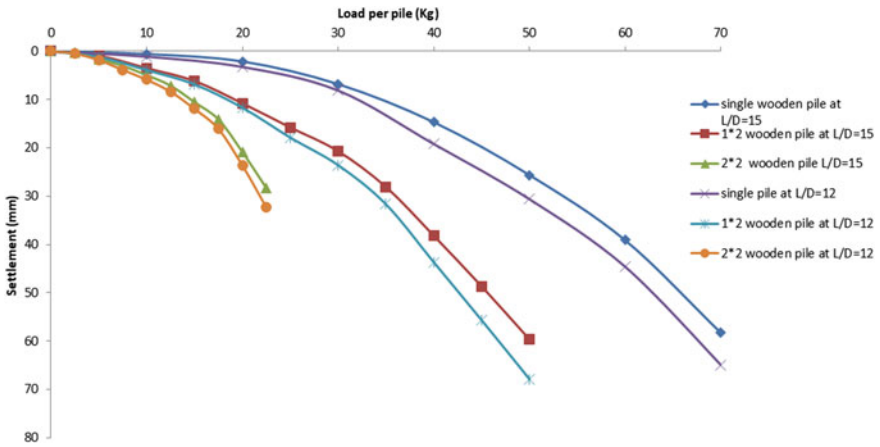


Fig. 7 Load settlement behaviour of wooden pile at RD = 70%

4.5 Effect of Pile Material

Pile material has different effect on the loading capacity of the pile group. Steel and wooden piles have been compared based on their loading capacity. At different L/D ratio and at different sand density, a comparative study is done to show that steel pile has more load carrying capacity. Behaviour of 1 × 2 and 2 × 2 pile group configurations has been shown for both wooden pile and steel pile. The difference in the load carrying capacity of pile group in both the configurations is due to more interaction

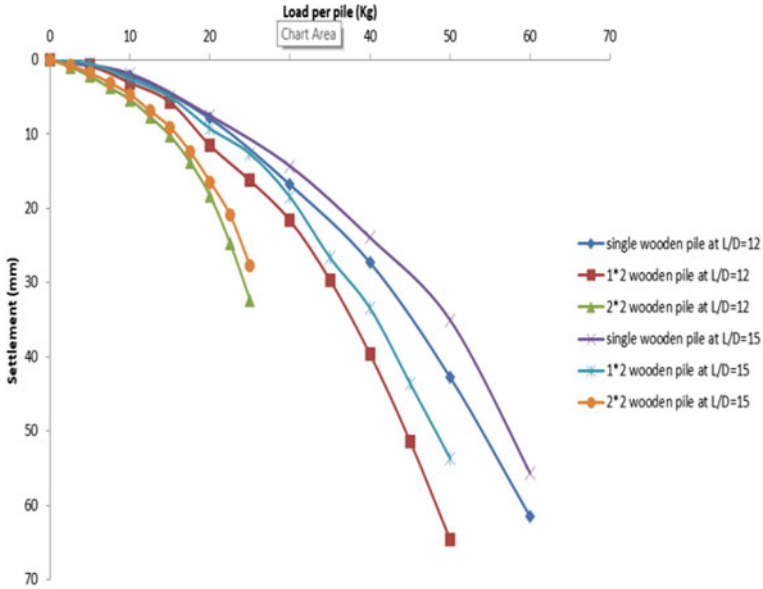


Fig. 8 Load settlement behaviour of wooden pile at RD = 85%

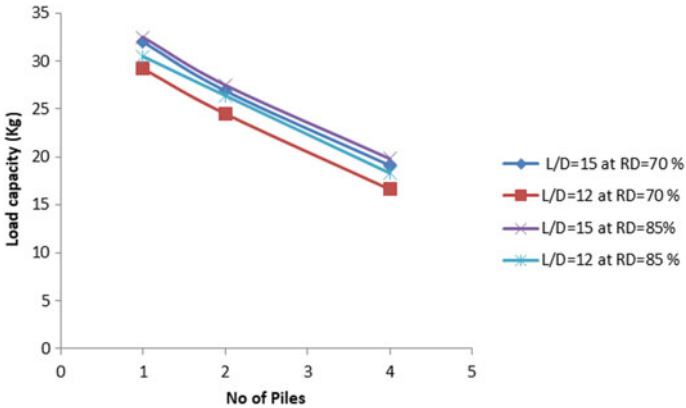


Fig. 9 Load capacity at different relative density and different L/D ratio

in case of 2 × 2 pile group configuration as compared to 1 × 2 configuration. This interaction occurring in both directions in case of 2 × 2 configuration causes it to deflect less as compared to that in case of 1 × 2 pile configuration in which only one side interaction occurs (Figs. 10 and 11).

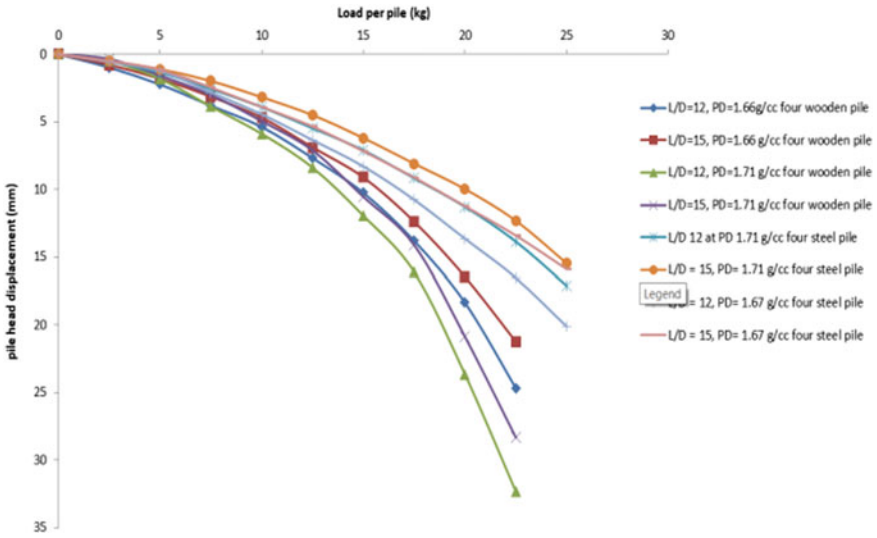


Fig. 10 Load displacement behaviour of 2*2 steel and wooden pile groups

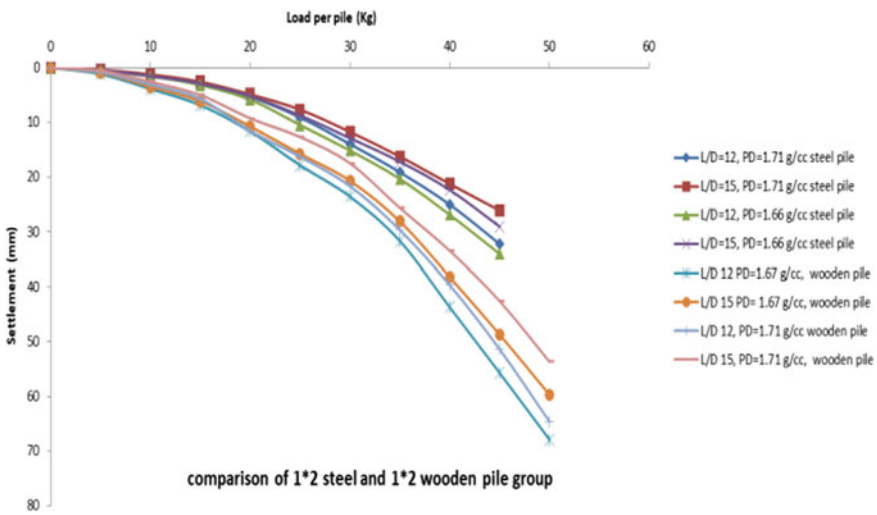


Fig. 11 Load displacement behaviour of 1*2 steel and wooden pile groups

4.6 Loading Capacity of Piles in Group

Piles in group show the decreasing efficiency with number of piles. Single pile shows maximum loading capacity as compared to piles in group due to interaction effect of piles in group. The piles have been studied for their capacity corresponding to the

Fig. 12 Load capacity of wooden piles versus number of piles

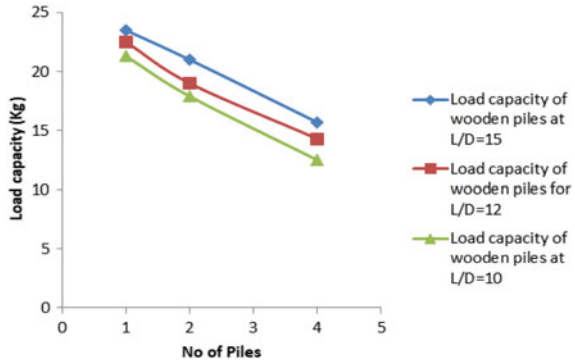
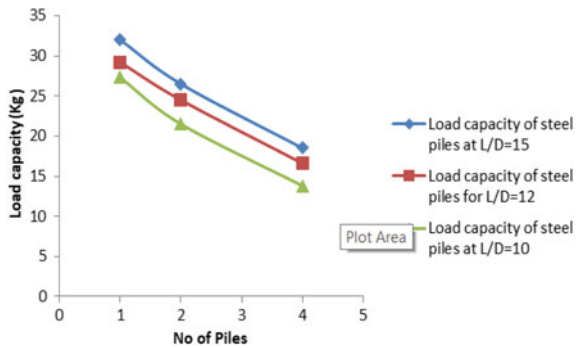


Fig. 13 Load capacity of steel piles versus number of piles



settlement of 0.23D for single as well as group of piles. Both the steel and wooden piles show the decreasing pattern of load carrying capacity with increase of number of piles. This behaviour of load carrying capacity occurs due to the interaction effect of piles. For a single pile, the load carrying capacity corresponding to 0.23D settlement is greater as compared to that of 2 pile or 4 pile group at the same settlement amount (Figs. 12 and 13).

Comparison curve is shown in Fig. 14 with previous study of Gandhi and Selvam (1997). The comparison curve is drawn on the dimensionless quantity to compare the test results effectively.

5 Software Test Results

5.1 Pile Head Displacements

Pile head displacements that have been obtained in the case of single steel and single wooden pile are analogous to that of experimentally obtained test results.

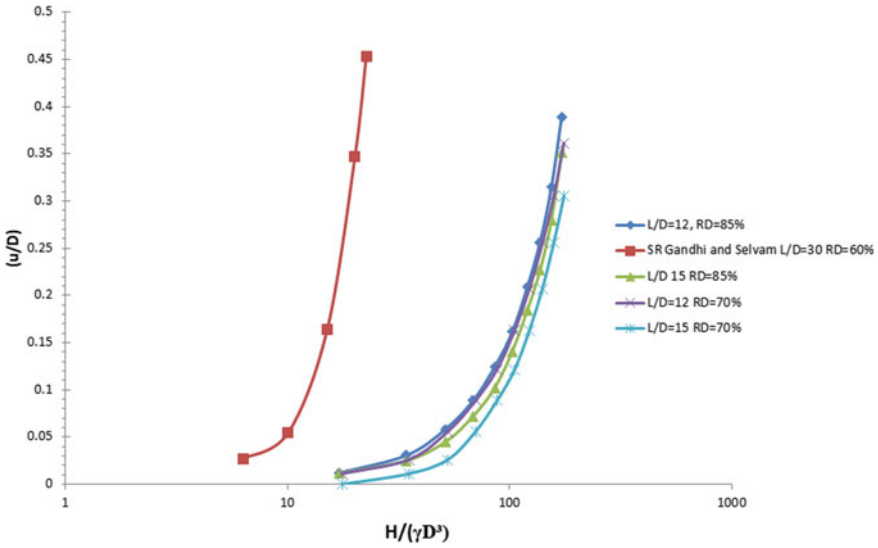


Fig. 14 Comparison of four steel pile groups

The soil properties in the case of the software analysis were kept the same as that of during the experimental tests. The pile head displacements in case of software analysis are somewhat greater as compared to that of load displacements obtained in experimental tests. Displacement behaviour of prototype pile in software analysis for each configuration has been depicted in subsequent figures. The difference in the displacement occurs due to change in the site condition, presumed analysis values in software and also due to the change of pile dimension and other factors (Figs. 15, 16 and 17).

Figure 18 shows the pile head displacements of single steel and single wooden pile with increase in the embedded length into sand layer. For the lesser embedded depth of the pile in the sand, the difference in the pile head displacements is larger as compared to that in case of larger embedded length of the pile into the sand. This occurs due to more resistant behaviour of the sand in larger embedded length of the pile in the sand. A comparative study of the steel and wooden pile can also be interpreted by the graph as for wooden piles the pile head displacements are greater as compared to that for steel pile due to its rigidity and larger modulus of elasticity as compared to wooden piles.

5.2 Moment Distribution Trends

The curve in Fig. 19 shows the trend analysis of moment distribution curve in the laterally loaded piles in sand. The comparison curve has been drawn with the results

Fig. 15 Load pile head displacement of single steel pile at $L/D = 12$ at 70% RD

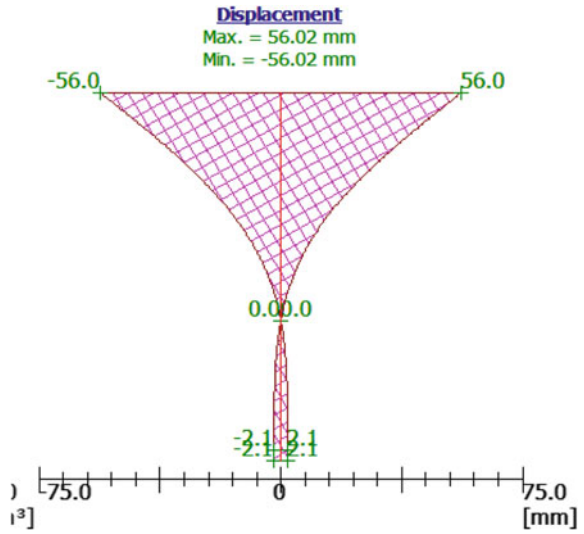
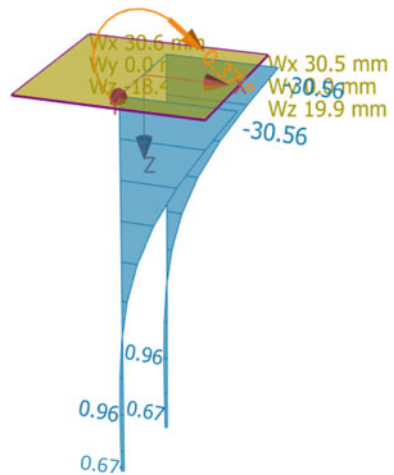


Fig. 16 Horizontal pile head displacements of two pile groups in prototype $L/D = 12$ and RD of 70%



of Poulos and Davis (1969). The results shown here have been converted into non-dimensional form to show the exact comparison study of laterally loaded piles.

6 Conclusion

Based on the results of the present experimental work on model pile groups embedded in sand, the following conclusions are drawn:

Fig. 17 Horizontal displacements of pile groups in prototype $L/D = 12$ and RD of 70%

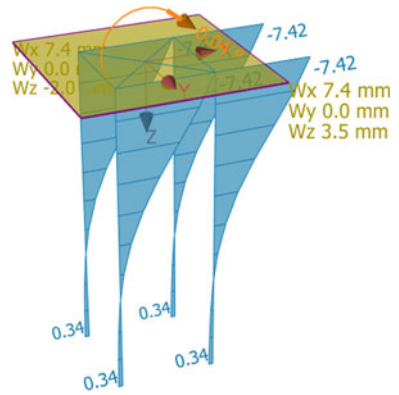


Fig. 18 Pile head displacements in computer analysis

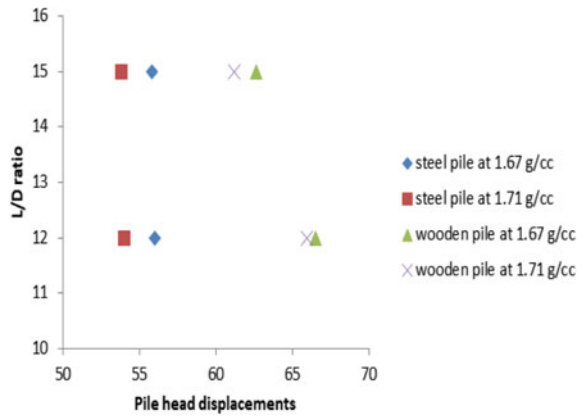
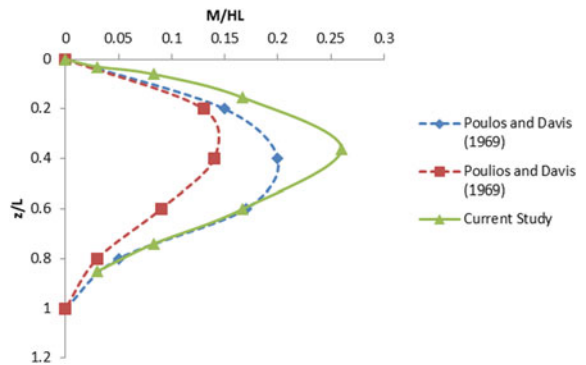


Fig. 19 Comparison study of moment distribution



1. Pile–soil–pile interaction leads to a considerable reduction in the lateral load capacity of piles in the groups as compared to the single pile. With the increase in number of piles in the pile group, the load capacity of the pile group increases significantly. For the same settlement value of $0.23D$ load taken up of 2×2 pile groups is more than single pile.
2. The density of sand affect the loading capacity of the pile groups and single as well. Increase in the density reduces the lateral load capacity of the pile group and single pile.
3. The embedment length is an important factor for the loading capacity and the interaction of the pile. With greater L/D ratio, the loading capacity of the group and single pile decreases. At L/D ratio of 15, the lateral loading capacity is 10–12% higher as compared to that at L/D ratio of 12 for steel piles and 14–18% for wooden piles.
4. Group efficiency decreases as the number of piles in the group increases due to the interaction effect. A reduction of 40% of efficiency has been obtained. Pile group efficiency decreases with the increase in the number of piles in the pile group. The efficiency obtained in case of pile group at the same S/D ratio has the decreasing order with change of L/D ratio and number of pile in the group. At the L/D ratio of 12, the difference in the efficiency that has been obtained for two pile group and four pile group is 42.85%. While for L/D ratio of 15, this difference in the efficiency obtained is 41.67%.
5. For $0.23D$ settlement value, the loading capacity of steel pile group increases by 14–18% for 1×2 configurations and 8–10% for 2×2 configurations.
6. The difference of the settlement of the single wooden pile and single steel pile has been observed up to 15–18% for the same average loading.

Notations:

The following symbols are used in this paper:

C_u	Uniformity coefficient
C_c	Coefficient of curvature
D	Diameter of the pile
E_m	Modulus of elasticity of model pile
E_p	Modulus of elasticity of prototype pile
E_S	Secant modulus of soil
I_m	Moment of inertia of model pile;
I_p	Moment of inertia of prototype pile;
K_{rc}	Relative stiffness factor
L	Length of the pile
P	Soil reaction
$1/n$	Scale factor for length
Q_G	Lateral load capacity of the group
Q_S	Lateral load capacity of the single pile
S	Spacing of pile in the direction of loading as well as in transverse to the loading
η_g	Number of piles in the group

Acknowledgments I would like to express my sincere gratitude to my Advisor Prof. Ashok Kumar Khan, Department of Civil Engineering, National Institute of Technology, Jamshedpur for the continuous support towards my study and related research, for his patience, motivation, and immense knowledge. His guidance helped me in completion of research and writing of this dissertation. He definitely provided me with the tools that I needed to choose in the right direction. His faith in me from the very start of the project helped me to complete it effectively and pushed me to realize my potential.

I am extremely grateful to my family, especially to my father and mother. Without their support by my side nothing could have possible. At the same time, all other family members have also been a constant source of support in my life.

References

- Broms B (1964) Lateral resistance of piles in cohesion less soil. *J Soil Mech Found Eng* 90(3):123–156
- Brown DA, Morrison C, Reese LC (1988) Lateral load behaviour of pile group in sand. *J Geotechn Eng ASCE* 114(11):1261–1276
- Gandhi S, Selvam S (1997) Group effect on driven piles under lateral load. *J Geotech Geo-environmental Eng*-123. [https://doi.org/10.1061/\(asce\)1090-0241\(1997\)123:8\(702\)](https://doi.org/10.1061/(asce)1090-0241(1997)123:8(702))
- Phanikanth VS, Choudhary D, Reddy CR (2010) Response of single pile under lateral loads in Cohesion-less soils. *Electron J Geotech Eng* 15:813–830
- Poulos HG, Davis EH (1980) *Pile foundation analysis and Design*. Wiley, New York
- Poulos HG (1971a) Behaviour of laterally loaded piles-single piles. *Proc ASCE J Soil Mech Found Eng Div* 97(SM5):711–731
- Poulos HG (1971b) Behaviour of laterally loaded piles: Pile groups. *Proc ASCE J Soil Mech Found Eng Div* 97(SM5):733–751
- Rollins KM, Peterson KT, Weaver TJ (1998) Lateral load behaviour of full scale pile group in clay. *J Geotech Geoenviron Eng* 124(6):468–474
- Rollins KM, Lane JD, Gerber TM (2005) Measured and computed lateral response of a pile group in sand. *J Geotech Geo-environmental Eng ASCE* 131(1):103–114
- Walsh JM (2005) Full scale lateral load test of a 3 x 5 pile group in sand. Department of Civil and Environmental Engineering, Brigham Young University

Review of Load Test Performance of Base Grouted Concrete Piles



D. Nagarajan, K. Raja Rajan, and T. Vijayakumar

Abstract Bangladesh is a low-lying country crisscrossed by many rivers. Large diameter bored piles are replacing caisson foundation in Bangladesh. Bored cast in situ pile is a popular choice for heavy loaded structures due to the ability to adjust the pile length suitably in case of any variation found in the actual geological strata. Geological strata are predominantly silt in nature and N-value in this region is less than 5 up to 15 m depth. Pile design is based on field N-values and laboratory test results. Pile capacities estimated through static formula are in co-relation of N-value and laboratory test results. Two 1.5 m diameter bored cast in situ piles without base grout and two 1.5 m diameter bored cast in situ piles with base grout were casted, and initial load test was performed on these piles to finalize the pile length. This paper presents the vertical load performance of 1.5 m diameter base grouted concrete piles in comparison with ungrouted bored piles.

Keywords Angle of internal friction · Base grouting · End bearing · Initial pile load test · N-value · Settlement

1 Introduction

A railway bridge of length 700 m is planned across the Rupsa river with approach viaduct running length of 2.2 km on both sides. Super structure is of steel girder in approach viaduct, and steel truss in main bridge portion has been planned. Substructure of approach viaduct portion comprises 1.5 m diameter bored cast in situ pile of 800 nos. approximately and main bridge is of 2.5 m diameter of 48 nos. bored cast

D. Nagarajan (✉) · K. Raja Rajan · T. Vijayakumar
CMPC division, EDRC, HCI, L&T Construction, Chennai, India
e-mail: nagarajan-d@Intecc.com

K. Raja Rajan
e-mail: k-raja@Intecc.com

T. Vijayakumar
e-mail: tvk@Intecc.com

Table 1 Project location details

Type	Details
Terrain type	Alluvial-cum piedmont plain
Hottest month	April–May
Coldest month	December–January
Annual average temperature	11.3° (in winter) 34.5° (in summer)
Rainfall season	June–September
Annual average rainfall	1842 mm

in situ pile. Pile designed during tender stages with the available soil reports carried out in initial stages. Pile capacity is estimated through static formula based on correlation of N-value and laboratory results. To verify the pile capacities predicted during tender stage, detail soil investigation and pile load tests were planned. Every pier as one borehole each with depth of 15 m below the pile termination level is ordered to evaluate the soil parameters for every change of layers. Every pile group in each pier as one initial pile load test to ensure the given pile length is sufficient to take the estimate safe working load.

1.1 Location

The southwestern coastal belt of Bangladesh, especially the Khulna-Satkhira coastal belt, is endowed with multi-layer prolific aquifers composed of deltaic sediments—a complex mixture of sand silt and clay. Hydrogeologically, the southwestern coastal belt of Bangladesh belongs to the Holocene Coastal Plains (Zone-V) (Table 1).

1.2 Soil Profile

Geotechnical investigations were carried up to 60 m depth at every pier location to ascertain the actual soil strata. Subsoil profile of the particular stretch is dominated by silt content, and the N-value in this region is less than 5 in top 10 m soil strata. Generally, top 10 m is of sandy silt with soft layer, followed by 15 m of poorly graded sand with loose to medium dense and then followed by silty sand till the termination of bore hole. Standard penetration tests were conducted at every 1.5 m up to 15 m depth and 3.0 m interval beyond 15 m depth up to exploration depth. Disturbed and undisturbed samples were taken from boreholes for testing soil parameters. Angle of internal friction was co-related based on SPT N-values, and laboratory values are used in order to perform pile capacity calculations. Subsoil profile encountered in the proximity of test pile location is presented in Fig. 1.

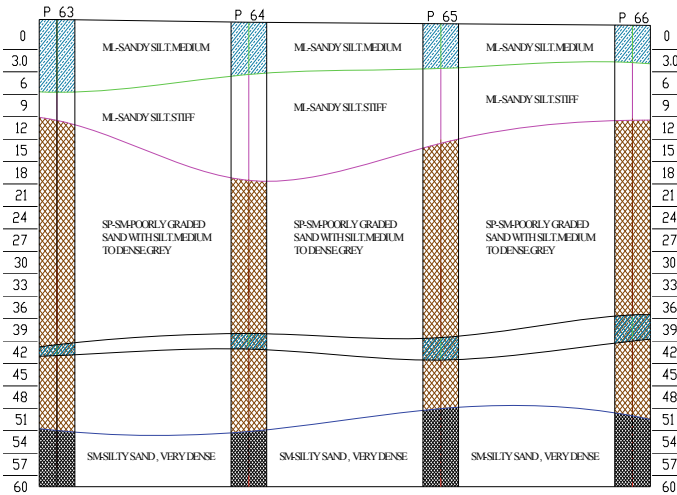


Fig. 1 Soil profile in the proximity of P63 to P66

2 Test Pile Arrangement

Kentledge system is designed to perform the initial pile load test. Water table is at the ground level during the initial pile load testing time, so ground improvement will not be effective to support the kentledge, so steel liner was used to support the kentledge load. Concrete blocks were stacked over steel girders in order to take reaction to test pile. Two hydraulic jacks of 1000 MT are used along with grillage beam to transfer the load to the pile. Four dial gauges were placed using supporting block in order to measure the settlement of the pile (Fig. 2).

2.1 Measurement of Load and Displacement

The jack, pressure gauge and power pack were checked and calibrated prior to commencement of test. Pressure developed in pressure gauge was monitored and the corresponding load was read from calibration certificate. The pile head movement was measured by using four dial gauges against independent reference beams. The supports are sufficiently embedded into the ground at distance more than 3D clear between support and test pile. Kentledge arrangement for test pile (TP-01) is shown in Fig. 3.

The readings were recorded in all the dial gauges, the load cell and the pressure gauge for the jack at 1-min intervals on the time-settlement data sheet. The loading pattern to the pile is 50, 100, 125, 150, 175, 200 and 250% of SWL and the settlement of the pile is monitored in both loading and unloading cycle at defined interval time.

Fig. 2 Test pile arrangement using kentledge method

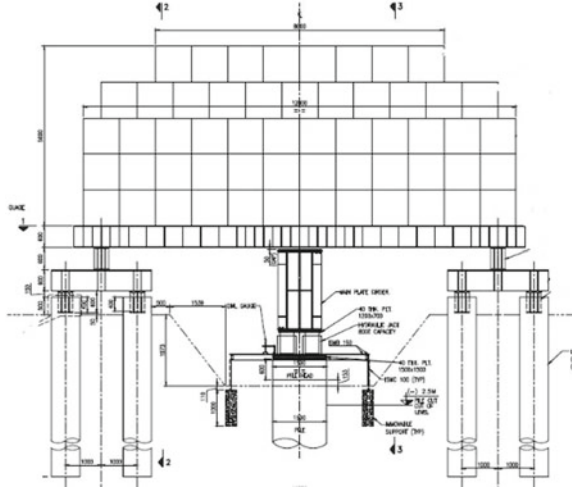


Fig. 3 Test pile arrangement—site photo



3 Test Pile TP-01 Details

Pile design carried out as per IS 2911 method and design is normally based on field test such as standard penetration test N-values and lab results. Coefficient of earth pressure taken as 1 and angle of wall friction between pile and soil was taken the same as angle of internal friction of soil. Overburden pressure was limited to 20 times the diameter of pile. By using the above said method and above assumptions, it has been estimated that 1.5 m diameter and 40 m length of pile would be sufficient to take safe working load of 570 MT.

Table 2 Details of test pile-01

Details	Test pile (TP-01)
Type of pile	Bored cast in situ pile
Diameter (m)	1.5 m
Termination depth	40 m
Design load	570 MT
Test load	1425 MT
Method of installation	Hydraulic rotary method under bentonite slurry
Drilling equipment	Hydraulic rig BG-25C

In order to validate the design, initial pile load test was planned. Details of pile load test are tabled in Table 2.

Test pile is constructed in a manner similar to that to be used for construction of working pile, and by the use of similar equipment and material. Permanent steel liner is installed and boring is done by hydraulic drilling rig under bentonite slurry. Concrete is mixed in batching plant and poured through tremie pipe. During drilling soil strata were checked and all the relevant data recorded. Pile head was trimmed and prepared before testing.

3.1 Results of Test Pile TP-01

The results were interpreted through load-settlement curves by applying various methods for determining the allowable load bearing capacity of the pile. Pile load test is terminated after reaching 777 MT load since the settlement exceeds 10% of pile diameter, that is, 150 mm. Load-settlement curve for test pile 01 is presented in Fig. 4.

4 Detailed Soil Investigation

Owing to unpredictable behavior of pile, consultant and contractor jointly proposed for detailed soil investigation, that is, borehole under each pier. A total of 144 boreholes has been planned to drill in the proximity of bridge pier alignment. Tests, like direct shear test, UCC, tri-axial test, grain size distribution and so on, to be performed at which depth were predetermined. Typical graph between SPT N-value and depth for P65 and P66 is shown in Fig. 5. Relative density range between loose and very dense increases with increase in depth (Fig. 5).

Fig. 4 Load-settlement curve for test pile-01

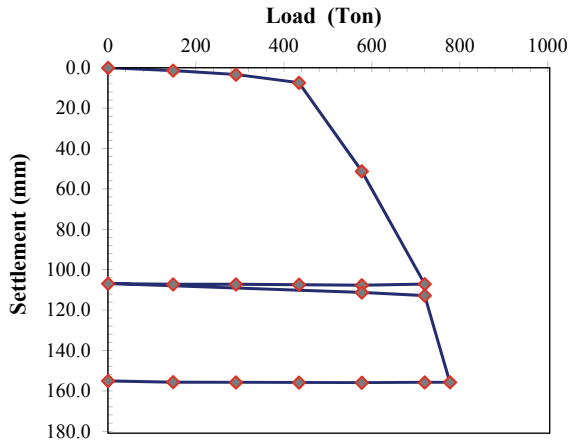
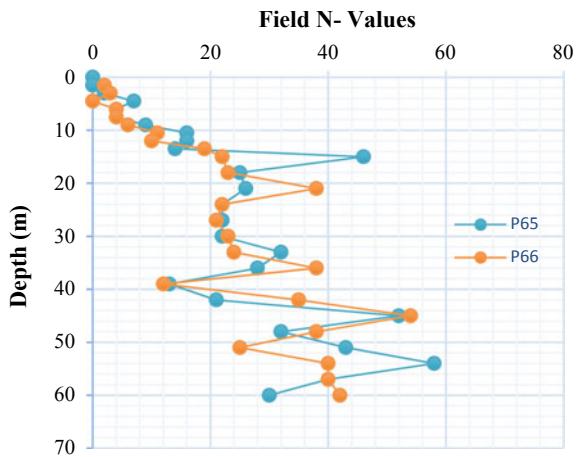


Fig. 5 Field SPT N-values versus depth for P65 and P66



5 Redefining Geotechnical Parameters

With detailed investigation data, pile capacity has been re-evaluated for two pier locations P65 and P66. Based on particle size distribution and SPT-N values, pile-soil friction angle is revised. Based on particle size distribution, soil layer encountered is separated as per Table 3 and then redefined as per SPT-N values as tabulated in Table 4.

Based on the above redefined soil properties, test pile (TP-010) reveals the pile capacity of 390 tons which is already verified by load test, so same redefined pile capacities were assumed for test pile (TP-02) design. Test pile (TP-02) of 1.5 m diameter pile is designed, pile capacity for 52 m length estimated as 450 MT and the same is presented in Fig. 6 (Table 5).

Table 3 Soil layer as per PSD requirement

Prefix	PSD requirement
1A	Clay + Silt $\geq 50\%$
1B	$20\% = < \text{Clay} + \text{Silt} < 50\%$
2	Clay + Silt $< 20\%$ and Coarse Sand $< 10\%$
3	Clay + Silt $< 20\%$ and Coarse Sand $\geq 10\%$

Table 4 Soil layer as per SPT N-values

Suffix	PSD requirement
a and b	$N \leq 10$
c	$10 < N \leq 17$
d	$17 < N \leq 32$
e	$32 < N \leq 50$
f	$N > 50$

Fig. 6 Estimation of pile capacity for TP-01 and 02

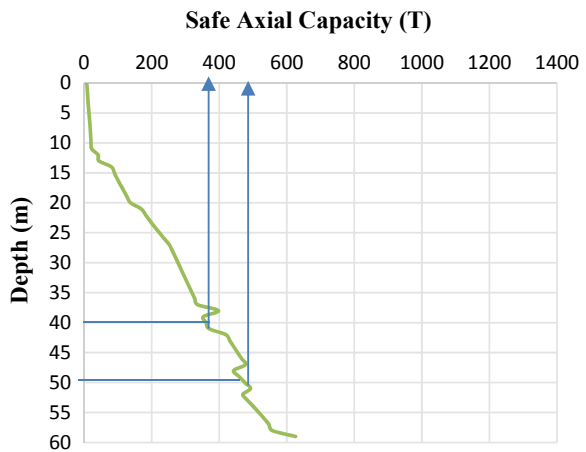


Table 5 Design parameter for pile design

Soil type	Unit weight (kN/m ³)	Friction angle (Φ)	Soil-pile friction angle (δ)
Unit 1a and 1b	16	–	–
Unit 2a, 2b and 2c	17	25	22
Unit 2d and 2e	18	28	25
Unit 2f	19	30	27
Unit 3e	19	30	27
Unit 3e	19	32	28

Table 6 Details of test pile-02

Details	Test pile (TP-02)
Type of pile	Bored cast in situ pile
Diameter (m)	1.5 m
Termination depth	52 m
Revised design load	450 MT
Test load	1140 MT
Method of installation	Hydraulic rotary method under bentonite slurry
Drilling equipment	Hydraulic rig BG-25C

6 Test Pile TP-02 Details

Test pile of depth 52.0 m is casted nearby location in the proximity of piers P65 and P66 to evaluate the pile capacity as per redefined soil parameters. Details of pile load test are tabled in Table 6.

6.1 Results of Test Pile TP-02

Test pile (TP-02) is carried out as per maintained load method. Test was terminated as pile reaches the settlement of 150 mm as it exceeds the 10% diameter of pile, and the corresponding load measured was 1212 MT. Load at 18 mm settlement was 690 MT and safe load was 460 MT obtained from test pile (TP-02) which validates the design assumption to estimate pile capacity. Load-settlement curve for test pile TP-02 is presented in Fig. 7.

7 Comparison of Test Pile Results

Test pile TP-01 test load estimated as 1425 MT for 40 m pile length, but after conducting pile load test for 10% of pile diameter, that is, 150 mm settlement occurred for the applied load of 777 MT. Load at 18 mm settlement was 469 MT, that is, safe load of 312 MT only obtained which leads to redesign the pile as it could not be able to meet the requirement. Test pile TP-02 working load estimated as 1140 MT for 52 m length, after conducting pile load test for 10% of pile diameter, that is, 150 mm settlement occurred for the applied load of 1212 MT. Load at 18 mm was 690 MT, that is, safe load as 460 MT which was parallel to the estimated pile capacity as per redefined soil properties in alluvial deposit (Table 7).

Fig. 7 Load-settlement curve for test pile-02

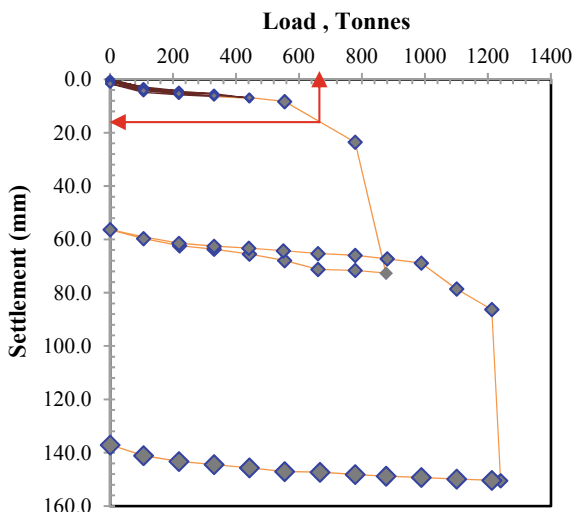


Table 7 Comparison of test pile results

Test results	Test pile (TP-01)	Test pile (TP-02)
Max. applied load (Ton)	777.6	1240.0
Total settlement, mm	155.7	150.4
Net settlement, mm	155.1	137.0
Final load at 18 mm settlement	469 MT	690 MT
Safe load (2/3*Load at 18 mm)	312 MT	460 MT

8 Base Grouting

Base grouting technique was introduced to increase the end bearing of the bored cast in situ pile. Base grouting techniques are widely used to increase the toe resistance of bored pile. Flat jack and tube-a-manchette method are generally employed and for this pile the latter one is selected. Access pipe and tube-a-manchette are shown in Fig. 10. Grout is prepared by mixing OPC and plain water with little bentonite. Grout pump model GI ET 2 of Soilmec SPA Italy was used for grout pumping.

The flowchart describes the activities involved in base grouting of pile in Fig. 8.

A pair of concrete-embedded strain gauge was placed near bottom of the pile to monitor load transfer behavior of the pile through the pile toe. The grouting technique carried out for test pile in order to increase the toe capacity and the details are presented in Table 8.

Grout controlling criteria based on the injected grout volume if it is lesser than 300 L and pressures achieves 3.0–6.0 MPa on second stage. Injection pressure is

Fig. 8 Flowchart of base grouting operation

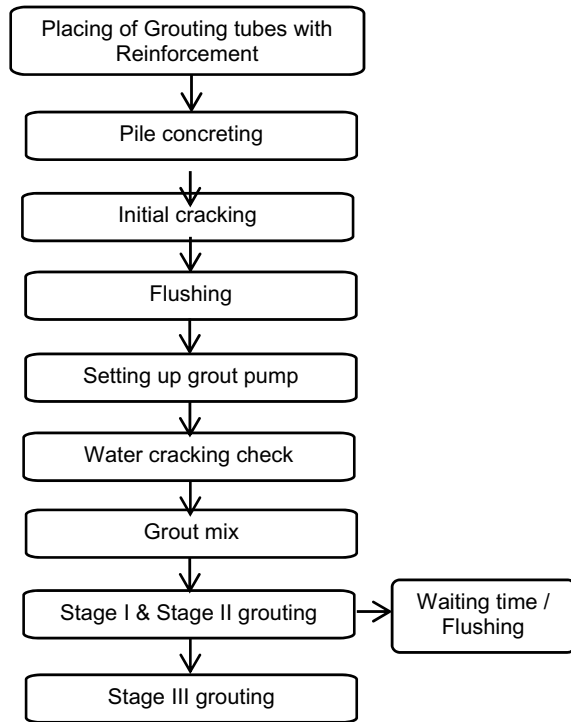


Table 8 Grouting technique details

Activity	Details
Setting time	Pile concrete strength achieves at least 20 MPa
Water cracking check	Done separately for each circuit less than 12 h
Grout mix (for 1000 L)	Cement—1115.7 kg, water cement ratio—0.5, water—557.7 kg, admixture 1% of cement weight
Injection rate	10 L/min for each separate circuit, then
Injection rate	5 L/min maximum,
Maintaining pressure	3.0–6.0 MPa maximum

monitored at inlets and outlets. Tentative cement grout pumped in three stages for test pile and quantities is as follows (Figs. 9, 10, 11 and 12):

- 1st stage: 600 L
- 2nd stage: 750 L
- 3rd stage: 450 L



Fig. 9 Site photo showing grout pipes on test pile

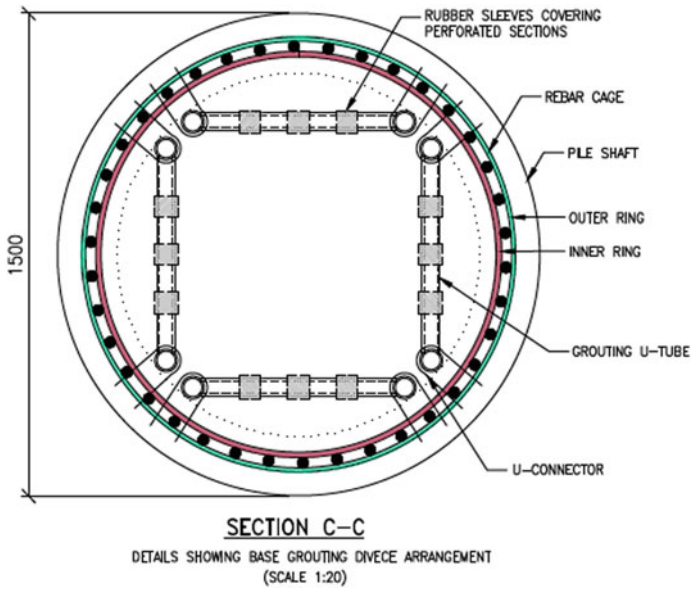


Fig. 10 Plan of pile showing grouting pipes

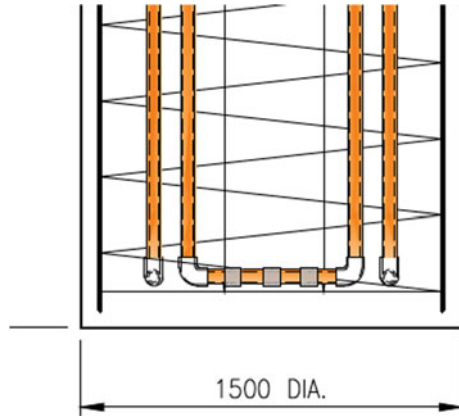
8.1 Grout Mix

Grout mix is a base parameter to achieve the desired capacity of pile. Cement, water, BASF and bentonite were the main ingredients for grout mix. As per specification, for 1000 L of grout volume the following are the mixing ratio: Cement 822 kg, water



Fig. 11 Site photo showing reinforcement cage with grout pipes

Fig. 12 Grout tube arrangement at the bottom of pile



cement ratio is 0.6, water is 493.2 kg, BASF Master flow 150 is 1% of cement, that is, 8.22 kg, and bentonite is 3% of cement content, that is, 24.66 kg. In order to ensure the flow ability of grout mix, initial temperature of mix shall not exceed 30 °C (Fig. 13).

Fig. 13 Grout mix preparation



8.2 Grouting Stages

Grouting has been done in stages in order to achieve the grout strength. I-stage is referred to as permeation grouting, whereas II-stage is referred to as compaction grouting. Grout mix is kept ready as per the specification. Grout pressure and grout injection rate is also predefined as per the specification. Pressure of 3 MPa is to be applied during initial stage of grouting and 6 MPa to be achieved during final grouting stage. Target grout volume for each circuit is estimated as 145 L. Holding time shall be 2 h with same pressure after initial grouting is completed. Water flushing shall be carried out immediately after holding time. Arrangement of grout pile in pile head is shown in Fig. 14.

Dial gauges are fixed and monitored for uplift of pile. If any uplift occurs, grouting shall be stopped for holding time, and then the remaining volume shall be applied in the third stage of grouting (Fig. 15).

9 Test Pile TP-03 Details

Test pile of depth 45.0 m with base grouting is casted in the nearby location in the proximity of piers P65 and P66 to evaluate the pile capacity. Base grouting was carried out on stages with different grouting pressure in order to densify the soil at the bottom of the test pile (Table 9).

Fig. 14 Arrangement of grout pipe at pile head

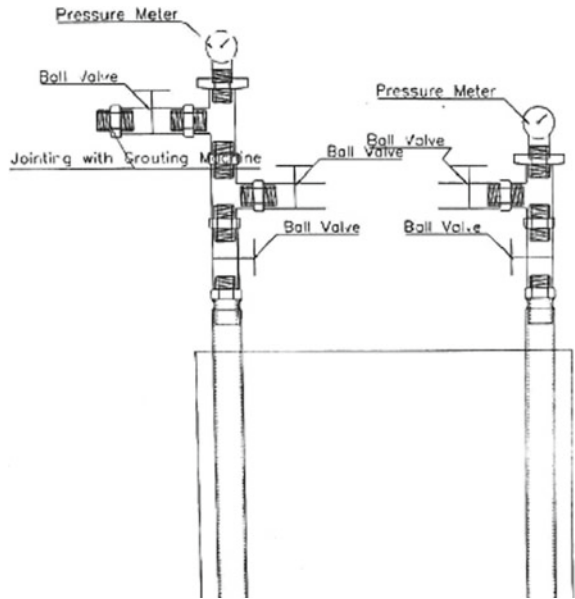


Fig. 15 Arrangement of grout pipe at pile head



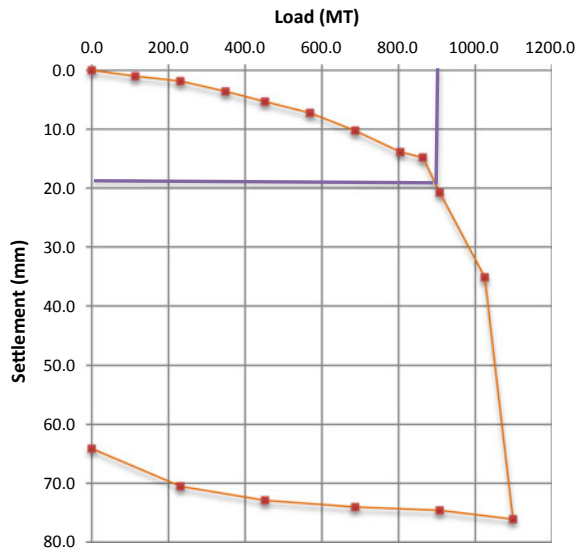
9.1 Results of Test Pile TP-03

Test pile with base grouting (TP-03) is carried out as per maintained load method. Test was terminated as pile reaches the settlement of 74 mm and the corresponding load measured was 1098 MT. Load at 18 mm settlement was 890 MT only and marginally safe load obtained was 590 MT and it did not reach the test load of 1425

Table 9 Details of test pile-03

Details	Test pile (TP-03)
Type of pile	Bored cast in situ pile with base grouting
Diameter (m)	1.5 m
Termination depth	45 m
Revised design load	570 MT
Test load	1425 MT
Method of installation	Hydraulic rotary method under bentonite slurry
Drilling equipment	Hydraulic rig BG-25C

Fig. 16 Load-settlement curve for test pile-03



MT. So it has been planned to cast test pile-04 with increased depth of 52.0 m to check the pile capacity increase. Load-settlement curve for test pile TP-03 is presented in Fig. 16.

10 Test Pile TP-04 Details

Test pile with increased depth 52.0 m with base grouting is casted in the nearby location in the proximity of piers P65 and P66 to evaluate the pile capacity. Similarly, as per TP-03, base grouting was carried out on stages with different grouting pressure in ordered to densify the soil at the bottom of the test pile (Table 10).

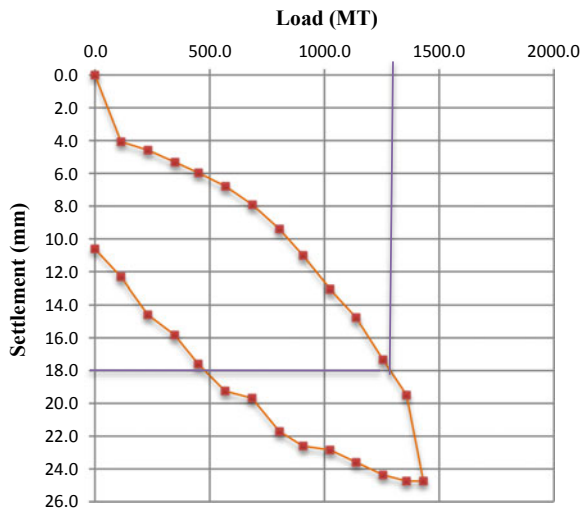
Table 10 Details of test pile-TP-04

Details	Test pile (TP-04)
Type of pile	Bored cast in situ pile with base grouting
Diameter (m)	1.5 m
Termination depth	52 m
Revised design load	570 MT
Test load	1425 MT
Method of installation	Hydraulic rotary method under bentonite slurry
Drilling equipment	Hydraulic rig BG-25C

10.1 Results of Test Pile TP-04

Test pile with base grouting (TP-04) is carried out as per maintained load method. Test was terminated as pile reaches the settlement of 24 mm, and the corresponding load measured was 1358 MT. Load at 18 mm settlement was 1300 MT and safe load was 866 MT obtained from test pile (TP-03) which satisfies the pile capacity requirement of superstructure. Load-settlement curve for test pile TP-04 is presented in Fig. 17.

Fig. 17 Load-settlement curve for test pile-03



11 Comparison of Test Pile Results

A total of four test piles has been carried out with different depths to finalize the pile capacity. Test pile (TP-01) of depth 40 m obtained safe load of 312 tons and test pile (TP-02) of 52 m depth obtained safe load of 460, which shows a 12.0 m increase in depth increases only 148 tons in pile capacity. Test pile (TP-03) with base grouting of depth of 45 m shows safe load capacity of 593 tons and test pile (TP-04) with base grouting of depth of 52 m shows safe load capacity of 866 tons, which shows an increase in pile capacity of 273 tons between base grouted piles. However, TP-02 and TP-04 with same depth of 52 m having base grout and without base grout piles show the increase in pile capacity of 406 tons which is 90% of safe load capacity. It shows base grouting considerably increase the pile capacity in alluvial deposits (Fig. 18).

In test pile TP-02 and TP-04, base grouting method improves the axial load-settlement performances by increasing the axial resistance of the pile and/or by improving the mobilization of shaft resistance. Potential benefits of postgrouting piles include reduced settlement under loading, decreased length of the shaft, better alignment of load transfer curves for end and side resistance and improved ground beneath the base of the pile. Test pile TP-01 without base grout and test pile TP-03 with base grouting of having depth difference of almost 7.0 m, however TP-03 of 45 m showing the higher safe load of 593 tons than the test pile TP-02 of 52 m, that is, 460 tons pile capacity. It clearly states that base grouting helps to reduce the pile depth with increase in base resistance (Table 11).

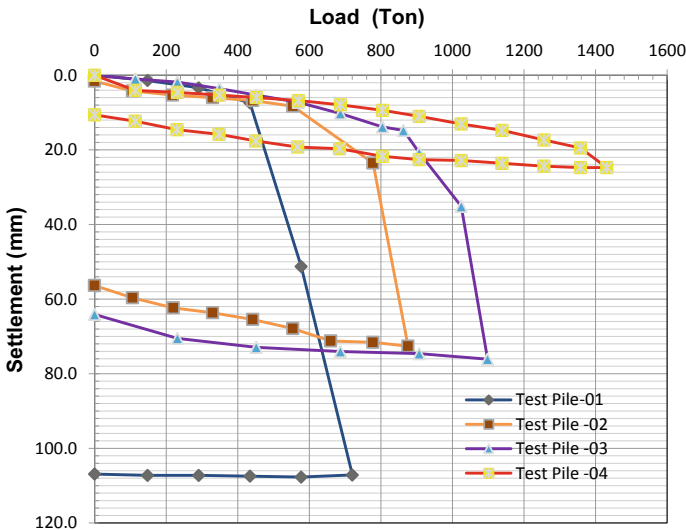


Fig. 18 Comparison of load-settlement curve for all test piles

Table 11 Comparison of test pile results

Test pile	Pile depth (m)	Max. applied load (MT)	Max settlement (mm)	Load at 18 mm	Safe load (MT)
(TP-01) Without base grout	40	777.6	155	469	312
(TP-02) Without base grout	52	1240	150	690	460
(TP-03) With base grout	45	1098	76	890	593
(TP-04) With base grout	52	1431	25	1300	866

12 Conclusion

Following are the conclusion made based on the test piles with and without base grouting with respect to pile capacity considered in substructure design:

- (a) Test pile (TP-01) conducted for estimated theoretical capacity of 1.5 m diameter with pile length 40 m for the safe load of 570 T, whereas actual soil condition reveals only 50% of capacity achieved for estimated pile length.
- (b) Increase in fine content of silty deposits reduces the angle of internal friction, which ultimately leads to reduced pile capacity.
- (c) Detailed borelog investigation planned, that is, one borelog under each pier, so a total of 144 borelogs has been planned with some additional laboratory tests for determining shear strength parameters at predetermined depths.
- (d) With redefined soil parameters pile capacity estimated and pile length increased to 52 m for pile load test (TP-02), which shows load-settlement curve close to theoretical pile capacity.
- (e) Though increase in pile depth increases skin friction marginally, considering the limitation on piling rig increase in pile depth has restriction after some extent.
- (f) With increase in pile length and adopting base grouting of piles found to be engineered economical solution.
- (g) In order to percolate the grout to base, grouting is carried out with different grout pressure, which will increase the percolation of grout to the bottom of the pile.
- (h) Test pile TP-03 and TP-04 conducted with 52 m length along with base grout shows satisfactory results of pile capacity.
- (i) TP-04 shows 46% more pile capacity than the actual required capacity.
- (j) Test pile settlement decreases with increase in pile capacity due to effective base grouting.

- (k) Pile capacities based on static formulas were calculated by not considering base grout effect, but increase in pile capacities is due to base grout considered as additional advantage.
- (l) However, time cycle decreased slightly due to base grout for each pile, but capacity increases rapidly.
- (m) After review of the above load test, base grout pile was proposed with pile length of 52 m.
- (n) All the piles in this project were revised to bored cast in situ piles with base grouting due to sufficient increase in vertical load capacity.
- (o) Lateral load test were carried out after vertical load tests, and lateral load test shows the satisfying lateral load carrying capacity of piles.
- (p) Time cycle of working piles with base grouting was increased, and it reduces by increase in the number of grouting pumps for base grouting.
- (q) It has been planned to monitor the performance of base grouted piles to understand the long-term behavior by placing inclinometer and strain gauges to record the displacement of pile if any.

Base grouting is becoming more widely accepted in the drilled shaft industry as a means to improve end-bearing response to load. There are a limited number of full-scale field comparisons of test shafts. This full-scale static load test of test piles conducted on piles with and without base grouting clearly estimates the increase in pile capacity and decreases the settlement with respect to load.

Acknowledgments The author is thankful to the management of L&T Construction for granting permission for this paper to be published. The author extends gratitude to project manager and project site team and colleagues in extending their support to the paper in their own way.

References

- Bowles JE (1996) Foundation analysis and design, 5th edn. McGraw-Hill, Singapore
- IS 2911(2013) Part 4, Design and construction of pile foundation—Code of practice—Load test on Piles
- IS 2911 (2010) Part 1-Sec 2, Design and construction of pile foundation: sect 2-Bored cast in-situ concrete piles
- IS 1888 (2002) Method of load test on soils. Bureau of Indian Standards, New Delhi, India
- Tomlinson MJ (1992) Pile design and construction practice, a view point publication. Cement and Concrete Association, 62 Grosvenor Gardens, London

Uplift Capacity of Single-Belled Anchor in Cohesionless Foundation Media



Tanaya Deb and Sujit Kumar Pal

Abstract This experimental investigation describes the variation in uplift capacity of single-belled anchors due to embedment ratios of 3, 4 and 5, diameter ratios of 0.28, 0.33, 0.38 and 0.46, and bell angles of 45°, 54°, 63° and 72°. The reason for variation in uplift behaviour is explained by failure diagrams. The uplift capacities show consistently increasing trend due to higher embedment ratios and lesser diameter ratios, and are found to be effective to gain uplift capacities for bell angles of 45°, 54° and 63° compared to 72° belled anchors.

Keywords Belled anchor · Breakout factor · Plaxis 3D modelling

1 Introduction

Belled anchors are generally favoured by geotechnical engineers when foundations have to provide extensive load bearing capacity and tension anchorage for the uplift resistance of foundation system. The anchors can be characterised as shallow and deep (Saran et al. 1986 and Tagaya et al. 1988). Ghaly et al. (1991) said that the anchors can also be categorised as shallow, deep and transition on the basis of failure response up to sand surface.

Anchor pile is a convenient and conventional method of foundation construction for works under water table and ocean structures; underground pumping station, oil storage tanks, pipe lines under sea water, buildings having several underground floors and built in coastal areas are the examples of such structures. Offshore structures (dolphins, jetty and wharf structures) are continuously subjected to thrust of wind, storm and hurricanes that produce cyclic wave, fluctuation in water level, thrust and pull of the berthing ships, and sometimes thrust of thick sheets of moving ice carried

T. Deb (✉) · S. Kumar Pal
Civil Engineering Department, NIT Agartala, Agartala, India
e-mail: debtanaya88@gmail.com

S. Kumar Pal
e-mail: skpal1963@gmail.com

by tide. More recently, anchors are being used to provide a simple and economical mooring system for offshore floating oil and gas amenities. Rao et al. (2006) sketched the mooring systems and presented in Fig. 1.

In case of on-land structures, beneath the structures the tensile forces are usually temporary and are almost always caused by the moment due to wind. For radar tower, television tower, power pole, road-side sign posts and outdoor sign pools, imbalance in horizontal forces is mainly due to severe wind velocity, and the resultant uplift load is more than their self-weight. The resultant pullout force in the legs of power transmission tower was presented by Davie (1973) due to wind load as shown in Fig. 2. Owing to high wind velocity and trembling in cables, there is severe vibration on the tower structure and if a cable would break, there are large unbalanced forces accounted. Both sets of forces are responsible for moment generation. Silos, overhead water tank and tall chimneys are not only concerned about large compressive load

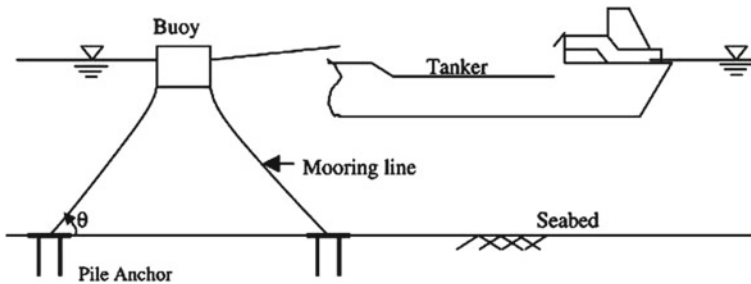
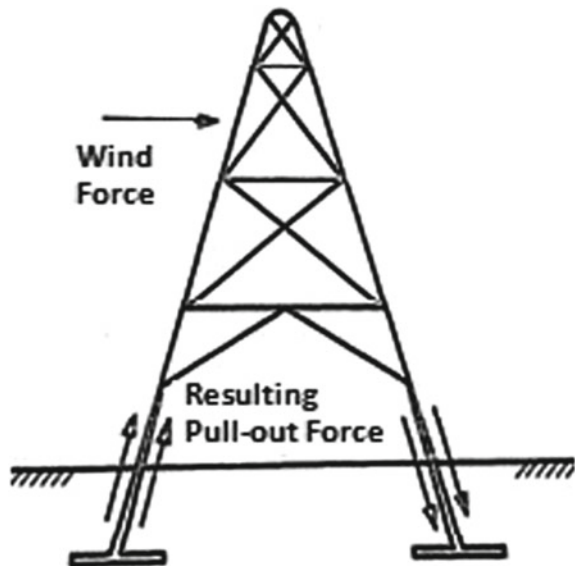


Fig. 1 Mooring system (after, Rao et al. 2006)

Fig. 2 Tensile forces on footings (after, Davie 1973)



transmission in sub-soil profile but also governed by uplift or overturning load and moment considerations. Rao et al. (2007) worked on the granular pile anchor to resist uplift due to swelling of expansive clay bed.

The uplift capacity of belled anchor had been studied by Dickin and Leung (1990, 1992), Pal (1992), Ghosh and Bera (2010), Bera (2014), Bera and Banerjee (2013), and Nazir et al. (2014). Uplift capacity of straight single pile and pile group had been studied by Dash and Pise (2003), and Deshmukh et al. (2010). Uplift resistance of screw anchors was studied by Ghaly et al. (1991) and Mittal and Mukherjee (2013). Sahoo and Kumar (2012) used group of coaxial horizontal anchors with a common vertical axis in cohesive soil.

The present experimental study aims to explore the variation in uplift behaviours of single-belled anchors in sand with several embedment ratios and anchor characteristics. The variation in uplift response is justified with the support of failure diagrams of those models.

2 Materials and Experimental Methodology

2.1 Materials

In the present study, locally collected sand is used as foundation media in a completely dry condition for all experiments. Figure 3 shows gradation of sand sample. The physical and engineering properties are obtained in accordance with the ASTM standards and are presented in Table 1.

Fig. 3 Gradation of sand sample

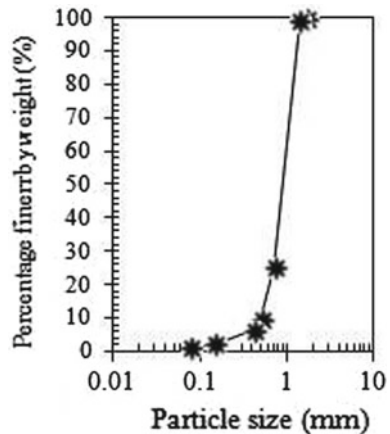


Table 1 Physical and engineering properties of sand sample

Physical and engineering properties	Test results
Medium sand (%)	93.50
Fine sand (%)	6.50
Silt and clay (%)	1.05
Effective grain size, D ₁₀ (mm)	0.70
Average grain size, D ₅₀ (mm)	0.93
Coefficient of curvature, C _c	0.91
Coefficient of uniformity, C _u	1.00
Name of soil (USCS)	SP
Specific gravity	2.67
Minimum void ratio	0.63
Maximum void ratio	0.88
Void ratio at placement density	0.71
Minimum dry density (kN/m ³)	14.20
Maximum dry density (kN/m ³)	16.50
Placement dry density (kN/m ³)	15.60
Relative density D _r (%)	64.38
Undrained cohesion, c (kN/m ²)	0.00
Soil internal friction angle, ϕ (°)	33.50
Coefficient of hydraulic conductivity, k (m/s)	1.83×10^{-4}
Modulus of elasticity, E _s (kPa)	31,600
Dilatancy angle, ψ , (°)	3.5

2.2 Models

Belled anchor is generally identified by its bell angle, shaft diameter and bell diameter. Table 2 presents the detailing of all the models. For all the models the shaft diameter (D_s) is kept constant at 26 mm and the variable bell diameters (D_b) are used as 92, 80, 68 and 56 mm, and these are having a bell angle of 45°, 54°, 63° and 72°. A hollow cylindrical arrangement and a couple of horizontally projected steel strips at 180° apart are welded at the top of all models to attach the proving ring and to hold dial gauges gently. Here, to study the failure diagram, both the sides of panels (in same scale as the models are mentioned already) are fabricated with 1 mm thick steel plates. These are denoted as 2D panels.

Table 2 The geometry, identifications and designations of models

α (°)	D_s/D_b	Model identifications	L/D_b	Model designations
(i)	(ii)	(iii)	(iv)	(v)
45	0.46	M:45-0.46	3	M:45-0.28-3
			4	M:45-0.28-4
			5	M:45-0.28-5
45	0.38	M:45-0.38	3	M:45-0.33-3
			4	M:45-0.33-4
			5	M:45-0.33-5
45	0.33	M:45-0.33	3	M:45-0.38-3
			4	M:45-0.38-4
			5	M:45-0.38-5
45	0.28	M:45-0.28	3	M:45-0.46-3
			4	M:45-0.46-4
			5	M:45-0.46-5
54	0.46	M:54-0.46	3	M:54-0.28-3
			4	M:54-0.28-4
			5	M:54-0.28-5
54	0.38	M:54-0.38	3	M:54-0.33-3
			4	M:54-0.33-4
			5	M:54-0.33-5
54	0.33	M:54-0.33	3	M:54-0.38-3
			4	M:54-0.38-4
			5	M:54-0.38-5
54	0.28	M:54-0.28	3	M:54-0.46-3
			4	M:54-0.46-4
			5	M:54-0.46-5
			3	M:63-0.28-3

2.3 Testing Tank

The size of the testing tank is 600 mm (L) × 600 mm (W) × 700 mm (H). The frame is made of steel and the bottom of the tank is enclosed by a steel plate. Vertical steel stiffeners are welded to three sides of the frame. The box is enclosed by a plaxi-glass sheet of 12 mm thick in four sides. To study failure diagram, stiffeners are not provided in front side to have a clear view from outside. The size of the tank is big enough to be free from boundary effects.

2.4 Sand Bed Preparation for Models and Panels

In the present study, the sand is used at placement density of 15.60 kN/m^3 , and these are achieved by raining technique (Ghosh and Bera 2010, Bera 2014, Bera and Banerjee 2013, Dickin and Leung 1990, and Pal 1992). For reproducing sand deposit of uniform density, two factors play a vital role, that is, the height of free fall and intensity of deposition, as suggested by Bouazza and Finlay (1990). The height of free fall is fixed by calibration and finalised as 70 cm in both the densities. Here, the rainfall procedure is maintained manually by soil tray. The local density of sand within the model tank is checked by several wooden cubes of 80 cc by placing them in different levels of the tank and variation has been found $\pm 1\%$ only.

To study the failure diagram in both sides of 2D panels homogeneous sand bed is prepared by placing successive layers of dyed sand (i.e., red colour) and non-dyed sand (i.e., natural colour), and both the layers belonging the same density of 15.60 kN/m^3 .

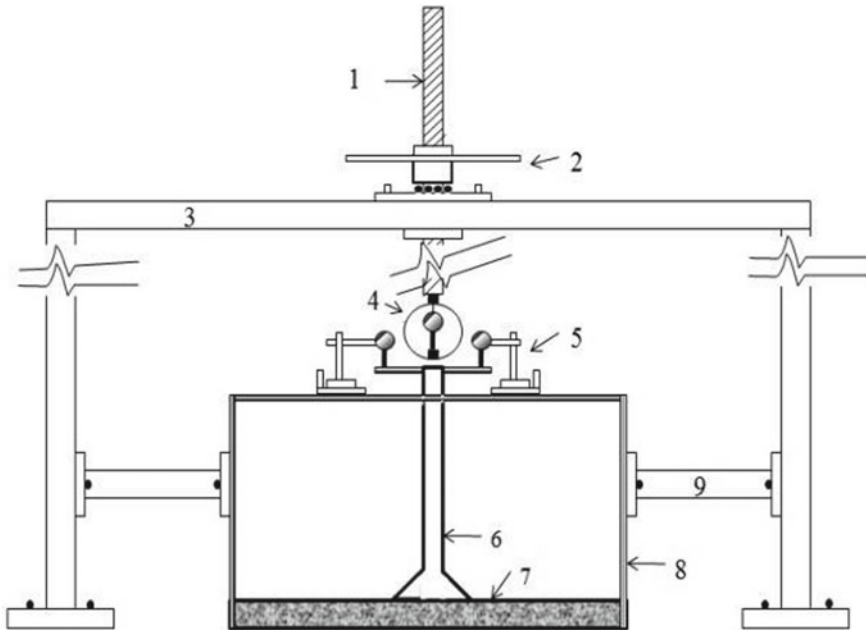
2.5 Experimental Set-up and Test Procedure

Figure 4 shows the schematic diagram of experimental set-up consisting of loading frame, anchor, model tank, proving ring, dial gauges and other accessories. The base of loading frame is bolted with the ground for stability and it is fabricated from steel channels. A reaction beam of steel channel is welded with the vertical frames. A pulling shaft (running as screw jack) is a mechanical tool working on the principle of nut and screw motion. At the bottom of pulling shaft the model is connected via proving ring. Upward movement of the shaft is manually controlled by rotating circular wheel fixed with nut arrangement (resting over the reaction beam), and nut and screw is functioning on the ball-bearing system. Prior to each test, a compacted sand layer of 100 mm thick is prepared inside the model tank to place the model. The sand filling is done up to desired embedment depth from the level of anchor base. Tension proving ring (1.0 kN capacity) and a couple of dial gauges (0.01 mm accuracy) are used to measure tensile loads and corresponding vertical displacements, respectively. The dial gauges are properly fixed with magnetic bases and the magnetic bases are placed on a couple of steel bar placed over the model tank.

3 Experimental Programme

In this test series, the variable parameters as considered are mentioned below:

- Embedment ratios (L/D_b) of models: 3, 4 and 5,
- Diameter ratios (D_s/D_b) of models: 0.46, 0.38, 0.33 and 0.28; and



1. Long screw, 2. Rotating wheel, 3. reaction frame, 4. Proving ring, 5. Dial gauge in magnetic base, 6. Model anchor, 7. Sand datum, 8. Test tank, 9. Stiffeners

Fig. 4 Schematic diagram of experimental set-up (after, Deb and Pal 2018)

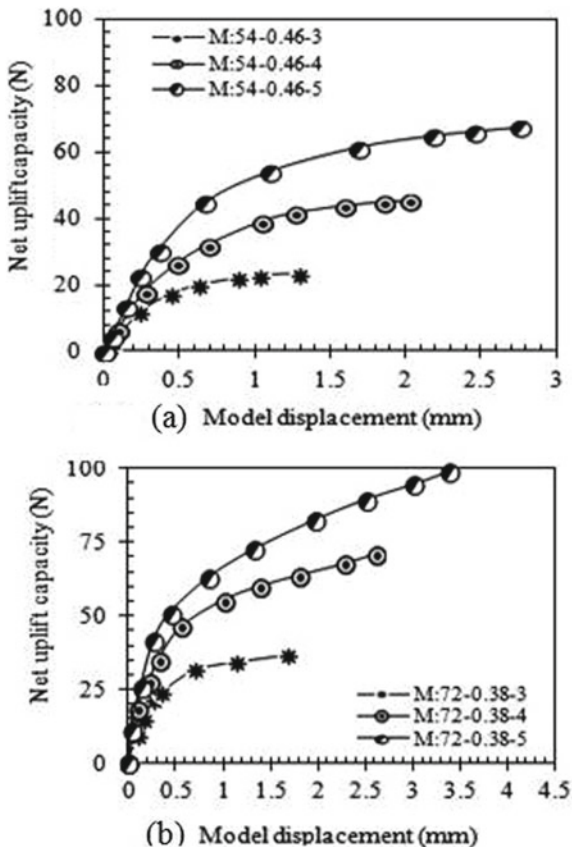
- Bell angles (α) of models: 45°, 54°, 63° and 72°.

In total, 48 (= 3 × 4 × 4) numbers of tests are performed to investigate uplift behaviour. 48 numbers of tests are conducted to show the variation in failure diagrams with 2D panels. In 2D panel T_s and T_b represents the thickness of shaft and bell base, respectively and these values are same as D_s and D_b . So, the values of T_s/T_b and L/T_b are identical to D_s/D_b and L/D_b respectively.

4 Observations on Uplift Capacity Versus Displacement Behaviour

The typical net uplift capacity versus anchor displacement behaviour is presented in Fig. 5a and b for models M:54-0.46 and M:72-0.38, respectively, both at L/D_b of 3, 4 and 5. In general, the curves pass through three phases. Initially, in the curves, linear part is presenting true elastic response and thereafter linear part trying to be

Fig. 5 Net uplift capacity versus anchor displacement behaviour for **a** M:54-0.46 and **b** M:72-0.38

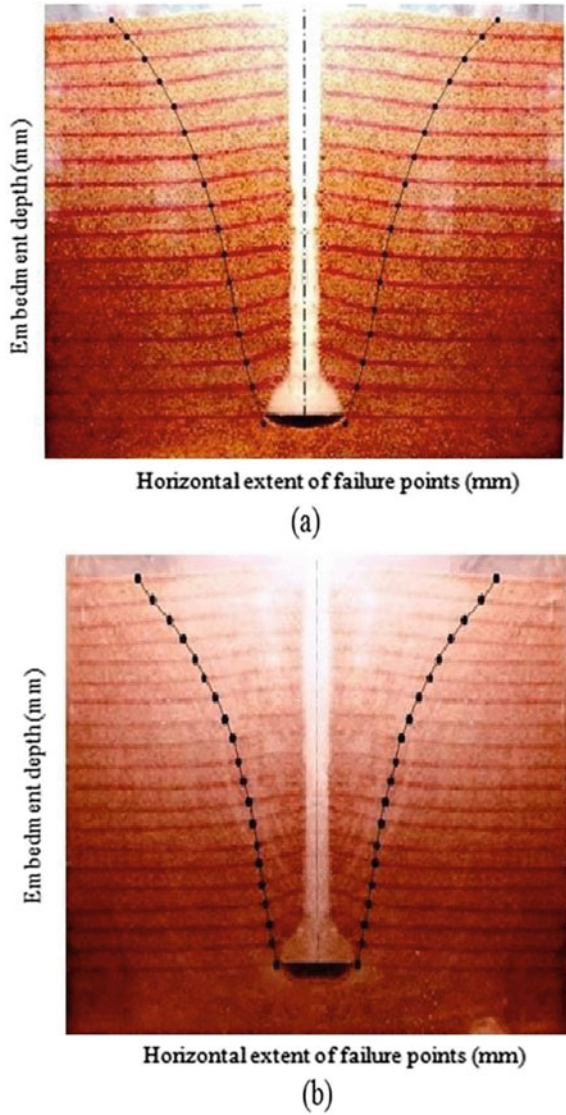


approximately curvilinear shape, and finally, the elasto-plastic response is seen with the truly curvilinear shape at the collapsed stage. The nature of the curves is similar as explained by Rowe and Davis (1982) in the sand for plate anchors. The gross ultimate uplift capacity (Q_g) and corresponding failure displacement (D_f) is pointed out, when uplift capacity is attained peak value in proving ring and displacement shows in dial gauge under that peak value. Net ultimate uplift capacity (Q_u) is always reported as self-weight subtracted from the Q_g .

The failure diagram obtained in both the sides of panels are presented in Fig. 6a and b. In the plots of failure diagram (Figs. 8, 10 and 12) “FS” indicates failure surface around the 2D panel. The failure points are plotted with the help of polynomial curves.

In Table 2 (column v) the detail designations of models are presented. Each model is represented by a coding system consisting of four parts. The first, second, third and fourth part represents the model, bell angle, diameter ratio and embedment ratio, respectively. For example, a model having α value of 54° , D_s/D_b of 0.33 and L/D_b of 5 is designated as M:54-0.33-5. The designation M:72-0.46-3 represents a

Fig. 6 Failure surfaces in both sides of panels **a** 2D:45-0.33-4 and **b** 2D:54-0.33-5 (after, Deb and Pal 2018)



model having α value of 72° , D_s/D_b of 0.46 and L/D_b of 3. The panels are similarly designated as models and to make understand the panel “2D” is used.

5 Failure Surface Mechanism and Observations

In case of 2D panels, it is observed from the present study that at primary stage of pulling with the application of tensile load, the sand layers around bell base tend to move along panel, resulting in formation of small cavity or gap underneath the anchor base, and this may be the stage of relief of stress beneath the anchor base and simultaneous increase of compression in the sand located above the ceiling of belled out portion. This phenomenon described by Saeedy (1987) that with initial uplift, sand above anchor base compressed under the action of anchor and at that stage compressibility was dependent on initial state of stress of sand. In this present study, the dyed sand layers near the base are gradually inclined in respect of horizontal with initial upward movement of anchor. With further pulling up to certain height from the base, the inclination of sand layers is steeper in respect of horizontal plane; thereafter the inclination in layers becomes gradually milder as migrate towards top surface of sand layer. Within the compressed zone for locking up of sands, the factors responsible are dilatancy of sand (Rowe and Davis 1982), and higher interlocking among the sand particles within failure zone than rolling and sliding (Ilamparuthi and Muthukrisnaiah 1999).

Continuous pulling results in expansion of cavity and migration of nonlinear slip surface with higher radial spreading progressively towards sand surface until shear stress level in the sand around anchor base reaches shear strength.

At the verge of failure, tension cracks are produced in sand around the base and a plastic flow of disturbed sand progress downward to fill the void. It is noticed that when the displaced sand around the base start to flow downward to fill the cavity, simultaneously the developing failure surface reaches top surface of sand layer. It has been observed from the present study that the failure wedge once generated remains unaltered even after further pulling and the domain outside of failure surface remains in rest condition. The pulling is continued after the failure indicated by the proving ring till the sand particles around the base of panel move downward to fill the cavity.

6 Discussions

Based on 48 numbers of experimental results and 48 numbers of observations on failure surfaces, the variations in the response of uplift behaviour of belled anchors in cohesionless foundation media due to different embedment ratios, diameter ratios and bell angles have been discussed in this section.

6.1 Net Ultimate Uplift Capacity (Q_u) of Belled Anchors Influenced by Embedment Ratio (L/D_b)

The plots of net ultimate uplift capacity (Q_u) of belled anchors versus embedment ratio (L/D_b) are illustrated in Fig. 7 for models M:63-0.28, M:63-0.33, M:63-0.38 and M:63-0.46, each at L/D_b of 3, 4 and 5. It reveals that with the increase in the value of L/D_b , for the same anchor, the values of Q_u gradually moves upward irrespective of D_s/D_b and α . In M:54-0.33, the values of Q_u raise from 75.65 to 149.65 N and from 149.65 to 224.19 N, as L/D_b increases from 3 to 4 and 4 to 5, respectively. The similar trend was observed in helical screw anchors (Mittal and Mukherjee 2013), in plate anchors (Vanitha et al. 2007, and Ilamparuthi and Dickin 2001), in belled anchors (Dickin and Leung 1990, Pal 1992, Ghosh and Bera 2010, Bera 2014, and Nazir et al. 2014) in sand, respectively.

It is obvious that progressively more overburden pressure would act on anchor base at gradually higher embedment ratios due to larger sand mass. In Fig. 8, from the failure diagram it is noticed that larger volume of sand is uplifted at higher embedment ratios. Hence, there is more the amount of breakout sand zone, the higher weight of sand inside the wedges as well as mobilised shear on surfaces of wedges; this phenomenon explains the reason of higher uplift capacity (Q_u) of belled anchors at embedment ratios which is independent of diameter ratios and bell angles.

Fig. 7 Net ultimate uplift capacity versus embedment ratio relation for models at $\alpha = 63^\circ$, $D_s/D_b = 0.28, 0.33, 0.38$ and 0.46 each at $L/D_b = 3, 4$ and 5

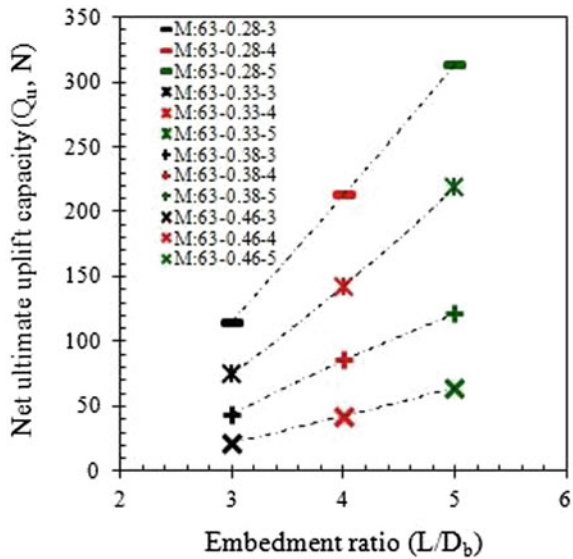
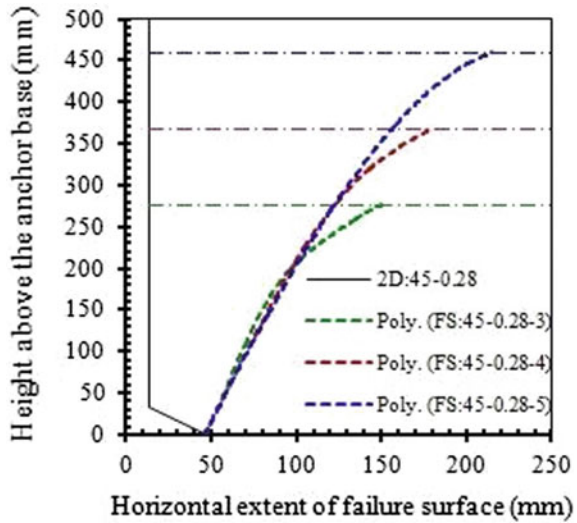


Fig. 8 Failure diagram besides panels having at $\alpha = 45^\circ$, $T_s/T_b = 0.28$ at $L/T_b = 3, 4$ and 5



6.2 Net Ultimate Uplift Capacity (Q_u) of Belled Anchor Piles Influenced by Diameter Ratio (D_s/D_b)

The plots of the net ultimate uplift capacity of belled anchors versus diameter ratio are presented in Fig. 9 for models of M:54-0.46, M:54-0.38, M:54-0.33 and M:54-0.28, at L/D_b of 3, 4 and 5. In models having α of 72° at L/D_b of 5, due to a decrease

Fig. 9 Net ultimate uplift capacity versus diameter ratio relation for models at $\alpha = 54^\circ$, $D_s/D_b = 0.28, 0.33, 0.38$ and 0.46 each at $L/D_b = 3, 4$ and 5

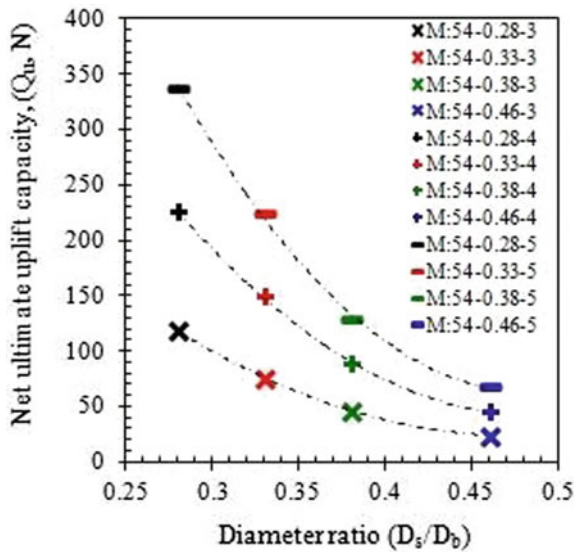
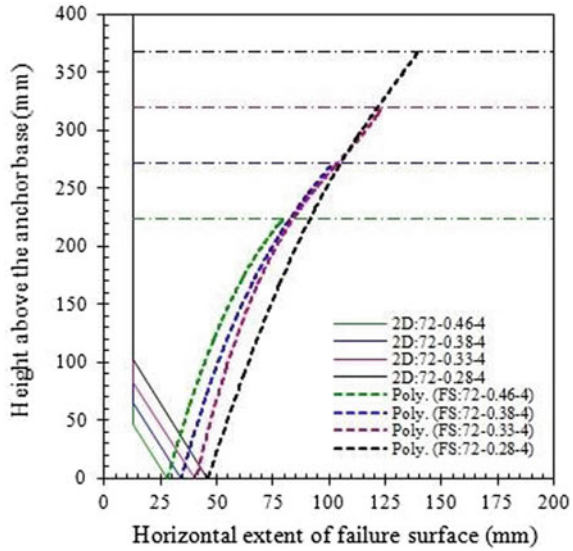


Fig. 10 Failure diagram besides panels having $\alpha = 72^\circ$, $T_s/T_b = 0.46, 0.38, 0.33$ and 0.28 at $L/T_b = 4$



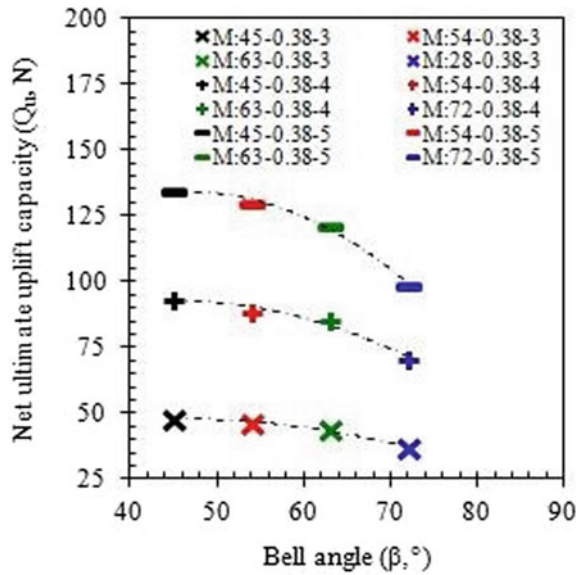
in the value of D_s/D_b from 0.28 to 0.33, 0.33 to 0.38 and 0.38 to 0.46, Q_u decreased from 95.14 to 60.86 N, 60.86 to 36.93 N and 36.93 to 19.65 N, respectively. The trend of these values of Q_u was the same as reported by Dickin and Leung (1990), Pal (1992), Nazir et al. (2014), and Ilamparuthi and Dickin (2001) for belled anchors installed in dry sand.

In Fig. 10, from the failure diagrams, it is observed that with the increase in the value of T_s/T_b , at constant L/T_b and α , the volume of breakout sand zone gradually decreases. From this figure, it is also revealed that the weight of sand column on the ceiling of the belled out portion is gradually lesser in FS:54-0.33-3 than FS:54-0.28-3, in FS:54-0.38-3 than FS:54-0.33-3 and in FS:54-0.46-3 than FS:54-0.38-3. Hence, combinations of gradually lesser weight of wedges, as well as mobilised shear, offer lesser uplift capacity.

6.3 Net Ultimate Uplift (Q_u) Capacity of Belled Anchor Piles Influenced by Bell Angle (α)

The plots of net ultimate uplift capacity of belled anchors versus bell angle are presented in Fig. 11 for models having D_s/D_b of 0.28, α of $45^\circ, 54^\circ, 63^\circ$ and 72° , and each model is installed at L/D_b of 3, 4 and 5. The Q_u values are reduced from 7 to 10% when the bell angle is increased from 45 to 63° . Dickin and Leung (1992) and Nazir et al. (2014) noticed the rate of reduction in uplift capacity of belled anchor due to change in bell angle from 45 to 60° and 22 to 63° , respectively. In the present study, as α increased from 63 to 72° , in most of the cases, uplift capacities decreased

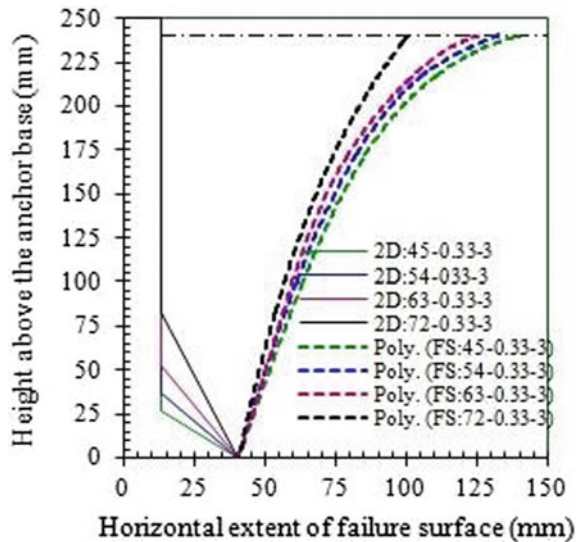
Fig. 11 Net ultimate uplift capacity versus bell angle relation for models at $D_s/D_b = 0.38$, $\alpha = 45^\circ, 54^\circ, 63^\circ$ and 72° each at $L/T_b = 3, 4$ and 5



within the range of 17–22%. Dickin and Leung (1992) found that there was a rapid decrease in uplift capacity beyond bell angle of 62° .

In Fig. 12, from the failure diagrams it has been found that FS:45-0.33-3, FS:54-0.33-3 and FS:63-0.33-3 are near each other; but FS:72-0.33-3 is comparatively far from FS:45-0.33-3 and close to anchor. This figure also indicates that volume of wedges is slightly reducing for anchors having the α within the range of 45° – 63° , and

Fig. 12 Failure diagram besides panels having $L/T_b = 3$, $T_s/T_b = 0.33$ and $\alpha = 45^\circ, 54^\circ, 63^\circ$ and 72°



for anchors possessing α of 72° the volume of the wedge is much lesser. Hence, at a constant value of L/T_b and T_s/T_b , the Q_u values are slightly lesser in anchors having α of 63° than anchors possessing α of 45° and Q_u values are much lesser for anchors having α of 72° than anchors possessing α of 45° .

7 Concluding Remarks

On the basis of the results, observations and discussions carried out in this study, the following significant conclusion can be listed:

- For higher embedment ratio, higher uplift capacity is obtained irrespective of diameter ratio and bell angle. With higher embedment ratios larger breakout wedges are formed due to failure.
- With the increase in diameter ratio, a gradual decreasing tendency in uplift capacity is found regardless of embedment ratio and bell angle. With higher diameter ratios smaller wedges are formed due to failure.
- With a gradual steeper bell angle (from 45° to 63°), for specific diameter ratio and embedment ratio, net ultimate uplift capacities become gradually lesser. When belled angle increased from 63° to 72° , uplift capacities decreased significantly. The breakout wedges formed surrounding 63° belled anchors are slightly lesser than those anchors formed around 45° belled anchors, but the wedges formed surrounding 72° anchors are considerably lesser than those anchors formed around 45° belled anchors.
- The belled anchors are found to be effective to gain uplift capacities when bell angles are 45° , 54° and 63° in comparison to 72° .

References

- Bera AK (2014) Parametric study on uplift capacity of anchor with tie in sand. *Korean Soc Civil Eng* 18(4):1028–1035
- Bera AK, Banerjee U (2013) Uplift capacity of model bell shaped anchor embedded in sand. *Int J Geotechn Eng* 7(1):84–90
- Bouazza A, Finlay TW (1990) Uplift capacity of plate anchors buried in a two-layered soil. *Geotechnique* 40(2):293–297
- Dash BK, Pise PJ (2003) Effect of compressive load on uplift capacity of model piles. *J Geotechn Geoenvironmental Eng, ASCE* 129(11):987–992
- Davie JR (1973) Behaviour of cohesive soils under uplift forces. PhD Thesis, University of Glasgow, Glasgow, U.K
- Deb T, Pal SK (2018) Study on the uplift behaviour and failure pattern of single belled anchor with 3d and 2d models in cohesionless soil bed. *Iran J Sci Technol Trans Civil Eng* 43(2):327–343
- Deshmukh VB, Dewaikar DM, Choudhury D (2010) Computations of uplift capacity of pile anchors in cohesionless soil. *Acta Geotech* 5:87–94

- Dickin EA, Leung CF (1992) The influence of foundation geometry on uplift behaviour of piles with enlarged bases. *Can Geotechn J* 29:498–505
- Dickin EA, Leung CF (1990) Performance of piles with enlarged bases subjected to uplift forces. *Can Geotech J* 27:546–556
- Ghaly A, Hanna A, Hanna M (1991) Uplift behavior of screw anchors in sand. I: dry sand. *J Geotechn Eng* 117(5):773–793
- Gosh A, Bera AK (2010) Effect of geotextile ties on uplift capacity of anchors embedded in sand. *Geotechn Geol Eng* 28:567–577
- Ilamparuthi K, Dickin EA (2001) Predictions of the uplift response of model belled piles in geogrid-cell-reinforced sand. *Geotext Geomembr* 19:89–109
- Ilamparuthi K, Muthukrishnaiah K (1999) Anchors in sand bed: delineation of rupture surface. *Ocean Eng* 26:1249–1273
- Mittal S, Mukherjee S (2013) Vertical uplift capacity of a group of helical screw anchors in sand. *Indian Geotechn J* 43(3):238–250
- Nazir R, Moayed H, Pratikso A, Mosallanezhad M (2014) The uplift load capacity of an enlarged base pier embedded in dry sand. *Saudi Society for Geosciences, Springer*. <https://doi.org/10.1007/s12517-014-1721-3>
- Pal SK (1992) Uplift capacity of shallow and deep belled anchors tied geofabric strips, M.Tech. Dissertation, Department of Civil Engineering IIT Kharagpur, West Bengal, India
- Rao SN, Latha KH, Pallavi B, Surendran S (2006) Studies on pullout capacity of anchors in marine clays for mooring systems. *Appl Ocean Res* 28:103–111
- Rao AS, Phanikumar BR, Babu RD, Suresh K (2007) Pullout behavior of granular pile- anchors in expansive clay beds in situ. *J Geotechn Geoenvironmental Eng* 1335:531–538
- Rowe RK, Davis EH (1982) The behaviour of anchor plates in sand. *Geotechnique* 32(1):25–41
- Saeedy HS (1987) Stability of circular vertical earth anchors. *Can. Geotech. J.* 24
- Sahoo JP, Kumar J (2012) Vertical uplift resistance of two horizontal strip anchors with common vertical axis. *Int J Geotechn Eng* 6:485–495
- Saran S, Ranjan G, Nene AS (1986) Soil anchors and constitutive laws. *J Geotechn Eng* 112(12):1084–1100
- Tagaya K, Scott RF, Aboshi H (1988) Pull-out resistance of buried anchors in sand. *Soils Found* 28(3):114–130
- Vanitha L, Patra NR, Chandra S (2007) Uplift capacity of pile group anchors. *Geotechn Geol Eng* 25:339–347

Effect of Footing Shapes and Reinforcement on Bearing Capacity of Three Adjacent Footings



S. S. Saraf and S. S. Pusadkar

Abstract The effect of geogrid reinforcement on bearing capacity was studied on three surface square footings in series. Parameters included under the reinforcement configuration were, length of reinforcement on either side beyond center of footings (L_x), depth of first geogrid layer (u), vertical distance between geogrid layers (h) and center to center distance between three footings (S). Also influence of footing shapes was studied for square, circular and rectangular shape of same cross-sectional area for optimum reinforcement configuration. In order to evaluate these effects, laboratory model tests were conducted at 55% relative density of sand. Bearing capacity of adjacent footings has been observed to be improved by providing geogrid reinforcement layer in the foundation soil under closely spaced footings. It was observed that the reinforcement configurations play a vital role in bearing capacity improvement. It was also observed that bearing capacity of the soil varies with the shape of footings.

Keywords Three footing · Bearing capacity · Geogrid-reinforced sand

1 Introduction

The lowest part of a structure which transmits its weight to the underlying soil or rock is the foundation. The foundation design is aimed at providing a means of transmitting the loads from a structure to the underlying soil without causing any shear failure or excessive settlement of the soil under the imposed loads. Bearing capacity is the supporting power of a soil or rock, which play important role in design of foundation. The bearing capacity may be determined by analytical methods, conducting field and laboratory tests and from the building codes. The scarcity of

S. S. Saraf (✉)

P.R. Pote College of Engineering and Management, Amravati 444 602, India

e-mail: sachinsaraf2014@gmail.com

S. S. Pusadkar

Department of Civil Engineering, Government College of Engineering, Jalgaon, India

e-mail: ss_pusadkar@yahoo.co.in

© Springer Nature Singapore Pte Ltd. 2020

M. Latha Gali and P. Raghuvver Rao (eds.), *Construction in Geotechnical*

Engineering, Lecture Notes in Civil Engineering 84,

https://doi.org/10.1007/978-981-15-6090-3_10

land due to growth in population and built-up area results in construction of heavy high-rise adjacent structures. Because of this, the footings are kept at close spacings and the interferences of footings occur. The interference of foundations may change the behavior, as compared to isolated foundations. The influence of the interference is directly related to the distance between adjacent footings. The soil improvement is necessary when the available soil is weak. The uses of geo-synthetic materials are mostly preferred as soil reinforcement for improving the performance of shallow foundations.

Numerous investigations have been carried out, to study the bearing capacity of two interfering footings on unreinforced sand (Das and Larbi-Cherif 1983; Khan et al. 2006; Kumar and Ghosh 2007; Kumar and Bhoi 2009; Mabrouki et al., 2010; Kouzer and Kumar 2010; Ghosh and Sharma 2010; Ghosh and Kumar 2011; Nainegali and Basudhar 2011; Srinivasana and Ghosh 2013; Nainegali et al. 2013) and reinforced sand (Khing et al. 1992; Al-Ashou et al. 1994; Kumar and Saran 2003; Ghazavi and Lavasan 2008; Ghosh and Kumar 2009; Pusadkar and Saraf 2012a; Ghazavi and Lavasan 2012; Pusadkar and Saraf 2012b; Naderi and Hataf 2014). The results of these research works show a significant improvement in bearing capacity and settlement after providing continuous geogrid reinforcement. It was also observed that the ultimate bearing capacity (UBC) of neighboring footings increases as the spacing between footing decreases. The literatures only show work on the interfering effects of multiple footings on unreinforced sand (Graham et al. 1984; Lee and Eun 2009; Kumar and Bhattacharya 2010; Daud 2012). However, the experimental study on the interfering effects of three adjacent footings on reinforced sand is not available. This reveals that study on the effect of reinforcement configurations, spacing between footings and shape of footings on bearing capacity of three adjacent footing on reinforced sand is the need of the future. In order to evaluate the performance of three adjacent footings on reinforced sand, laboratory experiments to simulate the various conditions of footing were performed and the results were compared for development of knowledge base in this regard.

2 Scope of the Study

From the literature study it was observed that most of the works on the interfering effects of three adjacent footings were for unreinforced sand. Limited information is available for reinforced sand. The main objective of this research work was to experimentally investigate the effect of footing shapes and reinforcement on bearing capacity of three adjacent footings. The effect of geogrid reinforcement on bearing capacity was studied on three surface square footings in series. Parameters included under the reinforcement configuration were length of reinforcement on either side beyond center of footings (L_x), depth of first geogrid layer (u), vertical distance between geogrid layers (h) and center to center distance between three footings (S). The influence of footing shapes was studied for square, circular and rectangular shape of same cross-sectional area for optimum reinforcement configuration. For

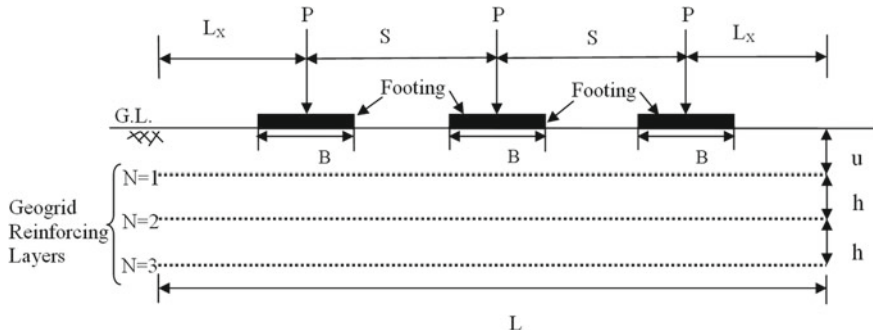


Fig. 1 Layout of geogrid reinforced sand bed

these purposes, extensive laboratory model tests were conducted at 55% relative density of sand for simulating the various conditions of footing. For reinforced sand three geogrid layers ($N = 3$) were used. Figure 1 shows typical layout of multi-layered geosynthetic reinforced sand bed adopted in the model tests.

3 Material and Experimental Program

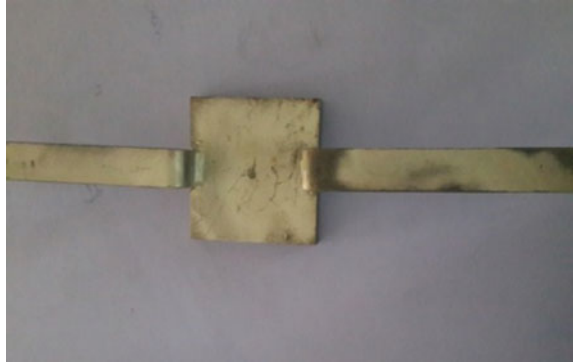
3.1 Materials

For the model load tests, cohesionless dry sand (Kanhana Sand) available in Nagpur region of Vidarbha, passing through 2 mm IS sieve and retaining on 1 mm IS sieve was used as the foundation material. The properties of sand used are shown in Table 1.

Commercially available continuous biaxial geogrid in three layers was used for reinforcing the sand bed. Three model footings of square, rectangular and circular shapes were fabricated by using cast iron material of same cross-sectional area. The sizes of footings for square, rectangular and circular shapes were 10 cm × 10 cm,

Table 1 Properties of sand used

Properties	Values
Specific gravity	2.53
Bulk unit weight (kN/m^3)	15.21
Maximum unit weight (kN/m^3)	16.26
Minimum unit weight (kN/m^3)	14.20
Angle of internal friction	34°
Coefficient of uniformity C_u	2.8
Coefficient of curvature C_c	1.37
Effective size D_{10}	0.50

Fig. 2 Model footing

14.1 cm \times 7.1 cm and 11.3 cm diameter, respectively. Every footing has a little groove at the center to facilitate the application of load. The base of the model footings was roughened by fixing a thin layer of sand to it with epoxy glue. The footings were provided with the two flanges on two sides of footings to measure the settlement of footing under the action of load with the help of dial gauges as shown in Fig. 2.

3.2 Test Setup

Laboratory plate load test setup consists of a test bed tank and loading frame assembly. The sand beds were prepared in a steel test tank of size 2.5 m \times 1.5 m \times 0.9 m stiffened at different levels to avoid volume change during preparation of reinforced sand bed. The tank was fabricated using steel plates of 6 mm thickness. A loading frame consisting of two vertical ISMB 200 girders bolted with ISMB 200 horizontal reaction beam for applying the load to the model footing is assembled. The load was applied with manually controlled hydraulic jack bolted on reaction frame. For transferring the symmetrical loads to three footings, load transfer beam of size 800 \times 50 \times 50 mm having arrangement to change the spacing between footings was fabricated and connected to hydraulic jack. Load on each footing was measured with the help of proving ring placed between footing and load transfer beam. Dial gauges were placed on each flanges of each footing to measure the settlement. The schematic diagram of the experimental setup used for studying the effect of footing shapes and reinforcement on bearing capacity of three adjacent footings is as shown in Fig. 3.

3.3 Testing Procedure

For the load test, initially the tank was filled with the dry sand of 2 mm passing and retaining on 1 mm IS sieve up to 600 mm depth. The sand was poured in the tank by

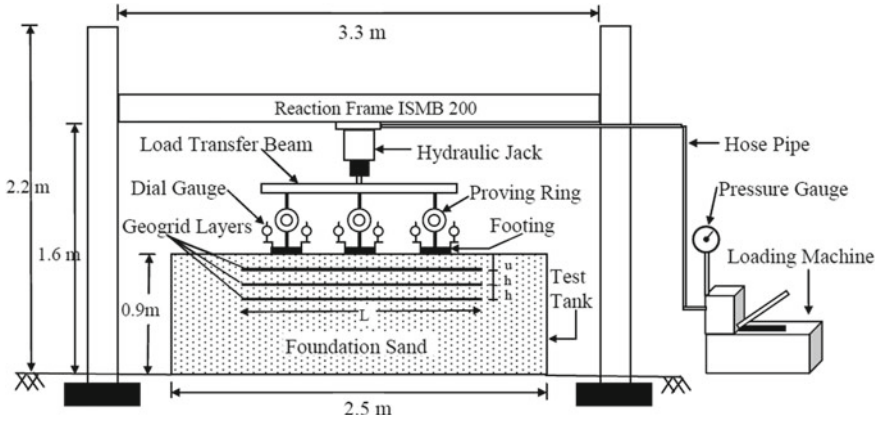


Fig. 3 Schematic diagram of test setup

rainfall technique keeping the height of fall as 25 cm to maintain the constant relative density and average unit weight of 55% and 15.21 kN/m³, respectively, throughout the bed. The height of fall to achieve the desired relative density was determined a priori by performing a series of trials with different heights of fall. Whenever the sand is deposited up to the desired location of the bottom layer geogrid reinforcement from bottom of footing, the top surface of the sand was leveled and the bottom geogrid reinforcement was placed. Again, the sand was filled over this geogrid reinforcement layer in the tank up to the desired location of the next layer, and similarly, the multi-layered geosynthetic-reinforced sand bed adopted in the model tests, as shown in Fig. 1, was prepared. The prepared top surface of sand was leveled and three surface square footings 10 cm x 10 cm size in series at different spacing are then placed on the prepared reinforced sand bed. The middle footing was placed exactly at the centre of the loading jack to avoid eccentric loading. A manually controlled hydraulic jack installed between the load transfer beam and strong reaction frame, as shown in Fig. 3, was used to provide the required load on the footings. A calibrated proving ring was used to measure the load transferred to the footing. The load was applied in small increments. Each load increment was maintained constant until the footing settlement was stabilized. All the three footings were simultaneously loaded vertically. The vertical displacement of each test footing was measured by taking the average of two dial gauges readings. By gradually increasing the load, a series of tests was carried out so as to monitor the complete load deformation plots till the ultimate failure occurs. Figure 4 shows the actual experimental setup used for load tests.

Fig. 4 Actual experimental setup used



3.4 Testing Program

Initially, one model plate load test was conducted on three surface square footings in series resting on unreinforced sand bed, each at varying spacing distance between footings of 1B, 2B and 3B, where B is the width of the footing. After that three different series of model tests (i.e. A–C) were carried out on footings resting on geosynthetic-reinforced sand beds by varying different parameters, such as depth of the top most reinforcement layer from the base of the footing (u), vertical spacing between consecutive layers of reinforcement (h), center to center distance between three footings (S) and length of geogrid reinforcement on either side beyond center of footings (L_x). Table 2 presents the description of each of these series with the parameters used. All the varying parameters are expressed in non-dimensional form in terms of the footing width (B) as u/B , h/B , L_x/B and S/B .

After performing the model load tests mentioned in the Table 2, the optimum geogrid reinforcement configuration ($u/B = 0.3$, $h/B = 0.3$ and $L_x/B = 3$, $N = 3$)

Table 2 Description of laboratory model test series for reinforcement configuration

Test series	Details of parameters used in tests			
	S/B	L_x/B	h/B	u/B
A	1	4, 3 and 2	0.2	0.2, 0.3, 0.4 and 0.5
			0.3	
			0.4	
B	2	4, 3 and 2	0.2	0.2, 0.3, 0.4 and 0.5
			0.3	
			0.4	
C	3	4, 3 and 2	0.2	0.2, 0.3, 0.4 and 0.5
			0.3	
			0.4	

Table 3 Description of laboratory model test series for different footing shapes

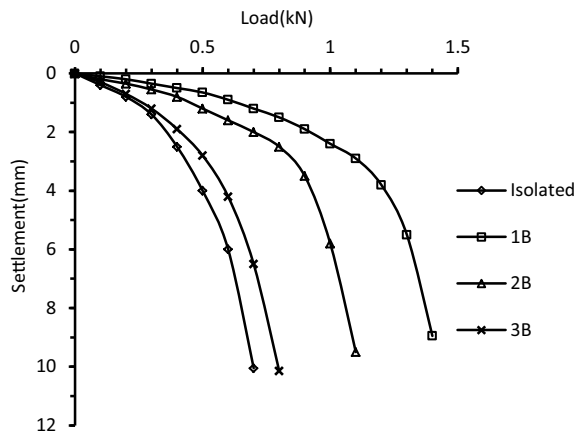
Test series	Details of parameters used in tests		
	Foundation bed type	S/B	Footing shapes
D	Optimum geogrid reinforcement ($u/B = 0.3$, $h/B = 0.3$ and $Lx/B = 3$, $N = 3$)	1, 2 and 3	Square, circular and rectangular
E	Unreinforced	1, 2 and 3	Square, circular and rectangular

was determined by comparing the results from Figs. 6, 7 and 8. After that, the two different series of model tests (i.e. D and E) were carried out to investigate the effect of footing shapes on bearing capacity of three adjacent footings for square, circular and rectangular shape of same cross-sectional area. Table 3 presents the description of each of these series with the parameters used.

4 Results and Discussion

The load settlement behaviors of footings were determined by conducting a model plate load tests as described in Tables 2 and 3. The load settlement curves were plotted for each case. The ultimate failure load was decided from load settlement curve, and thus ultimate bearing capacity was calculated. The typical load settlement curves for isolated and three square footing in series at different spacing for reinforced sand are as shown in Fig. 5.

Fig. 5 Typical load settlement curves for isolated and three square footings in series at different spacing for reinforced sand



4.1 Bearing Capacity Ratio (BCR)

The performance improvement in terms of the increase in the ultimate bearing capacity due to the provision of geosynthetic reinforcement is quantified through a non-dimensional parameter, the bearing capacity ratio (BCR), which is defined as follows and shown in Eq. (1).

$$B.C.R = \left(\frac{q_{u \text{ int}(\text{reinforced})}}{q_{u \text{ int}(\text{unreinforced})}} \right) \quad (1)$$

where $q_{u \text{ int}(\text{reinforced})}$ is the ultimate bearing capacity of an interfering footing on the reinforced sand and $q_{u \text{ int}(\text{unreinforced})}$ is the ultimate bearing capacity of the same footing on unreinforced sand.

4.1.1 Effect of Length of Reinforcement on Either Side Beyond Center of Footing

Figures 6, 7 and 8 show the variation in BCR with the length of reinforcement on either side beyond center of footing for test series A, B and C, respectively. From these figures it can be observed that initially up to $L_x/B = 3$ the BCR increases rapidly with increase in the length of reinforcement on either side beyond center of footing. After that the improvement in BCR is very marginal. It was also observed that the BCR is maximum for test series A when the ratio of center to center distance between the three footings and width of footing is unity ($S/B = 1$).

4.1.2 Effect of Depth of First Layer Reinforcement (U/B) and Vertical Distance Between Layers (H/B)

From the Figs. 6b, 7b and 8b, it can be observed that the BCR is optimum when the depth of inclusion of first layer geogrid reinforcements and vertical distance between consecutive layers is 0.3 times the width of footing for all the three test series. It was also observed that the BCR is maximum for test series A when the ratio of center to center distance between the three footings and width of footing is unity ($S/B = 1$).

After comparing the variation in BCR with L_x/B for test series A, B and C as shown in Figs. 6, 7 and 8, it was observed that the BCR is optimum for the geogrid reinforcement configuration with $u/B = 0.3$, $h/B = 0.3$, $L_x/B = 3$, and $N = 3$.

4.1.3 Effect of Footing Shapes

Figure 9a and b shows the variation in UBC with center to center distance between footings for optimum geogrid reinforced and unreinforced sand, respectively. From

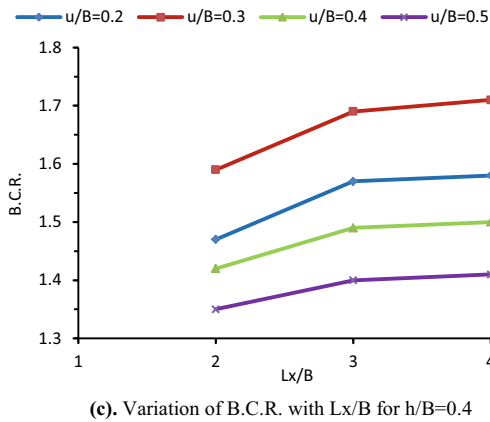
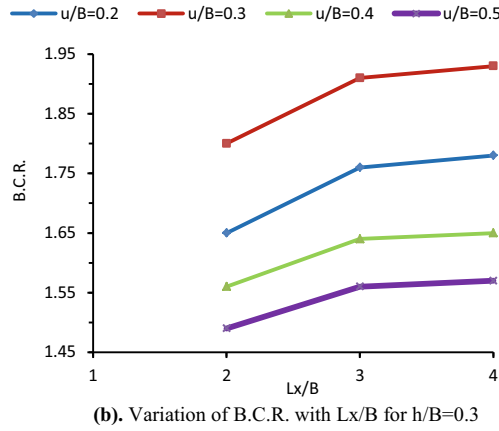
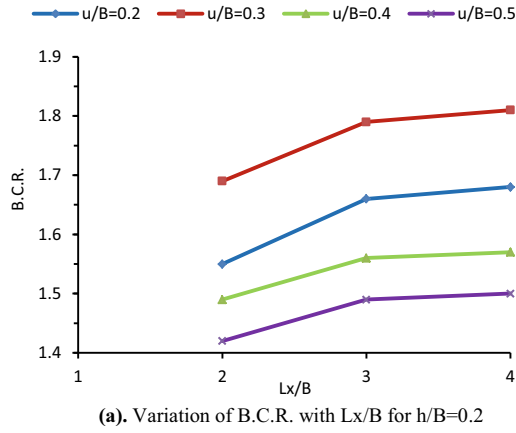
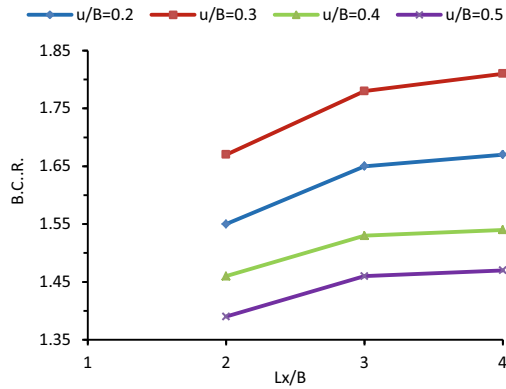
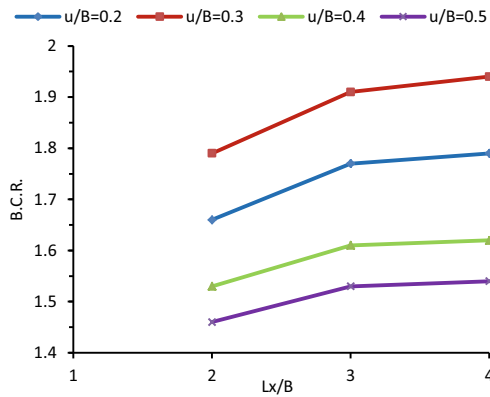


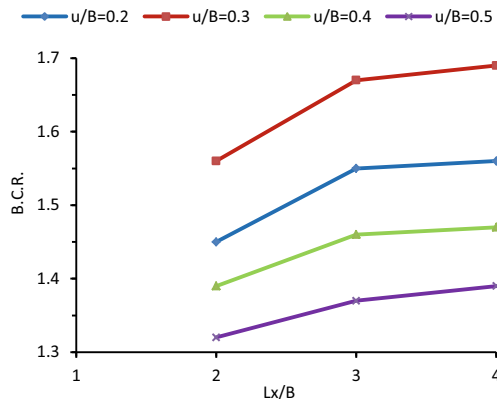
Fig. 6 Test series A for $S/B = 1$



(a). Variation of B.C.R. with Lx/B for h/B=0.2

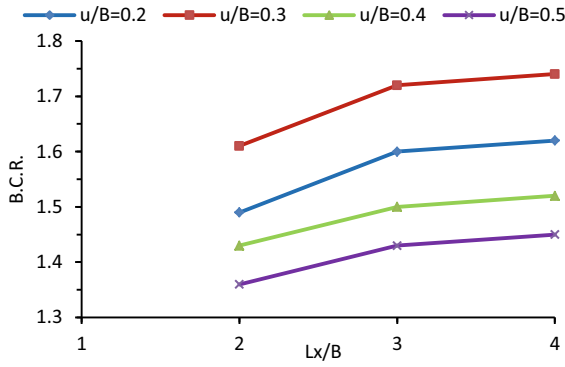


(b). Variation of B.C.R. with Lx/B for h/B=0.3

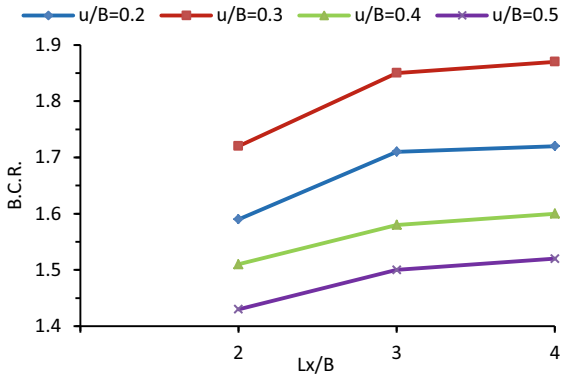


(c). Variation of B.C.R. with Lx/B for h/B=0.4

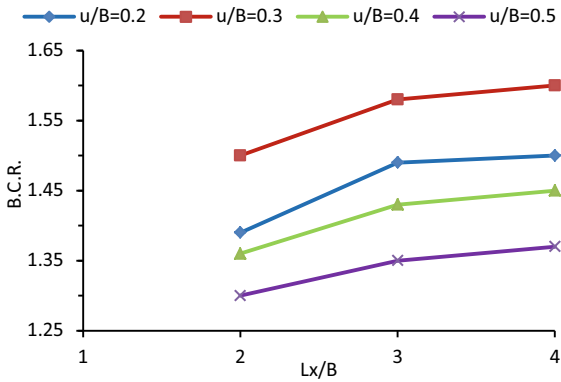
Fig. 7 Test series B for S/B = 2



(a). Variation of B.C.R. with L_x/B for $h/B=0.2$



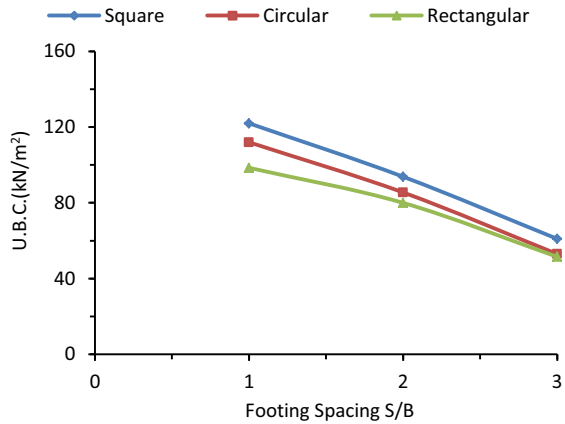
(b). Variation of B.C.R. with L_x/B for $h/B=0.3$



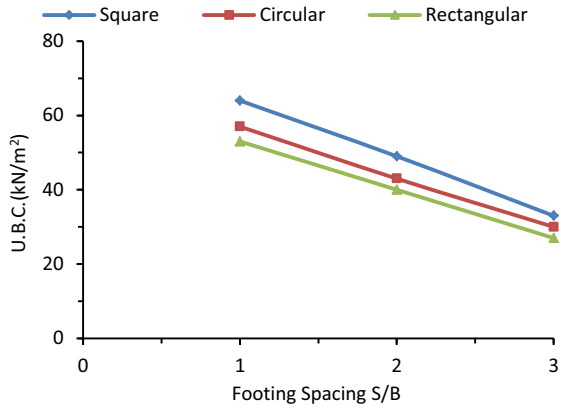
(c). Variation of B.C.R. with L_x/B for $h/B=0.4$

Fig. 8 Test series C for $S/B = 3$

Fig. 9 Variation in UBC with center to center distance between footings



(a). Test series D for optimum geogrid reinforced sand



(b). Test series E for unreinforced sand

the results it was observed that for both the test series D and E, the ultimate bearing capacity of square footing is more than the circular and rectangular footing of same cross-sectional area. Also the same trend was observed while finding the optimum geogrid reinforcement for footing spacing (S/B). As the center to center distance between footings decreases the ultimate bearing capacity increases. For all the three shapes it was observed that the UBC of three interfering footing is nearly equal to the UBC of isolated footing for S/B more than three.

5 Conclusions

From the present study, the following conclusions were drawn:

- Reinforcement configuration plays a very significant effect on the behavior of reinforced sand foundation.
- The optimum length of geogrid reinforcement on either side beyond center of footing is three times the width of the footing ($L_x/B = 3$).
- The optimum depth of first layer geogrid reinforcement is 0.3 times the width of the footing ($u/B = 0.3$) and the optimum vertical distance between geogrid reinforcing layers is also 0.3 times the width of the footing ($h/B = 0.3$).
- The ultimate bearing capacity of square footing is more than the circular and rectangular footing of the same cross-sectional area.
- The bearing capacity of interfering footing on unreinforced and reinforced sand increases as spacing decreases.
- A considerable improvement in bearing capacity and settlement has been observed by providing geogrid reinforcement layers in the foundation soil.
- When the footings are placed at a distance more than three times the width of the footing, there is no interference.

References

- Al-Ashou MO, Sulaiman RM, Mandal JN (1994) Effect of number of reinforcing layers on the interference between footings on reinforced sand. *Indian Geotechn J* 24(3):285–301
- Das BM, Cherif SL (1983) Bearing capacity of two closely spaced shallow foundations on sand. *Soils Found* 23(1):1–7
- Daud KA (2012) Interference of shallow multiple strip footings on sand. *Iraqi J Mech Mater Eng* 12(3):492–507
- Ghazavi M, Lavasan AA (2008) Interference effect of shallow foundation constructed on sand reinforced with geosynthetics. *Geotext Geomembr* 26:404–415
- Ghazavi M, Lavasan AA (2012) Behavior of closely spaced square and circular footings on reinforced sand. *Soils Found* 52(1):160–167
- Ghosh P, Kumar J (2009) Interference effect of two nearby strip footing on reinforced sand. *Contemp Eng Sci* 2(12):577–592
- Ghosh P, Sharma A (2010) Interference effect of two nearby strip footings on layered soil: theory of elasticity approach. *Acta Geotech* 5(3):189–198
- Ghosh P, Kumar S (2011) Interference effect of two nearby strip surface footings on cohesionless layered soil. *Int J Geotechn Eng* 5(1):87–94
- Graham J, Raymon GP, Suppiah A (1984) Bearing capacity of three closely spaced footings on sand. *J Geotechn* 34(2):173–182
- Khan IN, Bohara KC, Ohari ML, Sinfh AA (2006) Study on interference of surface model footing resting on sand. *Inst Eng Malays* 67:15–23
- Khing KH, Das BM, Puri VK, Cook ED, Yen SC (1992) Bearing capacity of two closely-spaced strip foundations on geogrid reinforced sand. In: *Proceedings of international symposium on earth reinforcement practice, Fukuoka, Japan, vol 1, pp 619–624*

- Kouzer KM, Kumar J (2010) Ultimate bearing capacity of a footing considering the interference of an existing footing on sand. *Geotechn Geol Eng* 28(4):457–470
- Kumar A, Saran S (2003) Closely spaced footings on geogrid-reinforced sand. *J Geotech Geoenvironmental Eng* 129(7):660–664
- Kumar J, Bhattacharya P (2010) Bearing capacity of interfering multiple strip footings by using lower bound finite elements limit analysis. *Comput Geotech* 37:731–736
- Kumar J, Bhoi MK (2009) Interference of two closely spaced strip footings on sand using model tests. *J Geotech Geoenvironmental Eng* 134(4):595–604
- Kumar J, Ghosh P (2007) Ultimate bearing capacity of two interfering rough strip footings. *Int J Geomech* 7(1):53–62
- Lee J, Eun J (2009) Estimation of bearing capacity for multiple footings in sand. *Comput Geotech* 36:1000–1008
- Mabrouki A, Benmeddou D, Frank R, Mellas M (2010) Numerical study of the bearing capacity for two interfering strip footings on sand. *Comput Geotech* 37:431–439
- Naderi E, Hataf N (2014) Model testing and numerical investigation of interference effect of closely spaced ring and circular footings on reinforced sand. *J Geotext Geomembr* 42:191–200
- Nainegali L, Basudhar P (2011) Interference of two closely spaced footings: a finite element modeling. *Geo-Frontiers* 3726–3735
- Nainegali L, Basudhar P, Ghosh P (2013) Interference of two asymmetric closely spaced strip footings resting on non-homogeneous and linearly elastic soil bed. *Int J Geomech* 13(6):840–851
- Pusadkar SS, Saraf SS (2012a) Interference of adjoining circular footings on reinforced sand. In: *Proceeding of the Indian geotechnical conference, advances in geotechnical engineering, New Delhi, India, vol 1, pp 373–375*
- Pusadkar SS, Saraf SS (2012b) Interference of adjoining rectangular footings on reinforced sand. *Int J Civil Eng and Technol(IJCIET)* 3(2):447–454
- Srinivasana V, Ghosh P (2013) Experimental investigation on interaction problem of two nearby circular footings on layered cohesionless soil. *Geomech GeoEngg* 8(2):97–106

Analysis of Torpedo Anchors for Mooring Operations



S. Keerthi Raaj , R. Sundaravadivelu, and Nilanjan Saha

Abstract A novel technique of dynamically installing torpedo-shaped anchors is investigated. A vast extent of uncertainties arises in pull-out capacity estimation due to the excessive tilt of a torpedo anchor during free-fall and subsequent embedment into the seafloor. This paper will investigate the issues encountered by the torpedo anchor during the vertical drop, which ultimately reduces the pull-out resistance. The pull-out resistance study offered by torpedo anchors is investigated using a finite element tool, PLAXIS 3D. A series of pull-out tests were conducted with anchors under four different ballast conditions (20, 40, 60 and 80%) with three chosen fin configurations (without fin, 3 fins and 4 fins). The anchors are tested for various inclinations (0° , 2.5° , 5° , 7.5° and 10°) and the effect of torpedo anchor tilt on pull-out resistance is studied, and the allowable range of anchor tilt was recommended. Thus, this study provides the benefit of ideal ballast and fins arrangements.

Keywords Torpedo anchors · Pull-out resistance · PLAXIS 3D

1 Introduction

Offshore construction requiring anchors is usually expensive and challenging. The cost of traditional anchoring systems (like drag anchors, plate anchors, piles, suction anchors and gravity structures) increases exponentially with an increase in water depth. Advanced and novel techniques of dynamically installing torpedo-shaped anchors are used nowadays to avoid external driving energy; easier, faster and simpler installation techniques; water depth independency; ability to withstand inclined load; limited use of anchor handling vessels (AHV) and remotely operated vehicles (ROVs); precise installation location positioning and needless installation time made them more economical. This most promising concept is successfully commissioned in Brazilian offshores and Goja, North Sea (Lieng et al. 2010; Medeiros 2002). These methods have been successfully used in offshore; however, there are

S. Keerthi Raaj (✉) · R. Sundaravadivelu · Nilanjan Saha
Indian Institute of Technology, Chennai, India
e-mail: mskraaj44@gmail.com

© Springer Nature Singapore Pte Ltd. 2020
M. Latha Gali and P. Raghuvver Rao (eds.), *Construction in Geotechnical Engineering*, Lecture Notes in Civil Engineering 84,
https://doi.org/10.1007/978-981-15-6090-3_11

no well-established practices or design guidelines on the precise embedment depth or on the model for prediction of pull-out capacity (de Aguiar et al. 2013; Kim et al. 2015; Liu et al. 2014; Soh et al. 2015). de Aguiar et al. (2013) remarked the prediction of pull-out capacity and stress in the structure remains a great challenge. There exist uncertainties in pull-out capacity estimation due to the excessive inclination of torpedo anchor during free-fall and subsequent embedment in the seafloor. This paper will investigate the issues encountered in the verticality of the torpedo anchor, which ultimately reduce the pull-out resistance.

Researchers have noted that the influence of the tilt angle of a free-fall torpedo pile anchor on pull-out capacity is significant (Ehlers et al. 2004; Liu et al. 2014; Brandao et al. 2006). Liu et al. (2014) noted widespread usage of torpedo anchors in offshore exploration but the unpredictability related to the verticality during penetration is a major cause to affect their long-term pull-out capacity. This tilt angle leads to a reduction in estimated theoretical pull-out capacity. In the Albacora Leste field test, anchors are retrieved and redeployed due to excessive anchor tilt of more than 10° which leads to huge operational costs. Added in situ field test from Brazilian offshore reveals that always there exists a small tilt angle even after embedment due to the resistance, which affects the overall pull-out capacity. The quantitative measurement of the tilt angle and their influence on pull-out capacity was analyzed numerically using PLAXIS 3D (Brinkgreve et al. 2016), a finite element commercial package. The focus of the present study is to assess the pull-out capacity of torpedo anchors by varying the amount of ballast, number of fins and inclination configurations.

2 Anchor and Soil Properties

A typical torpedo anchor consists of a bottom nose, a ballasted trunk with fluke and pad-eye. In this study, the importance of ballasted trunk with and without a varied number of fluke is studied. The uncertainty encountered in the verticality of the torpedo anchor will reduce the pull-out resistance incorporated into the analysis. In the present study, the torpedoes used by Medeiros (2002) in field study are analyzed and validated, which has a diameter of 0.762 m, 12 m long, dry weight of 24 tonnes without a fin and also vertical fins of $0.45 \text{ m} \times 9 \text{ m}$ are investigated in the study. The geometrical representation of the anchor is presented in Fig. 1a–c without and with 3 and 4 fins, respectively. The typical geometrical dimensions of the anchor with fins are shown in Fig. 1d. The included angle between the fins is 120° and 90° for 3 and 4 fins, respectively. The torpedo anchor has a conical tip with a taper angle of 30° and thickness of the fluke and ballasted trunk are 0.05 m. In the present study, the behavior of the torpedo anchor after the free-fall and embedment into the soil is considered, so the importance of hydrodynamic center and gravity center is neglected.

The shear strength profile of Campos Basin (Medeiros 2002) soil is represented by $S = 5 + 2x$, where x is a vertical distance below the ground (in meters). Pecorini and De (2015) used cohesion and frictional angle of 5 kPa and 17° to provide the

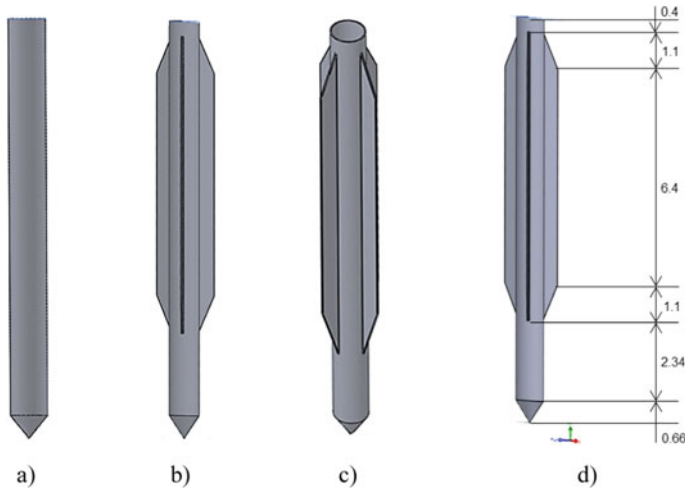


Fig. 1 Torpedo anchor **a** without fin, **b** with 3 fins, **c** with 4 fins and **(4)** anchor with the geometrical dimensions (all dimensions are in meters)

Table 1 Geotechnical properties of marine clay sediments and torpedo anchor

Clay sediment	
Material model	Modified Cam-Clay
Drainage type	Undrained
Cohesion, kN/m^2	5.00
Angle of internal friction, φ ($^\circ$)	17
Normal consolidation line slope, λ	0.205
Swell line slope, κ	0.044
<i>Torpedo Anchor</i>	
Model type	Linear elastic
Unit weight of an anchor	65 kPa
Modulus of Elasticity, kN/m^2	31×10^6 kPa
Poisson's ratio	0.2
Drainage type	Non-porous

required shear strength profile with the Mohr–Coulomb model. In the present case, the modified Cam–Clay model is used to represent the same soil profile shear strength with addition stiffness property using the slope of normal consolidation line (κ) and slope of the swell line (λ). The geotechnical properties of a typical marine site with clay sediments and the corresponding torpedo anchor employed are mentioned in Table 1.

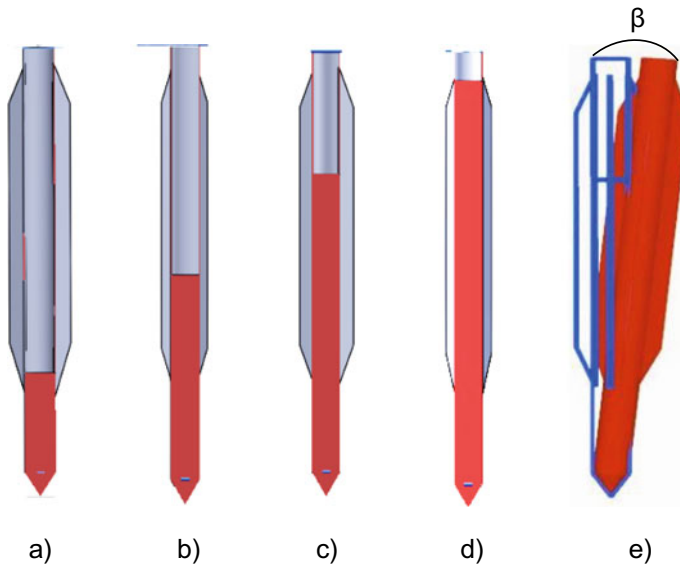


Fig. 2 Torpedo anchor with different ballast weights **a** 20%, **b** 40%, **c** 60%, **d** 80% and **e** with inclination

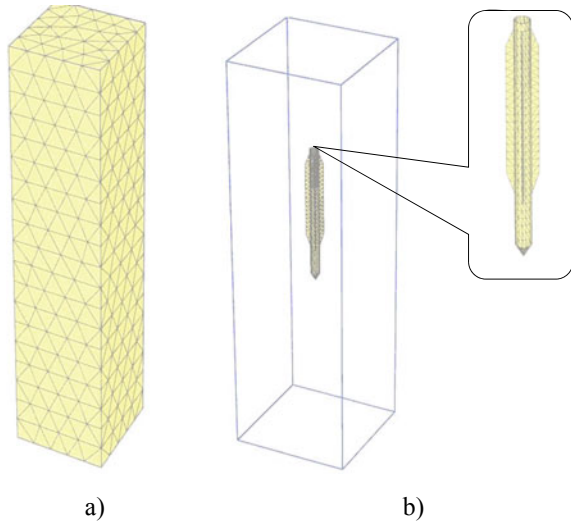
3 Numerical Procedures

In this set of experiments, the amount of ballast is varied in consonance with other parameters to study their influence on pull-out capacity. The parameters considered are: (i) the weight of ballast, (ii) the number of flukes and (iii) the anchor tilt angle. A series of pull-out tests are conducted with anchors under four different ballast conditions (20, 40, 60 and 80%) with three chosen fin configurations (without a fin, 3 fins and 4 fins). The anchors are tested for various inclinations ($\beta = 0^\circ, 2.5^\circ, 5.0^\circ, 7.5^\circ$ and 10.0°) and the effect of anchor tilt angle on pull-out capacity is studied. Each anchor model is denoted as BxxFyIz.z. For instance, B60F4I7.5 signifies that the torpedo anchor has a ballast weight of 60% with four fins and the anchor is tested for an inclination of 7.5° about the vertical axis in the positive x-direction. In total, around 60 numerical trials are conducted and they are discussed in this paper (Fig. 2).

4 Modeling of Torpedo Anchor

PLAXIS 3D, a commercial three-dimensional finite element tool was used to perform the real-time pull-out capacity estimation. Since the torpedo-shaped anchor has a complex geometry, to compute the pull-out capacity a numerical-based finite element model is used to assess the interface between the anchor and surrounding soil. The

Fig. 3 Numerical representation of torpedo anchors with the surrounding soil **a** total domain and **b** torpedo anchor (detail)

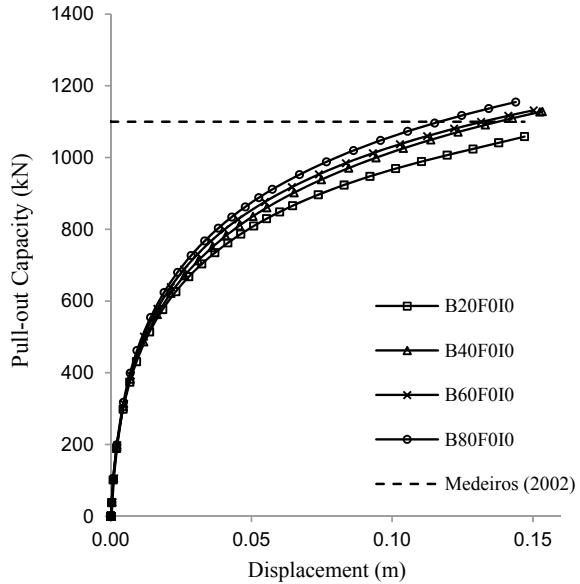


3D finite element model has a length of 35 m with a square cross-section of 10 m in lateral directions as shown in Fig. 3a. The torpedo anchor is modeled first using a mesh generation algorithm and later imported into the PLAXIS 3D program. The 3D model torpedo anchor possesses a diameter of 0.762 m and 12 m long, which is embedded in the soil domain (see Fig. 3b). The embedded 3D torpedo anchor is assumed as a rigid body, which has a negligible change in shape during operations (i.e., deformations during the entry/pull-out is neglected). This assumption is based on the fact that the stiffness of the torpedo is large compared to the stiffness of the soil. The rigid body motion is expressed in terms of translation and rotation. Here, the translation corresponds to tensile load application direction and rotation corresponds to the tilt of the torpedo anchor, respectively.

5 Validation

A full-scale field test is conducted by Medeiros (2002) in the Campos Basin, with 0.762 m torpedo piles and medium tip penetration of 20 m. The torpedo anchors offered a pull-out capacity of 1100 kN while applying a tensile load in a horizontal direction. The same condition is modeled in PLAXIS 3D, and the typical load–displacement curve is shown in Fig. 4. From Fig. 4, for 80% ballast weight the ultimate pull-out capacity is 1154 kN. The obtained results from the present simulation are close to the field observations. The difference in the field and the numerical result is about 4.6% and thus, the PLAXIS 3D numerical model can represent the full-scale field results. Consequently, for 20, 40 and 60% ballast condition the ultimate pull-out resistance are 1058, 1126 and 1131 kN, respectively, and the difference is within a

Fig. 4 Validation—pull-out resistance of finless torpedo anchor



permissible 5%. From Fig. 4, it is also noted that with an increase in ballast weight, the pull-out capacity of the anchor increases.

6 Results and Discussion

The deformed mesh and tilted torpedo anchor models are presented in Fig. 5a, b. de Sousa et al. (2010) studied the failure mechanism of the torpedo anchor in a cohesive soil and observed that for horizontal loading, there is a mobilization of large soil mass before the collapse followed by subsequent plastic deformation. The same type of failure is observed while applying the tensile load in the lateral direction as depicted in Fig. 5b, where large mobilization of soil around the torpedo anchor is evident. In this section, the effect of the tilt angle, number of fins and ballast weight are discussed in detail.

6.1 Effect of the Tilt Angle

Figure 6 indicates the typical load–displacement curve for various tilt angles for four-finned torpedo anchors with 40% ballast conditions. It is clearly observed that for an increase in tilt angle there is a gradual reduction in the pull-out capacity. For a torpedo anchor without any initial inclination (i.e., perfectly embedded vertically

Fig. 5 a 3D deformed torpedo anchor b deformed mesh slice

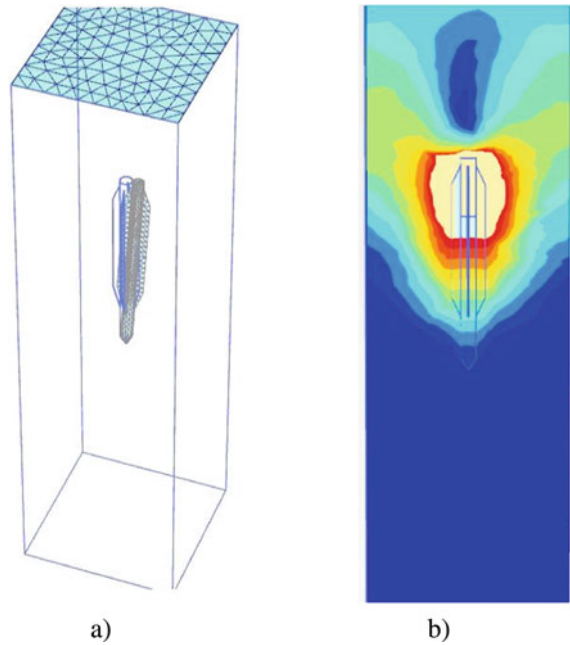
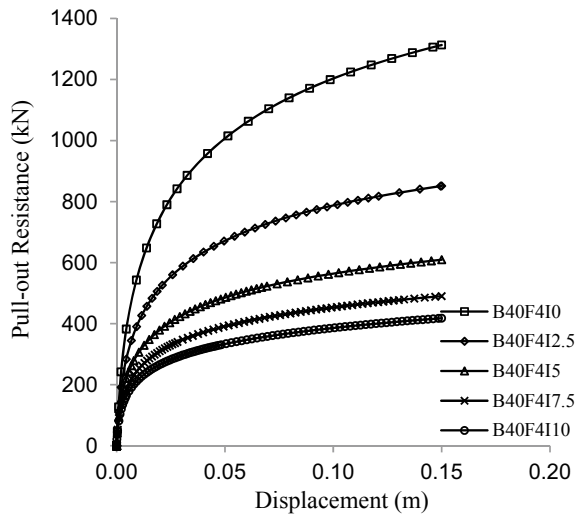
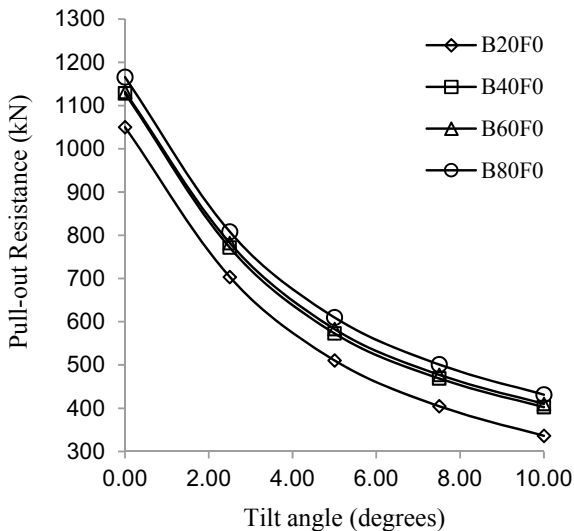


Fig. 6 Effect of the tilt angle



in the subsoil domain), the pull-out capacity is maximum. With an increase in tilt angle from 0° to 10° , the pull-out capacity drops from 1313 to 418 kN. The reduction in pull-out capacity is 35, 53, 63 and 68% for 2.5° , 5° , 7.5° and 10° , respectively. Therefore, the torpedo anchors with lesser tilt angle are stable and have an efficient pull-out capacity. For a more stable anchor the tilt should be less than 2.5° , even

Fig. 7 Effect of ballast weight



which at 2.5° the capacity is reduced by 35%. Hence, precise installation technique should be adopted for achieving lesser anchor tilt; otherwise even small tilt angles may cause substantially reduced pull-out capacity.

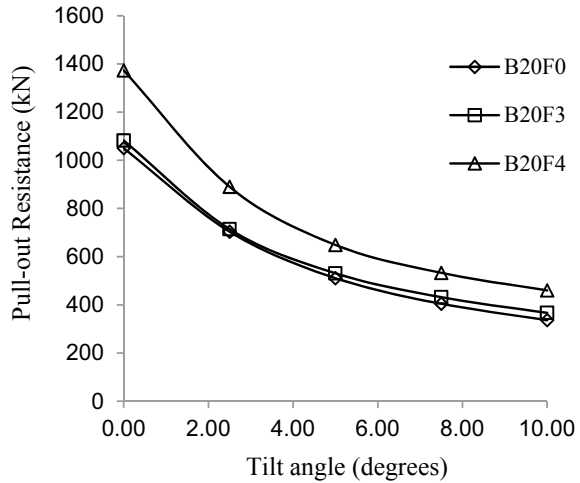
6.2 Effect of Ballast Weight

Figure 7 shows the typical load–displacement curve for different percentages of ballast conditions for finless torpedo anchor with zero inclination conditions. From the figure, one observes that with an increase in the percentage of ballast weight there is a gradual increase in the pull-out capacity. For a torpedo anchor with 80% ballast weight the pull-out capacity is maximum. With an increase in tilt angle from 0° to 10°, the pull-out capacity drops for all the ballast conditions. The reduction in pull-out capacity is about 31, 48, 57 and 63% for 2.5°, 5°, 7.5° and 10°, respectively, for 80% ballast weight. Therefore, the torpedo anchors with more ballast weight are more stable and have a maximum pull-out capacity. Hence, an anchor with larger scrap weight should be used for achieving more penetration depth and pull-out capacity.

6.3 Effect of the Number of Fins

Figure 8 represents the typical load–displacement curve for various finned torpedo anchor with 20% ballast conditions. One observes that for an increase in the number of fins there is a gradual increase in the pull-out capacity. For a torpedo anchor

Fig. 8 Effect of number of fins



without any fin, the pull-out capacity is minimum. The pull-out capacity drops for all the fin conditions, with an increase in tilt angle from 0° to 10°. The reduction in pull-out capacity is 35, 53, 61 and 65% for 2.5°, 5°, 7.5° and 10°, respectively, for four-finned torpedo anchor. Therefore, the torpedo anchors with more number of fins are stable and have the additional pull-out capacity. The stability of torpedo anchors is increased with an increased number of fins since they offer extra lateral stability to the anchor. Hence, extra fins not only help during free-fall but also in achieving additional stability in a pull-out stage, though they offer lesser embedment depth during anchor penetration in the subsoil.

7 Conclusion

This paper attempts a comprehensive study in analyzing the various design parameters of torpedo anchor, viz., the number of fins, the effect of tilt angle and the amount of ballast on the pull-out capacity. The soil is assumed to be marine clay sediment having properties of Indian offshore. The torpedo anchors are assumed to be made of linearly elastic material. The numerical results are validated through the established full-scale field results (Medeiros 2002), and the potential advantages of ideal ballast and fins arrangements with the goal of maximum ultimate capacity are discussed. The conclusions of the present study are:

- i. The torpedo anchors with lesser tilt angle are stable and have an efficient pull-out capacity. A stable anchor should have the tilt angle within 2.5°.

- ii. The torpedo anchors with more ballast weight are stable and have a larger pull-out capacity.
- iii. The stability of torpedo anchors increases with an increased number of fins since they offer extra lateral stability to the anchor.
- iv. The torpedo anchors with lesser tilt angle, more ballast weight, with fin are more stable and observed to offer maximum pull-out resistance.

Acknowledgments The first author gratefully acknowledges the support from the Ministry of Human Resources and Development, Government of India through Indian Institute of Technology Madras, Chennai. The author also thanks the Department of Ocean Engineering and the Department of Civil Engineering of IIT Madras for the research facilities.

References

- Brandao FEN, Henriques CCD, Araujo JB, Ferreira OCG, dos Santos Amaral C (2006) Albacora leste field development- FPSO P-50 mooring system concept and installation. In: Proceedings of offshore technology. Offshore Technology Conference. Texas U.S.A. <https://doi.org/10.4043/18243-ms>
- Brinkgreve RBJ, Swolfs WM, Engine E (2016) PLAXIS user's manual, PLAXIS bv, The Netherlands
- de Aguiar CS, de Sousa JM, Sagrilo LS, Ellwanger GB, Porto EC (2013) a simple approach for determining the holding capacity of torpedo anchors embedded in cohesive soils. Proc Int Conf Offshore Mech Arctic Eng. <https://doi.org/10.1115/OMAE2013-10809>
- de Sousa JM, de Aguiar CS, Ellwanger GB, Porto EC, Foppa D, de Medeiros CJ (2010) Undrained load capacity of torpedo anchors embedded in cohesive soils. ASME Proc Jo Offshore Mech Arctic Eng 133(2) (2010). <https://doi.org/10.1115/1.4001953>
- Ehlers CJ, Young AG, Chen J (2004) Technology assessment of deepwater anchors. In: Proceedings of 36th annual offshore technology conference, offshore technology conference, Houston, Texas, Paper No. OTC 16840 (2004)
- Kim YH, Hossain MS, Wang D, Randolph MF (2015) Numerical investigation of dynamic installation of torpedo anchors in clay. Ocean Eng 108:820–832. <https://doi.org/10.1016/j.oceaneng.2015.08.033>
- Lieng JT, Tjelta TI, Skaugset K (2010) Installation of two prototype deep penetrating anchors at the Goja Field in the North Sea. In: Proceedings of the 2010 offshore technology conference, paper OTC 20758
- Liu XD, Sun JJ, Yi JT, Lee FH, Gu HH, Chow YK (2014) Physical and numerical modeling of the performance of dynamically installed anchors in clay. ASME. Int Conf Offshore Mech Arctic Eng 1A: Offshore Technology. <https://doi.org/10.1115/omae2014-23769>
- Medeiros CJ (2002) Low cost anchor system for flexible risers in deep waters. In: Proceedings of offshore technology. Offshore Technology Conference. Texas U.S.A. <https://doi.org/10.4043/14151-ms>

- Pecorini D, De A (2015) Pull-out capacity analysis of offshore torpedo anchors using finite-element analysis. In: Proceedings of international society of offshore and polar engineers, Hawaii, USA. ISSN 1098-6189
- Soh BP, Pao W, Al-Kayiem HH (2015) Numerical analyses for improved hydrodynamics of deep water torpedo anchor. In: Proceedings of IOP conference series: material science engineering, 100. <https://doi.org/10.1088/1757-899x/100/1/012059>

Ground Improvement for Foundations of Structures Using Stone Column—Case Study on Road Connectivity to ICTT, Vallarpadam Port in Cochin, Kerala, India



Avik Kumar Mandal, S. Sailesh, and Pradyot Biswas

Abstract Vallarpadam ICTT Port in the state of Kerala was connected with NH-47 by 17.20 km long four-lane highway. Starting from the junction with NH-47, the first 8.40 km length of the project road was on land area. The rest of the project corridor was routed across reclaimed land and the last part of the road was in island of port area. Deep soft clay deposits were found along the project road. In the land area of project stretch, stone column had been adopted for the foundations of RCC retaining wall and box underpass structure as an alternative to pile foundations. The details of foundation adopted, design involving evaluation of load bearing capacity of stone columns-treated soft ground for the retaining wall and underpass structures, and results of load tests on stone columns are provided here in this paper. Details of machinery used, procedures adopted in the installation of vibratory stone columns, and different field controls adopted to ensure the proper formation of stone columns are presented here.

Keywords RCC retaining wall and box underpass · Vibratory stone columns · Field control and load test over stone columns

1 Introduction

Vallarpadam area of Cochin in the state of Kerala is a port hub and is located in marine backwater area. The ICTT Port at Vallarpadam area was connected with NH-47 by 17.20 km long four-lane highway. The initial 8.40 km length of the four-lane highway connecting ICTT Port was in the land portion and it had limited right of way

A. K. Mandal (✉) · S. Sailesh · P. Biswas
LEA Associates South Asia Pvt. Ltd, New Delhi, India
e-mail: avik@lasaindia.com

S. Sailesh
e-mail: sailesh@lasaindia.com

P. Biswas
e-mail: pradyotbiswas@lasaindia.com

to accommodate both the main carriageway and service road. The maximum height of main carriageway embankment was about 8.0 m in the land area and subsoil is having soft soil (SPT, $N < 5$) deposits up to 12.0 m. So the high embankment of main carriageway had to be confined by RCC retaining wall. However, problems in inadequate bearing capacity and rotational stability had to be overcome for the retaining walls separating the high embankment of main carriageway and service road. In addition to that, due to the presence of deep soft clay deposit in subsoil of land area, the required safe load bearing capacity was not available for the shallow foundations of RCC box-type underpass structure in original in situ ground condition. So the ground improvement measures by “Vibrofloat Stone Column” were adopted for the foundations of RCC retaining wall as well as for the RCC box underpass structure in the land portion of the project road. Brief details of design and construction methodology of stone column adopted, including the machinery used for installation and different field quality control tests for ensuring the formation of compacted stone column, are discussed in this paper.

2 Details of Typical Sections

The details showing typical cross-sections for the RCC retaining wall supporting the main carriageway embankment and longitudinal section for the RCC box type underpass structure along the land portion of ICTT port connecting road are given below.

2.1 *RCC Retaining Wall in Road Section*

The typical cross-section of RCC retaining wall in between the main carriageway and service road is shown in Fig. 1. The maximum height of embankment was up to 8.00 m and the design height of RCC retaining wall was varying from 4.00 to 8.00 m from the founding level. Generally, the side slope adopted for the retaining wall backfill soil embankments was 1 V: 2H. Locally available Moorum was used as backfill embankment material which had cohesion (c) 3.0 t/m², angle of internal friction (ϕ) 27°, and dry density (γ_d) 1.90 t/m³.

2.2 *RCC Box Underpass Structure*

The underpass of size 1 × 6.00 m (span) × 2.50 m (height) was provided to give access to the cross road traffic in the land area of the project road. The typical longitudinal section of RCC box-type underpass structure is shown in Fig. 2.

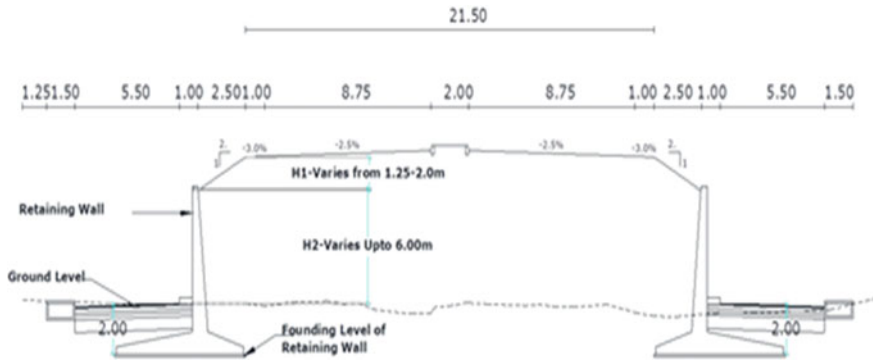


Fig. 1 Typical details of road cross-section with RCC retaining wall

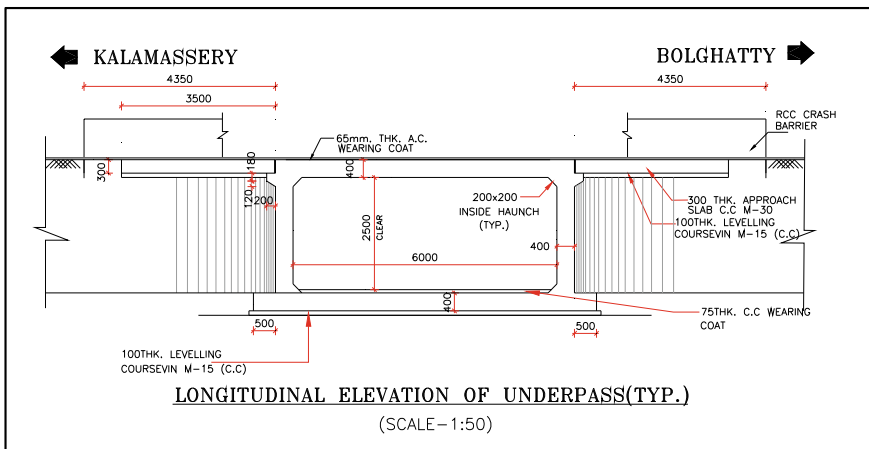


Fig. 2 Typical details of longitudinal section of RCC box type underpass

3 Geotechnical Investigations and Typical Properties of Foundation Soil

For the engineering assessment of foundation of structures, a detailed “geotechnical investigation work” comprising both field and laboratory tests were undertaken at retaining wall and underpass locations along the project road. A total of 37 numbers of boreholes of adequate depth were explored all along the alignment of project road in the land area.

The field investigation program consisted of exploration of minimum 150 mm diameter boreholes up to the desired depth and the recording of subsurface profile along with all related field tests and also the collection of different types of foundation soil samples following the related BIS guidelines.

The detailed laboratory investigations, namely soil classification tests (grain size analysis, Atterberg limits, i.e. LL, PL, PI, and SL), natural moisture contents (NMC), in situ density, specific gravity, shear strength tests (cohesion and angle of shearing resistance) and settlement parameters (compression index, recompression index, void ratio, and coefficient of consolidation) of the collected soil samples and chemical tests of subsoil and groundwater were conducted as per the relevant BIS guidelines.

The water table was found almost at the original ground level as observed through the exploratory boring.

The following section gives the broad range of the foundation soil stratifications below the existing ground level as found through investigations.

3.1 For Retaining Wall-Supported Road Section

A total of 35 numbers of boreholes of depth varying from 10.0 to 30.0 m were drilled along the retaining wall locations in the land area of the project road. Typical geotechnical engineering properties of the foundation soil layers in the retaining wall locations of land area are mentioned in Table 1, from which it is clear that the foundation soil was of soft nature with low shear strength and the compressibility of the foundation soil was also high.

3.2 For RCC Underpass Structure

Two numbers of exploratory boreholes of 18.00–20.00 m depth were conducted in one RCC box-type underpass location along land area of the project road. The typical range of geotechnical engineering properties of the foundation soil layers as found from the boreholes in the underpass locations are given in Table 2. From this table, the clear presence of very soft/soft to medium stiff and compressible clayey subsoil layers is observed in the underpass location.

4 Geotechnical Design of Foundation of Structure and Its Ground Treatment

Geotechnical design for the shallow, that is, open foundations of structures comprised the estimation of safe load bearing capacity of foundations against the shear failure of foundation soil without exceeding the permissible total settlement. This was done as per the relevant guidelines namely IS: 6403, IS: 8009 (Part 1), and IRC: 78-2014.

Table 1 Typical geotechnical engineering properties of foundation soil layers in retaining wall locations

Layer no.	Thickness of layer (m)	SPT values	Unit Weight i.e. γ_{bulk} (t/m^3)	Shear strength parameters		Compressibility parameters				
				Cohesion i.e. c (t/m^2)	Angle of internal friction i.e. ϕ (deg.)	Compression Index (C_c)	Recompression index (C_r)	Initial Void ratio (e_0)	Coefficient of consolidation i.e. C_v (m^2/day)	Preconsolidation pressure i.e. p_c (t/m^2)
Layer 1	4.2-5.3	2	1.70	1.50	0	0.75	0.075	2.00	0.004	5
Layer 2	2.5	4	1.80	2.50	0	0.45	0.045	0.71	0.004	10
Layer 3	2.9	5	1.85	1.30	26	0.25	0.025	0.71	0.008	15
Layer 4	9.9	8-14	1.95	4.50	15	0.20	0.02	0.68	0.008	25
Layer 5	11.2	18-50	2.00	0.00	30	-	-	-	-	-

- Layer 1: Soft clayey silt/silty clay
- Layer 2: Soft to medium stiff sandy silty clay
- Layer 3: Loose clayey silty sand
- Layer 4: Stiff lateritic silty sandy clay
- Layer 5: Medium dense to dense clayey silty sand

Table 2 Typical geotechnical engineering properties of foundation soil layers in underpass location

Layer No.	Thickness of layer (m)	SPT values	Unit Weight i.e. γ_{bulk} (t/m^3)	Shear strength parameters		Compressibility parameters					
				Cohesion i.e. c (t/m^2)	Angle of internal friction i.e. ϕ (deg)	Compression index (C_c)	Recompression index (C_r)	Initial void ratio (e_0)	Coefficient of consolidation i.e. C_v (m^2/day)	Preconsolidation pressure i.e. p_c (t/m^2)	
Layer 1	7.85	1	1.25	1.20	0	1.21	0.19	3.00	0.0005	5	
Layer 2	3.28	5	1.80	3.00	5	0.25 ¹	0.025	0.85	0.0040	15	
Layer 3	8.13	30	1.90	–	30	–	–	–	–	–	

Layer 1: Very soft silty clay/clayey silt with organic matter/decomposed wood

Layer 2: Soft to medium stiff sandy silty clay

Layer 3: Medium dense to dense clayey silty sand

The load bearing capacity analysis for the foundations of structures was performed in original ground conditions, that is, without any kind of ground treatment as well as with ground treatment condition.

The results of load bearing capacities for retaining wall and underpass structures are given separately in the following paragraphs.

4.1 For RCC Retaining Wall

The shallow foundation for retaining wall was strip footing with minimum foundation embedment depth as 2.00 m satisfying the requirement given in IRC: 78-2014.

The results of “Load Bearing Capacity Analysis” for the shallow foundations of RCC retaining wall in original ground, that is, without any kind of ground treatment condition are presented in Table 3.

From Table 3 it is clear that the load bearing capacities of the foundations of RCC retaining wall in original ground condition, that is, without any ground treatment condition were not adequate and the estimated total settlement corresponding to the required load intensity was also high. So to satisfy the requirement of safe load bearing capacity of shallow foundation, it was required to adopt the ground treatment under the foundation base of retaining wall.

To achieve the required safe load carrying capacity for the foundation of retaining wall, the ground treatment measures in the form of “removal and replacement of existing top weak compressible soil” was examined first considering the ease of construction, time, and economics. However, because of very high groundwater table and close proximity of soft soil, removal of existing foundation soil was found economical and practical up to a maximum depth of 2.50 m below OGL. In view of that a maximum of 2.50 m depth of removal and replacement had been considered and analyzed.

Table 3 Summary of load bearing capacity analysis for shallow foundations of retaining wall in “Original Ground Condition”

Design height (m)	Foundation width (m)	Depth of foundation from OGL (m)	Safe load bearing capacity of open foundation (t/m^2)	Required load bearing capacity (t/m^2)	Estimated total settlement corresponding to the required load bearing capacity (mm)	Remarks
4.00	3.65	2.00	2.00–3.65	7.50	36–171	Not ok
5.00	4.45	2.00	2.00–6.00	9.80	94–279	Not ok
6.00	5.85	2.00	2.85–6.75	11.20	96–210	Not ok
7.00	6.70	2.00	4.10–5.75	11.20	135–169	Not ok
8.00	7.40	2.00	4.00	11.80	185	Not ok

Table 4 Summary of load bearing capacity analysis for shallow foundations of retaining wall after doing “Ground Treatment by Removal and Replacement”

Design height (m)	Foundation width (m)	Depth of foundation from OGL (m)	Thickness of removal and replacement with granular material (m)	Safe Loadbearing capacity of open foundation (t/m^2)	Required Load bearing capacity (t/m^2)	Remarks
4.00	3.65	2.00	1.50–2.50	3.40–7.00	7.50	Not ok
5.00	4.45	2.00	1.00–2.50	3.00–8.50	9.80	Not ok
6.00	5.85	2.00	1.00–2.50	3.50–7.75	11.20	Not ok
7.00	6.70	2.00	2.50	5.00–6.50	11.20	Not ok
8.00	7.40	2.00	2.50	5.60	11.80	Not ok

The results of “Load Bearing Capacity Analysis” for the shallow foundations of RCC retaining wall with ground treatment, that is, after replacement of top soft compressible soil with compacted granular soil are presented in Table 4.

Form Table 4, it is found that even after replacing 2.50 m thick top soft soil below foundation base by compacted granular material, the available safe load bearing capacity of the foundation was not satisfying the requirement. Hence, for achieving the required load carrying capacity with less settlement, it was recommended to adopt the ground treatment by special method like stone column.

4.2 For RCC Box Underpass

The shallow foundation for RCC box underpass was raft foundation with minimum foundation embedment depth as 0.500 m from the OGL.

The results of “Load Bearing Capacity Analysis” for the shallow foundations of RCC box underpass without any kind of ground treatment condition, that is, in original ground condition are presented in Table 5.

Table 5 Summary of load bearing capacity analysis for shallow foundations of underpass in “Original in situ Ground Condition”

Foundation width (m)	Depth of foundation from OGL (m)	Safe load bearing capacity of open foundation (t/m^2)	Required load bearing capacity (t/m^2)	Estimated total settlement corresponding to the required load bearing capacity (mm)	Remarks
7.80	0.500	1.75	8.00	350	Not ok

Table 6 Summary of load bearing capacity analysis for shallow foundations of underpass after doing “Ground Treatment by Removal and Replacement”

Foundation width (m)	Depth of foundation from OGL (m)	Thickness of removal and replacement with granular Material (m)	Safe load bearing capacity of open foundation (t/m^2)	Required load bearing capacity (t/m^2)	Remarks
7.80	0.500	2.50	2.50	8.00	Not ok

From Table 5 it is clearly noted that the load bearing capacities of the foundations of RCC box underpass in original ground condition, that is, without any ground treatment condition were not adequate, and the estimated total settlement corresponding to the required load intensity was also quite high.

So to achieve the required safe load carrying capacity for the foundation of underpass, the ground treatment measures in the form of “removal and replacement of existing top weak compressible soil” was attempted first considering the ease of construction, time, and economics.

However, because of very high groundwater table, removal of existing top foundation soil was found economical and practical up to a maximum depth of 2.50 m below OGL. In view of that a maximum of 2.50 m depth of removal and replacement had been considered and analyzed.

The results of “Load Bearing Capacity Analysis” for the shallow foundations of underpass structure after ground treatment by replacement of top soft compressible soil with compacted granular soil are presented in Table 6.

For the underpass structure also, it is noted from Table 6 that even after replacing 2.50 m thick top soft soil below foundation base by compacted granular material, the available safe load bearing capacity of the foundation was not satisfactory. Hence, for achieving the required safe load carrying capacity with permissible settlement it was recommended to adopt the ground treatment by stone column which was preferred over the conventional deep foundation, like pile foundation, because of overall cost economy, time, and available of specialized agency in the close vicinity.

5 Ground Improvement for Foundation of Structure by Stone Column

In order to construct the structures, namely RCC retaining wall and box type underpass in land area, safe against collapsibility, and serviceability, the ground improvement by stone column was recommended, viewed from the foundation soil conditions, site and road requirements, construction ease, and schedule. Around 1.50 km length of RCC retaining wall and one RCC box type underpass along the land area of the project road was constructed over the ground improved with Stone Column.

5.1 *Design and Detailing of Foundations Treated with Stone Column*

Detailed design of ground treatment measures for structure foundations with stone column was carried out in accordance with “IS 15284 (Part 1): 2003, Design and Construction for Ground Improvement—Guidelines, Part 1 Stone Column”. The other guidelines namely IRC—HRB—Special Reports 13 and 14 dealing with design and construction of embankments on soft ground were also followed for finalization of detailing of the ground improvement.

The load carrying capacity of the stone column-treated ground was determined by summing up contributions of each of the following three components as per IS: 15284 (Part 1):

- (a) Capacity of the stone column resulting from the resistance offered by the surrounding soil against its lateral deformation (bulging/cavity expansion) under axial load,
- (b) Capacity of the stone column resulting from increase in resistance offered by the surrounding soil due to surcharge over it, and
- (c) Bearing support provided by the intervening soil between the columns.

The formulae for evaluation of above said individual load carrying component was considered from IS guidelines. The settlement of the stone column-treated ground was estimated using “reduced stress method” based on the “stress concentration factor” and “area replacement ratio” as defined, and the procedure given under Annex B of IS:15284 (Part 1).

The results of load bearing capacities for foundations of retaining wall and underpass structures rested over of the stone column-treated ground are given separately in the following sections.

For RCC Retaining Wall. The outputs of “Load Bearing Capacity Analysis” including the “Settlement Analysis” and “Rotational Stability Analysis” for the foundations of retaining wall with ground treatment by stone column are presented in Table 7.

For dispersion of applied load from retaining wall foundation base to the top of stone column and to aid drainage of the pore water, stone columns were topped with a compacted granular blanket of thickness varying from 500 to 1150 mm. The depth of stone column was generally so decided that very soft/soft and medium stiff clay layers, which were most significant weak strata were treated completely. Minimum two numbers of stone columns had been kept below foundation throughout the length in square pattern to utilize maximum resistance against bulging within the limited base width. The spacing of stone column was varying between 1.65 and 2.50 m to achieve overall economy. One additional row of stone column was also given on either side, beyond the base width of retaining wall, to ensure the lateral spreading of load through the projected portion of granular blanket over the column.

Table 7 Summary of analysis for foundations of retaining wall after doing “Ground Treatment by Stone Column”

Design height (m)	Foundation width (m)	Depth of foundation from OGL (m)	Safe load bearing capacity of open foundation (t/m^2)	Required load bearing capacity (t/m^2)	Estimated total settlement of stone column treated foundation Soil (mm)	Factor of safety in global stability	Remarks
4.00	3.65	2.00	7.50	7.50	24–89	1.35	Ok
5.00	4.45	2.00	9.80	9.80	44–130	1.60	Ok
6.00	5.85	2.00	11.20	11.20	76	1.35	Ok
7.00	6.70	2.00	11.20	11.20	76–129	1.55	Ok
8.00	7.40	2.00	11.80	11.80	86	1.50	Ok

The details of “ground treatment with stone column and compacted granular blanket” under the base of RCC retaining walls are given in Table 8.

The typical sectional elevation and plan showing the arrangement of stone columns and compacted granular blanket below the RCC retaining are given in Fig. 3.

For RCC Box Underpass. The results of “Load Bearing Capacity Analysis” including the “Settlement Analysis” for the underpass foundations with ground treatment by stone column are presented in Table 9.

A compacted granular blanket of thickness 1000 mm was provided over top of the compacted stone column for dispersion of applied load from underpass foundation base to the top of stone column and to aid drainage of the pore water. This blanket was extended 500 mm beyond the edge of last stone column all round. The depth of stone column is generally so decided that very soft/soft and medium stiff clay layers, which were most significant weak strata, were treated completely.

The details of “ground treatment with stone column and compacted granular blanket” under the foundation of RCC box type underpass structure are given in Table 10.

The typical sectional elevation and plan showing the arrangement of stone columns and compacted granular blanket below the RCC box underpass are given in Fig. 4.

5.2 Construction Materials and Installation Methodology of Stone Column

Construction Materials. The crushed stone, namely gravel, was used for stone column as well as for granular blanket at top of the stone column. That crushed stone, that is, gravel material consisting of clean, hard, angular, chemically inert, resistant

Table 8 Summary of details of “Ground Treatment with Stone Column and Compacted Granular Blanket” for retaining wall foundations

Design height (m)	4.00	5.00	6.00	7.00	8.00
Foundation width (m)	3.65	4.45	5.85	6.70	7.40
Diameter of stone column (mm)	1000	1000	1000	1000	1000
Spacing of stone column (mm)	1850–2500	1650–2250	1750–2000	1650–2000	1650
Type of arrangement	Square	Square	Square	Square	Square
Length of stone column from average OGL (m)	6–11	6.5–12.0	7.5–14.0	8.0–14.0	8.0
Safe load carrying capacity of single stone column and its tributary soil (ton)	24.6–44.0	22.4–49.0	29.0–43.0	29.0–43.0	29.5
Nos. of stone column under RCC retaining wall along foundation width (nos.)	2 nos. equally apart from C/L	2–3 nos. equally apart from C/L	3 nos. with center column along C/L	3–4 nos. with center column along C/L	4 nos. equally apart from C/L
Nos. of stone column under either side of the projected blanket along foundation width (nos.)	1 no.	1 no.	1 no.	1 no.	1 no.
Thickness of compacted granular blanket (mm)	500	500–1000	700–1150	500–1150	800

(continued)

Table 8 (continued)

Design height (m)	4.00	5.00	6.00	7.00	8.00
Width of granular blanket beyond edge of last row of stone column (mm)	500	500	500	500	500

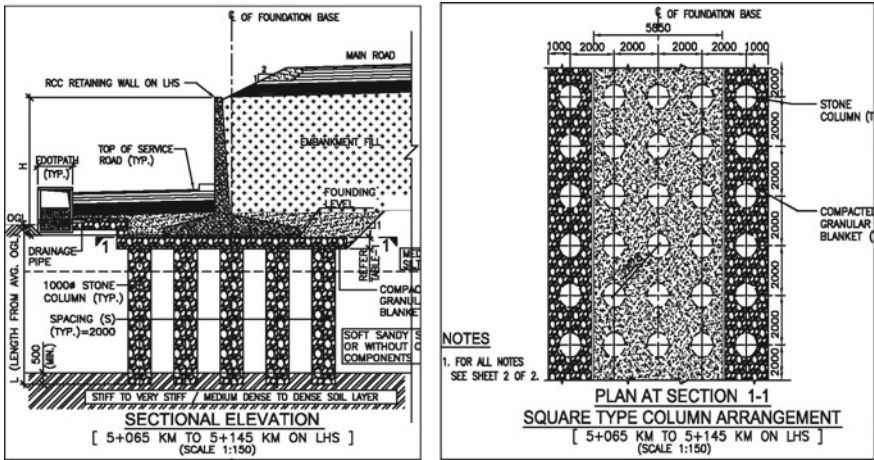


Fig. 3 Typical elevation and plan showing arrangement of stone columns and granular blanket below retaining wall

Table 9 Summary of analysis for foundations of underpass structure after doing “Ground Treatment by Stone Column”

Foundation width (m)	Depth of foundation from OGL (m)	Safe load bearing capacity of open foundation (t/m^2)	Required load bearing capacity (t/m^2)	Estimated total settlement of stone column treated foundation soil (mm)	Remarks
7.80	0.500	8.00	8.00	150	Ok

to breakage, and free from organic material, trash, or other deleterious materials and conforming to the gradation as given in Table 11 which is based on earlier same project work as mentioned in the technical paper of same author published in “Proceedings of IGC2011” given under reference no. [6] of this paper. The uniformity coefficient of crushed gravel was greater than 3, and grain size distribution curve

Table 10 Summary of details of “Ground Treatment with Stone Column and Compacted Granular Blanket” for underpass foundations

Foundation width (m)	7.80
Depth of foundation from OGL (m)	0.500
Diameter of sone column (mm)	1000
Spacing of stone column (mm)	1650
Type of arrangement	Triangular
Length of stone column from average OGL (m)	12.00
Safe lad carrying capacity of single stone column and its tributary soil (ton)	17
Projected row beyond width	2 nos.
Projected row beyond length	1 no.
Thickness of compacted granular blanket (mm)	1000
Width of granular blanket beyond edge of last row of stone column (mm)	500

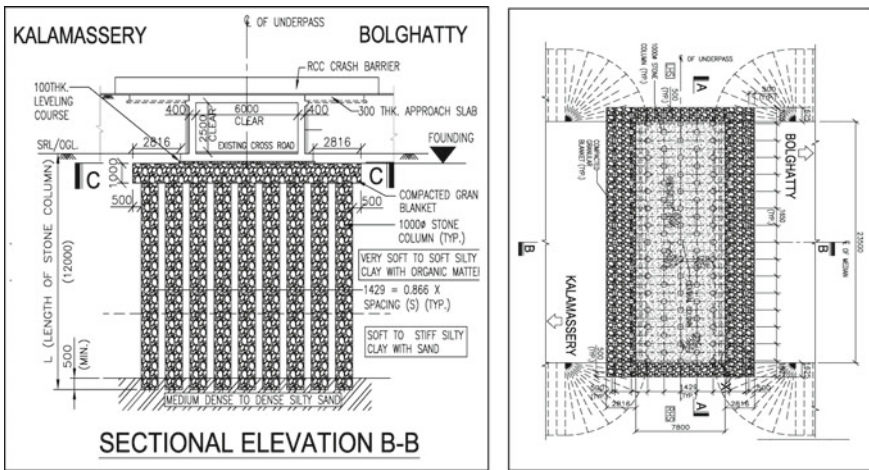


Fig. 4 Typical elevation and plan showing arrangement of stone columns and granular blanket below RCC box underpass

Table 11 Gradation of aggregates for stone columns (Ref: 6)

Size of crushed aggregates	% Passing
75 mm (3")	90–100
50 mm (2")	40–90
20 mm (3/4")	0–10
12 mm (1/2")	0–5

showed the material was well graded. The aggregate crushing value of the stone was not more than 30% and the impact value was not more than 25%.

The granular blanket was compacted in layers to a relative density of 75–80%. This blanket was exposed to atmosphere at its periphery for pore water pressure dissipation.

Construction Procedure and Stone Column Installation Methodology. The construction of stone column involved creation of a hole in the ground which was later filled with granular material in compacted manner. The stone columns were installed by Vibrofloat method. The wet method of Vibro-replacement was adopted as it was suitable for soft to medium stiff soil with high water table condition where borehole stability was questionable. Crushed stones of desired gradation were fed by mechanical means, that is, use of loader/hopper/chute, and so on. The slush, muck, and other loose materials at work site were removed suitably by the contractor as instructed by the engineer. Adequate measures were taken to ensure stability of boreholes made for installation of stone column.

The detailed installation procedure/method statement was submitted by the project contractor including the following:

- Mechanical arrangement for placing stones (s) around the probe point
- Quality control, quality assurance procedure covering details on automatic recording devices to monitor and record stone consumption
- Deployment of various equipment and machineries
- Manpower deployment
- The proposed sequence and timing for constructing stone columns having regard to the avoidance of damage to adjacent stone columns
- Bar chart for the entire foundation work.

The construction technique and probe was capable of producing and/or complying with the following:

- The hole was close to circular.
- The probe and follower tubes were of sufficient length to reach the elevations shown on the plans.
- The probe, used in combination with the flow rate and available pressure to the tip jet, was capable of penetrating to the required tip elevation. Pre-boring of stiff lenses, layers, or strata was permitted.
- The probe had visible external markings at one (1) foot/suitable increments to enable measurement of penetration and re-penetration depths.
- The equipment used was instrumented with sensors and the data processed by a micro-processing unit to enable continuous monitoring and capturing of data related to depth of vibrator and vibrator movements (i.e. depth of penetration) and power consumption (i.e. compaction effort) during construction of each stone column.

Data captured was continuously displayed on a LCD unit and graphical output (plots of depth versus time and power consumption) generated by automated computerized recording device throughout the process of stone column installation for each point was submitted to the engineer.

Sufficient quantity of wash water was provided to the tip of the probe to widen the probe hole to a diameter to allow adequate space for stone backfill placement around the probe. The flow of water from the bottom jet was maintained at all times during backfilling to prevent caving or collapse of the hole and to form a clean stone column. The flow rate was generally greater as the hole was jetted in, and decreased as the stone column came up to the top.

After forming the hole, the vibrator was lifted up a minimum 3 m, dropped at least twice to flush the hole out. The probe was, however, not completely removed from the hole. The column was formed by adding stone in lifts having each lift height between 600 and 1000 mm.

The stone aggregate in each lift was compacted by re-penetrating it at least twice with the horizontally vibrating probe so as to densify and force the stone radially into the surrounding in situ soil. The stone in each increment was re-penetrated a sufficient number of times to develop a minimum ammeter reading on the motor of at least 40 amps more than the free-standing (unloaded) ampere draw on the motor, but no less than 80 amps total.

Stone column was installed so that each completed column was continuous throughout its length.

The typical photographs of installation of stone column, laying granular blanket, and construction of retaining wall are given in Figs. 5, 6, 7, and 8.

Fig. 5 Typical installation of stone columns with Vibroflotation method (Wet)



Fig. 6 Typical Vibroflotation probe



Fig. 7 Typical laying process of granular blanket



Monitoring of Stone Column Installation. During construction of each stone column, all details and parameters were recorded and maintained and was made available for inspection by the engineer. The details were included but not limited to the following:

- Location, reference number, diameter, and depth (top and bottom elevation) of stone column.
- Stack measurement of stone (s) used in the works.

Fig. 8 Typical retaining wall construction over stone column-treated ground



- Monitoring stone consumption vis-à-vis theoretical requirements, information to include pressure gauge readings, depth versus time (time to penetrate and time to form each stone column), and so on.
- Computation of average quantity of back fill materials consumed per linear meter of the column.
- Vibrator power consumption during penetration of vibrator and during compaction of stone column.
- Details of obstructions, delays, and any unusual ground conditions.
- Any other information as required by the engineer.

Fig. 9 shows typical record of vibrator power consumption with respect to depth during making and washing of bore of stone column and finally compaction of stone column which helps in monitoring its degree of compaction. This is based on earlier same project work as mentioned in the technical paper of same author published in “Proceedings of IGC2011” given under reference no. 6 of this paper.

Section 1 in Fig. 9 shows advancement of borehole and Sect. 4 shows corresponding power consumed. Section 2 shows the washing of hole by moving the vibrator up and down the hole. There was no variation of power consumed for this process as clearly shown in Sect. 5. Sect. 3 shows the formation of column and corresponding power consumed is shown in Sect. 6. Section 6 shows more power consumption than Sects. 5 and 4. This is because more energy is required for doing compaction of the stone column. This energy difference indicates that a well-compacted stone column had been formed.

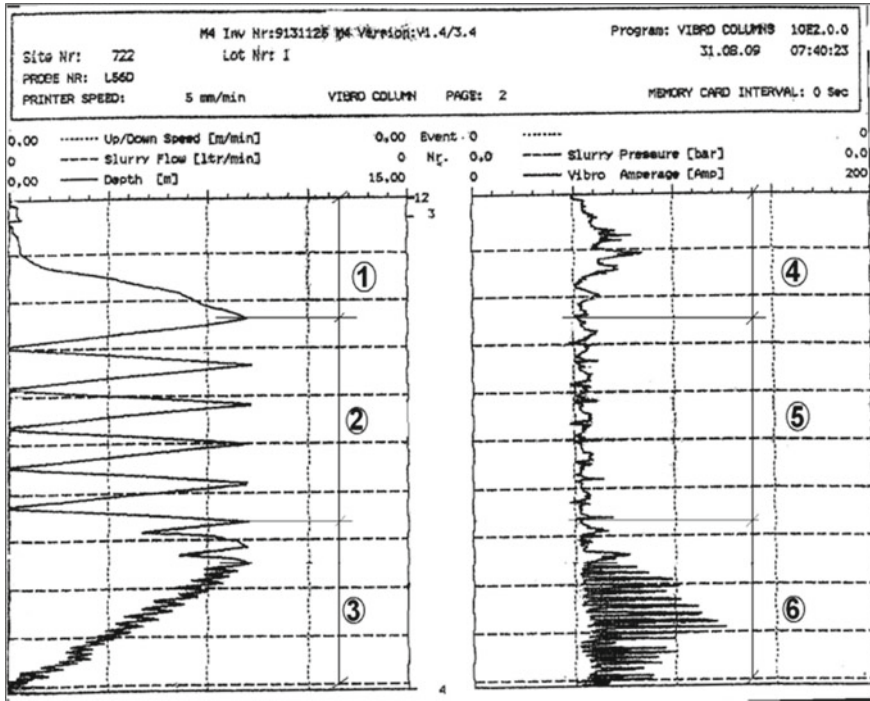


Fig. 9 Typical record of vibrator power consumption during installation of stone column (Ref: 6)

5.3 Load Tests of Stone Column

Two different types of vertical load tests, namely “Initial Load Test” over the “Test Column” and “Routine Load Test” over the “Working Column” were conducted for the stone column-treated foundations.

The initial load tests were performed at a trial test site to evaluate the load-settlement behavior of the soil-stone column system. The tests were conducted on a single and also on a group of minimum three columns in accordance with IS: 15284 (Part-1). The load-settlement observations were taken for the test load of 1.5 times of the safe design load in initial load test. The number of initial load tests was as follows:

- Single-column tests—1 test per 500 or part thereof stone columns
- Three column group tests—1 test per 1000 or part thereof stone columns

Figs. 10 and 11 show the typical photograph of conducting load tests over stone column.

The results of initial load test over stone column was accepted when settlement recorded was 10–12 mm at design load for a single column test and similarly settlement observed was 25–30 mm under design load for three column group test.

Fig. 10 Typical “reaction kentledge” for load test over stone column



Fig. 11 Typical arrangement for load test over group of stone columns



Figure 12 shows typical load-settlement graph of “initial load test” over single stone column which is based on earlier same project work as mentioned in the technical paper of same author published in “Proceedings of IGC2011” given under reference no. 6 of this paper.

The routine load tests over working column were carried out on a single column as well as over group of stone columns in accordance with IS:15284 (Part-1). The job column was loaded for a test load of 1.1 times the design load intensity with reaction kentledge minimum 1.3 times the design load pattern.

Figures 13 and 14 show the typical load-settlement graphs of routine load test over single stone column and group of stone columns under retaining wall.

Fig. 12 Typical load-settlement graph of initial test over single stone column (Ref: 6)

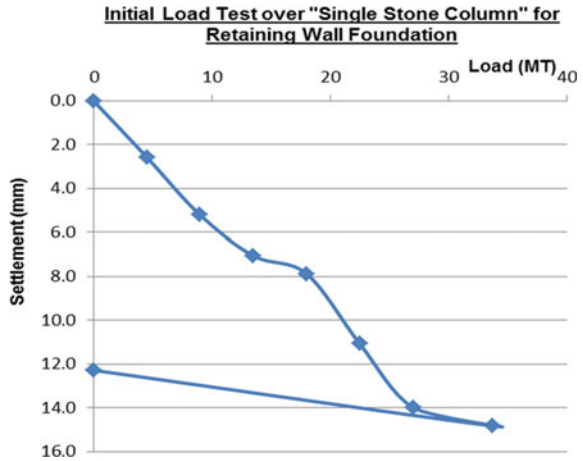
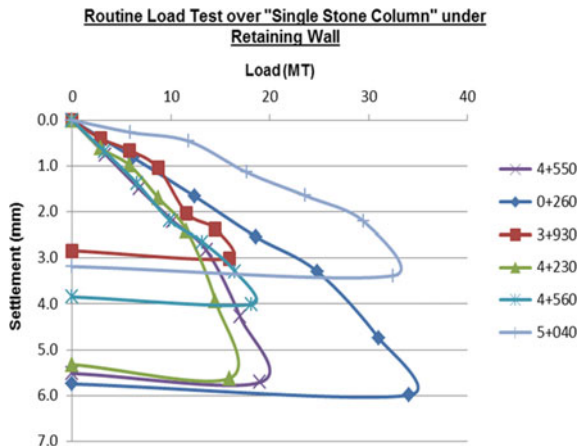


Fig. 13 Typical load-settlement graph of "routine load test" over single stone column



The typical load-settlement graph of routine load test over single column under RCC box underpass is also shown in Fig. 15.

5.4 Advantages of Using Stone Column in Place of Pile Foundation

Stone column was better alternative to pile foundation where soft compressible deposits of foundation soil exist below foundation of structure because:

- Installation of stone column was quite faster and around 50 numbers of stone columns of 10 m depth were installed in one day.

Fig. 14 Typical load-settlement graph of “routine load test” over group of stone column

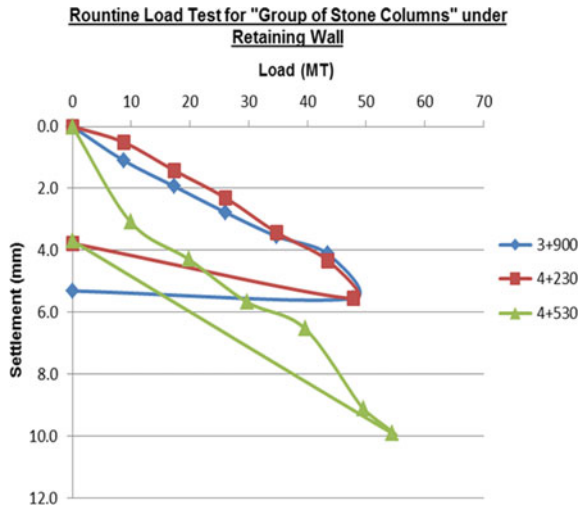
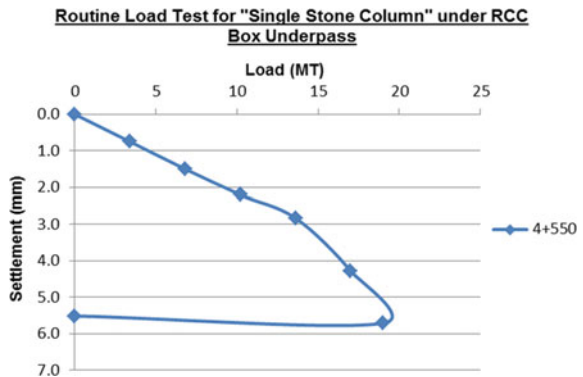


Fig. 15 Typical load-settlement graph “routine load test” over single stone column under box underpass



- Cost of construction of stone column was much less as compared to construction of pile foundation.
- As a result, there was reduction in overall cost of ground improvement for foundations.
- Small and insignificant settlement under the safe design load was observed in post stone column construction/installation stage.
- Generally, no waiting period was required to be adopted and loads were placed shortly after installation of stone columns in foundation soils.

6 Conclusions

There were 4–12 m deep soft compressible clayey deposits in the foundation soil of RCC retaining walls and box type underpass structures in land area of the Cochin ICTT Port road connectivity project. The ground improvement with stone column was effectively provided for the foundations of structures as an economical and safe alternative solution to the pile foundation. The details of design philosophy and construction methodology as adopted for the ground improvement works by “Vibrofloat Stone Column” under foundations of structures are described here. The field quality monitoring of stone column installation and load testing of stone column treated ground is also provided in this paper.

The following typical photo shows the completed project road with retaining wall supported over stone column-treated ground.



Acknowledgments The authors thank senior managements, design, and construction supervision team of engineers of M/s. LEA Associates South Asia Pvt. Ltd. (LASA), New Delhi, India for providing the support and encouragement in preparation of the paper.

As stated earlier, some of the contents of the paper on foundation treatment with stone column for RCC retaining wall are based on earlier same project work as mentioned in the technical paper of same author published in “Proceedings of IGC2011” given under reference no. 6 of this paper.

References

1. IS 6403 (1981) Code of Practice for Determination of Bearing Capacity of Shallow foundations
2. IS: 8009 (Part I) (1976) Code of Practice for Calculations of Settlement of Foundations, Part I Shallow Foundations
3. IRC 78 (2000) Standard Specifications and Code of Practice for Road Bridges, Section VII Foundations and Substructure
4. IS 15284 Part 1 (2003) Design and Construction for Ground Improvement—Guidelines Part 1 Stone Columns
5. IRC-HRB (1994) State of the Art: High Embankment on Soft Ground—Part A—Stage Construction and Part B—Ground Improvement

6. Mandal Avik Kumar, Rao P. J., Biswas Pradyot, Sailesh S (2011) - Foundations for retaining walls on soft clay deposits along highway to ICTT, Vallarpadam Port in Cochin. In: Proceedings of Indian geotechnical conference i.e. IGC 2011, namely "GEOCHALLENGES", organized by Indian Geotechnical Society (IGS) in KOCHI, Kerala, India, pp 1011–1014, December 2011

Combined Piled Raft Foundation (CPRF) System for Polymerization Loop Reactor Structure



P. Jayarajan and K. M. Kouzer

Abstract The current practice followed in the detailed engineering of foundations for critical industrial structures ignores the contribution of the raft (pile cap) and assumes that the loads are supported entirely by the piles. This approach would result in unduly conservative and uneconomical design where the settlement is reduced smaller than necessary with the use of significantly higher numbers of piles. In a combined piled raft foundation (CPRF), the pile cap provides a significant proportion of the required load capacity with the piles strategically placed to boost the performance of foundation by acting as settlement reducers. The paper presents a detailed step-by-step procedure for the implementation of a CPRF as a cost-effective and technically competent foundation system for a polymerization loop reactor structure which represents a critical component of polymerization plant in the refinery unit. The design process consisted of an initial stage of geotechnical site characterization and computation of required parameters based on the results of soil investigation report prepared for detailed engineering. The structural analysis was then undertaken for various code-prescribed critical load combinations to compute the support reactions for foundation analysis and design. The feasibility and further preliminary assessment of CPRF layout was done using Poulos-Davis-Randolph (PDR) method. The pile numbers, length and locations were then refined using finite element-based geotechnical program, PLAXIS 2D. It was found that the implementation of a CPRF versus a conventional piled only foundation provided the required strength and serviceability performance while delivering a cost saving in the order of 30–50%.

Keywords Piled raft · Foundation · PLAXIS

P. Jayarajan (✉)
National Institute of Technology, Calicut, Kerala, India
e-mail: puttatt1@gmail.com

K. M. Kouzer
Government Engineering College, Kozhikode, Kerala, India

© Springer Nature Singapore Pte Ltd. 2020
M. Latha Gali and P. Raghuvier Rao (eds.), *Construction in Geotechnical Engineering*, Lecture Notes in Civil Engineering 84,
https://doi.org/10.1007/978-981-15-6090-3_13

1 Introduction

Combined pile–raft foundations (CPRFs) are composite structures consisting of three bearing elements: piles, raft, and subsoil. They are normally used in two situations. In the first, piles are necessary for the consideration of bearing capacity, and taking into account the soil below the raft would lead to a reduction in the number of piles. In the second, piles are added below the raft system at strategic locations to control the total and differential settlements. The study of CPRF systems consists of various interactions, namely pile–soil–pile, raft–soil and pile–soil–raft interaction.

Current knowledge in the piled raft foundations allows the engineers to use it as an economical and efficient foundation system, in particular for high-rise buildings. Poulos et al. (2011) provide design guidelines for such foundations. Poulos and Bunce (2008) detail the analysis and design procedure of the piled raft system used in Burj Dubai, the world's tallest building. Poulos (2001) has demonstrated the economy and effectiveness of a CPRF in comparison to pile foundations through the case study of a high-rise building in Australia.

A number of methods are available for the analysis of piled raft foundation systems. Randolph (1994) provides a detailed review of various design methods applicable for a piled raft considering the load levels at which the piles are designed and their primary role in a CPRF. Poulos (2001) presents an approximate method of numerical analysis for piled raft foundations, which predicts well both the settlement behavior and the design loads on piles.

Phung (2010) provides a detailed account of the various finite element tools that are capable of modeling complex soil–pile–raft interactions. Finite element commercial programs such as FLAC 3D, ABAQUS 3D and PLAXIS 3D provide a good means of analyzing piled raft foundations considering the interaction between various elements. A parametrical study of piled raft was performed by Jayarajan and Kouzer (2015) using PLAXIS 3D software.

Experimental investigations also help to provide a better understanding of various factors that govern the performance of CPRF. Jaymin et al. (2016) carried out an experimental study on behavior of piled raft foundation system in sandy soil under vertical load and concluded that the number of piles underneath the raft had a significant effect on the load–settlement relationship. Further, the efficiency of piled raft foundation system in reducing settlement is minimal beyond a certain number of piles. Rasouli et al. (2015) carried out experimental centrifuge modeling to investigate the performance of connected and non-connected pile–raft systems on the load–settlement behavior. The results showed that where the purpose of using piles is to decrease the settlements, the non-connected pile–raft system performs better than the connected system.

2 Problem Definition

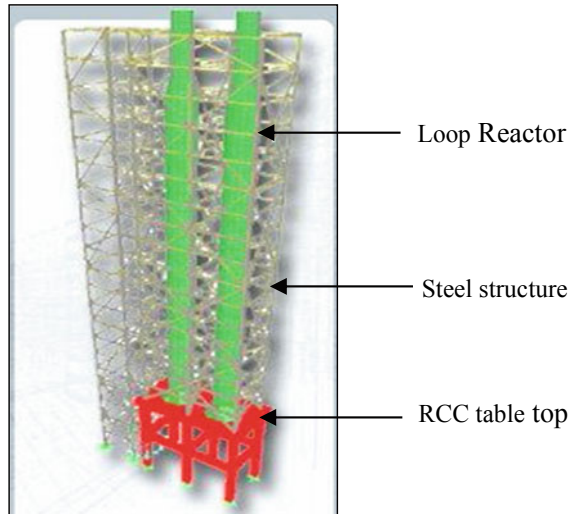
The detailed engineering consultants for petrochemical, refinery, and similar plants use either a raft or pile foundation system for critical industrial structures. This approach is unduly conservative and uneconomical. Though there is an increasing demand of combined piled raft foundations for high-rise structures, their use is very limited for critical structures in engineering plants. The above limitation is mainly due to the reluctance of design engineers in adopting a new foundation system in the absence of well-defined design guidelines. The broad objective of the paper involves explaining the step-by-step procedure involved in the sizing and detailed design of combined piled raft foundations for critical structures in engineering plants.

The paper describes the process of design of a piled raft foundation for a polymerization loop reactor structure which represents a critical component of polymerization plant in the refinery unit. The design process comprised an initial stage of geotechnical site characterization using the results of geotechnical investigation which is carried out as a part of detailed engineering. The geotechnical parameters for raft and pile design were then derived. Following this a preliminary foundation analysis was undertaken using the Poulos–Davis–Randolph (P–D–R) method for the loads obtained from analysis of the superstructure to assess the viability of such a foundation system and any potential advantages of a piled raft over conventional fully piled foundation systems. Finally, a detailed analysis was undertaken using the PLAXIS 2D (PLAXIS 2D Version 2002) finite element computer program. The results available from detailed analyses were used to finalize a more efficient piled raft system and to provide design actions for structural design of the foundation system for a variety of load combinations.

3 Description of Structure

Polypropylene unit is the main process unit of the naphtha cracker plant, and the structure for loop reactors represents a critical item in the unit. The loop reactor structure essentially consists of an RCC table top with the main reactors directly supported on it. The steel structure is essentially braced in one direction with the moment-resisting frames provided in the other. The loop reactors along with a part of the steel structure are in the scope of equipment supplier. The topmost steel platform attached to the reactor structure is at an elevation of 55 m above the ground. A pictorial view of the structure is given in Fig. 1.

Fig. 1 3D view of loop reactor structure



4 Geotechnical Conditions

In the job site the subsoil is alluvial in nature and consists of stiff sandy clayey silt to a depth of about 12.0 m from existing ground level with N values of 10–15 (layer-1a). The top layer is underlain by very stiff sandy clayey silt from 12 to 18 m with N values of 20–40 (layer-1b). From 18 m to termination depth of bore holes dense silty sand is observed with N values of 50–70 (layer-2). Based on the ground water levels measured in boreholes, the ground water level has been considered at 2.0 m below the ground level. Standard penetration tests (SPTs) have been carried out in the site at different depths in various locations. The summary of various geotechnical parameters derived from the empirical correlations with the SPT values is given in Table 1.

Table 1 Geotechnical parameters

Strata	N	γ	C_u or ϕ	E_u	E
1a	10–15	18	50–75	10–15	7–10
1b	20–40	20	100–200	20–40	15–30
2	50–70	20	38°	–	40–50

- N = Standard penetration values
- γ = Bulk unit weight (kN/m^3)
- C_u = Undrained shear strength (kN/m^2)
- ϕ = Angle of internal friction (degrees)
- E_u = Undrained Young's modulus (kN/m^2)
- E = Long-term drained Young's modulus (kN/m^2)

Table 2 Load combinations for foundation assessment

S. no.	Serviceability limit state	Ultimate limit state
1	DL + OP + LL	–
2	DL + OP + WL	–
3	DL + OP + 0.9LL + 0.9WL	–
4	–	1.35DL + 1.35OP + 1.35LL
5	–	1.35DL + 1.35OP + 1.5WL
6	–	1.35DL + 1.35OP + 1.35LL + 1.35WL

As per the geotechnical recommendations for the job site, shallow foundations on the stiff sandy clayey silt stratum may be used for structures subjected to limited static loads. However, for structures subjected to dynamic loads or large static loads and for those structures which are sensitive to settlements, pile foundations are recommended.

5 Loading and Structural Analysis

For the polymerization loop reactor structure, the critical load data for loop reactors at their support bases (8 nos.) is normally provided by the reactor vendor. Further, the support reactions from the vendor-supplied steel structure are also available. The basic loads considered for the analysis include dead load (DL), operating load (OP), live load (LL), and wind load (WL). The wind loads are considered in each of the two mutually perpendicular directions. Earthquake loads are not considered as they were not critical. The load combinations used for foundation assessment include both serviceability limit states (SLS) and ultimate limit states (ULS). The summary of critical load combinations taken from detailed project design specifications is given in Table 2. The structural analysis was performed using the STAAD-Pro software for basic loads and load combinations. A 3D analysis model for the structure is shown in Fig. 2.

6 Foundations Loads

The foundation loads are calculated at column locations for critical load combinations. The column layout is shown in Fig. 3. The layout basically consists of two rows of columns 7 m apart, their spacing being 4.2 m. The resultant column loads and moments transferred from superstructure to the foundation corresponding to the

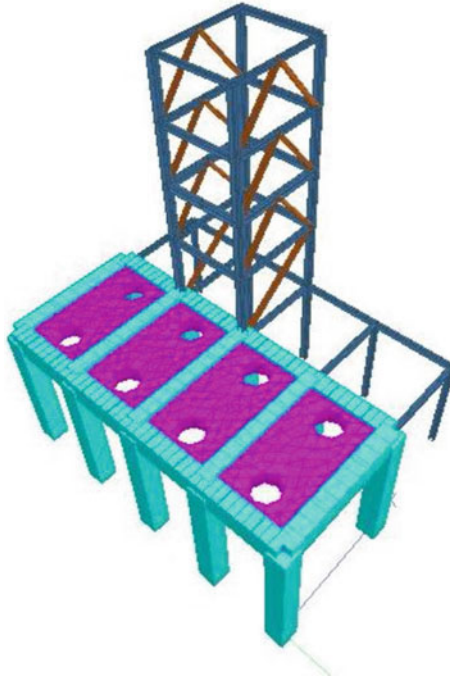


Fig. 2 3D structural analysis model

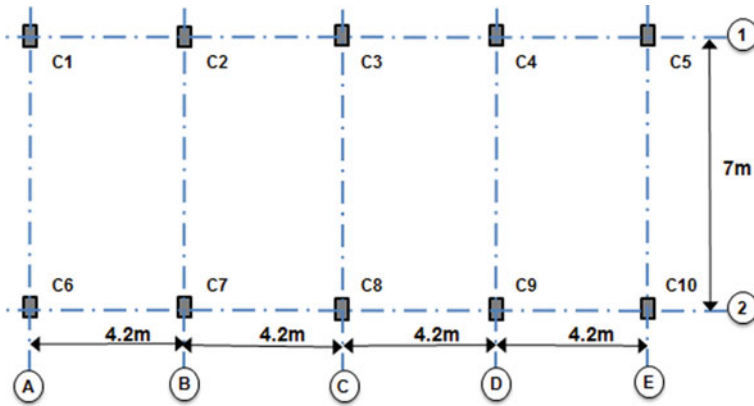
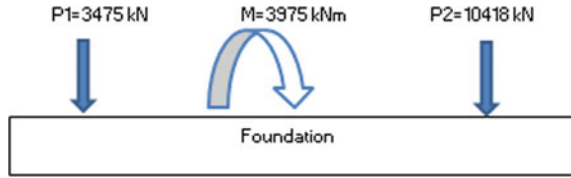


Fig. 3 Structural column layout

Fig. 4 Foundation loads from superstructure



most critical serviceability limit state are represented in Fig. 4. The review of loads indicates that the foundation is subjected to large eccentric loads.

7 Preliminary Foundation Assessment

Prior to the detailed foundation assessment, a feasibility study was conducted for various foundation schemes. The foundation assessment was carried out for (a) a raft alone without pile, (b) conventional pile foundation, and (c) combined piled raft foundation. For preliminary assessment, 450 mm diameter-driven cast in situ piles of 18 m length were considered. Based on previous experience with similar structures and considering adjacent constructions, a rectangular raft of size 20 × 10 m and 1.2 m thick was considered. The bottom of raft was kept 2.0 m below the ground level. The conclusions are presented in the following sections.

7.1 Raft Alone Without Piles

Considering the self-weight of raft and foundation soil and applying basic principles of engineering mechanics, the foundation loads shown in Fig. 4 could be represented by an equivalent load of 22460 kN at an eccentricity of 1.25 m. The modeling and detailed analysis of the raft foundation was done using finite element program PLAXIS 2D with a plane-strain model. The soil was represented using Mohr–Coulomb material model and raft by linear elastic material. The material properties used in the analysis are listed in Tables 1 and 3. The plane-strain model of the raft is shown in Fig. 5 and the deformed mesh in Fig. 6.

The load–settlement curve obtained from PLAXIS calculations is shown in Fig. 7. It was concluded from the above calculations that the raft foundation alone would

Table 3 Material properties used in PLAXIS analysis

Parameter	Raft	Piles
Material behavior	Elastic	Elastic
Axial stiffness (kN/m)	30E6	1.8E6
Bending stiffness(kNm ² /m)	3.6E6	2.3E4
Poisson's ratio	0.25	0.25

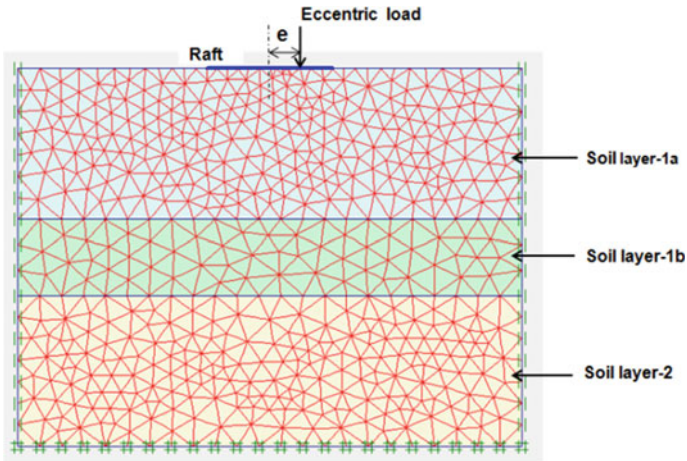
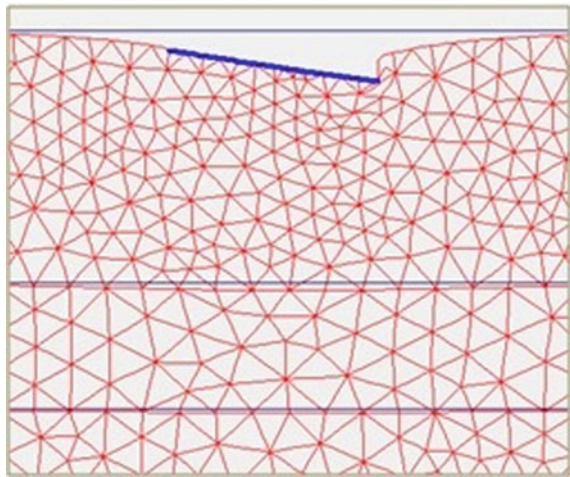


Fig. 5 Plane-strain model for the raft

Fig. 6 Deformed finite element mesh (raft)



have an overall safety factor of 2.0 under extreme wind loads and more than 3.0 under dead, operating, and live loads. However, the calculated maximum foundation settlement of 120 mm is much higher than the allowable value of 40 mm provided in project design specifications. Further, the calculated angular distortion of 1 in 140 is much higher than permissible value of 1 in 500. Therefore, the foundation design would be governed by the settlement and tilt considerations rather than by the ultimate bearing capacity.

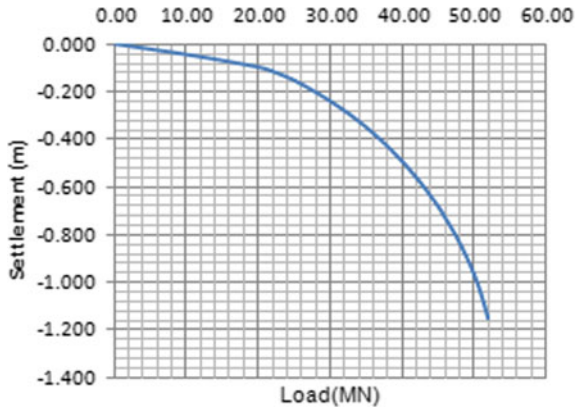


Fig. 7 Load versus settlement curve for raft

7.2 Pile Foundation

A preliminary assessment has shown that 45 numbers of 18 m long piles would be required as in the pile layout shown in Fig. 8. The pile foundation is modeled as a plane-strain model in PLAXIS 2D. The piles and raft were modeled using plate elements. The out of plane row of piles is modeled as plane-strain piles with an equivalent pile modulus of deformation in terms of the number of piles in the row considering the dimension of the pile and that of the raft. The interface strength coefficient R_{inter} in the model is adjusted so that the plane-strain piles develop the same shaft resistance of actual piles in the row. The plane-strain model of the pile foundation is shown in Fig. 9 and the deformed mesh in Fig. 10.

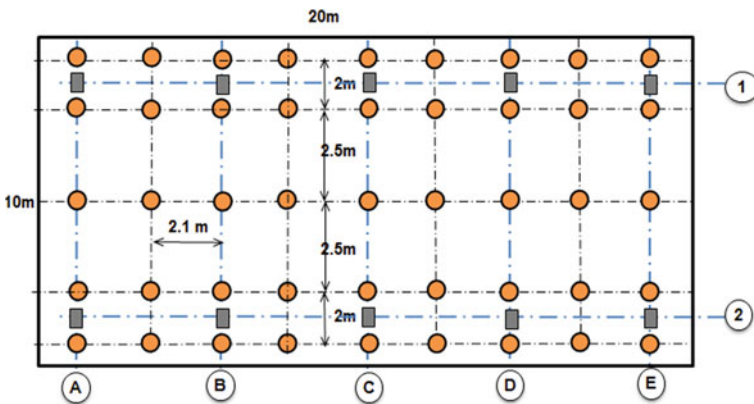


Fig. 8 Foundation pile layout (45 nos. of piles)

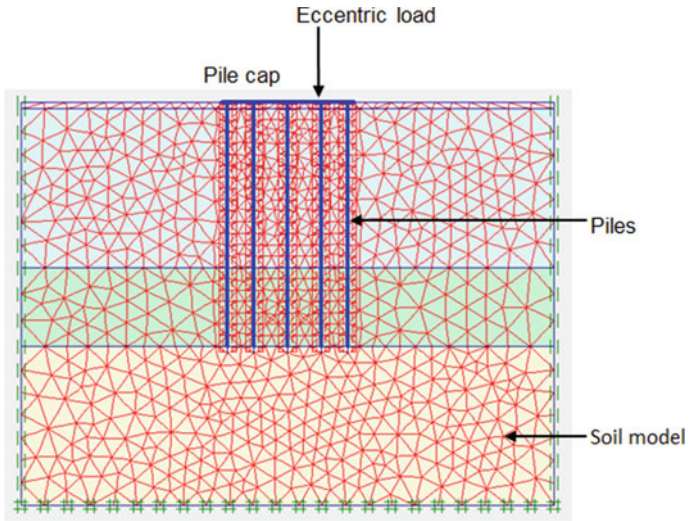


Fig. 9 Plane-strain model of pile foundation

Fig. 10 Deformed finite element mesh (piles)

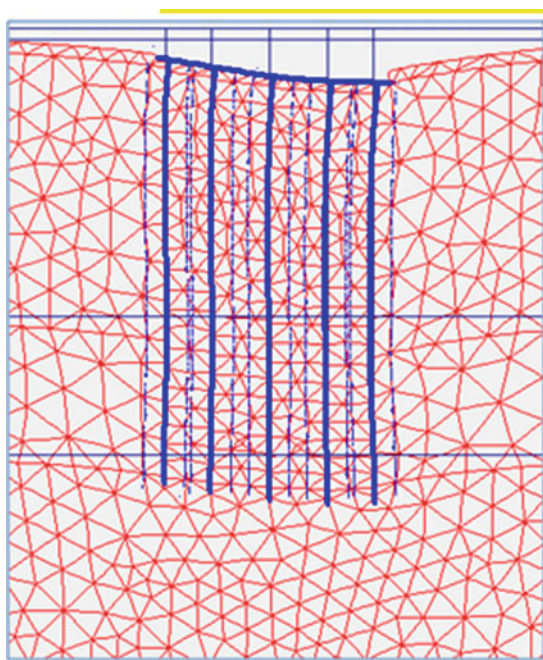
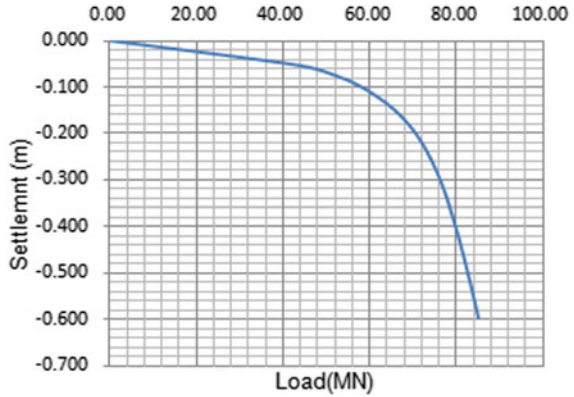


Fig. 11 Load–settlement curve for pile foundation



The load–settlement curve obtained from PLAXIS calculations is shown in Fig. 11. It was concluded that the pile foundation with 45 numbers of piles would have an overall safety factor of 4.0 under extreme windloads and the calculated maximum foundation settlement of 23 mm is well within the acceptable limits of 40 mm. Further the angular distortion of 1 in 900 is much less than permissible value of 1 in 500. Considering that the pile arrangement has excess capacity in terms of strength and serviceability, the possibility of using a combined piled–raft foundation is investigated with lesser number of piles.

7.3 Combined Piled–Raft Foundation (CPRF)

The behavior of a piled–raft foundation is determined by the interactions between the piles, raft, and soil. In reality, there are two basic interactions, pile–soil–pile interaction and pile–soil–raft interaction, as shown in Fig. 12. The feasibility of using a piled–raft is assessed using Poulos–Davis–Randolph (PDR) method. The method provides the number of piles to satisfy the design requirements relevant to strength and serviceability.

The simplified representation of piled–raft as used in PDR method is shown in Fig. 13. As per the method, the stiffness of the piled raft foundation can be estimated as:

$$K_{pr} = \frac{((K_p + K_r(1 - \alpha_{cp})))}{\left(1 - \alpha_{cp}^2 * \frac{K_r}{K_p}\right)} \tag{1}$$

where K_{pr} = stiffness of piled raft; K_p = stiffness of the pile group; K_r = stiffness of raft alone; α_{cp} = raft–soil–pile interaction factor.

The proportion of the total load carried by the raft is

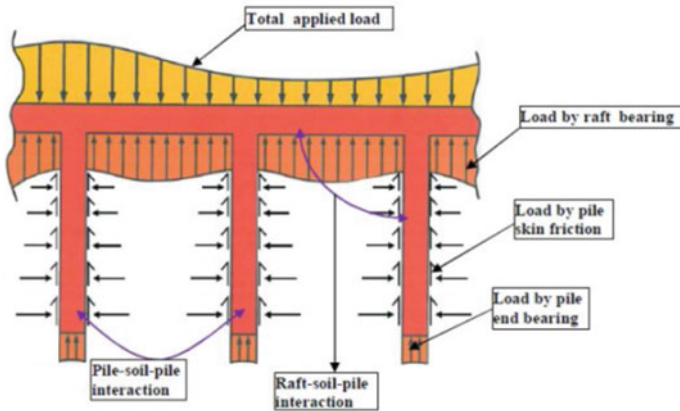


Fig. 12 Interactions in a piled raft foundation

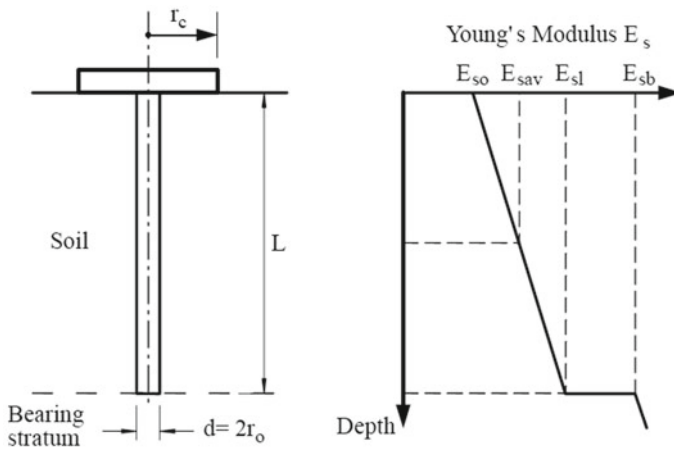


Fig. 13 Simplified representation of a piled raft unit

$$\frac{Pr}{Pt} = X = \frac{Kr(1 - \alpha cp)}{Kp + Kr(1 - \alpha cp)} \tag{2}$$

where Pr = load carried by the raft; Pt = total applied load.

If P_{up} is the ultimate load capacity of piles in the group, total load on the foundation at which the pile yields is given by

$$P1 = P_{up}/(1 - X) \tag{3}$$

The pile–soil–raft interaction factor αcp can be estimated as follows:

$$acp = 1 - \ln\left(\frac{rc}{r0}\right) / \beta \tag{4}$$

where rc = average radius of pile cap (corresponding to an area equal to the raft area divided by number of piles); $r0$ = radius of pile; $\beta = \ln(rm/r0)$; ν = Poisson's ratio of the soil; $rm = \{0.25 + \xi[2.5\rho(1 - \nu) - 0.25]\} * L$; $\xi = Es1/Esb\rho = Esav/Es1$; L = pile length; $Es1$ = soil Young's modulus at level of pile tip; Esb = soil Young's modulus of bearing stratum below pile tip; $Esav$ = average soil Young's modulus along pile shaft. A tri-linear load-settlement curve developed using the above equations is shown in Fig. 14.

The preliminary CPRF arrangement as shown in Fig. 15 is used to support the design loads. The CPRF considered consists of the raft of the same size but supported by lesser numbers of piles compared to the pie foundation. A total of 25 numbers of piles each of length 18 m is considered for the study. The calculations done using the

Fig. 14 Simplified load-settlement curve of CPRF

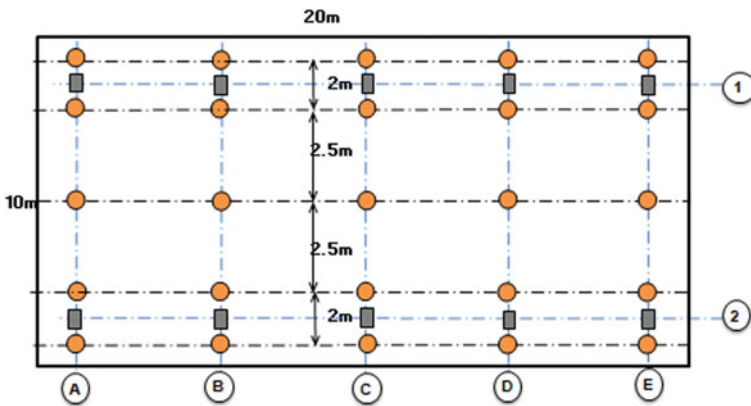
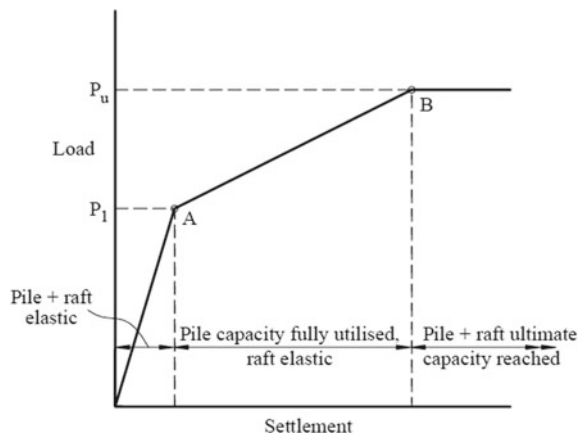


Fig. 15 Combined piled raft—pile layout (25 nos.)

MATHCAD worksheet developed by the authors give $P_1 = 52468$ kN, $P_u = 104538$ kN. Further, the settlement of 29.4 mm corresponding to a service load of 22460 kN is acceptable.

It shall be noted that the preliminary calculations using PDR method assumes a concentric load conditions. Accordingly, detailed assessment shall be done for the actual applied eccentric loads to understand the load transfer mechanism and the load–settlement characteristics.

7.4 Recommendations from Preliminary Geotechnical Assessment

Based on the results of the preliminary geotechnical assessment, it was recommended that a combined piled raft foundation system should provide a cost-effective solution for the foundations of polymerization loop reactor structure with required safety on strength and settlement.

8 Detailed Foundation Calculations

Based on the preliminary assessment, detailed calculations were done for CPRF layout shown in Fig. 15 using PLAXIS 2D. The thickness of the piled raft was considered same as 1.2 m. The water table has been modeled at 2.0 m below the ground level. A plane-strain model was considered for the analysis and computation of design forces in various elements. The deformed mesh of CPRF model is shown in Fig. 16. Two cases of loading were considered first with a concentric load system and the other with an eccentric loading. These cases were studied for the purpose of comparison with PDR method and also to examine the effect of load eccentricity on CPRF. A comparison of PDR method with PLAXIS analysis is shown in Fig. 17. It can be seen that behavior is almost the same in the linear portion corresponding to the development of full pile capacity and deviation is significant in the nonlinear portion. As the CPRF under consideration is subjected to highly eccentric loads, its behavior is also reviewed at different eccentricities ($e = 0, 0.5$ and 1.25 m) and the response is given in Fig. 18. As expected, the CPRF capacities decrease with increasing values of eccentricity.

The load–settlement behavior of the CPRF corresponding to applied eccentricity of $e = 1.25$ m is shown in Fig. 19. It is clear that the CPRF has a factor of safety of much higher than 3.0 under worst loading condition and maximum settlement of 36 mm is within the allowable value of 40 mm. Further, the angular distortion of 1 in 525 is less than permissible value of 1 in 500. Thus, the CPRF with much lesser numbers of piles satisfies the strength and serviceability requirements.

Fig. 16 Deformed finite element mesh

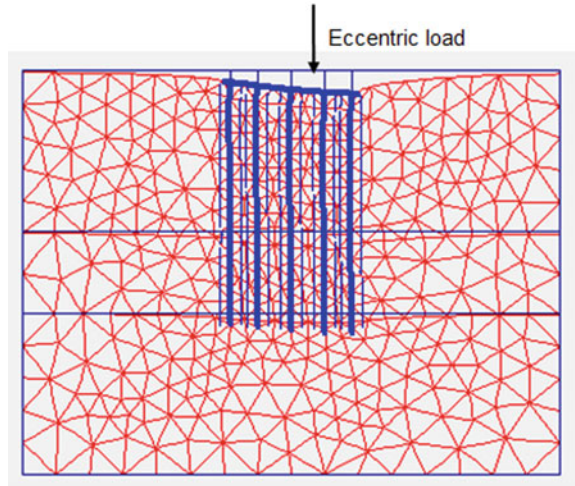


Fig. 17 Comparison of PDR method with PLAXIS

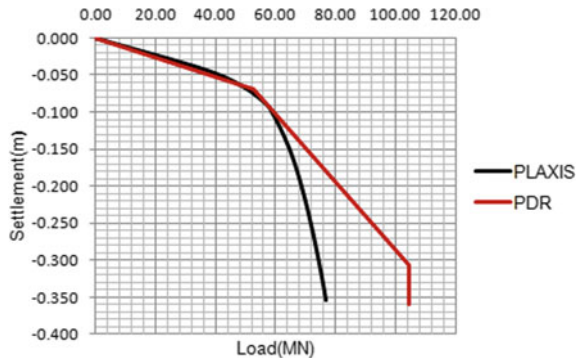


Fig. 18 Response of CPRF to different eccentricities

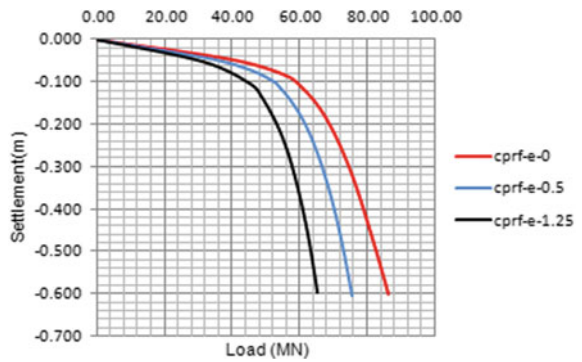


Fig. 19 Load–settlement curve for CPRF

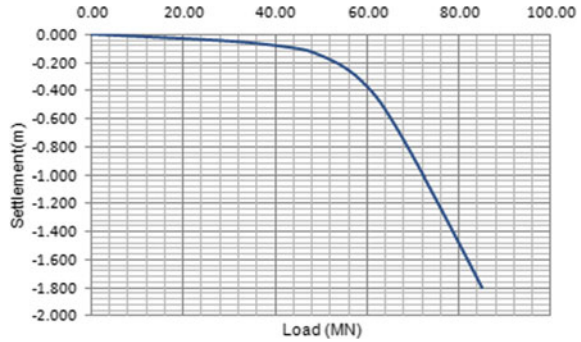
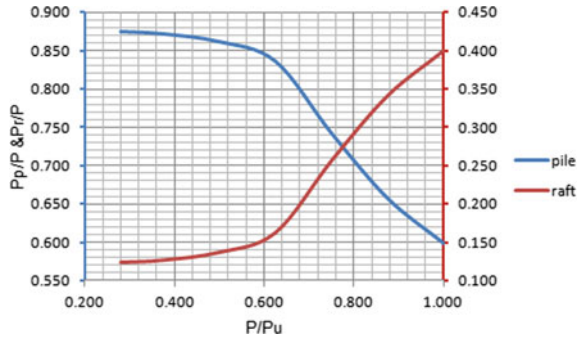


Fig. 20 Load-sharing mechanism for CPRF



It is very clear that the participation of piles takes place at low settlement levels where the raft starts contributing at higher settlements. Thus, the load distributed by raft and pile elements in a CPRF depends upon the settlement levels which are controlled by the applied load. The load sharing mechanism is demonstrated in Fig. 20. P_u = Ultimate load capacity of CPRF, P = applied load which is shared between piles (P_p) and raft (P_r) elements. Finally, a comparison of different foundations considered in the study, namely raft-only, pile-only, and combined raft foundation at an applied eccentricity of $e = 1.25$ m is shown in Fig. 21.

9 Ultimate Limit State Assessment CPRF

Using the ultimate limit state (ULS) loading combinations provided in Table 2, structural assessment of the piled raft was made. The computed values of maximum and minimum design values for the various structural actions are summarized in Table 4. It can be seen that the structural actions remain almost the same for raft element in CPRF and pile-only foundation. However, the pile loads appear to be much higher in CPRF compared to the pile-only foundation. This is obviously because of the lesser number of piles used in CPRF. Therefore, a part of the saving due to the

Fig. 21 Performance for reviewed foundations

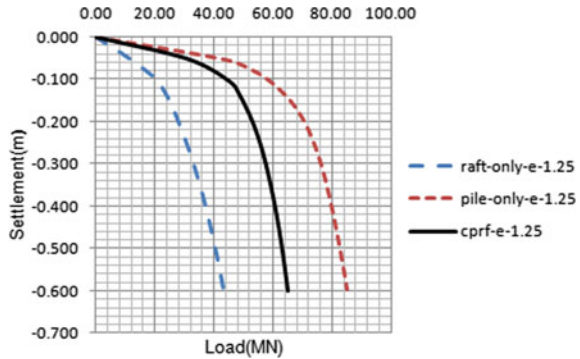


Table 4 Summary of design actions (ULS)

Parameter	Axial Force (kN)	Shear ^a Force (kN)	Bending ^a Moment (kN m)
(a) CPRF Pile	709	96	158
	1790	75	27
Raft	–	854	2170
(b) Pile-Only Pile	433	64	107
	1184	104	98
Raft	–	851	2074

^aRaft shear force and bending moments are per meter width

use of lesser number of piles in CPRF will be offset by correspondingly higher pile reinforcement.

10 Conclusions

The paper has provided a detailed procedure for the analysis and design of a combined piled raft foundation (CPRF) for the critical polymerization loop reactor structure in a refinery unit. The procedure involved characterization of soil profile using detailed geotechnical investigations, initial geotechnical assessment of possible types of foundation solutions, namely raft-only, pile-only, and the CPRF, and finally detailed calculations are done to verify the foundation response under critical loads. The objective of the paper is to provide necessary guidelines for detailed assessment of combined piled raft foundations for critical structures. It is expected that the paper will encourage practicing engineers involved in detailed engineering of sensitive and critical structures to come out with an efficient and economical foundation solution.

The Poulos–Davis–Randolph (PDR) method provides an efficient methodology for preliminary assessment of CPRF. The PLAXIS 2D finite element computer program can consider the complex interactions between various elements in a CPRF and provide the foundation response for various load combinations. The program also provides detailed summary of various design actions for ultimate limit state and can be used by structural engineers for design of raft and pile elements.

References

- Jayarajan P, Kouzer KM (2015) Analysis of piled raft foundations. In: Proceedings of international conference on recent innovations in engineering & technology, Coimbatore, India
- Patil JD, Vasanvala SA, Solanki CH (2016) An experimental study on behaviour of piled raft foundation, *Indian Geotech J* 46(1):16–24
- Phung DL (2010) Piled raft—a cost effective foundation method for high-rises. *Geotechn Eng J Seags & AGSSEA* 41:1–12
- PLAXIS 2D Version 2002, Reference manual, Delft, The Netherlands
- Poulos HG (2001) Methods of analysis of piled raft foundations, a report prepared on behalf of technical committee TC18 on piled foundations, International society of soil mechanics and geotechnical engineering
- Poulos HG, Bunce G (2008) Foundation design for the Burj Dubai—the world’s tallest building. In: 6th international conference on case histories in Geotechnical engineering, Arlington, VA
- Poulos HG, Small JC, Chow H (2011) Piled raft foundations for tall buildings. *Geotechn Eng J Seags & AGSSEA* 42(2):78–84
- Randolph MF (1994) Design methods for pile groups and piled raft, S.O.A. Report, 13 ICSMFE, New Delhi, 5:61–82
- Rasouli H, Saeedi Azizkandi A, Baziar MH, Modarresi M, Shahnazari H (2015) Centrifuge modeling of non-connected piled raft system. *Int J Civil Eng* 13(2):114–123

Bearing Capacity Estimation of Shallow Foundations on Dense Sand Underlain by Loose Sand Strata Using Finite Elements Limit Analysis



Pragyan Paramita Das and Vishwas N. Khatri

Abstract In the present paper, a statistical limit analysis was carried out to estimate the bearing capacity of the surface strip and the circular base resting on dense sand under the loose sand layer. The analysis was accompanied by a lower and upper bound limit analysis in combination with finite elements and second-order conic programming (SOCP). In this approach, the Mohr–Coulomb yield criterion was used to model soil behavior. Assuming an associated flow rule, rigorous lower and upper bounds on ultimate bearing capacity are obtained with the use of this technique. Comparisons were made with the available solutions from the literature wherever applicable.

Keywords Finite element limit analysis · Bearing capacity · Mohr–Coulomb · Conic programming

1 Introduction

Estimation of bearing capacity and settlement of the foundation has been a significant topic of interest since time immemorial. Although many research studies have been published in the literatures on layered soil media (Meyerhof 1974; Meyerhof and Hanna 1978; Hanna 1981, 1982, 1987; Georgiadis and Michalopoulos 1985; Oda and Win 1990; Michalowski and Shi 1995; Burd and Frydman 1997; Kenny and Andrawes 1997; Okamura et al. 1998; Shiau et al. 2003; Farah 2004; Kumar et al. 2007; Shoaie et al. 2012; Kumar and Chakraborty 2015), nevertheless, there are few experimental studies conducted by scientists in layered sand media (Meyerhof and Hanna 1978; Hanna 1981, 1982; Farah 2004; Kumar et al. 2007). Meyerhof and Hanna (1978) determined the ultimate bearing capacity of the strip and the circular

P. P. Das (✉) · V. N. Khatri
Civil Engineering Department, Indian Institute of Technology (I.S.M.), Dhanbad 826004, India
e-mail: pragyandas1403@gmail.com

V. N. Khatri
e-mail: vishuiisc@gmail.com

footing under inclined load using the limit equilibrium method. The results of the theoretical analyses were compared with small-scale model tests. Hanna (1981, 1982) developed design charts for estimating the bearing capacity of the strip and circular footing placed on layered sand media. That is a dense sand layer on loose sand strata and a loose sand layer on dense sand. Farah (2004) derived expressions for strip footing resting on layered soil. According to Farah (2004), the bearing capacity depends on the shear strength parameter of the upper and lower layers, the thickness of the upper layer and the width of the base to the depth ratio. Kumar et al. (2007) determined the carrying capacity of the dense sand layer overlying the loose sand deposit with and without geogrid on dense sand layer.

It is clear from the available literature that research has been carried out to determine the bearing capacity of layered sand media employing laboratory tests or the use of traditional approaches involving several simplified assumptions. Hardly any computational studies are available to determine the ultimate bearing capacity of layered sand media. This paper is trying to fill the gap. In the present paper, the bearing capacity of the strip and circular footing resting on layered sand media, that is, dense on loose sand is estimated using the lower and upper bound finite element limit analysis in conjunction with the second-order conic programming (SOCP). The analyses were conducted by varying the thickness of the upper dense layer and the angle of the internal friction of the two layers. The results are presented in a dimensionless manner and the comparisons are made with the available literature.

1.1 Problem Definition

A rigid rough strip and a circular footing are placed over a dense sand layer underneath the loose sand layer for analysis, as shown in Fig. 1. H is the thickness of the top

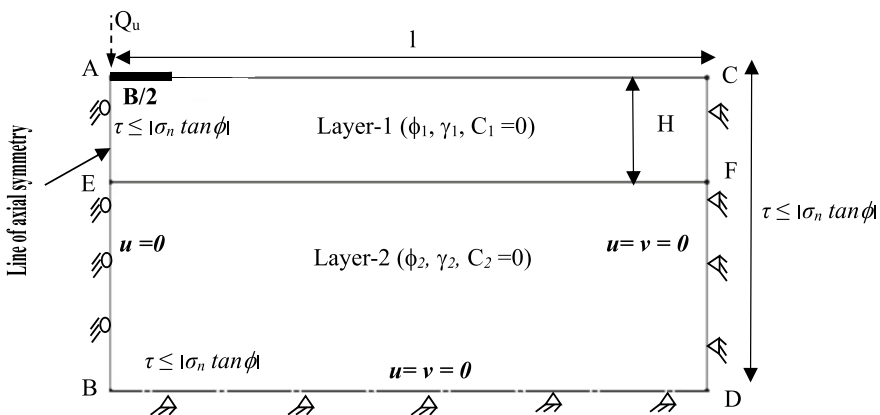


Fig. 1 Selected problem domain and associated boundary conditions

Table 1 The unit weights and the associated friction angles for sand in the analysis following Bowles (1977)

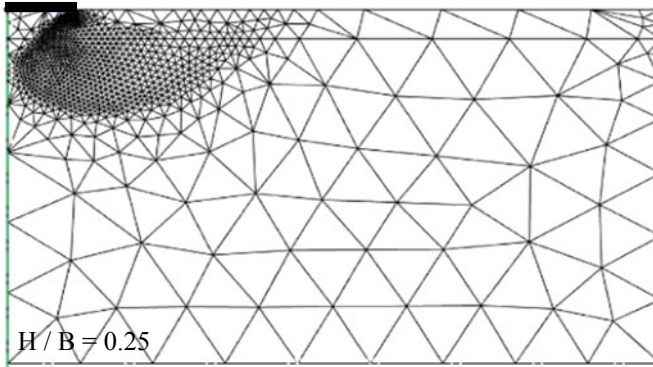
S. no.	Unit weight (γ) kN/m ³	Friction angle (ϕ) degrees
1	13.5	30
2	14.5	32
3	15	34
4	16	36
5	16.5	38
6	17.5	40
7	18	42
8	19	44
9	20	46

densified sand layer and B is the width/diameter of the base. It is intended to determine the ultimate bearing capacity of the base with variation in the frictional angle of the upper and lower layers and the thickness of the top dense layer. ϕ_1 , ϕ_2 , and γ_1 , γ_2 are the friction angles and unit weight of the top and bottom sand layers, respectively. Bowles (1977) provided the relationship between unit weight (γ) and friction angle (ϕ). These values were considered for analysis. The values are presented in Table 1. The soil is assumed to be completely plastic, comply with the associated flow rule and the Mohr–Coulomb failure criterion.

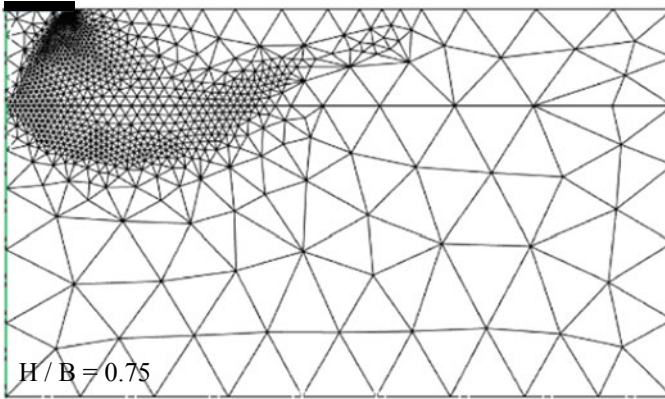
Problem domain and mesh details

The selected problem domain with associated boundary conditions is shown in Fig. 1. l and d are the length and depth of the chosen problem domain, respectively. Considering the corresponding stress and velocity conditions for the lower and upper bound analysis, one-half of the chosen domain on the x – y plane was used for analysis. At the base, at the bottom horizontal and the right vertical boundary (BC and CD), $\tau \leq |\sigma_n \tan \phi|$ was applied.

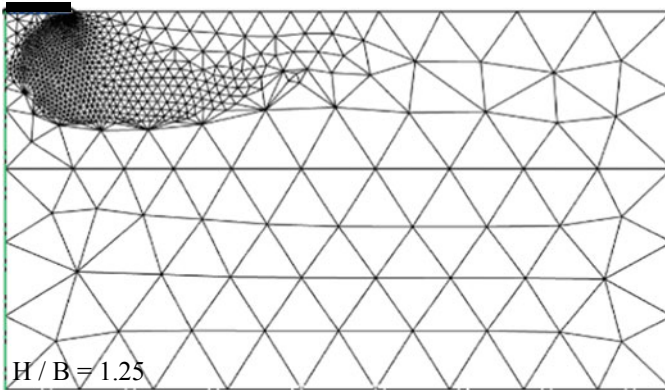
No horizontal velocity (u) along the base and line of symmetry was allowed during the upper bound analysis. The horizontal (u) and the vertical velocity (v) are kept to zero for the selected horizontal and vertical boundary. Only uniform vertical velocities were imposed along the footing base. The problem domain was selected by performing several trials so that patterns of failure lie within the domain without touching the horizontal bottom and the vertical boundaries right. l and d values of $7B$ and $5B$, respectively, are sufficient to satisfy the conditions. Adaptive meshes for footing with $H/B = 0.25, 0.75$ and 1.25 for $\phi_1 = 42^\circ$ and $\phi_2 = 32^\circ$ are shown in Fig. 2. The meshes are continuously updated based on the shear dissipation of the domain.



(a)



(b)



(c)

Fig. 2 Mesh details for footing on sand with $\phi_1 = 42^\circ$, $\phi_2 = 32^\circ$, with **a** $H/B = 0.25$, **b** $H/B = 0.75$ and **c** $H/B = 1.25$

2 Methodology

The numerical lower and upper bound finite element limit analyses were carried out using the lower and upper bound formulations given by Makrodimopoulos and Martin (2006, 2007) and Krabbenhoft et al. (2007, 2008), respectively. For the lower bound analysis, three-noded triangular elements with nodal stress σ_x , σ_y , τ_{xy} were used to represent the problem of the plane strain and the nodal stress σ_r , σ_z , σ_θ and τ_{rz} were used to represent the problem of the axisymmetrical strain. Statically admissible stress discontinuities have been introduced along with the interfaces of all triangular elements so that there will be a change in normal stress and shear stress at the nodes, but the stress remains continuous along the interface path. The main objective of the lower bound analysis is to maximize the collapse load. Six-noded triangular elements with horizontal and vertical velocity (u and v) were considered for the upper bound analysis. The interfaces have introduced kinematically admissible velocity discontinuities. The main objective of the upper bound analysis is to minimize the collapse. Lower and upper bound values of bearing capacity were obtained for dense on loose sand by varying the top (ϕ_1) and bottom friction angle (ϕ_2) and changes in the values of H/B . The results thus obtained are compared with the available literature, wherever applicable.

The methodology of the lower and upper bound analysis is explained in Sloan (1988), Sloan and Kleeman (1995), Lyamin (1999), Lyamin and Sloan (2002a, b), Krabbenhoft et al. (2007), Krabbenhoft et al. (2008), Makrodimopoulos and Martin (2006), (2007); Kumar and Chakraborty (2014) and Kumar and Mohapatra (2017). In the present study, numerical computations were carried out using the Optum G2 computer program.

3 Results and Comparison

After the determination of collapse load (Q_u), the ultimate bearing capacity (q_u) for circular and strip footing was determined following Eqs. 1 and 2.

$$q_u = Q_u/(\pi B^2/4) \quad (1)$$

$$q_u = Q_u/B \quad (2)$$

Before presenting the results for two-layered sand, it was thought of validating the model and software used for the present studies with the literatures for homogeneous

3.1 Footings on Homogeneous Sand

The analysis was performed for strip and circular base resting on a homogeneous sand layer. The angle of internal friction of sand varied from 30° to 45°. The ultimate bearing capacity was related to bearing factor N_γ (Eq. 3). The N_γ values are shown in Figs. 3 and 4 for strip and circular footing, respectively, following Terzaghi's equations as

$$N_\gamma = q_u / 0.5\gamma B \tag{3}$$

Fig. 3 Comparison of N_γ values for strip footing on homogeneous sand layer with literatures

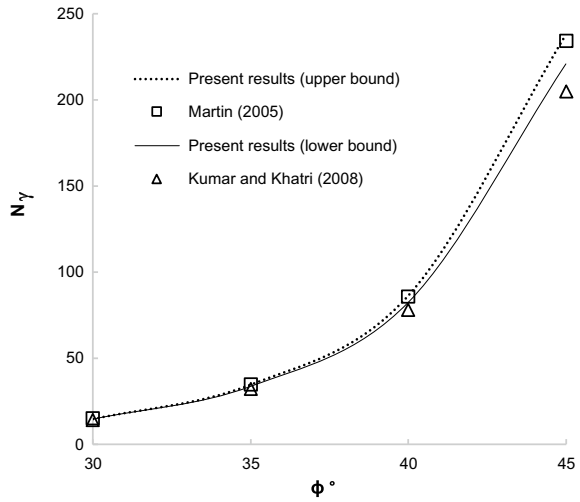
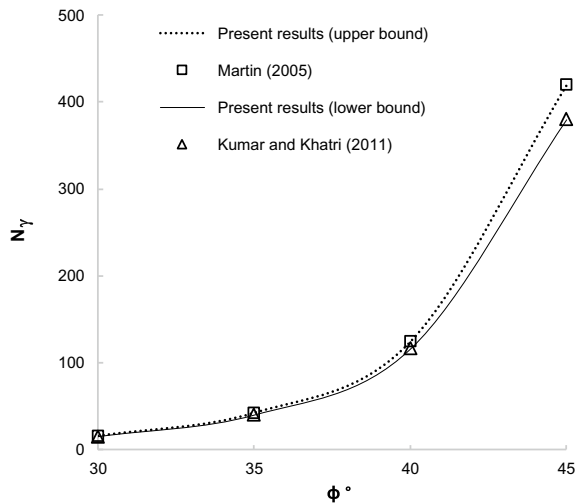


Fig. 4 Comparison of N_γ values for circular footing on homogeneous sand layer with literatures



The N_γ values presented in Figs. 3 and 4 show that the present analysis is quite comparable with those reported by Kumar and Khatri (2008, 2011) by using the lower bound limit analysis and linear optimization. Further, the N_γ values given by Martin (2005) by using the method of stress characteristics were found to lie between the lower and upper bound values of the present analysis.

3.2 *Footings on Layered Sand*

After carrying out the analysis for homogeneous cases, the analysis was carried out for layered sand media. The friction angle of the top dense layer varied from 42° to 46° and the bottom loose layer varied from 32° to 36° . The H/B ratio also varied until the bearing capacity became constant. The bearing capacity was expressed in terms of the efficiency factor, which is defined as the ratio of bearing capacity of the layered sand media to the ratio of bearing capacity of the homogeneous sand layer. The friction angle of the top dense sand is ϕ_1 and bottom loose sand is ϕ_2 . The efficiency factor was calculated by considering the average of lower and upper bound bearing capacity values.

3.3 *Variation of Efficiency Factor with H/B*

The variation of efficiency factor with H/B for different values of ϕ_1 and ϕ_2 is shown in Figs. 5 and 6 for strip and circular footings, respectively. From these figures, it can be observed that due to the inclusion of dense sand layer the efficiency factor increases with an increase in H/B and later it becomes constant with certain H/B values. It was also noticed that for the same values of H/B, ϕ_1 and ϕ_2 , the efficiency factor was found to be greater for circular footing in comparison to strip footing. For example, for H/B = 2, ϕ_1 and $\phi_2 = 42^\circ$ and 32° , the efficiency factor for circular and strip footings was found to be 8.41 and 3.95, respectively. It was also observed that the efficiency factor increased with the increase in ϕ_1 and decrease in ϕ_2 . From Figs. 5 and 6, it was also observed that the efficiency factor increases with H/B value. Further, the efficiency factor continues for a higher H/B value for strip footing compared to the circular footing. A similar observation was revealed by Meyerhof and Hanna (1978).

4 Comparisons

To compare the results of the present analysis with those available in the literature, the magnitude of bearing capacity was expressed in non-dimensional manner by dividing with $(g1B)$. The analysis was carried out by considering $\phi_1 = 47.7^\circ$, $\phi_2 = 34^\circ$, γ_1

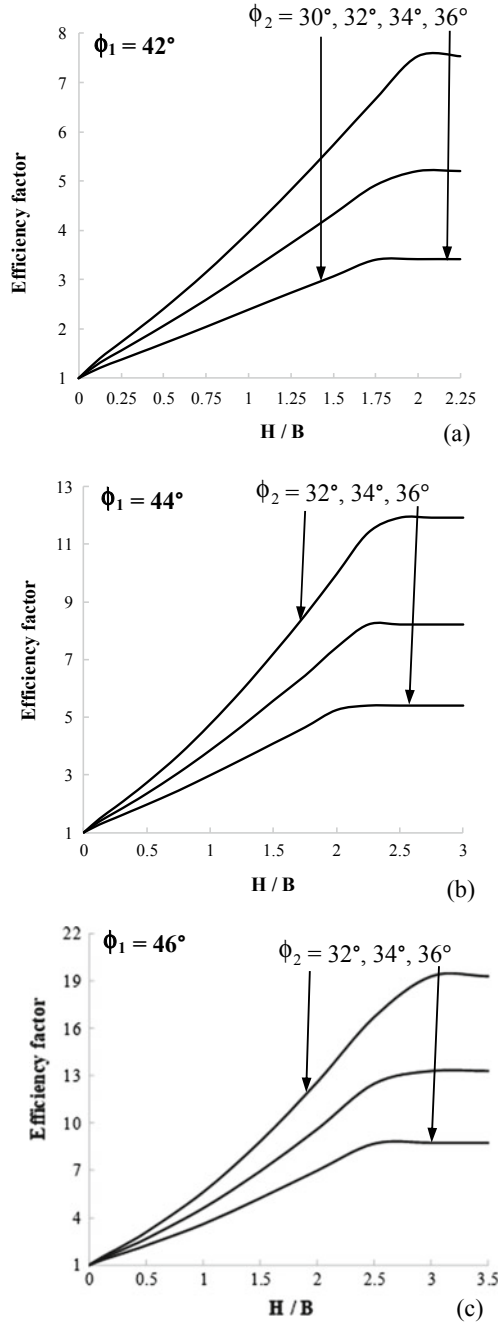


Fig. 5 Variation of efficiency factor with H/B and ϕ_2 for **a** $\phi_1 = 42^\circ$, **b** $\phi_1 = 44^\circ$ and **c** $\phi_1 = 46^\circ$ for rough strip footing

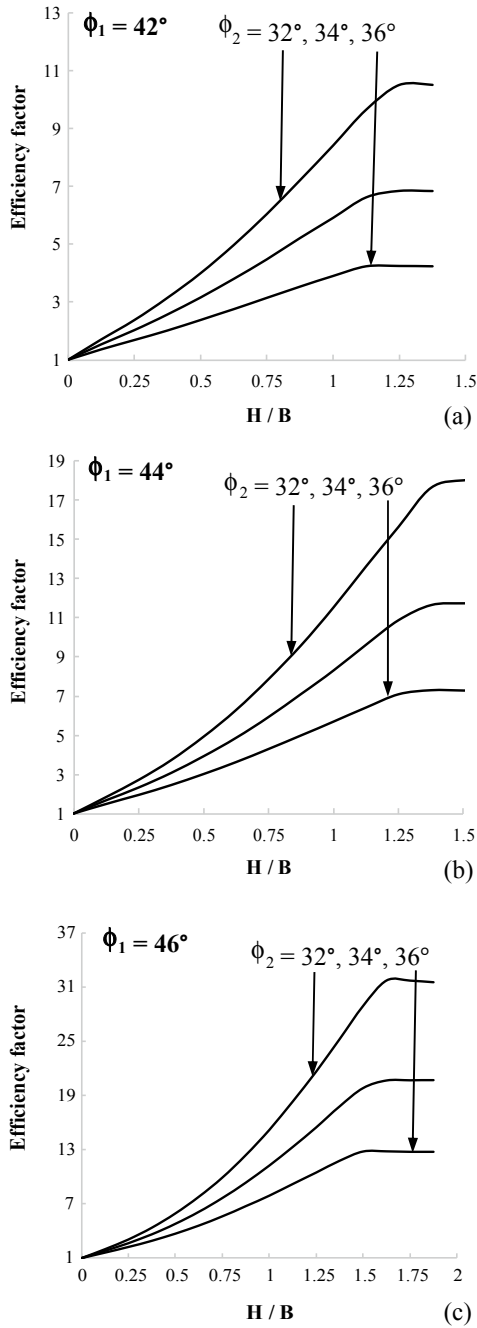


Fig. 6 Variation of efficiency factor with H/B and ϕ_2 for **a** $\phi_1 = 42^\circ$, **b** $\phi_1 = 44^\circ$ and **c** $\phi_1 = 46^\circ$ for rough circular footing

Table 2 Comparison of $q_u/(\gamma_1 B)$ values with Hanna (1981) and Farah (2004) for strip footing on layered sand strata

H/B	Present results		Hanna (1981)	Farah (2004)
	Lower bound	Upper bound		
0	11.92	12.4	18.79	20.38
0.25	19.15	19.93	23.5	25.71
0.5	30.76	32.04	31.16	34.82
1	54.31	56.54	44.92	50.56
1.5	83.16	87.03	67	77.14
2	108.33	113.86	89.09	101.35

Table 3 Comparison of $q_u/(\gamma_1 B)$ values with Hanna (1981) for circular footing on layered sand strata

H/B	Present results		Hanna (1981)
	Lower bound	Upper bound	
0	16.04	17.18	22.41
0.25	22.05	23.58	24.49
0.5	34.41	39.50	36.75
1	90.76	95.35	61.23
1.5	109.47	116.32	94.95
2	156.73	162.83	141.87

= 16.33 KN/m³ and $\gamma_2 = 13.78$ KN/m³. Table 2 shows a comparison of the present lower and upper bound results for strip footings with the corresponding experimental results of Hanna (1981) and Farah (2004). From Table 2 it can be noticed that the bearing capacity reported by Hanna (1981) and Farah (2004) was found to be either higher or close to the present results for H/B values up to 1. However, for values of H/B greater than 1, bearing capacity of the present analysis was found to be greater than those reported in the literature. Similar trends were also observed for circular footings. Table 3 shows the comparisons of the present analysis for circular footings with the corresponding experimental results of Hanna (1981).

5 Conclusions

The bearing capacity of the strip and circular base on dense sand, overlaid by loose sand strata, was numerically determined using lower and upper bound finite element limit analysis with conic optimization. The results are presented in terms of non-dimensional efficiency factors. The study concludes with the following conclusions:

1. For a given friction angle of top dense layer and bottom loose layer, the efficiency factor increases with an increase in the thickness of the top dense layer.

2. The increase in efficiency factor with the inclusion of a dense layer of specific thickness becomes more significant for a circular base than for a strip. That is to say, for the same thickness of the top dense layer, the circular base has more bearing capacity than the strip foot.
3. The increase in efficiency factor with the inclusion of a dense layer of specific thickness becomes more significant for the circular base compared to the strip foot, that is, for the same thickness of the top dense layer circular footing has more bearing capacity than the strip footing.

The generated adaptive mesh shows the variation of the bearing capacity with the thickness of the top dense layer.

The results of the present study suggest that with the inclusion of a thin, dense layer just below the footing resting on layered sand strata, the bearing capacity can be improved.

References

- Bowles JE (1977) *Foundation analysis and design*. McGraw-Hill, New York
- Burd HJ, Frydman S (1997) Bearing capacity of plane-strain footings on layered soils. *Can Geotech J* 34(2):241–253
- Farah CA (2004) *Ultimate bearing capacity of shallow foundations on layered soils*. MSc thesis, Civil and Environmental Engineering, Concordia Univ., Quebec
- Georgiadis M, Michalopoulos A (1985) Bearing capacity of gravity bases on layered soil. *J Geotech Eng* [https://doi.org/10.1061/\(ASCE\)0733-9410\(1985\)111:6\(712\)](https://doi.org/10.1061/(ASCE)0733-9410(1985)111:6(712)), 712–729 (1985)
- Hanna AM (1981) Foundations on strong sand overlying weak sand. *J Geotech Engrg Div* 107(7):915–927
- Hanna AM (1982) Bearing capacity of foundations on a weak sand layer overlying a strong deposit. *Can Geotech J* 19(3):392–396
- Hanna AM (1987) Finite element analysis of footings on layered soils. *Math Modell* 9(11):813–819
- Kenny MJ, Andrawes KZ (1997) The bearing capacity of footings on a sand layer overlying soft clay. *Geotechnique* 47(2):339–346
- Krabbenhøft K, Lyamin AV, Sloan SW (2007) Formulation and solution of some plasticity problems as conic programs. *Int J Solids Struct* 44(5):1533–1549
- Krabbenhøft K, Lyamin AV, Sloan SW (2008) Three-dimensional Mohr-Coulomb limit analysis using semidefinite programming. *Int J Numer Methods Eng* 24(11):1107–1119
- Kumar A, Ohri ML, Bansal RK (2007) Bearing capacity tests of strip footings on reinforced layered soil. *Geotech Geol Eng* 25(2):139–150
- Kumar J, Chakraborty M (2014) Upper bound axisymmetric limit analysis using Mohr-Coulomb yield criterion, finite elements and linear optimization. *J Eng Mech*, [https://doi.org/10.1061/\(ASCE\)EM.1943-7889.0000820](https://doi.org/10.1061/(ASCE)EM.1943-7889.0000820), 06014012
- Kumar J, Chakraborty M (2015) Bearing capacity of a circular foundation on layered sand-clay media. *Soils Found* 55(5):1058–1068
- Kumar J, Khatri VN (2008) Effect of footing roughness on lower bound N_y values. *Int J Geomech*, 176–187, [https://doi.org/10.1061/\(ASCE\)1532-3641\(2008\)8:3\(176\)](https://doi.org/10.1061/(ASCE)1532-3641(2008)8:3(176))
- Kumar J, Khatri VN (2011) Bearing capacity factors of circular foundations for a general $c-\phi$ soil using lower bound finite elements limit analysis. *Int J Numer Anal Methods Geomech* 35(3):393–405, Wiley

- Kumar J, Mohapatra D (2017) Lower-bound finite elements limit analysis for Hoek-Brown materials using semidefinite programming. *J Eng Mech*, 04017077 [https://doi.org/10.1061/\(ASCE\)EM.1943-7889.0001296](https://doi.org/10.1061/(ASCE)EM.1943-7889.0001296)
- Lyamin AV (1999) Three-dimensional lower bound limit analysis using nonlinear programming. PhD thesis, Univ. of Newcastle, Callaghan, Australia
- Lyamin AV, Sloan SW (2002a) Lower bound limit analysis using non-linear programming. *Int J Numer Methods Eng* 55(5):573–611
- Lyamin AV, Sloan SW (2002b) Upper bound limit analysis using linear finite elements and non-linear programming. *Int J Numer Anal Methods Geomech* 26(2):181–216
- Makrodimopoulos A, Martin CM (2006) Lower bound limit analysis of cohesive frictional materials using second-order cone programming. *Int J Numer Methods Eng* 66(4):604–634
- Makrodimopoulos A, Martin CM (2007) “Upper bound limit analysis using simplex strain elements and second-order cone programming. *Int J Numer Anal Methods Geomech* 31(6):835–865
- Martin CM (2005) Exact bearing capacity calculations using the method of characteristics. In: *Proceedings 11th Conference of IACMAG, Vol 4, International Association for Computer Methods and Advances in Geomechanics*, 441–450
- Meyerhof GG (1974) Ultimate bearing capacity of footings on sand layer overlying clay. *Can Geotech J* 11(2):223–229
- Meyerhof GG, Hanna AM (1978) Ultimate bearing capacity of foundations on layered soils under inclined load. *Can Geotech J* 15(4):565–572
- Michalowski RL, Shi L (1995) Bearing capacity of footings over two-layer foundation soil. *J Geotech Engrg*, 421–428, [https://doi.org/10.1061/\(ASCE\)0733-9410\(1995\)121:5\(421\)](https://doi.org/10.1061/(ASCE)0733-9410(1995)121:5(421))
- Oda M, Win S (1990) Ultimate bearing-capacity tests on sand with clay layer. *J Geotech Eng*, 1902–1906
- Okamura M, Takemura J, Kimura T (1998) Bearing capacity predictions of sand overlying clay based on limit equilibrium methods. *Soils Found* 38(1):181–194
- Optum G2 [Computer software]. Optum Computational Engineering, Copenhagen, Denmark
- Shiau JS, Lyamin AV, Sloan SW (2003) Bearing capacity of a sand layer on clay by finite element limit analysis. *Can Geotech J* 40(5):900–915
- Shoaei MD, Alkarni A, Noorzaei J, Jaafar MS, Huat BBK (2012) Review of available approaches for ultimate bearing capacity of two-layered soils. *J Civ Eng Manage* 18(4):469–482
- Sloan SW (1988) Lower bound limit analysis using finite elements and linear programming. *Int J Numer Anal Methods Geomech* 12(1):61–77
- Sloan SW, Kleeman PW (1995) Upper bound limit analysis using discontinuous velocity fields. *Comput Methods Appl Mech Eng* 127(1):293–314

Lateral and Uplift Capacities of Barrette Pile in Sandy Soil



Anju Kumari, S. W. Thakare, and A. I. Dhattrak

Abstract This paper presents the results of analyses of barrette piles. For this purpose models of barrette pile were developed in MIDAS GTS software, which is based on finite element method. Soil model was developed by Mohr–Coulomb and pile as linear elastic model. Various shapes of barrette, with similar cross-section area, viz., 1.5, 3 and 4.5 m² were considered for analysis and their lateral and uplift capacities were determined for different relative densities of soil. The capacities of barrette piles were compared with those of circular pile with the same cross-section area, and the improvement in lateral and uplift capacities of barrette piles was determined. Results indicate that the barrette piles have higher lateral and uplift capacities and percentage increase is in the range of 100–1300% as compared to circular pile. Also, cruciform shape barrette pile has higher lateral and uplift capacity among other shapes of barrette.

Keywords MIDAS GTS 3D · Circular · Rectangle · T-shape · L-shape · Cruciform barrette pile

1 Introduction

1.1 General

A barrette is a cast-in-place reinforced concrete pile, which can take high axial, lateral and uplift loads and also adaptable to the most types of ground. The word ‘barrette’ originates from the French language, which refers to a concrete replacement pile formed in a short and deep trench excavated under bentonite or polymer slurry by

A. Kumari (✉) · S. W. Thakare · A. I. Dhattrak
Government College of Engineering Amravati, Amravati, Maharashtra, India
e-mail: singh.anju245@gmail.com

A. I. Dhattrak
Department of Civil Engineering, University of Sant Gadge Baba Amravati University, Amravati, Maharashtra, India

diaphragm walling equipment. Barrettes have much of the same purpose and design as the conventional piles. Barrette piles are generally rectangular piles. However, various other shapes like T-shape and cruciform shape can also be constructed. Barrettes provide resistance to horizontal and vertical stresses better than circular piles of the same cross-section.

Barrettes provide an alternative to large diameter bored and cast-in-place piles or drilled shafts. This is because a barrette has a higher specific surface than a circular pile. The fact that a single barrette can replace a group of conventional circular piles in many applications results in a more compact, economical and reliable foundation system.

1.2 Literature Review


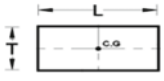
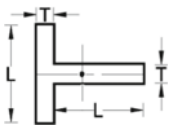
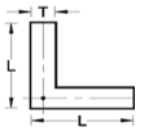
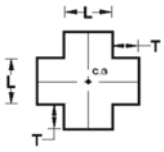
Wakil and Nazir (2012) had presented the study of behavior of laterally loaded small-scale barrettes in sand. Their aim was to investigate the response of laterally loaded rectangular cross-sectional barrettes. The lateral resistance of the barrette that was loaded in the direction of major axis was higher than that loaded in the direction of minor axis. Sand relative density had significant effect on the lateral capacity of the barrettes. Chu-Eu Ho and Lim (1998) described the performance of a fully instrumented test barrette subjected to an ultimate loading of 30932 kN. Ng et al. (2000) had presented field studies of well-instrumented barrette in Hong Kong. In Hong Kong, single barrette up to size of 1.5 m wide \times 6.6 m long had been constructed. Due to rectangular shape, barrette foundations are particularly suitable to resist large vertical and significant horizontal load in chosen direction. Zhang (2003) had described the behavior of laterally loaded large-section barrettes. The lateral load capacity was the greatest when the loading was along the major axis of the cross-section and smallest when the loading was along the minor axis. For loading directions in between, the lateral load capacity decreases gradually as the loading direction deviates from the major axis. Submanee Wong and Teparaksa (2009) studied on performance of T-shape barrette pile against lateral force. The lateral resistance of barrette pile was high along the longer side but low along narrow side.

2 Materials and Methods

2.1 Methodology

In this study, MIDAS GTS 3D software is used, which is a finite element-based software used for analyses. Initially, a three-dimensional geometry was created and the properties of the system were then assigned. Then a three-dimensional mesh was

Table 1 Various shapes of barrette piles

Shapes of piles	Sym	C/S area		
		1.5 m ²	3 m ²	4.5 m ²
	D	1.4	2	2.4
	L	1.5, 2 & 3	2, 2.5 & 3	3, 4.5 & 5
	T	1, 0.7 & 0.5	1.5, 1.2 & 1	1.5, 1.15 & 0.9
	L	1	1.5	2.2
	T	0.75	1	1
	L	1	1.5	2.2
	T	0.75	1	1
	T	0.75	1	1
	L	0.4	0.6	0.9

generated using the auto mesh function followed by the input of load and boundary conditions. Self-weight was calculated by the software itself by multiplying the unit weight and acceleration due to gravity. Lateral and uplift loads are analyzed individually.

Analysis for circular pile foundation system was carried out and its capacities were determined which served as a basis for comparison with performance of barrette pile foundation. The various shapes of the barrette pile considered for the analyses along with their cross-sectional dimensions are shown in Table 1.

The cross-sections of the barrette piles were the same as that of the circular pile, that is, 1.5, 3 and 4.5 m². The depth of piles was kept constant equal to 30 m in all cases.

2.2 Material Properties

The material properties adopted for pile and soil in the present study for the analyses are given in Tables 2 and 3, respectively.

Table 2 Material properties adopted for pile

Property	Unit	Pile
Material model	–	Elastic
Stiffness (E)	MPa	30,000
Poisson’s ratio (μ)	–	0.2
Unit weight (γ)	kN/m ³	25

Table 3 Material properties adopted for soil

Property	Unit	Loose soil	Medium dense soil	Dense soil
Material model	–	Mohr–Coulomb	Mohr–Coulomb	Mohr–Coulomb
Stiffness (E)	MPa	20	40	80
Angle of internal friction (ϕ)	Deg	30	33	38
Dilatancy angle (ψ)	Deg	0	5	10
Cohesion (c)	kPa	5	5	5
Poisson’s ratio (μ)	–	0.3	0.3	0.3
Unit weight (γ)	kN/m ³	15	17	20

2.3 Numerical Model and Analyses

The models of soil and barrette pile developed in MIDAS GTS software are shown in Fig. 1. The size of the soil model was 30 m × 30 m in plan and 100 m depth, whereas for pile it was 1.5 m × 1 m in plan and 30 m depth.

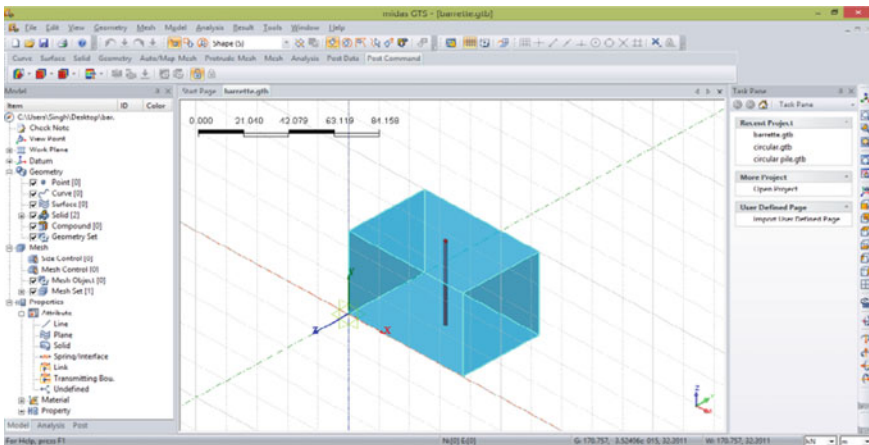


Fig. 1 Model created in MIDAS GTS software

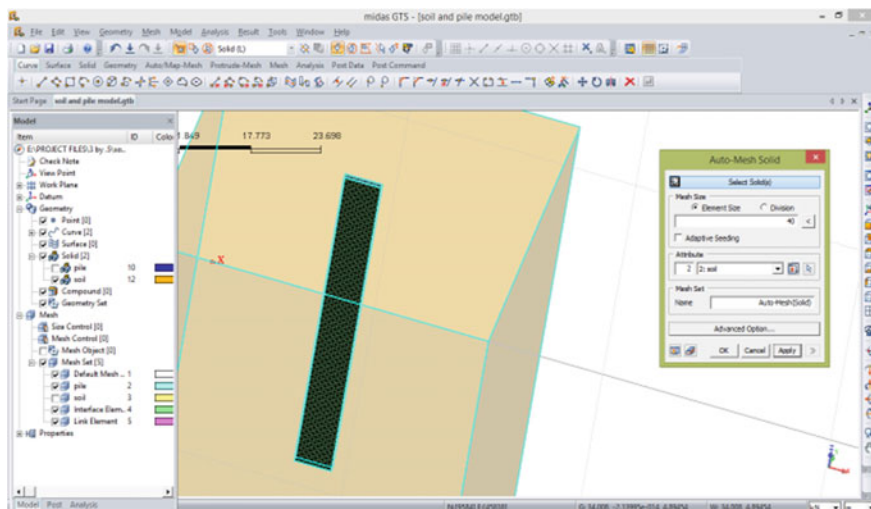


Fig. 2 Window of mesh generation in MIDAS GTS software

Separate meshing was provided for barrette pile foundation and soil model. In the present work auto mesh function was used for meshing. Number of elements chosen for meshing varies with variation of dimension. As far as possible, finer meshing was provided by increasing number of elements to achieve more accurate results. Figures 2 and 3 show window of mesh generation and geometry after mesh generation.

Model generated in previous stage was analyzed after calculations were carried out, and post-processing window was obtained, as shown in Fig. 4, which shows window of result extraction.

From the analyses carried out, load–settlement curve for each case was generated and ultimate lateral and uplift capacity was determined as per provisions of IS: 2911-1985. The effect of shape of barrette pile on ultimate capacities was studied. The capacities of the barrette of various shapes were compared with those of circular pile and percentage increases in the capacities are reported.

3 Results of Analyses

The analyses were carried out for circular pile and barrette piles of different shapes in loose sand, medium dense sand and dense sand.

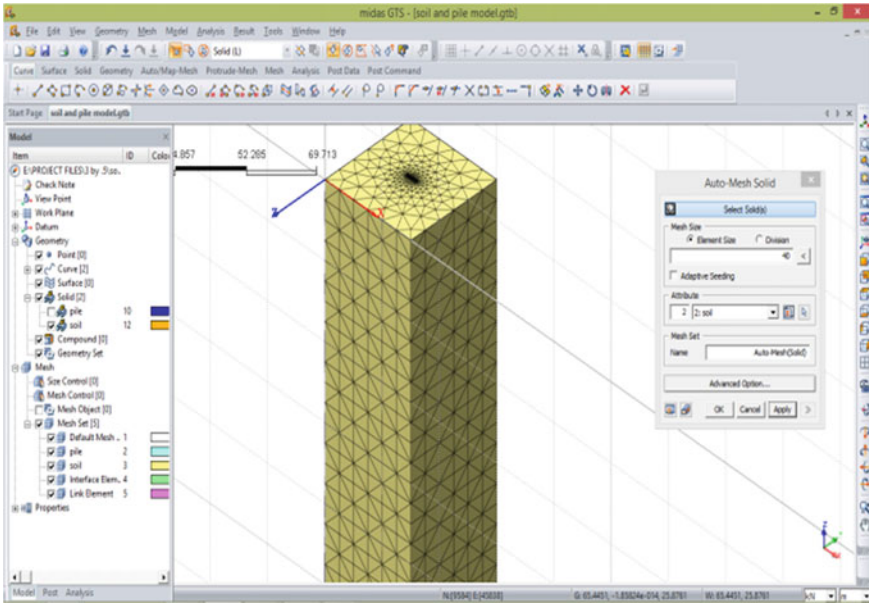


Fig. 3 Geometry after mesh generation in MIDAS GTS software

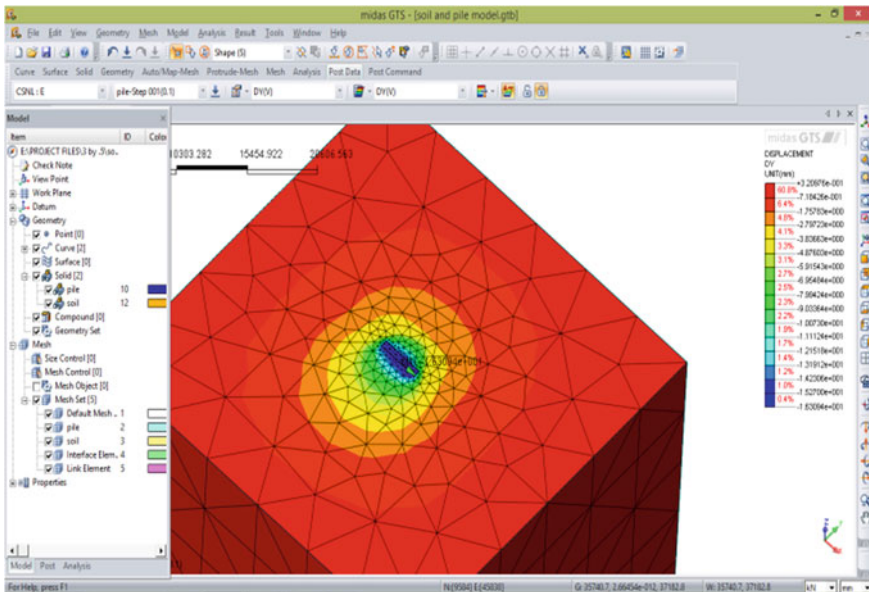


Fig. 4 Post-processing window in MIDAS GTS 3D

Table 4 Lateral and uplift capacities of piles with C/S area 1.5 m² in loose sand

Shape of pile	Lateral capacity along major axis (kN)	Lateral capacity along minor axis (kN)	Uplift capacity (kN)
Circular	600	600	300
Rectangle 1 (1.5 m × 1 m)	2980	1780	700
Rectangle 2 (2 m × 0.75 m)	3600	1680	1300
Rectangle 3 (3 m × 0.5 m)	4200	1500	2100
T-shape	4500	2100	2800
L-shape	3600	3200	2400
Cruciform shape	4800	–	3000

Table 5 Lateral and uplift capacities of piles with C/S area 3 m² in loose sand

Shape of pile	Lateral capacity along major axis (kN)	Lateral capacity along minor axis (kN)	Uplift capacity (kN)
Circular	800	800	600
Rectangle 1 (2 m × 1.5 m)	4000	3200	1960
Rectangle 2 (2.5 m × 1.2 m)	4800	2880	2400
Rectangle 3 (3 m × 1 m)	5400	2450	3500
T-shape	7000	4400	4000
L-shape	7500	5400	3600
Cruciform shape	8400	–	4200

3.1 Performance of Barrette Piles in Loose Sand

The analyses were carried out for circular pile and barrette piles of different shapes, but with the same cross-section area 1.5, 3 and 4.5 m² subjected to lateral and uplift loading in loose sand. From the results of the analyses, lateral and uplift capacities are determined for each case. These ultimate lateral and uplift capacities for different cross-section area are shown from Tables 4, 5 and 6.

3.2 Performance of Barrette Piles in Dense Sand

The analyses were carried out for circular pile and barrette piles of different shapes, but with the same cross-section area 1.5, 3 and 4.5 m² subjected to lateral and uplift

Table 6 Lateral and uplift capacities of piles with C/S area 4.5 m² in loose sand

Shape of pile	Lateral capacity along major axis (kN)	Lateral capacity along minor axis (kN)	Uplift capacity (kN)
Circular	1080	1080	1000
Rectangle 1 (3 m × 1.5 m)	5600	4800	3500
Rectangle 2 (4 m × 1.15 m)	6600	4000	3900
Rectangle 3 (5 m × 0.9 m)	7500	3600	4200
T-shape	10800	6600	5600
L-shape	11200	7500	4900
Cruciform shape	12000	–	6000

Table 7 Lateral and uplift capacities of piles with C/S area 1.5 m² in medium dense sand

Shape of pile	Lateral capacity along major axis (kN)	Lateral capacity along minor axis (kN)	Uplift capacity (kN)
Circular	700	700	490
Rectangle 1 (2 m × 1.5 m)	4030	2500	1500
Rectangle 2 (2.5 m × 1.2 m)	4500	2100	2250
Rectangle 3 (3 m × 1 m)	5400	1400	3200
T-shape	6500	3500	3750
L-shape	5000	4800	3200
Cruciform shape	7200	–	3850

loading in medium dense sand. From the results of the analyses, lateral and uplift capacities are determined for each case. These ultimate lateral and uplift capacities for different cross-section area are shown from Tables 7, 8 and 9.

3.3 Performance of Barrette Piles in Dense Sand

The analyses were carried out for circular pile and barrette piles of different shapes, but with the same cross-section area 1.5, 3 and 4.5 m² subjected to lateral and uplift loading in dense sand. From the results of the analyses, lateral and uplift capacities are determined for each case. These ultimate lateral and uplift capacities for different cross-section area are shown from Tables 10, 11 and 12.

Table 8 Lateral and uplift capacities of piles with C/S area 3 m² in medium dense sand

Shape of pile	Lateral capacity along major axis (kN)	Lateral capacity along minor axis (kN)	Uplift capacity (kN)
Circular	960	960	700
Rectangle 1 (2 m × 1.5 m)	5600	4200	2400
Rectangle 2 (2.5 m × 1.2 m)	6300	3850	3500
Rectangle 3 (3 m × 1 m)	7700	2450	4900
T-shape	10400	5600	5200
L-shape	9900	7200	4950
Cruciform shape	11200	–	5600

Table 9 Lateral and uplift capacities of piles with C/S area 4.5 m² in medium dense sand

Shape of pile	Lateral capacity along major axis (kN)	Lateral capacity along minor axis (kN)	Uplift capacity (kN)
Circular	1350	1350	900
Rectangle 1 (2 m × 1.5 m)	7900	6600	4800
Rectangle 2 (2.5 m × 1.2 m)	9100	5400	5200
Rectangle 3 (3 m × 1 m)	10400	4800	6000
T-shape	15000	9200	7600
L-shape	15750	10500	6650
Cruciform shape	16200	–	8400

Table 10 Lateral and uplift capacities of piles with C/S area 1.5 m² in dense sand

Shape of pile	Lateral capacity along major axis (kN)	Lateral capacity along minor axis (kN)	Uplift capacity (kN)
Circular	900	900	600
Rectangle 1 (2 m × 1.5 m)	4400	3500	2000
Rectangle 2 (2.5 m × 1.2 m)	5000	3000	3000
Rectangle 3 (3 m × 1 m)	6400	2500	3500
T-shape	8250	4500	4400
L-shape	7200	6000	4050
Cruciform shape	9000	–	5400

Table 11 Lateral and uplift capacities of piles with C/S area 1.5 m² in dense sand

Shape of pile	Lateral capacity along major axis (kN)	Lateral capacity along minor axis (kN)	Uplift capacity (kN)
Circular	1360	1360	1050
Rectangle 1 (2 m × 1.5 m)	8000	5600	3500
Rectangle 2 (2.5 m × 1.2 m)	9000	5000	4800
Rectangle 3 (3 m × 1 m)	11000	3600	6600
T-shape	14400	7650	7200
L-shape	13500	10800	6750
Cruciform shape	16500	–	7920

Table 12 Lateral and uplift capacities of piles with C/S area 1.5 m² in dense sand

Shape of pile	Lateral capacity along major axis (kN)	Lateral capacity along minor axis (kN)	Uplift capacity (kN)
Circular	1600	1600	1200
Rectangle 1 (2 m × 1.5 m)	10400	9200	6600
Rectangle 2 (2.5 m × 1.2 m)	12600	7700	7200
Rectangle 3 (3 m × 1 m)	14850	6600	8100
T-shape	20400	11200	10450
L-shape	21600	14000	9000
Cruciform shape	22500	–	11500

4 Discussion of Analyses

The results obtained from the analyses carried out on circular piles and barrette piles of various shapes with cross-section area as 1.5, 3 and 4.5 m² are discussed.

4.1 Effect of Shapes of Barrette Pile on Lateral and Uplift Capacity in Loose Sand

The percentage increase in lateral and uplift capacities of barrette piles of various shapes as compared to that of circular pile with the same cross-section area as 1.5, 3 and 4.5 m² in loose sand are shown in Figs. 5, 6, 7, 8, 9, 10, 11, 12 and 13.

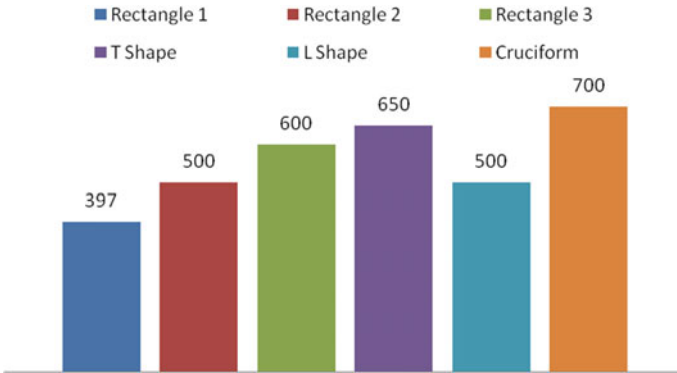


Fig. 5 Percentage increase in lateral capacity for barrette piles along major axis with C/S area 1.5 m² in loose sand

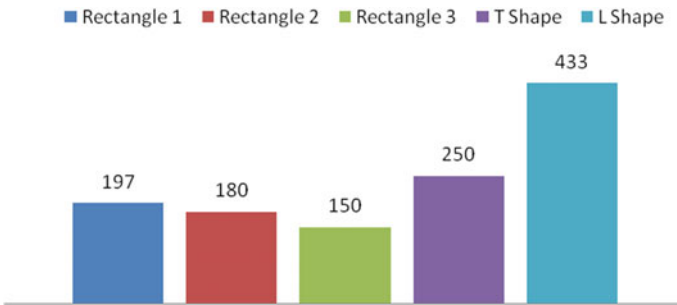


Fig. 6 Percentage increase in lateral capacity for barrette piles along minor axis with C/S area 1.5 m² in loose sand

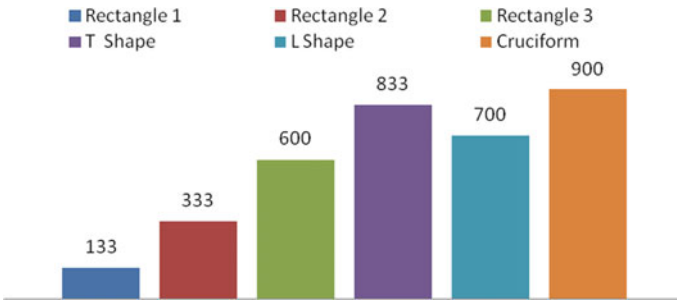


Fig. 7 Percentage increase in uplift capacity for barrette piles with C/S area 1.5 m² in loose sand

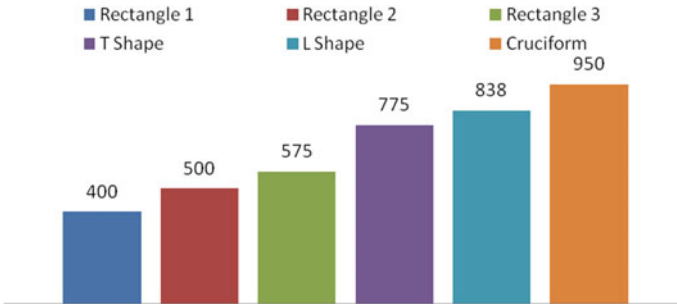


Fig. 8 Percentage increase in lateral capacity for barrette piles along major axis with C/S area 3 m² in loose sand

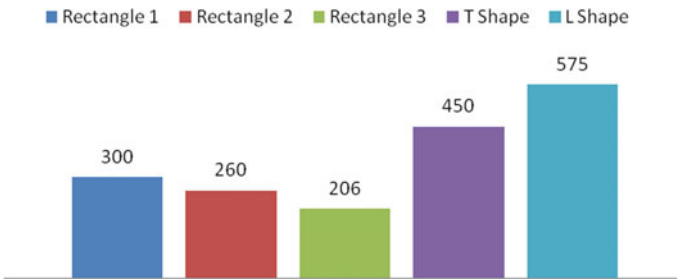


Fig. 9 Percentage increase in lateral capacity for barrette piles along minor axis with C/S area 3 m² in loose sand

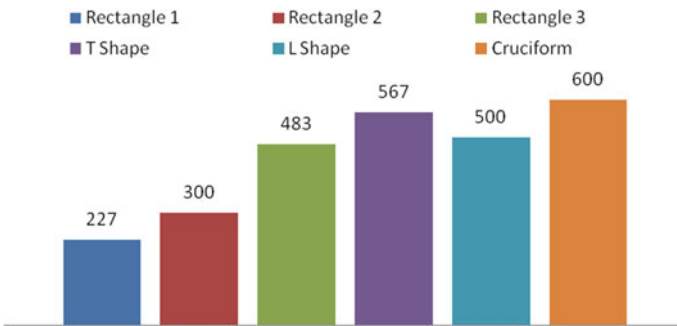


Fig. 10 Percentage increase in uplift capacity for barrette piles with C/S area 3 m² in loose sand

From Figs. 5, 6, 7, 8, 9, 10, 11, 12 and 13, it is seen that the lateral capacity and uplift capacity of barrette pile foundation for all cross-section area of 1.5, 3 and 4.5 m² are much higher for all shapes of barrette piles as compared to that of circular pile in loose sand bed. The percentage increase in lateral capacity along major axis is maximum for cruciform shape barrette pile, whereas it is maximum along the

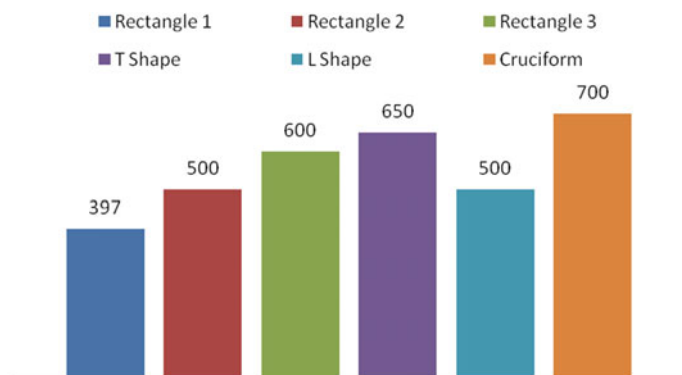


Fig. 11 Percentage increase in lateral capacity for barrette piles along major axis with C/S area 4.5 m^2 in loose sand

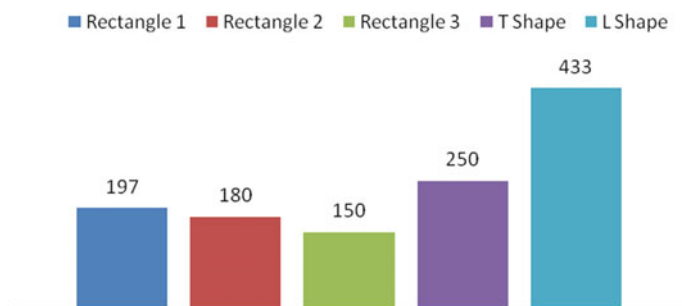


Fig. 12 Percentage increase in lateral capacity for barrette piles along minor axis with C/S area 4.5 m^2 in loose sand

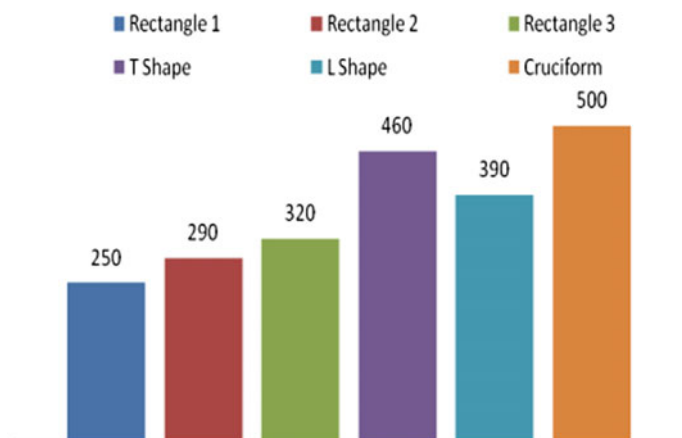


Fig. 13 Percentage increase in uplift capacity for barrette piles with C/S area 4.25 m^2 in loose sand

minor axis for L-shape barrette pile foundation for all cross-section area. Also, the percentage increase in uplift capacity is maximum for cruciform shape barrette pile as compared to other piles.

4.2 Effect of Shapes of Barrette Pile on Lateral and Uplift Capacity in Medium Dense Sand

The percentage increase in lateral and uplift capacities of barrette piles of various shapes as compared to that of circular pile with the same cross-section area as 1.5, 3 and 4.5 m² in dense sand are shown in Figs. 23, 24, 25, 26, 27, 28, 29, 30 and 31.

From the Figs. 14, 15, 16, 17, 18, 19, 20, 21 and 22, the percentage increase in lateral capacity along major axis is maximum for cruciform shape barrette pile, whereas it is maximum along the minor axis for L-shape barrette pile foundation for

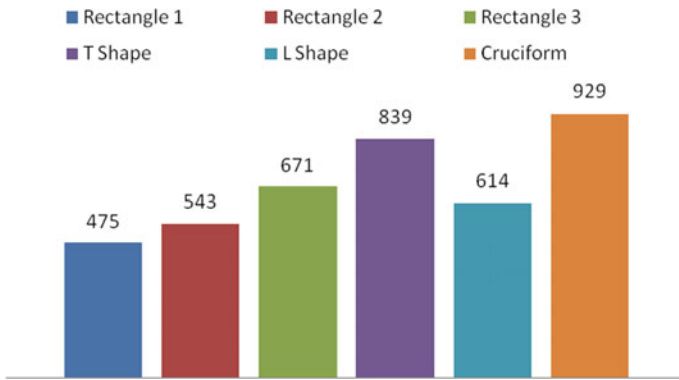


Fig. 14 Percentage increase in lateral capacity for barrette piles along major axis with C/S area 1.5 m² in medium dense sand

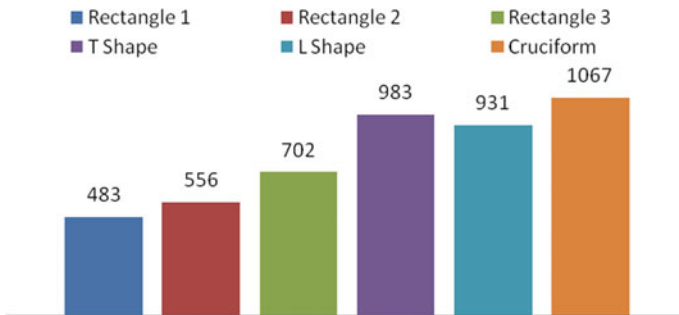


Fig. 15 Percentage increase in lateral capacity for barrette piles along minor axis with C/S area 1.5 m² in medium dense sand

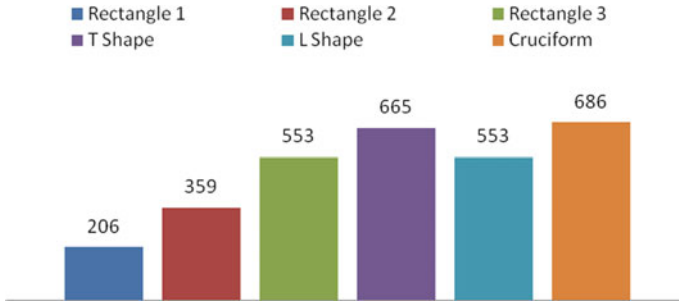


Fig. 16 Percentage increase in uplift capacity for barrette piles with C/S area 1.5 m² in medium dense sand

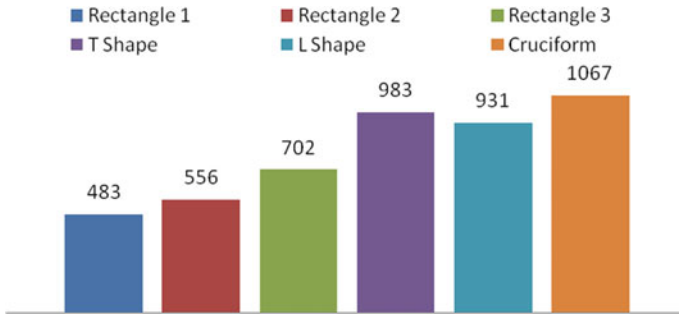


Fig. 17 Percentage increase in lateral capacity for barrette piles along major axis with C/S area 3 m² in loose sand

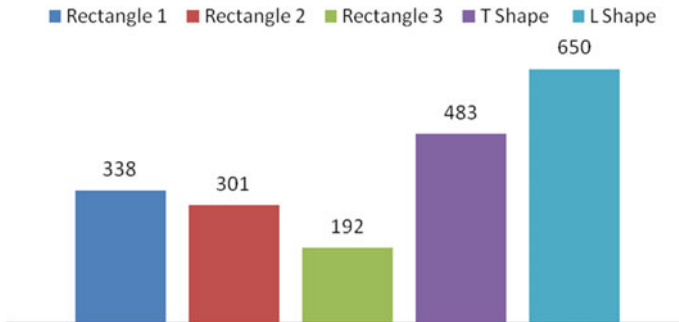


Fig. 18 Percentage increase in lateral capacity for barrette piles along minor axis with C/S area 3 m² in medium dense sand

all cross-section area. Also, the percentage increase in uplift capacity is maximum for cruciform shape barrette pile as compared to other piles.

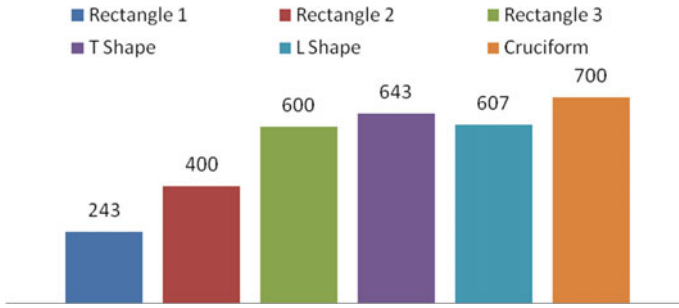


Fig. 19 Percentage increase in uplift capacity for barrette piles with C/S area 3 m² in medium dense sand

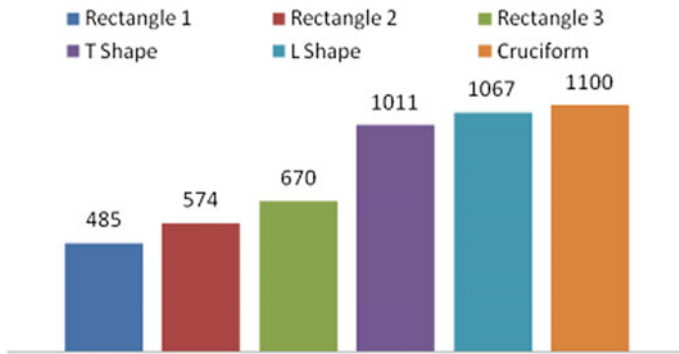


Fig. 20 Percentage increase in lateral capacity for barrette piles along major axis with C/S area 4.5 m² in medium dense sand

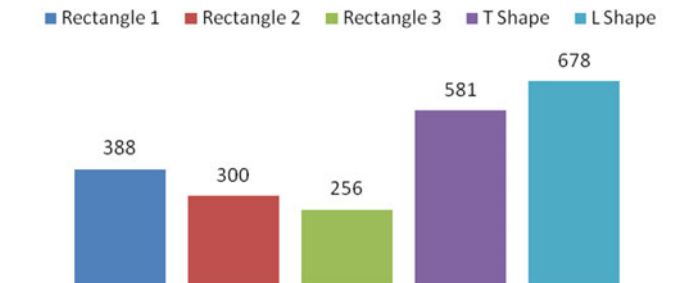


Fig. 21 Percentage increase in lateral capacity for barrette piles along minor axis with C/S area 4.5 m² in medium dense sand

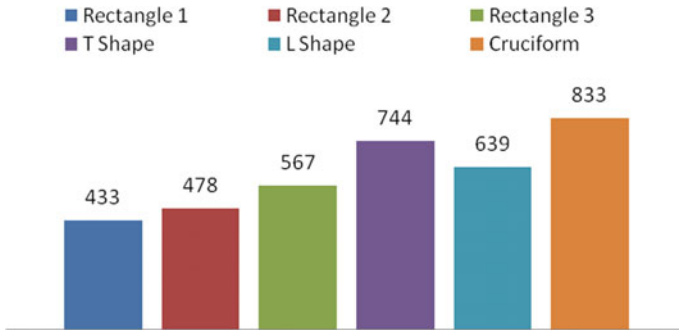


Fig. 22 Percentage increase in uplift capacity for barrette piles with C/S area 4.5 m² in medium dense sand

4.3 Effect of Shapes of Barrette Pile on Lateral and Uplift Capacity in Dense Sand

The percentage increases in lateral and uplift capacities of barrette piles of various shapes as compared to that of circular pile with the same cross-section area as 1.5, 3 and 4.5 m² in medium dense sand are shown in Fig. 14, 15, 16, 17, 18, 19, 20, 21 and 22.

From the Figs. 23, 24, 25, 26, 27, 28, 29, 30 and 31, it is seen that the lateral capacity and uplift capacity of barrette pile foundation for all cross-section area of 1.5, 3 and 4.5 m² are much higher for all shapes of barrette piles as compared to circular pile in medium dense sand. The percentage increase in lateral capacity along major axis is maximum for cruciform shape barrette pile, whereas it is maximum along the minor axis for L-shape barrette pile foundation for all cross-section area.

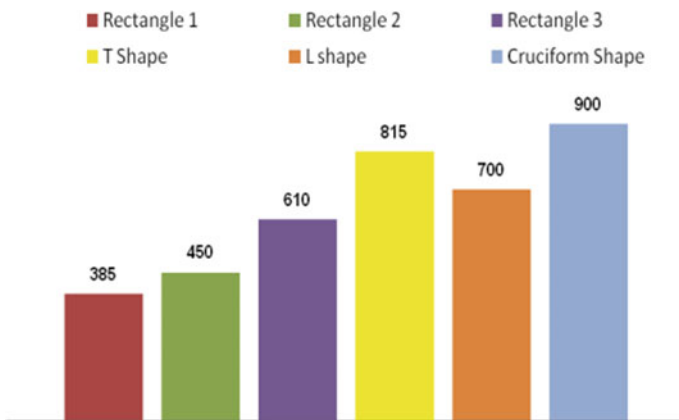


Fig. 23 Percentage increase in lateral capacity for barrette piles along major axis with C/S area 1.5 m² in dense sand

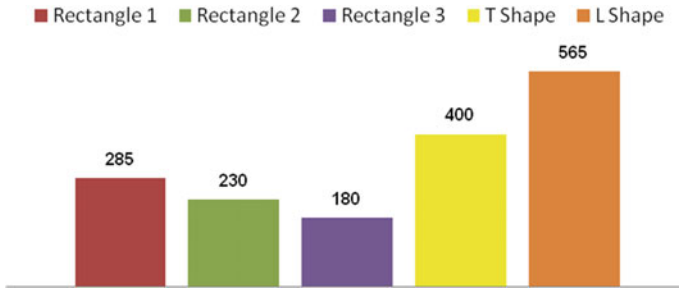


Fig. 24 Percentage increase in lateral capacity for barrette piles along minor axis with C/S area 1.5 m² in dense sand

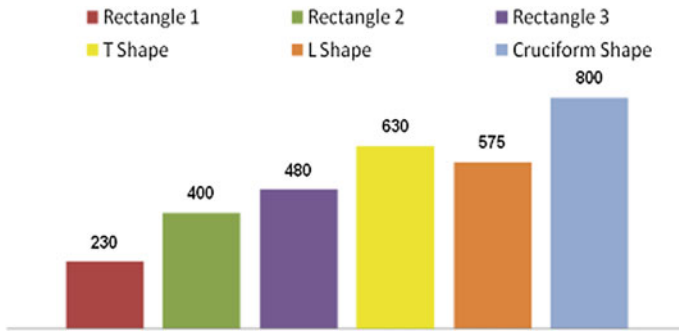


Fig. 25 Percentage increase in uplift capacity for barrette piles with C/S area 1.5 m² in dense sand

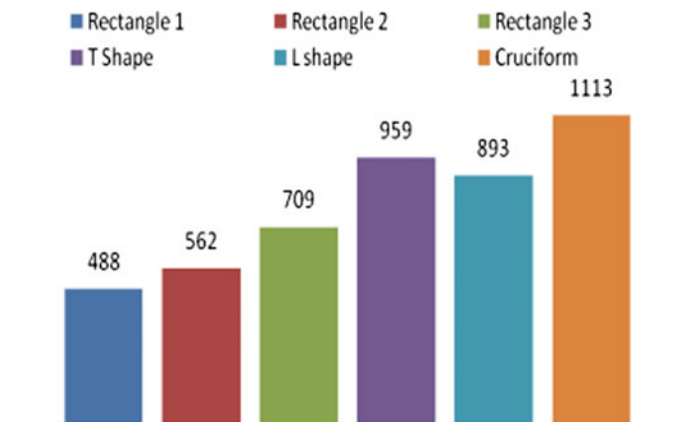


Fig. 26 Percentage increase in lateral capacity for barrette piles along major axis with C/S area 3 m² in dense sand

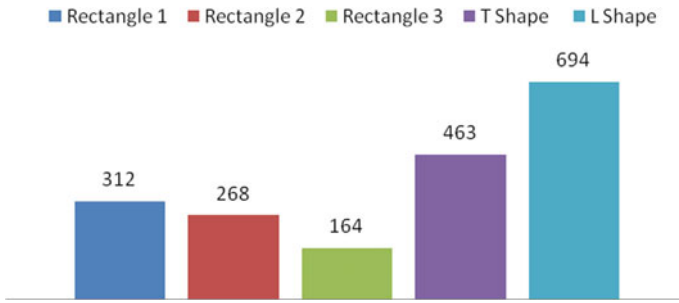


Fig. 27 Percentage increase in lateral capacity for barrette piles along minor axis with C/S area 3 m² in dense sand

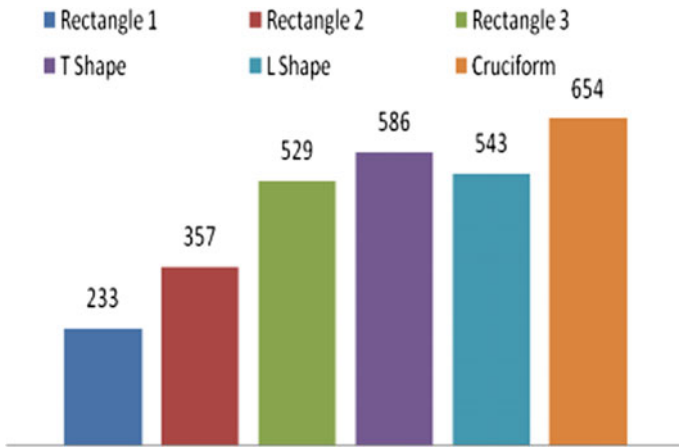


Fig. 28 Percentage increase in uplift capacity for barrette piles with C/S area 3 m² in dense sand

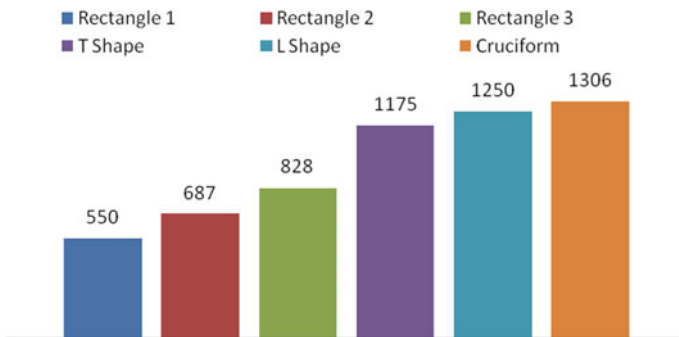


Fig. 29 Percentage increase in lateral capacity for barrette piles along major axis with C/S area 4.5 m² in dense sand

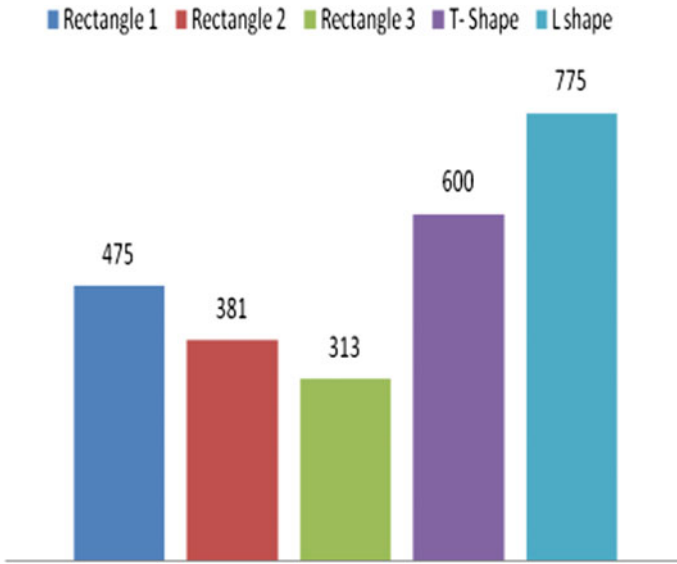


Fig. 30 Percentage increase in lateral capacity for barrette piles along minor axis with C/S area 4.5 m² in dense sand

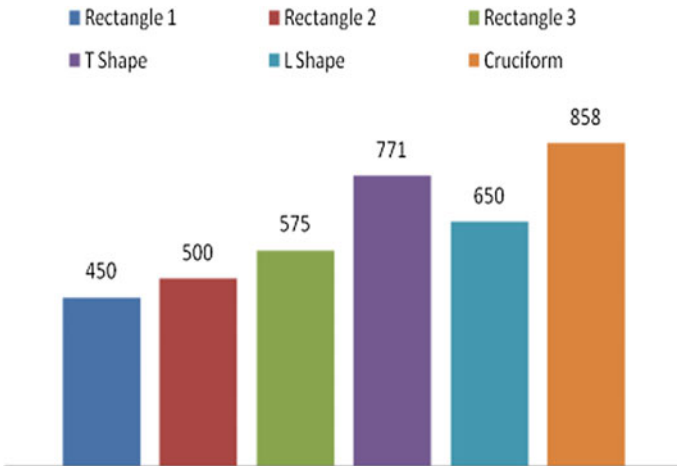


Fig. 31 Percentage increase in uplift capacity for barrette piles with C/S area 4.5 m² in dense sand

Also, the percentage increase in uplift capacity is maximum for cruciform shape barrette pile as compared to other piles.

5 Conclusions

Based on the results of the present study, the following broad conclusions are drawn:

1. The lateral capacities of barrette piles of various shapes, viz., rectangle, T-shape, L-shape and cruciform shape, are much higher as compared to those of circular pile of same cross-sectional area in loose sand, medium dense sand as well as dense sand.
2. The uplift capacities of barrette piles of various shapes, viz., rectangle, T-shape, L-shape and cruciform shape, are much higher as compared to those of circular pile of the same cross-sectional area in loose sand, medium dense sand as well as dense sand.
3. The lateral capacity of barrette pile foundation of any cross-section area along major axis is higher for cruciform shape barrette pile as compared to other shapes of barrette pile foundation in loose sand, medium dense sand and dense sand.
4. The lateral capacity of barrette pile foundation of any cross-section area along minor axis is higher for L-shape barrette pile as compared to other shapes of barrette pile foundation in loose sand, medium dense sand and dense sand.
5. The uplift capacity of barrette pile foundation of any cross-section area is higher for cruciform shape barrette as compared to other shapes of barrette pile foundation.
6. Ultimate lateral and uplift capacities of barrette piles of all shape increases as the cross-section area of barrette pile increases in loose sand, medium dense sand as well as dense sand.

References

- Chu-EuHo, Lim C-H (1998) Barrettes designed as friction foundations: a case study. In Fourth International conference on Case histories in geotechnical engineering, St. Louis, Missouri university of science and technology, (March 9–12,1998),pp 236–241, <http://scholarsmine.mst.edu/icchge>
- Indian Standard Code of Practice for Design and Construction of Pile Foundation Part 4 Load Test on Piles (1985) Bureau of Indian Standards (September 1985), IS:2911 (Part4)
- Ng CWW, Rigby DB, Ng SWL, Lei GH (2000) Field Studies of well instrumented barrette in Hong Kong. *J Geotechn Geoenviron Eng ASCE*, 126:60–73, p 60
- Submanee Wong C, Teeparaksa W (2009) Performance of T-shape barrette pile against lateral force in Bangkok. *J Southeast Asian Geotechn Soc*, 247–255
- Waki AZ, Nazir AK (2013) Behaviour of laterally loaded small scale barrettes in sand. *Ain Shams Eng J Egypt*, 343–350, <https://doi.org/10.1016/j.asej.2012.10.011>
- Zhang LM, M ASCE (2003) Behavior of laterally loaded large-section barrettes. *J Geotechn Geoenviron Eng* 129(7), [https://doi.org/10.1061/10900241\(2003\)1297\(639\)](https://doi.org/10.1061/10900241(2003)1297(639))

Analyses of Footing Resting on Confined Layered Sandy Soil



Apoorva M. Kulkarni, S. W. Thakare, and A. I. Dhatrak

Abstract The confinement of soil is one type of technique used for improving bearing capacity of soil and reduces the settlement. This paper presents result of analyses carried out on the effect of soil confinement on the behaviour of circular footing resting on loose, medium dense, dense and layered sand bed subjected to vertical, eccentric, inclined and eccentric-inclined load. The parameter includes the confinement height, diameter and placement of confinement from base of footing, varying depth of layered sand bed. Analyses was carried out in PLAXIS 2D which is based on finite element method. From the analysis, load settlement curves were developed and ultimate bearing capacity was determined for various cases. The optimum values of diameter and height of circular confinement and its placement below the base of footing have been determined for different soil conditions.

Keywords Confinement · PLAXIS 2D · Ultimate Bearing capacity · Bearing Capacity Ratio

1 Introduction

All civil engineering structures, whether they are buildings, dams, bridges, retaining wall and so on, are built on soil. The foundation of the structure should be in such a way that there is no shear failure as well as no excessive settlement of the structure. The conventional method of design of foundation is based on the concept of bearing capacity. The bearing capacity depends upon the shear strength of soil as well as shape, size, depth and type of foundation. For the safe design, the bearing pressure on the ground has to be kept within the safe permissible limit.

A. M. Kulkarni (✉) · A. I. Dhatrak
Government College of Engineering Amravati, Amravati, Maharashtra, India
e-mail: apoorvamkulkarni27@gmail.com

S. W. Thakare · A. I. Dhatrak
Department of Civil Engineering, University of Sant Gadge Baba Amravati University, Amravati, Maharashtra, India

In recent years, tremendous increase in population, tourism, scarcity of plain land and decreasing availability of good construction sites have led to increased use of sites with marginal soil properties. As per today's situation, the requirement for treatment of foundation soil to improve the bearing capacity has risen markedly. The more recent advancement in this field is to provide confinement to the soil by improving bearing capacity of soil and reducing the settlement. This new technique of confinement of soil, though applied in some areas of geotechnical engineering, has not received much attention in foundation applications. Sometimes, the bearing pressure of the soil is low due to the lateral movement of loose granular soil, and such a tendency can be checked by soil confinement. Confinement is carried out by providing sheet piles, skirts, cellular cells; cellular box made up of concrete, steel, PVC material or sheets. Confinement of footing is used to increase the safe bearing capacity and to reduce the settlement. Confinement also reduces the lateral loading effect.

2 Literature Review

Azzam and Elwakil (2015) had conducted laboratory experiments to show the effect of soil confinement on the bearing capacity of circular footing on sandy soil and had found that the bearing capacity increased 17 times that of without confinement. Elsaied et al. (2015) had conducted an experimental study on the influence of cell confinement on the bearing capacity and settlement of circular footing on silty sand. Prasad and Singh (2011) investigated experimentally the behaviour of soil footing system due to installing hollow cylinder surrounding isolated circular footing model on granular soil. El and Nazer (2005) had conducted experimental study to investigate the effect of soil confinement on the bearing capacity and settlement of circular footing. Zidan (2015) had conducted experimental and numerical study to investigate the mechanical behaviour of circular footing resting on confined cells on a sand bed adjacent to an earth slope. Gupta and Trivedi (2009) had conducted laboratory study to provide a better understanding of the behaviour of square and rectangular footings resting on confined Ganga sand under eccentric–inclined load. The aim of the present study was to investigate the effect of soil confinement on the behaviour of circular footing resting on loose, medium dense, dense sand bed subjected to vertical load, by finite element method. The influence of various parameters such as height, diameter and the placement of confinement from the footing on the performance of footing was investigated.

3 Materials and Methods

3.1 Methodology

The behaviour of footing on confined sand having specified geometry is modelled and analyzed in PLAXIS-2D finite-element software. PLAXIS-2D software was used for analyzing the performance of circular footing on the confined sand bed subjected to centric, eccentric and inclined loading. Initially, the analysis was carried out for 1.0 m diameter circular footing subjected to vertical centric, eccentric, inclined and eccentric–inclined loading on the loose, medium dense, dense and layered sand beds, which served as the basis for comparison with the performance of footing on confined sand beds with similar conditions. The parameters related with confinement considered for analysis were diameter of confinement, height of confinement, depth of confinement from base of footing and varying depth of layered sand bed. These are shown in Fig. 1.

3.2 Materials

The material properties selected for the analysis are shown in Tables 2, 3 and 4.

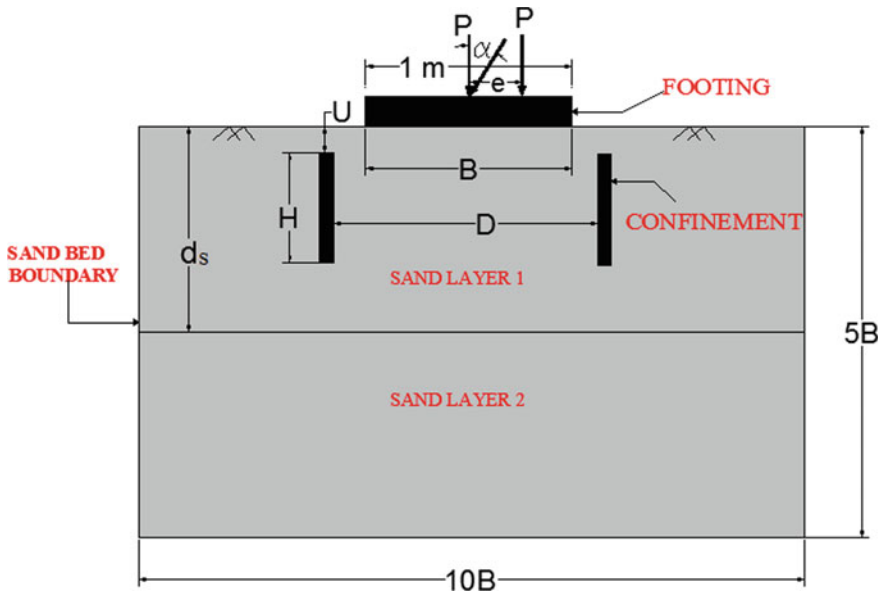


Fig. 1 Circular footing resting on sand bed with confinement with various parameters used for the analyses are shown in Table 1

Table 1 Details of parameter studied

S. no.	Parameter	Range selected
1	Confinement height ratio (H/B)	0, 0.5, 1.0, 1.5, 2.0, 5.0, 10.0
2	Confinement diameter ratio (D/B)	0.5, 1.0, 1.5, 2.0, 2.5
3	Confinement depth ratio (u/B)	0, 0.1, 0.25, 0.50, 0.75, 1.0
4	Load eccentricity ratio (e/B)	0.05, 0.1, 0.15, 0.2, 0.25
5	Inclination of load (α)	0°, 10°, 20°, 30°

Table 2 Properties of footing selected for analysis

Parameter	Name	Value	Unit
Type of behaviour	Material type	Elasto-plastic	–
Normal stiffness	EA	7.5×106	KN/m
Flexural rigidity	EI	56250	KNm ² /m
Equivalent thickness	D	0.3	M
Poisson's ratio	M	0.20	–

Table 3 Properties of confinement selected for analysis

Parameter	Name	Value	Unit
Type of behaviour	Material type	Elasto-plastic	–
Normal stiffness	EA	13.33×106	KN/m
Flexural rigidity	EI	1000	KNm ² /m
Equivalent Thickness	D	0.03	M
Poisson's ratio	M	0.20	–

Table 4 Properties assigned to soil bed for analysis

Properties	Symbols	Values for loose sand	Values for medium dense	Values for dense sand
Soil model		Mohr–Coulomb model	Coulomb model	Mohr–Coulomb model
Unit weight (kN/m ³)	Γ	17	18	18
friction angle	ϕ	30°	34°	38°
Dilatancy angle	Ψ	0°	5°	8°
Poisson's ratio	M	0.3	0.3	0.3
Young's modulus	E	13×103 kPa	30×103 kPa	50×103 kPa

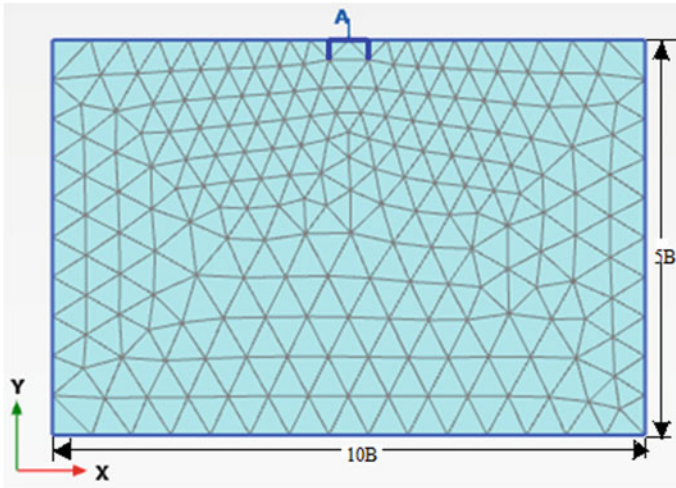


Fig. 2 Numerical model developed in PLAXIS-2D

3.3 Numerical Model and Analysis

Numerical model of the footing-soil bed system was developed in PLAXIS-2D as shown in Fig. 2. The dimensions of the soil model were: depth = $5B$ and width = $10B$.

From the analysis carried out, load–settlement curve for each case was generated and ultimate bearing capacity was determined as per provisions of IS: 1888-1982. The effect of selected parameters on ultimate bearing capacity was studied. The ultimate bearing capacity improvement due to the soil confinement was represented using a non-dimensional factor, called the bearing capacity ratio (BCR), which is the ratio of UBC of footing on confined sand bed to that on unconfined sand bed.

4 Results of Analyses

4.1 Performance of Circular Footing Without Confinement

The ultimate bearing capacities for circular footing resting on loose, medium dense, dense and layered sand bed without confinement are shown in Tables 5 and 6.

Table 5 UBCs of circular footing for various sand beds without confinement

S. no.	Sand bed	UBC (kN/m ²)
1	Loose sand	58
2	Medium dense sand	90
3	Dense sand	160

Table 6 UBCs of circular footing for various *ds/B* ratios without confinement

S. no.	ds/B	UBC (kN/m ²)
1	1	135
2	2	98
3	3	98
4	4	90
5	5	70
6	6	70
7	7	70

4.2 Performance of Circular Footing Subjected to Vertical Centric Load Resting on Loose, Medium Dense, Dense Sand Bed with Confinement

Ultimate bearing capacities for circular footing resting on loose, medium dense and dense sand bed for various (H/B) and (D/B) ratios with confinement are shown in Tables 7 and 8.

Table 7 UBCs for various (H/B) and (D/B) ratios for loose sand bed

S. no.	H/B ratio	UBC (kN/m ²)				
		D/B ratio				
		0.5	1.0	1.5	2.0	2.5
1	0.5	80	148	182	155	105
2	1.0	98	210	430	320	240
3	1.5	190	210	442	280	250
4	2	200	322	520	458	350
5	5	240	450	678	520	370
6	10	240	450	678	520	370

Table 8 UBCs for various (H/B) and (D/B) ratios for medium dense sand bed

S. no.	H/B ratio	UBC (kN/m^2)				
		D/B ratio				
		0.5	1.0	1.5	2.0	2.5
1	0.5	198	282	490	280	170
2	1.0	250	290	570	380	350
3	1.5	390	480	550	430	410
4	2	398	480	705	558	460
5	5	400	1000	1494	840	540
6	10	400	1000	1494	840	540

4.3 Performance of Circular Footing Subjected to Vertical Centric Load Resting on Layered Sand Bed with Confinement

The ultimate bearing capacities for circular footing on layered sand bed consisting of loose sand layer over dense sand layer with confinement for various (H/B) ratios and (D/B) ratios are shown in Figs. 3, 4 and 5 (Table 9).

4.4 Performance of Circular Footing Subjected to Eccentric Load Resting on Loose, Medium Dense, Dense and Layered Sand Bed with Confinement

The values of ultimate bearing capacities of circular footing on sand bed with confinement obtained from these load–settlement curves for various values of (e/B) ratios are shown in Tables 10 and 11.

Fig. 3 Variation of UBC for circular footing on layered sand bed with (D/B) ratio 1.0 and various (H/B) ratios of confinement

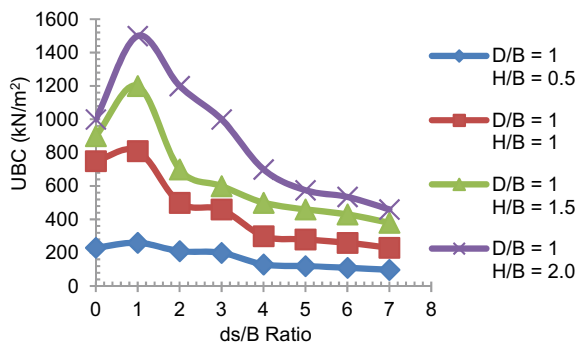


Fig. 4 Variation of UBC for circular footing on layered sand bed with (*D/B*) ratio 1.5 and various (*H/B*) ratios of confinement

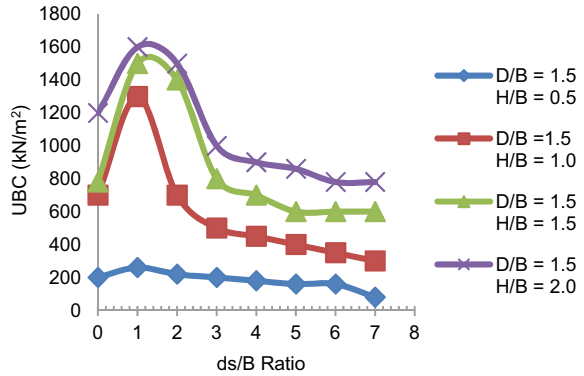


Fig. 5 Variation of UBC for circular footing on layered sand bed with (*D/B*) ratio 2.0 and various (*H/B*) ratios of confinement

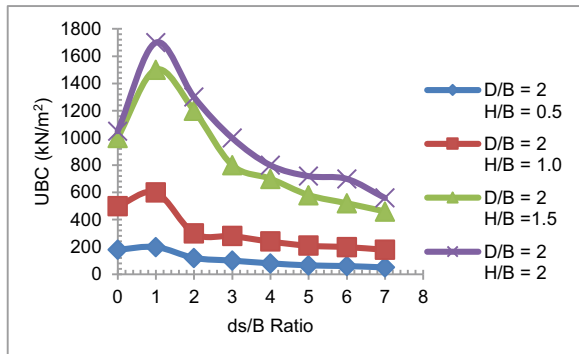


Table 9 UBCs for various (*H/B*) and (*D/B*) ratios for dense sand bed

S. no.	H/B ratio	UBC (kN/m ²)				
		D/B ratio				
		0.5	1.0	1.5	2.0	2.5
1	0.5	310	430	500	400	320
2	1.0	480	510	750	500	460
3	1.5	600	650	780	630	580
4	2	740	780	870	760	710
5	5	800	920	1500	830	815
6	10	800	920	1500	830	815

Table 10 UBCs for various (e/B) ratios for loose, medium dense and dense sand bed

e/B ratio	UBC (kN/m ²)		
	Loose sand bed	Medium dense sand bed	Dense sand bed
0	1200	1800	2000
0.05	1000	1500	1800
0.1	900	1400	1600
0.15	800	1200	1500
0.2	500	800	1200
0.25	500	800	1200

Table 11 UBCs for various (e/B) ratio for layered sand bed

e/B Ratio	UBC (kN/m ²)						
	(ds/B) ratio						
	1	2	3	4	5	6	7
0	1800	1700	1700	1500	1400	1300	1300
0.05	1700	1650	1600	1400	1300	1200	1200
0.1	1500	1500	1400	1300	1200	1200	1200
0.15	1400	1400	1300	1200	1000	1000	1000
0.2	1000	1000	900	800	800	700	600
0.25	1000	900	900	800	800	600	500

4.5 Performance of Circular Footing Subjected to Inclined Load Resting on Loose, Medium Dense, Dense and Layered Sand Bed with Confinement

The values of ultimate bearing capacities of circular footing on sand bed with confinement obtained from these load–settlement curves for various values of α are shown in Tables 12 and 13.

Table 12 UBCs for various α ratios for loose, medium dense and dense sand bed

A	UBC (kN/m ²)		
	Loose sand bed	Medium dense sand bed	Dense sand bed
0	1000	1800	2000
10	900	1700	1800
20	800	1600	1700
30	750	1500	1500

Table 13 UBCs for various α for layered sand bed

α	UBC (kN/m ²)						
	(ds/B) ratio						
	1	2	3	4	5	6	7
0	2000	1800	1700	1500	2000	1800	1700
10	1800	1700	1600	1400	1800	1700	1600
20	1700	1600	1500	1300	1700	1600	1500
30	1700	1600	1400	1200	1700	1600	1400

4.6 Performance of Circular Footing Subjected to Eccentric–Inclined Load Resting on Loose, Medium Dense and Dense Sand Bed with Confinement

The results obtained from the analyses in case of circular footing on loose, medium dense and dense sand bed with optimum size of confinement, that is, $(D/B = 1.5)$ and $(H/B = 2)$ subjected to eccentric–inclined loading are presented in Figs. 6, 7 and 8, which show the variations of ultimate bearing capacities of circular footing with respect to inclination ratio (α).

5 Discussion

The results obtained from the analyses carried out on circular footing are presented in the form of variation of BCR with respect to the selected parameter.

Fig. 6 Variation of UBC for circular footing on loose sand bed with confinement with respect to α for various eccentricity ratios (e/B)

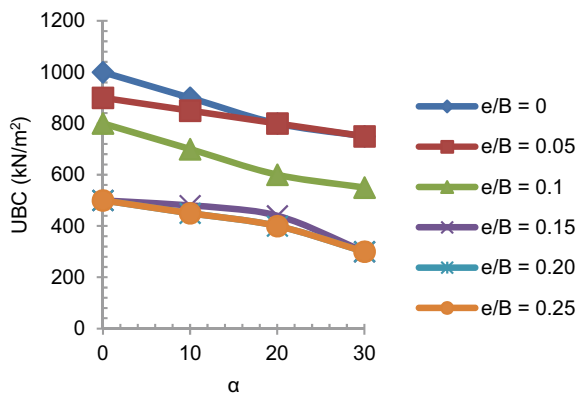


Fig. 7 Variation of UBC for circular footing on medium sand bed with dense sand bed with confinement with respect to α for various eccentricity ratios (e/B)

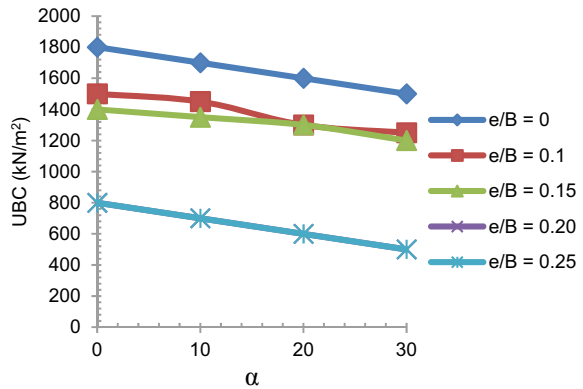
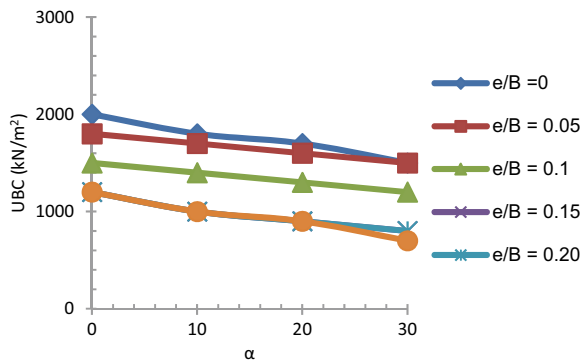


Fig. 8 Variation of UBC for circular footing on dense sand bed with confinement with respect to α for various eccentricity ratios (e/B)



5.1 Effect of Diameter of Confinement

The variation in BCR with respect to D/B ratio of confinement for layered sand beds is shown in Fig. 9.

From Fig. 9, it is observed that BCR initially increases with increase in D/B ratio up to 1.5 and thereafter BCR decreases with further increase in D/B ratio of confinement. Hence optimum D/B ratio of confinement may be taken as 1.5, that is, the diameter of confinement should be 1.5 times the diameter of footing. Hence, optimum D/B ratio of confinement may be taken as 1.5.

5.2 Effect of Height of Confinement

Variation in BCR with respect to H/B ratio of confinement, in case of circular footing on layered and bed with confinement, subjected to vertical loading, is shown in Fig. 10.

Fig. 9 Variation of BCR with respect to confinement diameter ratio (D/B) for optimum confinement height ($H/B = 2$) ratio for circular footing on layered sand bed

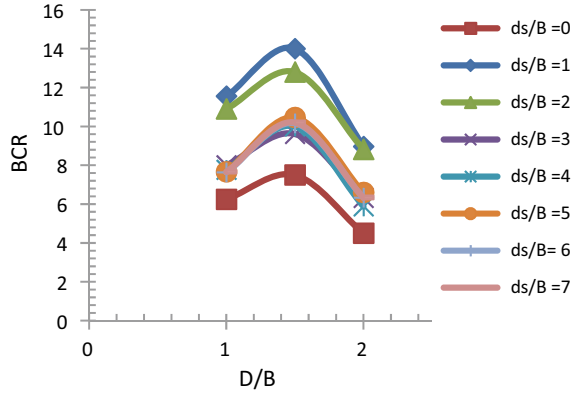
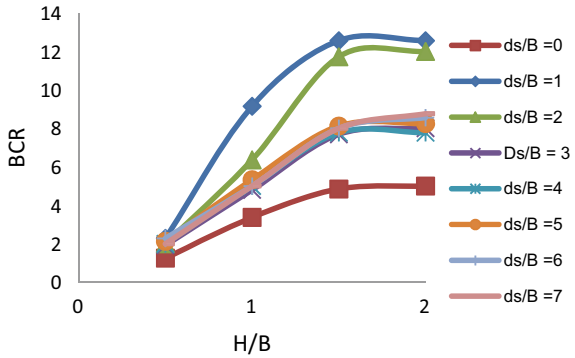


Fig. 10 Variation of BCR with respect to confinement height ratio (H/B) for optimum confinement diameter ($D/B = 1.5$) ratio for circular footing on layered sand bed



From Fig. 10, it is observed that the increase in BCR is more significant up to H/B ratio 2.0. The optimum H/B ratio of confinement may, therefore, be adopted as 2.0, that is, the height of confinement should be twice the diameter of footing.

5.3 Effect of Placement of Confinement

The variation in bearing capacity ratio of circular footing on layered sand bed with confinement with respect to placement of confinement ratio (U/B) is as shown in Fig. 11.

From Fig. 11, it is observed that BCR is maximum at (U/B) ratio = 0. Thereafter BCR decreases with increase in U/B ratio up to $U/B = 0.125$. With further increase in U/B ratio up to 0.75, there is no significant change in BCR. With further increase in U/B ratio, that is, $U/B > 0.75$, BCR reduces significantly. Thus, placement of confinement at the base of footing gives maximum benefit. However, the confinement may be placed up to depth of $0.125B$ from the base of footing.

Fig. 11 Variation of BCR of circular footing on layered sand bed with confinement for optimum diameter ratio 1.5 with respect to (U/B) ratio

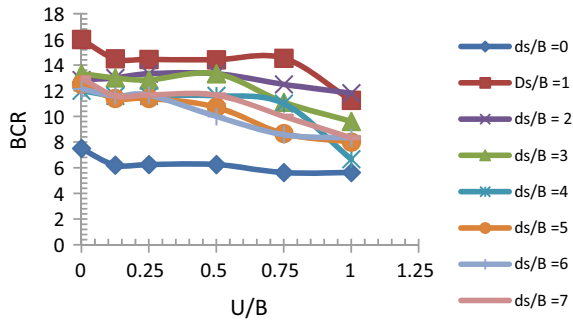
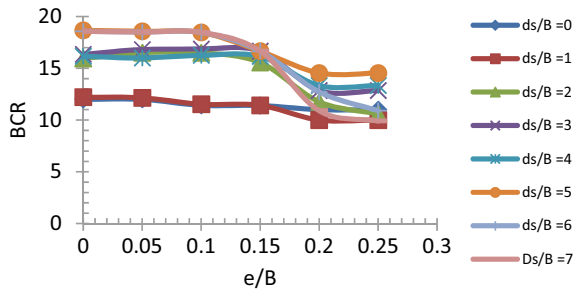


Fig. 12 Variation of BCR with eccentricity ratios (e/B) for layered sand bed with confinement of optimum size



5.4 Effect of Eccentricity of Loading

In case of circular footing placed on layered sand bed with optimum size of confinement, that is, ($D/B = 1.5$) and ($H/B = 2$), subjected to vertical eccentric loading, the results are shown in Fig. 12.

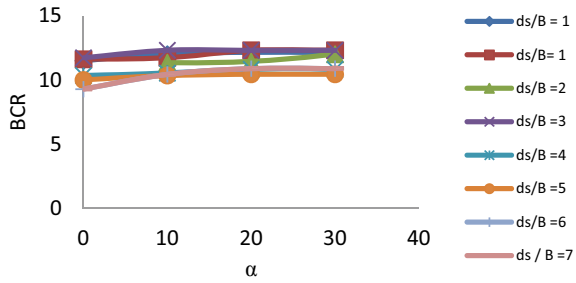
From Fig. 12, it is observed that BCR remains constant for eccentricity ratio up to 0.1. Thereafter, BCR decreases with further increase in the (e/B) ratio up to 0.2. With further increase in the (e/B) ratio, there is no significant decrease in BCR.

5.5 Effect of Inclination of Loading

In case of circular footing placed on layered sand bed with optimum size of confinement, that is, ($D/B = 1.5$) and ($H/B = 2$), subjected to inclined loading, the results are shown in Fig. 13.

From Fig. 13, it is observed that BCR increases with increase in α up to 10° , and for further increase in α , there is no significant effect on BCR, in case of circular footing resting on layered sand bed with confinement.

Fig. 13 Variation of BCR with inclined angle α for layered sand bed with confinement of optimum size



5.6 Effect of Combined Eccentricity and Inclination

In case of circular footing placed on layered sand bed with optimum size of confinement, that is, $(D/B = 1.5)$ and $(H/B = 2)$, subjected to eccentric inclined loading, the results are shown in Figs. 14, 15, 16, 17, 18, 19, 20 and 21.

From the above-mentioned graphs, it is observed that BCR increases with increase in α up to 20° , and for further increase in α BCR remains constant for layered sandy soil.

Fig. 14 Variation of BCR with inclination angle α for layered sand bed ($ds/B = 0$) with confinement of optimum size

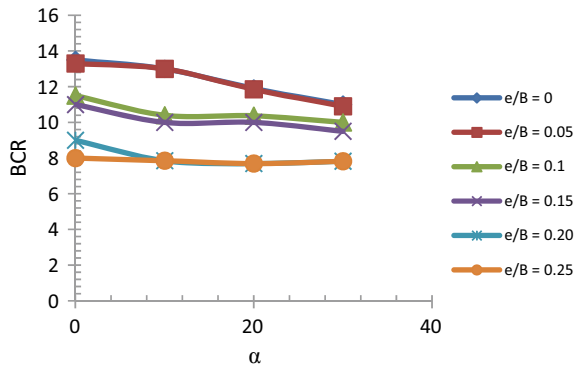


Fig. 15 Variation of BCR with inclination angle α for layered sand bed ($ds/B = 1$) with confinement of optimum size

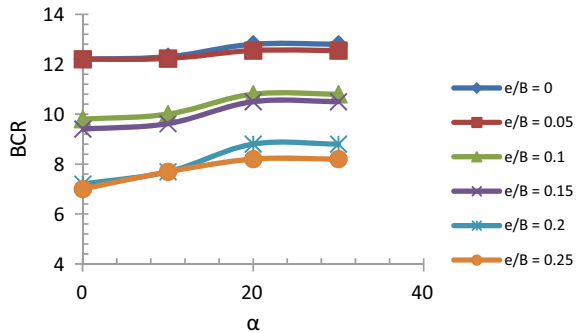


Fig. 16 Variation of BCR with inclination angle α for layered sand bed ($ds/B = 2$) with confinement of optimum size

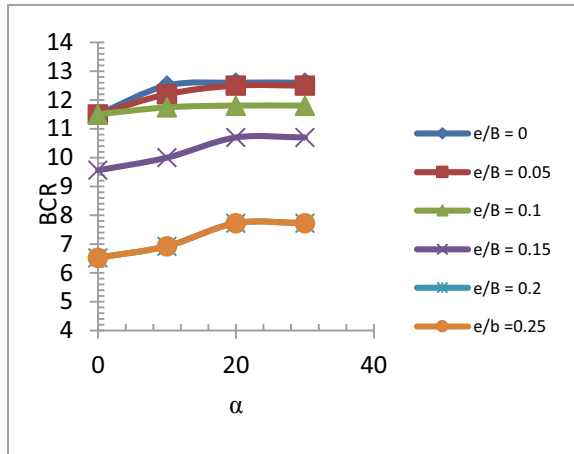


Fig. 17 Variation of BCR with inclination angle α for layered sand bed ($ds/B = 3$) with confinement of optimum size

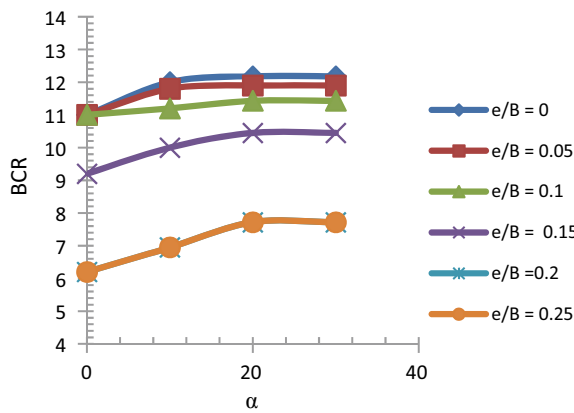


Fig. 18 Variation of BCR with inclination angle α for layered sand bed ($ds/B = 4$) with confinement of optimum size

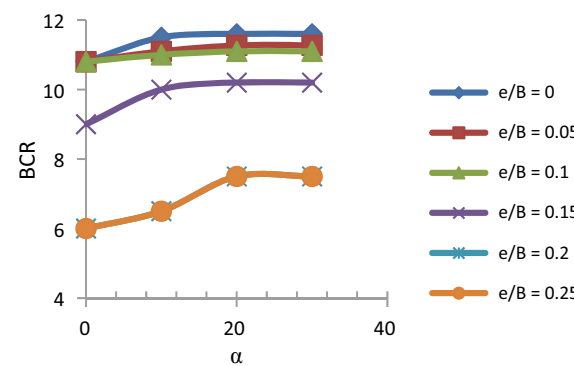


Fig. 19 Variation of BCR with inclination angle α for layered sand bed ($ds/B = 5$) with confinement of optimum size

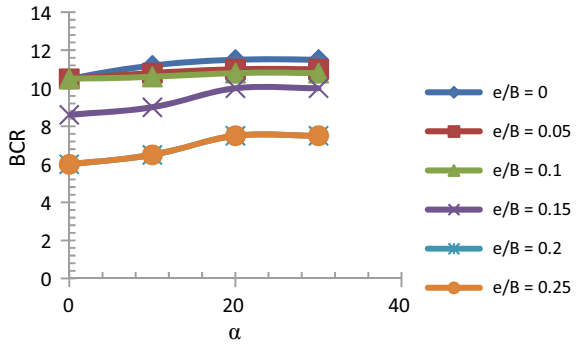


Fig. 20 Variation of BCR with inclination angle α for layered sand bed ($ds/B = 6$) with confinement of optimum size

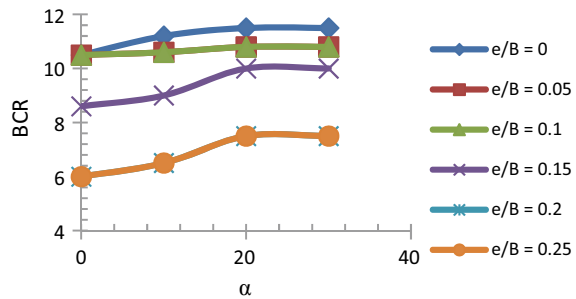
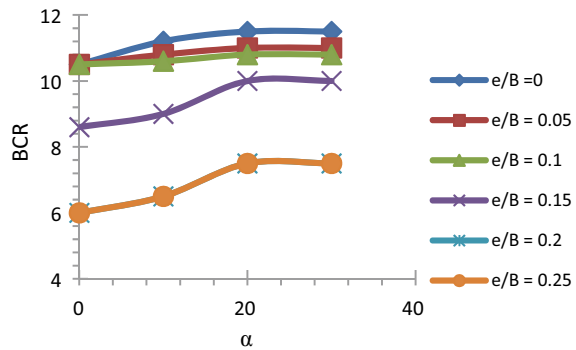


Fig. 21 Variation of BCR with inclination angle α for layered sand bed ($ds/B = 7$) with confinement of optimum size



6 Conclusions

The dissertation work was carried out to study the performance of circular footing of 1 m diameter resting in loose, medium dense, dense and layered sand bed with and without confinement subjected to vertical centric loads, vertical eccentric loads and inclined eccentric loads, using PLAXIS-2D, by considering the effect of diameter,

height and placement of confinement. Thickness of the top layer in case of layered sand bed was also varied.

Based on the results of present study, the following broad conclusions are drawn from the report:

1. Soil confinement has a significant effect on improving the performance of circular footing on granular soil.
2. Confinement provides substantial benefit in case of loose and medium dense sand bed and comparatively less in case of dense sand bed.
3. The optimum D/B ratio of confinement may be taken as 1.5 times the width of circular footing for all relative densities of sand.
4. The optimum H/B ratio of confinement may be adopted as 2.0, that is, the height of confinement should be twice the diameter of circular footing for all relative densities of sand.
5. Placement of confinement at the base of circular footing ($U/B = 0$) gives maximum benefit. However, the confinement may be placed up to depth of $0.125B$ from the base of circular footing for all relative densities of sand.
6. A circular footing placed on multilayered sand bed with confinement gives better results when the depth of top layer of sand bed is equal to the width of footing.
7. For circular footing resting on loose, medium dense and dense sand bed with confinement, the BCR decreases as (e/B) ratio increases. Decrease in BCR is not significant in case of loose sand bed.
8. In case of multilayered sand bed the BCR remains constant for eccentricity ratio up to 0.1. Thereafter BCR decreases with further increase in the (e/B) ratio up to 0.2. With further increase in the (e/B) ratio, there is no significant decrease in BCR.
9. For circular footing resting on sand bed with confinement, the BCR decreases slightly as angle of inclination increases. In case of multilayered sand bed, BCR increases with increase in α up to 10° . Further increase in α , there has no significant effect on BCR.
10. In case of combined eccentricity and inclination, circular footing resting on sand bed with confinement, BCR remains unchanged up to angle of inclination $\alpha = 20^\circ$ for all (e/B) ratios.
11. In case of combined eccentricity and inclination, circular footing resting on multilayered sand bed with confinement BCR increases with increase in α up to 20° . With further increase in α BCR remains constant for all (e/B) ratios.
12. Effect of combined eccentricity and inclination loading is significant up to $(ds/B) = 4$; after $(ds/B) > 4$, there is no change in BCR in case of layered sandy soil.

References

- Azzam WR, Elwakil AZ (2015) Experimental and numerical studies of circular footing resting on confined granular subgrade adjacent to slope. *Int J Geomech* (2015). [https://doi.org/10.1061/\(ASCE\)GM.1943-5622.0000500](https://doi.org/10.1061/(ASCE)GM.1943-5622.0000500)
- Elsaied A, Saleh NM, Elmashad ME (2015) Behavior of circular footing resting on laterally confined granular reinforced soil, 1687–4048 2015 Production and hosting by Elsevier BV on behalf of Housing and Building National Research Center (2015). <https://doi.org/10.1016/j.hbrcj.2014.03.011>
- Gupta R, Trivedi A (2009) Bearing capacity and settlement of footing resting on confined loose silty sands. *J Geotechn Eng* 14 bund A. <https://www.researchgate.net/publication/232723376>
- Prasad A, Singh V (2011) Behavior of confined square and rectangular footings under eccentric-inclined load. *Int J Geotech Eng* 5(2):211–221. <https://doi.org/10.3328/IJGE.2011.05.02.211-221>
- Sawwaf MEI, Nazer A (2005) Behavior of circular footings resting on confined granular soil. *J Geotechn Geoenviron Eng*. 131(3) [https://doi.org/10.1061/\(ASCE\)1090-0241\(2005\)131:3\(359\)](https://doi.org/10.1061/(ASCE)1090-0241(2005)131:3(359))
- Zidan AF (2015) Bearing capacity and settlement of Circular footing resting on confined sand. <https://doi.org/10.15224/978-1-63248-062-0-57> *Advances in Civil, Structural and Mechanical Engineering-CSM* (2015) Copyright © Institute of Research Engineers and Doctors, USA

Analyses of Shell Footing in Layered Sandy Soil



A. I. Dhatrak, P. S. Yaldarkar, and S. W. Thakare

Abstract Shell footing is economic alternative to long-established plain shallow foundations especially where heavy superstructural loads are to be transmitted to weaker soil. There are many shapes of shell footing such as circular, triangular (inverted and upright), conical, and cylindrical. In this paper, results of shell footing are presented. Models of upright and inverted triangular shell footings were developed in PLAXIS-2D software, which is a finite element-based software. Base to rise ratio (B/d or B/h) of the footing was varied. The results of the analysis were plotted as load settlement curves and ultimate bearing capacity were determined in each case. These were then compared with UBC of flat strip footing with similar conditions. The results indicated that shell footings have higher UBC than that of flat strip footing. The analyses were carried out on loose sand, dense sand, layered sand, reinforced sand bed.

Keywords Shell footing · Numerical study · PLAXIS · Ultimate bearing capacity · Reinforced sand

1 Introduction

Shell footing concept is not new in geotechnical engineering. The use of inverted brick arches as foundation has been used in different fieldwork in many parts of the world for long time. Shells are thin-wall structures which are required to reduce quantities of concrete material in their construction. A shell foundation is perhaps the antiderivative of the plain form, and it is typically made up of reinforced concrete material. Shell foundations depend on their geometrical shape and streamlined continuity to generate strength and perform efficiently in soil. There are many shapes of shell footing such as circular, triangular (inverted and upright), conical, and cylindrical. In this paper, results of analyses of shell footings are presented. Models of

A. I. Dhatrak · P. S. Yaldarkar (✉) · S. W. Thakare
Government College of Engineering, Amravati, Maharashtra, India
e-mail: panuy20@gmail.com

© Springer Nature Singapore Pte Ltd. 2020
M. Latha Gali and P. Raghuvver Rao (eds.), *Construction in Geotechnical Engineering*, Lecture Notes in Civil Engineering 84,
https://doi.org/10.1007/978-981-15-6090-3_17

255

upright and inverted triangular shell footings were developed in PLAXIS-2D software, which is a finite element-based software. The b/d ratios of the footings were varied. The results of the analysis were plotted as load settlement curves and ultimate bearing capacity were determined in each case. These were then compared with UBC of flat strip footing with similar conditions.

1.1 Literature Review

Hanna and El-Rahman (1990) presented the results of experimental work on ultimate bearing capacity of triangular shell strip footing on sand. Huat and Mohammed (2006) analyzed numerical and field study on triangular shell footing for low-rise building. Numerical analysis was done by finite element program (LUSAS) in both 2D and 3D. Rinaldi (2012) analyzed inverted shell foundation performance in soil by using PLAXIS software (FEM analysis). Loading on the footing-soil system was applied at 2 kPa load increments till shear strength failure of soil media.

2 Methodology

PLAXIS-2D software, which works on the finite element method approach, was used for analyzing the performance of shell footing when subjected to vertical centric loading. Initially, the analysis was carried out for 2.0 m wide strip footing subjected to vertical centric loading on the loose, dense sand beds, layered sand, and reinforced sand bed which served as the basis for comparison with the performance of shell footing with similar conditions. Figures 1 and 2 show the typical upright, inverted triangular shell footing model. Table 1 shows parameters for analysis when shell footing on sand bed.

2.1 Shell Footing on Sand Bed

2.2 Material Properties

The material properties selected for the analysis are shown in Tables 2 and 3.

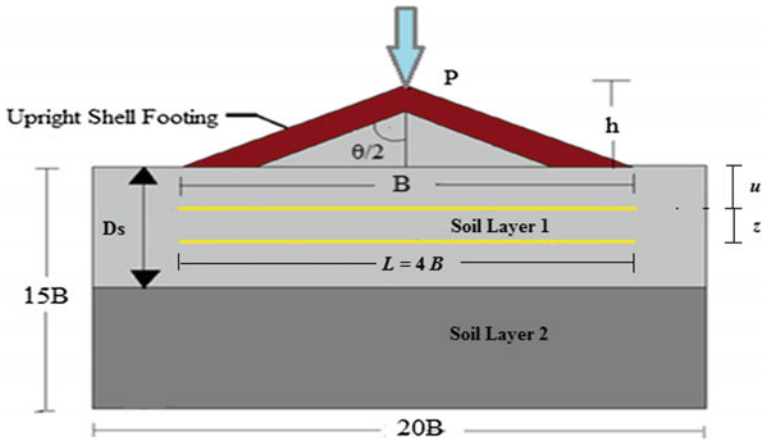


Fig. 1 Upright shell footing model

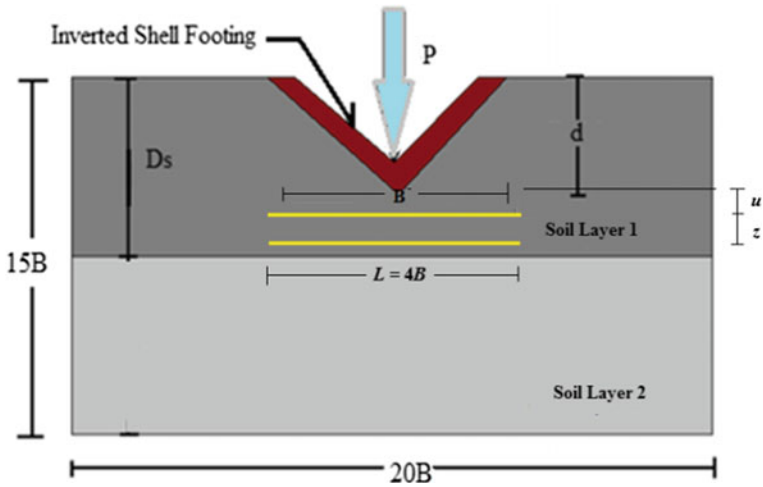


Fig. 2 Inverted shell footing model

3 Results of Analyses

The results obtained from the analyses carried out on shell footing and flat footing on loose sand, dense sand, layered sand, and reinforced sand bed are presented in this section.

Table 1 Parameters for analysis when sell footing on sand bed

Parameter	Range of parameter
Thickness of topsoil layer to width of footing ratio (D_s/B)	0, 1, 2, 3, 4, 5
Shell angle ($^\circ$)	180, 100, 90, 60, 50, 30
Types of shell footing	Flat, upright triangular, and inverted triangular shell footing
Base to rise ratio of Shell Footing (B/h or B/d)	3.73, 2.13, 1.73, 1, 0.83
Number of reinforcement layers (N)	1, 2, 3

Table 2 Properties of sand selected for analysis

Properties	Symbols	Values	Values
Soil model	–	Mohr–Coulomb model	Mohr–Coulomb model
Soil type	–	Loose sand	Dense sand
Unit weight	γ	14 kN/m ³	18 kN/m ³
Friction angle	ϕ	32 $^\circ$	41 $^\circ$
Dilatancy angle	Ψ	2 $^\circ$	11
Poisson’s ratio	M	0.3	0.3
Young’s Modulus	E	30 \times 10 ³ kPa	80 \times 10 ³ kPa

Table 3 Properties of footing selected for analysis

Parameter	Name	Value	Unit
Behavior type	Material type	Elastoplastic	–
Normal stiffness	EA	151,200	kN/m
Flexural rigidity	EI	20.1	kNm ² /m
Thickness	D	0.0399	M
Poisson’s ratio	γ	0.30	–

3.1 Performance of Shell Footing and Flat Footing on Loose Sand Bed

The load settlement curves obtained from the analyses for upright and inverted triangular shell footing for loose sand bed and for various B/d or B/h (base to rise ratio) ratios are presented in Fig. 3 and Fig. 4, respectively.

Fig. 3 Load settlement curves for upright shell footing on loose sand bed

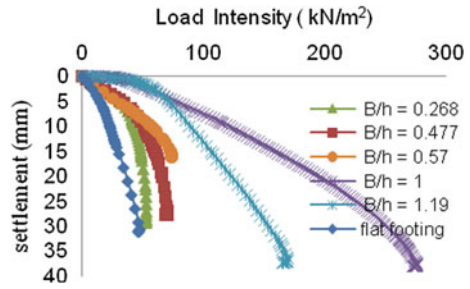
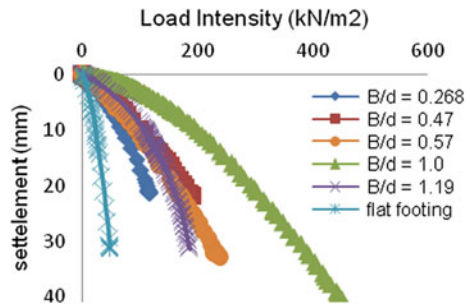


Fig. 4 Load settlement curves for inverted shell footing on loose sand bed



3.2 Performance of Shell Footing and Flat Footing on Dense Sand Bed

The results obtained from the analyses carried out on upright and inverted shell footing on dense sand bed, by varying b/d ratio are presented in Fig. 5 and Fig. 6, respectively.

Fig. 5 Load settlement curves for upright shell footing on dense sand bed

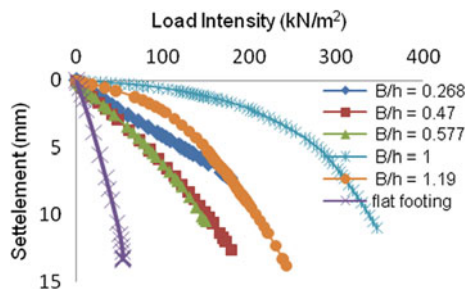
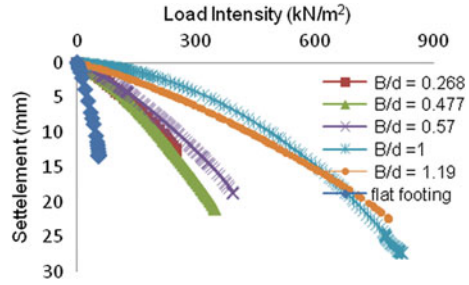


Fig. 6 Load settlement curves for inverted shell footing on dense sand bed



3.3 Performance of Shell Footing on Layered Sand Bed

Analysis was carried out for shell footing subjected to vertical centric loading, on the layered sand bed consisting of loose sand layer over dense sand layer. The parameter considered for analyses was thickness of the top layer of layered sand bed.

The ultimate bearing capacities of the shell footing on layered sand bed with loose sand layer over dense sand layer for vertical centric loading, for upright shell footing were determined by varying shell angles. The load settlement curves are shown in Figs. 7, 8, 9, and 10.

The Load settlement curves for inverted shell footing with varying shell angle under vertical centric loading on a layered sand bed are shown in Figs. 11, 12, 13, and 14. The corresponding values of UBCs determined from the curves are tabulated in Table 4.

Fig. 7 Load settlement curves for upright shell footing with shell angle 30° for different (D_s/B) ratios of layered sand bed

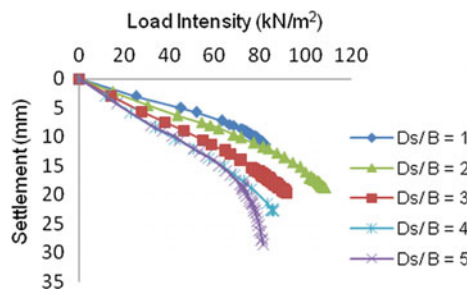


Fig. 8 Load settlement curves for upright shell footing with shell angle 50° for different (D_s/B) ratios of layered sand bed

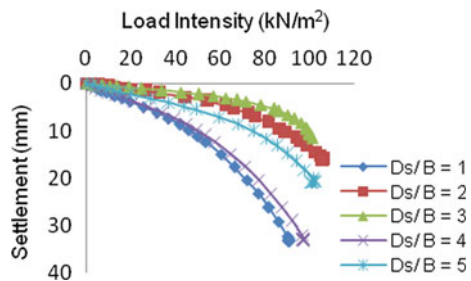


Fig. 9 Load settlement curves for upright shell footing with shell angle 60° for different (D_s/B) ratios of layered sand bed

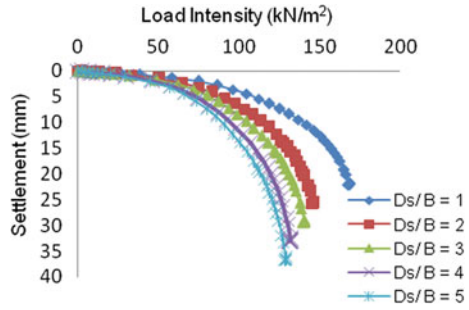


Fig. 10 Load settlement curves for upright shell footing with shell angle 90° for different (D_s/B) ratios of layered sand bed

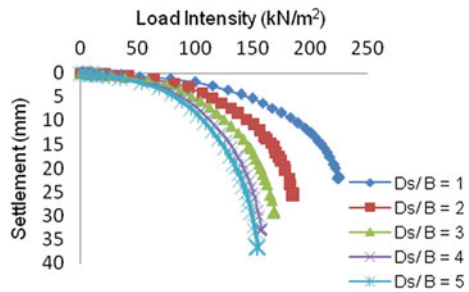


Fig. 11 Load settlement curves for inverted shell footing with shell angle 30° for different (D_s/B) ratios of layered sand bed

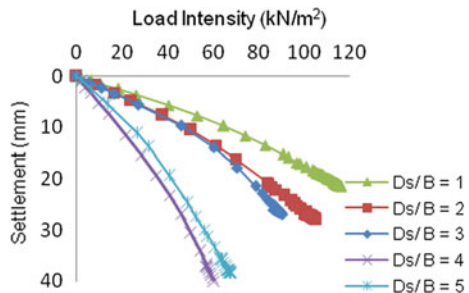


Fig. 12 Load settlement curves for inverted shell footing with shell angle 50° for different (D_s/B) ratios of layered sand bed

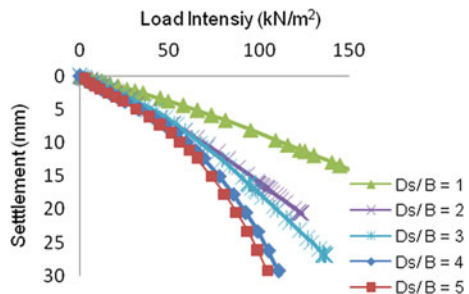


Fig. 13 Load settlement curves for inverted shell footing with shell angle 60° for different (D_s/B) ratios of layered sand bed

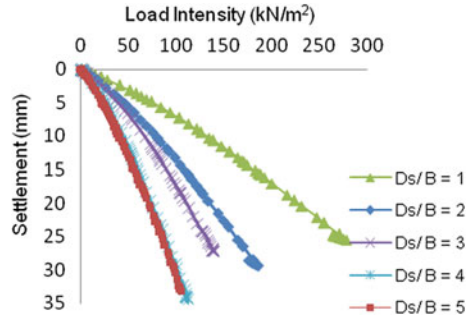


Fig. 14 Load settlement curve for inverted shell footing with shell angle 90° for different (D_s/B) ratios of layered sand bed

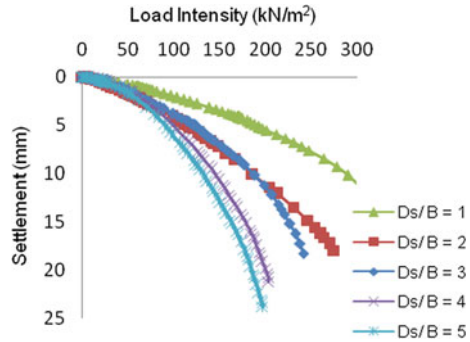


Table 4 UBCs of shell footing (upright and inverted) with respect to (D_s/B) ratio for vertical centric loading for layered sand bed

Type of footing	Shell angle (°)	UBC (kN/m ²)					
		D_s/B					
		0	1	2	3	4	5
Flat footing	–	40	35	33	30	28	28
Upright shell footing	30	80	70	65	63	52	52
	50	100	88	70	68	65	65
	60	140	125	99	79	75	75
	90	250	158	115	104	95	94
Inverted shell footing	30	110	85	60	55	40	39
	50	140	95	75	70	68	65
	60	210	140	115	85	82	79
	90	410	200	180	160	130	130

3.4 Performance of Shell Footing on Reinforced Sand Bed

Analysis was carried out for shell footing subjected to vertical centric loading reinforced sand bed with geogrid as reinforcement, that was placed at fixed depth $u = 0.25 B$ below the foundation base and length equal to $4 B$. The parameters considered for analysis were shell angle of the footing and numbers of layers of reinforcement. The load settlement curves for shell footing (inverted) with and without reinforcement shown in Figs. 15, 16, 17, 18, and 19. The corresponding values of UBCs determined from the curves are tabulated in Table 5.

The load settlement curves for shell footing (upright) with and without reinforcement are shown in Figs. 20, 21, 22, 23, and 24.

4 Discussion of Results

From the above study, the results of computational analysis are interpreted in terms of bearing capacity ratio (BCR), which is defined as the ratio of ultimate bearing capacity of shell footing to the ultimate bearing capacity of flat strip footing for similar conditions of loading and soil bed.

Fig. 15 Load settlement curves for inverted shell footing on reinforced sand bed (Shell angle 30°)

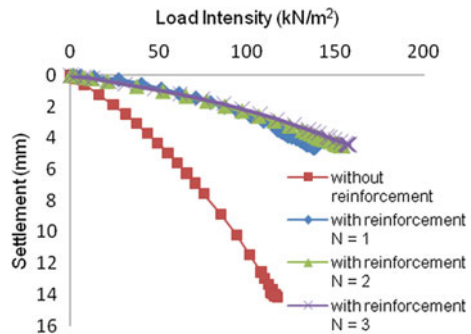


Fig. 16 Load settlement curves for inverted shell footing on reinforced sand bed (Shell angle 50°)

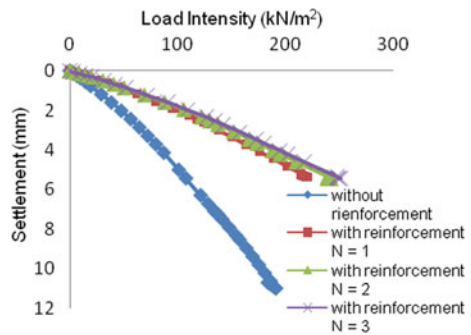


Fig. 17 Load settlement curves for inverted shell footing on reinforced sand bed (Shell angle = 60°)

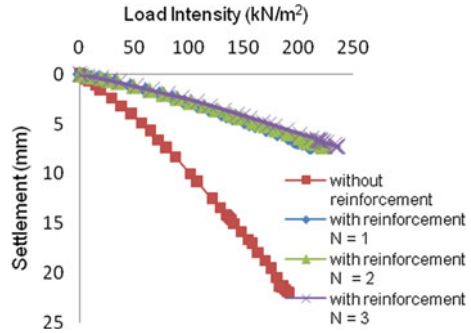


Fig. 18 Load settlement curves for inverted shell footing on reinforced sand bed (Shell angle = 90°)

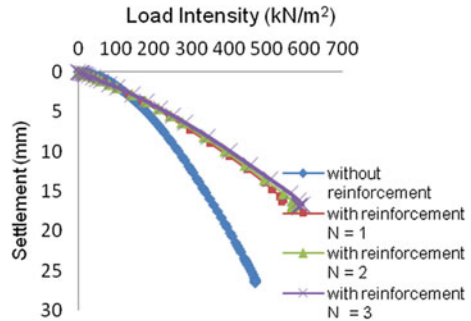
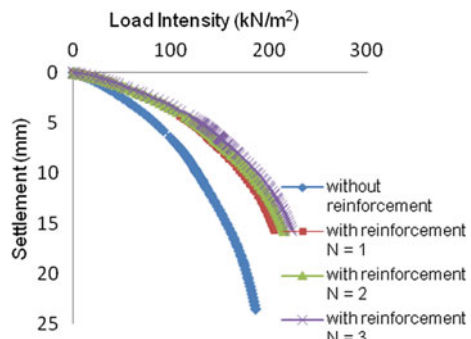


Fig. 19 Load settlement curves for inverted shell footing on reinforced sand bed (Shell angle = 100°)



$$(BCR) = \frac{\text{Ultimate Bearing Capacity of Shell Footing}}{\text{Ultimate Bearing Capacity of Strip Footing}}$$

The values of bearing capacity ratio are determined for each case in the computational analysis. These values of BCR are then plotted with respect to selected parameters, and its variation gives an idea about the performance of shell footing for the selected parameters. The results obtained from the computational analysis are suitably discussed in terms of bearing capacity ratio in the following section.

Table 5 UBCs for upright and inverted shell footing on reinforced sand bed

Type of shell footing	Shell angle (°)	UBC (kN/m ²)			
		Number of reinforcement layers			
		Without reinforcement	N = 1	N = 2	N = 3
Upright shell footing	30	34	42	46	46
	50	40	55	60	61
	60	58	100	120	122
	90	140	170	180	180
	100	85	130	150	150
Inverted shell footing	30	55	82	98	98
	50	80	118	140	142
	60	100	134	190	200
	90	200	300	360	362
	100	125	170	230	230

Fig. 20 Load settlement curves for upright shell footing on reinforced sand bed (Shell angle = 30°)

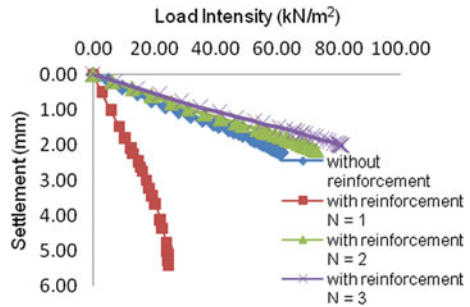


Fig. 21 Load settlement curves for upright shell footing on reinforced sand bed (Shell angle = 50°)

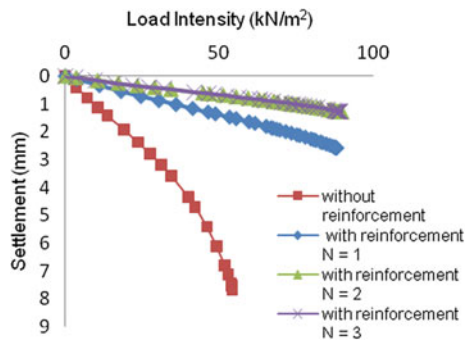


Fig. 22 Load settlement curves for upright shell footing on reinforced sand bed (Shell angle = 60°)

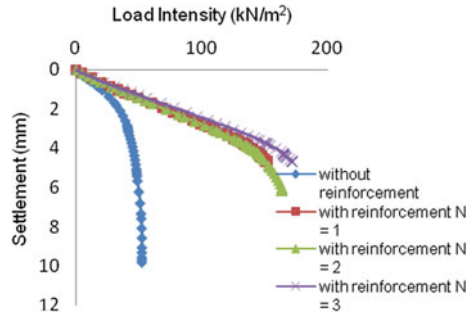


Fig. 23 Load settlement curves for upright shell footing on reinforced sand bed (Shell angle = 90°)

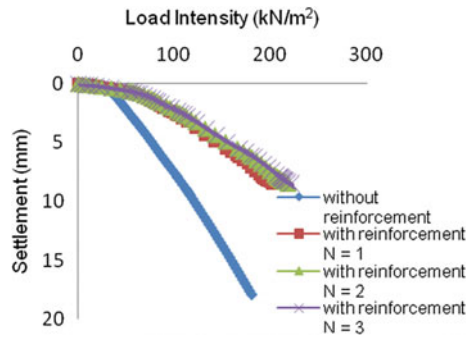
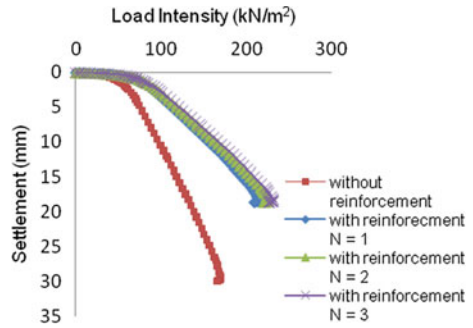


Fig. 24 Load settlement curves for upright shell footing on reinforced sand bed (Shell angle = 100°)



4.1 Effect of Shell Angle of Shell Footing

The percentage increase in UBC of shell footing corresponding to shell angle was evaluated as per the formula given in Sect. 1.

$$\% \text{ Increase in UBC} = q \times 100 \tag{1}$$

where

q_b = UBC of shell footing with varying shell angle in kPa.

q_c = UBC of strip footing in kPa.

Figures 25, 26, 27, and 28 show the variation of percentage increase in UBC for shell footing with different shell angles in loose and dense sand bed, respectively.

Fig. 25 Variation of % increase in UBC for upright shell footing on loose sand bed

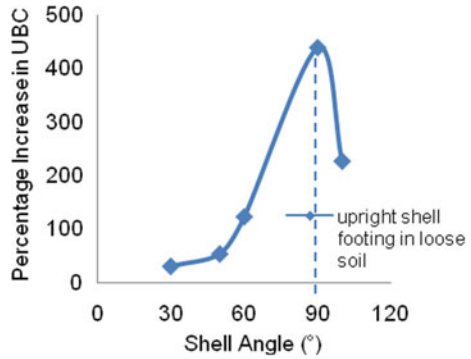


Fig. 26 Variation of % increase in UBC for upright shell footing on dense sand bed

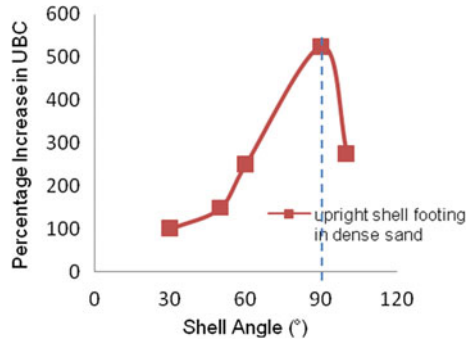


Fig. 27 Variation of % increase in UBC for inverted shell footing on loose sand

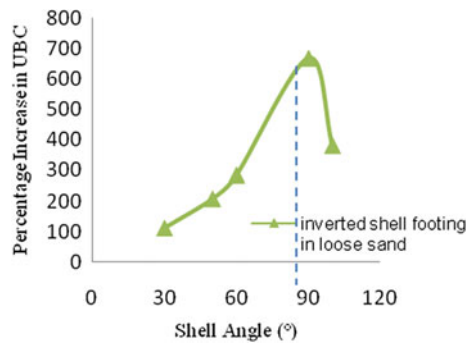


Fig. 28 Variation of % increase in UBC for inverted shell footing on loose sand

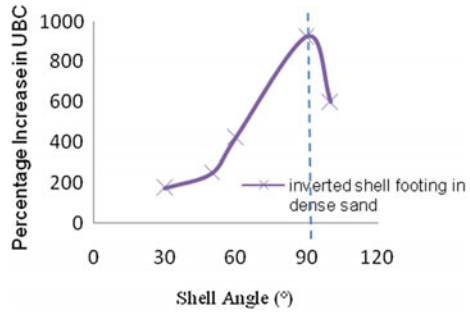
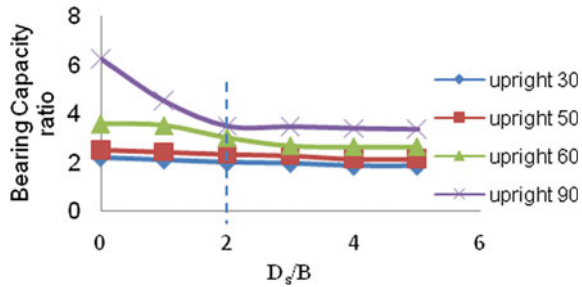


Fig. 29 Variation of BCR for vertical centric loading on upright shell footing with respect to (D_s/B) ratio on layered sand bed



From Figs. 25, 26, 27, and 28, it is observed that upright shell footing as well as inverted shell footing with shell angle 90° shows the maximum UBC than other shell angles. Thus the optimum shell angle for shell footing may be adopted as 90° .

4.2 Effect of Layering of Sand Bed

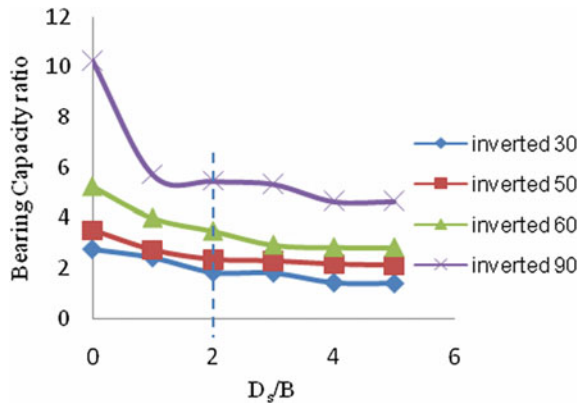
In case of multilayered sand bed, the variation of BCR with respect to depth of top layer of sand bed for upright and inverted shell footing subjected to vertical centric loading is shown in Fig. 29 and Fig. 30, respectively.

From Figs. 29 and 30, it is seen that BCR decreases as D_s/B ratio increases from $D_s/B = 0$ to $D_s/B = 2$. With further increase in D_s/B ratio, BCR remains unchanged.

4.3 Effect of Reinforcement in Sand Bed

Shell footing subjected to vertical centric loading on both unreinforced and reinforced sand bed using geogrid reinforcement was analyzed. First layer was placed at fixed distance u which was equal to $0.25 B$ below the foundation base with fixed length equal to $4 B$. Spacing between successive layers of reinforcement was $0.25 B$. The

Fig. 30 Variation of BCR for vertical centric loading on inverted shell footing with respect to (D_s/B) ratio on layered sand bed



effect of reinforcement in sand bed for upright and inverted shell footings are shown in Fig. 31 and Fig. 32, respectively.

From the above graphs, it is seen that BCR increases significantly with provision of two layers of reinforcement. Thereafter further increase in number of layers, ($N > 2$), BCR remains unchanged.

Fig. 31 Variation of BCR for vertical centric loading on upright shell footing on loose sand bed with respect to (N)

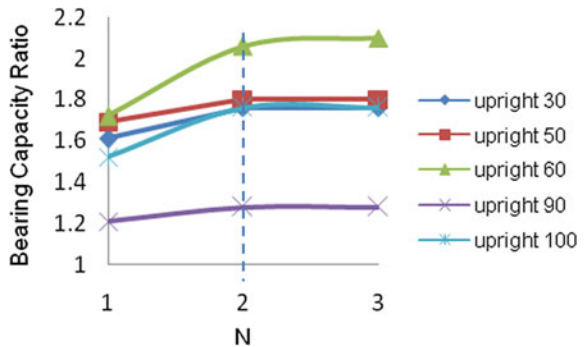
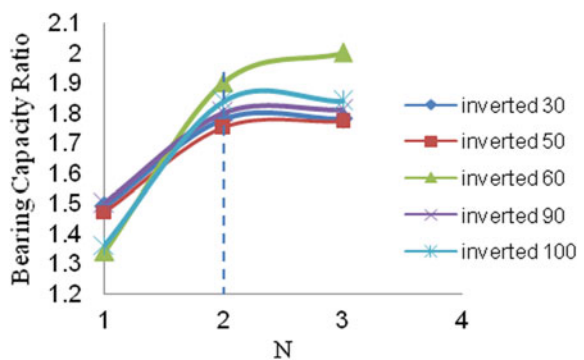


Fig. 32 Variation of BCR for vertical centric loading on inverted shell footing on loose sand bed with respect to (N)



5 Conclusions

Based on the results of the present study, the following conclusions are drawn.

1. Shell footing (upright and inverted) has higher ultimate bearing capacity on loose, dense as well as layered sand bed as compared to strip footing.
2. The ultimate bearing capacities of shell footing increases with increase in shell angle up to 90° . Ultimate bearing capacities of shell footing decrease with increase in shell angle after 90° . Thus 90° is the optimum shell angle for inverted shell footing.
3. For shell angle of 90° , UBC of inverted shell footing is higher than upright shell footing.
4. In case of layered sand bed, UBC of shell footing decreases with increase in thickness of top layer up to twice the width of footing. Thereafter, UBC remains constant.
5. BCR of shell footing increases significantly with provision of two layers of geogrid reinforcement. With further increase in number of layers BCR remains unchanged. Hence optimum number of layers of reinforcement may be considered as two, for shell footing on reinforced sand bed.

References

- Hanna A, El-Rahman MA (1990) Ultimate bearing capacity of triangular shell strip footings on sand. *J Geotech Eng* 116:1851–1863. ASCE, December 1990
- Huat BBK, Mohammed TA (2006) Finite element study using FE code (PLAXIS) on the geotechnical behaviour of shell footings. *J Comput Sci* 104–108
- Rinaldi R (2012) Inverted shell foundation performance in soil. Concordia University Montreal Quebec, Canada, April 2012

Performance of Suction Pile Anchor for Floating Offshore Structures



S. W. Thakare, Aparna H. Chavan, and A. I. Dhatrak

Abstract Offshore structures are huge concrete or steel structure used for extracting the oil and gas from earth's crust and used for producing renewable energy. The suction pile anchor is connected to the floating structure by mooring line which is attached to the pad-eye position on the side of suction pile anchor to maintain it in position. In this paper, the results of analyses of suction pile anchor in dense sand, medium sand, and clay soil bed are presented. For this purpose model of suction pile anchor was developed in MIDAS GTS 3D software. For a suction pile anchor of a particular dimension, mooring positions and load inclination angle of mooring line were varied. From the analyses, pullout force-displacement curves were developed and pullout capacities of the suction pile anchor were evaluated. Design charts were then developed which gives the length and diameter of suction pile anchors for a given pullout force.

Keywords Floating offshore structure · Suction pile anchor · Mooring position · MIDAS GTS 3D software

1 Introduction

Due to increasing global energy demand, major developments are taking place in harnessing renewable energy through wind turbines located offshore, where higher wind speeds are encountered and extraction of oil and gas from earth crust through platforms located offshore, where the oil and gas is available in large amount.

S. W. Thakare · A. H. Chavan (✉) · A. I. Dhatrak
Government College of Engineering, Amravati, Maharashtra, India
e-mail: aparanachavan93@gmail.com

S. W. Thakare
e-mail: sanjay.thakare1964@gmail.com

A. I. Dhatrak
e-mail: anantdhatrak@rediffmail.com

Sant Gadge Baba University, Amravati, Maharashtra, India

Offshore structure is huge concrete or steel structure used for extracting oil and gas in the earth's crust and used for producing renewable energy. The type of foundation element to be employed for such structures depends on the nature of loading, and stiffness and strength of the surface sediments. Offshore structures are generally classified as bottom supported fixed structures and floating structures. Floating structures are commonly used because of their cost-effectiveness. A floating structure is maintained in position by a mooring system, connecting the bottom end of the structure to anchors embedded in the seafloor. A Floating Production, Storage and Offloading (FPSO) unit is a floating vessel used by the offshore oil and gas industry for the production and processing of hydrocarbons, and for the storage of oil. Anchors are used as underwater foundation for offshore structures such as FOWT and oil and gas extraction platform. Anchors serve to secure moorings and foundations in a fixed position on the seafloor. Purpose of Anchor is to limit the vertical and lateral movement for offshore floating structure and submerged structure. The suction anchor is a hollow steel pipe, although the diameter of the pipe is much larger than that of the pile. Suction pile anchor is closed at the top and open at the bottom. The suction anchor is forced into the seabed by means of a pump connected to the top of the pipe, creating a pressure difference. The suction anchor is capable of withstanding both horizontal and vertical loads. The mooring line is directly attached to the upper part of the pipe. Suction anchor is suited for catenary and taut mooring lines. SPA is used for anchorage of FOWT and oil and gas extraction production. They have large diameters, typically more than 5 m in diameter and are 20–30 m in length, with a Length to Diameter ratio (L/D) in the range of 3–6. Plate anchors are large plates that resist extraction when embedded deeply into the seafloor. A Suction Embedded Plate Anchor (SEPLA) consists of a plate anchor attached to the tip of a suction caisson. Suction installation is very similar to that of a suction pile anchor, except that additional under pressure is required to overcome the added soil resistance acting against the plate. After installation to the target penetration depth, the suction pile is withdrawn, leaving behind the vertically oriented plate. The plate must be turned into the direction normal to the direction of applied loading, a process known as keying.

2 Problem Definition of Suction Pile Anchor

The analysis consisted of modeling of suction pile anchor embedded in dense sand, medium dense sand, and clayey soil to determine the uplift capacity. The suction pile anchor used as foundation for floating oil and gas extraction platform is shown in Fig. 1.

The various parameters which were considered for analyses were length and diameter of suction pile anchor. For a suction pile anchor, mooring positions and the load inclination angle with horizontal (θ) was varied as 0° , 22.5° , 45° , 67.5° , and 90° for each mooring position. The loads were applied at 5, 15, 35, 45, 55, 75, and 95% mooring positions ($Z_{cl}/L\%$) from the top of the suction pile anchor. Table 1 shows the properties of dense sand, medium sand, clayey soil for the analysis of suction

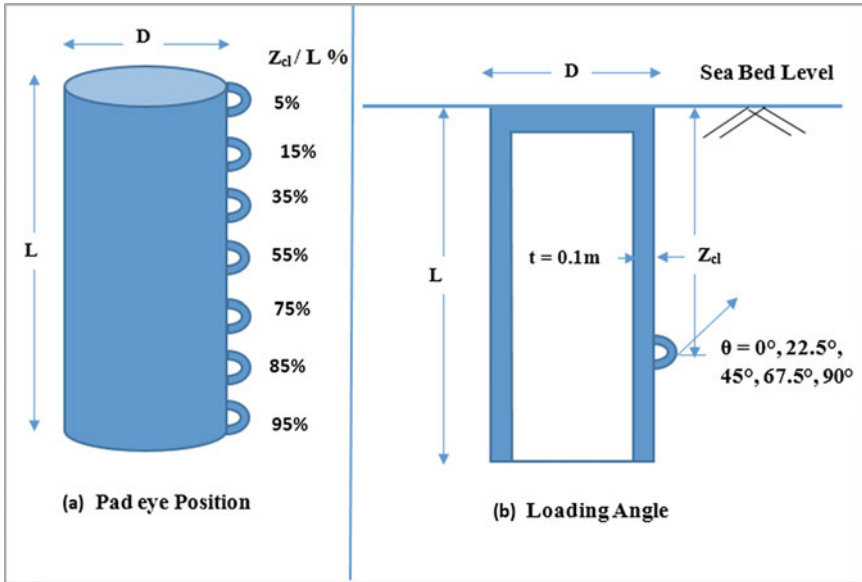


Fig. 1 Schematic diagram of suction pile anchor

Table 1 Properties of sand used for the analyses of suction pile anchor

Properties	Dense sand	Medium dense sand	Clayey soil
Unit weight (kN/m ³)	18	18	14
Young's modulus (kPa)	60,000	30,000	6000
Poisson's ratio	0.3	0.3	0.4
Angle of internal friction	39°	32°	0
Cohesion (kPa)	0	0	5

pile anchor in MIDAS 3D software. Properties of suction pile anchor are shown in Table 2.

Table 2 Properties assigned for suction pile anchor

Properties	Values
Young's modulus (kN/m ²)	2×10^8
Density (kN/m ³)	78
Poisson's ratio	0.30

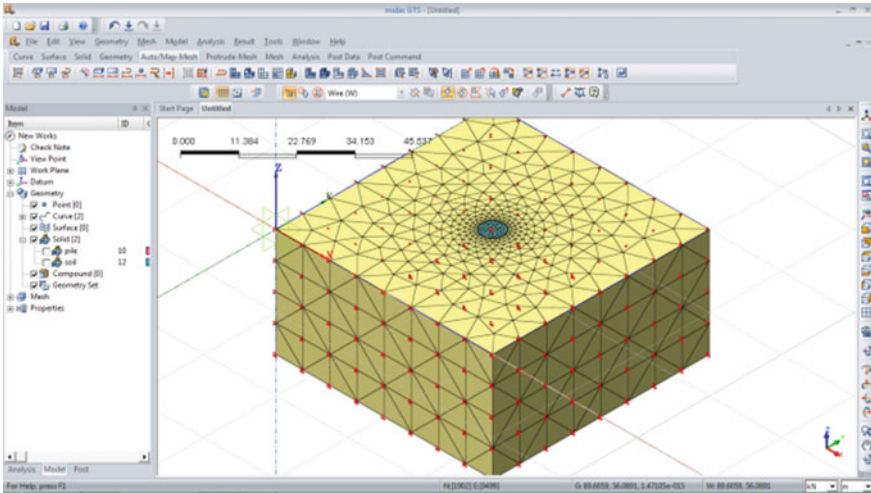


Fig. 2 Finite element model of suction pile anchor embedded in soil

2.1 Finite Element Model of Suction Caisson

The analysis in the present study consisted of modeling of suction pile anchor embedded in dense sand to determine the uplift capacity of suction caisson. Model of suction caisson was developed in MIDAS GTS 3D software, which is finite element-based software. Soil model of size $45\text{ m} \times 45\text{ m} \times 30\text{ m}$ was chosen for analysis. The finite element model of suction pile anchor embedded in dense sand bed developed in MIDAS GTS software is shown in Fig. 2.

3 Analysis of Suction Pile Anchor

There are many parameters for suction pile anchor design such as type of mooring system, soil type, anchor load direction, anchor pad-eye location, and anchor dimension ratio. The load angle was relative to a horizontal plane. The results are presented in the form of uplift force-total displacement curves for different combinations of mooring position. Each curve indicates the response of suction pile anchor under the application of uplift force at respective loading angle. The analyses were done until the horizontal component of movement of displacement controlled point reached 1.0 m.

The results of analysis carried out on suction pile anchor with aspect ratio 2.0, with $L = 9.0\text{ m}$, and $D = 4.5\text{ m}$ in dense sand are as shown in Figs 3, 4, 5, 6, 7, 8, 9, and 10.

Fig. 3 Pullout force—Total displacement curves of suction pile anchor for L = 9 m, D = 4.5 m (Mooring position 5 %, dense sand)

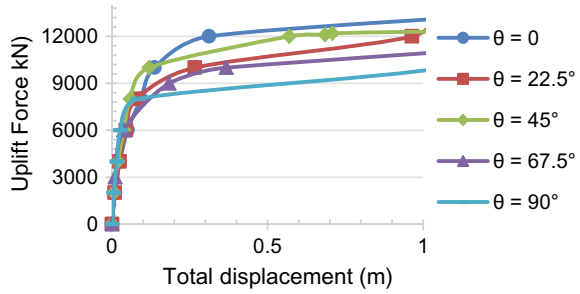


Fig. 4 Pullout force—Total displacement curves of suction pile anchor for L = 9 m, D = 4.5 m (Mooring position 15 %, dense sand)

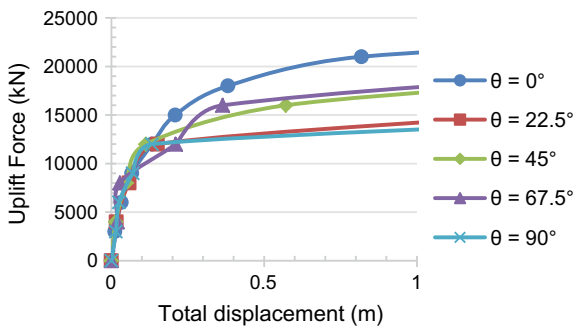


Fig. 5 Pullout force—Total displacement curves of suction pile anchor for L = 9 m, D = 4.5 m (Mooring position 35 %, dense sand)

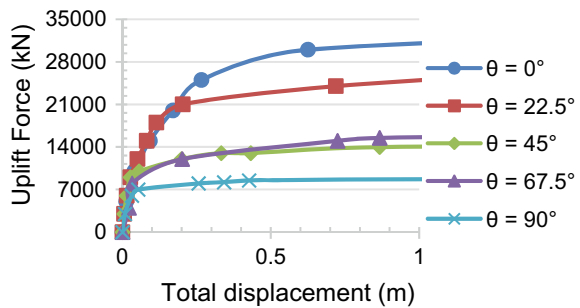


Fig. 6 Pullout force—Total displacement curves of suction pile anchor for L = 9 m, D = 4.5 m (Mooring position 45 %, dense sand)

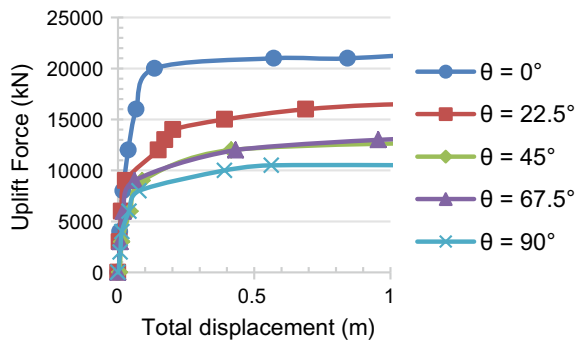


Fig. 7 Pullout force—Total displacement curves of suction pile anchor for $L = 9$ m, $D = 4.5$ m (Mooring position 55 %, dense sand)

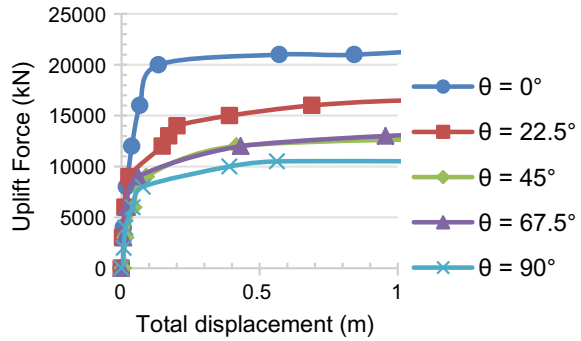


Fig. 8 Pullout force—Total displacement curves of suction pile anchor for $L = 9$ m, $D = 4.5$ m (Mooring position 75 %, dense sand)

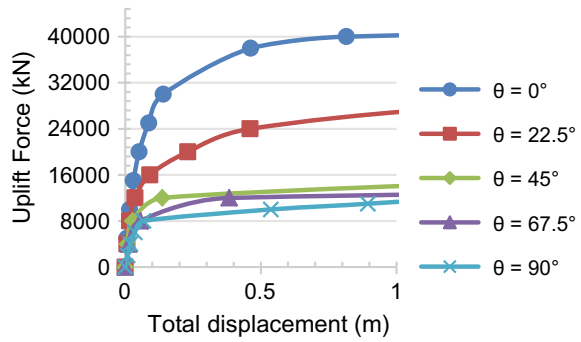
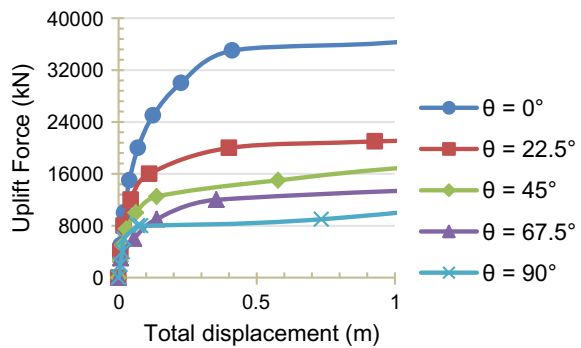


Fig. 9 Pullout force—Total displacement curves of suction pile anchor for $L = 9$ m, $D = 4.5$ m (Mooring position 85 %, dense sand)



The results of analysis carried out on suction pile anchor with aspect ratio 2.0, with $L = 9.0$ m, and $D = 4.5$ m in medium dense sand are as shown in Figs. 11, 12, 13, 14, and 15.

The results of analysis carried out on suction pile anchor with aspect ratio 2.0, with $L = 9.0$ m, and $D = 4.5$ m in soft clay are as shown in Figs. 16, 17, 18, 19, 20, and 21.

Fig. 10 Pullout force—Total displacement curves of suction pile anchor for $L = 9$ m, $D = 4.5$ m (Mooring position 95 %, dense sand)

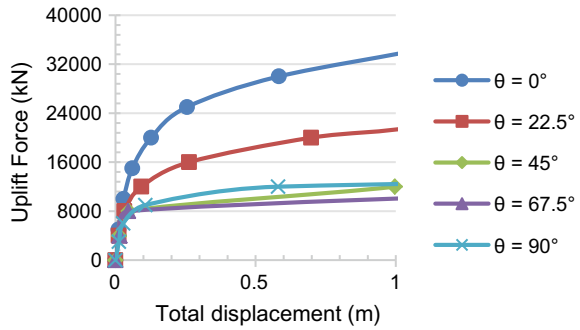


Fig. 11 Pullout force—Total displacement curves of suction pile anchor for $L = 9$ m, $D = 4.5$ m (Mooring position 15 %, medium dense sand)

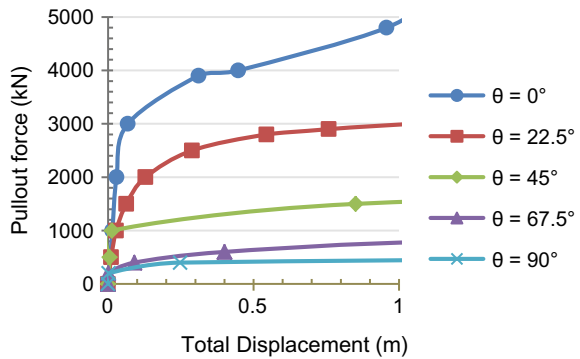
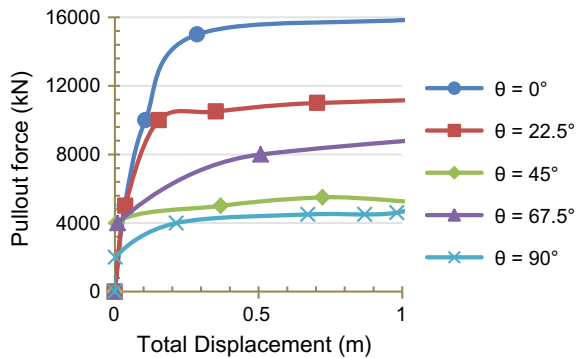


Fig. 12 Pullout force—Total displacement curves of suction pile anchor for $L = 9$ m, $D = 4.5$ m (Mooring Position 55 %, medium dense sand)



4 Discussion of Results for Suction Pile Anchor

From the results, it is observed that due to application of pullout force, suction pile anchor-soil system undergoes significant displacement and the displacement continued till certain limit, after which system fails to take further load and nature of the pullout—total displacement curve gets flat.

Fig. 13 Pullout force—Total displacement curves of suction pile anchor for $L = 9$ m, $D = 4.5$ m (Mooring position 75 %, medium dense sand)

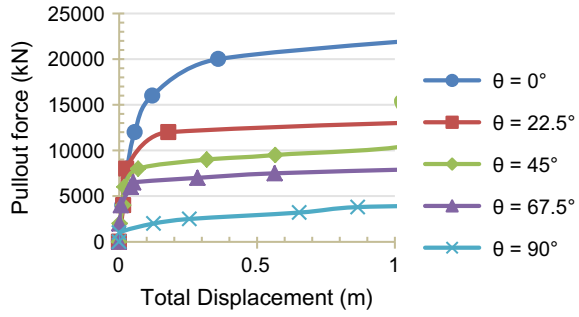


Fig. 14 Pullout force—Total displacement curves of suction pile anchor for $L = 9$ m, $D = 4.5$ m (Mooring position 85 %, medium dense sand)

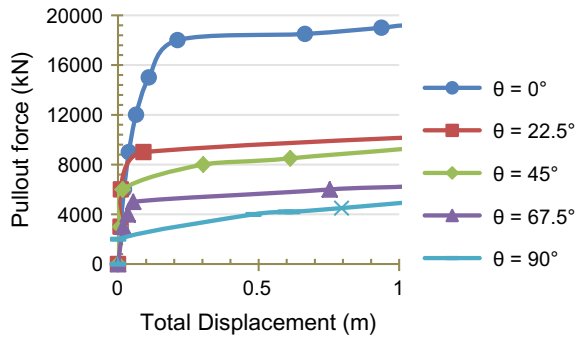


Fig. 15 Pullout force—Total displacement curves of suction pile anchor for $L = 9$ m, $D = 4.5$ m (Mooring position 95 %, medium dense sand)

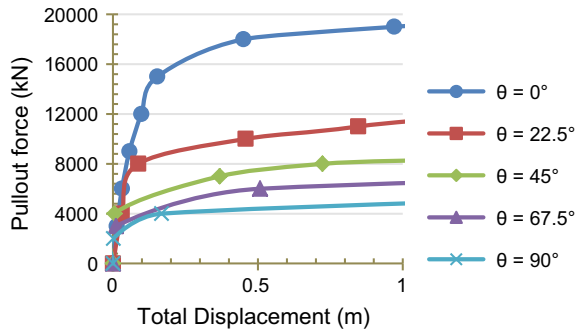


Fig. 16 Pullout force—Total displacement curves of suction pile anchor for $L = 9$ m, $D = 4.5$ m (Mooring position 5 %, soft clay)

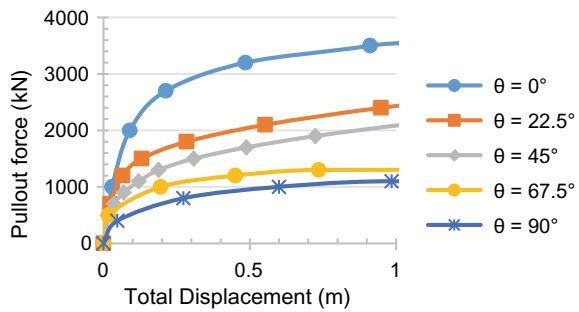


Fig. 17 Pullout force—Total displacement curves of suction pile anchor for L = 9 m, D = 4.5 m (Mooring position 35 %, soft clay)

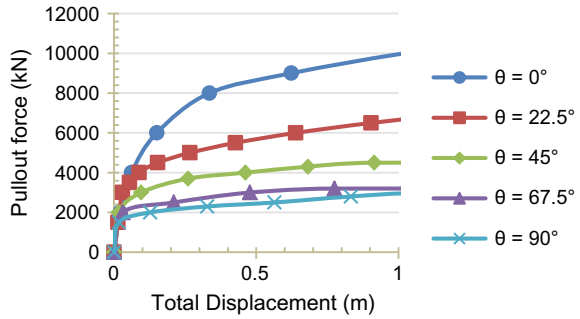


Fig. 18 Pullout force—Total displacement curves of suction pile anchor for L = 9 m, D = 4.5 m (Mooring position 55 %, soft clay)

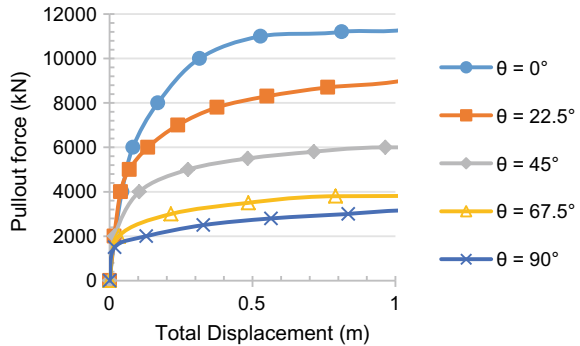


Fig. 19 Pullout force—Total displacement curves of suction pile anchor for L = 9 m, D = 4.5 m (Mooring position 75 %, soft clay)

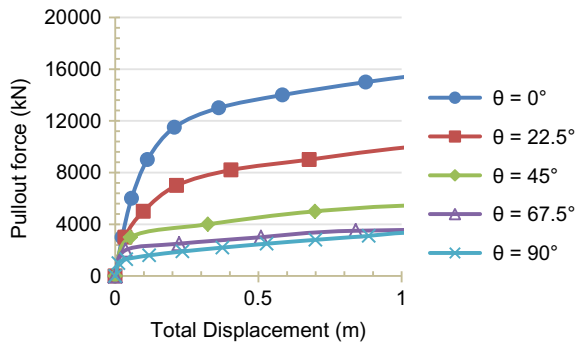


Fig. 20 Pullout force—Total displacement curves of suction pile anchor for L = 9 m, D = 4.5 m (Mooring position 85 %, soft clay)

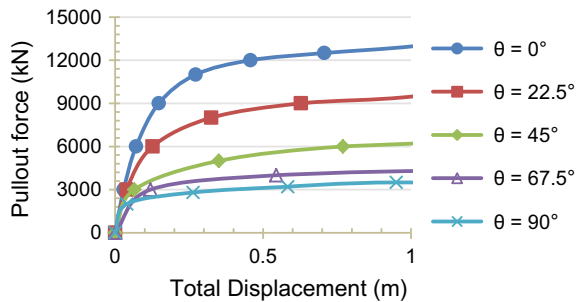
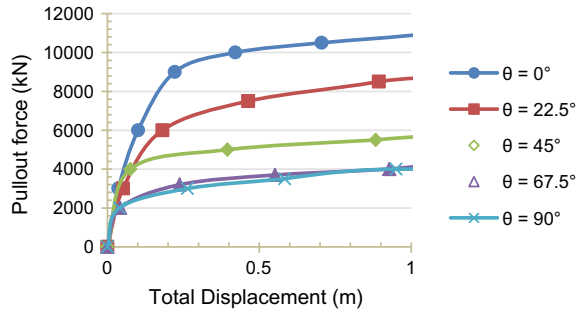


Fig. 21 Pullout force—Total displacement curves of suction pile anchor for $L = 9$ m, $D = 4.5$ m (Mooring position 95 %, soft clay)



The pullout capacities for different loading angles and mooring positions for suction pile anchor in dense sand, medium dense sand, and soft clay are shown in Figs. 22, 23, 24, and 25. From these figures, it is observed that for a given mooring position, the maximum pullout capacity is obtained for lateral loading ($\theta = 0^\circ$), while the minimum pullout capacity is obtained for $\theta = 90^\circ$. The difference between the pullout capacity for $\theta = 90^\circ$ and $\theta = 67.5^\circ$ is very small for mooring position up to 75 %, because in these cases, the suction pile anchor moves almost vertically, at $\theta = 90^\circ$ The suction pile anchor does not move purely vertically as the pad eye is located on one side of the caisson and therefore some counterclockwise rotation occurs.

Fig. 22 Variation of pullout capacity of suction pile anchor in dense sand with mooring position for different loading angles ($L = 6$ m, $D = 3$ m)

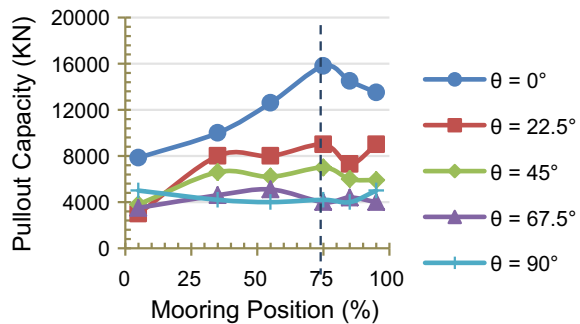


Fig. 23 Variation of pullout capacity of suction pile anchor in dense sand with mooring position for different loading angles ($L = 9$ m, $D = 4.5$ m)

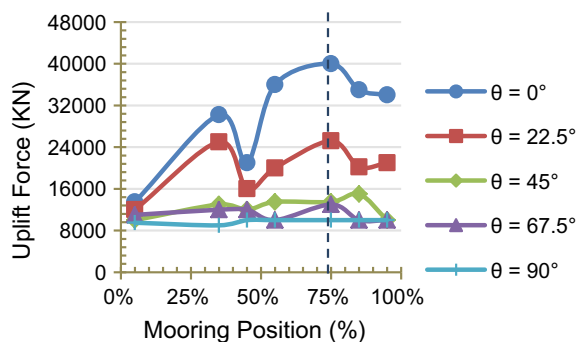


Fig. 24 Variation of pullout capacity of suction pile anchor in medium dense sand with mooring position for different loading angles (L = 9 m, D = 4.5 m)

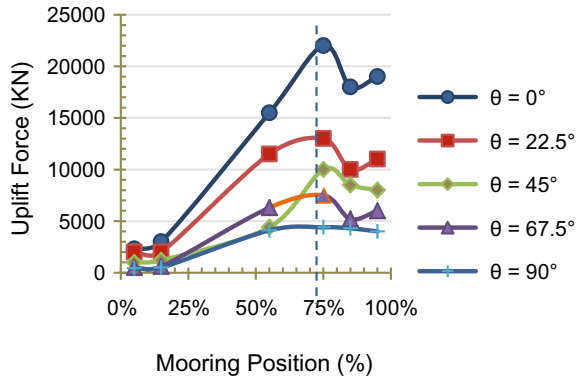
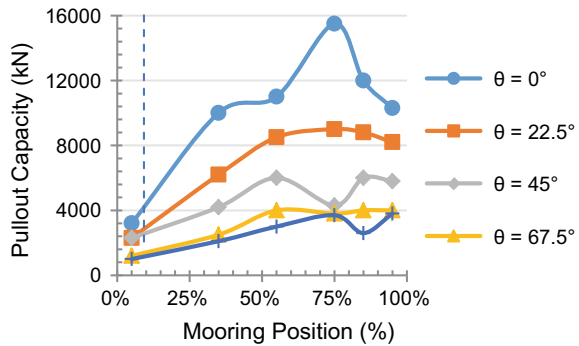


Fig. 25 Variation of pullout capacity of suction pile anchor in soft clayey soil with mooring position for different loading angles (L = 9 m, D = 4.5 m)



From these figures, it is observed that maximum pullout capacity is developed at about 75% mooring position and $\theta = 0^\circ$. Design charts are then developed for different L/D ratios of suction pile anchor for pad-eye position (mooring position) 75% for load inclination angle 0° , 22.5° , and 45° . These design charts may be used to determine the required length and diameter of suction pile anchor for the given uplift force. These design charts may be used for taut and catenary mooring line system. Figures 26, 27, 28, 29, 30, 31, 32, 33, and 34 show these design charts.

5 Conclusions

Anchors used as a foundation of floating offshore structure have been analyzed using MIDAS GTS 3D software. Behavior of suction pile anchor has been studied in dense sand, medium dense sand, and soft clayey soil.

From the results of this study, the following conclusions are drawn:

Fig. 26 Design chart for suction pile anchor (Mooring position 75 % and loading angle 0° in dense sand)

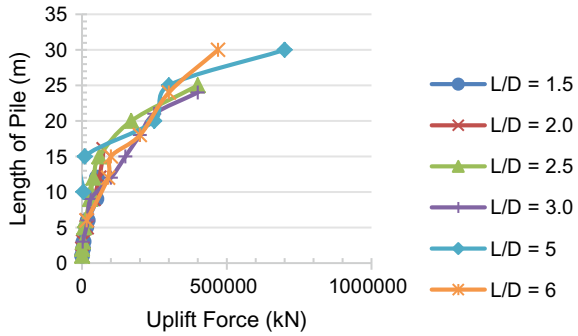


Fig. 27 Design chart for suction pile anchor (Mooring position 75 % and loading angle 22.5° in dense sand)

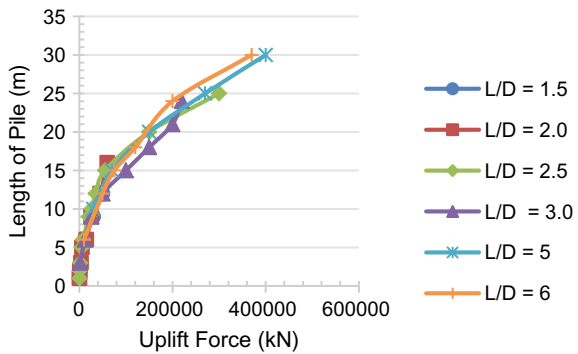
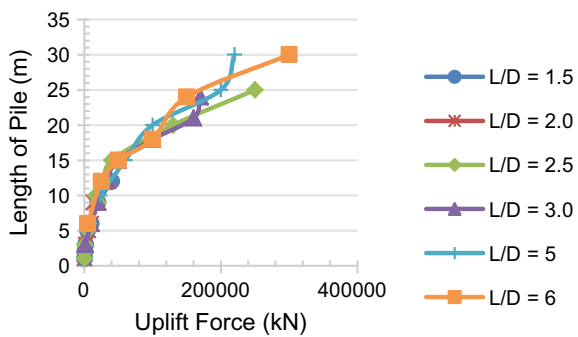


Fig. 28 Design chart for suction pile anchor (Mooring position 75 % and loading angle 45° in dense sand)



1. The maximum pullout force for suction pile anchor in dense sand, medium dense sand, and clayey soil is obtained for 75 % mooring position at 0° load inclination angle.
2. The maximum pullout capacity of suction pile anchor is obtained for lateral loading ($\theta = 0^\circ$), while the minimum pullout capacity is obtained for vertical loading ($\theta = 90^\circ$).

Fig. 29 Design chart for suction pile anchor (Mooring position 75 % and loading angle 0° in medium dense sand)

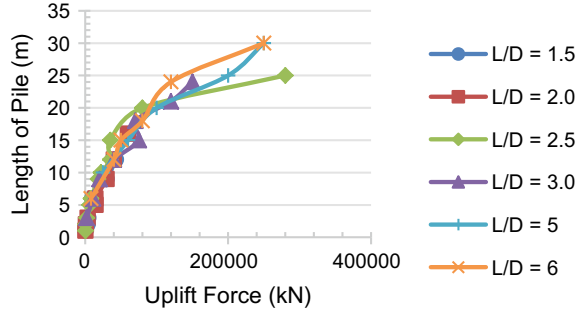


Fig. 30 Design chart for suction pile anchor (Mooring position 75 % and loading angle 22.5° in medium dense sand)

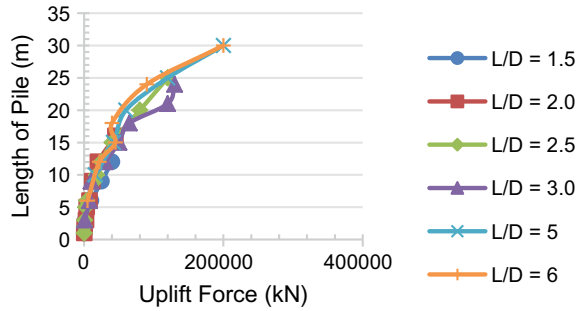


Fig. 31 Design chart for suction pile anchor (Mooring position 75 % and loading angle 45° in medium dense sand)

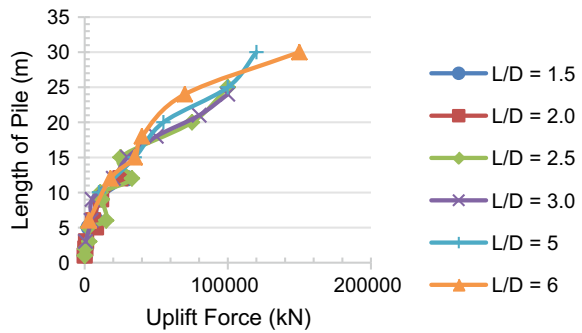


Fig. 32 Design chart for suction pile anchor (Mooring position 75 % and loading angle 0° in soft clay)

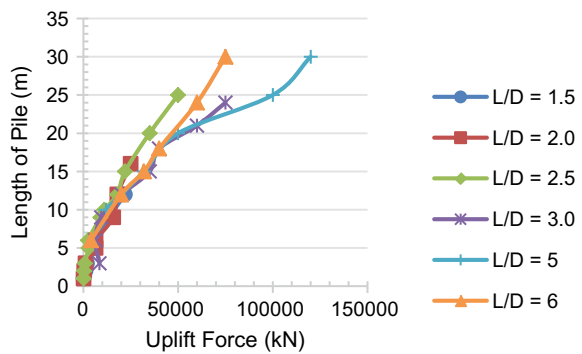


Fig. 33 Design chart for suction pile anchor (Mooring position 75 % and loading angle 22.5° in soft clay)

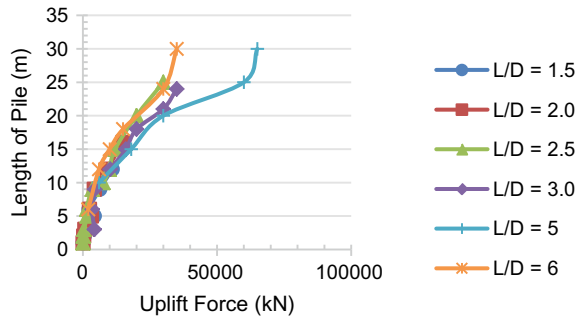
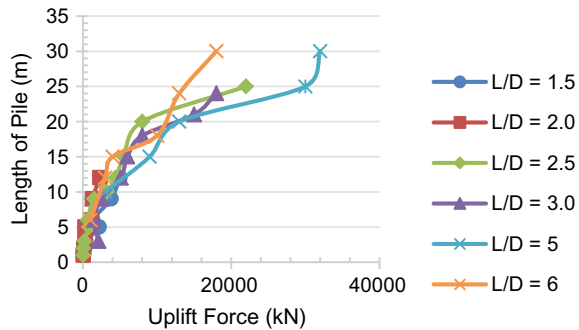


Fig. 34 Design chart for suction pile anchor (Mooring position 75 % and loading angle 45° in soft clay)



3. As aspect ratio (L/D) increases, the pullout capacity of suction pile also increases. The suction pile offers larger pullout force when angle of pull is 22.5° than that for pull at 45° .
4. Design charts developed may be used to determine the required length and diameter of suction caisson anchor for the given uplift force.

Bibliography

- Ahmed SS (2015) Finite element modeling of suction caisson and large diameter monopile In: Dense sand under oblique and lateral load. Faculty of Engineering and Applied Sciences Memorial University of Newfoundland
- Budiman I, Soedigdo I, Prakoso WA (2015) Analysis of suction piles for mooring floating structure foundations in clay soil at deep water levels. *Int J Technol* 2:254–263. ISSN 2086-9614
- Kim D, Lee J, Nsabimana E, Jung YH (2012) Numerical analysis of suction pile behavior with different loading locations and displacement inclinations. *Ocean Syst Eng* 2(3):205–215. <https://doi.org/10.12989/ose.2012.2.3.205>
- Vijaya R, Kiran AS, Ramesh R, Ramanamurthy MV, Ramadass GA, Atmanand MA (2014) Assessment of feasibility of suction pile/anchor installation and pullout testing through field tests. *Int J Ocean Clim Syst* 5:163–173

Image-Based Measurements to Estimate Bearing Capacity of Hollow Driven Piles Under Impact Loading



G. Sreelakshmi , Asha M. N. , Divya Viswanath ,
Y. N. Yogesh kumar , and S. Vinodini 

Abstract Hollow driven piles are long, slender columns made of concrete or steel and have a predetermined shape and size. They are installed by driving, jetting, screwing, jacking, vibrating, drilling, and grouting, or a combination of them. When a hollow pile (open-ended) is driven into the ground, a soil plug may develop within the pile during driving, which may prevent or partially restrict additional soil from entering the pile. It is known that the driving resistance and the bearing capacity of open-ended piles are governed largely by this plugging effect. Particle Image Velocimetry (PIV) technique has been adopted to understand pile-soil interaction during the installation of piles and to determine the effect of plugging on load-carrying capacity of piles. Experimental studies have been performed in a steel tank of dimensions 600 mm × 200 mm in plan and 450 mm deep. The top central part of front side of the steel tank is made of perspex sheet to facilitate image capture. Half section hollow aluminum piles modeled using wood's scaling law is used in the experiments. The infill material is cohesionless sand with different densities and impact load has been applied to drive the piles. Under axisymmetric conditions, the impact load is applied on the pile, and failure pattern at the interface region is captured using a high resolution digital camera that is later analyzed through Geo-PIV software. The number of blows required to drive the pile and rate of plugging induced is measured. The strain contours around pile-soil interface obtained through image analysis clearly indicated the effect of infill on pile driving. Bearing capacity of the hollow pile is estimated using three different methods, viz., IS 2911 (2010) SPT-based formula, American Petroleum Institute (API)'s design criteria, and SPT-based empirical equations proposed from literature. It is seen that SPT-based design method considering the plugging behavior gave a better estimate of bearing capacity values.

Keywords Bearing capacity · Driven pile · Soil plug

G. Sreelakshmi (✉) · Asha M. N. · D. Viswanath · Y. N. Yogesh kumar · S. Vinodini
Department of Civil Engineering, CMR Institute of Technology, Bengaluru 560037, Karnataka,
India
e-mail: sreelakshmi.g@cmrit.ac.in

1 Introduction

A driven pile has long and slender column-like structure made of predefined material and has a predetermined shape and size. Such piles are installed by impact hammering, vibration, or by pushing it into the ground for a design depth or till the required resistance is achieved. They are classified into two, viz., large and small displacement piles (a) Large displacement piles comprise of solid-section piles or hollow-section piles with a closed-end (b) Small displacement piles comprise rolled steel H- or I-sections, pipe or box sections and have a relatively small cross-sectional area driven with an open end such that the soil enters the hollow section Tomlinson (1994). Large displacement piles are generally preferred in loose cohesionless soil and develop greater shaft bearing capacities with tapered sections. Small displacement piles have been frequently used in the foundations of urban and coastal structures such as harbor terminals, long-span bridges, and offshore wind power structures.

The response of pile to transfer load depends on pile composition, pile configuration, environmental conditions, embedment depth, pile driving methods, and soil deformations associated with the same. For open-ended driven piles, soil displacement around pile results in the formation of soil plugging. It is found that for driven piles bearing capacity and stresses developed during pile driving are affected by soil plugging.

Most of the research works in the late twentieth century considers the behavior of open-ended hollow pile under static loading as similar to that of a closed pile (Brucy et al. 1991; Randolph et al. 1991; Raines et al. 1992; De Nicola and Randolph 1997; Lehane and Gavin 2001). However, in the recent years, research works have been carried out to investigate plugging behavior of driven piles. It is also reported that soil plug developed inside pile shaft depends on number of blows required to drive pile, relative density of infill medium, amount and type of infill, and pile diameter (Szechy 1959; Klos and Tejchman 1981; Murff et al. 1990; Froy 1993; Al-Ansari 1999). The bearing capacity of hollow driven piles is effected by plugging phenomenon which is explored by few researchers (Paik and Salgado 2003; Sangseom et al. 2015; Fattah et al. 2015). Empirical formulae have been developed to determine bearing capacity of hollow driven piles by incorporating the concept of Incremental Filling Ratio (IFR) to quantify soil plugging.

The suitability of particle image velocimetry to understand the deformation mechanism has been a matter of research in the recent years. Plane strain conditions and Particle image velocimetry (PIV) technique was used by White and Bolton (2004) to study the resistance offered by sand during pile installation. The model studies were carried out in a tank of 1000 mm length and 745 mm depth. It has been concluded that image analysis technique offered sufficient precision to measure pre-failure strains and offers the flexibility to capture non-homogenous soil deformations. Tran (2005) adopted PIV technique to capture soil deformations developed during installation of caissons in layered deposits. Ni and Hird (2010) carried out physical modeling to assess the impact of soil disturbance during pile installation. A vertical section aligned

with the pile centreline was illuminated by a laser light sheet, and a sequence of digital images was recorded. These were analyzed using particle image velocimetry, and the complete displacement distribution during the pile installation was obtained. The image analysis technique could estimate the soil displacement field developed from deep cone penetration test (Arshad et al. (2014)). It is found that image-based deformation measurement is suited best for geotechnical applications. Stanier et al. (2015) demonstrated that PIV measurements improved the clarity of the interpretation of all deformation modes, including rigid-body displacements, rotations, and strains. The pile-soil interaction behavior on hollow and solid closed-ended single pile and pile groups have been investigated through image analysis. They stated that surface heave developed around hollow pile under axisymmetric loading was more than solid pile due to lesser mass density of hollow pile than solid piles (Sreelakshmi et al. 2017).

From the literature, it is observed that PIV technique has been used by many researchers for investigating pile-soil interaction. Though image analysis can be used for measuring deformations, its potential toward estimating the plugging effect in piles has not been explored by any researcher. The main focus of the present study is to use the principles of particle image velocimetry, to estimate soil plug length in the hollow piles and analyze the deformation patterns at the pile-soil interface. An attempt has been made to estimate the bearing resistances of open-ended driven piles at different in situ densities.

2 Methodology

Methodology adopted to ascertain the bearing capacity of hollow open-ended can be sequenced as follows:

- Characterization of infill material and estimation of its friction angle at different dry densities.
- Fabrication of steel tank Parkin and Lunne (1982).
- Image acquisition using high resolution digital camera and obtain soil deformation profiles using Geo-PIV software.
- Assessment of pile drivability and soil plug length for different infill densities.
- Estimation of bearing capacity using different methods and comparison of the results.

3 Experimental Work

This section presents the material properties and the details of the experimental setup. Hollow open-ended piles are used for the experimental studies. The dimensions of the model pile and rammer have been determined by using scaling laws Wood et al. (2002), and Table 1 gives a summary of scaling factors. A factor of 1/10 is used for scaling length and $1/10^5$ has been used for scaling flexural rigidity.

Table 1 Scaling factors for pile modeling Wood et al. (2002)

Variable	Scaling factors
Length	1/10
Density	1
Stiffness	1/10
Stress	1/10
Strain	1

Aluminum half-section hollow piles of outer diameter 15.8 mm and inner diameter 13.4 mm (length to diameter ratios of 10) with open ends has been used for the present studies. Figure 1 shows the schematic sketch of pile cross section. Pen markings are made on pile at 1 cm interval to facilitate the measurement of plugging along the pile shaft through image analysis.

The steel tank (Fig. 2) has dimensions 600 mm × 200 mm in plan and 450 mm depth (Parkin and Lunne 1982) with perspex material on one side/face (longer direction) with vertical partitions to replicate plane strain conditions. Grid markings are made on front perspex sheet at 1 cm interval using CNG laser machine for tracking infill movement during pile penetration. Figure 3 shows the enlarged view of perspex window with its grid markings. Sandy soil with average of less than 3.8 mm has been used as the infill material. The sand is deposited by pluviation method to achieve uniform density. Three different heights of fall had been used in the present study, viz., 5, 10, and 15 cm. Table 2 presents the physical properties of infill used in the experiment. In the present experimental study, a hammer of weight 0.914 N falling

Fig. 1 Schematic sketch of model pile



Fig. 2 Perspex sheet with infill material and half-section pile

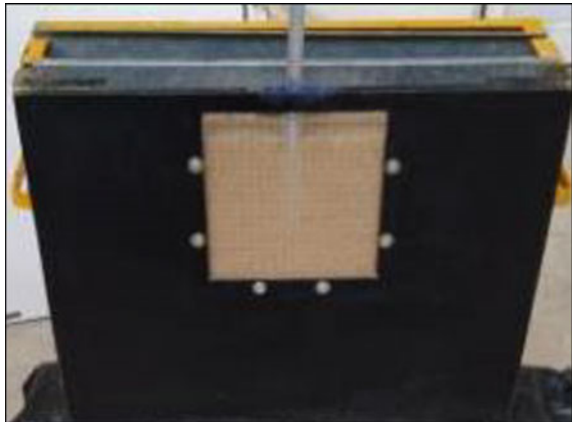


Fig. 3 Grid marked perspex sheet with sand infill and pile in background



Table 2 Physical properties of sand

Index property	Value
Coefficient of uniformity C_u	0.96
Coefficient of curvature C_c	0.66
Specific gravity G_s	2.47
Soil classification	Poorly graded sand
Unit weight (15 cm) height of fall	16.2 kN/m ³
Unit weight (10 cm) height of fall	15.4 kN/m ³
Unit weight(5 cm) height of fall	15.0 kN/m ³

from a height of 50 mm has been used to apply impact loads for driving the hollow piles. Figure 4 shows the standard penetration rammer model.

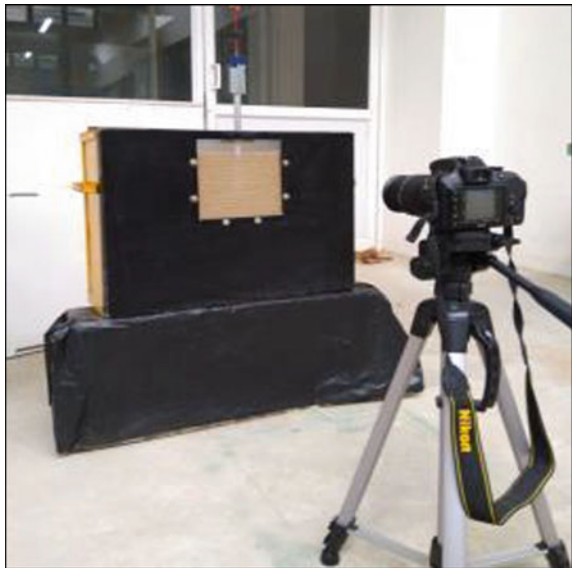
During pile driving, numbers of blows, soil plug length, and pile penetration depths are measured at every 15 mm for a total of 45 mm. The size of the soil plug and deformation around the pile during its driving is captured with the help of high resolution digital camera. When the pile is driven into the infill, a video is recorded and using an image grabber tool, still images at different microseconds are captured.

Figure 5 shows the photograph of detailed experimental test setup. The images are later analyzed using Geo-PIV software to capture the deformation profiles of the founded soil. The Geo-PIV software is a MATLAB-based tool which was originally developed for problems involving large displacements and deformations (Wood et al. 2002). In Geo-PIV, the displacement profiles for any application are obtained by comparing position coordinates of subsequent images. In the recent years, many researchers have used this tool to visualize the displacement and deformation of infill materials in various geotechnical processes through digital image correlation.

Fig. 4 Standard penetration rammer model



Fig. 5 Detailed experimental test setup



4 Bearing Capacity of Driven Piles

The axial load from a pile is transmitted to the soil through skin friction along the shaft and end bearing resistance at its tip. The ultimate load capacity of a pile is determined by means of static formula or by using a dynamic pile formula. Standard Penetration

Test (SPT) is commonly used for sub-soil exploration. An empirical equation for estimating ultimate load capacity of driven pile from standard penetration resistance, N was proposed by Meyerhof (1956). This is also mentioned in IS code (2010). For a saturated cohesionless soil, the ultimate load capacity (Q_u), in kN, is given in Eq. (1).

$$Q_u = 40 \times N \left(\frac{L_p}{D} \right) \times A_p + \bar{N} \times \left(\frac{A_p}{0.5} \right) \quad (1)$$

where

N = average N value at pile tip L_p = length of penetration of pile in the bearing strata, in m;

D = diameter or minimum width of pile shaft, in m;

A_p = cross-sectional area of pile tip, in m^2 ;

\bar{N} = average N along the pile shaft;

A_s = surface area of pile shaft, in m^2 .

Here, $40 \times N \left(\frac{L_p}{D} \right) \times A_p$ gives the end bearing resistance and $\bar{N} \times \left(\frac{A_p}{0.5} \right)$ gives the frictional resistance. For plugged piles, the bearing pressure is assumed to act over the entire cross section of the pile, and IS Code recommends a minimum factor of safety of 2.5. American Petroleum Institute (1993) estimates the bearing capacity of open-ended pile in a fully plugged mode or unplugged mode and is presented in Eqs. (2) and (3).

$$Q_{\text{unplugged}} = \sum f_{so} A_o + \sum f_{si} A_i + q_p A_p \quad (2)$$

$$Q_{\text{plugged}} = \sum f_{si} A_i + q_p A_p \quad (3)$$

f_{so} —Unit skin friction outside the pile (computed from ϕ)

f_{si} —Unit skin friction inside the pile (computed from ϕ)

A_o —Outside shaft area

A_i —Inside shaft area

A_p —Gross end area of pile

q_p —Unit end bearing capacity.

Here, $\sum f_{so} A_o$ gives the total external frictional resistance; $\sum f_{si} A_i$ gives the total internal frictional resistance, and $q_p A_p$ gives the end bearing resistance offered by the soil plug. For plugged piles, the bearing pressure may be assumed to act over the entire cross section of the pile, whereas for unplugged piles, the bearing pressure acts on the pile wall annulus only. In both codal methods, bearing capacity of a plugged pile is estimated by considering it as a solid pile and the plug length/extent of plugging is not considered. An empirical equation (Eq. 4) for calculating the inner bearing resistance of hollow piles by considering extent of plugging was proposed by Sangseom et al. (2015).

$$Q_{si} = f_{si} \times A_{si} = f_{si} \times \pi \times D_i \times L_{is} \quad (4)$$

where,

Q_{si} is the mobilized inner frictional resistance

f_{si} is the unit inner skin friction (kPa)

D_i is the inner diameter of the pile and

L_{is} is the length of mobilizing inner skin friction.

However, the total bearing capacity is the sum total of outside and inner frictional resistance. The outside frictional resistance is computed as the product of skin friction and its perimeter. The Eq. (5) is used to compute the unit inner skin friction.

$$f_{si} = K_O \sigma'_v \tan \delta \times 33.4 \times (\text{IFR} \times D)^{-0.48} \quad (5)$$

where, f_{si} is the unit inner skin friction (kPa),

K_O is the Rankine earth pressure coefficient before pile driving,

σ'_v is the average vertical effective stress over the entire penetration depth (kPa),

δ is the angle of interface friction between the soil and inner pile wall,

D is the pile diameter (m).

An empirical equation method was used to estimate Incremental Filling Ratio (IFR), Plug Length Ratio (PLR), and Soil Plugging Index (SPI) through regression analysis by Sangseom et al. (2015). In this, Incremental Filling Ratio (IFR) is defined as the increment of soil plug length per increment of pile penetration depth during pile installation. PLR or Plug length ratio is defined as the ratio of soil plug length to pile penetration. These can be estimated using Eq. (6) and (7).

$$\text{PLR} = 0.28 \ln \left(\frac{h D_i^2 \sigma'_h \sqrt{N}}{W L} \right) + 1.66 \quad (6)$$

Where, D_i is pile diameter, m,

L_{is} is the pile penetration depth, m,

W is the hammer weight, kN,

h is the height of fall, m,

N is the SPT value and σ'_h is the Horizontal effective stress of soil, kPa.

$$\text{IFR} = 110.3 \text{PLR} - 11.5 \quad (7)$$

Soil Plugging Index (SPI) is defined as

$$\text{SPI} = \frac{L_{is}}{L_i} \times 100$$

where L_i is the embedded length of the pile and L_{is} is the length of the developed inner skin friction region.

$$\text{SPI} = -0.03 D_i + 43.2 \quad (8)$$

where D_i is the inner pile diameter (mm).

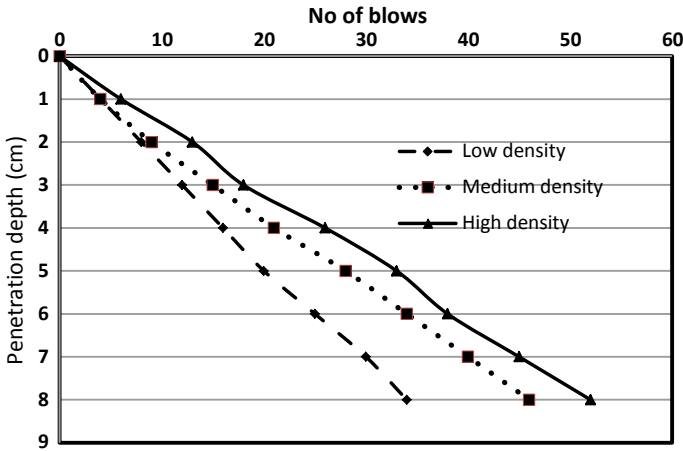


Fig. 6 Variation of number of blows vs penetration depth of pile under different densities

To understand the limitations of existing design methods, a comparison is carried between the bearing capacities values obtained through IS code, API code, and empirical expression suggested from literature by Sangseom et al. (2015).

5 Results and Discussions

5.1 Variation of Number of Blows Versus Penetration Depth

Figure 6 shows the variation of number of blows vs penetration depth of pile under low (15 kN/m^3), medium (15.4 kN/m^3) and high (16.2 kN/m^3) densities. It has been observed that as density increases, the resistance to penetration also increases. This is due to the greater frictional resistance offered by the dense packing of soil grains.

5.2 Effect of Soil Plugging Under Various Densities

Higher the density of the sand, higher will be the shear resistance offered by the sand and hence, more will be the resistance offered by the pile toward its deformation. This is in fact evident in Fig. 7, where plug length is highest for loose sands and lowest for dense sands. As the open-ended pipe pile is driven into the ground, the soil enters inside of the pile in the initial stage of pile driving at very shallow depths (up to 1 cm) and densification of the sand at the pile tip occurs.

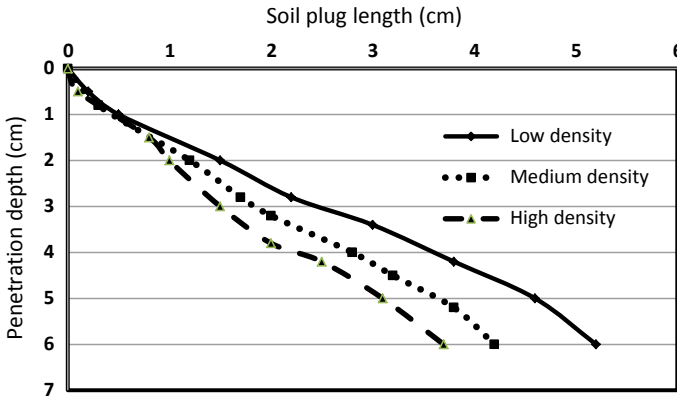


Fig. 7 Variation of soil plug length vs penetration depth

5.3 Shear Strain Contours Around Hollow Pile

Figure 8 shows the shear strain development of the soil domain due to the pile penetration under different in situ conditions (in pixels). Each image describes the maximum shear strain developed around the pile section. The color scale ranges from dark red, showing areas of greatest shear strain (75 %), to dark blue, showing no shear strain (0 %). The range between 0 and 75 % of shear strains was selected because it provided a better representation of the shear bands.

From the figure, it is observed that when density of sand is increased there is a decrease in area of strain contour developed around the pile with respect to its depth.

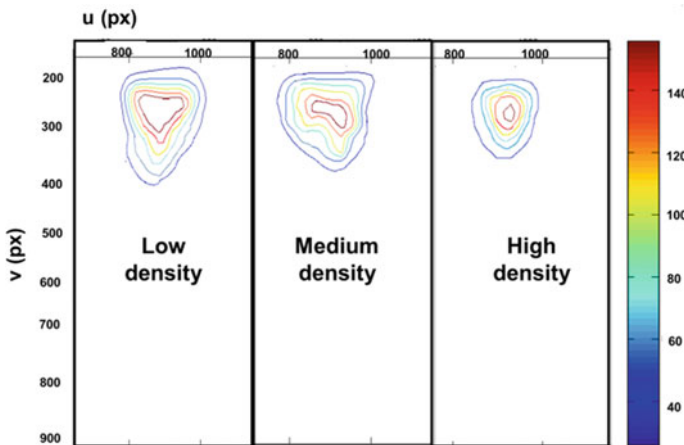


Fig. 8 Shear strain developed around soil under various low (15 kN/m³), medium (15.4 kN/m³) and high (16.2 kN/m³) densities

Table 3 Safe bearing capacity of driven piles

Infill density (kN/m ³)	SBC(kN) (IS 2010)* plugged condition	SBC(kN) (IS 2010)	SBC(kN) (Sangseom et al. 2015)
15.0	13.55	7.66	15.62
15.4	19.71	9.61	22.31
16.2	25.87	10.35	27.74

The simulation results are in agreement with the soil plugging results as presented in Fig. 8. The soil plug formed inside the pile prevents additional soil from entering the pile thereby allowing less displacement (strain) of soil around and beneath the pile.

5.4 Variation of Safe Bearing Capacity of Hollow Piles in Sand

From Table 3, it is observed that the bearing capacity predictions made by IS and API methods are less in comparison to the predictions made by Sangseom et al. (2015). In IS method, even for a partially plugged hollow pile, bearing pressure is assumed to act over the entire cross section of the pile tip. However, the N value recorded will not be in conjunction with the solid pile. This may cause an underestimation of bearing pressure. In API method, the skin friction which is function of soil pile friction angle is mainly dependent upon the density of the infill (0.27 for very loose sand to 0.70 for very dense sand). This narrow range of variation of the soil pile friction angle will lead to conservative bearing capacity estimation over other methods. The bearing capacity calculations proposed by Sangseom et al. (2015) is more realistic since the soil plug length is considered for the estimation of inner shaft friction.

The current code of practice emphasis on considering partially plugged pile as a solid pile in bearing capacity calculations which may not be realistic. Though many researchers have carried out extensive studies on soil pile interaction, bearing capacity calculations for partially plugged pile remains unexplored. Hence research studies needed to be carried out which help in developing design guidelines for partially plugged piles.

The bearing capacity of piles is calculated using IS (2010). Table 3 shows the bearing capacity values of hollow piles with respect to infill density with IS, API, and empirical equations taken from literature (Sangseom et al. 2015).

6 Conclusions

With increase in density of infill, there is an increase in number of blows with penetration depth. Also, there is a reduction in shear band formation in both vertical

and horizontal direction for hollow pile with increase in density. For hollow piles, driven in the field, rarely the plug length extends to the full length of inner shaft. There are no codal provisions to determine the bearing capacity of such partially plugged hollow piles. In the present study, bearing capacity estimated using the empirical equation proposed by Sangseom et al. (2015) is more realistic than the one estimated using codal recommendations.

References

- Al-Ansari (1999) Capacity and behavior of steel pipe piles in dry sand. PhD dissertation, University of Texas, USA
- American Petroleum Institute (API) (1993) Recommended practice for planning, designing and constructing of fixed offshore platforms—load and resistance factor design: RP2A-LRFD. 20th ed. American Petroleum Institute, Washington (DC), pp 66–68
- Arshad MI, Tehrani FS, Prezzi M, Salgado R (2014) *Geotechnique* 64(7):551–569
- Brucy F, Meunier J, Nauroy JF (1991) Behaviors of pile plug in sandy soils during and after driving. In: International proceedings of 23rd annual offshore technology conference, Houston, vol 1, pp 145–154
- De Nicola A, Randolph MF (1997) The plugging behaviour of driven and jacked piles in sand. *Geotechnique* 47(4):841–856
- Fattah M, Al-Soudani, Wissam (2015) Bearing Capacity of open ended pipe piles with restricted soil plug. *Ships Offshore Struct* 5(11):501–516
- Froy P, Colliat JL, Nauroy JF (1993) Bearing capacity of driven model piles in dense sands from calibration tests. In: Proceedings of the 25th annual offshore technology conference, Houston, OTC vol 7194, 655–665
- IS 2911 Part 1 (2010) Design and construction of pile foundations—code of practice
- Klos J, Tejchman A (1981) Bearing capacity calculation for pipe piles. In: International proceedings of the 10th international conference on soil mechanics and foundation engineering, Stockholm, June 1519, vol 2, pp 751–754
- Lehane BM, Gavin KG (2001) Base resistance of Jacked pipe piles in sand. *J Geotech Geoenvironmental Eng ASCE* 127(6):473–479
- Meyerhof GG (1956) The ultimate bearing capacity of foundations. *Geotechnique* 2(4):301–332
- Murff J, Raines R, Randolph M (1990) Soils plug behaviour of piles in sand. In: Offshore technology conference, Houston, TX, pp 25–32
- Ni QC, Hird IG (2010) Physical modelling of pile penetration in clay using transparent soil and particle image velocimetry. *Geotechnique* 2(60):121–132
- Paik K, Salgado R (2003) Determination of bearing capacity of open-ended piles in sand. *J Geotech Geoenvironmental Eng* 129(1):46–57
- Parkin AK, Lunne T (1982) Boundary effects in the laboratory calibration of a cone penetrometer for sand. In: Proceedings of 2nd European symposium on penetration testing, Netherlands
- Raines RD, Ugaz OG, O' Neill MW (1992) Driving characteristics of open-toe piles in dense sand. *ASCE J Geotech Eng* 118(1):72–88
- Randolph MF, Leong EC, Houlsby GT (1991) One-dimensional analysis of soil plugs in pipe piles. *Geotechnique* 41(4):587–598
- Sangseom J, Junyoung KN, Jinh W, Kwangwoo L (2015) Bearing capacity analysis of open-ended piles considering the degree of soil plugging. *Soils Found* 55(5):1001–1014
- Sreelakshmi G, Asha MN, Divya Viswanath (2017) Investigations on Pile-Soil interaction using image analysis. In: Proceedings of second Pan-American conference on unsaturated soils 2017, Dallas, Texas, pp 466–476

- Stanier SA, Blaber J, Take WA, White DJ (2015) Improved image-based deformation measurement for geotechnical applications. *Can Geotech J* 2016 53(5):727–739
- Szechy CH (1959) Tests with Tubular Piles. *Acta Technica* 24:181–219
- Tomlinson MJ (1994) *Pile design and construction practice*, Harlow. Prentice Hall, England
- Tran M (2005) Installation of suction caissons in dense sand and the influence of silt and cemented layers, PhD thesis
- White DJ, Bolton MD (2004) Displacement and strain paths during plane-strain model pile installation in sand. *Geotechnique* 54(6):375–397
- Wood DM, Crew A, Taylor C (2002) Shaking table testing of geotechnical models. *Int J Phys Model Geotech* 1:1–13

Experimental Analysis and Validation Techniques of Piled-Raft Foundation System



R. Vignesh and M. Muttharam

Abstract Due to urbanization, the high-rise building has become a common and growing phenomenon in all over the world. If a raft foundation does not meet the design requirement by itself, then the addition of a pile (piled-raft foundation system) may be possible with the raft. In this paper, the design of piled-raft foundation system has been carried out as the approximate assessment of the required number of piles, asses where piles may be required and refine piling requirements on their locations. The design strategies for the design of piles have been shown, and it has been demonstrated with the effective and efficient foundation can be designed by utilizing the significant capacity of pile. These strategies improve both the ultimate load capacity of the pile and settlement or differential settlement of the raft. In this analysis using of pile as settlement reducer and the condition in which the approach may be successful is derived. The characteristic behavior of the piled-raft foundation system has been considered in the effect of number of piles, nature of loading, raft thickness, and effect of load level on settlement. The behavior of piled raft is determined by complex soil-structure interaction effects, and understanding of these effects is useful for the reliable design of such foundations. The study brings out the effects of number of piles, pile length, raft thickness, and pile configurations; along with the soil-structure interaction by mean of the numerical modeling validation is compared with the measured and computed results.

Keywords Pile-Raft foundation · Pile configuration · Raft thickness · Numerical modeling on pile raft · And Load-settlement curve

R. Vignesh (✉) · M. Muttharam
Department of Civil Engineering, CEG, Guindy-Anna University, Chennai, Tamil Nadu, India
e-mail: vignesh.jec@gmail.com

M. Muttharam
e-mail: muttharam@annauniv.edu; muttharam@gmail.com

© Springer Nature Singapore Pte Ltd. 2020
M. Latha Gali and P. Raghuvver Rao (eds.), *Construction in Geotechnical Engineering*, Lecture Notes in Civil Engineering 84,
https://doi.org/10.1007/978-981-15-6090-3_20

1 Introduction

The performance of any foundation is to transmit the load to the soil so as to provide safety, reliability, and serviceability to the structure. Current practice is to provide a deep foundation, when the shallow foundation isn't sufficient to provide adequate safety and reliability. However, a combination of the shallow and deep foundation can be a price effective design approach. The pile-raft foundation is a grouping of a deep pile group and raft foundation, which has increased in very recent years.

It is evident from the available literature, the piled-raft foundation was constructed about fifty years past and also the attempt to capture its behavior was started within the early eighties, that has intense within the previous few years, however no appropriate design strategy has been formulated. This is often attributable to the complex interactions among the raft, pile, and soil, which is three dimensional in nature and cannot be captured by any analytical technique so far developed. With the advancement of engineering and numerical code, the researchers are currently attempting to model the complicated behavior of pile-raft foundation.

2 Literature

2.1 *Experimental Review*

According to Burland et al. (1977), the standard design methodology for the piled-raft foundation substructure suggests that the pile bears an interconnected load with the raft's input becoming ignored. This method is actually too restrictive as the product of the raft is in direct contact with the surface and therefore bears a significant portion of the load. In the case study of the piled-raft method in clay, Shukla et al. (2013) indicated that the building load, which causes stress within the pre-consolidated clay structure, is borne by piles in creeping loading and therefore the remaining load is held by the raft.

Horikoshi et al. (2003) reported that the settlement-reducing piled strategy is built to mistreat excess piled-raft systems.

Dauids (2008) shown that the various superstructures are distributed among raft and piles, carrying piles around 50–80% of the total load.

To examine the feasibility of the techniques endorsed by the elastic continuum principle for estimation of conformity with piled-foundation subjected to vertical loading.

Wiesner and Brown (1980) worked on raft foundation models in consolidated clay. Measured settlements, strains, and bending moments within the raft have been identified during this research. They suggested that the predictions of the hypothesis based upon the fact that soil can be a linearly elastic continuum would provide suitable predictions of piled-raft foundation behavior.

Cooke (1986) presented model test results on the foundation of piled raft. He contrasted with that of an unpiled raft and free-standing piled group with the behavior of a piled-raft foundation. Cooke (1986) noted that the distribution of loads between piles in a piled raft is reliant on the pile quantity and spacing. He noticed that the middle of the foundation of the raft is greater than that of the raft's sides.

Horikoshi and Randolph (1996) carried out centrifugal experiments on piled-raft foundations models to research the settling of piled-raft foundations on clay soil. They noticed that sometimes a small group of piles might significantly reduce the proportional raft settlement. This study suggested that the bearing efficiency of the system could be significantly increased by a small cap on a single pile.

Horikoshi et al. (2003) carried out centrifugal testing of piled-raft foundation models on sandy soil subject to vertically and horizontally loading. They evaluated the impact on the actions of piled-raft foundations of the rigidity of the pile head relation. These results showed that whenever the cap is in contact with soil the pile's strength increases due to the improvement in the confining stress around the pile. Horikoshi et al. (2003) reported that the piled-raft ultimate horizontal ability is greater than the unpiled-raft foundation.

Lee and Chung (2005) conducted tests on piled-raft foundations models to analyze the effect of pile installation and interaction between the raft and also the piles on the behavior of piled-raft system. They found that cap-soil-pile interaction impact is influenced by pile location and spacing. They determined that pile installation may compensate the decrease in cap capacity due to cap-soil-pile interaction effect.

Fioravante et al. (2008) conferred results of extensive centrifuge tests modeling of a rigid circular piled-raft on sand soil to assist in finding out the role of piles as settlement reducers and to quantify the load sharing between the raft and piles. They determined that raft settlement decreases as the number of piles will increase. The results showed that displacement piles are more effective in reducing the settlement of the raft than the non-displacement piles. Fioravante et al. (2008) found that the contribution of the raft starts when the piles approach the ultimate capability. They also determined that piled-raft stiffness increased with the increase within the number of piles supporting the raft.

2.2 Finite Element Method Review

One of the effective tools to evaluate piled rafts is the finite element method. The dissertation is required for both the structure and the soil foundations. The Hooper (1973), which used an axis symmetrical model of eight noded isoperimetric components, provided an early example of the study of a piled raft (The Hyde Park Barracks). In comparison, the relative rigidity of the pile group was approximated to the degree that the condensed rows of piles were based on a continuous annulus with a total rigidity equal to the overall rigidity of the piles.

Chow and Teh (1991) had presented a numerical method for examining the behavior, in a non-homogeneous soil of the static piled raft.

Liu and Novak (1991) used the approach for finite elements to analyze the output of a single-center pile raft.

The study of a circular piled raft made in Cairns was given by Wiesner (1980). The raft was viewed as a thin elastic plate and based on plate bending finite elements.

Clancy and Randolph (1993) stated a piled-raft foundation strategy for tall buildings.

Smith and Wang (1998) suggested the use of iterative methods using a finite element approach to analyze the behavior of a non-uniformly loaded piled raft.

Prakoso and Kulhawy (2001) studied the foundation of the piled raft through the use of finite element model linear elastic and non-linear strain planes, which included the evaluation of a piled three-dimensional raft in the form of a two-dimensional raft.

In the case of a rigid circular piled-raft models in over-consolidated clay Fioravante (2011) have conducted centrifugal experiments, which have shown that the load allocation under a rigid piled raft is not compatible within the working load range which is consistent with a linear/elastic analysis.

2.3 Theoretical Studies

Ta and Small (1996) developed a method of analysis for piled-raft foundations on layered soil which takes into account the interaction among the raft, piles, and soil by using the finite layer method for the analysis of the soil and the finite element method for the analysis of the raft to avoid the cost of a rigorous three-dimensional analysis. They claimed that their method can be used for the analysis of a raft with any geometry or stiffness because the raft is considered as a thin elastic plate and can be used for rafts on isotropic or cross-anisotropic horizontally layered soil with piles randomly distributed beneath the raft. They also found that the relative thickness and stiffness of soil layers can also influence the load distribution along the shafts of piles in piled-raft foundations. Some simplifications are needed to avoid the excessive computing time and other limitations when developing analysis methods of large piled-raft foundations.

Ta and Small (1997) proposed an approximate numerical method of analysis to estimate the influence factors for piled-raft foundations that can reduce computer run time. According to a numerical analysis, Ta and Small (1997) observed that the portion of the load carried by the piles increases and that by the raft decreases as the bearing stratum becomes stiffer.

Russo (1998) proposed an approximate numerical method (hybrid model) for the analysis of piled rafts which accounts for the non-linearity of the unilateral contact at the raft-soil interface and the non-linear load-settlement relationship. Russo (1998) stated that because piles are used as settlement reducers and their ultimate load capacity may be reached, non-linear analysis should be considered for piled-rafts analysis. Russo (1998) reported that most of the numerical analysis efforts have considered solving either simple axial-symmetric or plane strain problems to reduce the huge computational efforts of analyzing large piled foundations. He claimed that

introducing some approximations to the numerical methods can assist in solving such a problem.

Mendonca and de Paiva (2000) introduced a boundary element method for analyzing piled-raft foundations which accounts for the interaction among the raft, the piles, and the soil. The method developed by Mendonca and de Paiva (2000) can be used for analyzing piled-raft foundations with rigid or flexible caps. In the analysis method proposed by Mendonca and de Paiva (2000) each pile in the group, the soil, and the raft were modeled as a single element, an elastic linear homogeneous half space, and a thin plate, respectively.

Prakoso and Kulhawy (2001) used simplified linear elastic and non-linear (elastic-plastic) 2-D plane strain finite element models to predict the performance of piled-raft foundations and proposed a displacement-based design procedure for piled rafts based on this analysis. They used PLAXIS (software based on finite element method) in their study and they claimed that a 2-D plane strain analysis could yield satisfactory results for analyzing the piled-raft system without excessive time for modeling and computing.

Poulos (2001) introduced a simplified analysis method for piled-raft foundations as a tool for preliminary design of such foundations. Other solutions for the limitations of numerical modeling techniques were suggested by using hybrid models. Small and Zhang (2002) presented a method of analysis for piled-raft foundations on layered soil subjected to vertical loads, lateral loads, and moments by using the finite layer theory to model the layered soil and the finite element theory to model the piles and raft. El-Mossallamy (2002) employed a mixed technique of the finite element and boundary element methods to develop a numerical model which accounts for the raft stiffness, the non-linear behavior of the piles, and the slip along the pile shafts for analyzing piled-raft foundations.

Mendonca and de Paiva (2003) presented a static analysis of piled-raft foundations using a combination of finite element and boundary element methods in which interaction between soil, flexible raft, and piles was considered. Kitiyodom and Matsumoto (2003) developed a simple analytical method by using a hybrid model for piled-raft foundations embedded in non-homogenous soil considering the effect of vertical and lateral loads.

Reul (2004) conducted a rigorous numerical study using the three-dimensional finite element analysis to study the behavior of piled-raft foundations in over-consolidated clay. He used the finite element method to model the soil and foundation to obtain detailed information about soil-structure interaction. Reul (2004) stated that it is important to understand the interaction among the piles, the raft, and the soil which controls the behavior of piled-raft foundations. Reul (2004) observed that pile-raft interaction leads to an increase in the skin friction with an increase of the load or increase of the settlement.

Wong and Poulos (2005) presented a simplified method to estimate the pile-to-pile interaction factor between two dissimilar piles based on a parametric study which was conducted using the computer program GEPAN developed by Xu and Poulos (2000). The computer program GEPAN is based on the boundary element analysis. They claimed that this method can be beneficial for predicting the settlement

behavior of pile groups or piled-raft foundations with dissimilar piles. Garcia et al. (2005) studied piled-raft foundations supported by clay soil using a visco-hypoplastic constitutive law in a three-dimensional finite element analysis. Vasquez et al. (2006) used three-dimensional non-linear finite element analysis to predict the response of piled-raft foundations taking into account the non-linear behavior of the soil while linear elastic behavior was assumed for the raft and piles.

3 Methods of Analysis

Several methods for deciding the relationship of the piled-raft combination were available. It includes simplified methods of estimation, computer-based approaches, and more rigorous computer-based processes. The simplified methods of estimation are analytical methods with various simplifications, particularly with regard to the soil profile and the load. The raft is designed like a strip and the soil and piles are based on springs of varying stiffness in approximate computer methods. Computer-based, more rigorous approaches comprise different model methods such as boundary element approach, boundary elements combined with finite element analysis, a single strain problem finite element analysis, or an axisymmetrical issue. The main focus of this work is computational modeling of PLAXIS 3D applications relative to studies.

4 Soil Properties

An experimental testing program was conducted to determine the behavior of piled-raft foundation installed in sand. Sieve analysis for the sand soil was carried out. Physical properties, shear strength, and compressibility parameters are shown in Table 1.

5 Tank Description

In this analysis, on a plain raft and piled raft in identical homogeneous loose sand conditions, a small laboratory experiment was carried out. The sand characteristics used on the foundation medium were studied and recorded.

A square tank scale of 1000 mm \times 1000 mm \times 1000 mm was carried out for the laboratory prototype modeling as shown in the arrangement of the tank in Fig. 1. The piles used for this analysis were 1 \times 1, 2 \times 2, and 3 \times 3 pile setups. Studies have shown that settlement is substantially reduced relative to that of the plain raft foundation by the piled-raft foundation in sand.

Table 1 Soil properties

Sl. no.	Example description	Values
1.	Specific gravity	2.63
2.	Coarse sand	4.3
3.	Medium sand	60.7
4.	Fine sand	21.7
5.	Uniformity co-efficient	2.53
6.	Co-efficient of curvature	0.73
7.	Classification of sand	Poorly graded sand
8.	Maximum dry unit weight	17.59 kN/m ³
9.	Minimum dry unit weight	15.40 kN/m ³
10.	Maximum void ratio	0.71
11.	Minimum void ratio	0.46
12.	Unit weight	15.71 kN/m ³
13.	Relative density	26.63%
14.	Angle of internal friction	30°
15.	Module of elasticity	10.22 MN/m ²

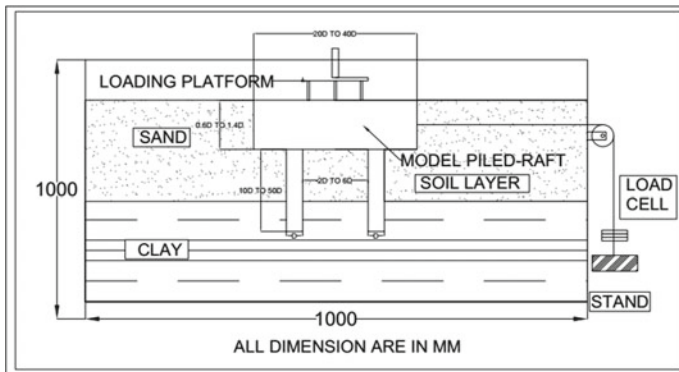


Fig. 1 Schematic diagram of the tank

6 Parametric Study

Parametric study is depending on the load sharing and the load-settlement relationships are the most important aspects in designing piled-raft foundations. El-Mossallamy et al. (2009) stated that the main criterion, which governs the design of piled-raft foundations, concerns the load sharing between the raft and piles and the effect of additional pile support on the foundation settlement. In this study, the effect of some parameters on the load-settlement relationship and the load sharing

between the raft and the piles was investigated. The aim of this study is to identify the very important parameters which affect the performance of piled-raft foundations and then to develop a model to predict the settlement and the load sharing between the raft and the soil.

Identifying the important parameters which significantly affect the performance of piled-raft foundations can assist in optimizing the design of such foundations. Therefore, studying the effect of different design parameters on the behavior of piled-raft foundations was carried out. This study focused on the effect of some parameters on the load-settlement relationship and the load sharing between the raft and piles of piled-raft foundations. The effect of the selected parameters on the load-settlement relationship will be investigated at small and large settlements. The tests in this study were carried out using the developed PLAXIS 3D model. Three-pile arrangements were considered in this study. Square piled rafts supported by 1, 4, and 9 piles, as shown in Fig. 2, were studied. The parameters considered in this study can be summarized in Table 2 as follows.

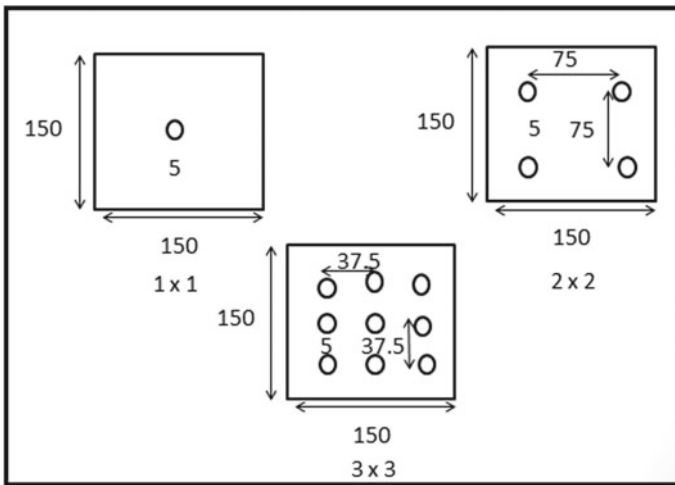


Fig. 2 Piled-raft model* 1 × 1, 2 × 2, and 3 × 3 pile

Table 2 Parameter validation study

Parameter name	Range of parameter				
Pile diameter D (mm)	3	4	5*	6	7
Pile spacing (mm)	10D	20D	30D*	40D	50D
Raft width (mm)	20D	25D	30D*	35D	40D
Raft thickness (mm)	0.6D	0.8D	D*	1.2D	1.4D

* indicates experimental model dimension is taken and analysed as shown in Fig. 2

7 Experimental Program and Numerical Validation

In this experimental setup, model pile is based on the mild steel rod having diameter 5 mm and length 150 mm, forming configurations 1×1 , 2×2 , 3×3 , and the piled-raft model used in the study. The piles are rigidly fixed to the raft by welding. The property of mild steel is shown in Table 3.

7.1 Loading Setup

The load frame consists of proving ring of 2kN capacity with 0.0025kN accuracy for load determination and two numbers of 25 mm dial gauge with 0.01 mm sensitivity for settlement prediction. The entire loading setup is shown in Fig. 3.

Table 3 Properties of mild steel rod

SI. no.	Properties	Values
1	Yield stress (N/mm ²)	411.21
2	Ultimate stress (N/mm ²)	432.61
3	Modulus of elasticity (N/mm ²)	2.34×10^5



Fig. 3 Loading frame setup

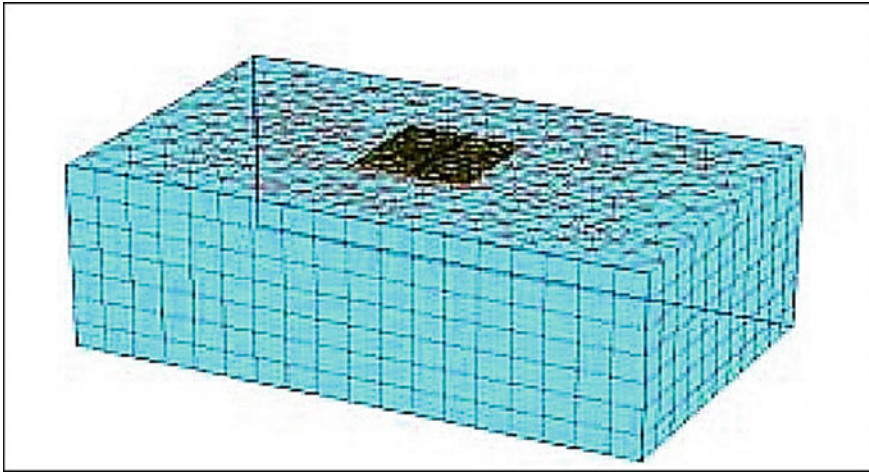


Fig. 4 Meshing

8 Numerical Validation Using Plaxis 3D

During the complete research process, vertical load was introduced at a constant loading pace of 1 mm/min. The remedy for each rise in load was calculated by means of dial gauges until the settlement is smaller than 0.02 mm/min. For each design of the piled-raft foundation, the load vs. settlement graph was compiled.

The values obtained are measured and calibrated using the Plaxis 3D tools and each configuration is shown in a cross section under Figs. 4, 5, 6, 7, and 8.

9 Comparison of Experiment and Plaxis 3D Result

The experimental study and FEM analyses reveal that the load-settlement difference across experiments and PLAXIS 3D is less than 15% up to the ultimate load, with FEM analytical review underestimating settlement and overestimating the ultimate load in contrast with experimental study. The load-settlement heterogeneity between experimental studies is 15% up to the final load, as well. The relation between the research sample and PLAXIS 3D is demonstrated in Figs. 8, 9, 10, and 11. In all these examples, it has been observed that the computational analysis has shown somewhat more load than the experimental work.

A contrast of raft load versus piled-raft load and raft with various configurations such as PR 1 × 1, PR 2 × 2, and PR 3 × 3 is shown in Fig. 12. The work-load capacity of the piled-raft system is significantly increased as the quantities of piles are increased.

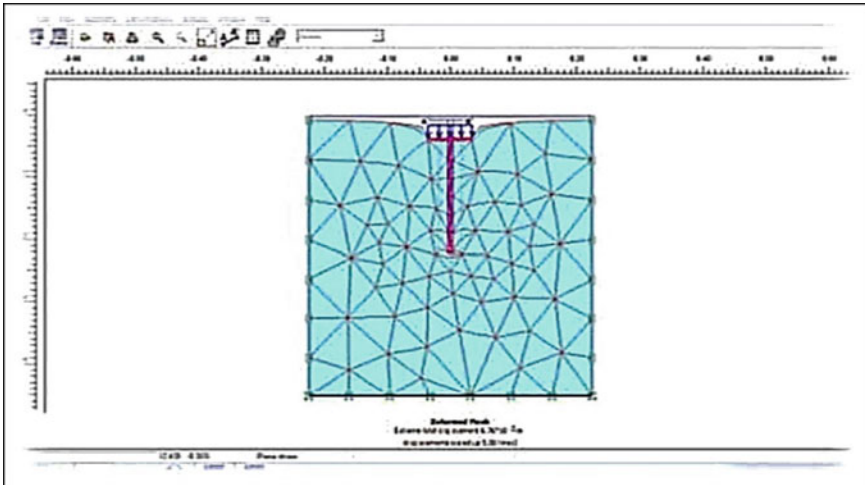


Fig. 5 Model piled raft 1 × 1

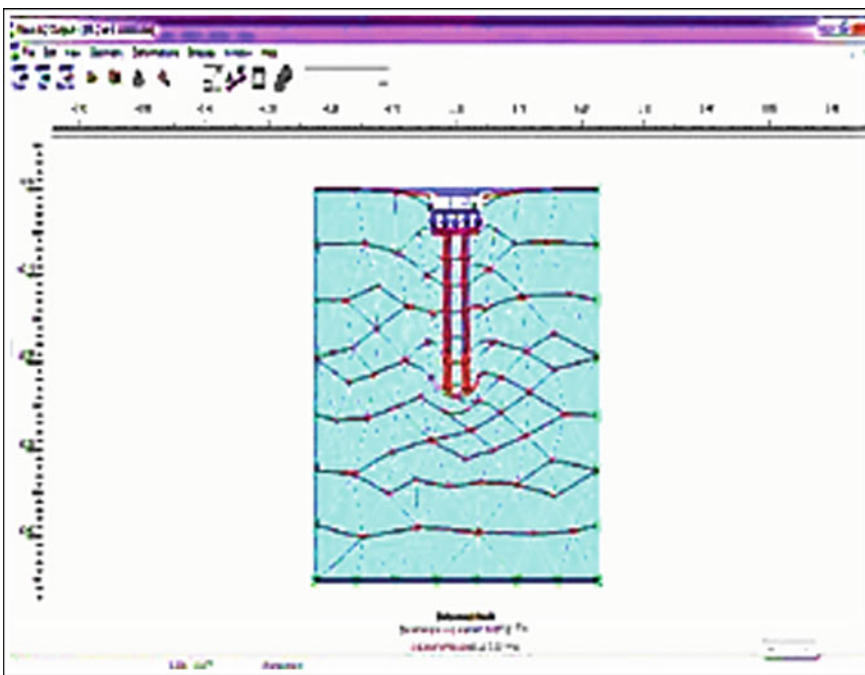


Fig. 6 Model piled raft 2 × 2

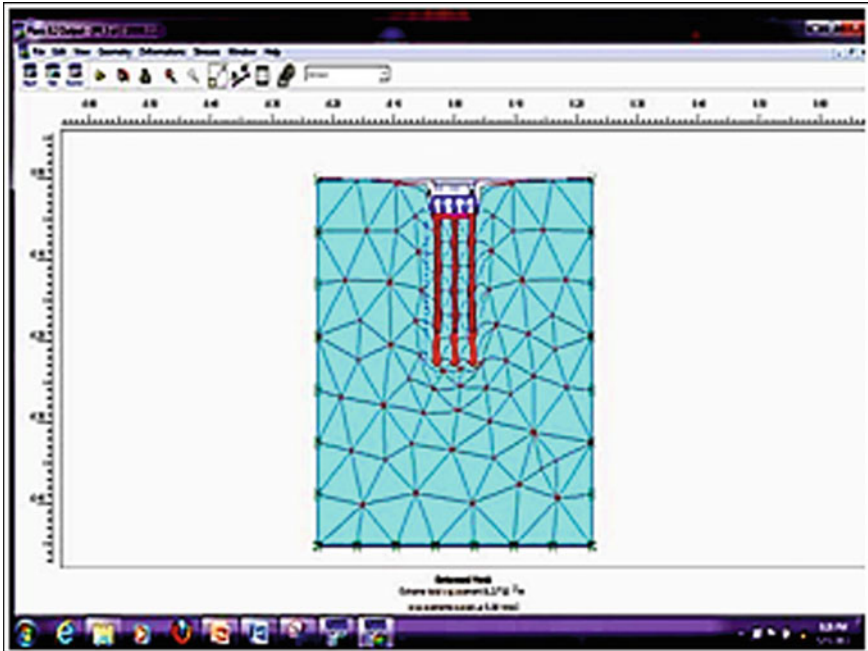
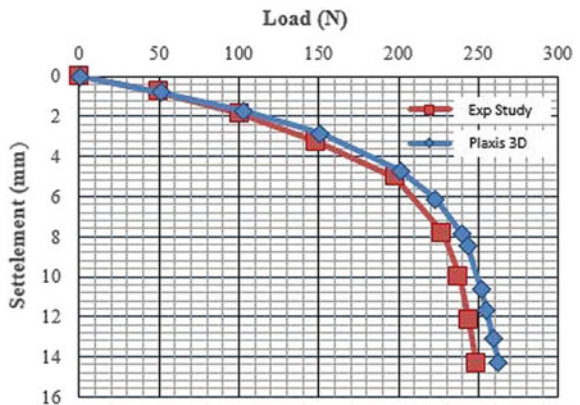


Fig. 7 Model piled raft 3 × 3

Fig. 8 Plain raft load versus settlement curve



10 Conclusion

It could be inferred on the basis of the current studies that the raft load rate in the piled-raft configuration is around 38% in sand. With the pile length and quantity decrease, the proportion of load borne by the raft increases. The raft load increases by up to 37% as the length of the piles reduces. The number of piles borne by the

Fig. 9 PRF 1×1 load versus settlement curve

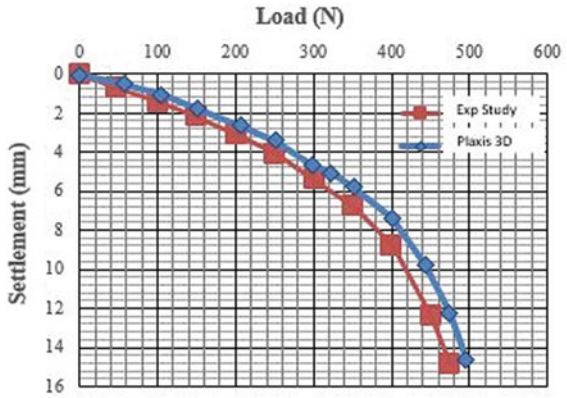


Fig. 10 PRF 2×2 load versus settlement curve

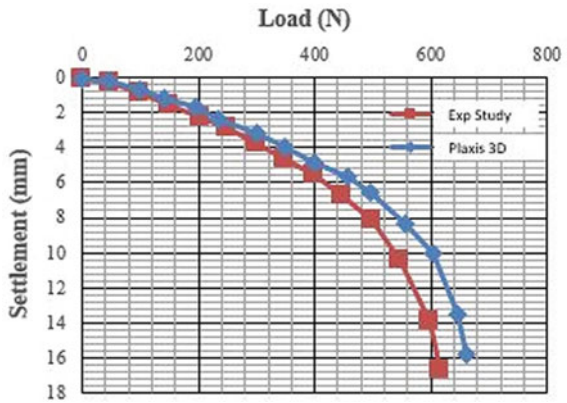


Fig. 11 PRF 3×3 load versus settlement curve

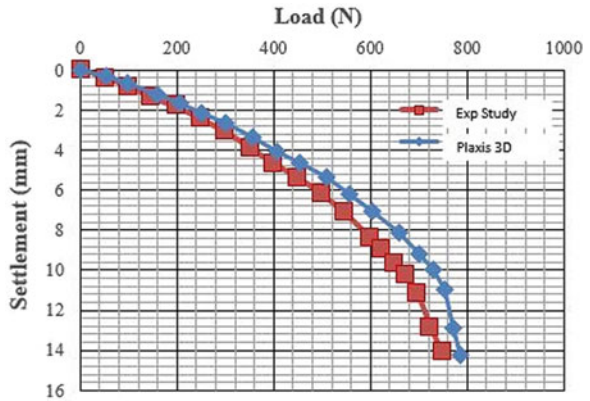
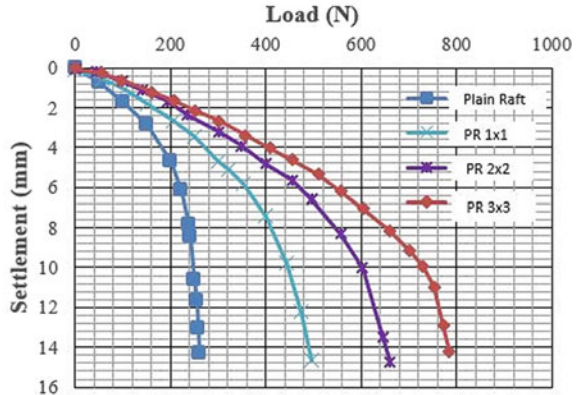


Fig. 12 PRF load versus settlement (Plaxis 3D Study)



raft raised to 57% as the number of piles decreased. With the settlement ratio S/B below or equivalent to 0.9, the load carried by piled raft is greater than the sum of raft's load and the pile load for each settlement ratio. The use of the piled raft as a settlement reducer is very helpful. For the best results, the piled raft at $S/B = 0.9$ should be designed. For pile rafts with 9 piles and the total load of piles raft with 4 piles is 27% higher. In this analysis, the computational model appears to work in a fairly reasonable direction, including the settlement magnitude. It reveals that the PLAXIS 3D model can be an efficient time tool for an advanced 3D model. The study of finite elements helped to better understand the piled-raft soil system's failure pattern.

References

- Chow YK, Teh CI (1991) Pile-cap-pile-group interaction in non-homogeneous soil. *J Geotech Eng* 117(11):1655–1667
- Clancy P, Randolph F (1993) An approximate analysis procedure for piled raft foundations. *Int J Numer Anal Meth Geomech* 17(12):849–869
- Cooke RW (1986) Piled raft foundations on stiff clays—a contribution to design philosophy. *Geotechnique* 36(2):169–203
- Davids A (2008) postcard from Dubai design and construction of some of the tallest buildings in the world. In: *Proceedings of the CTBUH 8 the world congress, 3–5 March, Dubai*
- EL-Mossallamy Y (2002) Innovative application of piled raft foundation in stiff and soft subsoil. *Deep Foundations, ASCE, Orlando, Florida*, pp 426–440
- El-Mossallamy Y, Lutz B, Duerrwang R (2009) Special aspects related to the behavior of piled raft foundation. In: *17 the international conference on soil mechanics & geotechnical engineering ICSMGE, Alexandria, Egypt*, pp 1366–1369
- Fioravante V (2011) Load transfer from a raft to a pile with an interposed layer. *Geotechnique* 61(2):121–132
- Fioravante V, Giretti D, Jamiolkowski M (2008) Physical modeling of raft on settlement reducing piles. In: *From research to practice in geotechnical engineering congress ASCE*, pp 206–229

- Garcia F, Lizcano A, Reul O (2005) Visco-hypoplastic model applied to the case history of piled raft foundation. In: *GeoCongress 2006*. ASCE, pp 1–5
- Horikoshi K, Randolph MF (1996) Centrifuge modelling of piled raft foundations on clay. *Geotechnique* 46(4):741–752
- Horikoshi K, Matsumoto T, Hashizume Y, Watanabe T, Fukuyama H (2003) Performance of piled raft foundations subjected to static horizontal loads. *Int J Phys Model Geotech* 2:37–50
- Burland JB, Broms BB, Demello V (1977) Behavior of foundation and structures. In: *Proceedings of the 9th ICSMFE*, Tokyo, pp 495–546
- Katzenbach et al (2003) Reducing the costs for deep foundations of high-rise buildings by advanced numerical modeling. *ARI Bull Istanbul Tech Univ* 53(2):9–18
- Lee S-H, Chung C-K (2005) An experimental study of the interaction of vertical loaded pile groups in sand. *Can Geotech J* 42:1485–1493
- Liu W, Novak M (1991) Soil-pile-cap static interaction analysis by finite and infinite elements. *Can Geotechn J* 28:771–783
- Mendonca AV, de Paiva JB (2000) A boundary element method for the static analysis of raft foundations on piles. *Eng Anal Bound Elem* 24:237–247
- Mendonca AV, Paiva JB (2003) An elastostatic FEM/BEM analysis of vertically loaded raft and piled raft foundations. *Eng Anal Bound Elem* 27:919–933
- Poulos HG (2001) Methods of analysis of piled raft foundations. A report prepared on behalf of technical committee TC18 on Piled Raft Foundations, International Society of Soil Mechanics and Geotechnical Engineering (2001)
- Prakoso WA, Kulhawy FH (2001) Contribution to piled raft foundation design. *J Geotech Geoenvironmental Eng* 127(1):17–24
- Reul O (2004) Numerical study on the behavior of piled rafts. *Int J Geomech ASCE* 4(2):59–68
- Russo G (1998) Numerical analysis of piled rafts. *Int J Numer Anal Meth Geomech* 22:477–493
- Shukla SJ, Desai AK, Solanki CH (2013) A dynamic behavioral study of 25 storey building with piled raft foundation with variable subsoil. *Int J Struct Civ Eng Res* 2(1):119–130 (2013)
- Small JC, Zhang HH (2002) Behavior of piled raft foundations under lateral and vertical loading. *Int J Geomech* 2(1):29–45
- Smith IM, Wang A (1998) Analysis of piled rafts. *Int J Numer Anal Methods Geomech*. 22:777–790
- TA LD, Small JC (1997) An approximate analysis for raft piled raft foundations. *Comput Geotech* 20(2):105–123
- Ta LD, Small JC (1996) Analysis of piled raft systems in layered soils. *Int J Numer Anal Methods Geomech* 20:57–72
- Vasquez LG, Wang ST, Isenhower WM (2006) Estimation of the capacity of pile-raft foundations by three dimensional non-linear finite element analysis. In: *GeoCongress 2006*. ASCE pp 1–6
- Wiesner TJ, Brown PT (1980) Laboratory tests on model piled raft foundations. *J Geotech Eng Div Proc Am Soc Civ Eng* 106(GT7):767–783
- Wong SC, Poulos GH (2005) Approximate pile-to-pile interaction factors between two dissimilar piles. *Comput Geotech* 32:613–618
- Xu KJ, Poulos HG (2000) General elastic analysis of piles and pile groups. *Int J Numer Anal Methods Geomech* 24:1109–1138

Prediction of Ultimate Uplift Capacity of Short Piles in Sandy Soils



R. M. Thejaswini, L. Govindaraju, and V. Devaraj

Abstract Short piles which are used for supporting the structural systems need to be checked for uplift capacity. In the present study, an attempt has been made to predict the ultimate uplift capacity of short piles embedded in sandy soils even when the piles are not subjected to uplift forces till their failure loads. A total of eight piles were tested with increasing pull out load increments; however the ultimate uplift capacity of these piles was estimated by the method suggested by modified Mazurkiewicz (1998). Based on these results, a comparative assessment on the ultimate uplift capacity of the piles has been made from the previous studies by Ireland (1975), Das (1983) and Chattopadhyay and Pise (1986) and Shanker et al. (2007). The results of the present study indicate that the ultimate uplift capacity of the piles is in close agreement with the expression proposed by Shanker et al. (2007).

Keywords Sandy soil · Short piles · Ultimate uplift capacity of pile

1 Introduction

Pile foundations are frequently used to transfer the super structure loads to the deeper strata. The piles which are used for supporting transmission line towers, tall chimneys, submerged platforms, and similar constructions need to be checked for uplift capacity, these uplift forces are caused due to overturning moments created by wind effects and seismic events. Moreover, uplift forces on piles are also exerted due to swelling of surrounding soils. In this study, an effort has been made to know the ultimate uplift capacity of short piles embedded in sandy soils even when the piles are not subjected to uplift forces till their failure loads. The field data used for installation of short piles to support solar panels at Krishnapuram Village, Trichy, Tamilnadu District, India, has been used in the present study. Field pull out tests were carried out on cast-in situ reinforced concrete (M25 grade) short piles having diameters of 300 mm and 350 mm and lengths varying from 1.35 m to 1.70 m (having embedment length

R. M. Thejaswini (✉) · L. Govindaraju · V. Devaraj
Department of Civil Engineering, UVCE, Bangalore University, Bengaluru, Karnataka, India
e-mail: thejaswini08@gmail.com

© Springer Nature Singapore Pte Ltd. 2020
M. Latha Gali and P. Raghuvver Rao (eds.), *Construction in Geotechnical Engineering*, Lecture Notes in Civil Engineering 84,
https://doi.org/10.1007/978-981-15-6090-3_21

315

to diameter 'L/d' ratio less than 5). A total of 8 piles were tested with increasing pull out load increments and corresponding movement of the pile was measured. But, all the piles were subjected to uplift loads until the pile movement was from 25 mm to 60 mm well before reaching the failure with an objective to calculate the allowable uplift capacity of the piles as per the guidelines. The ultimate uplift capacity of these piles was estimated by the method suggested by modified Mazurkiewicz (1998) and the results were compared with the previous studies by Ireland (1975), Das (1983), Shanker et al. (2007), Chattopadhyay and Pise (1986).

2 Previous Studies

Early studies showed that the uplift capacity of a pile depends on L/d ratios (Meyerhof 1973; Das 1983). Das (1983) proposed different formulae to calculate uplift capacity of piles having ratio $(L/d) \leq (L/d)_{cr}$, with respect to the relative density of compacted soil. However, recent studies have shown that the resistance of an uplift pile is a combination of both the skin friction resistance at the lower part of the pile and the shearing resistance mobilized on the failure surface in soil at the upper part of the pile (Chattopadhyay and Pise 1986; Shanker et al. 2007; Won-Pyo and Neatha 2014). Weeraya and Narinmarumdee (2013) have adopted modified Mazurkiewicz (1998) method to estimate uplift capacity of long piles in sand layers for the field data (Ammonia Storage Tank and Facilities project in Thailand) and the values were compared with Kulhawy et al. (1979), Das (1983) and Chattopadhyay and Pise (1986).

3 Present Studies

In this present study eight piles were considered which are having ratio L/d of 5. But $(L/d)_{cr}$ as per Fig. 1 amounts to 14.5 with relative density of 80%.

Approach adopted by Weeraya Chim-oye and Narin Marumdee (2013) to calculate the uplift capacity of piles has been followed in this study.

3.1 Characteristics of the Soil Layers in the Study Area

A total of seventeen bore holes were constructed to carryout subsoil investigation in the area. The first layer is of soft disintegrated weathered rock, and in some bore holes it is silty sand, and silty sand with gravels about 1.5 m thick. The lower layer is of soft disintegrated weathered rock. The engineering properties of each soil layer are summarized in Table 1 along with the details of 8 bored cast-in situ piles which were constructed with M25 grade concrete.

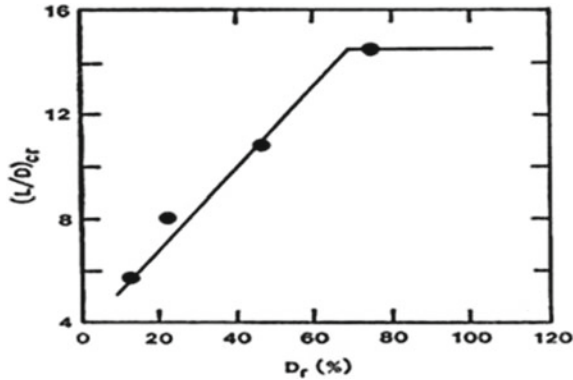


Fig. 1 Variation of (L/d)_{cr} with relative density of compaction (Das 1893)

Table 1 Details of soil and pile

Pile no.	N-value	Bulk density (kN/m ³)	φ	Pile diameter (m)	Pile length (m)
P1	>50	19.52	31	0.3	1.45
P2	>50	19.52	31	0.35	1.5
P3	>50	19.03	32	0.35	1.5
P4	37	19.32	33	0.3	1.35
P5	>50	19.71	31	0.35	1.35
P6	37	19.32	33	0.35	1.7
P7	>50	19.71	31	0.3	1.5
P8	>50	19.71	32	0.35	1.5

3.2 Pile Load Tests

The pile load tests were performed as per IS: 2911(Part-4)–1985. Piles were tested with increasing pull out load increments and corresponding movement of the pile was measured. But the piles were not tested to failure. Table 2 gives details such as the extent of load applied and their corresponding displacements. The safe load has been computed as 2/3 of the load in which the total displacement is 12 mm.

3.3 Evaluation of Ultimate Uplift Capacity of Pile

In the present study as the piles were not tested for their full capacity to attain failure, modified Mazurkiewicz (1998) method has been adopted to evaluate uplift capacity of piles. Figure 2a to h shows the computation of net ultimate uplift capacity of these piles.

Table 2 Summary of the test results

Pile no.	Extent of load applied (kN)	Load corresponding to 12 mm displacement (kN)	Safe load (kN)
P1	43.59	25.99	17.26
P2	49.54	27.47	18.34
P3	57.46	29.43	19.62
P4	43.59	19.62	13.04
P5	49.54	25.99	17.26
P6	59.44	35.32	23.544
P7	47.55	29.43	19.62
P8	47.55	23.544	15.69

Table 3 shows the summary of the assessed values of net ultimate uplift capacity of piles by modified Mazurkiewicz (1998) method.

4 Comparative Study

In order to compare the predicted net ultimate uplift load, the other alternative methods proposed by other researchers were also adopted and are as follows.

Ireland (1975) proposed an equation for predicting the net ultimate uplift capacity of piles in sandy layer

$$P_o = K \gamma_v^1 A_s \tan \phi \tag{1}$$

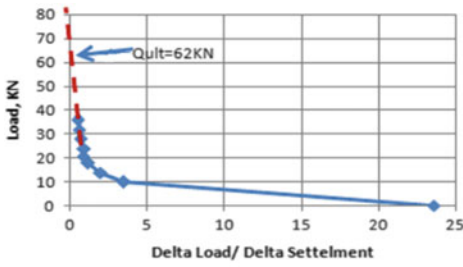
where P_o is the net ultimate uplift capacity, K is the lateral earth pressure co-efficient, γ_v^1 is the average effective overburden pressure and A_s is the surface area of the pile in contact with sand and ϕ is the angle of friction.

Das (1983) proposed different formulas for predicting ultimate capacity of the piles having the length $L \leq L_{cr}$ and $L \geq L_{cr}$ which are as given in Eq. 2 and 3 respectively.

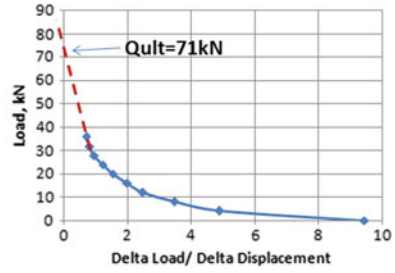
$$P_o = \frac{1}{2} \pi d \gamma L^2 K_u \tan \delta \tag{2}$$

$$P_o = \frac{1}{2} \pi d \gamma L_{cr}^2 K_u \tan \delta + \pi d \gamma L_{cr} K_u \tan \delta (L - L_{cr}) \tag{3}$$

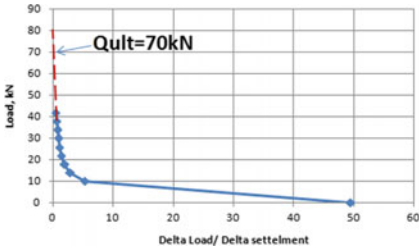
where γ is the effective unit weight, δ is the angle of pile friction and K_u is the uplift Co-efficient which depends on friction angle (ϕ).



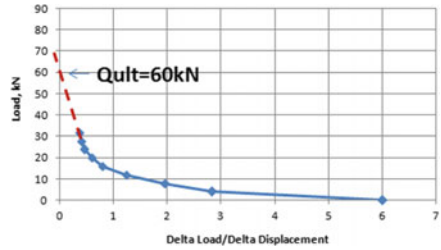
(a) Pile P1



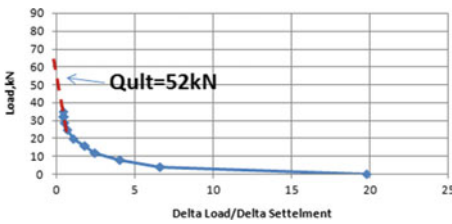
(b) Pile P2



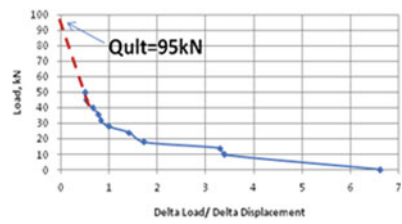
(c) Pile P3



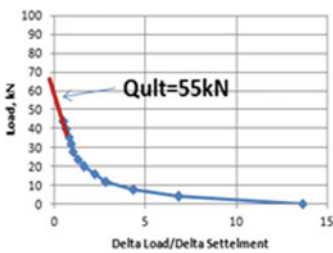
(d) Pile P4



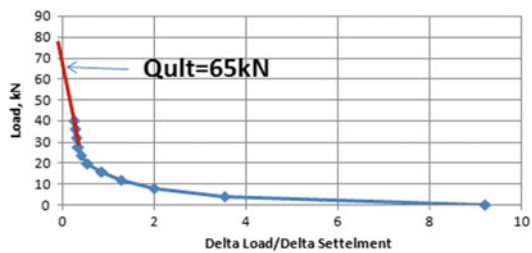
(e) Pile P5



(f) Pile P6



(g) Pile P7



(h) Pile P8

Fig. 2 Evaluation of net ultimate uplift capacity of piles (modified Mazurkiewicz 1998)

Table 3 Net ultimate uplift capacity of pile

Pile no.	Extent of load applied (kN)	Net ultimate uplift load (kN)
P1	39.63	62
P2	49.54	71
P3	46.46	70
P4	36.36	60
P5	49.54	52
P6	59.44	95
P7	47.55	55
P8	47.55	65

Chattopadhyay and Pise (1986) proposed a formulae to predict net ultimate uplift capacity of piles which is as given in Eq. 4.

$$P_{U_{net}} = A_1 \gamma \pi d L^2 \tag{4}$$

where L is the length of the pile, d is the diameter of the pile and A_1 is the net uplift capacity factor which depends on the angle of pile friction (δ) and slenderness ratio (λ).

The results of the net ultimate uplift load of piles computed by modified Mazurkiewicz method (1998) were compared with the above methods and summarized as in Table 4.

From the above Table 4, it is seen that the net ultimate capacity values calculated from theoretical expressions are not in the line with the predicted values from modified Mazurkiewicz method (1998).

Shankar et al. (2007) have clearly discussed about piles having different (L/d) ratios, they classified piles into two categories having $L/d \leq 20$ and $L/d > 20$. They also proposed an expression to calculate ultimate uplift capacity of piles. For the

Table 4 Comparison of ultimate uplift capacity (kN)

Pile no.	Ireland (1975)	DAS (1983)	IS: 2911 (Part-4)-1985	Chattopadhyay and Pise (1986)	Modified Mazurkiewicz Method (1998)
P1	21.25	21.88	27	28	62
P2	26.53	28.26	27	31	71
P3	30.71	29.39	31	31	70
P4	24.24	20.55	20	24.18	60
P5	18.98	18.11	25	24.7	52
P6	44.84	44.46	36	44.52	95
P7	12.09	8.58	30	11.3	55
P8	12	7.95	30	11	65

sake of simplicity, they assumed the failure surface is to be a truncated cone with the edges passing through the tip of the pile at an angle of β with respect to the vertical axis of the pile as shown in Fig. 3.

From their experimental results the net ultimate uplift capacity is obtained when the angle β is equal to $\phi/4$. Further Won-Pyo and Neatha (2015) also adopted the same failure theory and proposed their expression and concluded stating that net ultimate uplift capacity is obtained when angle β is equal to $\phi/2$. From these conclusions, it is clear that angle β plays a very important role in predicting ultimate uplift capacity of pile. Hence ultimate uplift capacity of piles for various values of angle β i.e. from $\phi/4$ to ϕ , were estimated using Shankar et al. (2007) formula which is as given in “Eqs. 5 to 8”, and presented in Table 5.

$$P_{Ug} = \frac{C_1}{2}L^2 + \frac{C_2}{6}L^3 \tag{5}$$

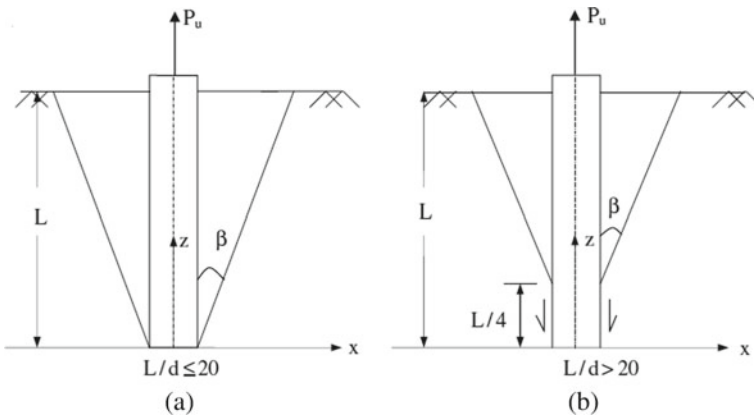


Fig. 3 Failure surface of the pile (Shankar et al. 2007)

Table 5 Ultimate uplift capacity (kN) of pile for various values of ‘ β ’

Pile no.	Extent of load applied	$\beta = \phi/4$	$\beta = \phi/2$	$\beta = 3\phi/4$	$\beta = \phi$	Modified Mazurkiwicz Method (1998)
P1	39.63	11.3	24.67	40.48	63.24	62
P2	49.54	13.23	27.44	46.58	72.4	71
P3	46.46	13.12	28.12	47.8	74.95	70
P4	36.36	10.22	21.55	37.13	58.78	60
P5	49.54	7.89	21.1	35.62	55.1	52
P6	59.44	19.81	40.13	72.51	97.38	95
P7	47.55	4.35	9.03	15.211	53	55
P8	47.55	3.91	10	16.91	68	65

$$P_{U_{net}} = P_{U_g} - \frac{\pi d^2}{4} \gamma L \tag{6}$$

$$C_1 = \pi d \gamma \left[\frac{1}{\tan \theta} + (\cos \theta + K \sin \theta) \tan \phi \right] \tag{7}$$

$$C_2 = \frac{2\pi \gamma}{\tan \theta} \left[\frac{1}{\tan \theta} + (\cos \theta + K \sin \theta) \tan \phi \right] \tag{8}$$

where K is the uplift Co-efficient which is equal to $(1 - \sin \phi)$ and θ is the angle which is equal to $(\frac{\pi}{2} - \beta)$ which is as shown in Fig. 4.

From the above results (Table 5), it is observed that net uplift capacity calculated using expression given by Shankar et al. (2007) for the piles are in correlation with the ultimate uplift capacity obtained by using modified Mazurkiewicz (1998) method when angle $\beta = \phi$. Figure 5 illustrates the comparison of ultimate uplift capacity of piles.

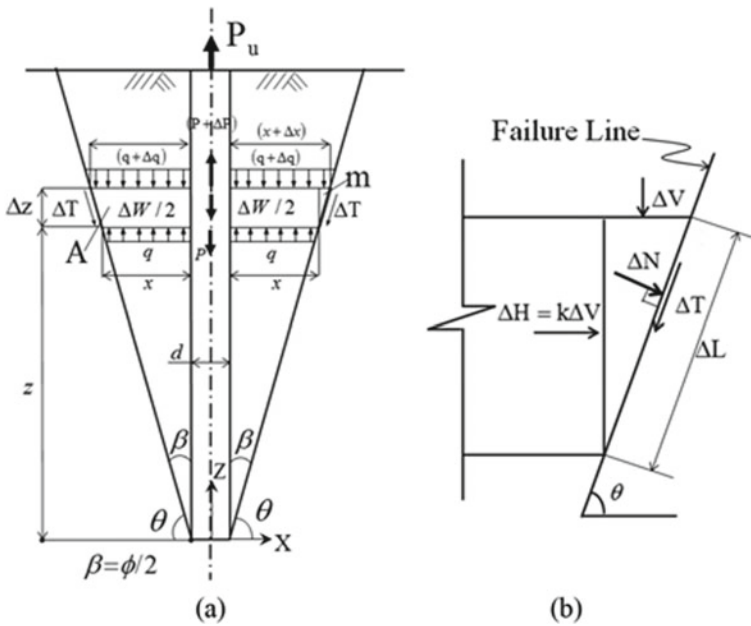
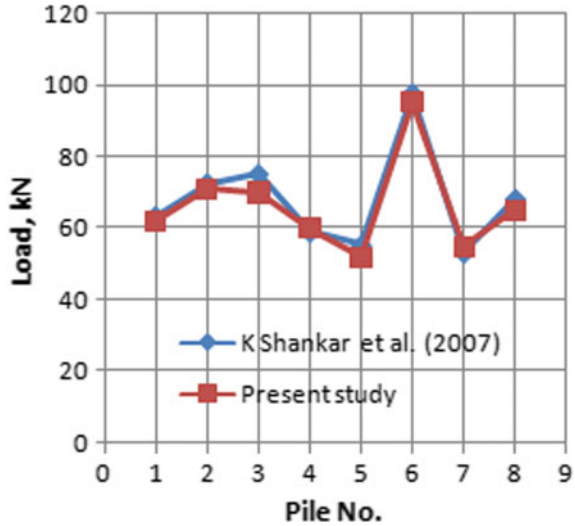


Fig. 4 Indication of angle θ and failure line (Won-Pyo and Neatha 2014)

Fig. 5 Comparison of ultimate uplift capacity of pile



5 Conclusions

Based on the data from field studies on pull out tests on short piles embedded in sandy soils, a comparative assessment on the ultimate uplift capacity of the piles was made with previous studies including IS code recommendations. The ultimate uplift capacity of the piles estimated from modified Mazurkiewicz method (1998) is in close agreement with the formulae proposed by Shankar et al. (2007) taking into account that the failure surface is a truncated cone with edges passing through the tip of the pile at an angle $\beta = \phi$.

References

Chattopadhyay BC, Pise P (1986) Uplift capacity of piles in sand. *Geotech Eng* 112(9):888–904

Das BM (1983) A procedure for estimation of uplift capacity of rough piles. *Soils Found* 23(3)

Ireland HO (1975) Pulling tests on piles in sand. In: *Proceedings of 4th international conference on soil mechanics and foundation engineering*, London, vol 2, pp 43–46

Meyerhof G (1973) Uplift resistance of inclined anchors and piles. In: *Proceedings of 8th international conference on soil mechanics and foundation engineering, USSR, Moscow*, vol 2(1), pp 167–172

Shanker K, Basudhar PK, Patra NR (2007) Uplift capacity of single piles: predictions and performance. *Geotech Geol Eng* 25:151–161. <https://doi.org/10.1007/s10706-006-9000-z>

WeerayaC-O, Narin M (2013) Estimation of uplift pile capacity in the sand layers. In *Trans J Eng Manag Appl Sci Technol* 4(1). ISSN 2228-9860

Won-Pyo H, Neatha C (2015) Prediction of uplift capacity of a micropile embedded in soil. *KSCE J Civ Eng* 19(1):116–126. Copyright at 2015

Experimental Investigation of Piled Raft Foundation Under Combined Vertical, Lateral and Moment Loads



Diptesh Chanda, Rajib Saha, and Sumanta Haldar

Abstract Piled raft foundation is a rational and economical solution for heavy and tall structures which are typically subjected to combined vertical, lateral and moment loadings. The interaction of lateral, vertical and moment load on piled raft foundation has not been well understood due to the complex interaction of raft, soil and piles. Studies on the behaviour of piled raft foundation system under combined vertical (V)-horizontal (H) and moment (M)-vertical (V) are limited. The V - M - H interaction study using model scale test can provide an insight into the failure mechanism of pile raft foundation. Present study is an attempt to investigate the combined interaction of vertical (V), lateral (H) and moment (M) loads on response of a model piled raft foundation system embedded in sandy soil maintaining relative density in the order of 50%. First, the ultimate vertical and lateral load capacity of only raft and piled raft foundation are obtained from load-deformation behaviour of raft and piled raft foundation. In the next phase, combined loading (i.e. V - M - H) test on piled raft system is carried out and horizontal displacement of piled raft foundation system is recorded with respect to gradually applied H or M loading at a uniform rate in presence of constant vertical load. The vertical load test results indicate that the bearing capacity is significantly enhanced due to inclusion of piles to the raft as a settlement reducer. However, the combined interaction of V - M - H loading exhibits significant variation in vertical and horizontal load capacity as well as horizontal displacement and settlement of piled raft system as compared to the response obtained with independent loading.

Keywords Piled-Raft foundation · Soil structure interaction · Experimental investigation · V-M-H interaction

D. Chanda (✉) · R. Saha

Civil Engineering Department, National Institute of Technology Agartala, Agartala 799046, Tripura, India
e-mail: diptesh279@gmail.com

S. Haldar

Department of Civil Engineering, School of Infrastructure, Indian Institute of Technology Bhubaneswar, Bhubaneswar 752050, Odisha, India

© Springer Nature Singapore Pte Ltd. 2020

M. Latha Gali and P. Raghuvver Rao (eds.), *Construction in Geotechnical Engineering*, Lecture Notes in Civil Engineering 84,
https://doi.org/10.1007/978-981-15-6090-3_22

325

1 Introduction

High rise buildings, towers are usually founded on piled raft foundation which is subjected to a combination of vertical, lateral and overturning forces. Combined pile raft foundations are an effective form of foundation system for tall buildings as the raft is able to provide a reasonable measure of both stiffness and load resistance and piles are acting as settlement reducer. A geotechnical assessment for design of such foundation system therefore needs to consider not only the capacity of the pile elements and the raft elements, but also their combined capacity and interaction under serviceability loading condition. State of the art research indicates that considerable effort was given for development of optimum design guideline of piled raft foundation system under static loading (e.g. Horikoshi and Randolph 1994, 1998; Poulos et al. 2011). In fact, the behaviour of piled raft foundation is complicated due to combined action of vertical (V), horizontal (H) and moment (M) loading and may be considered as governing design criteria for such robust foundation system. Horizontal loading, such as, earthquake, wave loading and wind may lead to significant horizontal forces and moment in addition to gravity loading to such foundation. Hence, sustainable design of piled raft foundation always requires consideration of combined interaction (V - M - H interaction) in obtaining design response. Previous studies primarily focused on horizontal deformation of foundation by restricting the rotational behaviour of foundation (e.g. Pastsakorn et al. 2002; Matsumoto et al. 2004a, b). However, the rocking of raft was reported to be an important behaviour during seismic loading (Kourkoulis et al. 2012). Limited studies are reported combined V - H and M - V loading by carrying out model experimental or full-scale field studies (Hamada et al. 2012; Sawada and Takemura 2014; Matsumoto et al. 2004a, b). In reality, V - M - H interaction study through experiments is expensive and challenging. However, model tests in geotechnical engineering offer the advantage of simulating complex systems under controlled conditions providing the opportunity of better understanding of the fundamental mechanisms of these systems. Such tests are often used as calibration benchmarks for numerical or analytical methods, or to make quantitative predictions of the prototype response. Hence experimental studies using model scale can provide an insight into the influence of V - M - H interaction of pile raft foundation. The V - M - H interaction study considering static load will also shed salient inputs on framing seismic design guideline for the structures supported on piled raft foundation, since such guidelines are still not explicitly addressed in literature.

In this context, present study is an attempt in this direction to examine the behaviour of piled raft foundation considering combined action of V - M - H load through model tests. A geometric scaling of 1:50 is assumed to prepare the pile raft model. The test is carried out in a cylindrical chamber filled with local sand. Sand pluviation technique (Lee et al. 2011) is used to prepare the uniform sand bed to achieve a desired relative density of 50%. In the first step, the vertical and horizontal load settlement behaviour of raft and piled raft foundation are obtained. In the next phase, combined loading test on piled raft system is carried out by applying moment (M) loading on piled raft foundation in the presence of constant vertical

load (V). Moment loading is applied at a constant rate and deformation of piled raft foundation is recorded with increase of load.

Moment load is applied at a height (h) from the raft base with M/H ratio as 3 and vertical load is applied in order of 10% of ultimate bearing capacity of the pile raft foundation which is kept constant throughout the test. Finally, the effect of interaction of V - M - H loading on piled raft foundation is investigated in the form of measuring deformation of piled raft system.

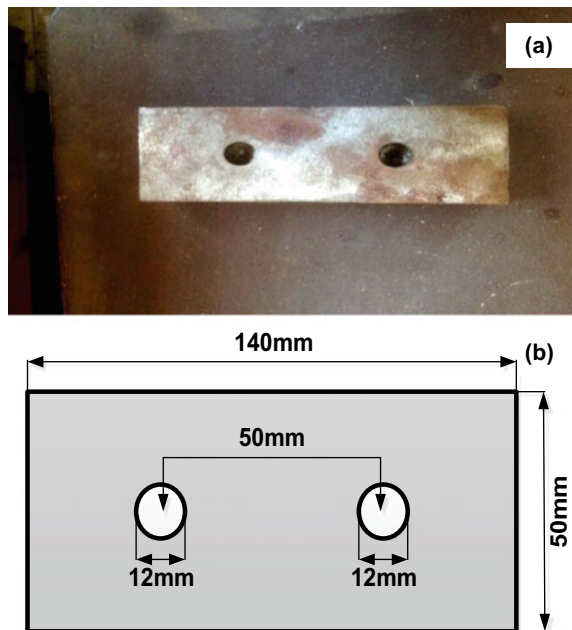
2 Experimental Set Up

2.1 Model Foundation System

The present study considers a prototype foundation system with raft dimension $7.0 \times 2.5 \times 1.4$ m and pile having a length of 24 m, outer diameter 0.6 m and thickness 0.1 m. A geometric scaling of 1:50 is adopted as a framework for modelling the pile raft foundation system. Scaling is done based on the proposed methodology by Meymand (1998). Figures 1 and 2 show the raft and pile model respectively, used in present study.

Mild steel raft with dimensions of $140 \times 50 \times 28$ mm is fabricated. Two circular grooves with centre to centre spacing of 50 mm and having a diameter similar to the

Fig. 1 a Photograph of model raft and b schematic diagram of model raft with dimensions



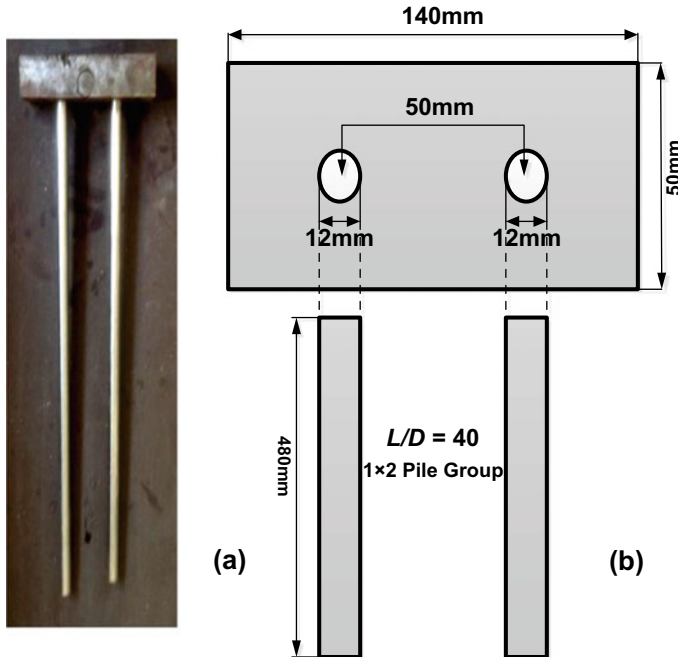


Fig. 2 **a** Photograph of model piled raft foundation system and **b** schematic diagram of model piled raft foundation system

outer diameter of piles are extruded in the raft. Further steel alloy piles with outer diameter 12 mm and thickness of 2 mm are rigidly fixed in the extruded groove of the model raft as shown in Fig. 2. Length to diameter (L/D) ratio of 40 is assumed for pile which ensures flexible behaviour of piles. 1×2 pile group is used in the present study. Conical driving shoes are fixed at the pile tips to facilitate easy installation of piles and to prevent soil plugging into the hollow model pile. Specifications of model pile and raft are presented in Table 1.

2.2 Soil Consistency

Locally available sandy soil is used in present study. Gradation of sand indicates that experimental sand is well-graded sand. Further, the shear strength parameters of sandy soil are determined from laboratory direct shear test. The average value of frictional angle (ϕ) and cohesion (c) is found to be 28° and 0.06 kN/m^2 respectively. Table 2 shows physical and engineering properties of sandy soil used in present study.

Table 1 Specification of model pile and raft

Properties of raft	Model	Prototype
Material	Mild steel	Steel
Unit weight	78.5 kN/m ³	78.5 kN/m ³
Dimensions	140 × 50 × 28 mm	7.0 × 2.5 × 1.4 m
Area of raft, A_r	7000 mm ²	17.5 m ²
Moment of inertia in lateral direction, I_{rx}	1.458 × 10 ⁶ mm ⁴	9.114 m ⁴
Moment of inertia in transverse direction, I_{ry}	11.433 × 10 ⁶ mm ⁴	71.45 m ⁴
Properties of pile	Model	Prototype
Material	Steel alloy	Steel
Unit weight	74.8 kN/m ³	78.5 kN/m ³
Outer diameter	12 mm	0.6 m
Thickness	2 mm	0.1 m
Length of Pile, L	480 mm	24 m
Cross sectional area, A_p	34.55 mm ²	0.086 m ²
Moment of inertia, I_p	527.002 mm ⁴	0.0032 m ⁴

Table 2 Properties of tested soils

Soil properties	
Soil consistency	Cohesionless soil
Coefficient of uniformity, C_u	2.016
Coefficient of curvature, C_c	1.369
Cohesion, c (kN/m ²)	0.06
Frictional angle, ϕ (in degrees)	28°
Relative density, D_r (%)	49.87

2.3 Test Tank

A soil container is designed to simulate the free field soil response efficiently by minimizing the boundary effects. The dimensions of the test tank are decided based on the effective stress zone from the periphery of the foundation model. For pile raft system, it is inferred from literature that the boundary effect is more predominant within 10 times the diameter of pile from the pile periphery (Matlock 1970). In present study the model pile diameter is 12 mm and hence the size of the tank shall be greater than 120 mm from face of pile. The diameter of the cylindrical test tank is taken as 550 mm and height as 900 mm which confirms negligible influence of boundary. Figure 3 shows the model test tank used in this study. The container is prepared with tin and strengthened with mild steel jacketing as shown in Fig. 4. The properties of the tin container and the retrofitting material are presented in Table 3.

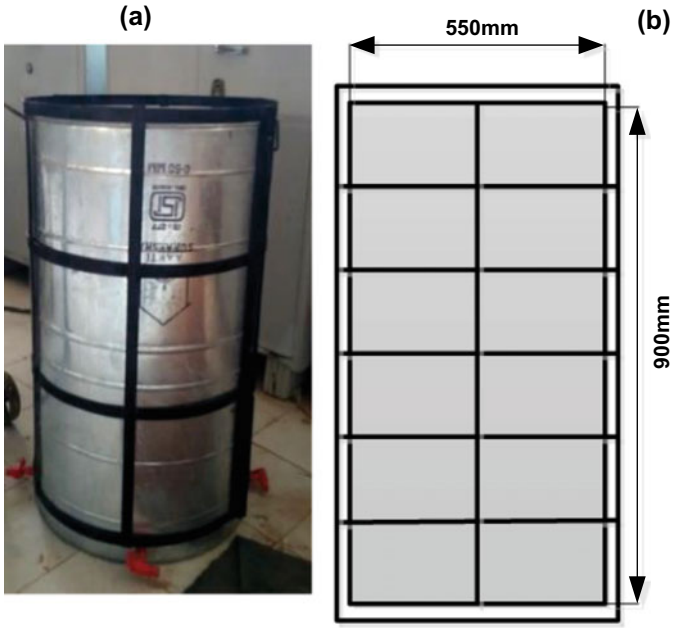


Fig. 3 a Photograph of test chamber and b schematic diagram of test chamber



Fig. 4 Sand pluviation technique

Table 3 Properties of test container and surrounding retrofit

Properties of test chamber	
Material	Tin (<i>Sn</i>)
Inner diameter (mm)	550
Thickness (mm)	3
Weight (gm)	4680
Yield strength (MPa)	7.32
Properties of strengthening material	
Material	Mild steel strips
Width (mm)	553
Thickness (mm)	4
Weight of jacket (gm)	12077
Yield strength (MPa)	250

2.4 Sand Bed Preparation and Installation of Pile

The sand is poured into the test chamber layer wise, with the help of sand pluviation method as shown in Fig. 4. Sand pluviation method offers several advantages with respect to the vibratory table method. The advantages are higher dry density, no particle crushing, less segregation of particle sizes, better uniformity of density and better repeatability (Lo Presti et al. 1992; Brandon and Clough 1991). Figure 5 presents the schematic representation of the sand pluviation chamber used in the present study. With each layer of poring of sand through sand pluviation method, simultaneous compaction was done using rammer so as to achieve a desired relative density of 50%.

Since the length of the pile is 480 mm (*L/D* ratio of 40) and raft is 28 mm deep, the sand bed is prepared to a depth of 600 mm keeping a clear spacing of 92 mm from

Fig. 5 Schematic representation of sand pluviation technique

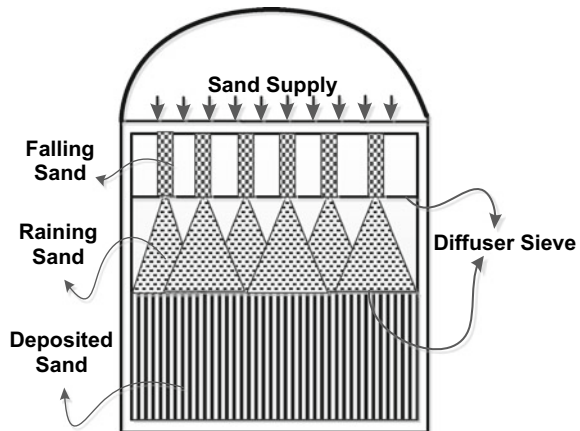
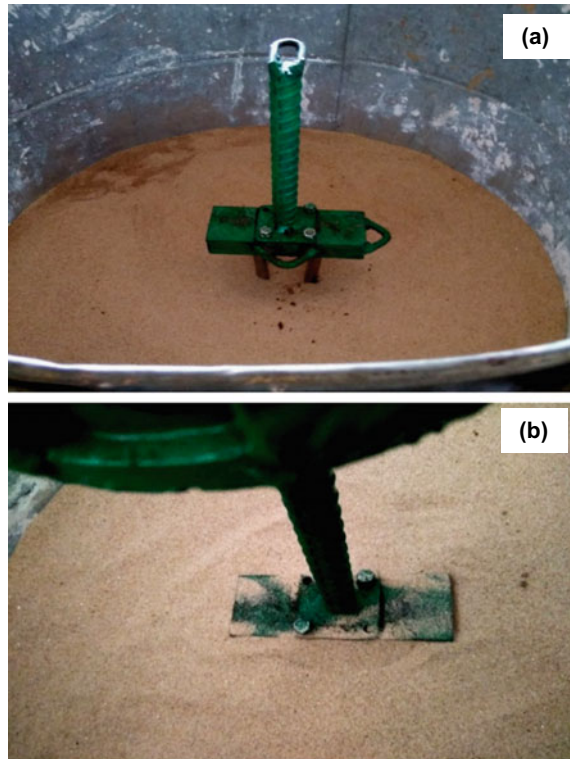


Fig. 6 a Pile Raft partially penetrated by hammering action b Pile Raft fully penetrated by hydraulic jack attached vertically



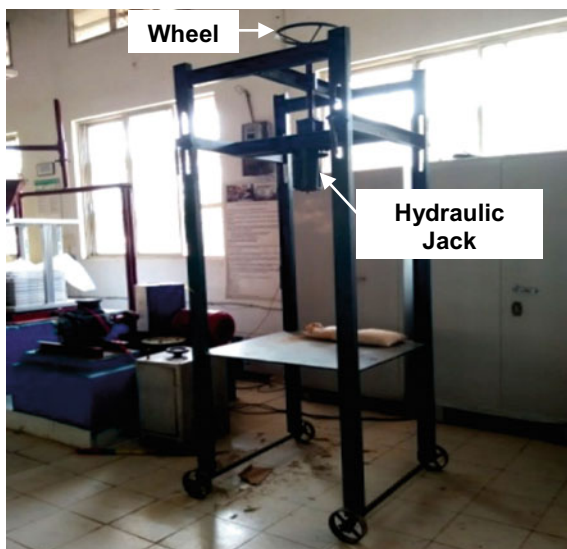
the bottom of the test tank so as to minimize the boundary effect from the bottom surface of the tank on the pile raft model.

After making the model ground, model piled raft foundation is penetrated vertically in the sand bed. Initially, the piled raft system is driven into the sand bed by hammering action. Further, hydraulic jack pressure is applied to push it further until the top surface of raft is in same level to the ground surface. Figure 6 represents the stages in pile raft installation in present study.

2.5 Test Setup and Loading Arrangement

At first, the bearing capacity of both raft and pile raft foundation is determined separately by applying the vertical load at the top of the raft using hydraulic jack. The amount of load applied on the model foundation is measured in terms of pressure on a pressure gauge connected to the hydraulic oil chamber. The jack is of 10 ton capacity and is attached to the loading frame as shown in Fig. 7. The loading frame is made up of 5 mm thick L section mild steel to resist heavy bending and shear stresses developed due to prolonged application of heavy load on it. Loading frame is made

Fig. 7 Loading frame with sliding and locking arrangement



adjustable, so that it could be lowered down to a maximum height of 40 cm, by a sliding and locking adjustment, as shown in the Fig. 7. A top wheel when rotated lowered the frame gradually, and when the desired height is achieved it is locked to its position by rotating arms provided at each corners. Iron wheels of diameter 10 cm are provided to make this heavy chamber movable.

Further, V - M - H interaction test on pile raft foundation is conducted in two phases. The gravity load in the form of dead load is kept on a steel platform supported on two rigid steel bars over the surface of the raft as shown in Fig. 8a. Vertical load is considered as 10% of the ultimate bearing capacity of the pile raft system. The model foundation has undergone a considerable settlement after application of vertical load. In the second phase, the vertical load is kept constant and gradually lateral load is applied at an eccentricity of ($e = M/H$) 20 cm as shown in Fig. 8b. The eccentricity is provided to create a moment load at the top surface of the pile raft foundation. A rigid bar attached to the centroid position of the raft is provided with a groove at the top so that it can be pulled in lateral direction with the help of a steel rope held through a pulley system. One end of the steel rope is attached with the groove in the rigid bar and the other end is attached with a 100 kg water carrying capacity plastic bucket. The bucket is calibrated by filling water and interval of 2.5 kg weight of water is marked on the inner surface throughout the height as shown in Fig. 8c. Free flow of water at a constant flow rate of 0.5 kg/min is allowed in the bucket from a water tank kept at a sufficient head from the bucket. Flow rate is controlled by a valve attached with water tank. The water bucket is provided with proper mild steel retrofitting all around as shown in Fig. 8d so as to withstand high vertical and lateral pressure due to weight of water in free standing condition. The loading frame has a provision to vary the height of the pulley so as to make the steel wire horizontal between the rigid bar over the raft surface and the bucket held through the pulley. Schematic diagram

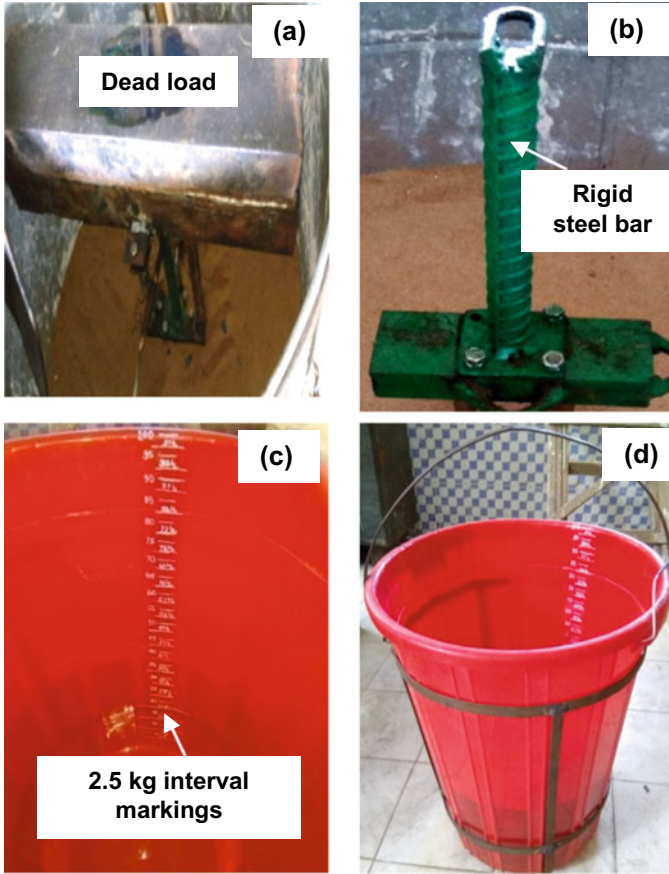


Fig. 8 a Dead Load supported on two rigid bars over the raft surface b Rigid bar at an eccentricity of 20 cm for lateral loading c Graduations on the inner side of the bucket d Retrofitted water bucket

of whole test setup for conducting the vertical bearing capacity assessment of pile raft foundation and V - M - H interaction behavior on pile raft foundation is shown in Fig. 10.

For determining the vertical load carrying capacity for both individual model raft and model pile raft foundation, the vertical settlement of the model foundation is recorded with an increase in vertical load by the hydraulic jack at a constant rate of 3.53 kgf/min. The settlement is recorded with a Linear Variable Displacement Transducer (LVDT) attached with the top surface of the raft as shown in Fig. 9a.

In case of V - M - H interaction test on pile raft foundation, the lateral displacement of the pile raft foundation is recorded with an increase in moment load due to gradually filling of water in bucket at constant rate. The lateral displacement is recorded using a LVDT connected with one edge of the model raft as shown in Fig. 9b. The LVDT readings in both the test are recorded in a data acquisition device (Fig. 10).

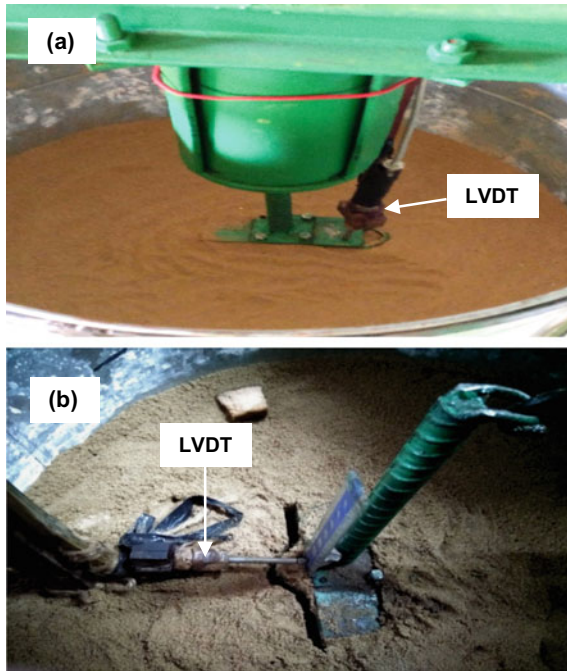


Fig. 9 a LVDT connected to raft top b LVDT connected to raft

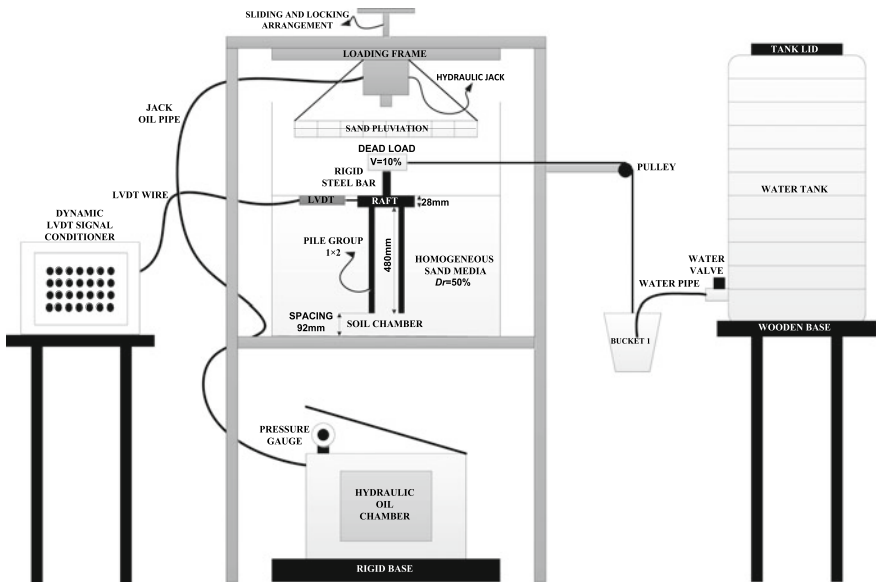


Fig. 10 Schematic diagram of the complete test setup and instrumentation used in present study

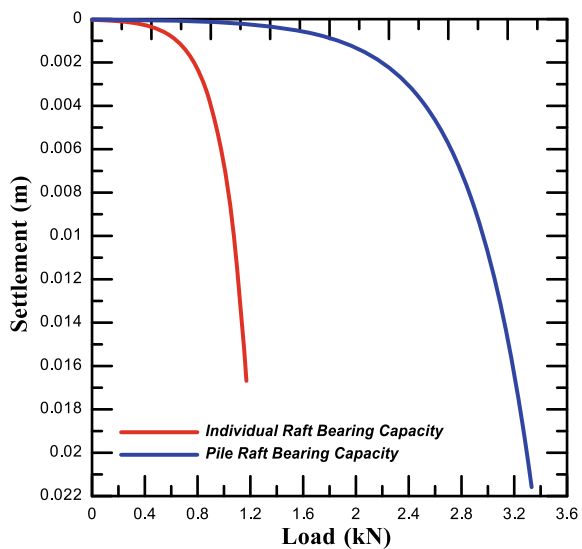
The vertical settlement and lateral displacement measured with LVDT are processed through Dynamic LVDT Signal Conditioner system and displayed on the monitor.

3 Results and Discussion

3.1 Bearing Capacity of Individual Raft and Combined Pile Raft Foundation System

Vertical loading tests are conducted in both model raft and piled raft foundation system prior to *V-M-H* interaction test on pile raft foundation system. The objective of the test is to find the vertical bearing capacity separately for individual model raft and pile raft foundation embedded in sandy soil. The load-settlement observed from the vertical loading test for both model raft and piled raft system is presented in Fig. 11. The tests are terminated when both the model raft and pile raft foundation has undergone a settlement of 20 mm. Figure 11 indicates that incorporation of piles in raft increases the vertical bearing capacity of foundation significantly. For instance, at a settlement of 0.00045 m, the corresponding vertical load for model raft and model pile raft foundation is found to be 0.085 kN and 1.56 kN respectively. The increase is around 18 times of load carrying capacity of raft.

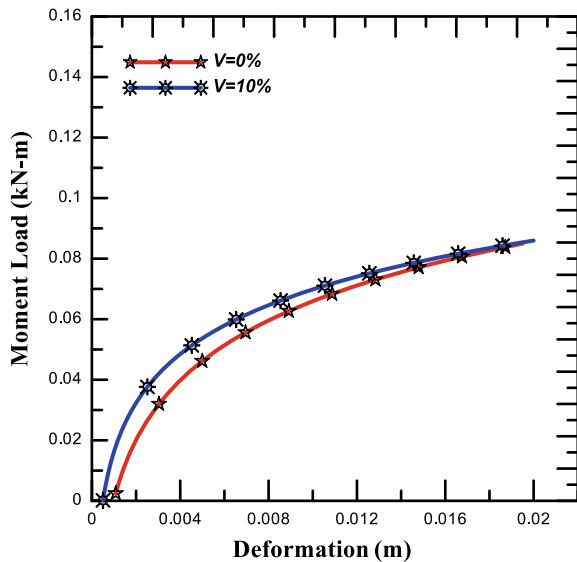
Fig. 11 Vertical load-settlement curve for model raft and piled raft foundation



3.2 Influence of Combined V-M-H Loading

This section presents the influence of interaction of *V-M-H* loading on lateral load-displacement behaviour of piled raft foundation system. In *V-M-H* loading condition, vertical load is applied as dead load which is equal to 10% of the ultimate bearing capacity of the pile raft foundation driven in sand. The vertical load carrying capacity of the pile raft foundation is found out from the vertical load-settlement curve presented in the previous section. The moment load is applied at an eccentricity of 20 cm. With the constant vertical load and increase in lateral load at a constant rate of 0.5 kg/min, the lateral displacement is recorded using a LVDT. Figure 12 presents the moment load deformation behaviour of the pile raft foundation model with 0% vertical Load and 10% vertical load. It is observed from Fig. 12 that combined *V-M-H* loading has notable effect on lateral load carrying capacity of piled raft system. For instance, at a yield displacement of 0.00045 m with 0% vertical load, the moment carried by the pile raft is 0.0021 kN-m. However, for 10% vertical load at same yield displacement the moment carried by the pile raft foundation is 0.0114 kN-m. The increase in load carrying capacity of pile raft foundation for 10% vertical load resulted to an increase up to approx. 440% with respect to zero vertical load on same pile raft foundation model. However, the effect may be more prominent with increase in vertical load on pile raft foundation. Further with increase in lateral load, the load displacement curve has shown a convergence at high level of displacement. The reason for this convergence at higher level of displacement may be due to increase in non-linearity of soil at higher lateral load. This limited study gives a clear indication of consideration of *V-M-H* condition for obtaining design forces in piled raft foundation system.

Fig. 12 Influence of combined *V-M-H* loading



4 Conclusions

The present study presents the interaction effect of combined *V-M-H* loading on piled raft foundation design response parameter. In addition, the use of piles as settlement reducer and raft carrying maximum amount of load in pile raft foundation is also studied experimentally through present study. Further experimental results on model structure indicate that load resistance is significantly influenced due to *V-M-H* interaction. Hence, present study offers valuable inputs for future development of design of piled raft foundation and indicates the necessity of detailed study in this direction encompassing other influential parameters.

References

- Brandon TL, Clough GW (1991) Methods of sample fabrication in the virginia tech calibration chamber. In: Proceedings of the first international symposium on calibration chamber testing, international society of soil mechanics and geotechnical engineering (ISSMGE), New York, pp 119–133
- Hamada J, Tsuchiya T, Tanikawa T, Yamashita K (2012) Lateral loading model tests on piled rafts and their evaluation with simplified theoretical equations. In Proceedings of the 9th international conference on testing and design methods for deep foundations, (IS- Kanazawa 2012), vol 1, pp 467–476
- Horikoshi K, Randolph MF (1998) A contribution to optimum design of piled rafts. *Geotechnique* 48(3):301–317
- Horikoshi K, Randolph MF (1994) Settlement of piled raft foundations on clay. *Proc Centrif* 94:449–454
- Kourkoulis R, Anastasopoulos I, Gelagoti F, Kokkali P (2012) Dimensional analysis of SDOF systems rocking on inelastic soil. *J Earthq Eng* 16:995–1022
- Lee J, Prezzi M, Salgado R (2011) Experimental investigation of the combined load response of model piles driven in sand. *Geotech Test J* 34(6):653–666
- Lo Presti DCF, Pedroni S, Crippa V (1992) Maximum dry density of cohesionless soils by pluviation and by ASTM D4253-83: a comparative study. *Geotech Test J* 15(2):180–189
- Matlock H (1970) Correlations for design of laterally loaded piles in soft clay. In: Proceedings of the 2nd annual offshore technology conference, pp 577–594
- Matsumoto T, Fukumura K, Kitiyodom P, Horikoshi K, Oki A (2004a) Experimental and analytical study on behavior of model piled rafts in sand Subjected to horizontal and moment loading. *Int J Phys Model Geotech* 4(3):1–19
- Matsumoto T, Fukumura K, Kitiyodom P, Horikoshi K, Oki A (2004b) Shaking table tests on model piled rafts in sand considering influence of superstructures. *Int J Phys Model Geotech* 4(3):21–38
- Meymand PJ (1998) Shaking table scale model tests of nonlinear soil pile superstructure interaction in soft clay, pp 1–404
- Pastsakorn K, Hashizume Y, Matsumoto T (2002) Lateral load tests on model pile groups and piled raft foundations in sand. In: Proceedings of international conference physical modelling in geotechnics, pp 709–714
- Poulos HG, Small JC, Chow H (2011) Pile raft foundations for tall buildings. *Geotech Eng J SEAGS & AGSSEA* 42(2)
- Sawada K, Takemura J (2014) Centrifuge model tests on piled raft foundation in sand subjected to lateral and moment loads. *Soils Found* 54(2):126–140

Study on Cyclic Pile Load Test of Pile Socketed in Rock



A. P. Sumisha and Arvee Sujil Johnson

Abstract In this study, different data of cyclic pile load test of pile resting and socketed in rock have collected and analysed to compare it with pile in sand for separating skin friction and end bearing. We all know that the transfer of load in different piles takes place differently, friction takes the load in friction piles and end bears in end bearing piles but in rock socketed piles both friction resistance and end bearing act together against the load. The load transfer is also depending on the type of soil in which the piles rest. Cyclic loading on pile is the best method to determine, how much of the total load takes up by the friction and by the point resistance. There already exists one graphical and analytical method to separate the skin friction and end bearing of pile resting on sand. In case of pile socketed in rock or resting on rock, the separation of skin friction and bearing is done with an assumption that rocks are in dense sand condition. The data of cyclic loading of pile in rock are analysed as per the IS method and found to be that the results are erroneous. So a separate method is essential to analyse the pile in rock. Initially a common trend in load versus settlement curve to be finalized for introducing a new method to separate skin friction and end bearing. The introduced new methods are worked out and that shows, graphical method gives almost acceptable results but the analytical method don't. Further studies are required for clarifying graphical method and to modify the analytical method.

Keywords Pile foundation · Cyclic plate load test · Rock socketing · Graphical method · Analytical study

A. P. Sumisha (✉) · A. S. Johnson
Geotechnical Engineering, College of Engineering, Trivandrum, India
e-mail: sumisha.ap@gmail.com

© Springer Nature Singapore Pte Ltd. 2020
M. Latha Gali and P. Raghuvver Rao (eds.), *Construction in Geotechnical Engineering*, Lecture Notes in Civil Engineering 84,
https://doi.org/10.1007/978-981-15-6090-3_23

1 Introduction

1.1 Background of the Present Study

The increment in load to foundation and available hard strata at higher depth are lead to deep foundation. The piles are classified into friction pile and end bearing pile based on the load transfer. The rock socketed pile possesses both skin friction and end bearing over the socketed depth. The skin friction and end bearing of pile can be separated by conducting cyclic loading on pile and the settlements are noted under loading and unloading. The cyclic loading test is safer because it tests the worst condition of pile under continuous loading and unloading.

The Piles resting on sand have a particular IS code graphical and analytical method to separate skin friction and end bearing. These same methods are used for the piles resting on the rock or socketed into the rock with an assumption that rock is dense sand. This assumption leads to this project. Why will not introduce a new method for separating skin friction and end bearing of pile on rock. A single project data is not sufficient to introduce such a method since the lack of clarification of load deflection curve. So have to collect different journals and case studies for analysis to fix the common trend of load deflection curve of pile on rock. This paper is the partial result of study dealing with the behaviour of pile in rock subjected to cyclic axial loads. As part of this project, an extensive search of existing data on the cyclic behaviour of piles in rock was performed. A large number of publications were collected dealing with laboratory tests, model pile tests and pile load tests. The data were analysed and the results of the analysis, which are represented in this paper served as guidelines for introducing a new method for separating skin friction and end bearing of pile resting or socketed in rock. The comparison of load deflection curves of pile on sand and rock is also included. The data of cyclic pile load test on rock were analysed as per the IS code method and it found to be erroneous. So a new method is essential to analyse the pile in rock. After finalizing the common trend of load versus settlement curve of pile in rock, a new graphical and analytical method are introduced. The acceptance of results of these methods is discussed in this paper and further study required areas are also mentioned in it the main objective of this study is

- To compare the results of cyclic pile load test of pile on both sand and rock and to determine how they are different.
- Determination of common trend p-y graph of pile socketed in rock.
- Comparison of graphical and analytical methods to separate skin friction and end bearing.
- To introduce a modified graphical and end bearing method for separating skin friction and end bearing.

1.2 Data Collected

The cyclic pile load test data were taken from these journals. Radhakrishnan (1989) ‘Load transfer behavior of rock socketed pile’, Omer and Delpakl (2002) ‘Instrumented load tests in mudstone: pile capacity and settlement prediction’.

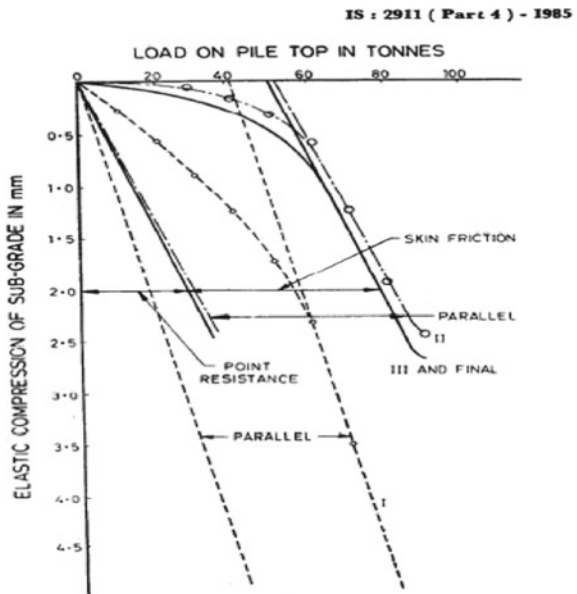
2 Methodology

2.1 General

Different journals and case studies of cyclic load test on pile resting on rock or socketed in rock were collected and the required data were taken. Mainly it requires the settlements on each loading and unloading. If the collected data is in graphical form it should be extracted to the values. The collected data were tabulated to find settlement of subgrade for each loading then plotted graph between settlement of subgrade and load. As per IS code method (2911 part 4) the graph was analysed to separate skin friction and end bearing. Actually this IS code is used for analysing cyclic pile load test on pile which is resting on sand so here we are going to do the analysis on pile resting on rock with an assumption that rock is a dense sand (Fig. 1).

This is the existing IS code graphical method for pile resting on sand and the analytical method is shown below. In graphical method a straight line is drawn which

Fig. 1 Separation of skin friction and end bearing



passes through the points in the straight line portions and another straight line which passes through zero and parallel to the previous line. For each load the end bearing and skin friction are shown in the above figure. In analytical method the value of m is found out by the equation and solved the two equations to find point resistance and skin friction. In other way the m is the slope of the load versus elastic compression of subgrade curve and can determine directly from the curve.

$$m = \frac{\Delta S - (\Delta T * (L/AE))}{\Delta T} \tag{1}$$

(IS code 2911 part 4 2013)

$m =$ a constant

$\Delta S =$ change in elastic settlement

$\Delta T =$ change in load, $L =$ length of the pile

$A =$ cross sectional area of pile, $E =$ modulus of elasticity

$S = mT$

($S =$ corrected settlement, $T =$ total load on pile)

$$T = P + F \quad \text{and} \quad S = m P + \frac{(T - (F/2)) * L}{AE} \tag{2}$$

$P =$ Point resistance, $F =$ skin friction

The graphs shown below are the collected data (Figs. 2 and 3).

For the study we require settlements on corresponding loading and unloading. The graphs are extracted to get settlements corresponding to loading manually which are shown below (Figs. 4 and 5).

Fig. 2 Cyclic pile load data
(Source Load transfer behavior of rock-socketed piles (Radhakrishnan 1989))

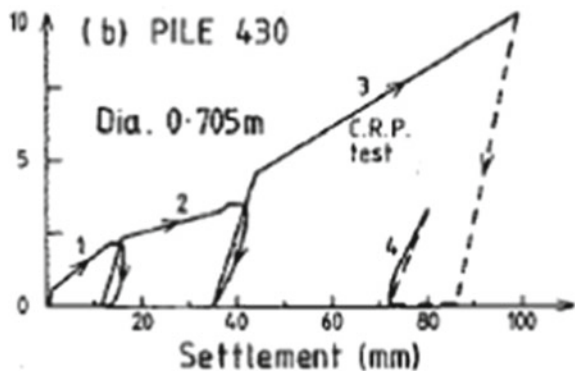


Fig. 3 Cyclic pile load data (Source Instrumented load tests in mudstone: pile capacity and settlement prediction (Omer and Delpakl 2002))

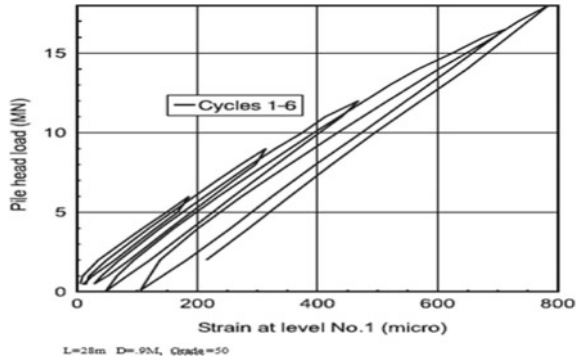
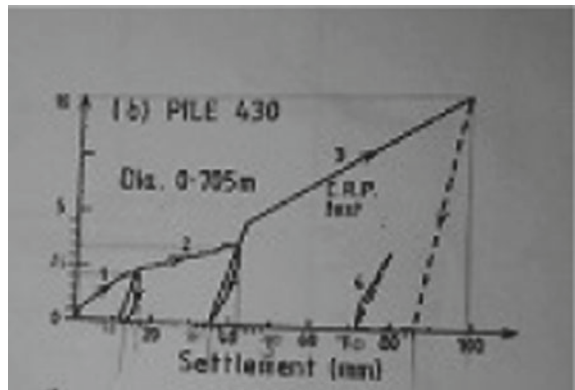


Fig. 4 Manual extraction of settlement (Source Load transfer behavior of rock-socketed piles (Radhakrishnan 1989))



The extracted data are shown below and tabulations to get elastic settlement of subgrade and load for the 1st data (Table 1).

The graph of load versus elastic settlement of subgrade was drawn as per IS code (2911 part 4) by assuming no frictional force and no elastic settlement on pile. Three trials are required to finalize the curve so in 2nd trial, the separated friction from 1st trial is taken as frictional resistance for calculating elastic settlement of pile. Then new curve was plotted and repeated this until the separated point resistance and skin friction in adjacent two trials are almost same (Table 2).

According to IS code method, the skin friction and end bearing are separated both graphically and analytically and compared the results obtained (Fig. 6 and Table 3).

In this curve, the settlement increases abruptly with initial loading and less settlement at the end of loading. This is clearer from the separated values of skin friction and end bearing. Both end bearing and skin friction act together to resist the load at all loading. The initial inclined straight line portion represents the development of frictional resistance and point resistance and curve shows both increases. Comparing to point resistance the frictional resistance is more all the time. By analysing the graph as is per IS code method at a particular portion the frictional resistance values

Fig. 5 Extraction of settlement (*Source* Instrumented load tests in mudstone: pile capacity and settlement prediction (Omer and Delpakl 2002))

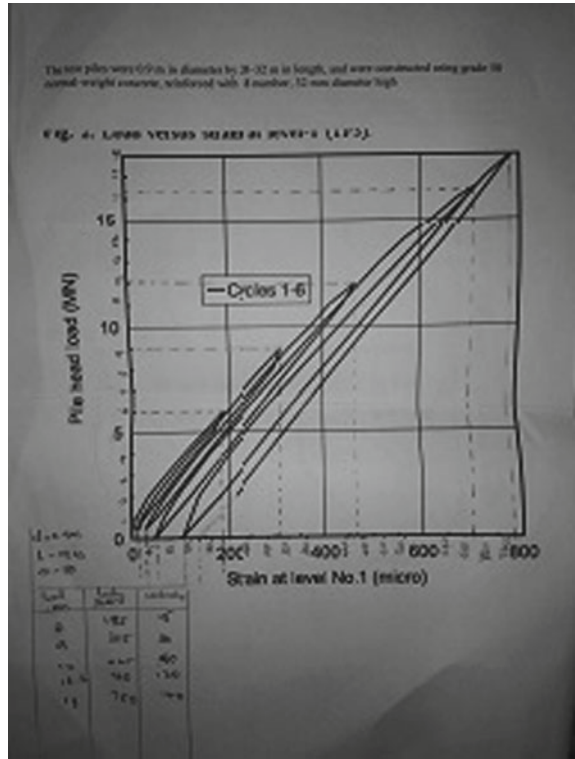


Table 1 Basic data of rock socketed pile

Basic data of pile		
Length of pile	12.4	m
Grade of concrete	35	N/mm ²
Elastic modulus of pile	33721654.76	kN/m ²
Dia of pile	0.705	m

Table 2 IS code trial analysis

Load (T)	Elastic recovery mm	Frictional resistance	Elastic settlement of pile mm	Elastic settlement of sub grade mm	Point resistance kN	Frictional resistance kN
0	0	0	0	0	0	0
203.9	6	0	0	6	90	113.9
356.8	12	0	0	12	180	176.8
1019.4	16	0	0	16	240	779.4

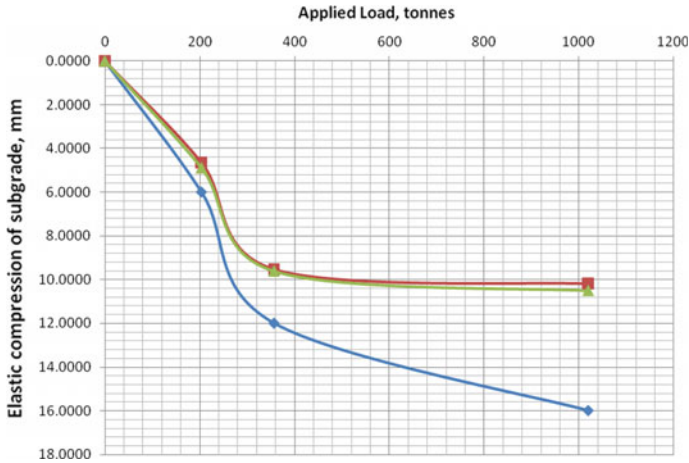


Fig. 6 Load versus elastic settlement of sub grade (three trials) for data 1

Table 3 Separated skin friction and end bearing

Load (T)	Graphical		Analytical	
	Point resistance kN	Frictional resistance kN	Point resistance kN	Frictional resistance kN
0	0.0	0.0	0.0	0
203.9	80.0	123.9	197.28	6.57
356.8	150.0	206.8	345.26	11.52
1019.4	180.0	839.4	986.54	32.85

are same. The further portion is analysed and that shows large increase in frictional resistance. The point resistance is increasing all the time.

The separation of skin friction and end bearing has done by analytical method that shows point resistance is greater all the time and only a small part of friction is there to resist the coming load (Fig. 7).

The frictional part is more than point resistance in graphical method but in analytical, frictional part is less than point resistance. The sudden downward fall of curve shows some type of failure or complete mobilization of load. From the previous analysis the skin friction is getting mobilized completely because the same value of friction has obtained. As per the IS code method further increase in skin friction is also shown here. If the continuous same value of friction shows frictional failure then it is not possible to see such increase in friction further so this is the part when the IS code method fails to determine or separate the skin friction and end bearing for rock socketed pile. So modification is required to separate skin friction and end bearing for rock socketed piles.

This is another data of rock socketed pile under cyclic pile load (Table 4).

Fig. 7 Separation of skin friction and end bearing

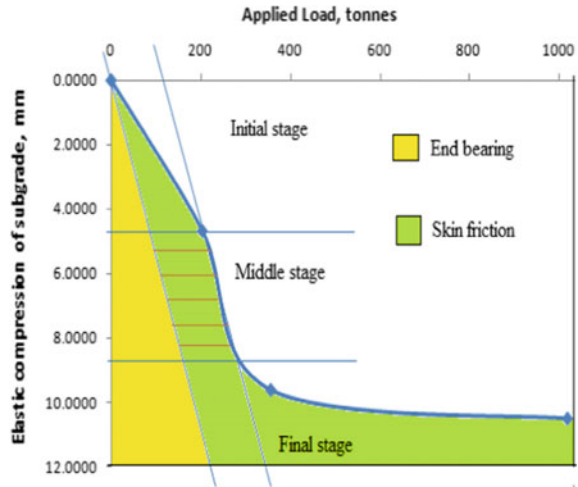


Table 4 basic data of rock socketed pile

Basic data of pile		
Length of pile	28	m
Grade of concrete	50	N/mm ²
Elastic modulus of pile	40305086.53	kN/m ²
Dia of pile	0.9	m

The same steps were done for the 2nd data (Tables 5 and 6 and Figs. 8 and 9).

A large settlement variation in initial loading and increment of settlement decreases after a particular loading. The frictional part obtained from graphical method is greater than the frictional part obtained from analytical part. An increase and decrease can be seen in graphical method and a slight continuous increase in analytical method. In graphical method the 4th and 5th loading gives almost same friction that means complete mobilization of friction. So further increase in friction

Table 5 IS code trial analysis

Load (T)	Elastic recovery mm	Frictional resistance	Elastic settlement of pile mm	Elastic settlement of sub grade mm	Point resistance kN	Frictional resistance kN
0	0	0	0	0.00	0.0	0
611.62	4.78	0	0	4.78	220	391.6
920.5	7.7	0	0	7.70	400	520.5
1220.2	11.6	0	0	11.62	600	584.5
1651.4	16.2	0	0	16.24	840	811.4
1834.9	17.9	0	0	17.92	940	894.9

Table 6 Separated skin friction and end bearing

Load (T)	Graphical		Analytical	
	Point resistance kN	Frictional resistance kN	Point resistance kN	Frictional resistance kN
0	0.0	0.0	0.0	0.0
611.62	270.0	341.6	605.4	6.2
920.5	550.0	370.5	908.09	9.34
1220.2	560.0	660.2	1210.78	12.46
1651.4	530.0	1121.4	1634.55	16.82
1834.9	620.0	1214.9	1816.17	18.69

Fig. 8 Load versus elastic settlement of sub grade data 2

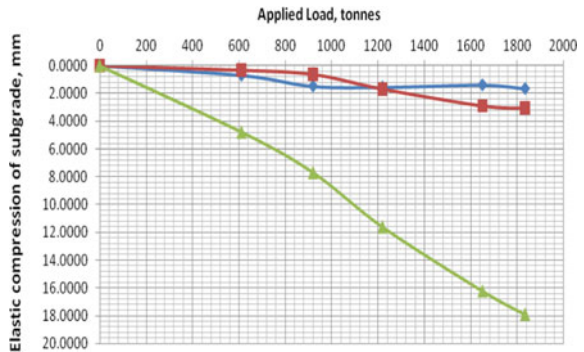
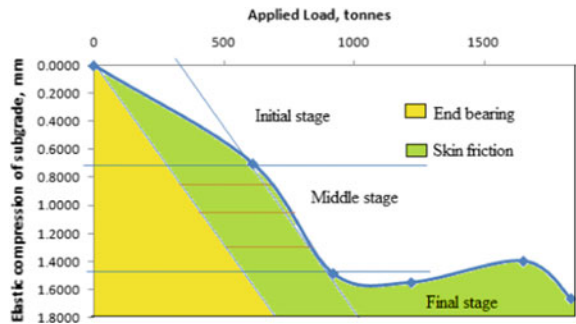


Fig. 9 Separation of skin friction and end bearing



is not possible but the method shows such increase in 6th loading so the method is not suitable for pile in rock. The graphically obtained frictional capacity is ten times the analytically obtained frictional capacity. In this it also shows, after a continuous same value of friction large increase is visible which is not acceptable in the sense of taking higher load after a failure. A new method is essential for separating skin friction and end bearing for a rock socketed pile.

2.2 Modification

The shape of the curve can be explained with the load transferred through the pile. First you should be aware that the load coming to the pile is always distributed to both skin friction and end bearing. Every load on pile has both frictional and end resistance but the proportions are different at different stages. The end bearing is always found in an increasing manner and the skin friction increases initially then attained a constant value. The parabolic shape shows the initial increase of skin friction and constant value is obtained from the straight line portion of the curve. The next straight line with less settlement shows the increase in skin friction as per the existing IS code method for sand. For a rock socketed pile the skin friction mobilizes before the mobilization of end bearing so the further increment of skin friction is not possible. This will be atypical variation of curve for rock socketed pile under cyclic pile load test (Fig. 10).

This is a typical trend of rock socketed pile under cyclic pile load test. The third portion which is in straight line shows a small increase in settlement with load. We all know that the skin friction values are constant for different loading means it is the maximum value that the skin friction can hold and in other way constant values mean complete mobilization of skin friction has occurred. But the third portion increases the skin friction as per the existing IS code method which is not possible since the skin friction has attained its maximum capacity. The less settlement means the bottom rock support is very much high which is known as end bearing. The point resistance is stronger and causes less settlement than a frictional resistance so the less settlement portion reveals the major part of the load is taken by point resistance. The capacity increase in curve at the end is the increase in end bearing not by the increase in skin friction by IS code method. So the method should be modified to show the actual process happening there.

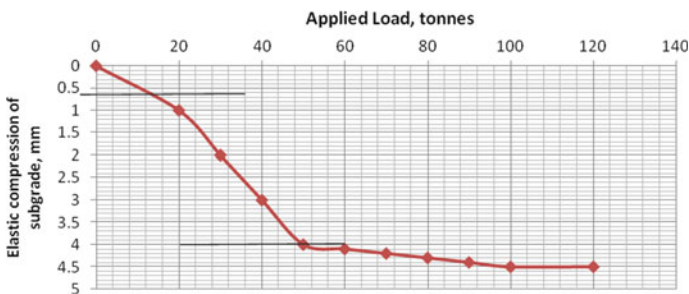


Fig. 10 Assuming trend of graph

2.3 Modified Graphical Method

The maximum value of skin friction is taken as constant for every load after the mobilization of friction as frictional part and the rest of the load on pile is taken as end bearing. For executing this, the mobilized skin friction value is taken as offset from all the next loads and drawn a new curve by joining the left tip of the offsets. The horizontal distance in x axis from y axis to the new curve corresponds to the point resistance and the new curve to previous curve (offset) corresponds to skin friction. The pictorial representation of this method is shown below (Table 7).

Comparing the modified and IS code graphical method, the mobilization of skin friction and increase in end bearing is only visible in modified graphical method. IS code method shows end bearing is less than skin friction at the end of loading (Fig. 11).

Table 7 Comparison of IS and modified graphical method

Load (T)	Graphical		Modified graphical	
	Point resistance kN	Frictional resistance kN	Point resistance kN	Frictional resistance kN
0	0.0	0.0	0.0	0.0
203.9	80.0	123.9	83.87	120.0
356.8	150.0	206.8	233.78	123.0
1019.4	180.0	839.4	896.4	123.0

Fig. 11 Modified separation of skin friction and end bearing data 1

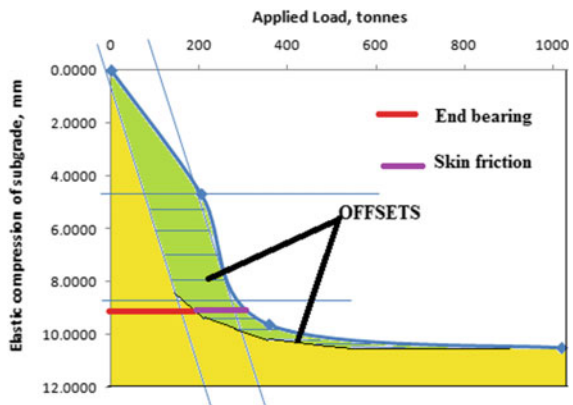


Fig. 12 Determination of slope of data 1

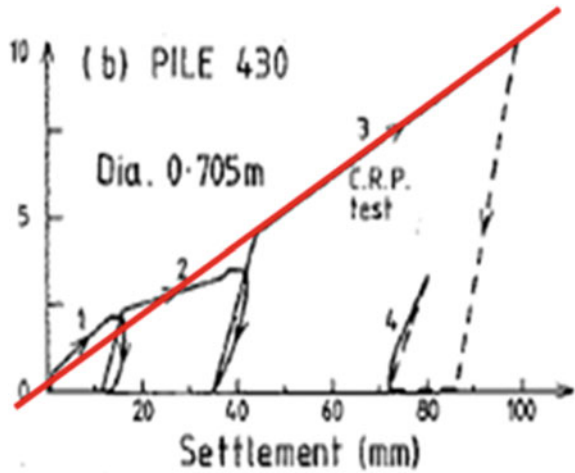


Table 8 Comparison of IS code and modified analytical method of data 1

Load (T)	Modified analytical		Analytical	
	Point resistance kN	Frictional resistance kN	Point resistance kN	Frictional resistance kN
0	0.0	0.0	0.0	0
203.9	152.46	51.41	197.28	6.57
356.8	304.9	51.88	345.26	11.52
1019.4	355.13	664.27	986.54	32.85

2.4 Modified Analytical Method

Determination of m from cyclic loading data of study Load transfer behavior of rock-socketed piles (Radhakrishnan 1989) (Fig. 12).

In IS code analytical method the value of m is taken as slope of load versus elastic settlement of subgrade. In new method the value of m is taken from cyclic pile load test curve as the slope of red line shown above. Then the results obtained are shown below (Table 8).

For the second data (Fig. 13 and Table 9).

3 Results and Discussion

Different data of cyclic pile load test of pile resting or socketed in rock were collected. And load versus elastic compression of subgrade curves have drawn. The drawn curves are analysed and a common shape is finalized. The common trend is explained

Fig. 13 Determination of slope of data 2

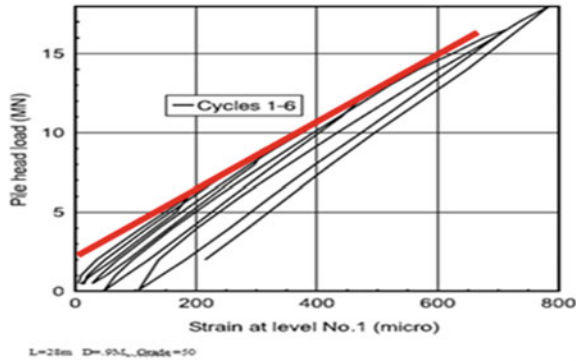


Table 9 Comparison of IS code and modified analytical method

Load (T)	Modified analytical		Analytical	
	Point resistance kN	Frictional resistance kN	Point resistance kN	Frictional resistance kN
0	0.0	0.0	0.0	0.0
611.62	389.55	222.07	605.4	6.2
920.5	633.69	283.74	908.09	9.34
1220.2	964.14	259.1	1210.78	12.46
1651.4	1350.43	300.94	1634.55	16.82
1834.9	1489.5	345.36	1816.17	18.69

by the load transferred through the pile which means the point resistance and skin friction corresponds to every load have determined and their magnitude variation gives such shape to the curve. The point resistance is increasing all the time but the skin friction increases initially and attains a maximum value then becomes constant. The further increment in load resistance capacity is by increment in point resistance.

The IS code graphical method is found to be erroneous since it gives such a result that skin friction is also increasing beyond the maximum mobilized value. An increase after maximum capacity is not a possible one. The mobilization is identified by the similarity in skin friction for different adjacent loading.

This error in IS code method led to the introduction of new graphical and analytical method. The introduced graphical method gives almost favourable results and further studies are required to modify the introduced analytical method since it is also erroneous.

4 Conclusion

- A common trend in load versus elastic compression of subgrade of pile under cyclic loading in rock has determined which is different from the trend of sand.
- The IS code method gives erroneous results for analysis of pile in rock under cyclic pile load test.
- For the same data, IS code graphical and analytical methods give different value for point resistance and skin friction.
- Modified graphical and analytical methods are introduced and verified its accuracy by considering number of trials of different cyclic pile load test data collected.
- Further study is essential to introduce most favourable analytical analysis.

References

- IS code part 4 (1985) Code of practice for the design and construction of the pile foundation load test on pile. Bureau of Indian standards, New Delhi, India
- Omer JR, Delpakl R (2002) Instrumented load tests in mudstone: pile capacity and settlement prediction. *Can Geotech J* 39:1254–1272
- Radhakrishnan (1989) Load transfer behavior of rock socketed pile. *J Geotech Eng* 115:755–768

Uplift Capacities of Inclined Double-Plate Circular Anchors at Shallow Depths in Sand



B. Vidya Tilak  and N. K. Samadhiya 

Abstract Inclined plate anchors are used to resist oblique loads in various civil engineering structures like the transmission towers, sheet pile walls, retaining structures, dams, etc. The use of single-plate anchors has been the interest of study from a long time by many researchers. However, the use of double-plate anchors and studies on the same has hardly been taken up. The present work discusses the uplift capacity of inclined double-plate circular anchors. The uplift capacity of 50 and 100 mm inclined circular plate anchors has been investigated. The double-plate anchors consist of two single plate anchors attached to the same tie rod at a spacing (s) equal to the size of the anchor (d). A comparison has been made between double-plate and single-plate anchors. The study summarizes the pullout load at failure for the anchor plates of different sizes and also presents the load-displacement curves of the various tests.

Keywords Inclined plate anchors · Single-plate anchors · Double-plate anchors · Pullout load · Sand

1 Introduction

Design of foundations supporting tensile loads requires the information on soil uplift resistance. The wide-ranging structures include the ones in land, offshore, highways, transmission towers, suspension bridges, and retaining walls, only to mention a few. The earlier construction practices involved the method of resisting the uplift by increasing the weight of the substructures. The consistent attempt by the research community, scientists, and engineers has brought-in the use of light-weight structures into practice. The use of artificial increase in weight by mobilizing passive resistance in the soil has proved to be an economically viable option. Anchors find a way here.

B. Vidya Tilak (✉) · N. K. Samadhiya
Indian Institute of Technology Roorkee, Roorkee 247667, UK, India
e-mail: vidyatilakb@gmail.com

N. K. Samadhiya
e-mail: nksamfce@iitr.ac.in

The anchors are of many types, viz., the ground anchors, plate anchors, screw anchors, suction anchors, torpedo anchors, grouted anchors, etc. The anchors are classified on the basis of mechanism they provide uplift resistance and the circumstances and location they are finally employed in.

Research involving laboratory studies, analytical studies, and numerical studies have been carried out all over the world. Kozlov (1967) conducted one of the pioneer studies on the use of anchorages. Das (1975) performed model studies on the vertical anchors. He studied the effect of size of anchor plates on the uplift resistance. He showed that the ultimate passive resistance of the circular anchor was about 66% that of the square anchor. Das and Seeley (1975a, b) worked on the use of inclined anchors in sand. They mentioned that the involvement of the unsymmetrical soil failure developed around the inclined anchors was the reason for an increase in the uplift resistance as compared to the horizontal anchor plates. The study on the vertical anchors led to the understanding of the factors involved in effecting the uplift resistance. Das and Seeley (1975b) attributed to the angle of internal friction, bulk density of the soil, and the involvement of the soil properties in providing efficient resistance in case of vertical anchors. They nondimensionalized the load-displacement curve and gave an empirical relation too. Similar laboratory studies in sand were conducted by Akinmusuru (1978a, b, 1984), Ranjan and Kausal (1977), Hoshiya and Mandal (1984). Stewart (1985) studied the uplift resistance of circular anchors in layered soil containing layers of sand and clay. Ilamparuthi et al. (2002) reviewed the design methods and analyzed the failure surfaces of the different sets of circular anchors at various embedment depth.

A fascinating improvement to the use of plate anchors was brought-in by the researching community in the form of inclined plate anchors, to resist the oblique loads. Goel et al. (2006) worked out a solution to find the break out resistance of inclined anchors using the limit equilibrium approach. Hanna et al. (2015) developed a theoretical model to study the pullout capacity of the inclined single plate anchors in sand. The research community working in the field of plate anchors have shown extensive interest in single-plate anchors.

Few researchers tested the effect of anchors being used in groups. Geddes and Murray (1996) tested a group of anchors resisting vertical pullout loads. They arranged a group of anchors in rows and found the collective behavior patterns. They also studied the behavior of the plate anchors in a square configuration. They applied static loading applied in displacement-controlled manner. The critical separation ratio between the anchors was analyzed. The end anchors provided a greater resistance as compared to the central ones. An innovative study on increasing the number of plate anchors being connected to a single stem was examined by Merifield and Smith (2010), and Kumar and Sahoo (2012). They have performed numerical studies to determine the ultimate uplift capacity of multi-plate anchors in undrained clay. Conversely, there has been hardly any experimental study on the multi-plate anchors in sand. The authors have in recent times shown interest in understanding the effectiveness of using multi-plate anchors in sand. Their work includes the study on the double-plate horizontal anchors on the pullout capacity (Tilak and Samadhiya 2017) and on the inclined double-plate square anchors in sand (Tilak and Samadhiya

2018). The present work compares the effect of the double-plate inclined circular anchors and the embedment ratio on the pullout load at failure.

2 Experimental Program

2.1 Methodology

The pullout tests on the single-plate and double-plate inclined anchors were performed in a tank of dimensions 1.1 m × 1.1 m × 0.75 m. Figure 1 shows the experimental setup. A uniformly graded sand was used. The dry sand was compacted to a relative density of 65% (medium-dense) using rainfall technique. The unit weight of sand was 14.80 kN/m³. The apparatus of the test includes a loading system consisting of a loading frame connected by a cable system, tie rod, and dial gauges with magnetic stand, strainer, and frame for sand raining.

The anchor plates were 50 and 100 mm, circular in shape and of thickness 5 mm. The anchor plate was inclined at an angle of 22.5° to the horizontal. The anchors were connected to a tie rod and pulled using a cable of 5 mm in diameter attached to the center of the pulley. The load was applied to the free end of the cable. The anchor was gradually subjected to pullout load. A set of two dial gauges were used to record the displacements after each application of the load. Thus, the load-controlled tests were performed, and the corresponding readings of Pullout Load-Displacement were recorded till the ultimate shear failure occurred and the anchor system failed. Figure 2 shows the image of the setup after the application of the initial load to the inclined plate anchor in the sand box. Figure 3 shows the image of the setup after the application of pullout load at failure to the inclined plate anchor in the sand box.

The total depth of the soil layer below the anchor plate was maintained to be 100 mm for all the tests conducted. The double-plate anchors basically consist of

Fig. 1 Test set-up. 1-pulley; 2-load hanger; 3-pedestal; 4-dial gauge; 5-tie rod; 6-inclined plate anchor; 7-sand; 8-sand box

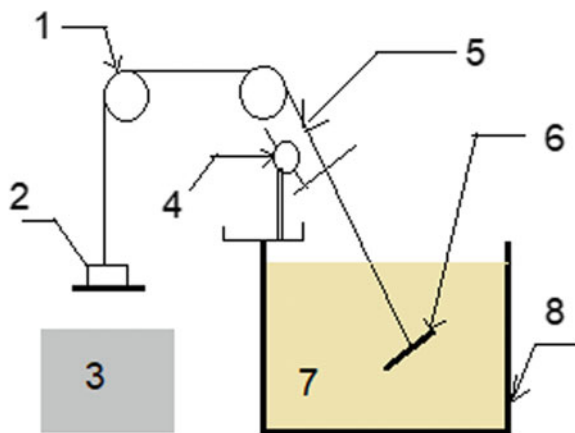




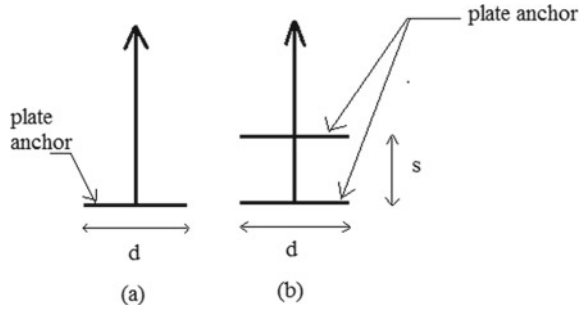
Fig. 2 Image of the setup after the application of the initial load to the inclined plate anchor in the sand box



Fig. 3 Image of the setup after the application of pullout load at failure to the inclined plate anchor in the sand box

two single plate anchors attached to the same tie rod at a spacing equal to the size of the anchor (Fig. 4). The weight of the double-plate anchor system increases by an anchor plate and a tie rod of length equal to the diameter, as compared to the single-anchor plate system. The spacing chosen between the two plates for all the

Fig. 4 Schematic diagram of **a** single-plate anchor
b double-plate anchor



double-plate anchor system was equal to size of the anchor plate. The embedment ratio (h/d) of 2–4 was selected for the study. The embedment length (h) is the height of the anchor plate from the top surface of the filled-up tank for a single anchor plate and is the height of the bottom plate of the double-anchor plate system, and “ d ” is diameter of the anchor plate.

The 50 mm single and double-plate anchor failed before loading, at shallower embedment ratios of 2 and 3. Therefore, the load-displacement data could not be obtained for the mentioned embedment ratios.

3 Results and Discussions

3.1 Load-Displacement of Single-Plate Anchors

The variation of load with displacement for the pullout test on 50 mm single-plate inclined anchor is presented in Fig. 5.

The ultimate pullout load of 55.4 N was obtained at a displacement of 150 mm for an embedment ratio 4. Similarly, the variation of load with displacement for the pullout tests on 100 mm single-plate anchors are presented in Fig. 6. The pullout loads of 124.6, 138.5, and 310.8 N were obtained at a displacement of 200 mm for an embedment ratio of 2–4 respectively.

A 5.6-fold increase in the pullout load was observed for an increase in the size of anchor, i.e., from 50 to 100 mm. For, the case of 100 mm single-plate anchor, the pullout load at failure increased with the increase in the embedment ratio from 2 to 3, and from 3 to 4.

Fig. 5 Load-displacement curve for 50 mm single-plate anchor

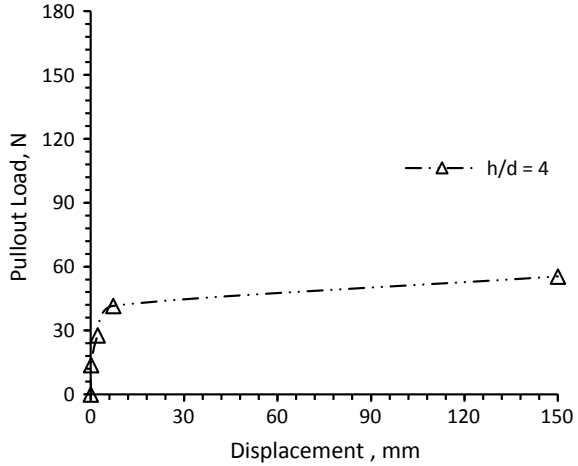
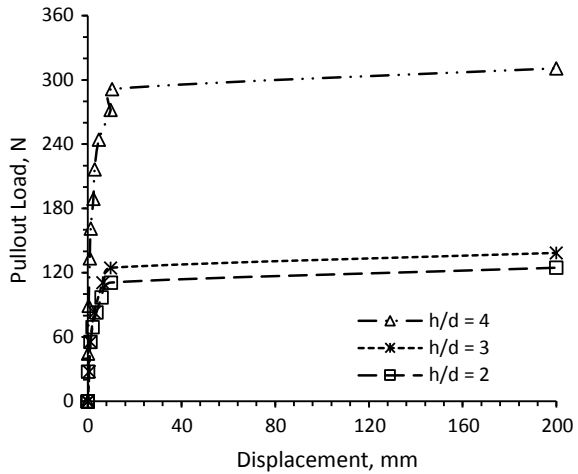


Fig. 6 Load-displacement curve for 100 mm single-plate anchor



3.2 Load-Displacement of Double-Plate Inclined Anchors

The variation of load with displacement for the pullout test on 50 mm double-plate anchor is presented in Fig. 7. The pullout load of 63.7 was obtained at a displacement of 150 mm for an embedment ratio of 4. Similarly, the variation of load with displacement for the pullout tests on 100 mm double-plate anchors for an embedment ratio of 2–4 are presented in Fig. 8. The pullout loads of 83.1, 166.2, and 277.6 N were obtained at a displacement of 200 mm for an embedment ratio of 2–4.

A 1.3-fold increase in the pullout load was observed for an increase in the size of anchor, i.e., from 50 to 100 mm. For, the case of 100 mm single-plate anchor, the pullout load at failure increased with the increase in the embedment ratio from 2 to 3, and from 3 to 4.

Fig. 7 Load-displacement curve for 50 mm double-plate anchor

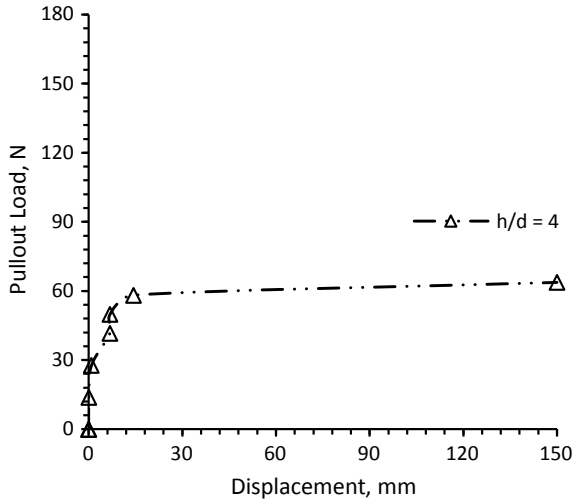
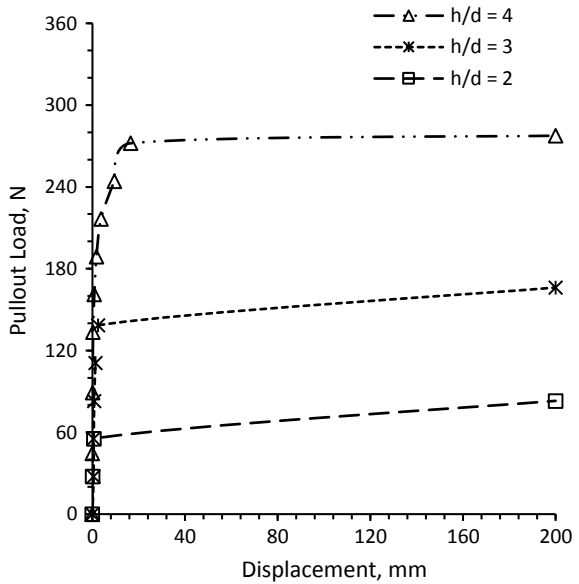


Fig. 8 Load-displacement curve for 100 mm double-plate anchor



For both the single-plate as well as the double-plate anchors, the increased embedment length and increased size of the anchor plate involves more soil volume responsible for the action of development of passive resistance and thereby increases the uplift capacity.

Table 1 Summary of pullout load of anchors at failure

Size of anchor plate, mm	Embedment ratio (h/d)	Pullout load at failure, N	
		Single-plate anchor	Double-plate anchor
50	4	55.4	63.7
100	2	124.6	83.1
	3	138.5	166.2
	4	310.8	277.6

3.3 Pullout Load of Anchors at Failure

The pullout load at failure for a 50 mm double-plate anchor is found to increase slightly compared to the single-plate anchor. The inclusion of additional plate in case of the double-plate anchor reduces embedment depth and may have reduced the pullout capacity. However, the increase in the pullout load being only 10% of the single-plate anchors, can be credited to the errors in the experimentation using the smaller sized plates. The authors are of the opinion that more sensitive tests are to be conducted with lesser weight of the tie rod and the steel wire system. The use of lesser weighted tie rod was not practiced in order to provide a uniform basis for comparisons.

Table 1 shows the trend for 100 mm circular plate. The decrease in the pullout load, due to addition of plate, may be due to the reduction in the effective embedment depth of the double-plate anchor. The upper plate is embedded at a lesser embedment depth. The reduction in the embedment length provides lesser soil volume for the passive resistance to mobilize, and the pullout load at failure was found to get lower, with the observation of heave. The test on the 100 mm single-plate anchor at an embedment ratio of 3 has given a pullout capacity lesser than the double-plate anchor of similar specifications. This can be credited to the errors in the nonuniformity of the sand raining technique and possible change in the inclination due to an unwarranted disturbance, specially observed in the tests at smaller depths.

A similar study by Kumar and Sahoo (2012), and Kumar and Naskar (2012), by using limit analysis approach on co-axial anchor plates in $c-\phi$ soil showed greater uplift component due to soil cohesion, for a group of two anchors compared to a single isolated anchor. Kumar and Naskar (2012) reported that the uplift resistance for two anchors and a single anchor remains almost identical in frictional material. The present laboratory study shows a decrease in the pullout load for the double-plate anchors. During the actual experimentation of the double-plate anchor system, the two plates of the anchors are co-axially joined to the same tie rod and placed at the same position in the tank. Subsequently, the soil material being sand is made to occupy the volume of the tank by using the devised rainfall technique to maintain the desired density. The way the sand particles, per se, occupy the space between the two co-axial anchors, specifically below the upper plate of the double-plate anchor

system could neither be controlled nor be judged to be uniform for all the tests. This inconsistency in the controlled distribution of the soil particles can be credited to an early failure of the double-plate anchor system.

4 Conclusions

An experimental study was conducted to study the use of multi-plate circular anchors inclined at an angle of 22.5° to the horizontal. The study shows the variation of pullout load with the displacement of anchors. The uplift capacity of single-plate inclined anchor increased with the increase in the size of the anchor and the depth of embedment depth. The uplift capacity, however, decreased by a thin margin with the addition of another plate in the case of double-plate anchor. The double-plate inclined anchors provided more resistance to the pullout forces with the increase in the size of the anchor and the depth of the embedment of anchor plate. The study summarizes the effect of inclusion of additional plate at shallow depths (for embedment ratios of 2–4) and proves the ineffectiveness of multi-plate anchors subjected to oblique loads at shallow depth.

References

- Akinmusuru JO (1978a) Horizontally loaded vertical plate anchors in sand. *J Geotech Eng* 104(GT2):283–286
- Akinmusuru JO (1978b) Vertical line groups of horizontal anchors in sand. *J Geotech Eng* 104(GT8):1127–1130
- Akinmusuru JO (1984) Mutlibell and block anchor capacities in sand. *Soils Found* 24(4):118–130
- Das BM (1975) Pullout resistance of vertical anchors. *J Geotech Eng* 101(GT1):87–91
- Das BM, Seeley GR (1975a) Passive resistance of inclined anchors in sand. *J Geotech Eng* 101(GT3):353–356
- Das BM, Seeley GR (1975b) Inclined load resistance of anchors in sand. *J Geotech Eng* 101(GT9):995–998
- Geddes JD, Murray EJ (1996) Plate anchors groups pulled vertically in sand. *J Geotech Eng* 122(7):509–516
- Goel S, Shalini, Patra NR (2006) Break out resistance of inclined anchors in sand. *Geotech Geol Eng* 24:1511–1525
- Hanna A, Foriero A, Ayadat T (2015) Pullout capacity of inclined shallow single anchor plate in sand. *Indian Geotech J* 45(1):110–120
- Hoshiya M, Mandal JN (1984) Some studies on anchor plates in sand. *Soils Found* 24(1):9–16
- Ilamparuthi K, Dickin EA, Muthukrisnaiah K (2002) Experimental investigation of the uplift behavior of circular plate anchors embedded in sand. *Can Geotech J* 39:648–664
- Kozlov SM (1967) Investigation of the behaviour of anchorages acted on by horizontal loads. Leningrad. Translated from *Osnovaniya, Fundamenty i Mekhanika Gruntov* 6:619–621
- Kumar J, Naskar T (2012) Vertical uplift capacity of a group of two coaxial anchors in a general $c-\phi$ soil. *Can Geotech J* 49:367–373
- Kumar J, Sahoo JP (2012) Vertical uplift capacity of a group of two coaxial anchors in clay. *J Geotech Geoenviron Eng* 138(3):419–422

- Merifield R, Smith C (2010) The ultimate uplift capacity of multi-plate anchors in undrained clay. *Soil Behavior and Geo-micromechanics*. Geotechnical Special Publication No. 200, pp 74–79. <http://ascelibrary.org/doi/abs/10.1061/41101%28374%2912>
- Ranjan G, Kausal YP (1977) Load-deformation characteristics of model anchors under horizontal pull in sand. *Geotechn Eng* 8:65–78
- Stewart W (1985) Uplift capacity of circular plate anchors in layered soil. *Can Geotech J* 22:589–592
- Tilak VB, Samadhiya NK (2017) Uplift capacities of double-plate square anchors at shallow depths in sand. In: *Indian geotechnical conference GeoNEst, IIT Guwahati, Assam, India*
- Tilak VB, Samadhiya NK (2018) Uplift capacities of inclined double-plate square anchors at shallow depths in sand. In: *International conference on advances in construction materials and structures (ACMS-2018), IIT Roorkee, Roorkee, Uttarkhand, India*

Analysis and Design of Pile Foundations for a Sewage Treatment Plant



S. Samarth, S. Nethravathi, M. S. Nagakumar, and G. Venugopal

Abstract In the present study, pile foundation underneath a single structural unit of a 90 MLD Sewage treatment plant is considered. The optimum configuration of pile arrangement with respect to number and spacing of piles for constant parameters of embedment depth of pile and subsoil characteristics and varying parameters of diameter of pile, eccentricity of loading, and pile material are investigated by using ETABS and SAFE softwares. The optimization, in terms of axial loads and slab stresses obtained, is considered for piles embedded in stratified soil with lower depths of pile shaft socketed in weathered rock, which has not been studied here to fore. Optimum pile configuration was found to be different than that which was originally provided for the considered structure. Next it was found that the endeavor to analyze pile foundation was justified in the case of provision of lesser number of piles and light-weight structural concrete but not for variation of pile diameter.

Keywords Pile foundation · Optimum configuration · SAFE software · Axial load · Weathered rock

1 Introduction

Pile foundation is one of the type of deep foundation, most often used in case of subsoil with loose upper layers, not suitable for a shallow foundation, wherein the piles are used to transmit the load to deeper harder layers. Pile foundation is being increasingly adopted due to disadvantages of traditional shallow foundation such as requirement of a large bearing area and excavation of a large volume of earth. Piles are classified depending upon type of soil, pile material, and load transmitting characteristic. The performance of the pile is influenced by its installation procedure; this variable distinguishes it from conventional foundation. Also pile foundations are more economical compared to shallow foundations when the structure is spread over a large bearing area.

S. Samarth · S. Nethravathi (✉) · M. S. Nagakumar · G. Venugopal
Department of Civil Engineering, R. V. College of Engineering, Bengaluru, India
e-mail: nethravathis@rvce.edu.in

© Springer Nature Singapore Pte Ltd. 2020
M. Latha Gali and P. Raghuvver Rao (eds.), *Construction in Geotechnical Engineering*, Lecture Notes in Civil Engineering 84,
https://doi.org/10.1007/978-981-15-6090-3_25

In the present study, pile foundation underneath a single structural unit of a 90 MLD Sewage Treatment Plant (STP) sanctioned by Bangalore Water Supply and Sewerage Board (BWSSB) and constructed in Bellandur in the outskirts of Bengaluru city is considered. M/s. Nippon Jogesuido Sekkei Co. Ltd Japan, Mott Macdonald Ltd. U.K. and Tata Consulting Engineers Limited, India (NMT), were the consultants for the project. The STP consists of numerous structures such as primary clarifiers, anaerobic digesters, etc., and also 4 units of anaerobic basin, anoxic basin, and aeration basin. For the present study, pile foundation underneath a single unit of anaerobic basin is considered.

The site is low-lying and frequently flooded by rains; large parts of it is swampy and water-logged. Information from available soil data shows that the site consists of sedimentary sandy clay and sand layers with relatively poor to moderate shear strength at shallow layers. Residual soil formation followed by weathered jointed rock (w.j.r.) and weathered fractured rock (w.f.r) is present at deeper layers. Geotechnical Solutions was commissioned by Vatech Wabag for carrying out detailed soil investigation. This consisted of 32 exploratory boreholes and carrying out of field tests in the boreholes and laboratory investigations on samples collected through the boreholes. The details of these tests and investigations are elaborated in the Geotechnical Investigation Report produced by M/s VaTech Wabag Ltd. The Geotechnical report along with other documents such as Pile load test report, Pile termination criteria report, Pile layout drawing, and Civil General Alignment (GA) drawing, etc., have been obtained from BWSSB for the sake of reference in the present study.

Ground improvement techniques, such as stone columns, cannot in-principle be considered as piles (Varaskin et al. 2016). Confusion in drawing a boundary between piling techniques and ground improvement techniques (such as vibro-stone columns) is due to the use of imprecise terminology. In vibro-stone columns, loads are not directly transmitted to depth but soft soil supports part of the load (between 60 and 90%) whereas in pile foundations, soft soil is just bypassed (or used for skin friction consideration). For model flexible pile arrangements embedded in clay, lateral load response and flexural behaviour were studied through experimental investigation (Kesavan and Chandrasekaran 2015). Various factors are evaluated for lateral response of pile arrangement such as magnitude of applied horizontal load, embedment depth of pile, size of pile arrangement, and position of pile within arrangement. It was found that flexible piles cannot be considered as flexible if they are subject to >60% of ultimate lateral load. Also, front row pile of 3×3 group had about 16% greater maximum bending moment than that of middle row pile.

The effect of pile configuration in terms of its number and spacing upon pile axial behavior has been investigated. This has been done for piles embedded in clayey soils, layered clayey soils, and layered sandy soils. According to, Comodromos et al. (2012) the response of various pile groups in clayey soils under lateral loading was investigated taking into consideration various factors including varying soil shear strength. It was found that pile response demonstrated maximum discrepancy for small deflection levels and as deflection increased, the discrepancy in pile response decreased. According to, Chandrasekaran et al. (2010) the response of various model pile groups in clayey soil under lateral loading was investigated taking into consideration various

factors including number and spacing of piles. The critical spacing was found to be 5ϕ for 1×2 group and 8ϕ for 2×2 group. According to, Maheetharan et al. (2016) optimum pile configuration was obtained for pile-raft foundation embedded in sand. The theoretical estimates of raft settlements were compared with the measured values and were found to be in reasonable agreement. The optimum configuration, in terms of axial loads and slab stresses obtained, is considered for piles embedded in stratified soil with lower depths of pile shaft socketed in weathered rock, which has not been studied heretofore.

2 Methodology

After the above mentioned literature review, an in-depth study has been made of the documents obtained from BWSSB. The salient details obtained from Geotechnical report include engineering properties of subsoil for a considerable depth at the site of borehole provision. The salient details obtained from Pile Termination Criteria report include the procedure whereby the process of evaluation of pile embedment depth is elaborated. The salient details obtained from Pile Load Test report include safe vertical compression load and safe lateral load of pile. The details required for modeling of super-structure and sub-structure in ETABS and SAFE is obtained from Pile layout drawing and Civil General Alignment (GA) drawing. These details include the material and sectional properties of all structural elements (example—dimensions of slab and wall sections can be obtained from Civil GA drawing). Also, details of number and position of piles underneath the considered structure are obtained from pile layout drawing and the same is modeled in SAFE.

Results through detailed soil investigation carried out by Geotechnical Solutions were obtained through the following process (based on reference of geotechnical report):

- Detailed soil investigation was carried out which comprised of 32 exploratory boreholes penetrated to varying depths of 7.70–20.00 m.
- Standard Penetration Tests (SPT) were conducted at regular intervals of depth to obtain Penetration Resistance (N).
- N is correlated with values of cohesive property (C_U) of soil.
- N is correlated with (M_V) Coefficient of volume compressibility of soil.
- Grain size distribution tests were carried out for soil samples collected at regular intervals of depth.
- Angle of shearing resistance is estimated using grain size distribution (Fig. 1).
- Thus the shear strength and compressibility parameters of soil samples are estimated.
- These estimated values are substantiated by 1-Dimensional Consolidation test (M_V is obtained) and Unconfined Compression strength test (Shear strength is obtained).

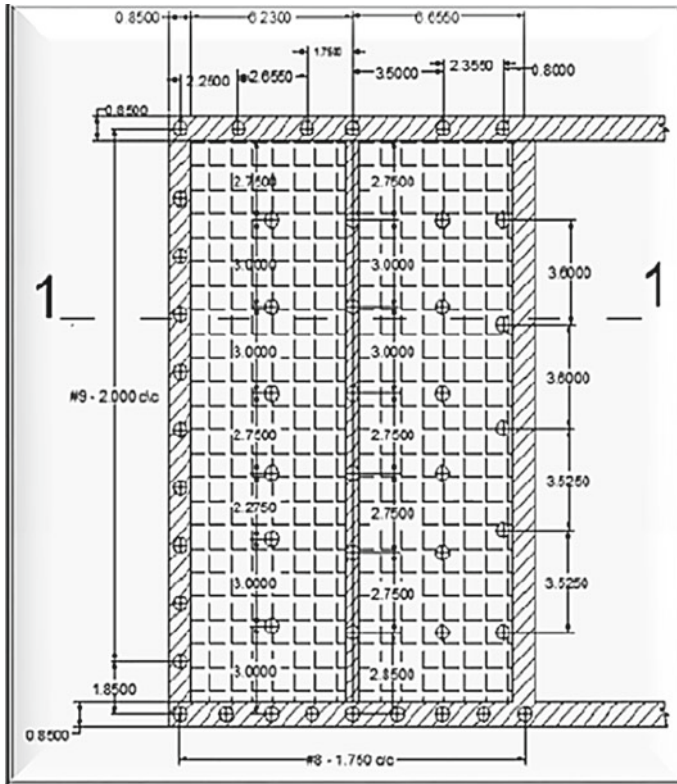


Fig. 1 Autocad rendering of pile layout

Bored Cast-in situ piles were chosen over other types of foundation for the following reasons process (based on reference of geotechnical report):

(I) Shallow footings in natural soil:

- G.W.T is lower than present G.L. during most of the year.
- Possibility of uplift pressure during no liquid condition.
- Maximum desired net S.B.C. for footings is 20 t/m^2 (for foundation portion supporting side wall).
- Amount of steel reinforcement in section/thickness of concrete footing would be too high.

(II) Shallow footings in engineered soil:

- This option is not very practical due to the requirement of deep excavations.
- Practical difficulties in ensuring adequate quality and quantity of materials.
- There is requirement of natural soil of moderate shear strength beneath the engineered soil to prevent undue settlements.

(III) Ground improvement technique of stone column:

- This consists of a relatively huge number of stone columns embedded at a relatively shallow depth in engineered fill.
- The problems mentioned above with regard to engineered fill are encountered in this option too.

(IV) Driven cast-in situ piles:

- They are not preferred to be used in a soil strata of $N > 50$.
- They are not preferable in case of uplift loads because of their relatively shallow embedment depth.

The type of boundary condition provided for the piles is studied and the values obtained for the same from Geotechnical report are corroborated. The pile axial stiffness (K), required for the modeling of piles, is obtained. The loads to be provided for the analysis of structure in ETABS are considered. The load intensities are either assumed from IS codes (example—live load intensity from IS 875 (Part-2) (1987) or calculated based on obtained drawings (example—lateral soil pressure intensities calculated based on Civil GA drawing). The seismic load details are provided based on IS 1893 (Part 1) (2002), and the various load combinations to be considered in structural analysis are noted (Fig. 2).

The structure has been modeled and analyzed in ETABS for the specifications thus obtained. Next, the structural loads are transferred exactly from ETABS model to one in SAFE. The pile foundations are modeled in SAFE for the constant parameters of embedment depth and subsoil characteristics and varying parameters of diameter of pile, eccentricity of loading, and pile material for the structural loads thus transferred. Optimum pile configuration, in terms of number and spacing of piles, is thus found from the analysis of these SAFE models.

Salient details of pile provided and surrounding subsoil are as shown in Table 1 follows (Table 1):

Safe vertical load in compression is obtained as 940 kN from pile load test report and 920 kN from geotech report as shown in above table. The allowable load on the pile is taken as the lower of geotech investigation report and the pile load test results. Socket bond strength between rock and pile was verified by Cole and Stroud approach (Tomlinson 1977) and was found to be 198.9 kN/m². This value is approximately equal to that obtained by geotechnical report (212 kN/m²). Pile is modeled as vertical spring in SAFE. The axial stiffness (K) of pile of 500 mm diameter, 6.9 m length and of M25 grade concrete is 711.41 kN/mm. Length of pile is a function of properties of subsoil and has been obtained through pile termination criteria report.

3 Results and Discussion

In the first model (pile foundation#1), piles were positioned with respect to number and spacing as per the pile layout drawing obtained from BWSSB. A total of 47

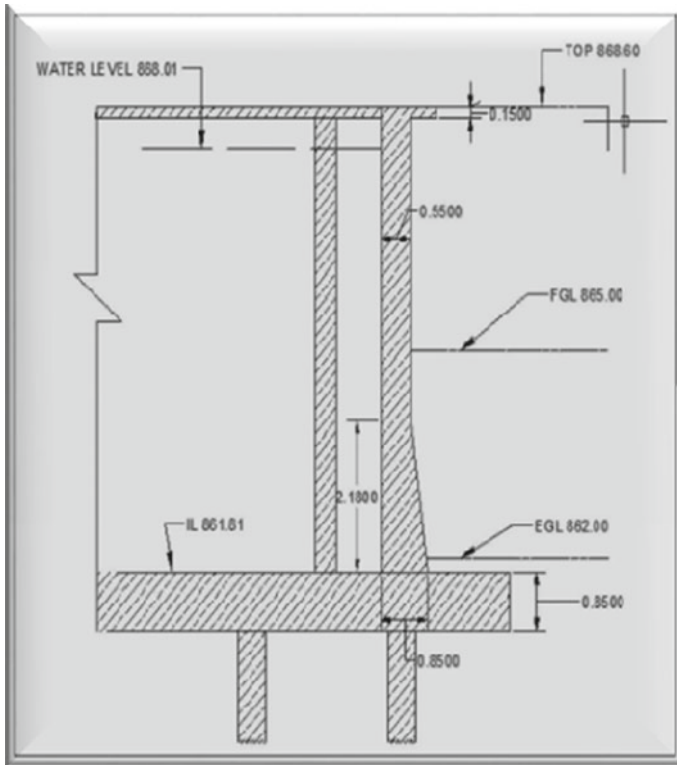


Fig. 2 Autocad rendering of partial elevation view of structure

number of piles of 500 mm diameter each with 22 of them interior piles and the rest along external wall perimeter were provided with a spacing varying from a minimum of 3.5 diameter to a maximum of 7.5 diameter. Minimum spacing of bored cast-in situ piles resting on rock is 2 times the pile diameter (IS 2911 2010). It was observed that the vertical axial load due to critical load combination coming on to each of the 47 pile is within its load carrying capacity ($920 \times 1.5 = 1380$ kN). Also moments in the horizontal plane of each pile are zero implying that all the moments have been transferred to base slab. The maximum of sum of vertical reactions for the entire pile foundation is found to be 28,406 kN.

In the next four models (#2, #3, #4, and #5) the number of piles were the same as in the first (47) but the position of the piles varied. For three of those four models (#2, #3, and #4), the maximum of sum of vertical reactions was 18,648 kN and for one of these models (#4), the vertical axial load due to critical load combination coming on to each of the 47 pile was found to be within its load carrying capacity ($920 \times 1.5 = 1380$ kN). Pile foundation #4, consists of 21 interior piles and 26 piles along external wall perimeter with a spacing varying from a minimum of 3.3 diameter to a maximum of 6.6 diameter. For the remaining model (#5), maximum of sum of

Table 1 Pile and subsoil details

High Flood Level (H.F.L.)	863.868 m R.L
Present Ground Level (G.L)	861.70–863 m R.L
Design Ground Water Table (G.W.T)	863.50 m R.L
Finished Ground Level (F.G.L.)	865.00 m R.L
Invert level (I.L.)	861.81 m R.L
Pile cut-off level	861.00 m R.L
Pile tip level RL	854.30 m R.L
Weak soil up to RL	862.20 m R.L
Length of pile, m	6.70
Pile diameter, mm	500
Eff overburden pressure at pile tip t/m ²	6.9
Ultimate end bearing resistance t/m ²	1080.0
Ultimate end bearing capacity tonnes	212.1
Ultimate skin friction capacity tonnes	63.5
Safe end bearing capacity tonnes	70.7
Safe skin friction tonnes	21.2
Total safe compression capacity tonnes	92.0
Soil at tip	w,j,r
Average SPT N	120
Skin friction from RL, m	856.40

vertical reactions was 19,213 kN. In the next two models (#6 and #7), investigation was continued for different pile diameter (450 and 600 mm), keeping the volume of pile material constant. The maximum of sum of vertical reactions was found to be 19,213 kN. In the next model (#8), 43 number of piles of 500 mm diameter each were provided. The maximum of sum of vertical reactions was 18,648 kN. In the next model (#9), all of the 47 piles were provided with light weight structural concrete. The maximum of sum of vertical reactions was 18,648 kN. In foundation #8 and #9, the vertical axial load due to critical load combination coming onto a few of the piles exceeded its load carrying capacity ($920 \times 1.5 = 1380$ KN). This can be remedied in foundation #8 by moving 4th column of interior piles towards the external wall and in foundation #9 by replacing the critical piles by piles made of conventional concrete. Next, models #1 to #8 are evaluated for slab stresses. It is observed that Pile Foundation #4 has the least slab stresses. Slab stresses of pile foundation #8 were found to be greater than that of #4.

The analysis details of pile foundations and of base slab (pile cap) as obtained in SAFE have been presented in Tables 2 and 3. The pile layout of the optimum pile configuration (#4) as modeled in SAFE is shown in Fig. 3.

Table 2 Pile foundation details

Pile foundation	Diameter (mm)	No. of piles			Spacing (diameter)		a	b (kN)
		Total	Internal	External	Minimum	Maximum		
#2	500	47	21	26	3.3	6.6	2	18,648
#3	500	47	23	24	3.3	6.6	4	18,648
#4	500	47	21	26	3.3	6.6	–	18,648
#5	500	47	16	31	2.66	8.0	4	19,213
#6	600	33	16	17	3.16	9.92	3	19,213
#7	450	58	22	36	2.46	8.82	5	19,213
#8	500	43	17	26	3.3	8.0	4	18,648
#9	500	47	21	26	3.3	6.6	6	18,648

^aNo. of piles exceeding its axial load carrying capacity

^bMaximum of sum of vertical reactions

Table 3 Slab stress details

Sl. no.	Pile foundation	Mxx in kN-m	Myy in kN-m	Slab stresses	
				M11 (max) in kN-m/m	M22 (max) in kN-m/m
1	#1	276,557	–57,480	403	366
2	#2	188,990	46,373	524	483
3	#3	188,990	46,373	489	658
4	#4	188,990	46,373	303.5	82.37
5	#5	194,589	–48,341	605.24	688.17
6	#6	194,589	–48,341	623.1	734.44
7	#7	194,589	–48,341	576.63	835
8	#8	188,990	–48,341	567	399

4 Conclusions

1. Optimum pile configuration in terms of number and spacing of piles is found to be different than that which was originally provided (in the planning and execution of actual work on site) for the considered structure with respect to axial loads obtained.
2. Spacing of interior piles in Global-X direction is dictated by site constraints to ensure that axial load coming onto all piles are within their capacity, whereas spacing of interior piles in Global-Y direction and spacing of external piles is based on general considerations.
3. Pile foundation #4, consisting of 21 interior piles and 26 piles along external wall perimeter with a spacing varying from a minimum of 3.3 diameter to a maximum

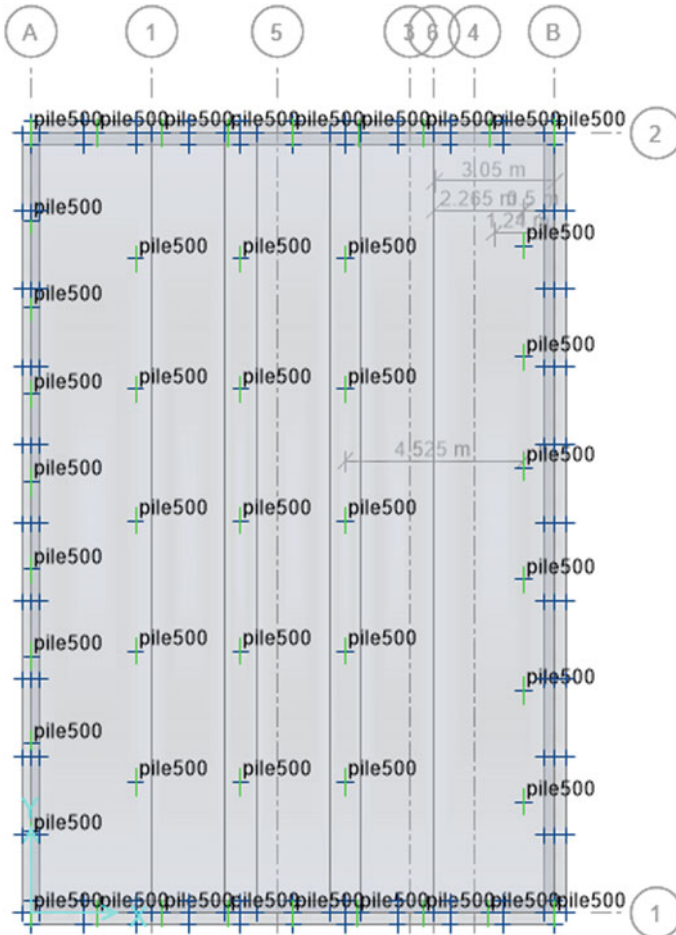


Fig. 3 Pile layout of pile foundation #4

of 6.6 diameter, was found to be the most suitable pile configuration with respect to axial loads and slab stresses obtained.

4. Sum total of vertical reactions (F_z) obtained is the same (18,648 kN) as that of pile foundation #4 for foundation provided with lesser number of piles and light weight structural concrete but not for foundation provided with pile of different diameter.
5. From (4), the endeavor to analyze pile foundation by varying the pile diameter (either by increase or decrease) of 500 mm, keeping the quantity of pile material consumed constant, can be disregarded but the endeavor to analyze pile founda-

tion by provision of lesser number of piles or piles provided with light weight structural concrete can be justifiably continued.

6. The reduction in number of piles may not be desirable due to a consequent increase in slab stresses.

References

- Chandrasekaran SS, Boominathan A, Dodagoudar GR (2010) Group interaction effects on laterally loaded piles in clay. *J Geotech Geoenviron Eng* 136:573–582
- Comodromos EM, Papadopoulou MC, Klimis NS (2012) Variation of p-multipliers for pile groups in clayey soils. In: *GeoCongress*. ASCE
- IS 1893-2002 (Part 1) (2002) Criteria for earthquake resistant design of structures, Part 1—General provisions and buildings. Fifth Revision, Bureau of Indian Standards 2002, New Delhi
- IS 2911 (Part 1/Sec 2) (2010) Design and construction of pile foundations—bored cast-in-situ concrete piles. Second Revision, Bureau of Indian Standards 2011, New Delhi
- IS 875 (Part-2) (1987) Indian Standard Code of practice for design loads for buildings and structures—imposed loads. Second Revision, Bureau of Indian Standards 1998, New Delhi
- Kesavan G, Chandrasekaran SS (2015) Factors influencing the behaviour of flexible pile groups under lateral loading in soft clay. *Indian Geotech J* 34:11–23
- Maheetharan A, Raveendiraraj A, Qusous O, May R (2016) Design of pile configuration for optimum raft performance. In: *Proceedings of the institution of civil engineers geotechnical engineering*, vol 169, pp 139–152
- Tomlinson MJ (1977) *Pile design and construction practice*. A View Point Publication, London
- Varaskin S, Hamidi B, Huybrechts N, Denies N (2016) Ground improvement vs. pile foundation. In: *International symposium on design of piles in Europe*, April 2016

Analytical and Numerical Analysis of Piled-Raft Foundation of Storage Tank



Mahdi O. Karkush  and Ala N. Aljorany

Abstract This paper focuses on the reanalysis of a piled-raft foundation used to support the primary digester of sewage treatment plant under construction in the Southern part of Iraq. Three of the constructed bored piles were failed in the pile test of working piles after applying a load of about 1.5 times the working load. The piled raft is reanalyzed considering the raft contribution. The ultimate carrying capacity of piles and raft settlement is calculated by using analytical equations and numerically by using the software SAFE 12. In order to obtain more accurate values for the required soil parameters, a further soil investigation was carried out, to amend the input data in both analytical and numerical analyses. The results obtained from numerical analysis showed the ability of designed piled raft to carry the working load of the primary digester with an acceptable factor of safety. The analysis results of the piled-raft foundation indicate a change in the load sharing and contribution of the constructed piles due to redistribution of the applied loads on the stiffer piles and the raft.

Keywords Piled-raft · Foundation · Analytical analysis · Numerical analysis · Digester tank

1 Introduction

The primary digester tank under consideration is one of the main parts of sewage treatment plant and is currently under construction. The primary digester can be described as a reinforced concrete tank that consists of three main parts. The upper part is of a conical shape with outer radius of 12.5 m and height of 6.5 m, the middle part which has a cylindrical shape with outer radius 12.5 m at its upper part (7.3 m height) and 12.8 m at its lower part (6.45 m height) and the lower part of the digester which is of an inverted conical shape with outer radius of 12.8 m. The total height of the tank will therefore be 29.25 m. The tank is supported by eight triangular radial

M. O. Karkush (✉) · A. N. Aljorany
Department of Civil Engineering, University of Baghdad, Aljadriah, Baghdad, Iraq
e-mail: mahdi_karkush@coeng.uobaghdad.edu.iq

© Springer Nature Singapore Pte Ltd. 2020
M. Latha Gali and P. Raghuvver Rao (eds.), *Construction in Geotechnical Engineering*, Lecture Notes in Civil Engineering 84,
https://doi.org/10.1007/978-981-15-6090-3_26

373

walls fixing the inverted conical base to the tank raft. The structure foundation is a reinforced concrete raft of 16.5 m radius and 1 m thickness resting at a depth of about 2.5 m below the ground level. This raft is supported by 193 piles distributed in a radial direction. The piles were cast in situ concrete (bored) piles of 0.6 m diameter and 15 m length.

The foundation of primary digester tank consists of 193 piles were constructed and the raft has been casted as well. The structural designer has defined the working load of each pile as 870 kN. After testing eleven working piles, it is found that three piles cannot support a load of 1.5 times the working load (1305 kN) safely or in other words the factor of safety of these failed piles is <1.5 (Al-Liqaa Engineering Bureau 2015). The problem was analyzed by the consulting engineering company who supervises the project by using SAAP2000 considering different combinations and probabilities of distribution for the (failed) piles and suggested a structural solution to the problem by adding a reinforced concrete ring beam around the existing raft, as mentioned by the consultant report (Rezae and Karami 2015).

In the present work, a detailed soil investigation data collected from the site of the tank and the foundation of tank reanalyzed considering piled-raft foundation to check the adequacy of such pile to support the design loads transmitted from the structure to the foundation. Also, the carrying capacity of piles and consolidation settlement of foundation have been calculated by using theoretical equations. The primary digester is currently under construction. The 193 piles were constructed and the raft has been casted as well. The structural designer (SGI Company) has defined the working load of each pile as 870 kN. After testing eleven working piles, it is found that three piles cannot support a load of 1.5 times the working load (1305 kN) safely or in other words the factor of safety of these failed piles is <1.5 .

2 Site Description and Investigation

The whole site of treatment plant was investigated by drilling 12 boreholes extended to a depth of 20 m below the existing ground surface (Al-Mawal Company 2013). The soil stratification and bearing capacity of soil can be described as follows:

- The surface layer consists of brownish to greyish silty clay with sand (CL-CH) of soft to medium consistency. This layer extended from the existing ground level to a depth of 15.5 m. The thickness of this layer is variable in the site.
- In some locations in the site, a subsurface layer of green silty sand with clay (SW-SP), the density of this layer varies from loose to medium dense and extended from a depth of 2.5–7.5 m.
- A layer of green silty sand with gypsum (SW-SP). The density of this layer varies from dense to very dense and this layer extended from a depth of 14.0 to the end of boring (20.0 m) in some locations of the site.
- A layer of green silty clay with sand (CL) and has stiff consistency, this layer extended from a depth of 18.5–20.0 m.

- The allowable bearing capacity of shallow foundation ranged 80–98 kPa at a depth ranging from 2 to 3 m below ground level.
- The allowable carrying capacity of bored piles of 600 mm diameter and 15 m length is 1092 kN. The carrying capacity of piles based on a factor of safety of 2.5, so that the ultimate carrying capacity of such piles as suggested by the previous site investigator is 2730 kN.

It is believed that the suggested carrying capacity is a little bit overestimated as none of the pile tests indicates such high values for the ultimate carrying capacity. For this reason, it is suggested to perform an additional soil exploration by drilling another three exploring boreholes that may help in obtaining more precise soil parameters to be used in the analysis of the problem. Two boreholes were drilled to a depth of 20 m and the third borehole was drilled to a depth of 10 m. The additional boreholes and soil samples obtained from these boreholes indicated that the soil in the site at its most is silty clay that differs in its constituents from depth and location to another with some sand at some locations. According to the results of standard penetration tests and laboratory tests, the results of allowable bearing capacity of foundation at depth 1.5 m is ranging from 55 to 80 kPa and at depth 4.5 m is ranging from 57.5 to 110 kPa. Also, it's concluded that a bored pile of 0.6 m diameter and 15 m depth has an allowable carrying capacity of 710 kN (Aljorany and Karkush 2015). This conservative value of allowable carrying capacity is almost consistent with the results of working pile tests.

3 Geotechnical Parameters of Soil

In order to perform a sound analysis to the problem, it is very important to define a reasonable value for the soil parameter that will be used in the analysis. After carefully reviewing the soil investigating reports, the following parameters are considered as representative values for the soil parameters in the site, see Table 1 (Al-Mawal Company 2013; Aljorany and Karkush 2015).

$$E = E_{oed} (1 + \mu)(1 - 2\mu)/(1 - \mu) \quad (1)$$

The shear modulus (G) can be obtained by using three different correlation expressions (Kulhawy and Mayne 1990; Lambe and Whitman 1979):

$$G = E/2(1 + \mu) \quad (2)$$

$$G = (100 \text{ to } 300)S_u \quad (G \text{ in Mpa and } S_u \text{ in kPa}) \quad (3)$$

$$G = 0.6 \times 25^{S_u/100} \quad (G \text{ in MPa and } S_u \text{ in kPa}) \quad (4)$$

Table 1 Geotechnical parameters of soil

Property	Value
The undrained shear strength (S_u)	34 kPa
The compression index (c_c)	0.10534
The swelling index (c_s)	0.01115
The initial void ratio (e_o)	0.735
The preconsolidation pressure (P_c)	111 kPa
The coefficient of volume change (mv)	$1.2 \times 10^{-4} \text{ m}^2/\text{kN}$
The constrain modulus (E_{oed})	8.05 MPa
The dry unit weight (γ_d)	15.26 kN/m ³
The saturated unit weight (γ_{sat})	19.76 kN/m ³
The Poisson's ratio (μ)	0.4 (assumed)
The water table level	1.5 m below EGL

Equation (2) gives a value of G about 1.342 MPa but it depends on the elastic properties of soil and doesn't account for shear strength of soil (S_u), while Eq. (3) and by using its lower limit gives a value of 3400 kPa. Equation (4) results in a value of 1.792 MPa for G . By considering the three values of (G), a conservative value of $G = 2$ MPa is quite reasonable to be considered as a representative value for the foundation soil layer in the analysis. Regarding the modulus of subgrade reaction of the supporting soil (K_s) in the site, the geotechnical report assumes that at depth 2.5 m, (K_s) is ranging from 2 to 13 MN/m³ (Aljorany and Karkush 2015). This value is obtained by using the following formula:

$$K_s = 40 \times FS \times \text{Allowable Bearing Capacity} \quad (5)$$

and

$$K_s = E/B(1 - \mu^2) \quad (6)$$

4 Theoretical Analysis of Piled-Raft

Before starting the theoretical analysis, it is important to calculate the applied load on the soil by the primary digester tank. The main load of this structure is resulting due to its dead load plus the weight of water inside. The live load which implicitly considered constitutes a very low portion of the total weight of the tank and water inside. The total weight of the concrete tank and the water at its maximum capacity is about 160 MN. The applied stress on the soil will be about 187 kPa by considering the raft footing area of about 855 m². Regarding the wind load, a calculation was

performed by considering a wind speed of about 136.75 km/h and an importance factor of 1.15 (Bowles 1996). It is found that for such structure of height about 30 m, the wind pressure is ranging from 1.4 kPa at its top to 1 kPa at its bottom. This will give a resultant horizontal force of about 1000 kN and a resulting moment on the foundation of about 20 MN m. To calculate the eccentricity (e) of the total applied loads, this value of moment is divided by the axial force (160 MN) to give an eccentricity value of about $e = 0.125$ m which is less than $B/6$ of the footing ($B = 33$ m). Therefore, the wind load can be neglected in the analysis. In the beginning, the foundation of the structure will be analyzed as raft foundation at depth 2.5 m. The ultimate bearing capacity of such raft can be calculated as follows (Das 2011):

$$q_{ult} = 5.14Su \left(1 + \frac{0.2B}{L} \right) \left(1 + \frac{0.4D}{L} \right) + \gamma D \quad (7)$$

In which B and L are width and length of the raft and D is the depth of footing placing. For circular footing, both L and B are substituted by the raft diameter (33 m). This equation gives a value of about 254 kPa. This means that the foundation soil can carry applied stress with a factor of safety of about 1.357. Due to its large diameter, raft foundation usually causes a settlement more than that permissible by different codes of practice. Therefore, the factor of safety should be increased to control the foundation settlement to be within allowable limits. It's recommended to adopt the values presented by Skempton and McDonald in checking the settlement of the structures foundation (Skempton and MacDonald 1965). Regarding the circular raft of the primary digester tank, the anticipated settlement can be calculated as follows (Fleming et al. 2009):

$$S_c = \frac{C_c}{1 + e_o} H \log \left(\frac{\sigma_o + \Delta\sigma_v}{\sigma_o} \right) \quad (8)$$

Considering normally consolidated clay, the following input data used in the calculation of consolidation settlement: $P_c = 111$ kPa, thickness of consolidated layer ($H = 17.75$ m), the overburden pressure at the mid of consolidated layer ($\sigma_o = 104$ kPa), and incremental stress increase resulting from tank load ($\Delta\sigma_v = 116$ kPa). The structure load transferred to the mid of consolidated layer by using a method of 2 V:1H, the resulting settlement is about 350 mm which is much greater than that allowed (65–100) mm. In such situation, piles are usually used and the foundation should be considered as piled raft. The main function of piles in such foundation is to reduce the settlement of the raft to its allowable limit and to increase the factor of safety of soil bearing capacity. It is documented that when the raft diameter (or width) is greater than the pile length the pile will no longer work as a pile group, rather the foundation will work as piled-raft. To analyze the piled-raft foundation, it is important to calculate the pile stiffness and the raft stiffness individually then calculate the piled raft stiffness. Regarding the piles in hand (diameter, $D = 0.6$ m

and length, $L = 15$ m) installed in such soil, the following equation is used to define whether the pile is long (flexible) or short (rigid) pile. For short rigid piles (Wood 2004; Poulos 2001):

$$L/D < 0.25 \sqrt{\left(\frac{E_p}{G}\right)} \quad (9)$$

L/D is about 25 while the right-hand side term is 27, therefore the pile is considered as short (rigid) pile and the stiffness of an individual pile (K_{p1}) is calculated by the following equation (Poulos and Davis 1980):

$$K_{p1} = \frac{2DG}{1 - \mu} + \frac{2\pi GL}{\zeta} \quad (10)$$

where (ζ) value is ranging from 3 to 5 and considered as 4 in this analysis. The calculated value of (K_{p1}) is 51.124 MN/m. The stiffness of 193 piles (K_p) cannot be considered as the sum of individual pile stiffness (K_{p1}) because of the interaction between piles. The suggested equation to calculate the stiffness of whole group of piles (K_p) is (Poulos and Davis 1980):

$$K_p = K_{p1}(\text{No of Piles})^\beta \quad (11)$$

A reasonable value of $\beta = 0.66$ can be considered in the analysis. This yields a value of K_p of about 1.6485 GN/m. The raft stiffness (K_r) is calculated as follows (SAFE 2009):

$$K_r = 2DG/(1 - \mu) \quad (12)$$

That gives $K_r = 220$ MN/m. The piled raft stiffness (K_{pr}) is calculated by using (SAFE 2009):

$$K_{pr} = \frac{K_p + (1 - 2\alpha_{pr})K_r}{1 - \alpha_{pr}^2 \left(\frac{K_r}{K_p}\right)} \quad (13)$$

where (α_{pr}) represents the factor of interaction between piles and raft, its value can be considered as 0.8. The calculated value of K_{pr} is about 1.65919 GN/m. Considering an applied load on the piled raft of 160 MN, the resulting displacement will be 96 mm which is much less than that of raft alone and within the acceptable limits.

5 Analysis of Field Pile Tests

The working carrying capacity or design carrying capacity of a pile can be defined as the load can withstand by the pile safely within allowable settlement. The allowable settlement depends on the importance of building, geotechnical properties of soil, type of pile, and life design of proposed structure. Generally, the design carrying capacity of pile is pre-calculated theoretically depends on the field and laboratory tests, then the factor of safety is checked by conducting field loading of test piles. As mentioned earlier, the circular raft is supported by 193 piles of 0.6 m diameter and 15 m length. The piles are reinforced concrete bored piles. Eleven working piles were tested by considering the working load of each pile is 870 kN. The maximum axial loading reached in the pile tests is 1305 kN that represents 1.5 times the working load. By considering the total applied load of about 160 MN and dividing this load by the total number of piles, one can get a load of about 830 kN. It is thought therefore that the structural designer presumed that the piles will work as (pile group) with a value of group efficiency of about 95%. The pile test reports indicate that three of the tested piles cannot carry a working load of 870 kN with a factor of safety (SF = 1.5) and mentioned that these piles are considered as (failed) piles. The calculated value of pile ultimate load is (Orense et al. 2010; Tomlinson and Woodward 2014):

$$P_{ult} = \pi D L S_u + \frac{\pi D^2}{4} N_c S_u \quad (14)$$

where D is the diameter of pile, L is the length of pile, S_u is the undrained shear strength of soil, and N_c is the bearing capacity constant. Considering $N_c = 9$, the ultimate carrying capacity (P_{ult}) will be about 1047 kN. If the factor of safety is considered as (SF = 2), the allowable carrying capacity will be about 524 kN. Therefore, the assumed working load of each pile (870 kN) could be an overestimated value. To reanalyze the pile test results, two criterions have been adopted to obtain the ultimate carrying capacity of the pile from pile test results. The first one is Davisson's criteria and the second is Brinch-Hansen (1963) criteria. The results of six piles test are reanalyzed; two of the failed piles, namely Pile Nos. 138 and 184 and four of the piles that passed test, namely, Pile No. 20, 22, 70, and 142.

5.1 Davisson's Method (1972)

The ultimate carrying capacity of pile can be estimated from load-settlement curve by using a well-known and widely used method called Davisson's method. Davisson's method offers the ultimate carrying capacity corresponding to the maximum allowable settlement taken into consideration the dimensions of cross-sectional area and length of pile. This method considered conservative to determine the ultimate

Table 2 Values of P_{ult} obtained from pile test results

Pile no.	Davisson's method, P_{ult} (kN)	Brinch-Hansen method, P_{ult} (kN)	Remarks
P20	>1305	1643	Passed
P22	1152	1360	Passed
P70	1222	1410	Passed
P138	576	872	Failed
P142	1300	1580	Passed
P184	726	1080	Failed

carrying capacity of pile without dividing by the factor of 0.9 which reduces the conservation of the method.

5.2 Brinch-Hansen's 80% Criterion (1963)

Brinch-Hansen proposed 80% failure criteria for stress-strain behavior of cohesive soils. The failure load can be defined as the load that causes four times the settlement of the pile head that corresponding to 80% of the load estimated directly from the load-settlement curve. The pile test results are reanalyzed to obtain the ultimate capacity by using both Davisson's method and Brinch-Hansen method. The calculated values are shown in Table 2. It can be noticed that Davisson's method gives conservative values for the ultimate carrying capacity and cannot predict that value when it exceeds the maximum load reached during the pile test. Since the number of tested piles is limited (only eleven piles), it is important to generalize a representative value for all the piles that passed the test and another value for all the failed ones. To be more reasonable, an averaging for the values obtained by the two adopted method; Davisson and Brinch-Hansen will be made then another averaging for the tested piles. This will result in an average value for the ultimate carrying capacity for the piles that passed the test of about 1380 kN and that value for the (failed) piles is 815 kN.

6 Analysis of Field Pile Tests Results

A computer program SAFE 12 (SAFE 2009) is used to model and analyze the problem. Only the pile raft will be modeled as reinforced concrete mat foundation and the rest of concrete and other members of the primary digester will be represented as vertical loading applied on the circular raft. This simulation disregards the additional stiffness resulting due to the tank structure and could be in the safe side as the adopted stiffness of the raft is less than its actual value. In the program SAFE 12, each pile is modeled as an individual spring of a certain stiffness value K_{p1} . In

this analysis, the pile test results will be adopted to define this value of pile stiffness because it is more reasonable than that obtained by theoretical analysis. After reviewing the pile test results, it is found that the secant stiffness values are ranging from 40 kN/mm for the failed piles up to more than 240 kN/mm for the other piles. Therefore, an average value of 140 kN/mm will be considered as a conservative value as the number of failed piles is less than half of the total tested piles. To account for piles interaction, the equivalent value of pile stiffness that will be input in the analysis is only 10 kN/mm which is almost equal to $K_{p1} * (193)^{0.5}/193$ (Orense et al. 2010; Tomlinson 2014). The value of soil subgrade reaction is also required by the program SAFE 12 and the adopted value is 2 MN/m³. Regarding the raft itself is modeled as reinforced concrete with a unit weight of 24 kN/m³.

SAFE 12 analysis results are shown and discussed with the aids of figures and a table in the following paragraphs. The contours of raft displacements are shown in Fig. 1. It can be noticed that the displacement is almost uniform with an average value of 43.8 mm. The maximum value is 44.2 mm occurs not at the raft center, as expected, but at a radial distance of about 7 m from the center. This is mainly because of the smaller pile spacing close to raft center. The minimum displacement value occurs at the raft edge as expected with a value of 43.5 mm. The average value of displacement is within the acceptable limits (less than 50 mm) and more than 90%

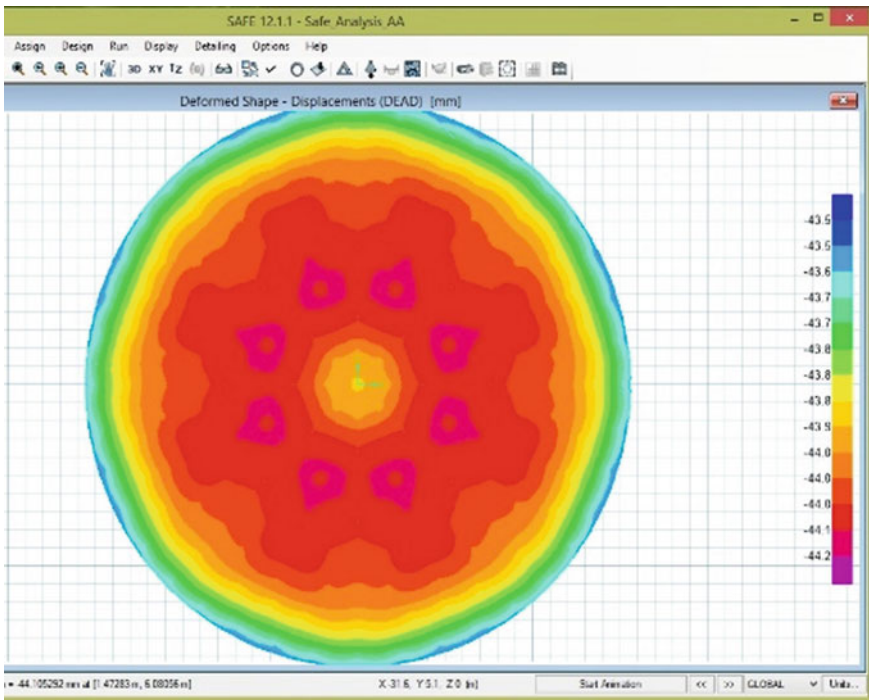


Fig. 1 Contours of the displacements of raft foundation

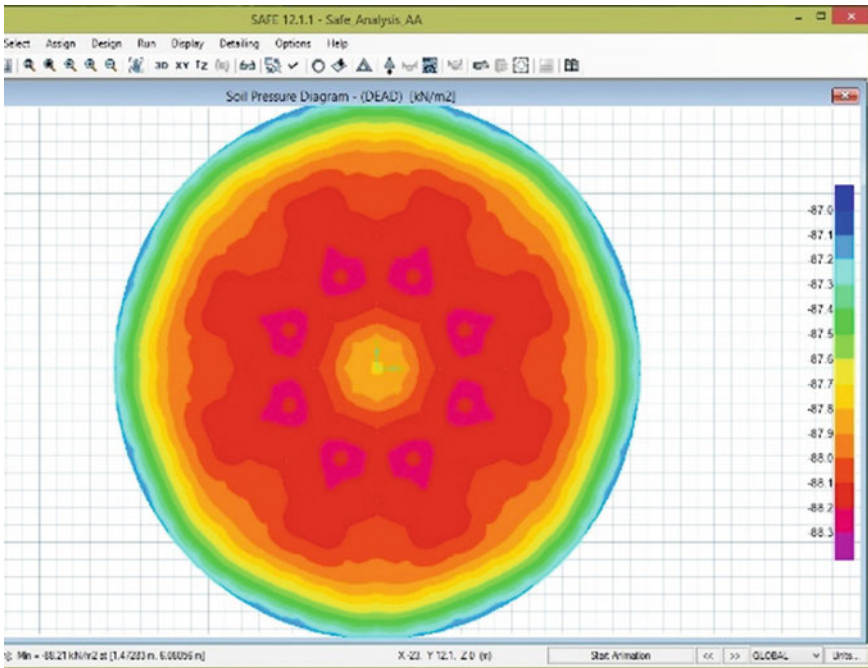


Fig. 2 Contours of subgrade soil pressure resulted from the loading of digester tank

of this displacement will take place during the construction as it is resulting mainly due to the digester self-weight and equipment plus the weight of water inside the tank. The differential settlement which is about 0.7 mm is very small and is expected to be reduced if the stiffness of the tank is added to the raft stiffness.

The resulting soil pressure on the footing of digester tank is shown in Fig. 2. It can be noticed that the distribution of subgrade soil pressure is consistent with the raft displacement. The average value of soil pressure is 87.6 kPa which is less than the allowable bearing capacity obtained by theoretical analysis. The values of the axial load carried by each pile vary from 440 kN to about 483 kN depending on the pile position. Considering the average ultimate load values for both failed and passed piles, the average value of factor (SF) for the failed piles is about 1.85 and for the piles that passed the test is 2.86. These values of factor of safety obtained by considering all the piles are of the same stiffness, the average value of pile stiffness as mentioned earlier. Therefore, for stiffer piles the carried load will increase and then the factor of safety will increase. It is known that the failed piles have a less stiffness value. It is expected therefore that both failed and passed piles will have a reasonable value of factor of safety of 2 or more.

7 Conclusions

After reviewing the previous soil investigating report and pile tests reports, the foundation of the primary digester tank is reanalyzed. Both analytical and numerical analysis has been performed considering conservative and representative values for the soil parameters in the site. The following points are deduced as concluding remarks:

- The foundation of primary digester which consists of circular raft and the supporting 193 piles are analyzed as “piled-raft foundation” rather than pile group or a circular pile cap. This is mainly because the diameter of the raft is much greater than the pile depth. In piled-raft foundation analysis, both the supporting piles and the subgrade soil will share the applied load of the structure. The main function of piles is to reduce the anticipated settlement of large diameter raft.
- According to the results of theoretical analysis for foundation of primary digester which based on the parameters of soil tested in the field and laboratory, the foundation (pile-raft interaction) of primary digester can be considered acceptable with a factor of safety at least equal 2.
- After reanalyzing the pile test reports by using two well-known methods; Davisson and Brinch-Hansen methods to determine the ultimate carrying capacity of the tested piles. The analysis results and the theoretical calculations have shown that the adopted ultimate and allowable bearing capacity values by the foundation structural designer (SGI) and by the site investigation report editor are over-estimated. Thus, the consultants from Baghdad University conducted field and laboratory soil tests to get accurate values for soil parameters which were used in the analysis of piled-raft foundation system.
- Using SAFE 12 software to analyze the problem numerically, it is found that the anticipated settlement of the raft is <100 mm which is within the acceptable limits. It is also found that the piles can support the applied load with a factor of safety of 1.85 for the failed piles and 2.86 for the piles that passed the tests. These values are believed to converge to more than 2 for both groups of piles. This is mainly because stiffer piles will tend to carry greater load while piles of less stiffness will carry a less load.
- To increase the factor of safety and reduce the anticipated consolidation settlement of pile-raft footing, it is recommended to increase the diameter of raft footing by adding a ring beam to the existing raft footing. Also, it is important to reduce the differential settlement especially in the locations of failed piles in the test.

References

- Aljorany AN, Karkush MO (2015) Analysis report of primary and secondary digesters tanks of sewage treatment plant. University of Baghdad, Unpublished confidential report
- Al-Liqaa Engineering Bureau (2015) Pile testing report No. 614, Unpublished confidential report

- Al-Mawal Company (2013) Soil investigation report for the site of Al-Dewainiya treatment plant project. Unpublished confidential report
- Bowles LE (1996) Foundation analysis and design. McGraw-Hill, New York
- Das BM (2011) Principles of foundation engineering, 7th edn. Thomson Brooks, Cole, USA
- Davisson MT (1972) High capacity piles. In: Proceedings, Lecture Series, Innovations in Foundation Construction, ASCE, Illinois Section, Chicago, March 22, pp 81–112
- Fleming K, Weltman A, Randolph M, Elson K (2009) Piling engineering, 3rd edn. Taylor and Francis Group, London and New York
- Hansen BJ (1963) Discussion of hyperbolic stress-strain response: cohesive soil. *J Soil Mech Found Div ASCE* 89(4):241–242
- Kulhawy FH, Mayne PW (1990) Manual on estimating soil properties for foundation design. Cornell University, Ithaca, NY, USA
- Lambe TW, Whitman RV (1979) Soil mechanics, SI version. Wiley, Chichester
- Orense RP, Chouw N, Pender MJ (eds) (2010) Soil-foundation-structure interaction. CRC Press
- Poulos HG (2001) Method of analysis of piled raft foundations. A report prepared on behalf of Technical Committee TC18 on Piled Foundations. ISSMGE
- Poulos HG, Davis EH (1980) Pile foundation analysis and design. Wiley, New York
- Rezae M, Karami M (2015) Review of the failed piles and their effects on the digester foundation, Unpublished confidential report
- SAFE (2009) Slab analysis by the finite element method. Computers and Structures, Inc., Berkeley, CA
- Skempton AW, MacDonald DH (1965) The allowable settlements of buildings. *Proc Inst Civ Eng* 5(6):727–768
- Tomlinson M, Woodward J (2014) Pile design and construction practice. CRC Press
- Wood DM (2004) Geotechnical modelling. CRC Press, Boca Raton

Comparative Study of Methods for Analysis of Laterally Loaded Well Foundation



Ramyasri Rachamadugu and Gyan Vikash

Abstract Well foundation is commonly used in India for road and railway bridges over rivers. It is a massive structure and hence it is generally considered to be safe under laterally loaded condition. Indian Roads Congress Codes (IRC:45-1972 and IRC:78-1983) suggests limit equilibrium approach to determine lateral load capacity of well foundation. It considers well foundation as a rigid body and surrounding soils as elastic in design state and plastic in limit state. Design procedure stated in Indian standard codes determines ultimate lateral load capacity of Well-Soil system. However, it does not yield the magnitude of lateral displacement of a well foundation at the ultimate load. Because of this, it is difficult to decide whether the lateral displacement at estimated ultimate lateral load capacity of a well foundation is allowable or not. Over the years, few methods to analyze the lateral response (both force and displacement responses) of well foundation are developed. These methods consider surrounding soil as linear elastic material which is modeled by linear elastic springs, and well foundation as a rigid body. Recently developed methods consider lateral stiffness as well as rotational stiffness of the surrounding soil and represent soil by parallel combination of lateral linear springs and rotational springs. Some of these methods also consider flexibility of well foundation and model well foundation by Euler-Bernoulli beam element. In this article, we present a comparative study of the available methods of analysis of laterally loaded well foundation. This study indicates significant differences in the response of Well-Soil system obtained from different methods. Validation of existing methods is done with two-dimensional continuum model to identify accuracy in existing models. It highlights the need for proper evaluation of available methods of analysis with realistic incorporation of foundation stiffness and interface effect in modeling the Well-Soil system for pseudo static loading conditions.

R. Rachamadugu · G. Vikash (✉)

Department of Civil Engineering, School of Engineering, Shiv Nadar University, Gautam Buddha Nagar, Greater Noida, Uttar Pradesh, India

e-mail: gyan.vikash@snu.edu.in

R. Rachamadugu

e-mail: rr783@snu.edu.in

© Springer Nature Singapore Pte Ltd. 2020

M. Latha Gali and P. Raghuvver Rao (eds.), *Construction in Geotechnical*

Engineering, Lecture Notes in Civil Engineering 84,

https://doi.org/10.1007/978-981-15-6090-3_27

Keywords Well Foundation · Lateral response · Winkler Spring Model

1 Introduction

Well foundation are commonly used in India to support bridge piers and abutments of major road and railway bridges on rivers with erodible bed (Mondal et al. 2012a, b). This type of foundation is generally preferable when no firm bed is available for larger depth below the river bed. Indian standard codes (IRC:45-1972, IRC:78-1983) applies elastic limit state theory to determine the ability of soil to withstand the failure of the foundation. It considers location of point of rotation is dependent on load magnitude. No clear explanation stated on location of point of rotation at the bottom in design state or 0.2 times scours depth in ultimate state. Soil reaction is considered as parabolic with zero at top and bottom. Soil reaction at zero indicates no resistance offered by soil at top. Deflection variation is considered linearly decreasing from ground surface to bottom of the foundation. The coefficient of horizontal subgrade reaction of soil increases linearly with depth. Failure settlement is calculated by considering full stability in structure to withstand applied load and assumes little foundation settlement will occur and do not include soil structure interaction in calculations. Stiffness calculation of cohesive soil in well foundation is approximated by not considering skin friction which acts as a shear tractions between soil and foundation. Hence, Indian standarad codes considers a simplified approach for analysis which assumes foundation as rigid, elastic, linear, and homogeneous soil and soil–well interactions not included in standard codes.

The point of rotation is an important parameter in determining sharing of moments with in sides and bottom of the foundation. The coefficient of horizontal subgrade reaction (K_h) determines stiffness of soil. Consideration of linearly increasing variation of K_h with depth accounts for continuous increase in stiffness of soil with depth. This consideration is not valid for soft layer present in between the layers. Interaction between soil and foundation indicates separation, sliding, and base lifting at interface. Huge dimensions of well lead to high area of contact with soil and lead to high skin friction between soil and well. Hence neglecting shear tractions and soil-well interaction will not account for side resting moment of soil and soil nonlinearity. Indian code considers rectangle and circular solid foundations. To design a hollow cylinder, value of shape factor and alpha to determine moment of inertia of foundation is not mentioned in the code. Field tests available for determination of coefficient of subgrade reaction exist for pile and caissons but not for well foundations exclusively (Chiou et al. 2012). In the absence of field tests to determine coefficients of subgrade reaction, ratio of vertical to horizontal subgrade reaction is considered as unity. This cannot capture multilayer effect. These assumptions in analysis can result in significant difference in response pattern of foundation from reality. Hence greater clarity is needed on considerations in code for accurate modeling of Well-Soil system.

Many researchers have proposed several design procedures for predicting well foundation response for static loading condition where soil is modeled as springs

attached to foundation (Tsigginos et al. 2008; Varun et al. 2009). But these methods do not consider separation, sliding, and uplifting at interface of soil and well. To incorporate nonlinearity at the interface, some researchers proposed two-dimensional nonlinear analysis (Mondal et al. 2012a, b). This analysis considers soil as continuum medium and foundation is embedded in it. Incorporation of interaction between soil and well is modeled using contact elements. Few methods, models foundation as rigid block (Gerolymos and Gazetas 2006a, b, c; Mondal et al. 2012a, b; Zafeirakos and Gerolymos 2014; Karapiperis and Gerolymos 2014) and some consider it as flexible by modeling foundation as Euler beam elements (Varun et al. 2009; Chiou et al. 2012). Response of rigid structure will be different than flexible structure due to their stiffness variations. Rigid structure modeling considering rotation and lateral displacement of foundation for lateral loading condition. Unlike rigid, flexible considers bending of foundation with displacement. Hence different methods with different considerations are available for well foundation analysis. For accurate determination of lateral response of foundation realistic consideration of foundation's stiffness and soil foundation interaction is important (Varun et al. 2009). Hence for accurate modeling of well foundation, this study considers two-dimensional continuum method for static loading with hollow consideration of the foundation with contact elements at soil-foundation interface.

Multi spring models are preferred methods as they are easy to implement in design offices than continuum model (Mondal et al. 2012a, b). Available multi spring models for static loading case proposed in literature are mostly for Caissons which are rigid, soil foundation with large diameter and shallow embedment (Gerolymos and Gazetas 2006a, b, c; Chiou et al. 2012). Noteworthy models available for well foundation are very few. In literature, model verification of multi spring models is done considering three dimensional finite element model by considering foundation as rigid block and surrounding soil as elastoplastic material with perfect bonding conditions at interface. Foundation has been considered as rigid in both finite element validation and approximate method as these methods are proposed for caissons. But for well foundation, rigid consideration over estimates foundation stiffness as it is a hollow cylinder made up of different concrete materials for strength and filled with excavated soil. Hence it is of interest to see if these models are applicable for well foundation analysis. Hence a comparative study has done in this study between Indian code practices with multi spring model and performance of these models are evaluated with elastic two-dimensional continuum model with four nodes quadrature element modeling for both soil and foundation with interface elements for validation of approximate method and IRC code practices. This study highlights the importance of consideration of foundation stiffness, interaction between soil and foundation, and also questions the practice of considerations of Indian code.

2 Theoretical Methods

2.1 Indian Standard Code Procedure

Indian standard codes (IRC:45-1972; IRC:78-1983) considers the depth of the foundation below the scour depth for stability. Design of well foundation is checked by both elastic and ultimate soil resistance methods. Soil is considered elastic in design load and plastic in ultimate load. Well foundation is assumed as a rigid body. Applied loads are considered at scour level. In elastic state, point of rotation is considered at the bottom of the foundation. Figure 1 depicts deflection profile of the well at sides as linear and soil reaction profile at sides as parabolic. Code considers skin friction from cohesive soil to be very less. Hence, skin friction is not accounted for foundation. Code presumes the load acting on the foundation will be limited to safe bearing capacity and therefore catastrophic settlements are not calculated. Computation of settlements does not take account of slip of foundation structure with respect to soil.

In ultimate conditions, failure is considered at 3 rotation at 0.2 times the depth below scour depth distance from the bottom of the foundation (Fig. 2).

Fig. 1 Displacement profiles and soil reaction profiles of well in elastic state (from IRC:45-1972)

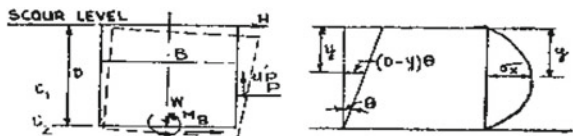


Fig. 2 Ultimate soil pressure distribution at the front and rear faces of the well foundation [IRC:45-1972]

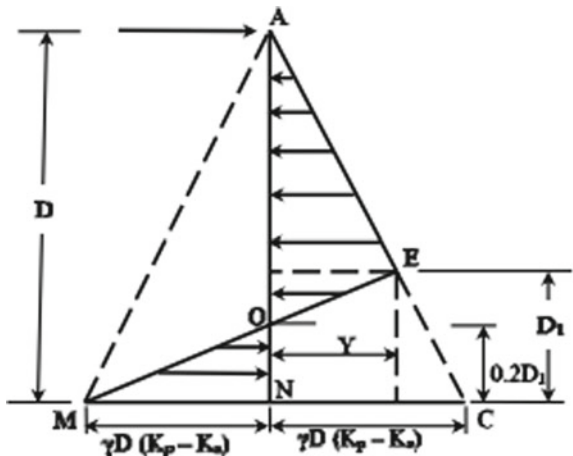
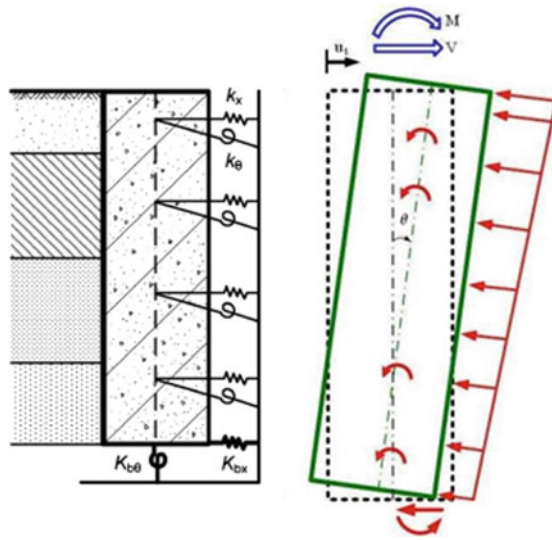


Fig. 3 Macroscopic representation of multi Winkler model (Gerolymos and Gazetas 2006a, b, c)



2.2 Approximate Method

Gerolymos and Gazetas (2006a, b, c) developed a four type Winkler spring method to model soil and considered foundation as rigid block as shown in Fig. 3. Their study highlighted the importance of skin friction of soil across foundation and included side rotation springs to capture shear tractions. The model attempts to consider couple between rotational and translation springs and also soil structure interaction. But their model is valid only for slender ratio from range 0.5 to 2.

Varun et al. (2009) developed three type Winkler spring to model soil and considers foundation as solid and flexible by modeling it by Euler beam element. Their study indicates base rotation spring is not significant for foundation with slender ratio 2–6. This method considers independent springs and did not take into account the interface interaction.

Chiou et al. (2012) propose a six type Winkler model accurately by performing field test at old Niu-Dou Bridge in Italian country. However the testing is done for caisson foundation and no field testing details exist performing on well foundation in literature. Mondal et al. (2012a, b) propose a Winkler model for dynamic loading case. However proposed model is for particular site conditions and validation of the model is needed with 3D soil well pier model.

2.3 Continuum Method

Mondal et al. (2012a, b) consider a two-dimensional nonlinear analysis for dynamic loading condition. Soil is modeled as pressure dependent multi yield surface

modeling to accurately capture soil nonlinearity and address complex phenomenon as liquefaction in seismic condition. Pier and well are considered nonlinear and modeled as bilinear kinematic element. Interface interaction is considered realistically using contact elements with compression-gap elements for normal elements and elastic perfectly plastic for tangent elements. This approach covered important aspect of material and geometry nonlinearity but needs extension of three dimensional modeling.

Zafeirakos and Gerolymos (2013) perform a three dimensional modeling of nonlinear pier and caisson foundation considering surface to surface contact interaction using exponential pressure-over closure relationship. The model considers a simple elastoplastic constitutive model for capturing nonlinear soil behavior in static loading condition.

3 Problem Statement

The studied problem is portrayed in Fig. 4. A Well foundation of hollow cylinder with length 70 m and diameter of 12 m with steining thickness of 1.5 m on each side with curb height of 5 m. It's embedded depth in saturated cohesion less oil stratum of depth 65 m and bedrock layer of depth 35 m present at bottom of the foundation. Undrained strength (S_u) of sand is 1.57 MPa and bedrock is 41.799 Mpa. Hollow cylinder is filled with sand. Well cap, steining, and bottom plug are constructed using M30, M25, and plain M15 concrete grade. A static lateral load of $P = 1000$ kN is applied at well cap. The discharge of river ganga at Balawali was recorded as 94,000 cumsec and maximum scour depth predicted is 36 m below LWL (Kumar and Rao 2012) (Table 1).

Fig. 4 Schematic diagram of stimulated field problem in this study

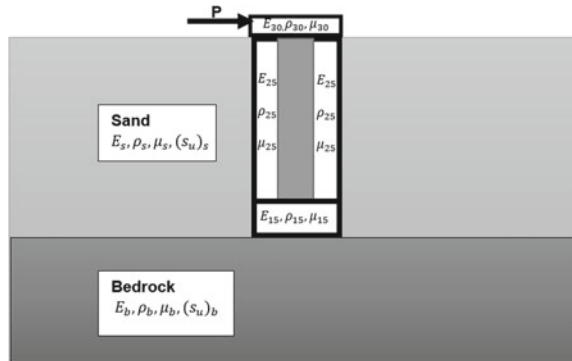


Table 1 Material properties of soil are given in are according to stated values in Yang et al (2008)

Material	Youngs modulus (MPa) (E)	Possion ratio (μ)	Density (kg/m^3) (ρ)
Sand (s)	100	0.3	1922
Bedrock(b)	57,500	0.284	2638
M30	25742.96	0.15	2500
M25	23500	0.15	2500
M15	18203.021	0.15	2400

Table 2 Characteristics of design parameters of IS code

Parameters	Values
Friction angle	33
Side friction angle	22
Horizontal coefficient of subgrade reaction (kN/m^3)	4400
Saturated unit weight (kN/m^3)	21.2
Passive pressure coefficient	0.254
Active pressure coefficient	0.264

4 Methodology

4.1 IS Code Design

Considering Indian standard procedure, response of an embedded foundation subjected to lateral loading has determined by considering parameters as listed in Table 2.

4.2 Approximate Method

Out of all the available methods, Varun et al. (2009) model is applicable for slender ratio of 5.4.

$$\frac{k_x}{E_c} = 1.828 \left(\frac{L}{D} \right)^{-0.15} \tag{1}$$

$$\frac{k_{bx}}{E_b B} = 0.669 + 0.129 \left(\frac{L}{D} \right) \tag{2}$$

$$\frac{k_\theta}{E_c B^2} = 1.1060 + 0.227 \left(\frac{L}{D} \right) \tag{3}$$

Equations (1)–(3) determine the stiffness of lateral translation springs (k_x), lateral rotational springs (k_θ) and (k_{bx}) base translation spring for foundation embedment depth (L) with diameter (D). The model considers a solid foundation. Hence equivalent young’s modulus of hollow cylinder is calculated using Eq. (4)

$$E_c = \left(\frac{(E_{30} \times A_{WC}) + (E_{25} \times A_{WS}) + (E_s \times A_s) + (E_{15} \times A_{bp})}{A_r} \right) \quad (4)$$

E_c is the equivalent young modulus where, the young modulus of concrete with grade 30, 25, 15, is the young modulus of sand and E_b is the young modulus of bedrock. A_{WC} is the area of well cap, A_{WS} area of well stenting, A_s is the area of the sand, A_{bp} is the area of the bottom plug and A_T is the total area, E_c value in this study is 8236.60 Mpa.

4.3 Two-Dimensional Finite Element Analysis

4.3.1 Modeling of the System

OpenSees-2.5 command language is employed for 2-D finite element analysis and visualization of geometry and deformed shape has been done by using pre-post processing software GID-13.01. In the analysis both soil and foundation are assumed to remain in linear elastic range and discretized using quadrilateral four noded elements. After performing sensitivity analysis, optimum domain size obtained is 680 m × 100 m domain. Mesh size for sand domain is gradually varying from 0.08 m × 4 m at the sides of foundation to 3 m × 4 m till influencing zone and it is maintained constant till boundaries to avoid coarse meshing at boundaries. Mesh size of foundation is 0.5 m × 4 m. Width of mesh size for bedrock is similar to sand layer but height is considered as 7 m for computational efficiency.

Hollow cylinder filled with sand is assumed to be perfectly bonded within the foundation. Soil-well interaction is modeled using node to node zero length frictional contact element available in OpenSees (Mazzoni et al. 2009). Fixed boundary conditions are considered at bottom and roller supports at the sides of domain (Fig. 5).

Fig. 5 Schematic representation of modeling of 2D soil-well model

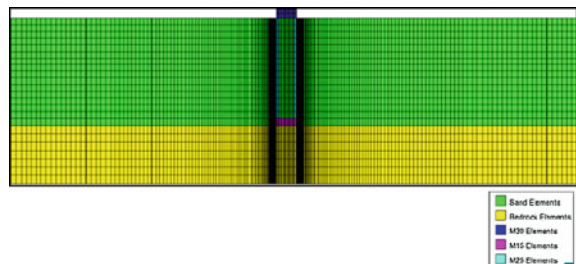


Table 3 Iteration scheme for penalty study (Mondal et al. 2012a, b)

Iterations	Normal penalty	Tangential penalty
1	Es	$0.01 \times Es$
2	$10 \times Es$	$0.01 \times 10 \times Es$
3	$100 \times Es$	$0.01 \times 100 \times Es$
4	$200 \times Es$	$0.01 \times 200 \times Es$
5	$100 \times Es$	$0.1 \times 100 \times Es$
6	$100 \times Es$	$100 \times Es$

4.3.2 Interface Algorithm

Friction contact problem, penalty method is used for analysis. Penalty parameter tangential penalty (K_T) and normal penalty (K_N) determines penetration of well nodes into soil and vice versa. It indicates maximum expected separation and sliding at interface. Selection of optimum values of parameters is needed to avoid numerical instability in solving global system with high values and not to consider low values which gives unreasonably high amount of separation and sliding (Table 3).

In every iteration corresponding well cap displacement is determined. After 4th iterations, displacements are converged. In the study iteration 6 is considered with $K_N = K_T = 100 \times Es$. In this study failure stress is calculated using von misses yield criteria for pure shear condition ($\sqrt{3}X S_u$).

5 Results

In this section, deflections of foundation and soil reaction across sides of foundation are determined from above mentioned methods to estimate lateral response profile of well foundation.

Fig. 6 Variation of soil reaction along the depth of the foundation

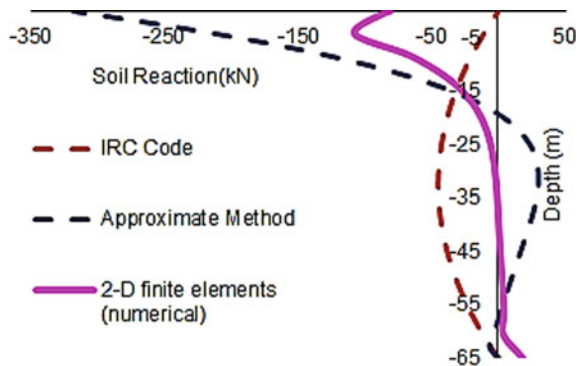


Fig. 7 Variation of soil reaction estimated by IRC code in secondary horizontal axis (X2) and 2D finite modeling and approximate method in primary horizontal axis (X1)

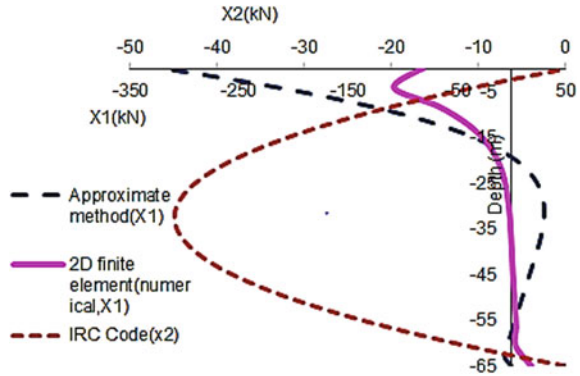


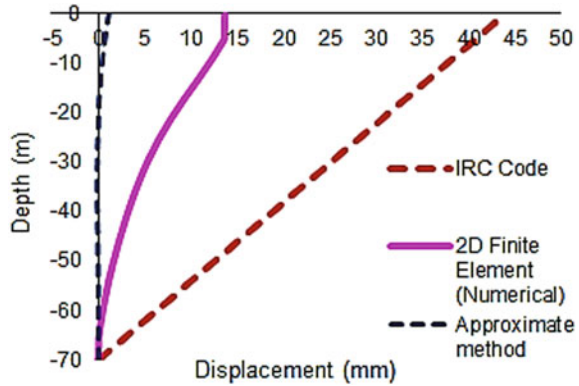
Figure 6 indicates approximate method calculations yield high soil reaction values compared to IRC code and two-dimensional (2D) finite elements. It is due to the consideration of high soil stiffness in approximate method by modeling soil with lateral and rotational springs. For more clarity IRC code is plotted in secondary axis and rest in primary axis in Fig. 7 to observe response pattern.

Figure 7, indicates that soil reaction profiles computed from approximate method are similar to two-dimensional finite modeling than IRC code. This is because of consideration of flexibility in foundation modeling which was missing in Indian codes. IRC code predicts maximum soil reaction of 44.9 kN at 32.5 m depth and minimum soil reaction of 0 at top and bottom of the foundation. Approximate method estimates 318.145 kN at top and zero at bottom of the foundation. 2D finite modeling predicts maximum soil reaction of 107.742 kN at 4.17 m and minimum of 0.46483 kN at 36.4402 m depth. Computed soil reaction values from IRC code are negative indicating that soil exerts force opposite to the movement of foundation. Where as in approximate method and 2D finite model have both positive and negative values indicating soil exerts force in same direction of foundation response. Positive values of soil reaction force were from 56.875 m depth to 20.3125 m depth in case of approximate method. But 2D finite element modeling, changes in sign from negative to positive at 40.47 m and remained positive till the bottom of the foundation.

Variations in soil reaction force values influence foundation displacements as foundation displacement is resultant of inertia of foundation due to its stiffness and overcome of resting force of soil. Hence displacement profiles predicted by all methods are plotted in Fig. 8.

From Fig. 8 it is observed that approximate method estimates top and bottom displacements of foundation as 1.121 and 0.031 mm. Whereas IRC code predicts 44 mm and 0 mm at top and bottom foundation displacements. 2D finite method predicts top and bottom displacements of foundation as 14.421 and 0.0105 mm. It is interesting to note approximate method underestimates deflection in foundation when compared to 2D finite model and IRC code. This is due to consideration of high foundation and soil stiffness in approximate method analysis. Unlike IRC code, displacement profile pattern of foundation is not linear in approximate method and

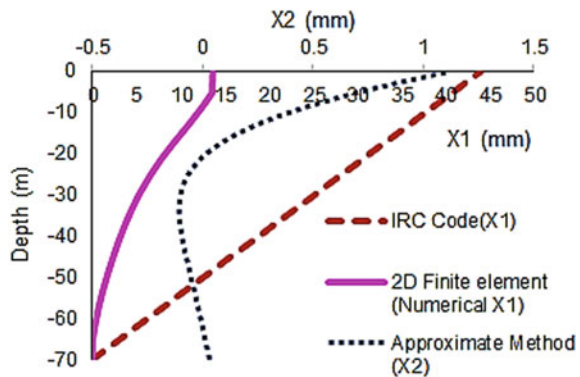
Fig. 8 Variation of deflection profiles across the side well foundation



2D finite element modeling. Huge variations are seen in calculated displacement values. Even consideration of point of rotation along vertical axis plays a main role in estimating displacement magnitudes of foundation and pattern of deformation profile. For clear observation of response variation approximate method is plotted in secondary axis in Fig. 9.

From Fig. 9, it is observed that location of point of rotation is considered at bottom by IRC code, whereas 2D finite element predicts it at 57.5773 m depth. Approximate method shows two point of rotation at 63.43 and 19.68 m depth. Displacement plots, in figure clearly show, that IRC code predicts only sliding of foundation without any deformation of shape in foundation for applied load. This states that foundation is rigid enough to resist applied load without any change of shape. Whereas for the same conditions approximate method predicts change of foundation's shape. This is due to consideration of approximate method to model foundation as Euler beam element neglecting width of the foundation and refers its original position with 0. Flexibility in beam captures bending of foundation for applied load. Resulting displacements in foundation due to bending is depicted by negative values to indicate foundation

Fig. 9 Variation of soil reaction estimated by approximate method in secondary horizontal axis (X2) and IRC code and 2-D finite element in primary horizontal axis (X1)



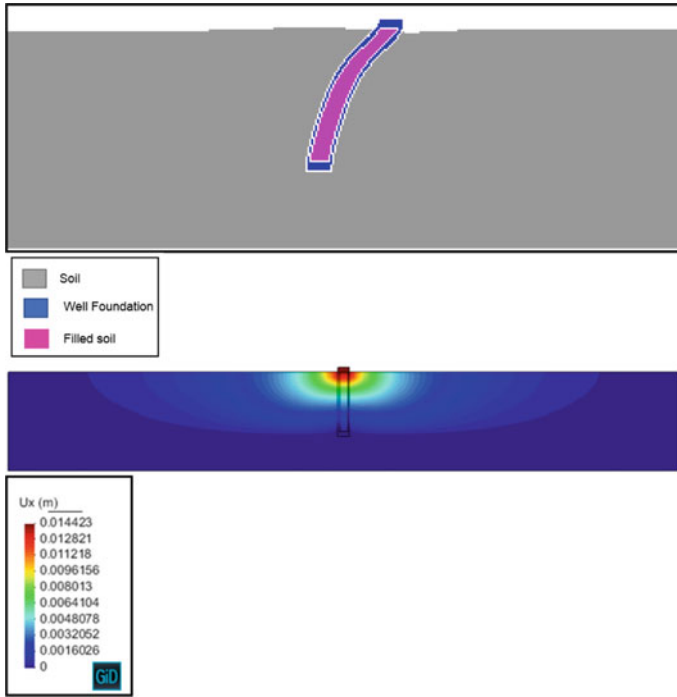


Fig. 10 Deflection profile of well foundation and displacement contour plot of well-soil system predicted by two dimensional Finite elements

movement opposite to applied load with reference to original position. Bending of foundation according to approximate method is from 61.25 to 21.875 m.

To validate whether foundation consideration of IRC code and approximate method, 2D finite element modeling considers realistic foundation stiffness with its shape effects and also consider soil interactions at interface. Deflection profile of well foundation by two-dimensional finite element modeling is given in Fig. 10.

Figure 10 clearly indicates deformation of well foundation which is ignored by IRC code due to their consideration of rigid. Unlike in approximate method, bending of foundation is not concentrated at particular depth. Bending in foundation was gradually increasing from bottom to top along the foundation length.

6 Conclusion

This study started with questioning the considerations of IRC code in analyzing well soil system. To understand reliability of code considerations on location of point of rotation, foundation rigidity, linear deflection profile, and parabolic distribution of soil reaction, a comparative study is done between IRC code and approximate

method. Results of the methods predicted completely different responses. IRC code calculated soil reaction with only lateral spring and approximate method considered both lateral and rotational springs. Deflection profile predicted by approximate method is nonlinear, bending in foundation which is not considered in IRC code. Unlike in IRC code, location of point of rotation is not at bottom and it is inside the foundation according to approximate method. To validate these most commonly practiced methods, this study considered two-dimensional (2D) continuum model with finite element analysis. Foundation and soil are modeled with using quadrilateral four noded elements, and their interactions at interface are modeled with contact elements. Results of 2D finite element methods indicate both sliding and bending in foundation response and point of rotation location near to bottom. It is interesting to note approximate method underestimates deflection magnitude and IRC code predicts it conservatively. Hence 2D continuum model results are intermediate between IRC and approximate method and highlights on how practices of Indian code and approximate method are way away from reality and need to consider realistic foundation stiffness and soil foundation interaction in modeling for analysis.

However, lateral response of well soil system is three-dimensional phenomenon and highly nonlinear in behavior. Hence authors are working on considering three-dimensional (3D) continuum modeling with elastoplastic consideration of soil and concrete for incorporation of material nonlinearity in future for more accurate validation and helpful to improve approximate methods accordingly for better results. This study considered only horizontal load application, it can be extended by considering vertical load on foundation to notice buckling effect of foundation and compare base pressure distributions obtained with IRC code predictions.

References

- Chiou J-S et al (2012) Testing and analysis of a laterally loaded bridge caisson foundation in gravel. *Soils Found* 52(3):562–573. <https://doi.org/10.1016/j.sandf.2012.05.013>
- Gerolymos N, Gazetas G (2006a) Development of Winkler model for static and dynamic response of caisson foundations with soil and interface nonlinearities. *Soil Dyn Earthq Eng* 26(5):363–376
- Gerolymos N, Gazetas G (2006b) Static and dynamic response of massive caisson foundations with soil and interface nonlinearities—validation and results. *Soil Dyn Earthq Eng* 26(5):377–394
- Gerolymos N, Gazetas G (2006c) Winkler model for lateral response of rigid caisson foundations in linear soil. *Soil Dyn Earthq Eng* 26(5):347–361
- IRC:45-1972 Recommendations for estimating the resistance of soil below the maximum scour level in the design of well foundations of bridges. IRC, New Delhi
- IRC:78-1983 Standard specifications and code of practice for road bridges. Section: VII, Foundations and substructure. IRC, New Delhi
- Karapiperis K, Gerolymos N (2014) Combined loading of caisson foundations in cohesive soil: finite element versus Winkler modeling. *Comput Geotech* 56:100–120. <https://doi.org/10.1016/j.compgeo.2013.11.006>
- Kumar ND, Rao SN (2012) Lateral load: deflection response of an embedded caisson in marine clay. *Mar Georesour Geotechnol* 3(1):1–31. <https://doi.org/10.1080/1064119X.2011.562444>
- Mazzoni S, McKenna F, Scott MH, Fenves GL (2009) OpenSees command language manual. Univ. of California, Berkeley, Calif

- Mondal G, Prashant, A, Jain SK (2012a) Significance of Interface Nonlinearity on Seismic Response of Well-Pier System in Cohesionless Soil. *Earthq Spectra* 28(3) 1117–1145. <http://dx.doi.org/10.1193/1.4000074>
- Mondal G, Prashant A, Jain SK (2012b) Simplified seismic analysis of soil–well–pier system for bridges. *Soil Dyn Earthq Eng* 32(1):42–55. <http://dx.doi.org/10.1016/j.soildyn.2011.08.002>
- Tsigginos C et al (2008) Seismic response of bridge pier on rigid caisson foundation in soil stratum. *Earthq Eng Eng Vibr* 7(1) 33–43. <https://doi.org/10.1007/s11803-008-0825-8>
- Varun et al (2009) A simplified model for lateral response of large diameter caisson foundations—Linear elastic formulation. *Soil Dyn Earthq Eng* 29(2):268–291. <https://doi.org/10.1016/j.soildyn.2008.02.001>
- Yang Z, Lu J, Elgamal A (2008) Open Sees soil models and solid-fluid fully coupled elements: user's manual. Dept. of Structural Engineering, Univ. of California, San Diego
- Zafeirakos A, Gerolymos N (2013) On the seismic response of under-designed caisson foundations. *Bull Earthq Eng* 11(5):1337–1372
- Zafeirakos A, Gerolymos N (2014) Towards a seismic capacity design of caisson foundations supporting bridge piers. *Soil Dyn Earthq Eng* 67:179–197. <https://doi.org/10.1016/j.soildyn.2014.09.002>

Influence of Shape of Footing on Coefficient of Elastic Uniform Compression of Soils



C. N. V. Satyanarayana Reddy and S. Swetha

Abstract Coefficient of elastic uniform compression (C_u) of soil used in design of vibrating bases is generally determined from cyclic plate load test conducted at the site. The value of C_u determined for test plate is correlated to the size of actual footing based on Barkan's equation. The bases of machines may be square or circular and hence, the values of C_u are required accounting for shape of the footing. The effect of shape of footing on C_u will be different in cohesive and cohesionless soils. So, correlations between C_u values of square and circular footings are required to tackle the different field requirements. In the present study, an attempt is made to correlate the coefficients of elastic uniform compression of square and circular plates of same size in cohesive soils based on cyclic load tests conducted on specimens prepared in CBR moulds. Self straining loading frame is used in the test for application of cyclic loading as it facilitates maintenance of load with settlement, easy loading and unloading of the specimen. Cohesive soils considered in the study are clayey sand and clay of low compressibility. The results of study revealed the ratio of coefficients of elastic uniform compression of circular plate to square plate in cohesive soils under study as 1.2.

Keywords Shape of footing · Cyclic load test · Soil spring stiffness · Machine foundation

C. N. V. Satyanarayana Reddy (✉)
Department of Civil Engineering, College of Engineering, Andhra University, Visakhapatnam
530003, Andhra Pradesh, India
e-mail: prof.cnvsreddy@andhrauniversity.edu.in

S. Swetha
Department of Civil Engineering, Sri Venkateswara College of Engineering and Technology,
Etcherla, Andhra Pradesh, India

© Springer Nature Singapore Pte Ltd. 2020
M. Latha Gali and P. Raghuvver Rao (eds.), *Construction in Geotechnical Engineering*, Lecture Notes in Civil Engineering 84,
https://doi.org/10.1007/978-981-15-6090-3_28

399

1 Introduction

The foundations of Industrial structures are to be designed for static and dynamic loads. Hence, foundation design requires soil stiffness in addition to bearing capacity. Computations of natural frequency of foundation soil system and amplitude of vibration are based on equivalent soil spring stiffness. Soil stiffness is determined under different modes of vibration using coefficients of elastic uniform compression, non uniform compression, uniform shear and non uniform shear. As established correlations are available, the elastic coefficients determination requires only coefficient of elastic uniform compression (C_u). Thus, the coefficient of elastic uniform compression of soil (C_u) is the most important parameter in dealing with dynamic loads. It is defined as the ratio of uniform compressive pressure (P) to the corresponding elastic settlement (S_e).

Soil spring constant (k) for vertical excitation is determined by multiplying coefficient of elastic uniform compression C_u with base area of foundation. The coefficient of elastic uniform compression is determined from cyclic plate load test (IS 5249-1992) as the slope of linear portion of load-elastic settlement plot. The values of C_u are influenced by shape of footing, contact area of foundation block, modulus of elasticity, poisson's ratio, type of soil and moisture content of soil (Barkan 1962; Prakash and Basavanna 1969; Moghaddas Tafreshi et al. 2008).

2 Review of Literature

Though elastic constants can be used for determination of coefficient of elastic uniform compression of soil, cyclic plate load tests are widely recommended. The value of C_u for original footing is obtained upon correlation based on Barkan's equation (Barkan 1962) using generally square test plates. As coefficient of elastic uniform compression depends upon shape of footing, the value of C_u obtained from square plates cannot be used for circular foundations of vibrating bases. Hence determination of shape factor for C_u is required to switch from square footing to circular footing.

Recent studies (Satyanarayana Reddy et al. 2017) reported the ratio of coefficients of elastic uniform compression of circular plate to square plate in fine sand as 0.85. More studies are essential to evaluate the shape effect on C_u in cohesive soils. As conduction of field cyclic plate load test is costly and time taking, small scale cyclic load tests using self straining load frames may be considered for the studies. In the present study, an attempt is made to evaluate coefficient of elastic uniform compression of two cohesive soils by performing cyclic loading tests on small scale specimens in CBR Mould using square and circular plungers using a loading frame of 50 kN capacity.

3 Details of Study

Two cohesive soils are considered for the study and are procured from neighbourhood of Visakhapatnam. Laboratory tests are performed to determine engineering properties of the soils as per IS codes of practice (IS 2720 parts 3 and 4-1985, IS 2720 part 8-1983) and the evaluated engineering properties are presented in Table 1.

The soils are classified based on gradation and plasticity characteristics as per IS 1498 (1970). The soils are classified as Clay of Low Compressibility (CL) and Clayey Sand (SC). Compaction characteristics are evaluated by conducting IS Heavy Compaction tests.

Small scale cyclic load tests are done on soil specimens prepared in CBR moulds at OMCs and respective MDDs after soaking for 96 hours. The loading is applied through self straining loading frame of 50 kN capacity using standard CBR plunger (IS 2720 part 16-1997). The load applied on the test sample through plunger is measured with the help of calibrated proving ring of 200 kg capacity. The soil specimen under a surcharge of 5 kg is placed in position for testing and load is applied in increments. The load applied at each stage is released and the plate is allowed to rebound. The load is applied in increments of $1/10^{\text{th}}$ of anticipated safe load up to the safe load. The elastic settlement under each stage of loading is determined based on dial gauge readings in loading and unloading stages.

The load-elastic settlement data is plotted on graph sheet and the value of coefficient of elastic uniform compression of soil (C_u) is obtained as the slope of the linear portion of the plot. The load tests are done on clayey sand and low compressible clay using standard CBR plunger and a square plunger of size and mass equal to CBR

Table 1 Engineering properties of soils

Engineering property	Soil 1	Soil 2
Specific gravity	2.70	2.68
<i>Grain size distribution</i>		
(a) Gravel (%)	0	0
(b) Coarse sand (%)	–	0
(c) Medium sand (%)	–	30
(d) Fine sand (%)	16	56
(e) Fines (%)	84	14
<i>Plasticity characteristics</i>		
(a) Liquid limit (%)	33	32
(b) Plastic limit (%)	21	20
(c) Plasticity index (%)	12	12
IS classification	CL	SC
<i>Compaction characteristics</i>		
(a) Optimum moisture content (%)	10.8	10
(b) Maximum dry density (g/cc)	1.69	1.78

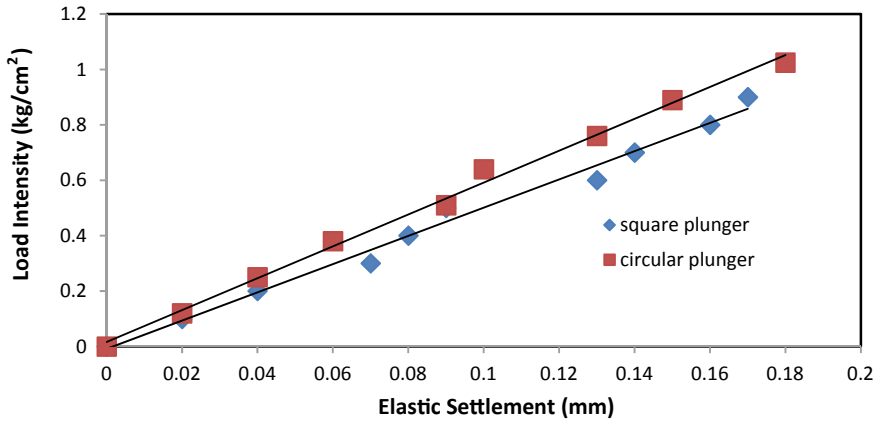


Fig. 1 Load-elastic settlement plots of clayey sand with circular and square plates

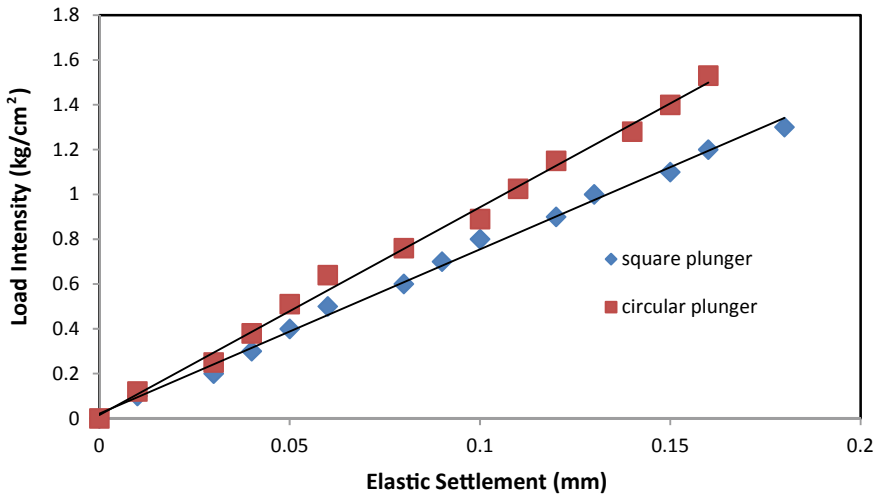


Fig. 2 Load-elastic settlement plots of clay of low compressibility with circular and square plates

test plunger. The load-elastic settlement plots generated from model cyclic plate load tests on clayey sand and clay of low compressibility with circular and square test plates (plungers) are presented in Fig. 1 and Fig. 2 respectively.

Table 2 Coefficients of elastic uniform compression of clayey sand and low compressible clay

Type of soil	Shape of test plate	Coefficient of elastic uniform compression (kg/cm ³)
Clayey sand	Circular	58.2
	Square	48.9
Low compressible clay	Circular	75.6
	Square	62.2

4 Discussion

From the small scale cyclic plate load test results, the values of C_u for clayey sand under study using circular and square plates are obtained as 58.2 and 48.9 kg/cm³ respectively. In clay of low compressibility, values of C_u for circular and square plates are obtained as 75.6 kg/cm³ and 62.2 kg/cm³ respectively. It is found that the value of C_u for circular plate is higher than the square plate in clayey sand and clay of low compressible clay under study.

The ratios of coefficients of elastic uniform compression of circular plate to that of square plate are determined as 0.84 and 0.82 in clayey sand and clay of low compressibility, respectively from the study. Hence, the value of C_u of circular test plate is about 1.2 times the value of C_u of square plate in clay of low compressibility and clayey sand (Table 2).

5 Conclusion

The value of coefficient of elastic uniform compression of (C_u) for circular vibrating base/foundation based on m small scale test results may be taken as 1.2 times the coefficient of elastic uniform compression of square footing in cohesive soils.

References

- Barkan DD (1962) Dynamics of bases and foundations. McGraw-Hill, New York
- IS 1498 (1970) Indian Standard for classification and identification of soils for general engineering purposes. Bureau of Indian Standards, New Delhi
- IS 5249 (1992) Indian Standard on determination of in-situ dynamic properties of soils. Bureau of Indian Standards, New Delhi
- IS 2720 Part 8 (1983) Indian Standard Code of practice—methods of tests for soils-determination of water content-dry density relation using heavy compaction. Bureau of Indian Standards, New Delhi
- IS 2720 Part 16 (1997) Indian Standard Code of practice—methods of tests for soils-laboratory determination of CBR. Bureau of Indian Standards, New Delhi

- IS 2720 Part-4 (1985) Indian Standard Code of practice—methods of tests for soils-grain size analysis. Bureau of Indian Standards, New Delhi
- IS 2720 Part-5 (1985) Indian Standard Code of practice—methods of tests for soils-determination of liquid and plastic limit. Bureau of Indian Standards, New Delhi
- Moghaddas Tafreshi SN, Zareian SE, Soltanpour Y (2008) Cyclic loading on foundation to evaluate the coefficient of elastic uniform compression of sand. In: The 14th world conference on earthquake engineering, Beijing, China
- Prakash S, Basavanna BM (1969) Effect of size and shape of foundation on elastic coefficients in a layered soil mass. In: Proceedings of IV world conference on earthquake technology, Chile
- Satyanarayana Reddy CNV, Usha Rani GV, Nagalakshmi M (2017) Effect of shape of footing on coefficient of elastic uniform compression of fine sand. In: Proceedings of Indian geotechnical conference, IIT Guwahati

Effective Cut Slope of Rock Slope Along NH-44



Promit Kumar Bhaumik, Rituraj Devrani, Apurba Das, S Sreedeeep,
and S. B. Prasath

Abstract Development of national highways in the hilly terrain plays a vital role in the economic development of the country. Landslides or instability of the slopes is more common in the developing hilly terrain due to unscientific cutting of the toe of rock slope for the construction or widening of roads and/or bridges. The NH-44 in the Jaintia Hills district (Meghalaya, India) connecting Malidor to Sonapur (approx. 30 km), have experienced many landslide events causing huge loss of life and property. The two locations along the NH-44 are considered and different cut sections of slopes were studied to support the further extension of the NH-44. Kinematic analysis reveals that the possible type of failures such as wedge failure, planar failure and toppling failure occurs at the selected locations. The stability assessment of in situ rock slope and different cut slope sections were investigated to determine the effective cut slope. Potentially unsafe in situ slopes/different cut slopes were identified using PHASE², which is a finite element method, based on shear strength reduction technique. The unstable slopes were further stabilized with the installation of shotcrete and bolt. A parametric study has been done to understand the stability of rock slope under various bolting conditions.

Keywords Rock slope · Stability · Finite element method · Cutting · Reinforcement

1 Introduction

The north eastern states of India are prone to numerous slope failures along the roads and highways. These states also frequently affected by heavy intensity monsoon rainfall and earthquakes of moderate to high intensity. The highway roads connecting the

P. K. Bhaumik (✉) · R. Devrani · A. Das · S. Sreedeeep
Department of Civil Engineering, Indian Institute of Technology Guwahati, Guwahati, India
e-mail: promit.bhaumik@gmail.com

S. B. Prasath
Department of Civil Engineering, Bannari Amman Institute of Technology, Sathyamangalam,
Tamilnadu, India

© Springer Nature Singapore Pte Ltd. 2020
M. Latha Gali and P. Raghuvver Rao (eds.), *Construction in Geotechnical Engineering*, Lecture Notes in Civil Engineering 84,
https://doi.org/10.1007/978-981-15-6090-3_29

major cities and commercial places play a crucial role in the economic development of the country. The national highway NH-44 connecting Malidor to Sonapur (approx. 30 km) runs along the Jaintia Hills district (Meghalaya, India) is the only road that presently connects Barak Valley of Assam, Tripura and Mizoram with mainland of India (Sarkar et al. 2016). The national highway NH-44 has experienced many landslide events causing disruption in traffic and huge loss of life and property. The geodynamic activity in the region is intense due to heavy rainfall during the monsoon period. These developing hilly terrain has witnessed more frequent landslide and slope instability events due to unscientific cutting of the toe of rock slope for the construction of roads or widening of roads and/or bridges. The instability of the rock slopes was highly influenced by the structural discontinuities in the rocks such as joints, bedding planes, fractures, fissures, cracks, fault plane, etc. The discontinuities are the weakest part of the rock mass and got affected by shearing during the application of load on the rock mass (Jana et al. 2017). The anisotropic property of the rock mass was influenced by the discontinuities and it alters the stress-strain behaviour within the rock mass. The rock slopes considered has more joints and seepage of water along the discontinuities, which makes the rock slope highly unstable. This article deals with the economical slope cut along the NH-44 for the further widening of the highway road from 2 lanes to 4 lanes. The stability of the in situ slopes was checked and further, the stability of different possible slope cuts was investigated with and without nailing to find out the potentially economical slope cut. The utilization of finite element method (FEM) has considerably increased due to its simplicity in analyzing the complex slope stability problems (Hammah et al. 2005).

The kinematic analysis reveals the potential failure direction and the possible type of failures such as wedge failure, planar failure and toppling failure for the given discontinuities properties of selected locations in Dips (Rocscience 2016a). The finite element-based shear strength reduction (SSR) is used to compute the factor of safety of the in situ slope, cut slope of different geometry and reinforced unstable cut slopes. In the present study modelling is performed in combined continuum interface method in PHASE² (Rocscience 2016b). A parametric study has been done to understand the stability of rock slope under various bolting conditions.

2 Study Area

Sarkar et al. (2016) have calculated the CSMR value for the vulnerable slopes in five locations along the NH-44. The study area is located along NH-44 in the Jaintia Hills district of Meghalaya state (India) connecting the places Malidor and Sonapur at a distance of 141.74 km from Shillong city. The area under investigation falls between latitudes 25°09'19"N-25°11'03"N and longitudes 92°26'20"E-92°27'09"E. The two locations with different failure conditions namely L1 and L4 are used for the present study to find out the effective cut slope for the further widening of the national highways.

Table 1 Joint properties

Description		L1 (Dip/Dip direction)	L4 (Dip/Dip direction)
Joint sets	J1	28°/305°	60°/295°3
	J2	90°/290°	58°/25°
	J3	32°/185°	NA
Orientation of slopes		30°/330°	47°/173°

3 Description of Rock Slope

The two locations among the five locations in Sarkar et al. (2016) namely L1 and L4 are considered for the present study. The joint properties were taken from Sarkar et al. (2016) as shown in Table 1. The slope height along the location L1 and L4 was considered as 20 m high. The rocks are highly folded and jointed in the study area. The rock slopes consist of three sets of highly weathered and exposed joint sets, namely J1, J2, J3 and the corresponding orientation of slopes, dipping angle and dip direction are shown in Table 1.

4 Methodology

The different cut slopes ensure the extra width required for widening of the road. The different cut slopes are made by doing any one of the following; exact vertical cut of the adjacent slope by removing the toe of the slope (cut surface perpendicular to horizontal surface); uniform cutting or removal of the rock on the slope face to maintain the existing slope angle and partial cutting of the toe with partial removal of the soil from the slope face. The stability assessment of in situ rock slope and different cut slope sections were investigated to determine the effective cut slope. The potentially unsafe in situ slopes/different cut slopes were identified by using PHASE², which is a finite element method, based on shear strength reduction technique.

4.1 Shear Strength Reduction Technique

Strength reduction means reducing the parameters of shear strength (cohesion and internal friction angle) of rock slopes in the finite element calculation. The strength reduction method using FEM can be used to simulate the failure limit states of slopes and to determine their critical sliding surfaces along with the factor of safety of the rock slope. The shear strength reduction technique is used widely in the numerical modelling, which gives better results compared to the conventional methods. In the SSR technique, it is not required to assume the failure shape, location and failure mechanism. The shear strength reduction (SSR) technique automatically satisfies all

the equilibrium conditions.

$$C_f = \frac{C}{SRF} \tag{1}$$

$$\phi_f = \tan^{-1} \left[\frac{\tan \phi}{SRF} \right] \tag{2}$$

where,

C_f —reduced cohesion

C —cohesion

ϕ_f —reduced friction angle

ϕ —friction angle

4.2 Evaluation of Rock Mass Property

The Generalized Hoek–Brown Failure criterion was used to determine the rock mass strength parameters. The rock without any discontinuities are termed as intact rock and rock with joints are termed as rock mass.

$$\sigma_1 = \sigma_3 + \sigma_{ci} * \left\{ m_b * \frac{\sigma_3}{\sigma_{ci}} + s \right\}^a \tag{3}$$

where,

σ_1 and σ_3 are major and minor principal stresses at failure

σ_{ci} is the uniaxial compressive strength of the intact rock

m_b is the reduced value of the material constant

m_i is given as

$$m_b = m_i * \exp \left\{ \frac{GSI - 100}{28 - 14 * D} \right\} \tag{4}$$

s and a are constants for the rock mass given as

$$S = \exp \left\{ \frac{GSI - 100}{28 - 14 * D} \right\} \tag{5}$$

$$a = \frac{1}{2} + \frac{1}{6} * \left(e^{-\frac{GSI}{15}} - e^{-\frac{20}{s}} \right) \tag{6}$$

GSI is the geological strength index, and D is the disturbance factor which depends upon the degree of disturbance to which the rock mass has been subjected by blast damage and stress relaxation. The value of the D varies from 0 for undisturbed rock mass and 1 for disturbed rock mass (Table 2).

Table 2 Rock mass properties

Description	Value
GSI	35
Unit weight (kN/m ³)	27
Elastic Modulus (GPa)	7
Intact compressive strength (GPa)	35
Poisson's ratio	0.3
m_b	6
S	1
a	0.5

4.3 Kinematic Analysis

The rock failure is governed by the series of discontinuities such as joint sets, faults, foliation, shear zones, bedding planes, cut slopes, etc. The angle of friction governs the progress of failure over the nature of discontinuities. The friction cone is the zone within which the all poles belong to the planes that dip at angle less than the angle of internal friction is safe against failure (Hoek and Brown 1980; Hoek et al. 2002). The nature of failures is planar, wedge and toppling failure. The planar failure occurs when the sliding plane is near parallel to the slope and the sliding occurs relatively along the slope face. The upper edge of sliding surface either intersects with upper slope or terminates in a tension crack and when the angle of sliding plane is greater than the angle of internal friction. The wedge failure in rock occurs when the rock mass slides along two intersecting discontinuities and the cut slopes from oblique shaped dip to form a wedge-shaped block. The kinematic analysis was carried out for the in situ slopes in the location L1 and L4. The failure was found to planar failure in location L1 as shown in Fig. 1 and wedge failure in location L4 as shown in Fig. 2. The cut slopes are made in three different forms by changing the angle of slope to provide sufficient width along the road for widening of the road. The kinematic analysis of the cut slopes namely S1, S2 and S4 for the locations L1 and L4 are compared in Table 3. It was found to be no change in the mode of failure of the slopes but the severity of the failure of the slopes is increased.

4.4 Combined Continuum Interface Method

The combined continuum interface numerical method has been attempted in order to incorporate the joints in the intact rocks. These joint elements open up a relaxed connectivity between two adjacent intact rock portions. The joint element is considered as three-nodded triangular one-dimensional finite element of zero thickness. At the edge of interface, the relative displacement of nodal points are simulated for normal and shear displacement. Mohr–Coulomb failure criteria is used to determine

Fig. 1 Planar failure (L1)

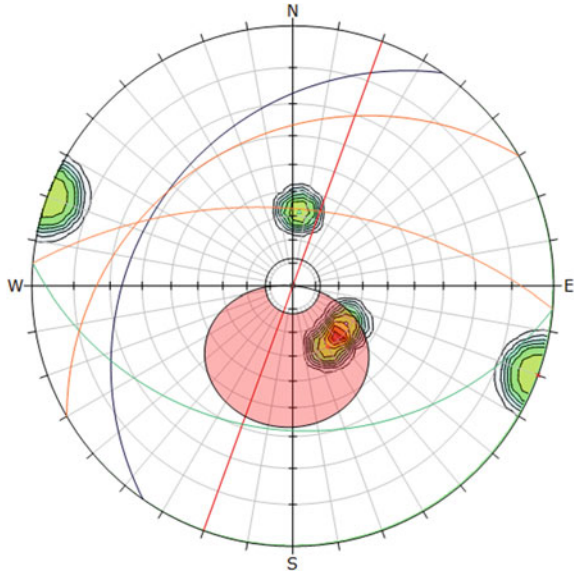


Fig. 2 Wedge failure (L4)

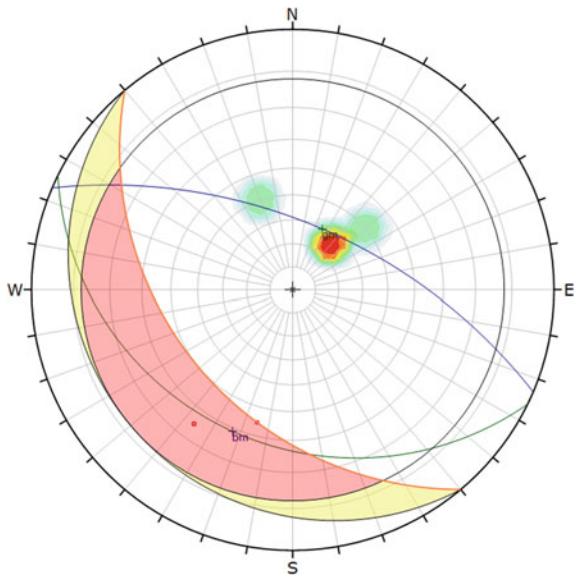


Table 3 Mode of failure of cut slopes (kinematic analysis)

Condition	L1	L4
In situ condition	Planar	Wedge
S1	Planar	Wedge

the shear strength parameters of the joint. The joint properties used in the analysis are shown in Table 1. All the three joint sets having a spacing of 0.3 m throughout the slope are used in the analysis. The shear strength reduction (SSR) technique (Matsui and Sam 1992) is used to find the factor of safety value of jointed rock slope.

5 Result and Discussion

The stability analysis of the in situ condition for rock slope at location L1 in Fig. 3 was found to be stable ($SRF = 1.53 > 1.5$). The rock slopes are cut in three different manner as shown in Figs. 4, 5 and 6. The first slope cutting is just vertical cut of the available slope and removing the rock in the toe of the slope as shown in Fig. 4 and termed as S1. The second slope cutting is removing the rock entirely throughout the slope by maintaining the in situ slope angle as shown in Fig. 5 and termed as S2. The third slope cutting is modifying the slope angle by removing the rock only to a certain distance from toe of the slope as shown in Fig. 6 and termed as S3. Due to the different rock cuttings for widening of roads, the slope was rendered unstable. The modified slopes S2 and S3 for the location L1 are stable but cutting of huge quantity of rocks is uneconomical compared to S1. The modified slope S1 is nearly safe and the slope S1 is strengthened by soil nailing. Similar stability analysis for rock slopes at location 4 showed the in situ slope is unstable. The slopes are modified in a similar manner and the factor of safety values are found to be unsafe. The factor of safety value and the quantity of rock cut are compared. The modified slope S3,

Fig. 3 In situ slope

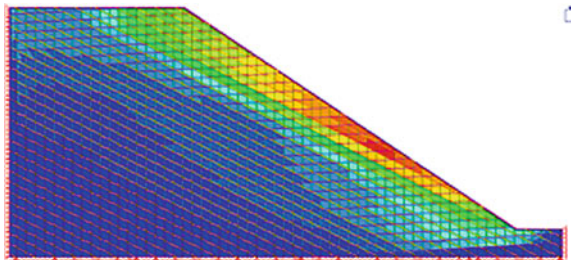


Fig. 4 Modified slope or cut slope (S1)

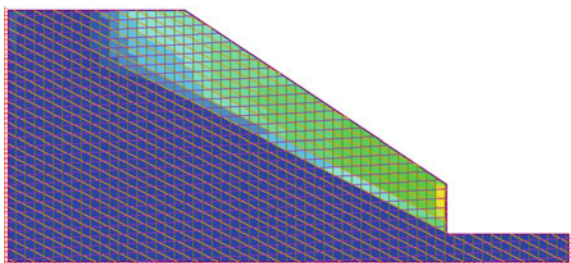


Fig. 5 Modified slope or cut slope (S2)

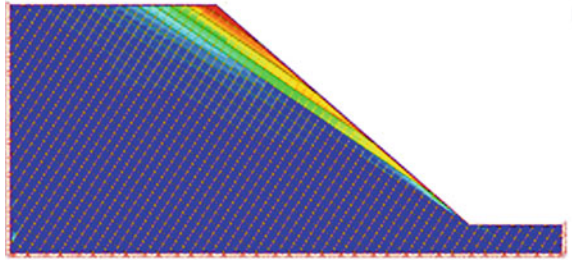


Fig. 6 Modified slope or cut slope (S3)

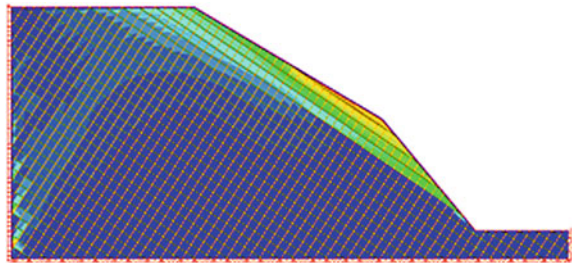


Table 4 SRF value of the cut slopes

Cut slopes	L1	L4
In situ	1.53	0.89
S1	1.43	0.55
S2	1.94	1.19
S3	1.80	1.08

comparatively has more factor of safety and low volume of rock cut. Hence, quite naturally, the rock cuttings of the slope at location 4 were also unstable. The factor of safety of the different modified slopes (S1, S2 and S3) for locations L1 and L4 are compared in Table 4. The volume of the rock is more in S2 compared to S1 and S3. The volume of rock cut is minimum for the modified slope S1 compared to S2 and S3.

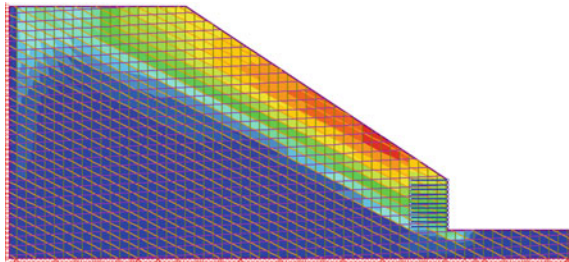
6 Design of Reinforcement

The analysis of the in situ and modified slopes using the finite element method clearly shows that most of the slopes in L4 and S1 of the L1 are unstable slopes. These slopes need proper stabilization technique to make them stable. In the present study, end anchored bolts are used for rock slope stabilization and the properties are shown in Table 5.

Table 5 Bolt properties

Description	Value
Bolt type	End anchored
Bolt diameter (mm)	24
Bolt Modulus E (GPa)	200
Tensile capacity (MN)	0.1
Residual tensile capacity (MN)	0.1
Out of plane spacing (m)	1

Fig. 7 Reinforced cut slope (L1–S1)



In PHASE², end anchored rock bolts are modelled as one-dimensional deformable element. A parametric study involving various bolt lengths and inclination of rock bolts are done to compute the corresponding SRF values. Taking into consideration the above parameters, deduction of the most optimal design of reinforcement and also the most safe rock cut is identified. The modified slope S1 is considered for the location L1 and soil nailing was applied as shown in Fig. 7. The orientation of the nails were used from 75° to 120° and the factor of safety for different inclination of the soil nails were compared in Figs. 8 and 9. The modified slope S3 is considered for the location L4 and the soil nailings were applied as shown in Fig. 10. The orientation of the nails were changed from 75° to 120° and the factor of safety for different inclination of the soil nails were compared in Fig. 9. The angle or orientation of the nails are taken with respect to the face of the slope. The optimum angle of the nails with respect to the face of the slope was found to be 105°.

7 Shotcreting

The shotcreting was applied on the slope face of the cut slopes as shown in Fig. 11a, b. The function of shotcreting is to provide uniform distribution of the loads from reinforcement or soil nailing and to avoid falling of scalps. The area adjacent to the slopes are used for vehicle transport and falling of scalps from the disturbed surface while cutting the rocks may harm the life or property. The cut slopes with the shortcreting are analyzed and the factor of safety with and without shotcreting are compared in Table 6.

Fig. 8 Variation of SRF with respect to orientation of the bolt (Location-L1)

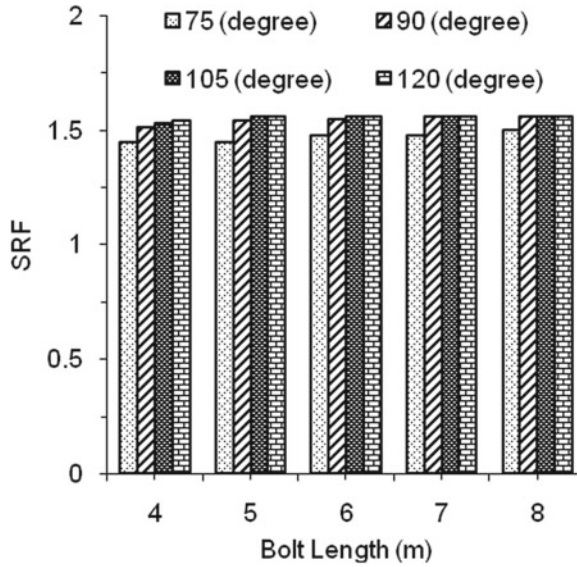
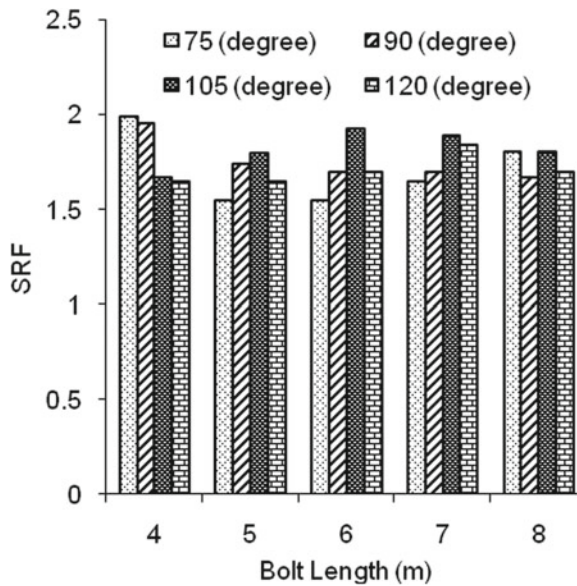


Fig. 9 Variation of SRF with respect to orientation of the bolt (Location-L4)



8 Conclusion

In the present study, the stability analysis of the different cut slopes and parametric analysis of the orientation of the bolts are studied. The stability analysis shows, the modified slope S1 for the location L1 and the modified slope S3 for the location L4 gives economically better factor safety in terms of the volume of rock cut. The

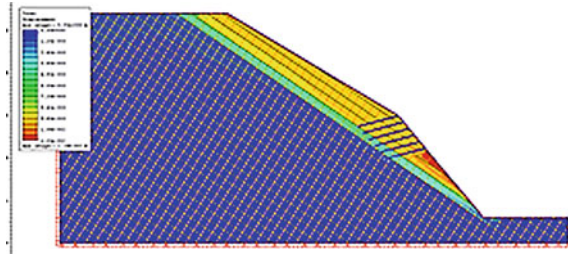


Fig. 10 Typical reinforced cut slope (L4-S3)

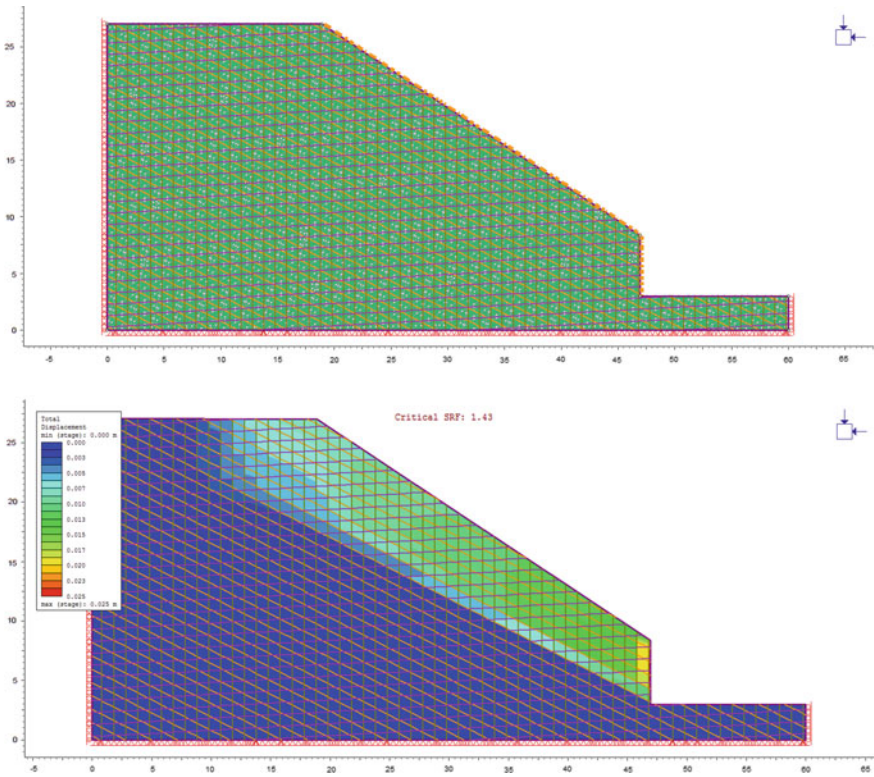


Fig. 11 a Typical cut slope model with shotcrete, b analysis result of typical cut slope with shotcrete showing no considerable improvement in SRF

economical cut S1 for the location L1 and S3 for the location L4 are stabilized using the soil nailing technique. The parametric analysis of the angle of the anchors shows 105 degree with respect to the face of the slope. The effective modified slope and the optimum angle of the bolting are only for the specific slope and the specific property of the bolt.

Table 6 SRF value of the cut slopes with shotcreting and nailing

Cut slopes		Without shotcreting	With shotcreting
L1	S1	1.43	1.43
	S2	1.94	1.94
	S3	1.80	1.80
L2	S1	0.55	0.55
	S2	1.19	1.19
	S3	1.08	1.08

References

Hammah RE, Yacoub TE, Corkum BC, Curran JH (2005) The shear strength reduction method for the generalized Hoek-Brown criterion. In: Alaska rocks 2005. American Rock Mechanics Association, Anchorage

Hoek E, Brown, ET (1980) Empirical strength criterion for rock masses. *J. Geotech. Engng Div., ASCE* 106(GT9), 1013–1035

Hoek E, Carranza-Torres C, Corkum B (2002) Hoek-Brown criterion—2002 edition. In: Proceedings of the NARMS-TAC conference. Toronto, Canada, pp 1, 267–273

Jana A, Dey A, Sreedeeep S (2017) Stability analysis of rock slope using combined continuum interface element method. In: Indian geotechnical conference 2017 GeoNEst, pp 1–4

Matsui T, Sam KC (1992) Finite element slope stability analysis by shear strength reduction technique. *Soils Found* 32(1):59–70

Rocscience (2016a) Dips version 7.0, Graphical and statistical analysis of orientation data. Rocscience Inc., Ontario

Rocscience (2016b) Phase2 version 9.020, Finite element analysis for excavations and slopes. Rocscience Inc., Ontario

Sarkar K, Buragohain B, Singh TN (2016) Rock slope stability analysis along NH-44 in Sonapur area, Jaintia hills district, Meghalaya. *J Geol Soc India* 87(3):317–322

Raising of Ash Pond for Augmented Storage



B. V. Sushma

Abstract In thermal power plants, a huge amount of ash will be generated as a result of combustion of coal in large quantities. The generated ash will generally be transported and stored in designated areas called ‘ash pond’, before finding use in cement plants or any other engineering purposes. Ash pond is generally formed by creating an earthen embankment all along the identified periphery. In primary phase, the earthen embankment is constructed to contain the ash slurry up to maximum ash fill level, which is termed as ‘starter bund’. In the secondary phase for augmenting the ash storage volume, the ash bund height will be increased by formation of bund of equal heights in stages over and above the starter bund, which is termed as ‘raisings’. This paper covers the raising of bund, construction material, design and construction aspects.

Keywords Ash pond · Starter bund · Augmented storage · Raising · Design · Construction

1 Introduction

Coal-based thermal power plants generate fly ash during steam generation by burning of coal. Fly ash generated is collected in Electro Static Precipitator (ESP). Fly ash from ESP is transported in dry or wet form and disposed in a pond formed by constructing earthen embankment around an identified place within the plant site. After commissioning of power plant, ash will be deposited in the pond till it gets filled up to the design fill level termed as maximum ash fill level. Once the pond is filled, second stage of pond formation will be started using the settled ash. The raising of ash pond is generally carried out by 3 methods:

- (a) Upstream construction method
- (b) Downstream construction method
- (c) Centre line construction method.

B. V. Sushma (✉)
Tata Consulting Engineers Ltd., Bengaluru, Karnataka, India
e-mail: bvsushma@tce.co.in

© Springer Nature Singapore Pte Ltd. 2020
M. Latha Gali and P. Raghuvver Rao (eds.), *Construction in Geotechnical Engineering*, Lecture Notes in Civil Engineering 84,
https://doi.org/10.1007/978-981-15-6090-3_30

In upstream construction method the deposition of ash for raising is carried out on upstream face of the ash pond. In downstream construction method deposition of ash for raising is carried out on downstream face of the ash pond. In centre line construction method the deposition of ash for raisings is carried out from the centre of the ash pond. Out of the elaborated three methods, the upstream method is commonly adopted and regarded as the most viable technique (Gandhi 2005).

The ash from the plant will be transported to ash pond by (i) dry method and (ii) wet method.

In dry method, the ash in dry form is transported by trucks whereas in wet method the ash is mixed with water and conveyed to ash pond through pipes in slurry form. The ash slurry is pumped to the ash pond through various discharge points. The ash slurry can be in lean slurry form or High Concentrated Slurry Disposal (HCSD) form depending on the concentration of ash in the slurry (Biswas et al. 2000). The transportation of ash in slurry form to the ash pond is considered to be the most economical, environmental friendly and hence generally adopted. The lean slurry ratio is generally maintained 1 (ash): 4 (water) by weight.

When ash slurry is disposed to the ash pond, ash gets accumulated at the discharge point end where the ash laid water flows towards the other end. Ash particles take sufficiently long time to settle and further the water need to be steady condition without any turbulence for ash particles to get settled. The turbulence of water can be cut down by discharging ash slurry in multiple points in phased manner and recovering the water at the end, opposite to that of the discharge end. Alternatively the ash water flow can be channelised in the pond by creating baffles and recovering the clear water at the end opposite to the discharge end.

The process of sedimentation of ash particles and collecting the relatively clear water for reuse is termed as decantation system. The clear water thus recovered is again used for mixing with ash to obtain lean slurry.

Fig. 1 Existing ash pond with ash slurry filled up to the maximum ash fill level



The project under consideration is raising of ash pond for a thermal power project in coal belt region near Odisha. Ash pond is around 170 acres and created by constructing starter bund of height around 7 m all along the identified periphery. The ash was filled up to the max ash fill level in around 4 years. Figure 1 shows the site photo of the max ash fill level of the earlier constructed starter bund. Further raising of bund was initiated from this level in multiple of 4 m using the upstream method of construction. Ash disposal by lean slurry discharged at multiple points.

2 Design Philosophy

The starter bund is an existing earthen embankment of 7 m height. The slopes of the bund were 1 in 2 with provision of berm of 1.5 m at 3.5 m height. The section of the starter bund is shown in Fig. 2.

The requirement of project was to create a divider bund for each stage of bund raising so as to facilitate parallel operation of ash slurry filling and bund construction. If fully earthen bund is planned as divider bund, it will reduce the capacity of ash pond, hence the partition wall was planned by constructing bund using majorly ash material. Earth cover of around 0.5 m was provided for each raising of ash bund to provide more stability. Thus the partition bund will be a notional bund which will exist till the completion of each raising of the considered stage.

The partition bund was formed as illustrated in Fig. 3 creating Area 1 and Area 2 for raisings of ash pond. This bund was formed little earlier than filling of ash slurry into the pond. This will facilitate ash filling in Area 1 while raising the peripheral bund of Area 2. The ash filling to be carried out in the Area 1 and raising of the ash bund on periphery was carried out in the Area 2. After filling is reached up to maximum ash fill level in the Area 1, the ash slurry pipelines were shifted to the Area 2 and ash filling was carried out till desired ash fill level in Area 2 was attained. Parallely further raising of the ash pond was taken up in the Area 1. The construction and raising of ash bund sequence repeated as required up to the final designed raising of the bund.

HDPE liner is provided in the upstream slope and a certain portion of bottom of the raising bund to prevent the seepage from the bund raising. HDPE liner is protected by sand and fly ash brick layer which are provided over the HDPE liner.

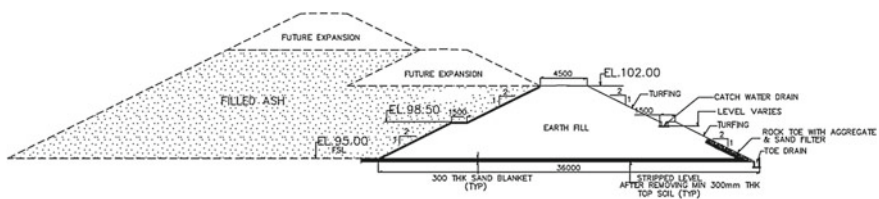


Fig. 2 Section of starter bund

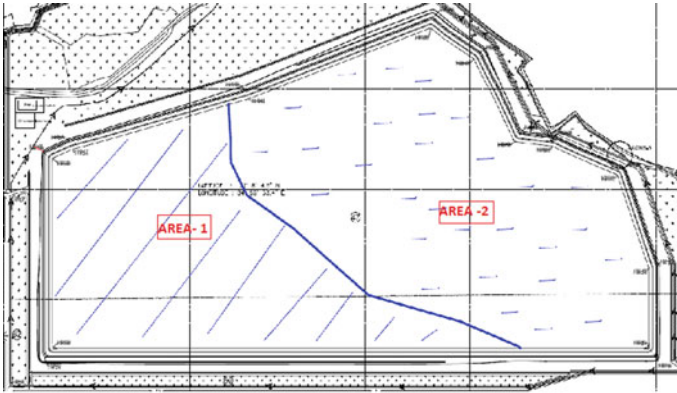


Fig. 3 Plan showing demarcation of Area 1 and Area 2 for raisings of ash pond

3 Slope Stability Analysis of the Raising of Ash Pond

The slope stability analyses were carried out using Geostudio 2007 Slope/w software. The slopes were checked for various loading conditions against minimum factor of safeties for respective conditions, as per clause 5.1.1 of IS 7894. The applicable stability conditions for ash bund raising are end of construction and steady seepage condition.

The end of construction condition will be applicable for the empty condition of the ash pond, soon after construction. This condition is checked for both upstream and downstream slopes. In the steady seepage condition, the seepage is considered from upstream slope to downstream slope and hence this condition was checked only for downstream slopes. The above conditions were analysed for both normal and seismic cases.

3.1 Material Properties

For the economic considerations, suitable soil, available from nearby borrow pits was considered for the bund raisings. Soil available nearby borrow pit was of 'SC' type of soil classification as per IS 1498 which was selected for ash bund extensions. The soil properties were considered based on the 'ash test report & soil test report' shared by the customer. The subsoil properties are inferred from the available Geotechnical investigation report. The properties used for stability analysis are tabulated in Table 1.

Table 1 Soil strength parameters

Sl.no	Soil type	Cohesion (kpa)	Angle of Internal friction (deg)	Bulk unit weight (kN/m ³)	Permeability (m/sec)
1	Fly ash	0	30	13.5	1 e-008
2	Embankment material	10	28	18	1 e-006
3	Soil cover	10	28	18	1 e-006
4	Foundation	10	30	18	1 e-006

3.2 Analysis

Surcharge load of 20 kPa was considered for the movement of trucks on top of the embankment.

The site is located in Seismic zone III as per IS 1893. The below seismic co-efficients were calculated from IS 1893 and used in seismic co-efficient method for slope stability analysis.

- (a) Horizontal seismic co-efficient = 0.136
- (b) Vertical seismic co-efficient = 0.091.

The above co-efficients were adopted for seismic case in slope stability analysis. The slopes were analysed in the software for both seismic normal cases.

As the HDPE liner is provided on the upstream slope, practically seepage will not be expected in the bund raising. However to consider the critical case of HDPE lining getting ruptured and resulting in seepage inside the bund raising, the bund is checked for steady seepage condition. Hence the slopes were analysed for end of construction and steady seepage conditions under normal and seismic cases.

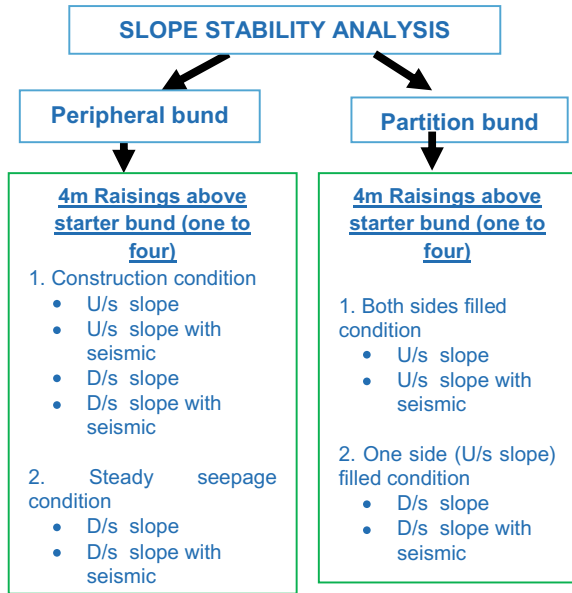
The maximum ash fill level in the ash pond was designed up to 1 m from the top of the bund. For steady seepage conditions, this level was considered for start of the phreatic line which travels into the section of the bund raising.

Figure 4 shows the flow chart of the slope stability analyses iterations carried out for peripheral and partition bund. U/s represents upstream face of the slope whereas D/s represents downstream face of the slope.

3.3 Peripheral Bund

The peripheral bund needs to be critically designed as this will be permanent bund storing the entire ash fill. For the enhanced stability of the peripheral bund, it is considered to be constructed with ash as core material and earth as shell material. The width of the earth shell material is kept minimum to the extent corresponding to the roller width of the compacting equipment. As the width of vibratory roller proposed to be deployed would be around 1.5 m. The earth shell material thickness is generally considered to be 1.5 m.

Fig. 4 Flow chart of iterations of slope stability analyses



The top width of the raising bund was considered as 4.5 m, which is same as that of the starter bund. The upstream and downstream slopes of both soil (shell) and ash (core) are considered as 1 in 3. The same is depicted in Fig. 5.

In the Geostudio analysis software, the starter bund and each raising were modelled as in Fig. 6. The ash fill and soil properties were considered as in Table 1.

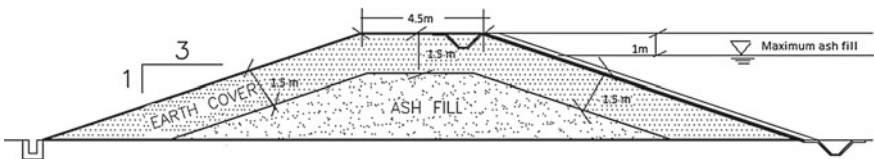


Fig. 5 Peripheral raising bund

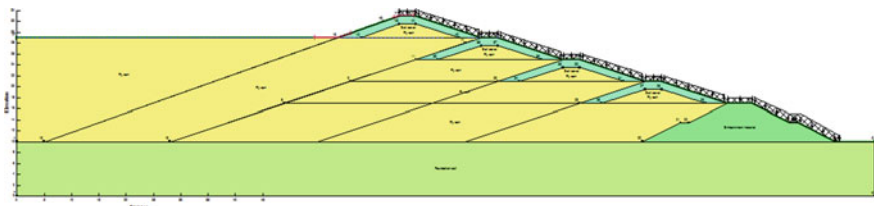


Fig. 6 Input model showing 4th stage raising of ash pond

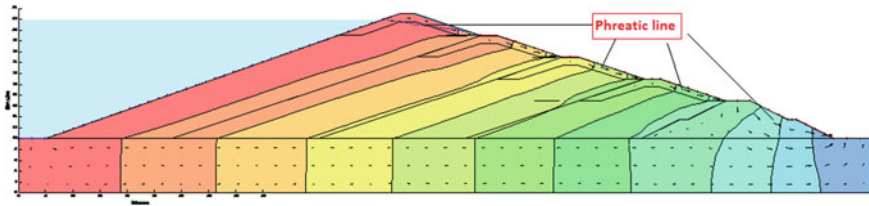


Fig. 7 Output model showing phreatic line from steady seepage condition

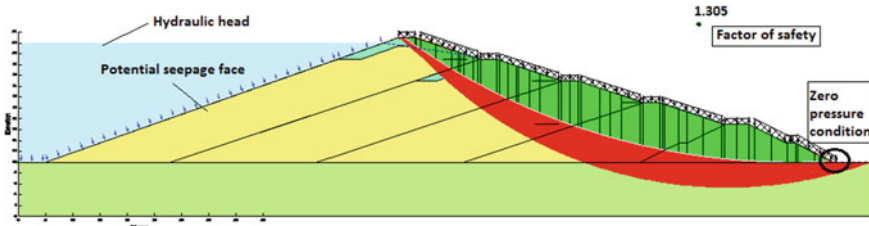


Fig. 8 Output model showing steady seepage condition—with earthquake forces

The model was analysed for end of construction and steady seepage condition as mentioned in the flow chart (Fig. 4). The analysis is repeated for each raising of the bund.

The steady seepage condition was modelled by defining the below inputs: zero pressure head as downstream toe, potential seepage face as the total upstream face with 4 raisings stage and the water head as max ash fill level at 4th stage that is 22 m. The phreatic line thus obtained as output from the steady seepage condition is shown in Fig. 7.

The factor of safeties obtained for downstream slope for steady slope seepage with seismic condition is shown in Fig. 8.

The ash bund up to 4 raisings for both construction and steady seepage conditions were found safe. The further extensions of the bund were attempted, but the slope stability was failing beyond 4 extensions of the bund. Hence the final height of the ash bund was concluded as 7 (starter bund height) + (4 × 4) (4 raisings of 4 m height each) = 23 m from the lowest RL in the area. Considering 1 m freeboard, the total ash fill possible is 22 m.

3.4 Partition Bund

The partition bund is a temporary bund which will exist at each bund raising. As explained earlier the partition bund is constructed with maximum ash fill and with minimum earth cover just to prevent erosion of ash during construction. The top width of the partition bund was considered as 4.0 m and earth cover was considered

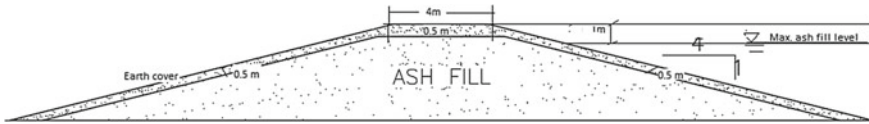


Fig. 9 Partition raising bund

of minimum 0.5 m thickness. The upstream and downstream slopes of both soil (shell) and ash (core) are considered as 1 in 4. The above cross-section was analysed for stability and found satisfactory for each stage of ash bund raising. The same is depicted in Fig. 9.

Partition bund is a notional bund that exists only for one stage of bund raising. After ash filling, the partition bund will be fully submerged with ash and for the next stage again, it will be created. The partition bund of 4th stage is found to be critical as it rests on the total ash fill of 19 m (7 (starter bund height) + (4 × 3) (3 raisings of 4 m height each) = 19 m). Hence 4th stage raising bund was modelled for partition bund in Geostudio analysis software as in Fig. 10.

It is noted that partition bund will be having ash slurry on one side and empty on the other side during construction phase. During operation phase, both sides of the

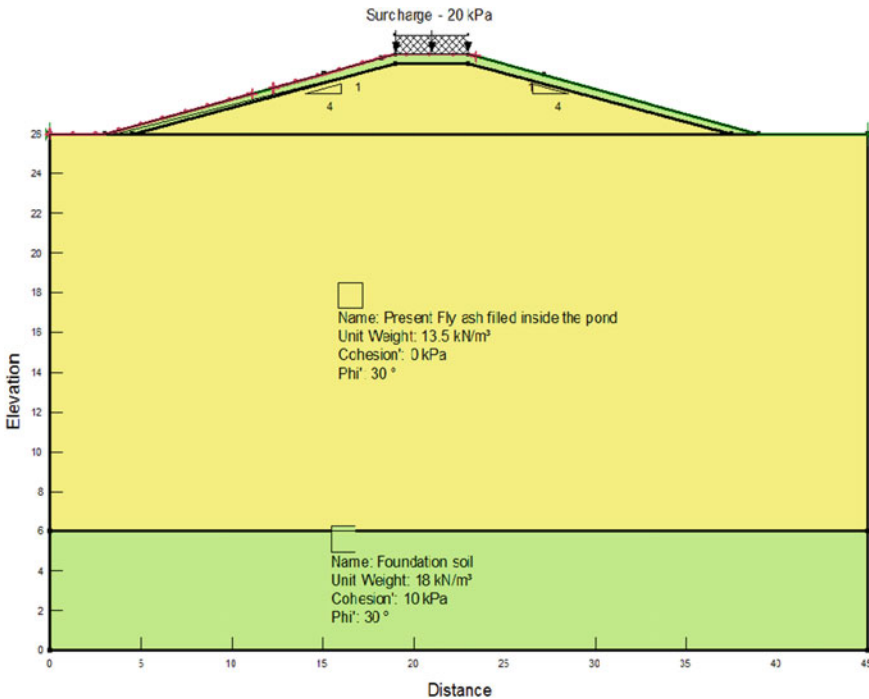


Fig. 10 Input model showing partition bund at 4th stage

partition bund will be filled with ash slurry. As the raisings are provided on upstream face, upstream slopes will be more critical, for ‘one side filled’ condition, hence only upstream slope was checked. For ‘Both sides filled’ seepage condition was analysed considering seepage indicated by phreatic line from the upstream slope and moving towards downward slope as illustrated in Figs. 11 and 12. Hence ‘both sides filled’ condition was checked for downstream slopes only. The above conditions were analysed for both normal and seismic cases. The factor of safeties obtained for

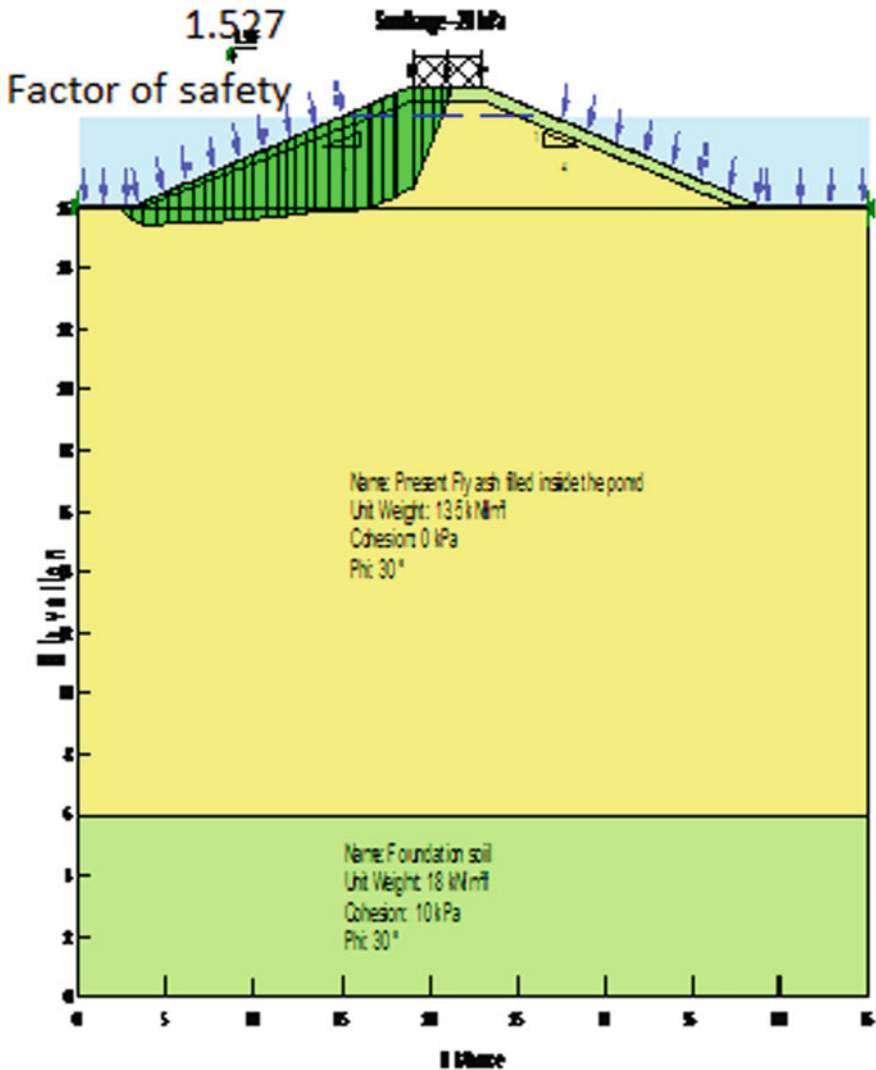


Fig. 11 Output model showing partition bund—stability of upstream slope—both side filled condition

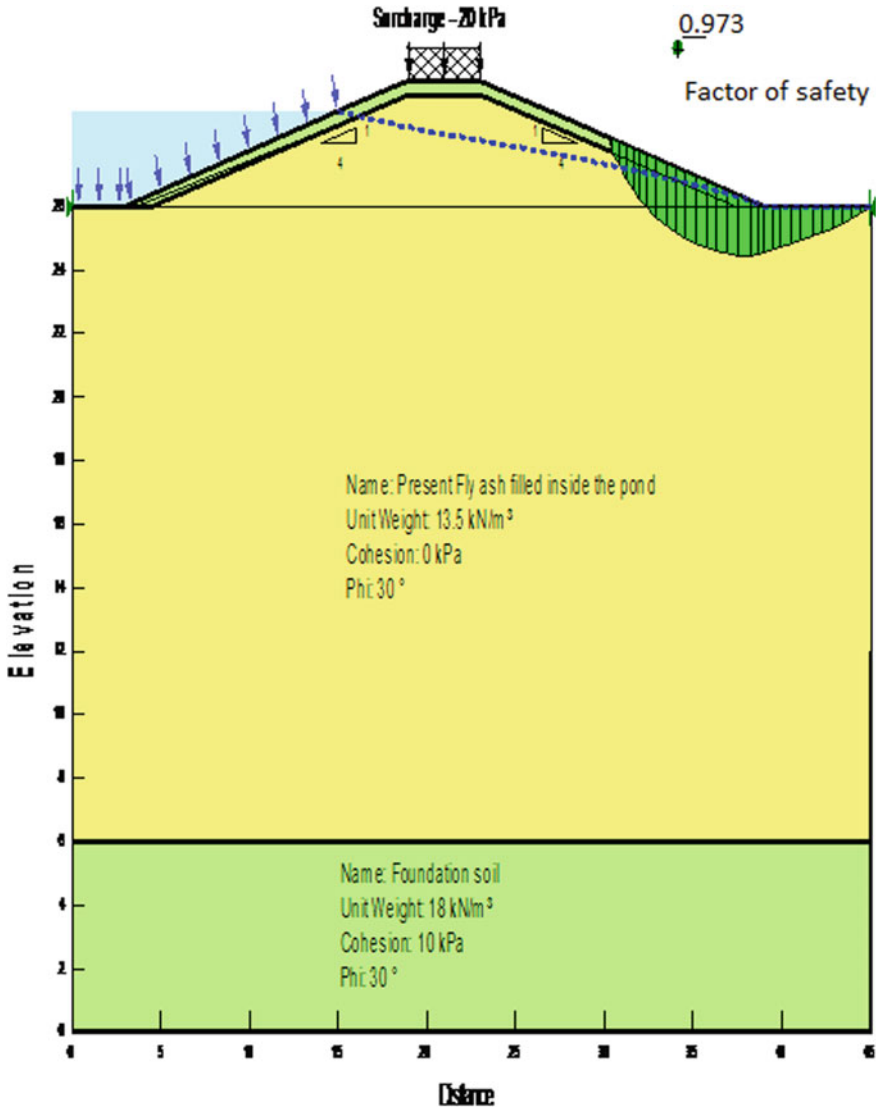


Fig. 12 Output model showing divider bund—stability of downstream slope—one side filled steady seepage condition

raising is shown in Fig. 12, the slopes were found to safe for both ‘one side filled’ and ‘both sides’ filled conditions.

The factor of safety obtained for 4th stage bund raising under steady seepage condition and seismic case was lower compared to all other cases and hence this was considered the governing case in the slope stability analysis.

4 Specification and Construction Sequence of the Raising of Ash Pond

Raising of ash bund will be done in four stages by the construction of peripheral bunds along the inner side of ash pond. One partition bund at each stage is proposed inside the ash pond area to facilitate the parallel operation of ash bund raising and ash filling. The total height of proposed ash bund raising is considered to be 16 m.

4.1 Material

The materials used for the construction of raisings are hereby elaborated.

4.1.1 Ash Available at Ash Pond

The available ash from the ash pond having properties mentioned in Table 1 was used for the construction.

4.1.2 Earth Material

The earth from one of the identified borrow pit having properties given in Table 1, have been considered for the construction. Earth material used for earth cover shall be free from clods, salts, sulphates, non-expansive, neutral in pH and organic or other foreign material. All clods of earth have been broken or removed. It was to conform to SC/GC/CL/CI as per IS 1498 soil classification system. The soil from the borrow pits were tested for plasticity, compaction and gradation characteristics for checking conformity with requisite characteristics. This was carried out for every 3000 cubic metres of earth from borrow pits.

4.1.3 HDPE Liner

The HDPE liner provided was 1 mm smooth UV resistant type and the properties conforming to GM 13 GRI standards.

4.1.4 Fine Sand Cover

The fine sand cover used as a protective layer above HDPE was of non-expansive clayey/silty sand or a mixture of these. The sand cover was fine and free from

kankar/gravel and other sharp-edged material. The sand material having particles passing through 2.36 mm IS sieve was used.

4.1.5 Fly Ash Bricks

Fly ash bricks were hand/machine moulded and have been made from the admixture of suitable soils and fly ash in optimum proportioned as per IS 2117 and are used for protection of U/s and D/s slopes of the bund.

4.2 Methodology of Raising of Ash Bund

A layer of soil of around 1 m was spread above the maximum ash fill level of the starter bund before starting of each raising of the ash pond. This layer acts as a drainage layer for draining out, seepage water if any.

Peripheral and Partition ash bund raising at each stage was constructed using ash and earth. The ash was used as the core layer and the selected earth from the identified borrow pits was used as the covering for the bund raising.

4.2.1 Peripheral Bund

The raising of each peripheral ash bund was started by spreading the ash in the centre and soil covering at the edges. The sufficient quantity of earth and ash was delivered to the proposed embankment location at a uniform rate to permit bund construction process.

The bund formation was done in layers of thickness not less than 225 mm. The compaction was carried for each layer up to 95% modified proctor density using rollers and by sprinkling the required quantity of water. The achievement of the desired compaction was tested for optimum moisture content and field density for every 1000 m² of the compacted area. After completion of filling by compaction up to the top bund level, both upstream and downstream slopes the slopes were trimmed to the required 1 V: 3H slopes. The typical section of the peripheral bund is shown in Fig. 12.

On the prepared even surface HDPE geomembrane was laid. The geomembrane was securely anchored at both ends of the slope by provision of anchor trench. A protective layer in the form of 50 mm thick sand was laid on HDPE liner on part of the pond bed and U/s slope. A 75 mm thick ash brick lining was laid over the sand layer along the slope and top of the bund in correct line set in 25 thick cement mortar (Fig. 13).

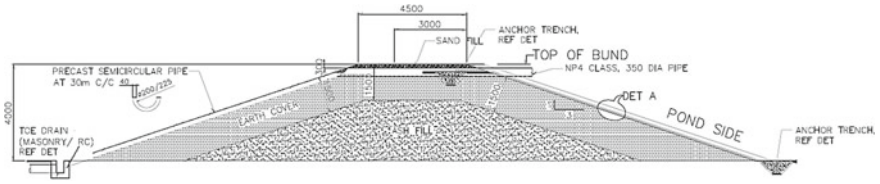


Fig. 13 Typical cross-section of peripheral bund

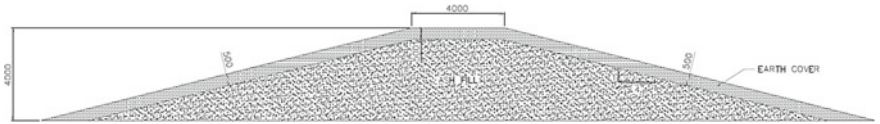


Fig. 14 Typical cross-section of partition bund

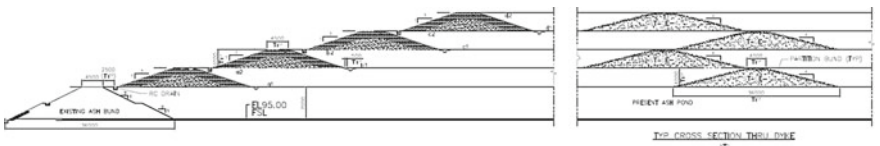


Fig. 15 Typical cross-sectional arrangement of peripheral and partition bund raising

4.3 Partition Bund

The raising of partition bund at each stage was constructed by dumping the ash to minimum 1 m height and compacting it by moving the roller over the dumped ash. The 3.5 m high ash core was constructed in this manner, subsequently 0.5 m wide earth cover was provided all around the ash core. The typical section of the partition bund is shown in Fig. 14.

The typical section of raising of partition bund and peripheral bund is shown in Fig. 15.

5 Decantation System

After construction of raising of peripheral and partition bund the ash slurry is disposed to the ash pond at the discharge points. The ash gets accumulated at the discharge point end where the ash laid water flows towards the other end, which is shown in site photo in Fig. 16.



Fig. 16 Construction of first stage raising of ash bund

The ash laid water is made stagnant, so that fine particles of ash get deposited by sedimentation, this process is known as decantation system. After sedimentation, sufficient clear water exists as a water head which can be collected for reuse.

Dewatering pumps were deployed to collect clear water for reuse purposes. The pipe end of dewatering was covered with fine mesh so that fine particles of ash will not escape.

The process of ash deposition on discharge end and recovery on opposite end was continued till the ash gets deposited up to the maximum ash fill level of the raising. Subsequent to that, the discharge point was shifted and the above process was repeated till the maximum ash fill level is reached.

6 Conclusions

- Raising of ash bund is the secondary phase considered for augmenting the ash storage. However the design and feasibility of raisings of the ash bund, needs to be finalised during the initial design of starter bund.
- Partition bund made of ash could be considered while raising of ash bund to facilitate parallel operation of ash slurry filling and construction of bund raising.

- The factor of safety obtained for 4th stage bund raising under steady seepage condition and seismic case was lower compared to all other cases and hence was considered the governing case in the slope stability analysis.
- Maximum 4 raisings of ash bund over and above starter bund were proved to be safe for considered ash and soil properties.

References

- Biswas A, Gandhi BK, Singh SN, Seshadri V (2000) Characteristics of coal and their role in hydraulic design of ash disposal pipelines. *Indian J Eng Mater Sci* 7:1–7
- Gandhi SR (2005) *Design and maintenance of ash pond for fly ash disposal*. In: Proceedings of Indian geotechnical conference. Ahmedabad, India, pp 85–86

Possible Use of High Draining Material in Core of Earth Dam with Admixtures



Saroj Kundu , Pritam Dhar, and B. C. Chattopadhyay

Abstract In construction of earthen dams, impervious materials are used in the core and pervious materials are placed in the upstream and downstream portion. Most of the construction sites of earthen dam have abundant availability of pervious materials but lacks in the availability of impervious materials. In earthen dams, impervious materials are responsible for the control of seepage loss of the dam. But due to the shortage of impervious materials, there occurs a need to meet the demand of core materials of the dam. To establish the requirement of low permeable soil, it needs to be transported from lower terrain to the construction site at high transportation charge. To minimise the construction cost of the earthen dam, there is a need to upgrade the locally available materials to the desired requirement. This can be achieved by Gradation method or by addition of foreign materials in a small ratio. In the repeated experimental programme, the permeability of locally available soil was reduced by adding industrial and agricultural wastes like fly ash or rice husk ash. Some further experiments have been performed to reduce further permeability by adding various percentages of bentonite mixed with fly ash and rice husk ash.

Keywords Permeability · Fine admixture · Earth dam · Plastic waste

S. Kundu

Meghnad Saha Institute of Technology, Kolkata 700150, India

e-mail: kundu.saroj44@gmail.com

P. Dhar (✉)

IRClass Systems & Solutions Private Limited, Kolkata, West Bengal, India

e-mail: pritamdhar21feb@gmail.com

B. C. Chattopadhyay

Bengal Engineering and Science University, Shibpur, Howrah 711103, India

e-mail: ccbikash@yahoo.com

© Springer Nature Singapore Pte Ltd. 2020

M. Latha Gali and P. Raghuvver Rao (eds.), *Construction in Geotechnical*

Engineering, Lecture Notes in Civil Engineering 84,

https://doi.org/10.1007/978-981-15-6090-3_31

1 Introduction

The India is a land full of rivers. Majority of these rivers become lively during monsoon due to heavy rainfall. A high percentage of these river water mixes up with sea through innumerable rivers originating from high altitude areas and hilly regions. If this valuable water could be collected and utilised in a proper approach during the lean period without causing any environmental hazards, then it can serve the society in its development by using the water for drinking and irrigation purpose and distributing it in a planned eco-friendly way. This is possible only when a cost-efficient dam is built across the river at suitable location along the flow of the river. These dams are generally constructed in hilly terrain to obtain the topographical advantage for distribution of water. The agricultural requirement of water should be judiciously stored ensuring proper storage during lean periods by the construction of reservoir. Cost-effective dams are constructed at suitable location along the path of river to ensure easy availability of raw materials having low cost. Seepage loss can be minimised by the use of soil with low permeability. Since low permeability soil is not easily available leading to their increased transportation cost, locally available materials of high permeability are modified to the required and suitable extent by cost-effective methods. So, sand is used in the core of earthen dam. But, as it is a highly pervious material, it needs to be graded and mixed with bentonite of different percentages (Dhar and Chattopadhyay 2014). But using a mixture of sand and bentonite only, the requirement about seepage loss concern as core materials of the dam cannot be met. Also, bentonite is a high-cost material. So, incorporation of some other materials is required to reduce the construction cost and obtain the required standards. This present study deals with the incorporation of some waste materials like fly ash and rice husk which is used as a core material with a small amount of bentonite is capable of arresting the seepage loss in the dam in a cost-effective way.

2 Cored Earth Dam

Homogeneous dams are generally constructed of single embankment material. Such dams have been built since the earliest times and are used today whenever only one type of material is economically available. But there are some benefits of a zoned dam, which also includes the availability of local materials that can be conveniently incorporated in a homogeneous dam by placing the materials selectively or by different construction methods in different parts of the dam.

Homogeneous core dams are constructed mainly of impervious or semi-pervious soil. When a large source of pervious and impervious soil near the construction site of a dam is existing, even then, the construction of homogeneous core earth dams will be cost-effective, because of a variety of reasons such as a cheaper cost of construction and less construction time requirement for such dams.

But, when there is the availability of only pervious material near the construction site of a dam, and only a limited supply of impervious soil then it is possible to construct only core dams.

In thin core dams, core may be placed upstream or placed in the vertical position near the centre of the embankment. The pervious zones are made up of sand and gravels or rocks. But even in such case, feasibility of constructing such dams depends upon the availability of scarce impervious materials. This requirement of such material for construction of thin core dams depends on the minimum thickness of the impervious core which should be safe enough for its stability and serviceability.

It had been opined (Sherard et al. 1963) that a core with a width of 30–50% of water head is generally satisfactory under diverse conditions for any type of soil and any height of dam. The core of a dam with a width, much less than 10% of the water head has not been used widely and it should be considered only in circumstances where a large leak through the core would not lead to the failure of the dam.

3 Scope of the Study

In most of the possible location of future earth dam, it is expected that such sites would have deficiency of deposits of impervious soil but will be abundant in gravel or sand. Where no such natural deposit of cohesive soil is available, attempt has been made to construct impervious core from the mixture of the locally available materials and a minimum percentage of bentonite. In this aspect, the above programme has been undertaken to seek the experimental solutions to decrease permeability of high draining sand with the help of mechanical stabilisation and addition of low draining material in optimum percentage by weight.

In the previous work, silver grey sand obtained from Hooghly river was used. The sand had been mechanically segregated in different fraction and permeability of each fraction has been determined. By proportional mixing of different grades, the permeability of each mix has been found to have visible effect on the value of the permeability.

When bentonite has been mixed in a ratio of 2.5% of the weight, it is seen that the value of K decreases to 0.000124 cm/sec (Dhar and Chattopadhyay 2014). This value of K is quite small, and is not enough for being used as a core material but it may be used in a zoned earth dam.

Regarding the concern of core materials, some series of experimental programmes have been performed. Initially Silver grey sand has been mixed with fly ash and rice husk ash, following which, the permeability values have been checked. Thereupon, some fine-grained material like bentonite, fly ash or rice husk ash has been used to find out the permeability values

4 Materials

Hooghly River sand has been mainly used, which is a fine sand. The sand particles passing through 150 μ sieve and retained on 75 μ was has been used in this study. The characteristic properties of the sand are exposed in Table 1 and grain size distribution of silver sand is shown in Fig. 1.

The characteristic properties of other materials except silver sand such as fly ash, rice husk ash and bentonite have been incorporated accordingly in Tables 2, 3 and 4.

From the analysis of the above tables (Tables 2, 3 and 4) are detailed knowledge on the characteristics of fly ash, rice husk ash and bentonite can be obtained. These

Table 1 Summary of properties of silver sand

Sl No.	Properties	Values obtained
1	Specific gravity	2.505
2	Percentage fineness	8.42%
3	Loose bulk density	1.093 gm/cc

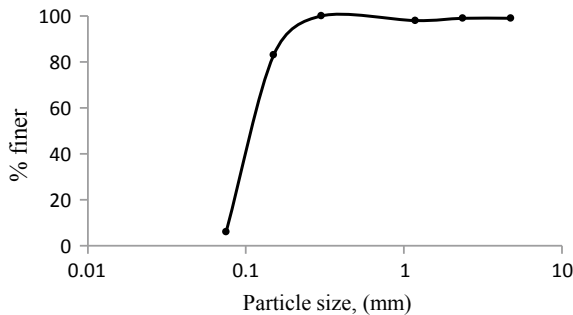


Fig. 1 Grain size distribution curve of silver sand

Table 2 Summary of Properties of Fly Ash

Sl No.	Properties	Values obtained
1	Colour	Whitish grey
2	Specific gravity	2.1
3	OMC (%)	30
4	MDD(gm/cc)	1.247
5	CBR value	6.9
6	Specific surface (Blaine's Permeability)	335.9
7	Particle retain on 45 μ sieve (wet sieving method)	32.03
8	Percentage of Fineness	22.42%

Table 3 Summary of properties of rice husk ash

Sl No.	Properties	Values obtained
1	Specific gravity	1.235
2	Water absorption (%)	0.62
3	Effective size, (D10)	0.075
4	MDD	1.28 gm/cc
5	OMC	29%

Table 4 Summary of properties of bentonite

Sl No.	Properties	Values obtained
1	Density	1.03 gm/cc
2	pH value	970.00%
3	Marsh cone viscosity	1.093 s
4	liquid limit	427.40%

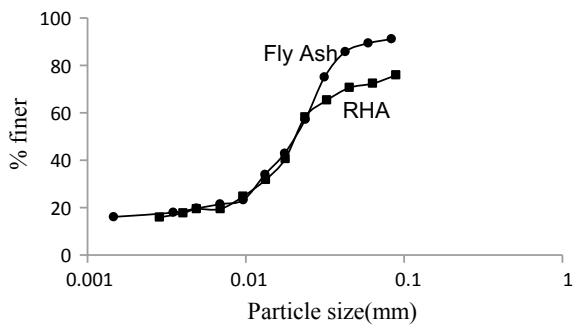
materials possess the property which fits the requirement to be a core material of an earthen dam.

The grain size distribution curves of fly ash and rice husk ash are shown in Fig. 2.

The grain size analysis is widely used in classification of both, fine and coarse material. The data obtained from the grain size distribution curve is used in the design of the core in an earthen dam. Information obtained from the grain size analysis predicts that the fineness property of both the material is nearly same.

Falling head permeability tests have been conducted for the determination of permeability value of this sand. All tests have been conducted by placing all materials at same density of 1.40 gm/cc for which the mould of volume 1021.01 cc has been filled with 1434 gm of samples.

Fig. 2 Grain size distribution curve of rice husk ash (RHA) and fly ash



5 Result and Discussions

In view of this, the value of coefficient of permeability of silver sand has been obtained from the falling head method. The experimental result shows the average value of coefficient of permeability for silver sand which is 0.003 cm/sec.

It has been already shown that permeability of such cohesion less soil can be improved by mixing various percentages of fly ash and rice husk ash. However, in this paper, some alternative techniques have been adopted to improve the coefficient of permeability for such soil in a cost-effective way.

This new technique uses the industrial and agricultural waste materials to upgrade the soil in such a manner that it is fit to be used as a core material of an earthen dam. The use of rice husk, an agricultural waste and fly ash, an industrial waste makes the procedure more economical.

The first experimental programme has been sorted out by mixing fly ash and silver grey sand in different proportion of 5%, 8% and 12%, respectively, by volume.

Again, rice husk ash has been used in same fashion with silver sand, and the different permeability values for each have been obtained and shown in Table 5.

The variation of K values of silver sand and locally available materials (fly ash and rice husk ash) in different proportion is shown in Fig. 3.

From Fig. 3 it is visible that with an increase in the percentage of locally available materials, i.e. fly ash and rice husk ash when mixed with silver sand, permeability

Table 5 K values for different % of locally available materials (fly ash and rice husk ash) with silver sand

Percentages additive material (%)	K values in cm/sec	
	Silver grey sand mixed with fly ash	Silver grey sand mixed with rice husk ash
5	0.001689	0.00297
8	0.000754	0.00218
12	0.000462	0.00178

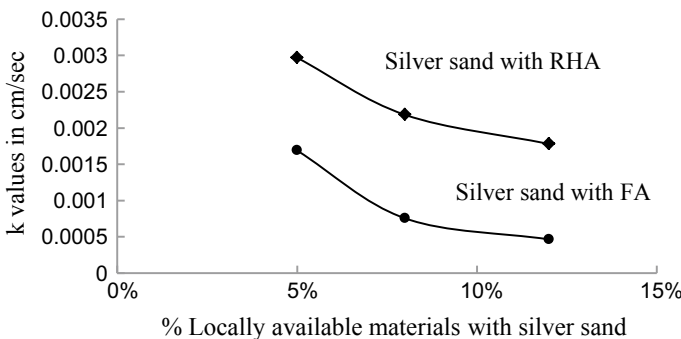


Fig. 3 Comparison of Permeability values using fly ash and rice husk ash with silver sand

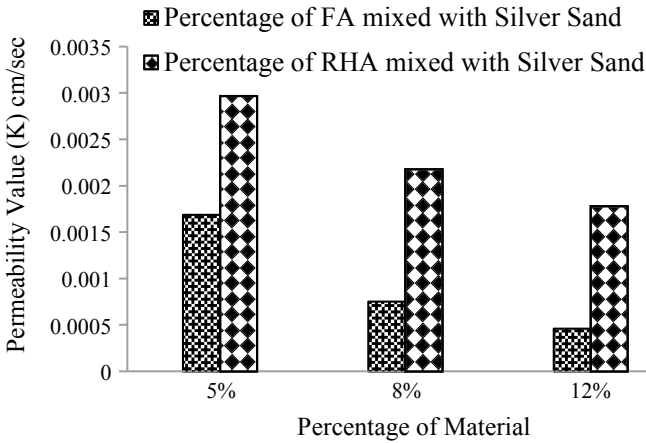


Fig. 4 Variation of K values when fly ash and rice husk ash is mixed with silver sand in various percentages

values decrease. But the decrement in permeability values is quite satisfactory for the mixture of fly ash and silver sand in comparison with the mixture of rice husk ash and silver sand. Thus it could be stated that fly ash is a more compatible material with respect to Rice Husk Ash when it mixed with silver sand for being used as a core material in an earth dam.

The comparison of the permeability values of silver grey sand when mixed with fly ash and rice husk ash in same percentages is shown in Fig. 4.

From Fig. 4, it is observed that for every percentage of material used, the permeability value (K) undergoes a prominent decrement when fly ash is incorporated into silver grey sand in comparison with fly ash when added to silver grey sand.

From the above chart, for the use of 5% of materials, the individual permeability value for fly ash is 0.001689 while K value for RHA is 0.00297. So it is evident that though there is a decrement of K value in both the cases, but K value obtained from the use of fly ash is more satisfactory. This similar fashion of decrement in K values carries on for all other percentages of material used. While using in the core of the earthen dams, as they are the waste materials from industrial and agricultural field, they may be used as alternative materials in the core of an earthen dam for cost-effectiveness.

Another experimental programme has been performed for improvisation of permeability values to an acceptable value for being used in core mixing of some fine-grained foreign material like bentonite which is a readily available material in the market like fly ash and rice husk ash. If bentonite is mixed with fly ash and rice husk ash in various proportions by volume, the permeability value may decrease in a way of cost-effective method. In this experimental programme, rice husk ash and fly ash have been kept same. So the properties of the materials are also same. For conducting the test, the density (i.e. 1.40 gm/cc) has been kept constant for the entire

Table 6 Permeability values with different percentage of bentonite with fly ash

% of bentonite with fly ash	Values of permeability (k) in cm/sec
0	0.000054
5	0.00000996
10	0.00000506

Table 7 Permeability values for different percentage of bentonite with rice husk ash

% of bentonite with rice husk ash	Values of permeability (k) in cm/sec
0	0.0000938
5	0.00001263
10	0.00000865

permeability test of different percentages of bentonite mixing with rice husk ash and fly ash.

At first permeability test has been conducted on 100% fly ash, which gives a permeability value $k = 0.000054$ cm/sec. Then the amount of bentonite used has been increased gradually by 5% and then 10%, for which, the permeability values are gradually decreasing, i.e. 0.00000996 cm/sec and 0.00000506 cm/sec, respectively. Permeability values (k values) with different proportion of bentonite, fly ash mixture is shown in Table 6.

After that Permeability values are checked for 100% RHA and then different percentages of bentonite was mixed with rice husk ash is as follows.

The Permeability value was found to be 0.000938 cm/sec when the test was performed on 100% rice husk ash. On increasing the amount of bentonite used gradually by 5% and then 10%, the permeability values gradually decrease to 0.00001263 cm/sec and 0.00000865 cm/sec, respectively. The results are systemising in Table 7. From Tables 6 and 7, it is seen that the permeability values are gradually decreasing with the increase in the percentage of bentonite. The graphical representation of the permeability curve of rice husk ash and fly with different percentage of bentonite result is shown in Fig. 5. Both the permeability curve is plotted between the % of bentonite as abscissa and corresponding permeability value, K (cm/sec) as ordinates.

On the other case when bentonite is mixed with fly ash and rice husk ash in various percentages by volume it is seen that, experimentally, the permeability value of 100% rice husk ash and fly ash are 0.0000938 cm/sec and 0.000054 cm/sec, respectively. When 5% bentonite is used with rice husk ash and fly ash, the permeability values increase to 0.00001263 cm/sec and 0.00000996 cm/sec, respectively. These variations are shown in Fig. 6. To compare the result of permeability values of fly ash and rice husk ash when mixed with various percentages of bentonite.

It is clearly visible from Fig. 7 that the permeability values decrease gradually in both cases with increase in the percentage of bentonite. When 5 and 10% bentonite is mixed with rice husk ash and fly ash, the permeability values decrease in a good

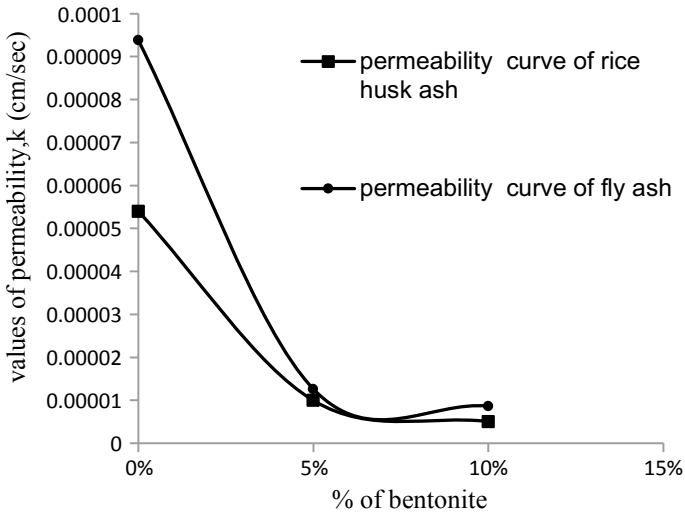


Fig. 5 Permeability values for different percentage of bentonite mixing with fly ash and rice husk ash

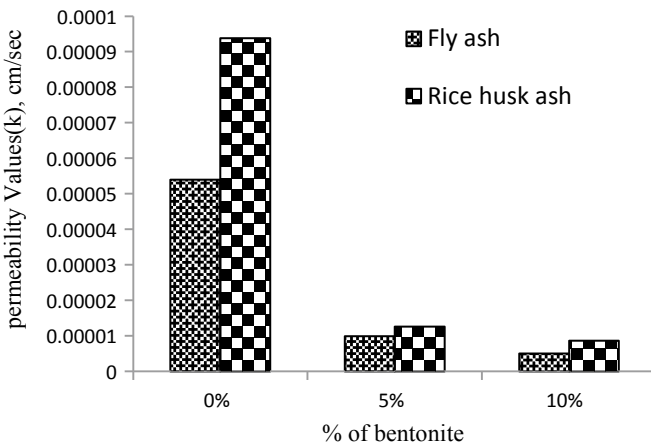
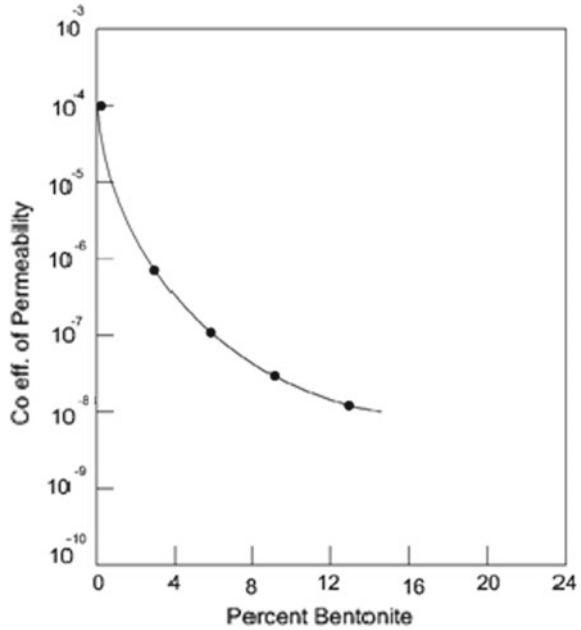


Fig. 6 Permeability values for different percentage of bentonite mixing with fly ash and rice husk ash

manner. The result indicates that adding bentonite by still higher percentage, value of K will decrease to a much lesser value. Published data on the decrease of value of coefficient of permeability with addition of bentonite by EPA (1984), shown a Fig. 7 indicate same.

Fig. 7 Effect of Sodium Bentonite on coefficient permeability of silty sand



6 Conclusions

In high altitude or high terrain, the presence of impervious materials is limited, but availability of pervious materials is high. By modifying the pervious materials, it cannot achieve the permissible value for being used as core materials of earth dam. So, there remain some factors which may affect the permeability values. Having discussion and analysis on such factors, a prominent effect on permeability value is seen where grain size decreases and the application of foreign materials in various proportion which gradually decrease in permeability value. The test has been conducted through the rice husk ash and fly ash medium which has been already reported as discussed above. When 5% and then 10% is used for both the case and the permeability is conducted in same fashion, the result shows that the effect of the quantity of the bentonite still exists. It may be because of its affects on the grain size which decreases the capillary ways and as a result of which, the permeability will decrease compared to the initial test result where the poor medium has been used.

But, this effect is visibly prominent while using fly ash compared to the rice husk ash. Further increment in the amount of bentonite mix (i.e. 10%) maintains its effect but it is poor during the comparison result of 5% use of bentonite. The permeability value tends to achieve the nearby variation as the occurrences initial condition.

In IGC (2014), fine silver sand, $k = 0.003$ cm/sec. When bentonite is mixed at a rate of 2.5% weights the value of k decreases to 0.000124 cm/sec, i.e. 1×10^{-4} cm/sec. But it is not sufficient for the desirable value of core materials of earth dam which is lesser than the value of 1×10^{-5} cm/sec. In this paper, after addition of

10% of bentonite with rice husk ash, $K = 8.65 \times 10^{-6}$ cm/sec and for fly ash it comes down at 5.06×10^{-6} . But value of K for clay, i.e. 1×10^{-6} is smaller, so it may be used in place of clay in core of a earth dam.

References

- Dhar P, Chattopadhyay BC (2014) Modification of sand for use in core of earth dam. IGC, pp 203–206
- Sherard JL, Woodward RJ, Gizienski SF, Clevenger WA (1963) Earth and Earthen dams, engineering problems of design and construction. Willey, IVC, New York
- Environmental protection agency (1984) Requirement for Hazardous waste land fill design, construction closure. publication ND EPA-625/4-89-022, Cincinnati, Ohio

Experimental Study on Cantilever Sheet Pile Wall



Aparna and N. K. Samadhiya

Abstract This paper presents the result of an experimental study conducted for evaluating the effect of depth and distance of adjacent footing on the behaviour of cantilever sheet pile wall. Model sheet pile wall tests have been performed in the medium dense sand. Lateral load on sheet pile wall is obtained by four proving rings attached to the sheet pile wall along with its depth, with the help of four titanium hollow pipes. The lateral load coming onto the sheet pile wall is observed decreasing with increasing depth of footing and distance of footing from the wall face. The position of footing from the sheet pile wall and depth of footing have been varied in this study. The footing is placed at 20, 40, 60 and 80 cm from the wall face at the backfill side with three different depths of footing (at surface, 7.5 cm, 15 cm) in different cases. The effect of sequential excavation has also been presented in this paper.

Keywords Sheet pile wall · Lateral load · Footing

1 Introduction

A cantilever sheet pile wall consists of a row of vertical structural elements embedded in the ground below the retained material. Sheet pile walls are generally sections of sheet material with interlocking edges. These are made up of steel, wood or RCC. Cantilever sheet pile wall is used up to 4–5 m height but beyond this height anchors are added to sheet pile walls to provide more passive resistance to it from backfill side. If lesser margins are available at the site for excavation with safe slopes, top-down approach is required where the soil retention system in form of sheet pile walls is installed first and then excavation is made.

Aparna (✉) · N. K. Samadhiya

Department of Civil Engineering, Indian Institute of Technology Roorkee, Roorkee, Uttarakhand, India

e-mail: aparnaiitr2018@gmail.com

N. K. Samadhiya

e-mail: samadhiyank@gmail.com

© Springer Nature Singapore Pte Ltd. 2020

M. Latha Gali and P. Raghuvver Rao (eds.), *Construction in Geotechnical Engineering*, Lecture Notes in Civil Engineering 84, https://doi.org/10.1007/978-981-15-6090-3_32

445

Sheet pile walls can be constructed by two different methods, as Backfilling method and Dredging method (Bilgin 2010). The Sheet pile wall is driven into the ground and then the backfill is placed in backfilling method whereas the sheet pile wall is first driven into the ground and the soil in front of it excavated in dredging or excavation method. The cantilever sheet pile derives its stability mainly from the lateral resistance of the soil in which the sheet pile is installed (Ranjan and Rao 2000).

Rowe (1952) studied the influence of different parameters like surcharge, position of anchors, dredge level, type of soil, flexibility of pile and distribution of soil pressure on flexible retaining wall. Milligan (1983), Rajgopal and Sri Hari (1998), Hanna and Khurdi (1974) had conducted experimental studies on anchored flexible retaining walls in sand by considering certain primary factors like anchor geometry, initial design assumption, soil density and initial stress state. Georgiadis and Anagnostopoulos (1998) conducted an experimental study as well as numerical analysis to investigate the influence of surcharge loads on the behaviour of sheet pile wall. Sowers and Sowers (2000) had discussed many cases of anchored bulkhead failures. They have concluded that inadequate consideration of allowance for deflection, excessive earth pressures and lack of consideration of effects of construction operations were among the factors leading to the failure of anchored sheet pile wall. Endley et al. (2000) showed unexpectedly larger than the originally calculated deformations for a 12-m high anchored sheet pile wall. They have concluded that the backfill construction method and the way the fill was placed produced large sheet pile deflections and stresses. Finno et al. (2007) conducted a finite element simulation on deep excavation in clays to find out the effect of excavation geometry, factor of safety against basal heave and wall system stiffness on the behaviour of ground movements. Sawwaf and Nazir (2012) presented the outcome of laboratory experiments on the influence of deep excavation-induced lateral soil deflections on the behaviour of a model strip footing adjacent to the excavation and supported on the reinforced granular soil.

The present study focuses on the change in the behaviour of sheet pile wall by changing few parameters around it. Sheet pile wall is placed adjacent to pre-existing footing where excavation has to be made. The distance between sheet pile wall face and footing has been varied. The footing is placed at different levels so as to vary the depth of footing.

2 Methodology

Model tests are conducted in laboratory with sand as backfill to understand the significance of various parameters affecting the system of sheet pile wall supported excavation nearby a strip footing. Sheet pile wall of 1 mm thickness has been installed 61 cm away from the outer plywood wall in the model test tank. The depth of excavation (H), depth of footing (D_f) and distance between sheet pile wall and adjacent footing (X) have been varied in this study. The load is applied on the strip footing by means of mechanical jack and sequential excavation is made and corresponding

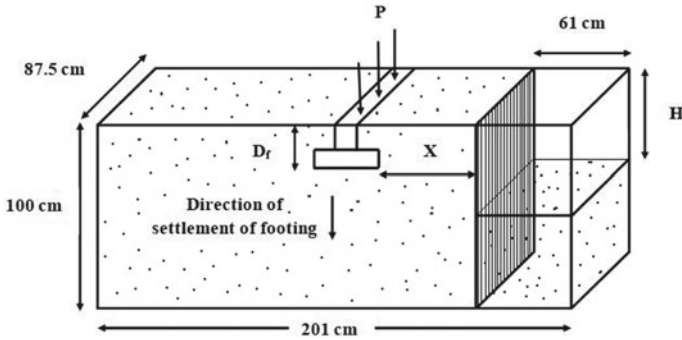


Fig. 1 Experimental setup

changes in the values of lateral load coming onto the sheet pile wall are observed. The experimental set up is shown in Fig. 1.

2.1 Test Facility

It comprises of one test tank of dimension $201 \times 87.5 \times 100$ cm, one mechanical jack for applying load on footing, one sheet pile wall of dimension $100 \times 86 \times 0.1$ cm and a footing of dimension $86 \times 15 \times 2.5$ cm. The sheet pile wall is placed inside the tank which is filled up with medium dense sand.

The lateral load on sheet pile wall has been measured by proving rings but these cannot be installed inside the tank because sheet pile wall is surrounded by sand from both sides as one side has to be excavated. Four 80 cm long hollow titanium pipes of 1.2 cm outer diameter have been used to connect sheet pile wall to the proving rings. Proper holes are made in sheet pile wall and then pipes having inside threads are fitted with bolt connection to the sheet pile wall. Holes of 0.4 cm diameter are created at 0.5, 25, 50 and 75 cm from the top of the sheet pile wall to connect these pipes. Front side of test tank is made up of plywood sheet, so these pipes are connected and pass through the small openings of plywood wall. These pipes are fitted with small plates of dimension $4 \times 4 \times 0.2$ cm at their free end. These small plates are removable and these are connected to the pipe after passing it through the plywood wall. For observing the load on sheet pile wall, the arrangement is shown in Fig. 2. The angle connection with the round turning bar holds the device properly and titanium pipes are used to connect sheet pile wall to the proving rings using small dimension plates to rest the tip of it on that.



Fig. 2 Model test tank: **a** Proving ring arrangement, **b** Inside view of tank with titanium pipes

2.2 Test Procedure

Dry sand is poured from a constant height to maintain a uniform density of 15 kN/m^3 throughout the test tank. Medium dense sand of properties listed in Table 1 has been used to fill the test tank with 55% relative density. Initially, the sheet pile wall placed inside the tank and it is clamped to both sides of the top of tank to stand vertically and titanium pipes are connected to it then whole tank is filled with medium dense sand by pouring the sand from a fixed height to achieve desired relative density.

After preparing the sand bed, footing is placed over it with loading block on centre of it. A mechanical jack is used to apply load onto the footing equivalent to a load intensity of 20 kN/m^2 . The load has been measured with the help of a proving ring. Initial readings of all four proving rings are taken then load is applied and corresponding changes in proving ring readings are noted down. Then excavation is made in front of the sheet pile wall. Successive excavation is made having 15 cm sand layers each excavated at a time. After first layer excavation, readings are noted down and like this till fourth layer all readings are noted down. The total 60 cm height

Table 1 Physical properties of sand

Properties	Values
D_{60} (mm)	0.243
D_{30} (mm)	0.175
D_{10} (mm)	0.15
C_u	1.62
C_c	0.84
φ°	34
G_s	2.67
Classification of soil	SP

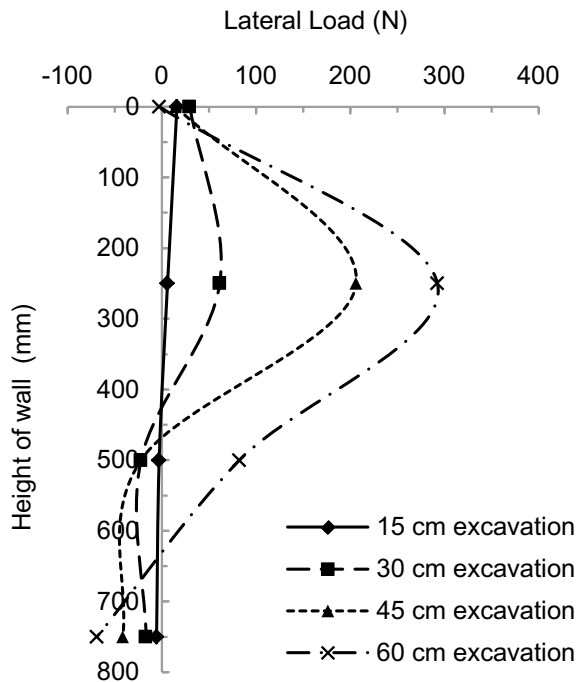
of sand has been excavated in four layers. The proving ring readings (load readings) are observed.

Sequential excavation is made in four layers. 15, 30, 45 and 60 cm soil height is removed, respectively in first, second, third and fourth layer of excavation. X is varied as 20, 40, 60 and 80 cm from the wall face at the backfill side as shown in Fig. 1 and depth of footing has been varied as at surface, at 7.5 cm, at 15 cm below sand bed level. All experimental findings are presented in next section.

3 Results and Discussion

Figure 3 shows the lateral load coming on the sheet pile wall at different levels of excavation without the application of surcharge load. It is observed that the lateral load coming on sheet pile increases as the excavation continues. Active pressure condition is developed after deflection of 0.3% of height of wall (Bowles 1982) and the wall experiences higher active pressure on it with each successive excavating layer. The maximum load found is 293 N at 25 cm below the top of the wall. Figures 4, 5 and 6 show the lateral load on sheet pile wall when footing is placed at 20 cm behind the wall for depth of footing varied as 0 cm, 7.5 cm and 15 cm, respectively. Maximum lateral load on sheet pile wall is observed at 25 cm below the top of the wall for each

Fig. 3 Lateral load on sheet pile wall without surcharge load



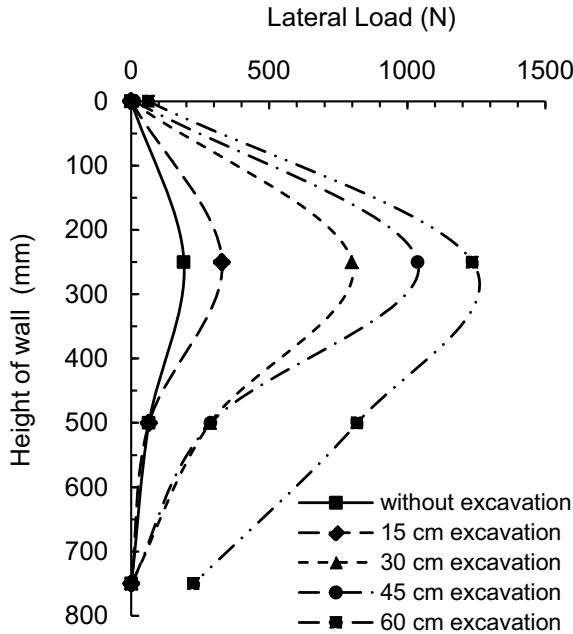


Fig. 4 Lateral load on sheet pile wall with $X = 20$ cm and $D_f = 0$ cm

case because applied load on footing is said to be dispersed in 2 V:1 H through the soil mass and in this way the top of the sheet pile wall experiences negligible load whereas the maximum load is found at the position of proving ring 2 which is placed at 25 cm below the top of the sheet pile wall. The maximum lateral load observed are 1236 N, 1164 N and 1042 N for footing placed at the surface, at 7.5 cm depth, and at 15 cm depth, respectively.

Figure 7 shows the lateral load on the sheet pile wall when footing is placed at 20 cm behind the wall with different depths of footing for full excavation case. It can be seen from Fig. 7 that as the depth of footing increases the lateral load on the sheet pile wall decreases. Load on the wall is observed maximum when footing is placed at surface. For cases when footing is placed below the top sand bed level ($D_f = 7.5$ or 15 cm), load applied on footing causes less deflection at the top of the sheet pile wall as the lateral load is distributed from that level of footing. Maximum distributed load on sheet pile wall also shifted downwards and causes less lateral load on proving rings.

Figure 8 shows the effect of increase in the distance between footing and excavation face when the footing is placed on the surface ($D_f = 0$ cm). The position of the footing is varied as 20, 40, 60 and 80 cm behind the sheet pile wall. This graph shows the full excavation case ($H = 60$ cm). A decrease in the lateral load on the sheet pile wall was observed with increase in the value of X . The main reason behind

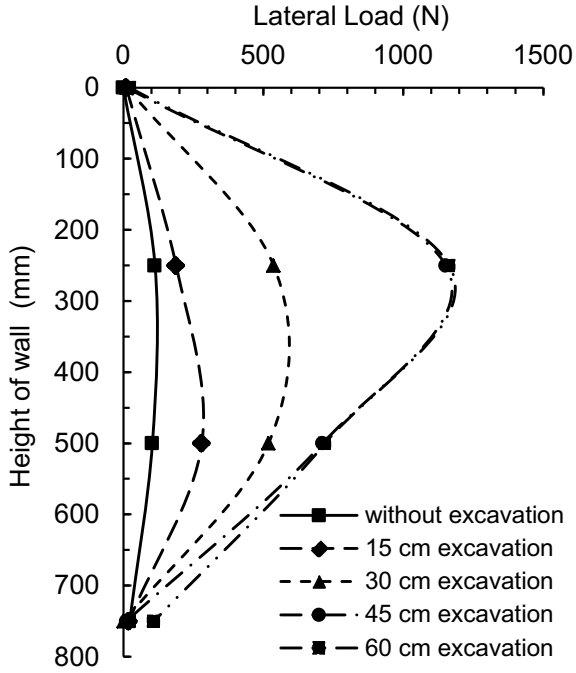
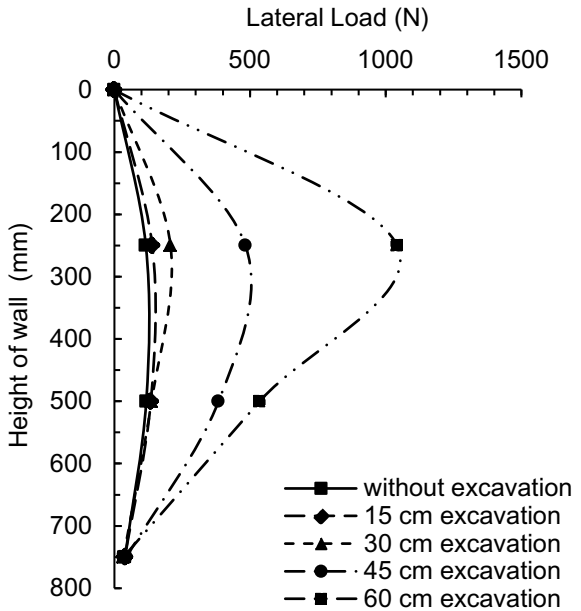


Fig. 5 Lateral load on sheet pile wall with $X = 20$ cm and $D_f = 7.5$ cm

Fig. 6 Lateral load on sheet pile wall with $X = 20$ cm and $D_f = 15$ cm



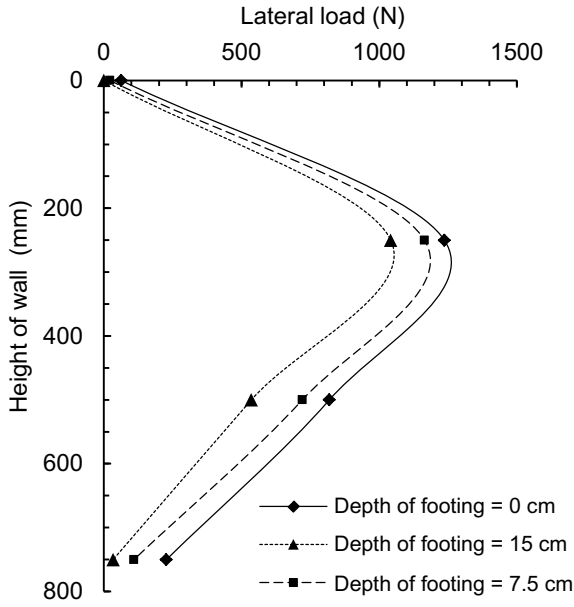


Fig. 7 Variation in load coming on the sheet pile wall with depth of footing D_f , for $X = 20$ cm, $H = 60$ cm

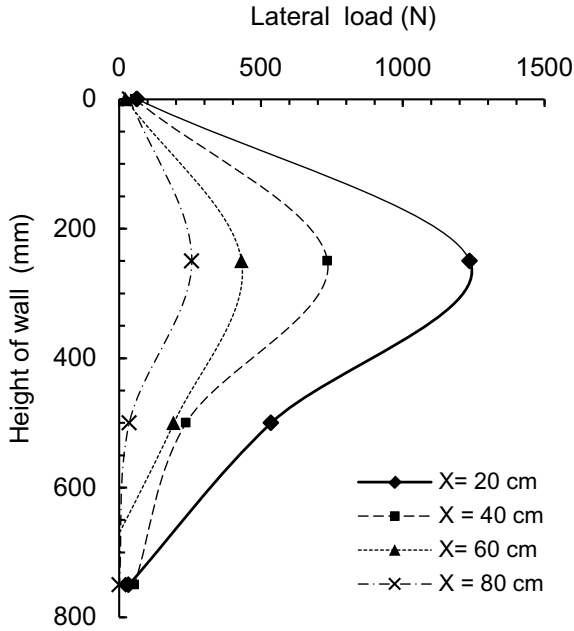


Fig. 8 Variation of lateral load on sheet pile wall with X , for $H = 60$ cm and $D_f = 0$ cm

this behaviour of the wall may be due to the fact that as the loading shifted away from the sheet pile wall, the influence of applied load reduces on the sheet pile wall.

4 Conclusions

Main conclusions of the present study are as follows.

1. The lateral load coming on the sheet pile increases with the excavation height and it is found maximum for 60 cm excavation for each case.
2. The maximum lateral load coming onto the sheet pile wall reduces with increase in footing distance from the wall. It is found maximum when footing is placed at 20 cm behind the excavation edge.
3. As the depth of footing increases the maximum lateral load coming on the sheet pile wall decreases. It is found maximum when footing is placed at the surface.
4. Excavation near to the existing structures causes differential settlements to the building so it is necessary to avoid such constructions at close proximity of the pre-existing structure and provide better support system.

References

- Bilgin Ö (2010) Numerical studies of anchored sheet pile wall behavior constructed in cut and fill conditions. *Comput Geotech* 37(3):399–407
- Bowles JE (1982) *Foundation analysis and design*, 3rd edn. McGraw Hill, New York
- Endley SN, Dunlap WA, Knuckey DM, Sreerama K (2000) Performance of an anchored sheet pile wall. *GeoDenver 2000 Geotechnical Measurements—Lab and Field*, ASCE, pp 179–97
- Finno RJ, Blackburn T, Roboski JF (2007) Three-dimensional effects for supported excavations in clay. *J Geotech Geoenviron Eng* 133(1):30–36
- Georgiadis M, Anagnostopoulos C (1998) Lateral pressure on sheet pile walls due to strip load. *J Geotech Geoenviron Eng* 124(1):95–98
- Hanna TH, Kurdi I (1974) Studies on anchored flexible retaining walls in sand. *J Geotech Eng* 100:1107–1122
- Milligan GWE (1983) Soil deformation near anchored sheet-pile walls. *Geotechnique* 33(1):41–55
- Rajagopal K, Sri Hari V (1998) Experimental study on retaining walls supported by vertical plate anchors. *Indian Geotech J* 28(3):270–296
- Ranjan G, Rao ASR (2000) *Basic and applied soil mechanics*, 2nd edn. New Age International Publishers, New Delhi
- Rowe PW (1952) Anchored sheet-pile walls. Institution of Civil Engineers. Paper No. 5708 (1952)
- Sawwaf ME, Nazir AK (2012) The effect of deep excavation-induced lateral soil movements on the behaviour of strip footing supported on reinforced sand. *J Adv Res* 3(4):337–344
- Sowers GB, Sowers GF (1967) Failures of bulkhead and excavation bracing. *Civil Eng* 37

Effects of Geogrid and Floating Piles on Performance of Highway Embankment Constructed Over Clayey Soil



Dinesh Kumar Verma and Baleshwar Singh

Abstract In this study, a highway embankment is modeled using 3D finite element package, for a deep medium clay soil site reinforced with piles along with a geogrid layer within the embankment. The pile length, pile spacing, and the geogrid stiffness are then varied. From the numerical analysis, settlement of the embankment surface, foundation surface, and pile cap as well as the lateral deformation of the foundation soil, and embankment toe are computed and compared. The distribution of vertical stresses among the piles and the foundation soil is also determined. The results of the numerical analysis show that inclusion of the piles has a greater influence on reducing the settlement of embankment and foundation surfaces, with the geogrid restricting the lateral deformation at the embankment toe and foundation soil due to enhanced load transfer mechanism.

Keywords Embankment · Geogrid · Piles

1 Introduction

Embankment is mainly used for the construction of highway, runway, and dam. Nowadays, due to rapid construction of pavements, geotechnical engineers are forced to construct embankment in such regions also where mostly soft soil layers are present. Due to poor quality of soft soil, it will lead to construction problems like excessive total settlement and differential settlements, bearing capacity failure, and lateral spreading of soil. To encounter these problems, soil improvement methods such as consolidation of soil using vertical drains and preloading, replacement of soft soil with suitable fill, piled raft foundation, and piled embankment with or without geosynthetic are available.

Consolidation of soil using vertical drains and preloading will take more time whereas replacement of soft soil with suitable fill and piled raft foundation will make project costly. So to reduce the construction time and project cost, piled embankment

D. K. Verma (✉) · B. Singh
Indian Institute of Technology Guwahati, Assam 781039, India
e-mail: dineshverma307@gmail.com

© Springer Nature Singapore Pte Ltd. 2020
M. Latha Gali and P. Raghuvver Rao (eds.), *Construction in Geotechnical Engineering*, Lecture Notes in Civil Engineering 84,
https://doi.org/10.1007/978-981-15-6090-3_33

with or without geosynthetic can be used. Embankment supported with only piles is called piled embankment, and embankment supported with piles and incorporated with geosynthetic reinforcement is called geosynthetic piled embankment.

Hewlett and Randolph (1988) estimated that the piles covering as much as 10% of the area below the embankment may carry more than 60% of weight of the embankment due to arching action in the fill. It was also observed that geosynthetic enhances the load transfer mechanism and it also reduces the lateral spreading of foundation soft soils. The design of geosynthetic reinforced piled embankment systems includes the design of embankment geometry, geosynthetic reinforcement, pile dimensions, and center to center spacing between the piles.

Abusharar et al. (2009) presented a new theoretical analysis for geosynthetic embankments on soft ground supported by a rectangular grid of piles which is similar to Low et al. (1994) with some modifications. The main modifications were the inclusion of a uniform surcharge load on the embankment, the use of individual square pile caps and taking into account the skin friction mechanism at the soil geosynthetic interface.

Han and Gabr (2002) proposed that the use of geosynthetic in the fill above the piles enhances the load transfer efficiency, minimizes yielding of soil above piles, and reduces the total and differential settlement. Ariyaratne and Liyanapathirana (2015) did a numerical analysis for geosynthetic piled embankment and a review of seven previously available design methods, and found that results of each method are different from each other.

In the literature, the majority of the study is based on piled embankments which are constructed on end bearing piles. If very thick soft clay soil layers are present below the ground surface, so in that case it is not economically feasible (Bhasi and Rajagopal 2013, 2015). Therefore, for such a condition floating piles (where the pile tip does not locate at hard stratum) should be used. In this study, a highway embankment is modeled using *Plaxis 3D* finite element package, for a deep medium clay soil site reinforced with piles along with a geogrid layer within the embankment.

2 Numerical Modeling

Since embankment is symmetrical about the center line of embankment, so half of the embankment is considered for the modeling. The horizontal length of model is considered as 66 m which is three times the width of half the embankment base so that boundary effect can be eliminated. In the x-direction base width and in the y-direction length of embankment are considered. The length of models is taken as 6 m, 7.5 m, and 9 m for the spacing (center to center spacing between piles) of 2 m, 2.5 m, 3 m, respectively. After that soil layers and its properties are defined.

The depth of groundwater table is set at -0.5 m height from the ground surface. Soft soils have been modeled using modified Cam-Clay model and both the embankment and pebble layer have been modeled by Mohr-Coulomb model. The displacement at $x = 0$, $x = 66$ m and $y = 0$, $y = 6$ m plane is not allowed in x-direction

Table 1 Properties of embankment fill, pile and pile cap

Material	γ (kN/m ³)	E (MPa)	Φ' (degree)	ν
Embankment fill	21	15	32	0.30
Pile and pile cap	24.5	35000	–	0.15

Table 2 Properties of foundation soil layers

Property	Silty soil	Clayey soil
γ (kN/m ³)	19.3	16.7
ν	0.35	0.40
λ	0.06	0.15
κ	0.012	0.030
M	1.20	0.95
e	0.818	1.286
k_h/k_v (cm/s)	$7.2 \times 10^{-6}/7.8 \times 10^{-6}$	$1.0 \times 10^{-7}/1.5 \times 10^{-7}$

and y-direction, respectively. The flow of water is allowed only from top and bottom boundaries of model and lateral flow is not allowed.

In the analysis, 3 rows of piles are considered. Number of piles in the case of 2 m, 2.5 m, 3 m center to center spacing of piles are 33, 27, and 21, respectively. Piles are created using embedded beam row and pile caps are created using plate elements. Piles and pile caps are modeled as isotropic linear elastic material. The construction of embankment is simulated in six stages. The height of first lift is 0.25 m and on that geogrid is provided and construction time is 2.5 days. The second lift height is 0.95 m and construction time is 10.5 days.

Thereafter, in each stage lift height is 1.2 m and construction period is 13 days. Thus after 65 days, construction of embankment is completed. After the construction of embankment, consolidation is allowed for 260 days.

Table 1 shows the properties of embankment fill, pile and pile cap whereas Table 2 presents the constitutive model parameters of foundation soil layers. In these tables, γ is unit weight, E is Young's modulus, Φ' is effective friction angle, ν is Poisson's ratio, λ is Cam-clay compression index, κ is Cam-clay swelling index, M is slope of compression line, e is void ratio, k_h (m/day) is permeability in horizontal direction, and k_v is permeability in vertical direction. Figure 1 is showing the front view of the embankment and foundation soil layers. Figure 2 depicts the finite element mesh.

3 Results and Discussion

Settlement of foundation surface, embankment surface, and pile cap and also lateral deformation of foundation embankment toe and foundation soil have been computed. Moreover, vertical stress on pile caps and foundation soil have been calculated and compared.

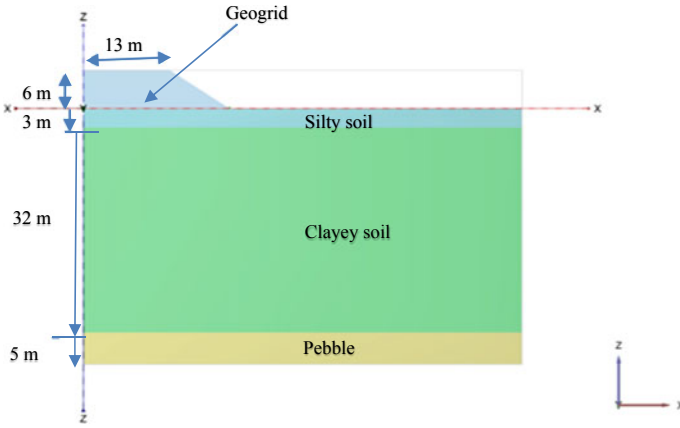


Fig. 1 Front view of the embankment and foundation soil layers

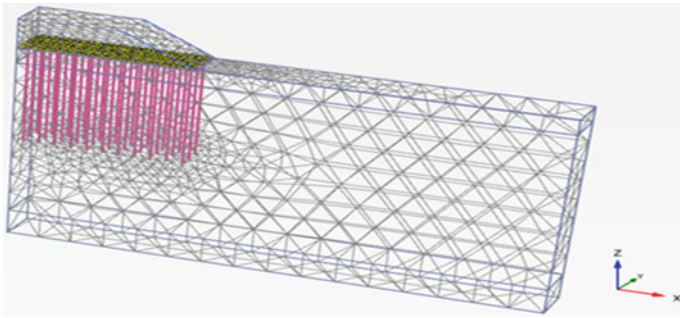


Fig. 2 Finite element mesh (2 m center to center pile spacing and 20 m pile length) with geogrid

3.1 Settlements of Foundation Surface and Embankment Surface

Settlement is calculated at the center line of the embankment. Figures 3 and 4 show the variation of settlement of foundation surface with time after 325 days, in the case of 20 m and 25 m pile length, respectively, along with 1500 kN/m geogrid stiffness. In these figures, settlement of foundation surface is compared for three different pile spacing (2, 2.5, and 3 m).

It is found that settlement of foundation surface is minimum in the case of 2 m pile spacing and maximum in the case of 3 m pile spacing for both pile lengths, because in the case of 2 m pile spacing more load is transferred to the pile caps compared to 3 m pile spacing. Further, settlement is less in the case of 25 m pile length compared to 20 m pile length. Settlements of foundation surface in the case of 1500 kN/m geogrid stiffness and 20 m pile length are 204, 218, and 306 mm, and in the case of

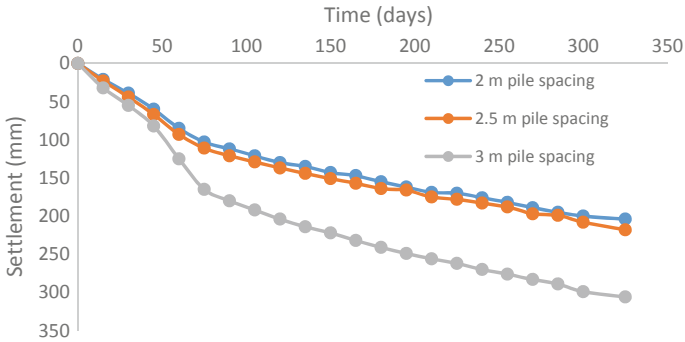


Fig. 3 Variation of settlement of foundation surface with time (in the case of 20 m pile length)

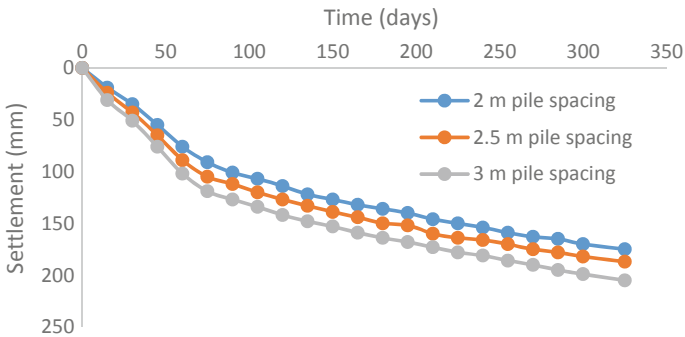


Fig. 4 Variation of settlement of foundation surface with time (in the case of 25 m pile length)

3000 kN/m geogrid stiffness are 197, 211, and 298.8 mm for the 2, 2.5, and 3 m pile spacing, respectively.

Settlements of foundation surface in the case of 1500 kN/m geogrid stiffness and 25 m pile length are 175, 188, and 205 mm, and in the case of 3000 kN/m geogrid stiffness are 167, 180, and 196.7 mm for the 2, 2.5, and 3 m pile spacing, respectively. Table 3 shows the comparison of settlements of embankment surface. Settlements of embankment surface in the case of 20 m pile length and 3000 kN/m geogrid stiffness for 2, 2.5, and 3 m pile spacing are 206, 214, and 303.8 mm, respectively. Settlements of embankment surface in the case of 25 m pile length and 3000 kN/m geogrid stiffness for 2, 2.5, and 3 m pile spacing are 177, 182.3, and 199.7 mm, respectively.

Table 3 Comparison of settlements of embankment surface

		Settlement (mm) at center of embankment surface after 325 days		
Pile spacing (m)	Pile length (m)	With no piles or geogrid	With only piles	With both piles and geogrid (1500 kN/m stiffness)
2	20	1150	240	212
	25		226	184
2.5	20		245	220
	25		229	191
3	20		350	310
	25		243	208

3.2 Settlement of Pile Cap

Settlement of pile cap is determined for the first pile from the center line of embankment along the 2nd row of piles. Figures 5 and 6 show the variation of settlement

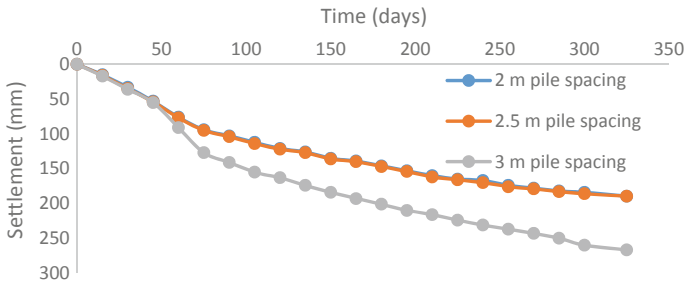


Fig. 5 Variation of settlement of pile cap with time (in the case of 20 m pile length)

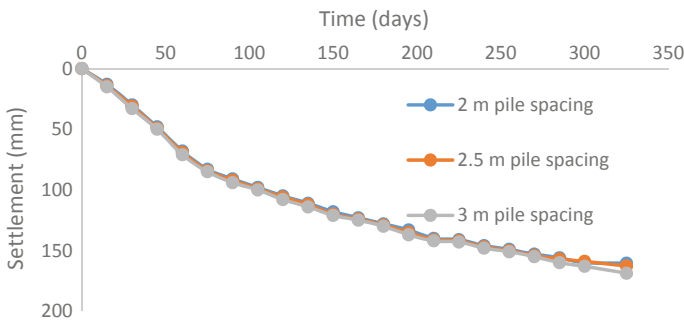


Fig. 6 Variation of settlement of pile cap with time (in the case of 25 m pile length)

of pile cap with time after 325 days, respectively, for the cases of 20 and 25 m pile length along with 1500 kN/m geogrid stiffness.

In these figures, the pile cap settlement is compared for three different pile spacing (2, 2.5, and 3 m). It is found that settlement of pile cap is minimum in the case of 2 m pile spacing and maximum in the case of 3 m pile spacing for both pile lengths, because in the case of 2 m pile spacing more load is transferred to the pile caps compared to 3 m pile spacing. In the case of 3000 kN/m geogrid stiffness, the pile cap settlement increases. This is mainly due to greater load transferred by the geogrid compared to 1500 kN/m geogrid stiffness.

3.3 Lateral Deformation of Embankment Toe and Foundation Soil

Figures 7 and 8 show the variation of lateral deformation of embankment toe and foundation soil with depth after 325 days, respectively, for the cases of 20 and 25 m pile length along with 1500 kN/m geogrid stiffness. In these figures, the lateral deformation is compared for three different pile spacing (2, 2.5, and 3 m).

It is found that lateral deformation of embankment toe is minimum in the case of 2 m pile spacing and maximum in the case of 3 m pile spacing for both pile lengths (20 and 25 m), because in the case of 2 m pile spacing more load is transferred to the pile caps compared to 3 m pile spacing. Table 4 shows the comparison of lateral deformation of embankment toe for three different cases: with no piles and geogrid, with only piles, and with both piles and 1500 kN/m geogrid stiffness. Lateral deformations of embankment toe in the case of 3000 kN/m geogrid stiffness and 20 m pile length for 2, 2.5, and 3 m pile spacing are 27.2, 45.36, and 85.82 mm, respectively. Lateral deformations of embankment toe in the case of 3000 kN/m geogrid stiffness

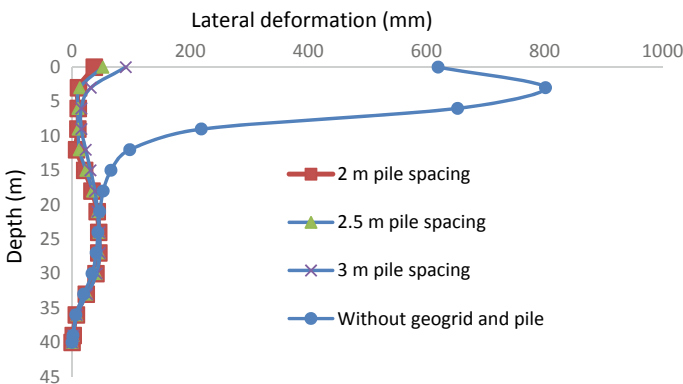


Fig. 7 Lateral deformation of embankment toe and foundation soil with depth (in the case of 20 m pile length)

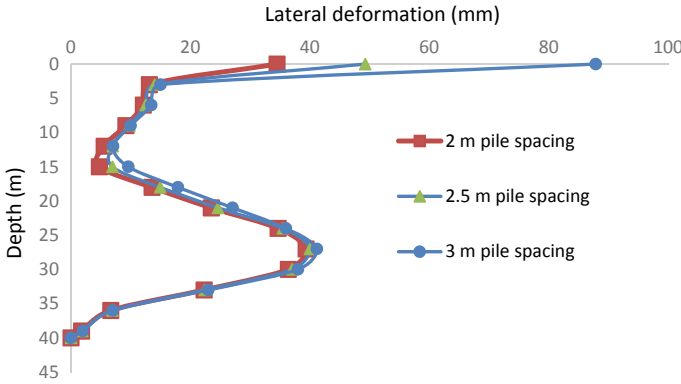


Fig. 8 Lateral deformation of embankment toe and foundation soil with depth (in the case of 25 m pile length)

Table 4 Comparison of lateral deformation of embankment toe

Pile spacing (m)	Pile length (m)	Lateral deformation (mm) of embankment toe after 325 days		
		With no piles or geogrid	With only piles	With both piles and geogrid (1500 kN/m stiffness)
2	20	620	85.6	37.8
	25		82.7	34.5
2.5	20		89.12	52.13
	25		86.25	49.25
3	20		110.5	90.95
	25		107.5	86.84

and 25 m pile length for 2, 2.5, and 3 m pile spacing are 23.5, 41.32, and 82.2 mm, respectively.

3.4 Variation of Vertical Stress

Vertical stress on the pile caps is calculated along the 2nd row of piles, and for foundation soil stress points are selected between two consecutive pile caps. Figures 9, 10 and 11 show the variation of vertical stress among pile caps and foundation soil in case of 2 m, 2.5 m, and 3 m pile spacing, respectively. From these figures, it is clear that vertical stress on pile caps is much greater than that on the foundation soil. This is mainly due to the occurrence of soil arching during the transfer of embankment load. Embankment load transfer proportions to the piles, in the case of 20 m pile length

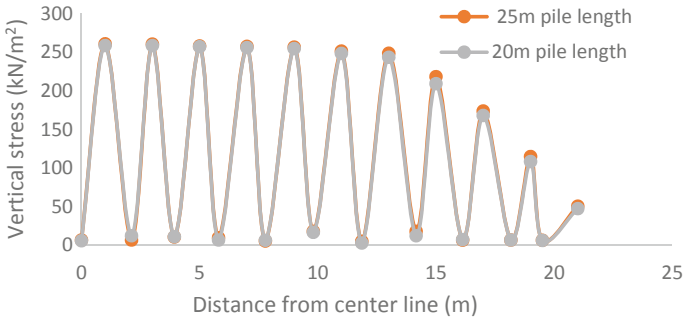


Fig. 9 Variation of vertical stress among pile caps and foundation soil (in the case of 2 m pile spacing)

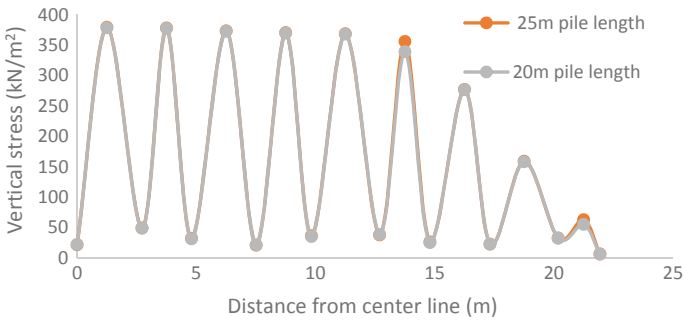


Fig. 10 Variation of vertical stress among pile caps and foundation soil (in the case of 2.5 m pile spacing)

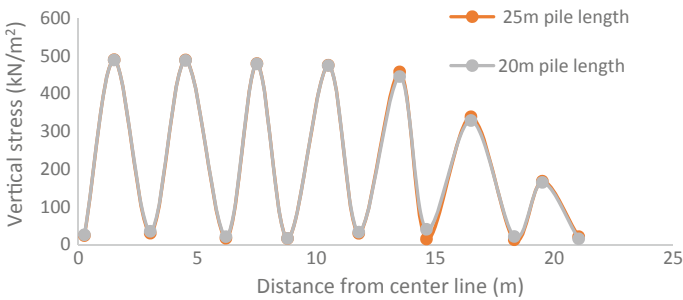


Fig. 11 Variation of vertical stress among pile caps and foundation soil (in the case of 3 m pile spacing)

are 86.73%, 81.14%, and 72.75%, respectively, for 2, 2.5, and 3 m pile spacing. In the case of 25 m pile length, embankment load transfer magnitudes to the piles are 87.43%, 81.39%, and 72.92%, respectively, for 2, 2.5, and 3 m pile spacing.

4 Conclusions

From the above modeling of a highway embankment constructed over clayey soil profile, the following conclusions can be made:

- Inclusion of floating piles reduces the settlement of foundation and embankment surfaces significantly, and are suitable for construction purpose.
- Inclusion of floating piles also reduces the lateral deformation, which can be further decreases by providing geogrid reinforcement.
- Settlements of foundation surface and embankment surface are found to be minimum in the case of 25 m pile length with 3000 kN/m geogrid stiffness and 2 m pile spacing.
- Settlement of pile cap is found to be minimum in the case of 25 m pile length and pile spacing 2 m.
- Embankment load proportions transferred to piles, in the case of 20 m pile length are 86.73%, 81.14%, 72.75%, respectively, for 2, 2.5, and 3 m pile spacing
- Embankment load magnitudes transferred to piles, in the case of 25 m pile length are only marginally greater at 87.43%, 81.39%, and 72.92%, respectively, for the pile spacing of 2, 2.5, and 3 m.

References

- Abusharar SW, Zheng JJ, Chen BG, Yin JH (2009) A simplified method for analysis of a piled embankment reinforced with geosynthetics. *Geotext Geomembr* 27(1):39–52
- Ariyaratne P, Liyanapathirana DS (2015) Review of existing design methods for geosynthetic-reinforced pile-supported embankments. *Soils Found* 55:17–34
- Bhasi A, Rajagopal K (2013) Study of the effect of pile type for supporting basal reinforced embankments constructed on soft clay soil. *Indian Geotech J* 43(4):344–353
- Bhasi A, Rajagopal K (2015) Geosynthetic-reinforced piled embankments: comparison of numerical and analytical methods. *Int J Geomech* 15(5):04014074(12)
- Hewlett WJ, Randolph MF (1988) Analysis of piled embankments. *Ground Eng* 21(3):12–18
- Han J, Gabr MA (2002) Numerical analysis of geosynthetic reinforced and pile supported earth platforms over soft soil. *J Geotech Geoenviron Eng* 128(1):44–53
- Low BK, Tang SK, Choa V (1994) Arching in piled embankments. *J Geotech Eng* 120(11):1917–1938

Dynamic Behavior of Retaining Wall Back Paneled by Waste Tire Shredded Rubber Fiber—An Experimental Study



Upendra Modalavalasa , Shyam A. Hatiwala, Brijesh K. Agarwal, Swapnali Pawar, and Jignesh B. Patel

Abstract An attempt was made in this paper to use waste tire shredded rubber (WTSR) fiber as a damping material back paneled to the Cantilever Retaining (CR) wall. WTSR fibers placed to absorb seismic-induced thrust on CR wall effectively, thus resulting in reduction of lateral displacement. A series of tests on models of cantilever retaining wall were conducted on uniaxial shaking table. A displacement of 10 mm in z-direction and frequencies of 5, 10, 15, and 20 Hz were selected for all the configurations of fiber panel widths. Four configurations were chosen based on fiber panel width, back to the CR wall which, are 0, 50, 75, and 100 mm. The deflections of the wall, with respect to frequency were measured. It is observed that inclusion of WTSR fiber effectively adsorbed the dynamic trust acting on the CR wall.

Keywords Shaking table · Cantilever retaining wall · Waste tire shredded rubber fiber

1 Introduction

Modern society resulted in the use of tires throughout the globe. Beukering and Jansen (2001) have stated that approximately 800 million tires are—discarded annually. Discarded worn out tires can cause environmental problems due to the time they take to complete decomposition and low compressibility to dispose in landfill as well. Effective use of waste materials in the geotechnical engineering applications has attracted recently to reduce disposal problems. The 54% of the Indian land mass is vulnerable to Earthquakes. The effects of seismic activities cause damage to many structures like buildings, retaining walls, etc. Seismic activity introduces a dynamic force on retaining wall. The objective of the study is to use waste tire fibers as a damping material, so as to decrease the deflection of the CR wall. To study the effect of fibers panel width on lateral deflection of the wall. To study the surface

U. Modalavalasa (✉) · S. A. Hatiwala · B. K. Agarwal · S. Pawar · J. B. Patel
Applied Mechanics Department, SVNIT, Surat, Gujarat, India
e-mail: upendarjntuk@gmail.com

© Springer Nature Singapore Pte Ltd. 2020
M. Latha Gali and P. Raghuvver Rao (eds.), *Construction in Geotechnical Engineering*, Lecture Notes in Civil Engineering 84,
https://doi.org/10.1007/978-981-15-6090-3_34

settlement (S_{sb}) and horizontal failure plane length ($H_{\bar{n}}$) of the backfill material after the dynamic phase. To study the effect of frequency on lateral deflection of the CR wall.

2 Literature Review

The use of vertical compressible layers placed against rigid soil retaining wall structures to reduce lateral static earth pressures has been reported in the literature by different researchers (Partos and Kazaniwsky 1987; Horvath 1997; Karpurapu and Bathurst 1992). Recycled tires can be applied as an alternative for backfills of mechanically stabilized earth (MSE) walls and bridge abutments, aggregate in leach beds for septic systems, additive to asphalt, substitute for leachate collection stone in landfills, sound barrier, admixture in bituminous concrete, scrap tire pad as a low-cost seismic base isolation pad, infrastructure for train roads for damping vibration, and insulation to reduce the freezing effect (Humphrey 2003; Salgado et al. 2003; Edinçliler 2007; Balunaini et al. 2009; Mashiri et al. 2016).

The total wall fore reduced on fixed base flexible cantilever retaining wall subjected to dynamic pressure using Lagrange's equation (Veletsos and Younan 1997). Permanent displacement was observed when propped and cantilevered retaining walls subjected to earthquake accelerations due to the mobilization of backfill shear strength (Madabhushi and Zeng 2007). Rigid and non-yielding retaining wall models were tested on 1-g shaking table. The dynamic wall forces by placing urethane deformable panels behind the retaining wall were reduced (Hazarika et al. 2003). The numerical analysis concluded that the inclusion of geofoam against flexible retaining wall reduced earthquake load (Athanasopoulos et al. 2007). The maximum reduction in dynamic force was 32% when non-yielding rigid walls compared with no-geofoam and with geofoam back paneled at a peak base acceleration of 0.7 g by physical shaking table test (Bathurst et al. 2007). A numerical modeling study to simulate the results of the 1-g shaking table tests reported by Bathurst. The dynamic stresses were in the plastic range by a elasto-plastic model based on Mohr–Coulomb failure criteria (Zarnani and Bathurst 2009). The inclusion of EPS geofoam of thickness of 15–20% of all height reduced 20% of seismic pressure (Trandafir and Ertugrul 2011).

3 Shake Table

Shaking tables are now-a-days a valuable tool for the study of seismic behavior assessment of civil engineering structures. The physical tests presented in this paper were conducted on shaking table located in SVNIT, Surat (India). The base of the table has holes at a distance 100 mm \times 100 mm center to center to hold the test

model on it. The model box is shown in Fig. 1. The salient features of the shake table were presented in the Table 1.

The input of frequency, displacement, number of cycles, and number of data to the actuators given by the control system through display screen as shown in Fig. 2.

The input motor frequency is different from frequency of the shake table while performing the experiment. Frequency of shake table was calibrated at different motor frequency through control system. Total 40 number of cycles were taken at a horizontal displacement of 10 mm. Time required for the completion of 40 cycles were noted for all the motor frequencies 5–50 Hz at frequency interval of 5 Hz. Frequency of shake table calculated by dividing the number of cycles with corresponding time. The calibration chart was prepared for shake table as shown in Table 2.

Fig. 1 Retaining wall model placed on shake table

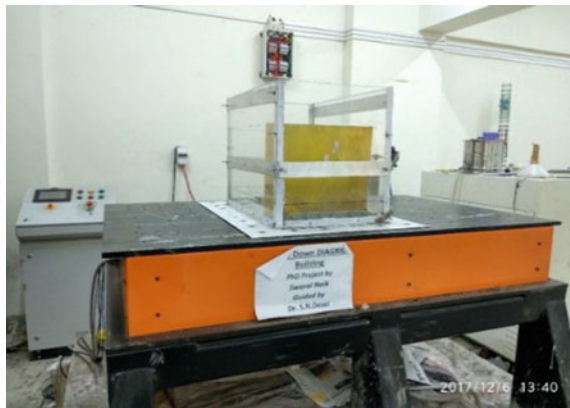


Table 1 Salient features of shake table facilities of SVNIT, Surat

Description	Specifications
Maximum payload	100 kN
Table Dimensions	900 mm × 1500 mm
Exciting direction	Z-direction
Degree of freedom	1 (translational)
Displacement/maximum stroke in Z-direction	+50 mm to –50 mm
Acceleration	1.0 g
Frequency range	1–50 Hz
Horizontal actuators	1
Control system	Digital control system (DCS), 2014

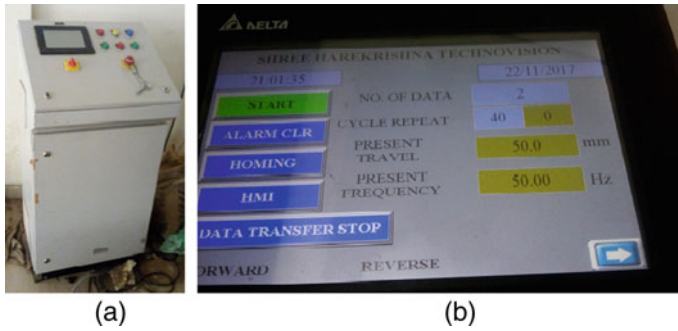


Fig. 2 Control system for shake table. **a** control system, **b** display for giving input to control system

Table 2 Calibration chart of shake table

Sr. No.	Input frequency of motor (Hz)	No. of cycles	Displacements (mm)	Time for 40 cycles (sec)	Frequency of shake table (cycles/time)
1	5	40	10	33.39	1.19796
2	10	40	10	21.56	1.85529
3	15	40	10	17.6	2.27273
4	20	40	10	15.92	2.51256
5	25	40	10	13.86	2.88600
6	30	40	10	12.33	3.24412
7	35	40	10	12.05	3.31950
8	40	40	10	11.21	3.56824
9	45	40	10	11.06	3.61664
10	50	40	10	10.59	3.77715

4 Retaining Wall

A model box of size of 600 mm × 380 mm × 450 mm is prepared using acrylate sheets and the box is supported by metal strips. The box is ensured of any leakages during the shaking process using silicone gel. Cantilever wall of size 380 mm × 300 mm × 1 mm (width × height × thickness) is prepared using a MS plate and it is connected to the base of the model box to have the cantilever action. Metal strips are used to support the bulging action of the acrylate sheets. The model box is fully bolt tightened to ensure no leakage during the shaking process.

Table 2 Physical properties of sand

Sr. No.	Property	Value
1	Specific gravity	2.6
2	Effective size of particles (D_{10} , mm)	0.16
3	Mean size of particles (D_{50} , mm)	0.3
4	Coefficient of curvature (C_u)	2.06
5	Coefficient of uniformity (C_c)	0.76
6	IS ¹ classification	SP ²
7	Minimum Unit Weight (γ_{min} , kN/m ³)	14.36
8	Maximum unit weight (γ_{max} , kN/m ³)	17.80
9	Minimum void ratio (e_{mini})	0.54
10	Maximum void ratio (e_{max})	0.91

¹Indian standard, ²poorly graded sand

5 Materials Used in the Study

5.1 Sand

A relatively uniformly graded sand was used in this study which was collected from Dumas Beach, Surat, Gujarat. The physical properties of the sand are performed in the laboratory and presented in the Table 3.

5.2 Tire Shredded Rubber Fibers

The waste tire rubber fibers (WTRFs) were collected from “National Procured Retreaders,” National Highway-8, Surat, Gujarat, India. Rubber fibers obtained were free from steel strands and threads (i.e., steel, 0% and thread, 0%). The fibers obtained were sieved through IS sieve sizes 4.75, 2.36, 2.0, 0.6, 0.425, 0.3, and 0.075 mm. The size distribution of the fibers as per IS 1498 (1970) is found to be the same as of poorly graded sand in nature. The fibers used in this study are those, having 19 mm length and 4.5 mm width (aspect ratio L/B equals to 4.22). It is noted that the larger size rubber fibers, i.e., 4.75 mm and above will have a boundary effect in the direct shear test. It is difficult to separate the smaller size tire fibers by sieving. The experimental program includes the reuse of sand tire mixture and hence the fibers of length 4.75 mm and above were used in the study (Fig. 3).

The fibers can be separated easily by sieving. The longest dimension of the fiber is recorded as its length. The specific gravity of tire fiber is 1.15. The Particle-size distributions of sand and tire fibers are shown in Fig. 4.



Fig. 3 Tire fibers

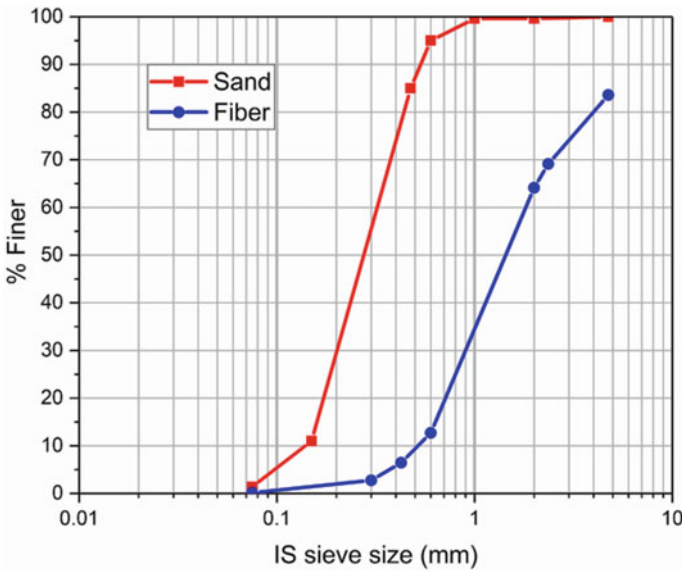


Fig. 4 Particle-size distribution of sand and rubber tire fibers

6 Test Methodology

Shake table was used to study the dynamic behavior of the retaining wall when back paneled with tire shredded rubber at various widths such as 50, 75, 100 mm. A 10 mm displacement is selected and the test was carried on different frequencies like 5, 10, 15, and 20 Hz.

A model box of size of 600 mm × 380 mm × 450 mm, MS sheet of size 380 mm × 300 mm × 1 mm as a retaining wall was prepared. Marine sand at relative density of 73% was used as the backfill. To avoid the intermixing of sand and fiber, a geotextile is placed at the interface.

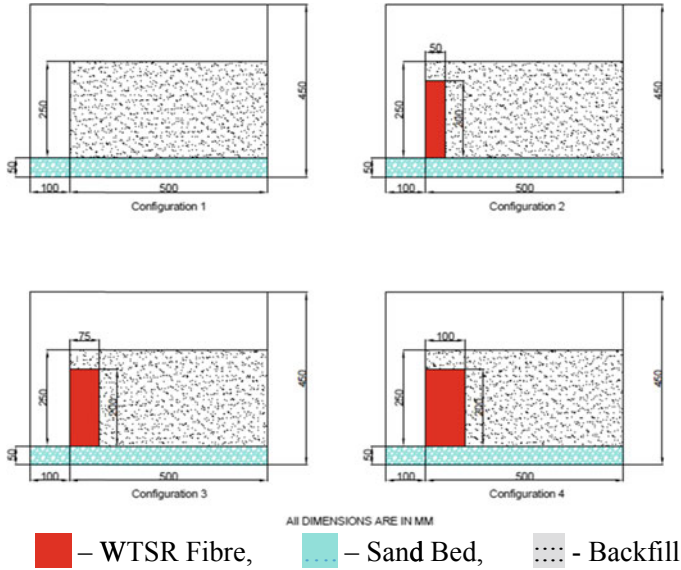


Fig. 5 Different configurations

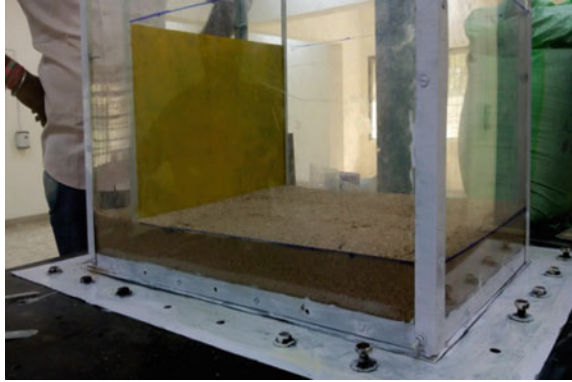
Total four number of configurations were considered to study the deflection of retaining wall back paneled by tire fibers at different width to retaining wall. Configuration 1: The CR wall is back paneled with only sand, Configuration 2: The CR wall is back paneled with a fiber width of 50 mm, Configuration 3: The CR wall is back paneled with a fiber width of 75 mm, Configuration 4: The CR wall is back paneled with a fiber width of 100 mm. Four configurations were presented in the following Fig. 5.

6.1 Experimental Procedure

Procedure includes the following stages after placing the CR wall model on shaking table.

- (1) Preparation of sand bed for foundation
- (2) Placing of fibers back panel to the CR wall
- (3) Preparation of backfill material by weight–volume relationship
- (4) Measurement of initial angle of inclination of the CR wall due to self-weight of the backfill material
- (5) CR wall subjected to dynamic loads through the control system unit to shake table
- (6) Measurement of final angle of inclination of the CR wall due to self-weight and dynamic loads

Fig. 6 Preparation of foundation sand bed



- (7) Measuring Surface settlement and horizontal failure plane length after the dynamic phase
- (8) Removing the backfill material, fibers, and foundation bed, repeated the same procedure for all the four configuration tests.

6.2 Preparation of Sand Bed

The sand bed was prepared with fine to medium coarse grained sand. For each test a uniform sand bed was prepared before placing the backfill material at a relative density of 90%. Specific gravity, coefficient of uniformity, and mean size (D50) of the sand are 2.71, 4.76, and 0.7 mm, respectively.

Natural dry unit weight of sand was 16 kN/m^3 . The 90% relative density is achieved by placing sand in two layers and gently compacted with piece of wood. Amount of sand required to prepare bed is calculated by volume method. Prepared sand bed was shown in Fig. 6. This sand bed acts as a foundation for the backfill material to the CR wall. The relative density (90%) and depth (50 mm) of sand bed were kept constant for all the configuration tests.

6.3 Preparation of Backfill

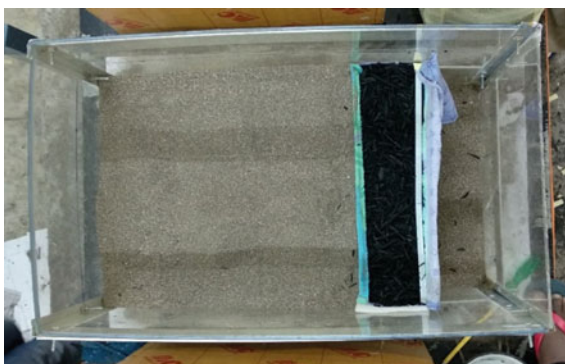
The backfill was prepared at 70% relative density by allowing test sand passing through funnel having a diameter of 20 mm from a height of 10 mm. Volume methodology was adopted to fill the model tank up to 250 mm height from the foundation level. The total height of the tank was marked at different height intervals of 50 mm from the foundation bed. The total weight of sand to be placed in the tank was calculated by volume unit weight relationships. After placing the calculated amount of sand in the tank, sand was gently compacted with wooden box to make height

Fig. 7 Placing of sand

up to interval of 50 mm. This process of placing sand was adopted to maintain uniform density throughout the depth and maintain constant relative density 70%. Sand placing method was shown in Fig. 7.

6.4 *Placing of Fibers*

The fibers were placed back paneled to the retaining wall as shown in Fig. 8. Geotextile rectangular box was prepared to hold the fibers up to required width. Three boxes of 50, 75, and 100 mm width were prepared to obtain different fiber width

Fig. 8 Fibers back paneled to the retaining wall (top view)

back paneled to the wall. In Fig. 8, the box of width 100 mm was shown to understand the placing method of fibers. First the empty box was placed backside to the CR wall and a smooth sponge of 10 mm thickness was placed at the vertical ends of the fiber box as shown in figure to avoid friction between the wall and the retaining wall and to arrest leakage of backfill sand from the sides. Fibers were placed in the empty box and sand was placed simultaneously to the height 250 mm from the foundation sand bed.

7 Results and Discussions

The top view photographs of the retaining wall models subjected to different motor frequencies and different fibers panel width back to the wall were presented. Horizontal length of failure planes of the retaining wall and surface settlement of the backfill material were observed in all four configurations. The deflections of the wall, acceleration in z-direction with respect to frequency were measured. The results are compared with conventional retaining wall backfilled with sand.

7.1 Configuration-1

The results of Configuration-1 were presented in Fig. 9. Horizontal length of failure planes of the retaining wall is 20, 55, 75, and 110 mm for 5, 10, 15, and 20 Hz of motor frequencies, respectively, for 40 cycles. Surface settlements of the backfill material (Ssb) are 23 mm, 38 mm, 55 mm, and 63 mm, respectively. From the test results, wide range of Horizontal length of failure planes (Hfl) and surface settlements were observed, compared to the other configurations. The entire dynamic thrust directly acted on to the retaining wall leads to the maximum inertial forces, causes the largest magnitudes in both the displacements.

7.2 Configuration-2

Reduction in failure plane length at 20 Hz is 50 mm ($110 - 60 = 50$) from the Figs. 9 and 10, which is 45.45% decrement. The Horizontal length of failure planes and surface settlements are 20 mm, 35 mm, 45 mm, 45 mm and 25 mm, 35 mm, 55 mm, 60 mm at motor frequencies of 5, 10, 15, 20 Hz, respectively.

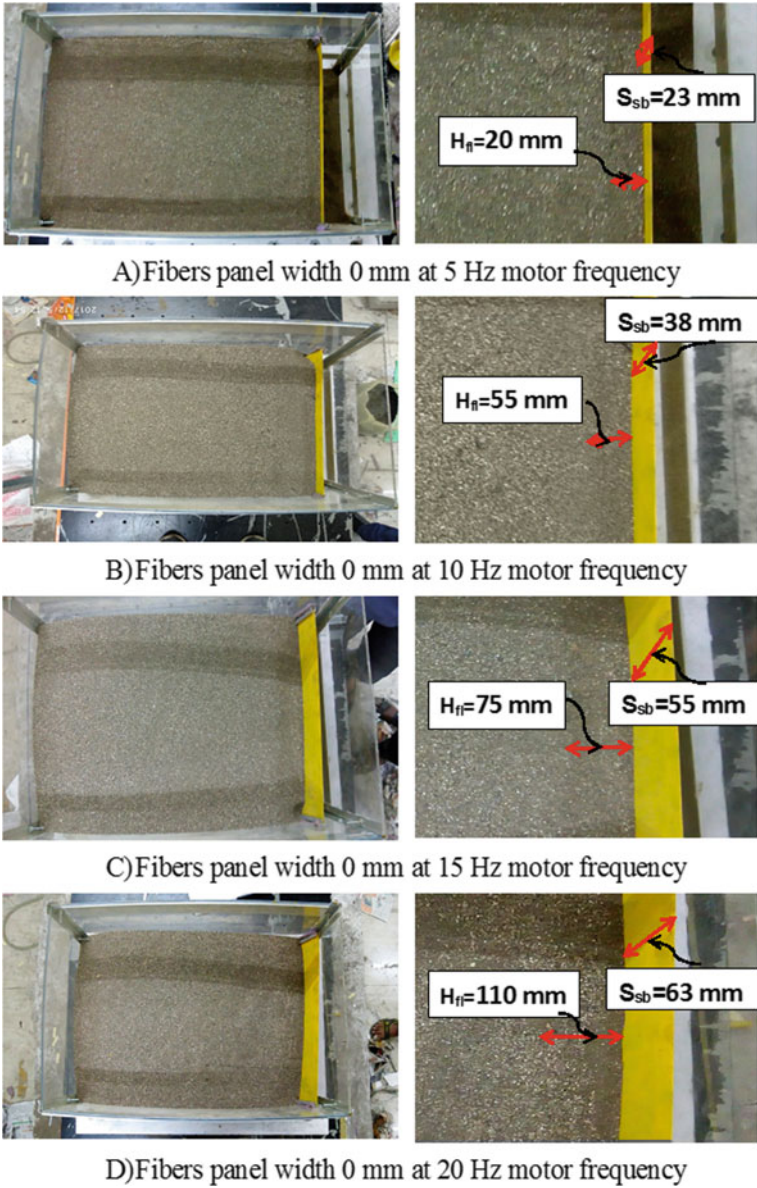


Fig. 9 Retaining wall without fibers panel inclusion after the dynamic phase

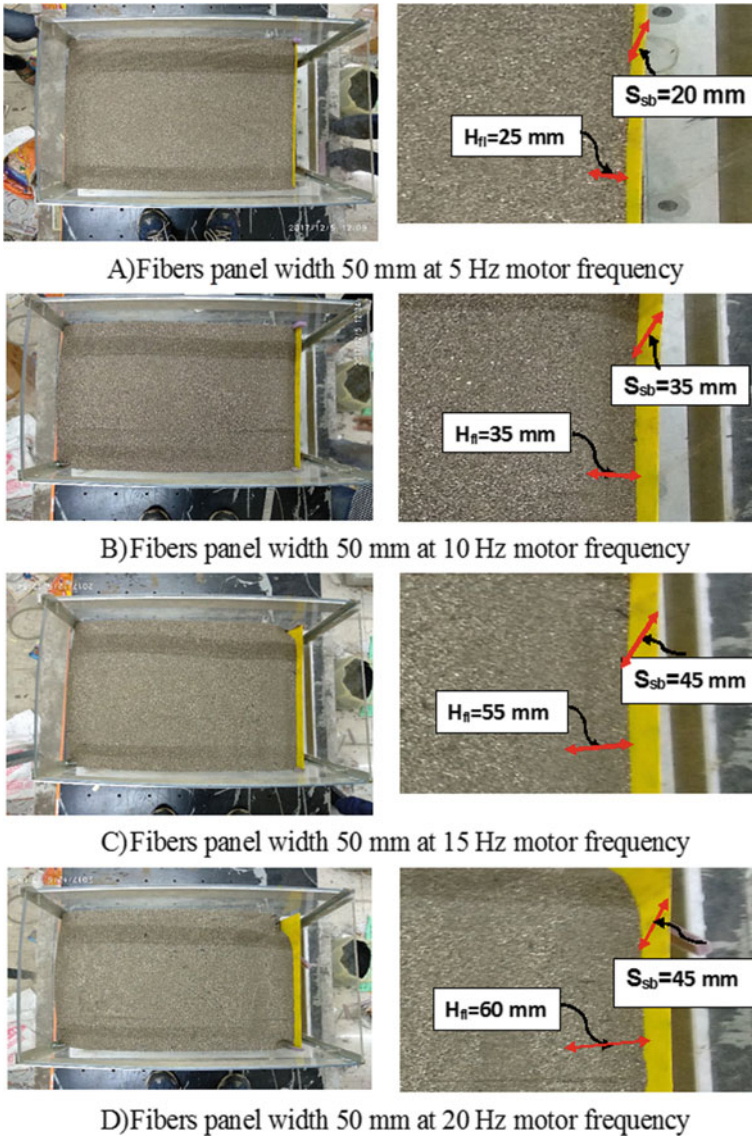


Fig. 10 Retaining wall with 50 mm fibers panel inclusion after the dynamic phase

7.3 Configuration-3

Reduction in surface settlement and failure plane length over 0 mm fiber width at 20 Hz are 38 mm and 60 mm, respectively. The results of Configuration-3 were presented in Fig. 11. The Horizontal length of failure planes and surface settlements

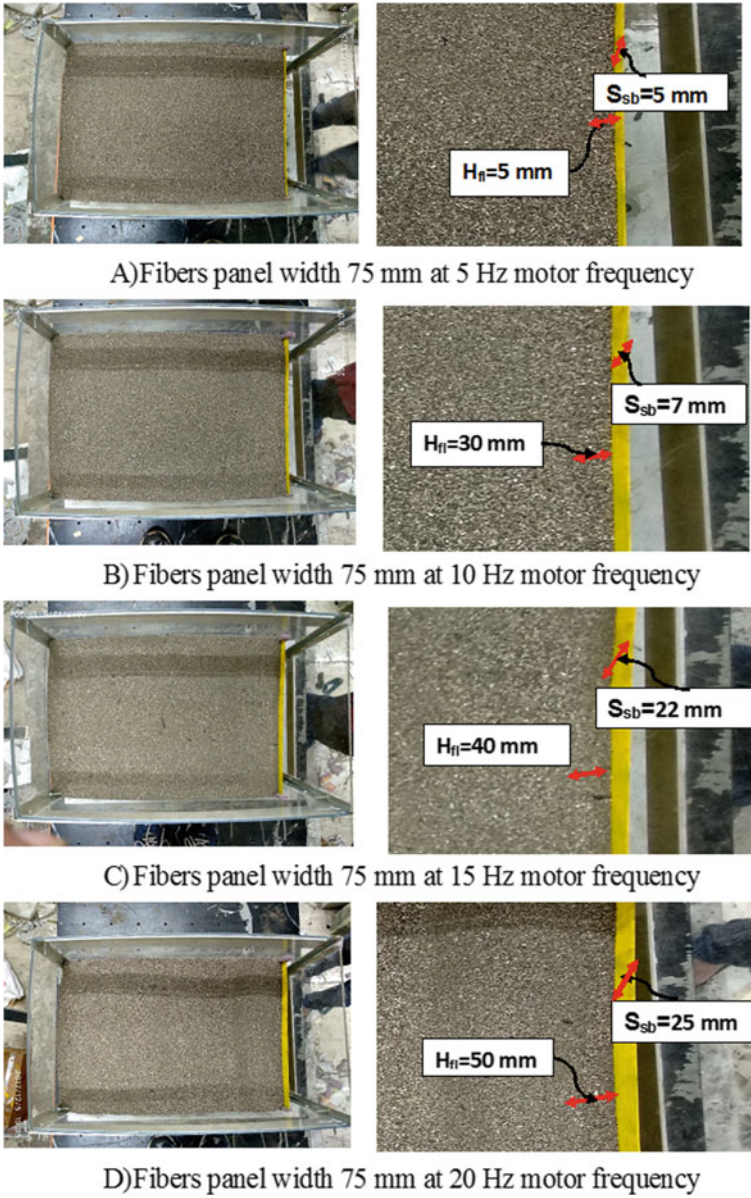


Fig. 11 Retaining wall with 75 mm fibers panel inclusion after the dynamic phase

are 5 mm, 30 mm, 40 mm, 50 mm and 5 mm, 7 mm, 22 mm, 25 mm at motor frequencies of 5, 10, 15, 20 Hz, respectively.

7.4 Configuration-4

The results of Configuration-4 were presented in Fig. 12. The Horizontal length of failure planes and surface settlements are 5 mm, 10 mm, 20 mm, 35 mm and 2 mm, 6 mm, 20 mm, 30 mm at motor frequencies of 5, 10, 15, 20 Hz, respectively.

The deflection of the CR wall was measured by measuring angle of inclination of wall before and after the dynamic phase. Initial inclination of the wall is due to the self-horizontal weight component of the backfill material. Initial inclination of the wall reduced with the inclusion and increase of fibers panel width, due to the self-weight of backfill material component reduced. Initial and final inclinations of the retaining wall were presented in Table 4.

From the Table 4, inclination of the retaining wall decreases with the inclusion of fibers panel to the retaining wall. With the increase in panel width inclination of wall decreases. For better understanding, inclination of the retaining wall after dynamic phase at 0 mm and 100 mm fibers panel widths are 13 and 3 at 20 Hz, respectively, which is about 76.9% reduction in the inclination of the wall. Frequency and deflection of wall are plotted for different fiber width and the plot is shown in Fig. 13.

8 Conclusions

In this study, physical tests on cantilever retaining wall with the inclusion of waste tire fibers back paneled to the wall were discussed. Based on the experimental results the following observations are drawn.

- Surface settlement of the backfill material increases with the increase in motor frequency for all four configurations. With the inclusion of tire fibers panel back to the wall decreases the magnitude of surface settlement due to the low compressibility of tire fibers.
- Horizontal failure length increases with the increase in motor frequency and reduces with the inclusion of tire fibers panel back to the wall.
- Lateral deflection of the retaining wall increases with the increase in motor frequency and reduces with the inclusion of tire fibers panel to the wall. With the increase in fibers panel width, furthermore reduction in lateral deflection of the wall. The results showed that, a decrease of 47%, 54%, 77% deflection of retaining wall back paneled by 50 mm, 75 mm, 100 mm width fiber, respectively, at a maximum frequency of 20 Hz.

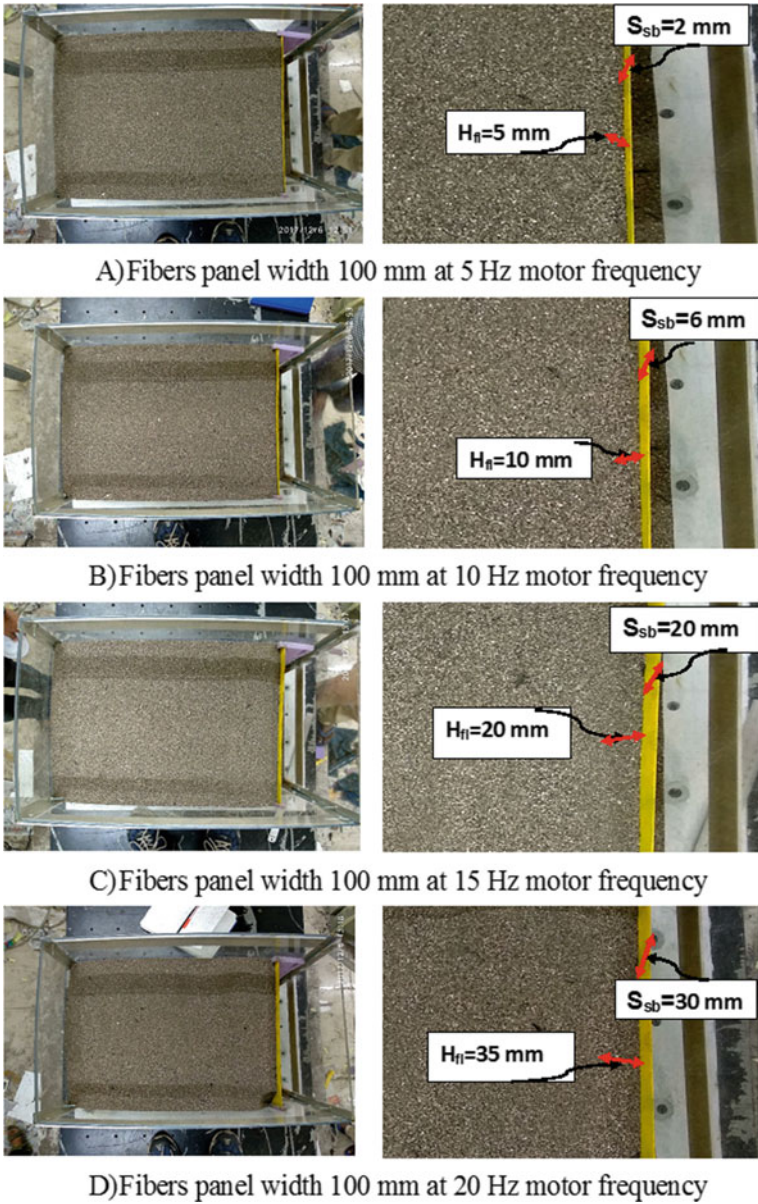


Fig. 12 Retaining wall with 100 mm fibers panel inclusion after the dynamic phase

Table 4 Angles of inclination of retaining wall before and after dynamic phase

Sr. No.	Input frequency of motor (Hz)	No. of cycles	Displacements (mm)	Time for 40 cycles (sec)	Frequency of shake table (cycles/time)
1	5	40	10	33.39	1.19796
2	10	40	10	21.56	1.85529
3	15	40	10	17.6	2.27273
4	20	40	10	15.92	2.51256
5	25	40	10	13.86	2.88600
6	30	40	10	12.33	3.24412
7	35	40	10	12.05	3.31950
8	40	40	10	11.21	3.56824
9	45	40	10	11.06	3.61664
10	50	40	10	10.59	3.77715

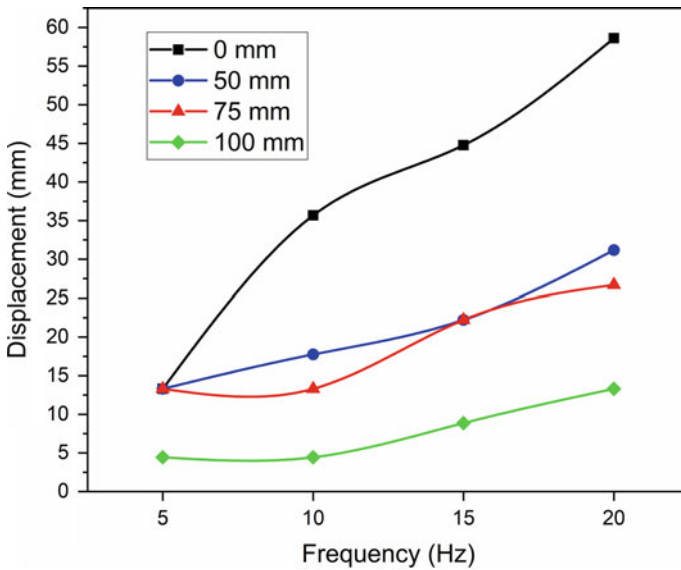


Fig. 13 Frequency vs displacement of CR wall for different fiber panel width

- The lateral deflection of the cantilever retaining wall reduced with the inclusion of tire fibers panel back to the wall due to the absorption of inertial force in fibers during dynamic phase and final thrust on retaining wall was reduced greatly.

These include areas of research covered in this paper which require further investigation, and those are not been addressed. Optimum size of tire fibers for particular

geotechnical applications, absolute method for inclusion of tire fibers, stress distribution of retaining wall along with fibers inclusion in the form of randomly distributed or horizontally stratified layers or vertical back paneled to the wall and mechanical properties of tire fibers with time in the soil. Larger scale testing trails should be conducted using equipment available on site in order to further assess the possibility of adopting the method industrially.

Acknowledgments The technical support from the Sardar Vallabhbhai National Institute of Technology (SVNIT) laboratory, Venkateswarlu Polugari is gratefully acknowledged.

References

- Athanasopoulos GA, Nikolopoulou CP, Xenaki VC (2007) Reducing the seismic earth pressure on retaining walls by EPS geofoam-buffers-numerical parametric study. In: Proceedings of the 2007 geosynthetics conference, vol I
- Athanasopoulos-Zekkos A, Lamote K, Athanasopoulos GA (2012) Use of EPS geofoam compressible inclusions for reducing the earthquake effects on yielding earth retaining structures. *Soil Dyn Earthq Eng* 41:59–71
- Balunaini U, Yoon S, Prezzi M, Salgado R (2009) Tire shred backfill in mechanically stabilized earth wall applications. Final report FHWA/IN/JTRP-2008/17. Purdue University, West Lafayette, USA
- Bathurst RJ, Zarnani S, Gaskin A (2007) Shaking table testing of geofoam seismic buffers. *Soil Dyn Earthq Eng* 27(4):324–332
- Edinçliler A (2007) Using waste tire-soil mixtures for embankment construction. In: Hazarika H, Yasuhara K (eds) *Scrap tire derived geomaterials e opportunities and challenges: proceedings of the international workshop IW-TDGM 2007*. CRC Press, p 319e28
- Hazarika H, Okuzono S, Matsuo Y (2003) Seismic stability enhancement of rigid nonyielding retaining walls. In: Proceedings of the 13th international offshore and polar engineering conference on international society of polar and offshore engineers. Honolulu, Hawaii
- Horvath JS (1997) Compressible inclusion function of EPS geofoam. *Geotext Geomembr* 15(1–3):77–120
- Humphrey D (2003) Civil engineering applications using tire derived aggregate (TDA). California Integrated Waste Management Board, Sacramento, USA
- Karpurapu R, Bathurst RJ (1992) Numerical investigation of controlled yielding of soil-retaining wall structures. *Geotext Geomembr* 11:115–31
- Madabhushi SPG, Zeng X (2007) Simulating seismic response of cantilever retaining walls. *J Geotech Geoenviron Eng* 133(5):539–49
- Mashiri M, Vinod J, Sheikh MN (2016) Constitutive model for sand/tire chip mixture. *Int J Geomech* 16(1):04015022. [https://doi.org/10.1061/\(asce\)gm.1943-5622.0000472](https://doi.org/10.1061/(asce)gm.1943-5622.0000472)
- Partos AM, Kazaniwsky PM (1987) Geoboard reduces lateral earth pressures. In: Proceedings of Geosynthetics'87, industrial fabrics association international. New Orleans, LA, USA, pp 628–39
- Salgado R, Yoon S, Siddiki N (2003) Construction of tire shreds test embankment. Final report FHWA/IN/JTRP-2002/35. Indiana Department of Transportation, Purdue University, West Lafayette, USA
- Trandafir AC, Ertugrul OL (2011) Earthquake response of a gravity retaining wall with geofoam inclusion. In: Proceedings of the geo-frontiers 2011, ASCE GSP.211. ASCE, Dallas

- van Beukering PJH, Janes MA (2001) *J Ind Ecology* 4(2):93
- Veletsos AS, Younan AH (1997) Dynamic response of cantilever retaining walls. *J Geotech Geoenviron Eng* 123:161–72
- Zarnani S, Bathurst RJ (2009) Numerical parametric study of expanded polystyrene geofam seismic buffers. *Can Geotech J* 46:318–38

Suitability of Fly ash in Raising the Embankments



Teja Munaga, Pothula Sai Charan, Mathew Sai Kiran Raju, Lahir Yerra, Bilal Kothakota, and Gonavaram Kalyan Kumar

Abstract The production of fly ash in India has increased tremendously due to coal-based thermal power plants. The fraction of fly ash re-used for any engineering purposes is merely 0.4–0.5. Hence, the storage and disposal of fly ash is a serious concern. The reserves for fly ash storage were built with specific capacity and needs further expansion for storage. Distinct techniques are available for construction of raising namely inward, outward and central raisings. Although being the most familiar and preferred, the inward raising, being resting on the hardened pond ash and subjected to fresh pond-ash filling, has pertinent stability and seepage concerns. The present study aims at determining safety of existing ash dyke by assessing geometric parameters of dyke, properties of ash and material used for further upraising of dyke. Using computer modelling and simulations, the factor of safety and critical slip surface of the ash dyke at various stages of construction are determined and analysed.

Keywords Embankments · Single and double staged ash dykes · Slope stability analysis · SLOPE/W

1 Introduction

1.1 General

Generation of Thermal power from Coal has been the backbone of power generation in India. The large quantity of ash is disposed by thermal power stations as a by-product. A large part of the fly ash is disposed on to the onsite storage ponds known as fly ash dykes (Gandhi 2005). Subsequent storage of fly ash needs expansion of

T. Munaga · P. Sai Charan · M. Sai Kiran Raju · L. Yerra · B. Kothakota · G. Kalyan Kumar (✉)
Department of Civil Engineering, NIT Warangal, Hanamkonda, Telangana, India
e-mail: kalyan@nitw.ac.in

T. Munaga
e-mail: mteja@student.nitw.ac.in

these dykes and it occurs in the vertical direction by constructing new dykes above the existing embankments known as Raisings. The raising rests on the existing weak deposited ash, thus leading to insufficient bearing capacity for the new dykes and thereby prone to seepage and stability concerns. Hence, there is a need to analyse the stability of these dykes. The choice of method is based on stability criteria, which is of utmost necessity.

1.2 Types of Embankment Raising

Centre Line Method

In this method, the raising of existing embankment is attained by raising the downstream and upstream slopes simultaneously to dispose the ash in the dyke. As shown in Fig. 1, material is placed on either side of the dyke such that the location of centre line remains same after the first stage of filling.

Upstream Raising

The construction sequence of upstream raising is shown in Fig. 2. With proper design, the starter dam can serve the purpose of toe filter for the embankment. Limitations of this method are as below:

- Due to the presence of finer particles, care should be taken during the deposition of ash along the bund which may lead to lowering the bearing capacity.

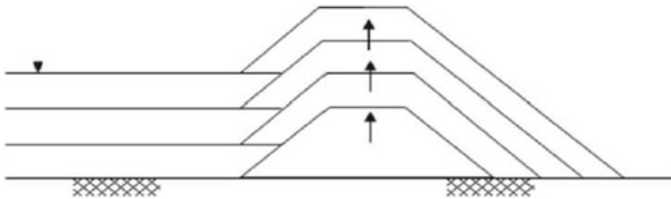


Fig. 1 Centre line method

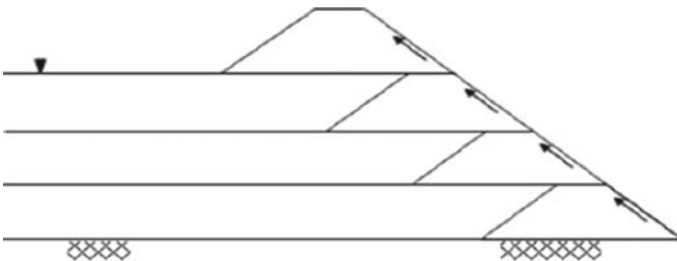


Fig. 2 Upstream raising

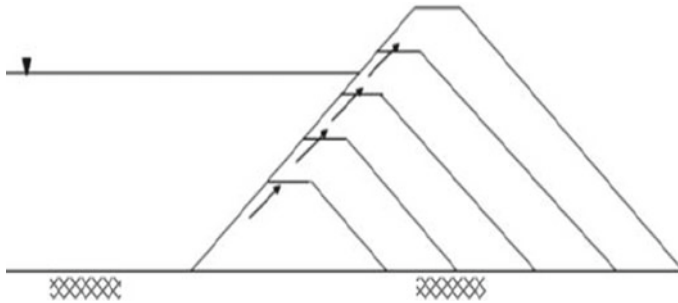


Fig. 3 Downstream raising

- Special care should be taken to analyse the liquefaction potential of the pond ash.
- The drains should be designed properly to maintain the connectivity to dissipate the excess seepage pressure.

Downstream Raising

The method of construction for downstream raising is shown in Fig. 3. It is evident from the figure that the construction is carried out on the downstream side of the embankment. This method is preferably chosen for the execution of new dykes. The embankment is consequently shifted towards the downstream and thereby the starter dam forms the upstream toe of the final dam. The advantages of downstream raising are listed below:

- The embankment is partially constructed on existing ash dyke. Hence, the issue of reduction in bearing capacity beneath the raisings does not occur due to placement of extensions on an existing earth dam.
- The variation of compaction and placement is possible at all stages of construction as per the requirements.
- This method facilitates for increasing the height of the ash dyke even during stage of operation.

1.3 Slope Stability

Slope stability is defined as the resistance of slope to failure by collapsing or sliding. Stability can be computed as the ratio of shear stress and shear strength. A slope failure can be triggered due to climatic events like excessive rainfall leading to mass movements. Instead, shear strength may be decreased by changes in pore water pressure and weathering.

The main objectives of slope stability analysis are to identify possible mechanisms of failure, areas that are susceptible to slope failure, mechanisms that are capable of

triggering the sensitivity of slopes and optimal design of safe, reliable and economic slopes (Deepankar et al. 2013).

The prerequisites for optimal design of a slope are reliable geological and geotechnical properties. It includes geometry and location of the slope, subsurface conditions at the slope, seismic activity, discontinuities, joints, soil properties, etc. The conditions prevailing at the site and mode of failure govern the choice of method of analysis. In addition, risk assessment concept provides a clear idea of consequence of slope failure and the probability of failure.

1.4 Stability Analysis

Several methods are available to analyse the stability of an embankment out of which Ordinary Method of Slices known to be most simple (Ashutosh et al. 2013). It is also known as Swedish circle or Fellenius method.

According to this method, the failure mass is made into slices as shown in Fig. 4. The failure surface is assumed as the arc of a circle. The free body diagram of a typical vertical slice is shown in Fig. 5. The factor of safety (FS) along the failure surface against sliding is computed as shown in Eq. 1 (Ranjan and Rao 2000; Arora 2004).

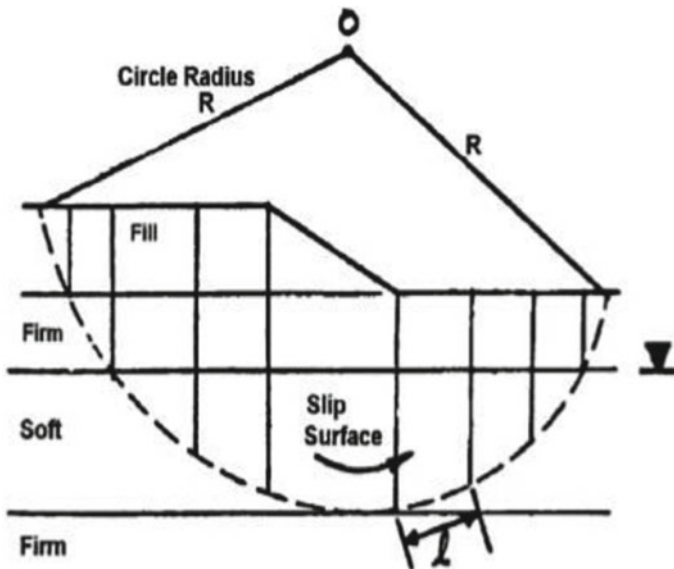


Fig. 4 Schematic view of ordinary method of slices

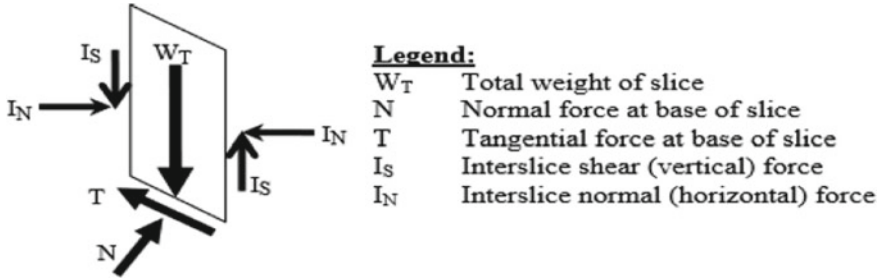


Fig. 5 Typical static forces on a slice of sliding mass without seepage

$$FS = \frac{\text{Sum of Resisting forces} \times \text{Moment Arm (R)}}{\text{Sum of Driving forces} \times \text{Moment Arm (R)}} \tag{1}$$

The resisting and driving forces in the current system are considered with respect to the failure arc, and therefore Moment arm (R) remains same. Thus, Eq. 1 reduces to Eq. 2.

$$FS = \frac{\text{Sum of Resisting forces}}{\text{Sum of Driving forces}} \tag{2}$$

The shear strength of the soil according to Mohr–Coulomb equation is shown in Eq. 3 (Ranjan and Rao 2000).

$$T = C + (\sigma - u)\tan\varphi \tag{3}$$

where,

- T = shear strength
- C = cohesion
- σ = total normal stress on the failure surface
- u = pore water pressure
- φ = angle of internal friction of soil

1.5 Slope/W

SLOPE/W is numerical modelling software mainly used to perform the slope stability analysis. The governing principle of SLOPE/W is method of slices in which the failure mass is analysed along its slip surface. This method satisfies moment and force equilibrium (Anbalagan 2017). In order to delineate the extent of the study slope and to save computing time, the radius and tangent slip surface grid of the computed slip surfaces are specified.

2 Methodology

Soil samples are obtained from selected bore hole locations. Fly ash samples are collected from National Thermal Power Corporation (NTPC), Ramagundam, Telangana. The geotechnical properties of soil and fly ash are determined according to IS: 2720 (Indian Standard 1975a, 1986, 1980, 1975b). The proposed dimensions of single and double staged ash dykes are decided on trial and error basis. Further, the stability of these ash dykes is analysed with proposed dimensions and geotechnical properties as input parameters for SLOPE/W.

2.1 Dimensions of Dyke

The single staged ash dyke is designed as shown in Fig. 6. The top width of the single staged ash dyke is 6 m with an slope of 2H:1 V and 2.5H:1 V on upstream and downstream, respectively. A Rock toe is designed at downstream with a top width of 1 m and side slopes of 2H:1 V on upstream and 2.5H:1 V on downstream. A sand chimney is designed at a depth of 0.5 m from top of the embankment and a sand blanket of 0.5 m thick is provided for drainage purposes.

In order to increase the capacity of the single staged dyke, a 5 m vertical upraising was proposed thereby making it a double staged dyke. The top width, bottom width, upstream and downstream slopes are assumed similar to that of single staged ash dyke. The dimensions of the double staged dyke are shown in Fig. 7.

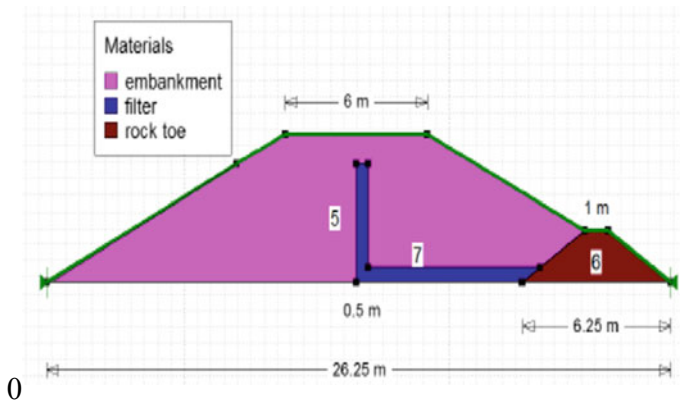


Fig. 6 Dimensions of single staged ash dyke

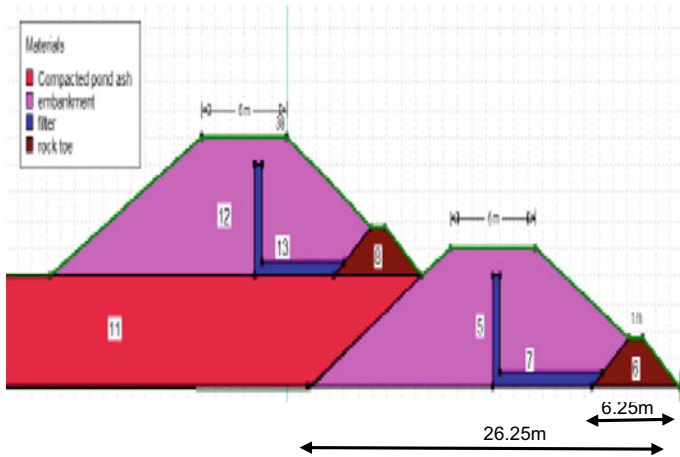


Fig. 7 Dimensions of double staged ash dyke

2.2 Analysis

Multiple analyses are performed to arrive at the preliminary dimensions of ash dykes. After arriving at the dimensions, it is proposed to maintain the dimensions of the single and double staged ash dykes constant at all the bore hole locations. The input parameters (i.e. soil and fly ash properties) are varied at respective bore hole locations and analysis is performed for the stability of single staged and double staged ash dykes.

3 Results

3.1 Material Properties

Soil

The soil samples obtained from 5 different bore hole locations are tested to determine shear strength parameters and bulk density according to IS: 2720 (Indian Standard 1975a, 1986, 1993). The variation of shear strength parameters and bulk density along the depth are presented in Table 1.

Fly Ash

The fly ash sample obtained from NTPC, Ramagundam is tested to determine the geotechnical properties according to IS: 2720 (Indian Standard 1980, 1975b, 1980, 1993). The results are listed in Table 2.

Table 1 Properties of soil

Depth (m)		Soil	Bulk density (kN/m ³)	Cohesion (kPa)	Friction angle (°)
From	To				
<i>Bore hole 1</i>					
0	2	Clay	17.9	30	0
2	3	Sand	16.8	0	29
3	6.5	Silty clay	18.7	30	0
6.5	20		17.4	0	28
<i>Bore hole 2</i>					
0	1.5	Clayey sand	17.9	5	35
1.5	15	Silty sand	20	0	31
<i>Bore hole 3</i>					
0	5	Silty clay	18.9	25	0
5	20	Silty sand	17.9	0	30
<i>Bore hole 4</i>					
0	2.5	Silty clay	15	35	0
2.5	5	Silty sand	20	0	32
5	11	Silty sand	20	0	30
11	20	Fine silty sand	20	0	29
<i>Bore hole 5</i>					
0	2	Silty sand	20	35	28
2	5		20	0	32
5	12.5	Silty sand	20	0	31
12.5	15		20	0	27

Table 2 Geotechnical properties of Fly ash

Property	Value
Specific gravity	2.0
Particle size classification	Poorly graded
Optimum moisture content (%)	11.75
Maximum dry density (g/cc)	1.65
Cohesion (kN/m ²)	0.2
Angle of friction (°)	28

3.2 Analysis of Single Staged Ash Dyke

The Single staged ash dykes are analysed for stability using SLOPE/W. The factor of safety of single staged ash dykes at different bore hole locations are listed in Table 3.

Table 3 Factor of safety for single staged ash dyke

Location	Factor of safety
Bore hole 1	1.783
Bore hole 2	2.082
Bore hole 3	1.520
Bore hole 4	1.851
Bore hole 5	2.372

Table 4 Factor of safety for double staged ash dyke

Location	Factor of safety
Bore hole 1	1.437
Bore hole 2	1.653
Bore hole 3	1.315
Bore hole 4	1.420
Bore hole 5	1.311

3.3 Analysis of Double Staged Ash Dyke

The Double staged ash dykes are analysed for stability using SLOPE/W. The factor of safety of double staged ash dykes at different bore hole locations are listed in Table 4.

4 Conclusions

Slope stability analysis of single and double staged ash dykes performed using SLOPE/W yielded satisfactory values of factor of safety.

Factors of safety for single staged dyke vary between 1.5 and 2.1. The results indicate that no susceptible damage is expected with the proposed dimensions of the ash dykes at all the bore hole locations.

Factors of safety for double staged dyke vary between 1.3 and 1.7. However, the factor of safety for double staged dyke is quite less at bore hole locations 3 and 5. Hence, it is suggested to either reduce the height of the second stage or increase the base width of first stage dyke.

References

- Arora KR (2004) Soil mechanics and foundation engineering. Standard Publishers Distributors, Delhi
- Ashutosh K, Dhananjai V, Rahul T, Singh TN (2013) A review on numerical slope stability analysis. *Int J Sci Eng Technol Res* 2(6)
- Deepankar CH, Jaykumar S, Amey K, Vilas P, Padma T (2013) Slope stability and settlement analysis for dry bulk terminal at mozambique: a case study. *EJGE* vol 18, Bund E
- Durga DNL, Anbalagan, R (2017) Study on slope stability of earthen dams by using geostudio software. *Int J Adv Res Ideas Innov Tech* 3(6)
- Gandhi SR (2005) Design and maintenance of ash pond for fly ash disposal. In: Indian Geotechnical Conference, Ahmedabad
- Indian Standard: 2720-Part 29 (1975a) Determination of dry density of soils in-place by the core-cutter method. Bureau of Indian Standards, New Delhi
- Indian Standard: 2720-Part 13 (1986) Direct shear test. Bureau of Indian Standards, New Delhi
- Indian Standard 2720-Part 3 Sect. 1 (1980) Determination of specific gravity-Fine-grained soils. Bureau of Indian Standards, New Delhi
- Indian Standard: 2720-Part 4 (1975b) Grain size analysis. Bureau of Indian Standards, New Delhi
- Indian Standard: 2720-Part 7 (1980) Determination of water content-dry density relation using light compaction. Bureau of Indian Standards, New Delhi
- Indian Standard: 2720-Part 11 (1993) Determination of the shear strength parameters of a specimen tested in unconsolidated undrained triaxial compression without the measurement of pore water pressure, Bureau of Indian Standards, New Delhi
- Ranjan Gopal, Rao ASR (2000) Basic and applied soil mechanics, 2nd edn. New Age Publishers, Delhi

Displacement-Based Analysis of Retaining Wall with Constrained Backfill



Godas Srikar, Satyendra Mittal, Sumit Bisht, and Ankarapu Sindhuja

Abstract In some practical circumstances retaining structure has to stabilise the limited width of backfill which ends with a hillock or a rigid wall. A displacement-based analysis is proposed to analyse a retaining wall with narrow backfill. A retaining wall with backfill that could not mobilise full Rankine's failure plane due to spatial constraint such geotechnical structure is considered to be a retaining wall with 'Narrow' backfill. A finite element modelling followed by plastic analysis is carried out to study such a practical application. Active earth pressure distribution on the wall is presented by prescribing displacement to the wall. It is observed that earth pressure reduces with an increase in the inclination of the rock face with respect to horizontal due to the constraint effect. The critical failure surface for narrow backfill wall is compared with that of an unconfined backfill wall. Results imply that conventional methods of estimation of earth pressure over-estimates in such circumstances.

Keywords Narrow backfill · Active earth pressure · Retaining wall · Critical failure plane

1 Introduction

Population increase in the coming decades always results in high traffic demands. Extra-widening of existing roads is a frequently adapted solution for such a problem. If there is a spatial limitation, to be on the economic side, the construction of retaining structures in constrained space is advisable than the construction of right-of-way. If a retaining wall is constructed in front of an intact rock or a stable wall, then the backfill width provided will be much less than a conventional retaining wall. In these circumstances, applying conventional earth pressure theories results in over-

G. Srikar (✉) · S. Mittal · S. Bisht
Indian Institute of Technology Roorkee, Uttarakhand 247667, India
e-mail: gsrikar@ce.iitr.ac.in; srikar3433@gmail.com

A. Sindhuja
Government polytechnic Korutla, Telangana 505326, India

© Springer Nature Singapore Pte Ltd. 2020
M. Latha Gali and P. Raghuvver Rao (eds.), *Construction in Geotechnical Engineering*, Lecture Notes in Civil Engineering 84,
https://doi.org/10.1007/978-981-15-6090-3_36

estimation of earth pressure further affecting the economy of the project. Spangler and Handy (1984) suggested Janssen's arching theory (see Janssen (1895)) to estimate lateral earth pressure for constrained backfill. Spangler and Handy (1984) did not discuss the choice of the value of the pressure coefficient to be used in the calculation. Frydman and Keissar (1987) conducted a centrifugal model test for the problem of constrained backfill in at-rest and active conditions. Frydman and Keissar (1987) did not discuss the scattering of earth pressure on the wall as they have used only two pressure cells in the experimental setup. Take and Valsangkar (2001) performed a series of centrifuge tests using the number of pressure cells in both vertical and lateral directions. To overcome the drawback of the previous study, the authors had come up with a variation of earth pressure with depth. The study also describes the effect of stiffness of pressure cells on measured lateral stress. Leshchinsky et al. (2004) analysed a reinforced earth wall with narrow backfill with an assumption that all the reinforcement layers are replaced by an equivalent reinforcement layer at a height of one-third of the height of the retaining wall to enable the development of non-dimensional design charts. This assumption also enables in extending the analysis for estimation of lateral earth pressure coefficient for a gravity retaining wall. Design charts are developed to estimate the coefficient of earth pressure for narrow backfill which requires bottom width, angle of rock slope as input parameters. The authors have performed both limit equilibrium analysis and finite difference analysis. Yang and Liu (2007) for the first time modelled a problem to perform finite element analysis. The authors have shown the variation of coefficient of earth pressure for at-rest case and active case with depth at the face of the wall and at mid-width of backfill for different aspect ratios. The results obtained from the study are compared with Janssen's arching theory (Janssen 1895) and Leshchinsky et al. (2004). The important contribution of the work is the authors have developed design charts for reduction factors to estimate at-rest and active pressures for narrow backfill retaining walls. The reduction factor can be used in combination with FHWA design charts. Fan and Fang (2010) performed numerical analysis using finite element modelling for varying width of the backfill. Nadukuru and Michalowski (2012) modelled problem in discrete element modelling. The paper presents local equilibrium (horizontal slice) whereas in Coulomb's analysis global equilibrium was carried out. Thereby load distribution over the height of the wall is presented which is not possible in the case of Coulomb's analysis as it is force equilibrium.

Greco (2013) performed limit equilibrium analysis for the problem. Based on the width of the backfill, the problem is divided into three mechanisms. Mechanism-1 is just similar to Coulomb's analysis with a single wedge. If backfill width is narrow enough to generate two failure wedges then it is categorized as Mechanism-2. Here the author assumed that first wedge slides over the other. If three wedges are formed then it is categorized as Mechanism-3. With knowledge of Coulomb's theory, Mechanism 1 can be solved. For Mechanism-2, thrust wedges are described by a cubic equation and Mechanism 3 thrust wedges are described by a cubic equation and the other quartic. Greco (2014) extended the above mechanisms including seismic pseudo-static force in the force equilibrium. Yang and Tang (2017) had conducted an experimental study for the problem for different modes of failure, viz., rotation

about top, translation and rotation about bottom. It is observed that the test yields different coefficients of earth pressure values for different modes of failure and in contradictory to limit equilibrium analysis conducted by Greco (2013) failure plane was observed to be nonlinear. In the present study, the same has been explored in a finite element framework for translation mode of wall movement.

2 Analysis

Figure 1 shows orientation of rock, backfill in the finite element model to investigate the effect of backfill space on active earth pressure. ‘b’ is the width of the backfill at the base of the wall, β is the angle made by rock surface with the horizontal and ‘H’ is the height of the retaining wall. In order to induce active condition, the wall is allowed to move away from the backfill in the lateral direction. In the course of movement of the wall, it is not allowed to bend by providing adequate flexural stiffness to the wall. To replicate the practical scenario, the fill material is placed in a staged manner. During the fill, the wall is not allowed to move. The movement of the wall is initiated only after construction is completed, displacements due to application of construction loads are cleared, i.e., reset to zero.

A displacement-based finite element modelling is carried out to understand the behaviour of a retaining wall with constrained backfill. The problem is modelled as shown in Fig. 2. Considering an assumption that the length of the retaining wall is infinite, wall-backfill-rock system is modelled as plane strain problem. Elements in finite meshing are considered to be six-noded. The model constitutes of wall, cohesion-less backfill, an intact rock mass behind the backfill. Wall is modelled as a ‘plate’ element behaving as an elastic material with flexural rigidity of $4.2 \times 10^5 \text{ kN.m}^2/\text{m}$ and a normal stiffness of $1.26 \times 10^7 \text{ kN/m}$ which gives rise to an equivalent width of 0.632m. Sand is modelled as Mohr–Coulomb material. Unit weight of the sand is considered to be 15.5 kN/m^3 . Elastic modulus and Poisson’s ratio is considered as 60MPa and

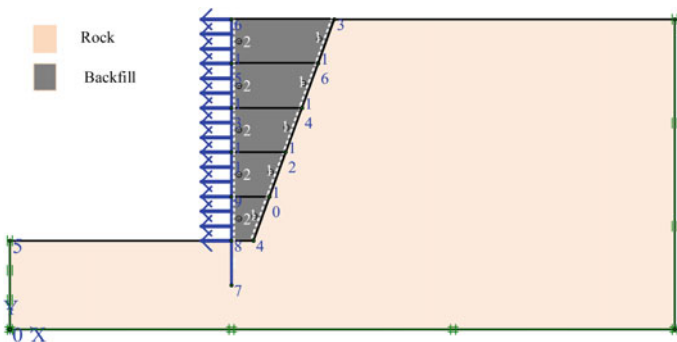


Fig. 1 Typical model showing the orientation of different components of the model

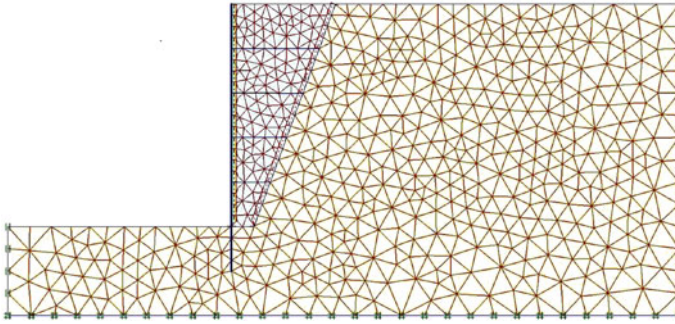


Fig. 2 Six-noded finite element mesh generated for the analysis

0.3, respectively. As backfill is considered as sand, a small negligible amount of cohesion is considered to avoid numerical instability in the analysis, friction angle is taken as 31° . A very small dilation angle of 1° is incorporated in the analysis. Rock modelled behind the backfill is assumed to behave as linearly elastic with elastic modulus of 2100MPa and Poisson's ratio of 0.15. The unit weight of the rock is taken as 24kN/m^3 . Interface between soil and wall; soil and rock play an important role in the present study. A separate interface is created with properties similar to sand and interface reduction factor of 0.9, 1 for wall and rock interfaces, respectively. Vertical boundaries of the model are restrained in the horizontal direction, whereas the bottom horizontal boundary is restrained in both horizontal and vertical directions. Seepage stresses are neglected in the analysis. The total height of the backfill is constructed in five stages by filling to a depth of 1m in each stage. Throughout the construction-stages, the wall is provided with required stiffness to resist lateral thrust from the backfill. After the construction stages, all the displacements due to construction are set to zero and soil-wall interface; soil-rock interfaces are activated. Active condition is created in the system by allowing the wall to move in the lateral direction. Plastic analysis with staged construction loading type is assigned to extract the results in terms of lateral earth pressure distribution just behind the wall.

3 Results and Discussion

Figure 3 shows the distribution of earth pressure on the height of the wall for different rock inclinations. The distribution of active earth pressure at a section just behind the wall is extracted. The plot also compares the results obtained from present finite element modelling and results obtained from Coulomb's earth pressure theory. Results obtained from the finite element analysis are observed to be always less than conventional earth pressure theory. Though the difference at the shallow depth is observed to be lesser but at the bottom of the wall this difference is observed to be considerable. Total active thrust obtained from Coulomb's active wedge theory is 55.218

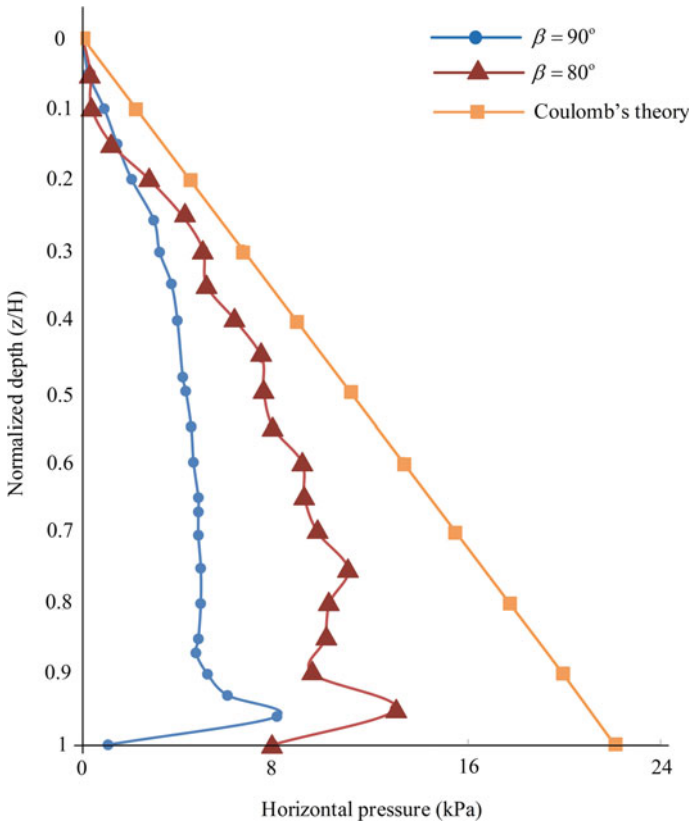


Fig. 3 Comparison of active pressure on wall for $\beta = 80^\circ, 90^\circ$ with Coulomb's theory

kN/m whereas the same active thrust which is so-called normal equivalent force acting on wall in FE analysis is 33.36kN/m, 17.79kN/m for $\beta = 80^\circ$ and $\beta = 90^\circ$, respectively. The point of application of active thrust for the case of constrained backfill is observed to be higher compared to that of Coulomb's theory. The point of active thrust on the wall is observed to be 1.88m, 2.05m from bottom of the wall for $\beta = 80^\circ$ and $\beta = 90^\circ$, respectively. From Fig. 3 it is also observed that for $\beta = 90^\circ$ earth pressure remains constant below a certain depth.

To know the critical rock slope that effects active earth pressure, a parametric study is conducted by changing β values which is shown in Fig. 4. It is observed that for the present width of the wall ($b = 0.5m$) the effect of constraint is evident for the rock inclination greater than 70° . The obtained results are also compared with the finite element model without rock. For $\beta = 70^\circ, 60^\circ$ the earth pressure distribution is almost the same as that of no rock condition. From this, it can be inferred that for the adopted geometry the effect of confinement on earth pressure acting on the wall is between $\beta = 70^\circ$ and $\beta = 80^\circ$.

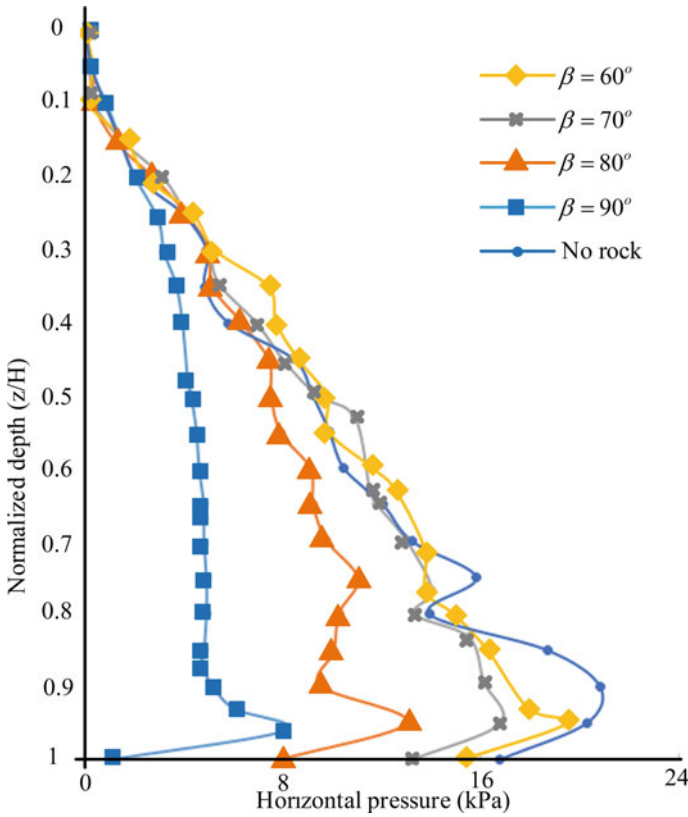


Fig. 4 Active earth pressure distribution for varying rock inclinations

Figure 5 shows the plot with the ratio of the coefficient of earth pressure obtained from FE analysis and Coulomb’s theory on the Y-axis and rock inclination on the X-axis. It can be observed that as rock inclination increases the ratio decreases. For rock inclination of 60° , the ratio is around 0.9, which implies that the active earth pressure obtained from present analysis is almost equal to Coulomb’s earth pressure. For the rock inclination of 90° , the ratio is reduced to a value of 0.363 which implies that the active pressure acting on the wall is reduced considerably.

In general, as friction angle increases total active thrust acting on a conventional retaining wall decreases, this can be attributed to an increase in shear strength resulting in resistance towards the formation of failure wedge. The same phenomenon is also observed in the case of retaining walls with narrow backfill. Figure 6 shows the variation of active thrust acting on the wall with a friction angle of backfill material for rock slopes $\beta = 80^\circ$ and $\beta = 70^\circ$. From the plot, it is also evident that for any value of friction angle, active thrust corresponding to 80° rock slope is always lesser than that compared to 70° rock slope.

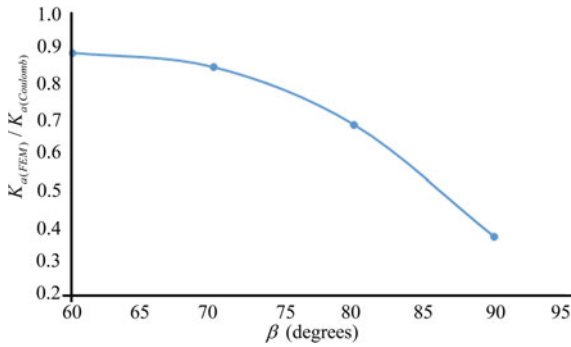


Fig. 5 Influence of rock slope on the coefficient of active pressure obtained from FE analysis

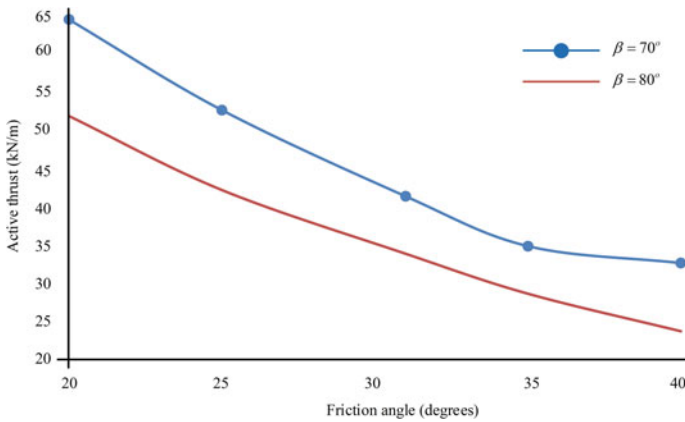


Fig. 6 Influence of friction angle on active thrust for different rock inclinations

Figure 7 shows the formation of critical failure surface for different rock inclinations and for conventional retaining wall. In the latter case, the formation of critical failure plane starts from the bottom of the wall and clearly extends to the surface of the backfill as shown in Fig. 7d. This failure resembles the same as that obtained from proposed conventional earth pressure theories. Figure 7a–c shows the formation of a failure plane for different rock inclinations. From Fig. 7, it is evident that the critical failure plane disappears as the inclination of the rock changes from 60° to 80°. This is because the presence of rock at particular orientations interrupts the formation of a critical plane. This interruption is observed to be minimum for the rock with slope angle $\beta = 60^\circ$ resulting in the formation of a failure plane just interacting the rock surface which is not that evident in the case of $\beta = 70^\circ$ and $\beta = 80^\circ$.

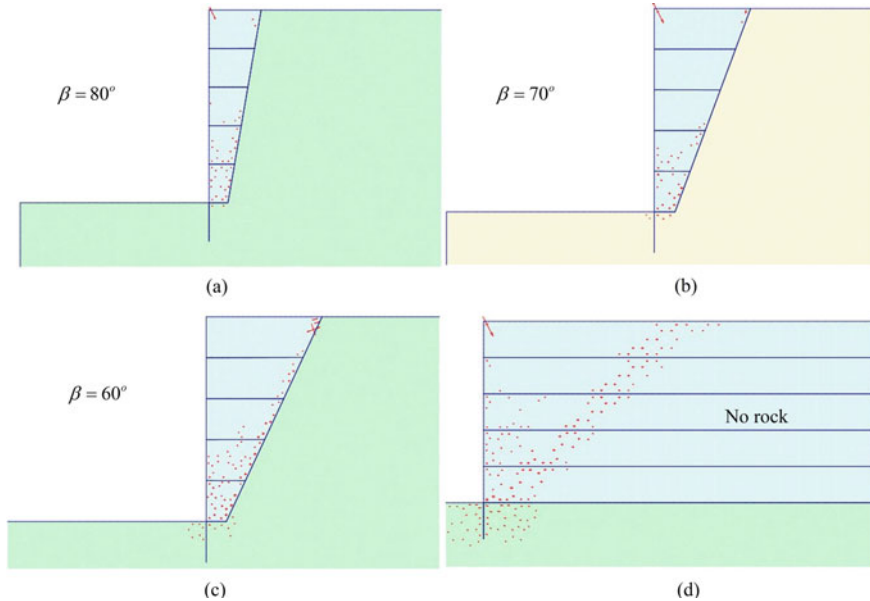


Fig. 7 Formation of critical failure surface for corresponding inclinations of rock surfaces

4 Conclusions

Displacement-based approach is used to estimate active earth pressure distribution acting on the retaining wall with narrow backfill. From the study, it can be concluded that the total active thrust estimated is far less than that computed from conventional earth pressure theories which in turn depends on angle made by rock face behind the backfill. The rationale behind the reduction in the magnitude of earth pressure distribution is the confinement of backfill against the formation of failure wedge. It can also be concluded that as the inclination of rock surface increases, active thrust acting on the wall reduces which results in a rise of point of application of active thrust. Finally, it is suggested that for an economical design of retaining wall with narrow backfill, the present study can be used.

References

- Fan CC, Fang YS (2010) Numerical solution of active earth pressures on rigid retaining walls built near rock faces. *Comput Geotec* 37(7–8), 1023–1029 (2010). <https://doi.org/10.1016/j.compgeo.2010.08.004>
- Frydman S, Keissar I (1987) Earth pressure on retaining walls near rock faces. *J Geotech Eng* 113(6), 586–599. [https://doi.org/10.1061/\(ASCE\)0733-9410\(1987\)113:6\(586\)](https://doi.org/10.1061/(ASCE)0733-9410(1987)113:6(586))

- Greco VR (2013) Active thrust on retaining walls of narrow backfill width. *Comput Geotech* 50, 66–78 (2013). <https://doi.org/10.1016/j.compgeo.2012.12.007>
- Greco VR (2014) Analytical solution of seismic pseudo-static active thrust acting on fascia retaining walls. *Soil Dyn Earthq Eng* 57, 25–36 (2014). <https://doi.org/10.1016/j.soildyn.2013.09.022>
- Janssen HA (1895) Versuche uber getreidedruck in silozellen. *Z Ver Dtsch Ing* 39(35):1045–1049
- Leshchinsky D, Hu Y, Han J (2004) Limited reinforced space in segmental retaining walls. *Geotext Geomembr* 22(6), 543–553. <https://doi.org/10.1016/j.geotextmem.2004.04.002>
- Nadukuru SS, Michalowski RL (2012) Arching in distribution of active load on retaining walls. *J Geotech Geoenviron Eng* 138(5), 575–584. [https://doi.org/10.1061/\(ASCE\)GT.1943-5606.0000617](https://doi.org/10.1061/(ASCE)GT.1943-5606.0000617)
- Spangler MG, Handy RL (1984) *Soil engineering*, pp 482–484 . Harper & Row Publishers, New York
- Take WA, Valsangkar AJ (2001) Earth pressures on unyielding retaining walls of narrow backfill width. *Can Geotech J* 38(6), 1220-1230. <https://doi.org/10.1139/t01-063>
- Yang KH, Liu CN (2007) Finite element analysis of earth pressures for narrow retaining walls. *J Geoenviron Eng* 2(2):43–52
- Yang M, Tang X (2017) Rigid retaining walls with narrow cohesionless backfills under various wall movement modes. *Int J Geomech* 17(11), 04017098. [https://doi.org/10.1061/\(ASCE\)GM.1943-5622.0001007](https://doi.org/10.1061/(ASCE)GM.1943-5622.0001007)

Behaviour of Strip Footing Resting on Pretensioned Geogrid-Reinforced Ferrochrome Slag Subgrade



Atul Kumar, Anil Kumar Choudhary, and Sanjay Kumar Shukla

Abstract Ferrochrome slag is one of the major industrial wastes produced in huge quantities during the manufacturing of high-carbon ferrochromium alloy and it resembles the coarse dark-colored sand. The use of ferrochrome slag as a substitute for natural soil for major geotechnical projects shall not only mitigate the problems of its disposal but also reduce the problem of environmental degradation. Keeping this in view, a series of model footing tests were conducted with unreinforced ferrochrome slag subgrade, as well as subgrade reinforced with a single layer of geogrid without pretension and pretensioned geogrid. Embedment depth for the geogrid was varied corresponding to the width of the footing for both the cases. For pretensioned geogrid, pretensions in the geogrid were varied as 1, 2, and 3% of tensile strength of geogrid. It is concluded that pretensioning of the geogrid is quite beneficial in enhancing the reinforcement efficiency.

Keywords Geogrid · Strip footing · Ferrochrome slag · $U/B = 0.4$

1 Introduction

With rapid industrialization, increasing quantities of pollutants are being spewed into the atmosphere and water sources in solid, liquid and gaseous forms. The pollutants pose a major health hazard in most urban and semi-urban areas. There is a vital need to find a solution to this problem. The profitability of industrial organization now depends upon the effective management and uses of its by-products. Due to the

A. Kumar · A. K. Choudhary (✉)
Department of Civil Engineering, National Institute of Technology, Jamshedpur, India
e-mail: akchoudhary.ce@nitjsr.ac.in

A. Kumar
e-mail: atulnitjsr008@gmail.com

S. K. Shukla
Discipline of Civil and Environmental Engineering, Edith Cowan University, Joondalup, Perth, Australia

lack of natural resources industries are trying to utilize their waste as a construction material. Some examples of industrial waste which are used as construction material are fly ash, bottom ash, blast furnace slag, red mud, etc. From the manufacturing of high-carbon ferrochromium alloy, a waste material named as ferrochrome slag is obtained and the main constitution of ferrochrome slag is SiO_2 (28%), Al_2O_3 (25%), and MgO (23%).

Generally, we know that engineers face difficulties in constructing roads and railways over low bearing capacity soils, and controlling the erosion of soil caused by water, and safeguarding the growth of vegetation. The UK-based company Nelton Limited, made the synthetic grid and were used for the first time for reinforcement of soft soil in Japan in 1967. Since then this has inspired the development of geogrids. Because of polymeric origin, they are non-biodegradable, anti-toxic inert products and are UV protected for long-term applications. They are used today with confidence in many structures around the world including India and provide a cost-effective, long-term solution to many civil engineering problems. It is well established that the reinforced earth technique is quite beneficial for improving the strength and deformation characteristics of soil especially the granular soils. It has been previously observed that for low levels of settlement, strains in the soil are insufficient to mobilize tensile load in the reinforcement. This may not be a desirable feature for shallow footings where deformation allowed is very limited. To overcome this problem, reinforcement can be pretensioned

2 Literature Review

Guido et al. (1985) performed a sequence of experimental laboratory model footing tests on the geosynthetic-reinforced sand bed. The model tests were performed in a tank having dimensions of 1.5 m long, 0.91 m wide and 0.91 m deep steel. The model footings used in the tests were having thickness of 25.4 mm made of steel plates with dimensions of 152 mm \times 152 mm ($B \times L$) for square footings and for rectangular footing dimensions were 152 mm \times 254 mm ($B \times L$) chosen based on the dimension of box, in order to minimize the boundary effect.

The result from the experiment showed that the magnitude of settlement ratio (s/B) is 7–10% at ultimate bearing capacity for embedded footings and for surface footing the settlement ratio (s/B) is 4–7% on both unreinforced and reinforced sands.

From the results, the following conclusions were obtained:

- $0.33B$ (B : Width of footing) is the optimum top layer spacing for the embedded square model footing ($D_f/B = 1.0$) on geogrid-reinforced sand.
- An influence depth of $1.25B$ for placing the geosynthetic reinforcement regardless of the type of reinforcement and embedment depth.
- Immediate settlement of footing reduced by 20% at all footing pressure levels with two or more layers of geogrid.

- A “surcharge effect” brought by the inclusion of geosynthetic reinforcement for surface footing conditions.

Shukla and Chandra (1994) analytically showed the effect of prestressing the geosynthetic reinforcement on the settlement behaviour of geosynthetic-reinforced granular fill-soft soil system. They developed a foundation model element that has a rough membrane embedded in a granular layer which has been modified to include the prestressing effect in the geosynthetic reinforcement. Parametric studies tell that the reductions in settlement within the loaded region were observed even for low prestress in the reinforcement. They have concluded that prestressing the geosynthetic reinforcement is a significant ground improvement technique in order to increase the settlement characteristics of the low-bearing capacity soils where the membrane effect of reinforcement is felt.

Lovisa et al. (2010) performed physical model tests on laboratory and finite element analyses concept was used to study the behaviour of two dimensionally prestressed geotextile-reinforced sand bed which is supporting a circular footing on which the load is acting. A single layer of woven geotextile (SG40/40) was used to reinforce the sand bed. Loading tests were carried out on a circular rigid footing, which was made of by mild steel. The thickness of model footing was 20 mm and diameter was 100 mm. The test was performed at three different footing embedment depths of 0, 50, and 100 mm. The prestressing load applied was 2% of the allowable tensile strength of the geotextile (approximately 0.84 kN/m) and was distributed over pulleys in both x and y directions. The test tank was made of perspex with following dimensions: 0.8 m × 0.8 m plan and 0.6 m high.

The study came up with the following conclusions:

- The application of prestressing force to the geotextile reinforcement significantly improved the settlement response and load-bearing capacity of the soil.
- The beneficial effects of geotextile reinforcement without prestress were insignificant beyond a footing embedment depth of 50 mm for low strains (i.e. small displacements). However, the addition of prestressing force to the geotextile reinforcement enhanced the settlement response and load-bearing capacity for all footing depths.
- To obtaining the beneficial effects of prestressed geosynthetic in field conditions, the geosynthetic should be pulled out by following the laboratory method in principle, and anchored in trenches surrounding the area to be reinforced before placement of the granular fill over it. The pulling out process may not be easy to simulate in field conditions, especially to have a high prestress in the geosynthetic.
- Results obtained from finite element analysis using the program, PLAXIS, were generally in good agreement with those obtained from physical model tests. This validated the equation in the literature, relating the modulus of elasticity to the modulus of subgrade reaction, where the parameter H was approximately 2.5–3 times the footing width.

Konnur and Rakaraddi (2017) conducted the laboratory test on the model square footing which rests on prestressed reinforced granular beds embedded at different depths in sand.

The study came up with the following conclusions:

The load-bearing capacity of the soil was enhanced and the settlement of the footing was decreased due to the application of prestressed geogrid and geotextile.

It was found that 2.5% of prestressing of geogrid and geotextile gives the maximum load-carrying capacity of the soil.

The optimum depth of geosynthetic material is found to be at u/B of 0.25 and with an increase in the depth of pre-stressed geosynthetic, the load-carrying capacity of soil gets decreased.

BCR and PRS values tell that the geogrid material gives better result under prestress condition as compared to geotextile material.

3 Experimental Program

3.1 Materials Used

3.1.1 Ferrochrome Slag

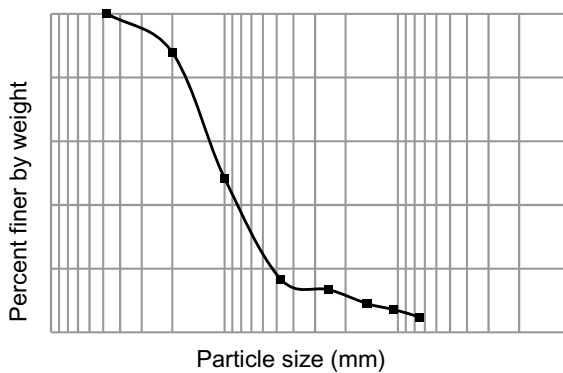
Ferrochrome slag in the crushed form obtained from the TATA steel plant Jamshedpur was used for the experiment. During the experimental program, the ferrochrome slag was air-dried and passed through 4.75 mm sieve (Fig. 1).



Fig. 1 Ferrochrome slag

Table 1 Properties of ferrochrome slag used

Property	Value
Specific gravity	2.73
Gravel content (%)	Nil
Sand content (%)	95.00
Silt and clay content (%)	5.00
Coefficient of uniformity, C_u	7.22
Coefficient of curvature, C_c	2.03
Soil classification as per ISSCS	SP
Maximum dry unit weight (kN/m^3)	14.40
Minimum dry unit weight (kN/m^3)	11.80
Cohesion, c (kPa)	Nil

Fig. 2 Particle-size distribution of ferrochrome slag

3.1.2 Particle Size Analysis Test

The particle size grading was carried out in the laboratory (Table 1, Fig. 2).

3.1.3 Geogrid

Knitted polypropylene geogrid (SG-40) manufactured by STRATA INDIA was used in the study (Fig. 3).

Basic Properties of geogrid are given in Table 2.

Fig. 3 STRATA geogrid used



Table 2 Basic properties of geogrid used

Properties	Value
Geogrid material	Polyester, Uniaxial
Type of geogrid	Knitted
Tensile strength (kN/m)	40
Aperture sizes (mm)	
MD	22
CMD	23

3.2 Methodology

3.2.1 Test Setup

The setup consists of test tank and loading system having an inner dimension of the test tank as 1.0 m in length, 0.51 m in width, and 0.70 m in height. The back and side faces of the tank were made of steel plates welded to stiff channel sections. To allow the visual observations of the reinforcement system, as well as photo scanning, the front face of the tank is made of a plexiglas sheet.

The setup used for this experiment program consisted of a loading frame and a mechanical jack. The loading frame had two vertical steel columns supporting the horizontal crosshead acting as a reaction frame. The hand-operated mechanical jack with proving ring suspended from the horizontal crosshead served for the application of compressive axial load to the footing and the load was measured by the proving ring. The jack was capable of applying a compressive load of up to 10 tons. The dimension of strip model footing was 50 cm in length 10 cm in width and 5 cm in thickness was made of seasoned teak wood. The top of the model footing was reinforced with 50 cm long, 6 cm wide and 10 cm high-steel I section. A depression was made at the centre of I section to receive a steel ball through which vertical loads

were applied to the footing. Load was applied on the footing by the mechanical jack fixed to the horizontal crosshead. The footing base was made rough by cementing a thin layer of sand by using epoxy glue. The pre-calibrated 5t proving ring was placed between the loading jack and steel ball and this pre-calibrated proving ring measured how much load was acting on the model strip footing. Two dial gauges that were attached to either side of the loading point at equal distances from the centre were used for observing the settlement of the footing. The pretension load was applied on the geogrid along the length of the tank across two pulleys as shown in Fig. 4.

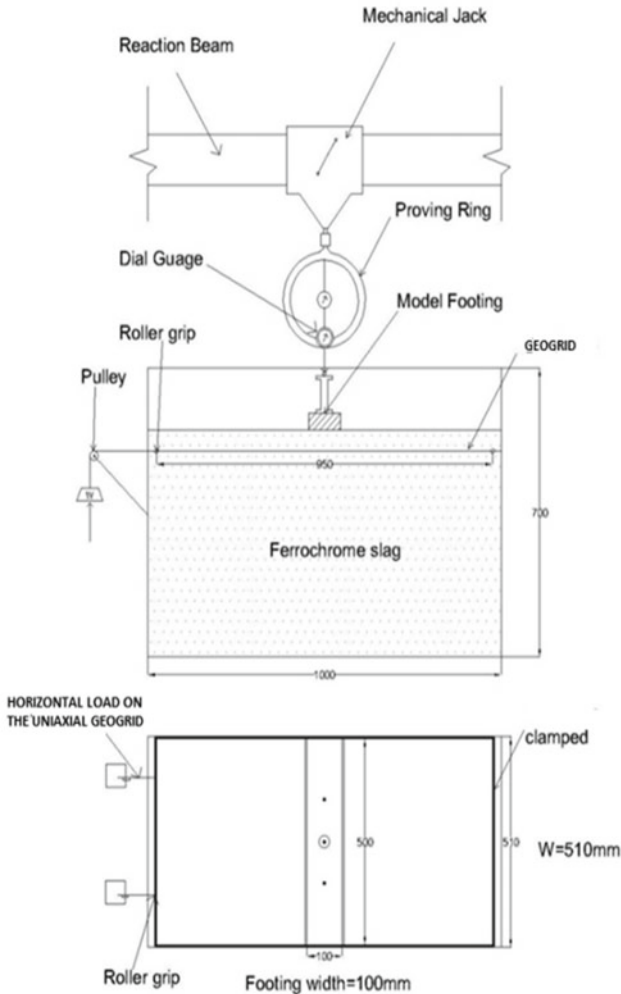


Fig. 4 Elevation and plan of the test setup (dimensions in mm)

In my experimentation, Geogrid was anchored on one end of the tank and the other end was connected to the two-pulley system. For uniform distribution of the pretensioning force, a roller grip was used. The pretension load was applied as 1, 2, and 3% percentage of tensile strength of the geogrid.

3.2.2 Preparation of Test Bed

The test is conducted on ferrochrome slag with two relative densities to check the performance of pretensioning of geogrid. Thus, the relative density of 60% and 30% were selected. In order to fill the tank, the raining technique was used to drop the ferrochrome slag in the testing tank at a known height and uniform density. For filling the tank with ferrochrome slag by raining technique, pouring device with 5 mm slit was used.

Desirable densities for the experimentation were obtained by conducting numerous trials of pouring at different heights. A free fall of ferrochrome slag into the tank was now done from the predetermined height to maintain the relative densities. Ferrochrome slag was then rained from a pre-calibrated height of 70 cm which was used to maintain a relative density of 60% for all the tests conducted and pre-calibrated height of 45 cm which was used to maintain the relative density of 30%. For checking the relative density which was used to fill the tank, the placement density was achieved by collecting samples in small aluminium cans of known volume placed at different locations during rainfall of ferrochrome slag. In the case of reinforced test bed, both the position of the footing and the position of the geogrid layer was marked on the inner face of the tank.

The ferrochrome slag was now rained into the tank from the determined height. On reaching the geogrid position, the raining of ferrochrome slag was temporarily stopped and the geogrid was placed on the ferrochrome slag bed by fixing it at one end of the tank's width face. At other width face of the tank, the pretensioning load to the geogrid was applied across the two pulleys. After placement of geogrid and application of pretensioning force, the filling of the tank with ferrochrome slag is now again continued from the top of the geogrid till the footing level by using the raining technique.

3.2.3 Test Procedure

When the test tank was filled up to the footing level, then before placing the footing on bed of slag the ferrochrome slag surface was levelled with a ruler. Upon filling the test tank to the footing level, the ferrochrome slag surface was first levelled with the help of a ruler with great care so that the relative density of the soil is not disturbed.

After levelling the surface of the test bed, the model strip footing is placed on the surface. The model strip footing is placed accurately so as to minimize the eccentricity as if this is not checked then it can cause the concentric load to not be generated at the footing and proper settlement will not take place. A seating load of 70 g/cm²

(as per code) was applied for a minute and then released. The dial gauges were attached to the footing. A normal compressive load was applied in increments of 1.0 kN to the model footing by means of a mechanical jack suspended from the reaction beam. The settlement of footing was measured by two dial gauges. For obtaining the footing settlement at the centre the average of the readings of two dial gauges was determined. The least count of both dial gauges is 0.01.

The test procedure is completed in any of the three following situations. (1) If excessive tilting of the footing takes place. (2) When failure occurred within the soil as the predefined amount of displacement and (3) If the load capacity of the jack was reached. Now the test tank was emptied and again refilled with accuracy for each test to be conducted to ensure standardized conditions were maintained throughout the investigation (Figs. 5, 6).

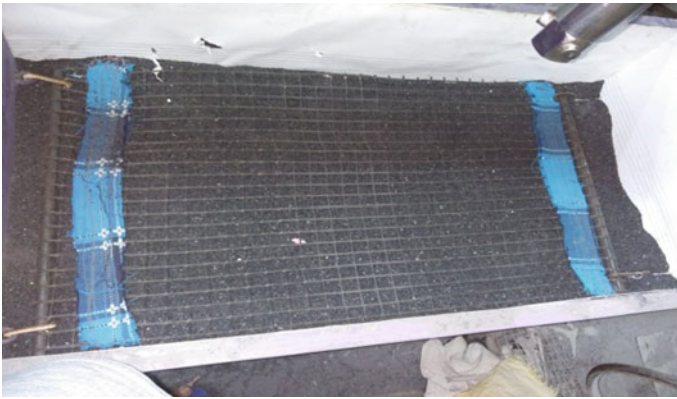


Fig. 5 Placement of geogrid



Fig. 6 Test arrangement

3.2.4 Test Variables

The width of footing (B), width of the geogrid (b) and density of the fill were kept constant throughout the entire investigation. Totally six different series of tests (i.e. A, B, C and 1, 2, 3) were conducted by varying test parameters as the depth of the geogrid layer below the footing level (u) and amount of pretension force. The test series A, B and C was carried out for ferrochrome slag having a relative density of 60% and the test series 1, 2 and 3 were carried out for having relative density of 30%. Now for unreinforced condition, the test series A and test series 1 were conducted. Test series B was carried out in unpretensioned geogrid by varying the depth of the geogrid layer (u). Test series 2 was carried out in unpretensioned condition by placing the geogrid at the optimum depth which was determined from test series B. The main aim of the test series B was to identify the optimum embedment depth of geogrid layer. The variable parameters used in this test series are expressed in a non-dimensional form with respect to model footing width (B) as u/B . Test series C and Test series 3 were conducted by varying the pretensioning force on the geogrid layer which was placed at optimum embedment depth. The pretensioning force is applied as a percentage of tensile strength of the geogrid used. The main objective of test series C and 3 was to find out the influence of pretensioning force on the overall performance of the footing (Fig. 7).

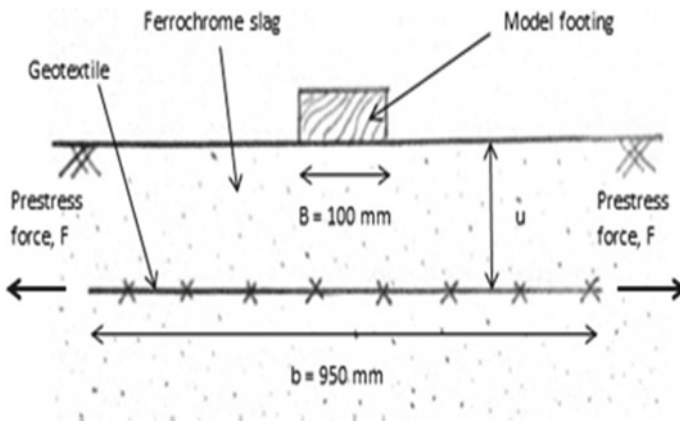


Fig. 7 Geometry of the pretensioned geogrid-reinforced foundation bed

4 Results and Discussion

4.1 Behaviour of Pretension Geogrid Reinforcement in Medium Dense Slag

The test series B results indicate that an embedment ratio of $u/B = 0.4$ is found to be optimum. Hence, for test series C, the geogrid layer was placed at an embedment ratio u/B of 0.4. Geogrid was pretensioned to 1, 2 and 3% of its tensile strength.

For unreinforced condition of the slag, the load-bearing pressure corresponding to 5 mm settlement was 51 kPa and in case of reinforcement with geogrid condition (at optimum depth) it is increased to 86 kPa whereas for pretensioning of 1, 2 and 3%, the load-bearing pressure corresponding to 5 mm settlement were found to be 97 kPa, 144 kPa, and 118 kPa, respectively. These observations indicate that the pretensioning of geogrid is effective in comparison to simply reinforcing the soil with geogrid and Fig. 8 also depicts that the 2% pretensioning is optimum pretensioning.

Allowable bearing capacity ratio (BCR_s) is defined as the ratio of q and q_R , which are load-bearing capacity values for unreinforced and reinforced foundations, respectively, at the same settlement s .

Allowable bearing capacity ratio corresponding to 5 mm settlement was calculated for all test series. Figure 9 presents the variation of allowable bearing capacity ratio at 5 mm settlement across different test series.

Figure 10 indicates the improvement of the slag at different settlements for all test series. It is clearly shown that the maximum improvement in the slag will take place at 5 mm settlement. Simply reinforcing the soil with geogrid without pretensioning, the improvement in load-carrying capacity of ferrochrome slag is 1.65 times of the unreinforced condition and at the application of 2% pretensioning the improvement in load-carrying capacity corresponding to 5 mm settlement is 2.79 times of unreinforced condition so this data states that pretensioning with geogrid is more beneficial in comparison to simply reinforcing with geogrid. The 2% pretensioning yielded the maximum improvement in comparison to 1 and 3% pretensioning.

Percentage reduction in settlement (%):

$$PRS (\%) = (S_u \pm S_r \text{ or } S_p) \times 100 / S_u \quad (1)$$

where S_r , S_p and S_u are the settlement of the reinforced, pretension reinforced and unreinforced soil, respectively, at a given pressure.

From Fig. 11, it is evident that the PRS for 2% pretension showed the maximum value of 66.20% and hence it is identified that 2% pretension is optimum for PRS consideration, corresponding to 200 kPa pressure.

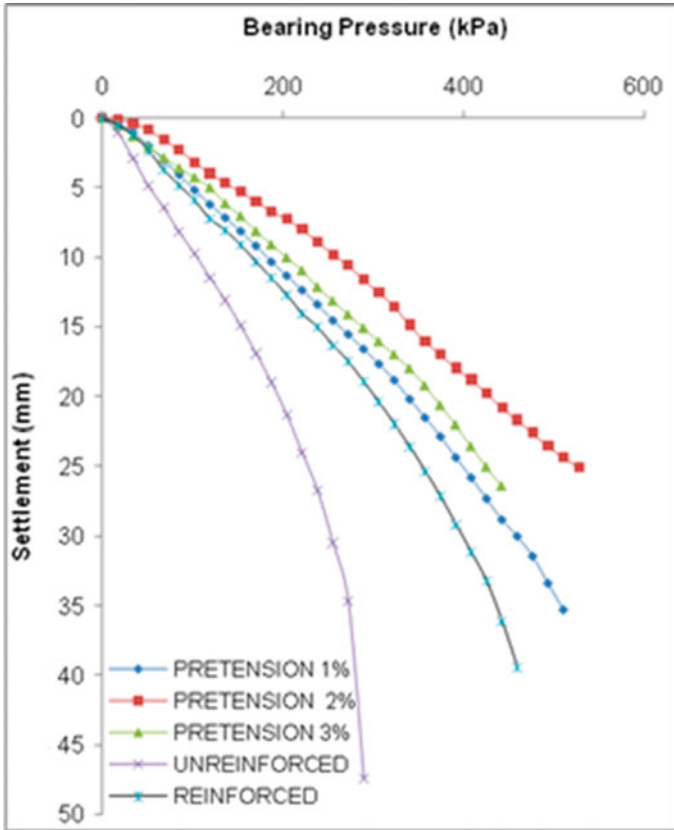


Fig. 8 Bearing pressure versus settlement curves for test series A, B and C

4.2 Behaviour of Pretensioned Geogrid Reinforcement in Loosely Filled Slag

For loosely filled ferrochrome slag, the optimum depth of geogrid ($u/B = 0.4$) was used which was obtained from medium densely filled slag and pretensioning is done at optimum depth.

From Fig. 12 the load-carrying capacity of ferrochrome slag was 52 kPa for unreinforced condition and for reinforced condition, the load-carrying capacity was obtained as 66 kPa and for 1, 2, and 3% pretensioning, the load-carrying capacities of ferrochrome slag corresponding to 5 mm settlement were found to be 72 kPa, 116 kPa and 108 kPa, respectively. This data also signifies that the pretensioning is effective in loosely filled ferrochrome slag in comparison to simply reinforced condition (unpretensioned condition).

Figure 13 indicates that the allowable bearing capacity ratio corresponding to

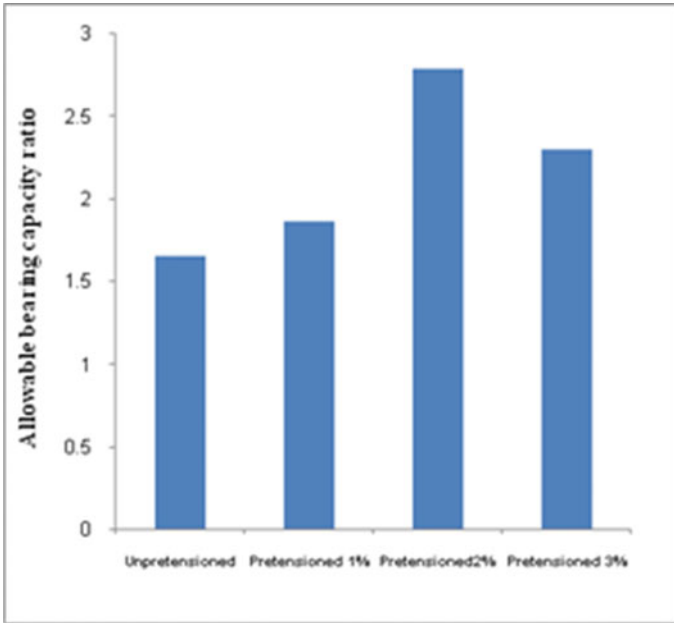


Fig. 9 Variation in allowable bearing capacity ratio corresponding to 5 mm settlement

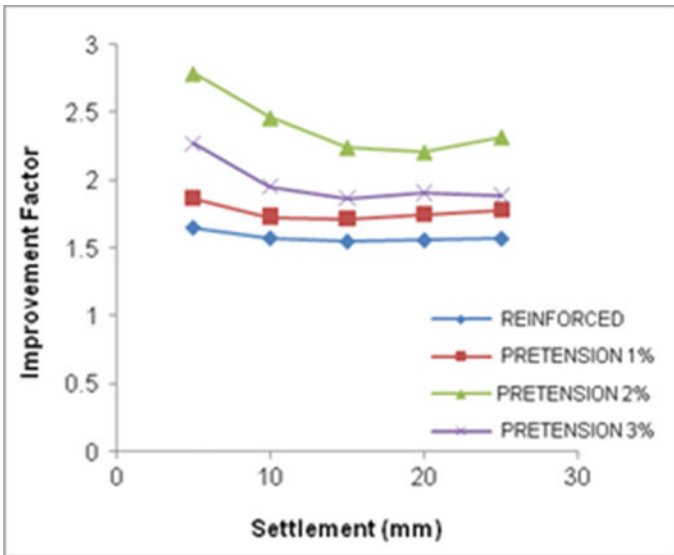


Fig. 10 Improvement factor curve for medium densely filled ferrochrome slag

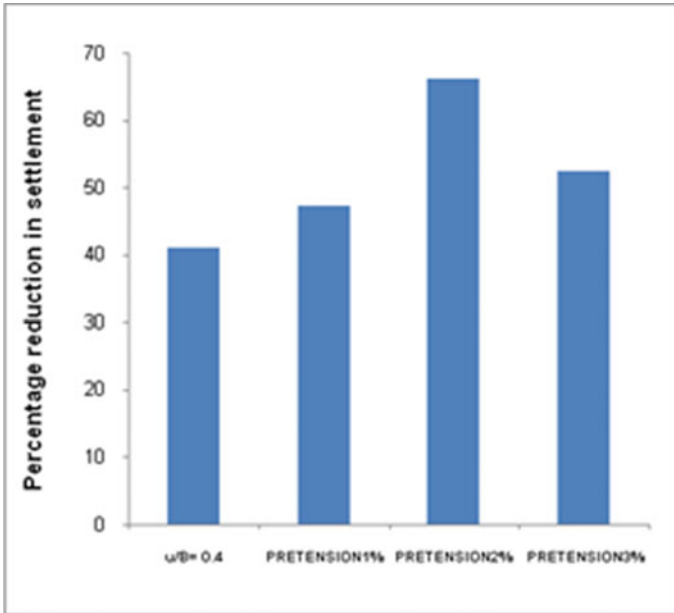


Fig. 11 Percentage reduction in settlement of footing for test series B and C

5 mm settlement is maximum for 2% pretensioning in comparison to 1 and 3% and unpretensioned condition.

From Figs. 13 and 14, it is clearly shown that after simply reinforcing the soil with geogrid without pretensioning the improvement in load-carrying capacity of loosely filled ferrochrome slag is 1.31 times of the unreinforced condition whereas after pretensioning the improvement in load-carrying capacity corresponding to 5 mm settlement is 2.23 times of unreinforced which is the maximum value as compared to 1 and 3% pretensioning of geogrid. This indicates that the 2% pretensioning is again more effective in comparison to all the above cases for improving the load-carrying capacity of ferrochrome slag.

From Fig. 15, the PRS value corresponding to 200 kPa for unpretensioned condition is 34.43. Now the PRS value corresponding to 200 kPa for 1%, 2%, 3% are 41.90%, 62.65%, 51.45%, respectively. This data indicates that the reduction in settlement is maximum for 2% pretensioning. Thus, 2% pretensioning is effective compared to all cases in loosely filled ferrochrome slag.

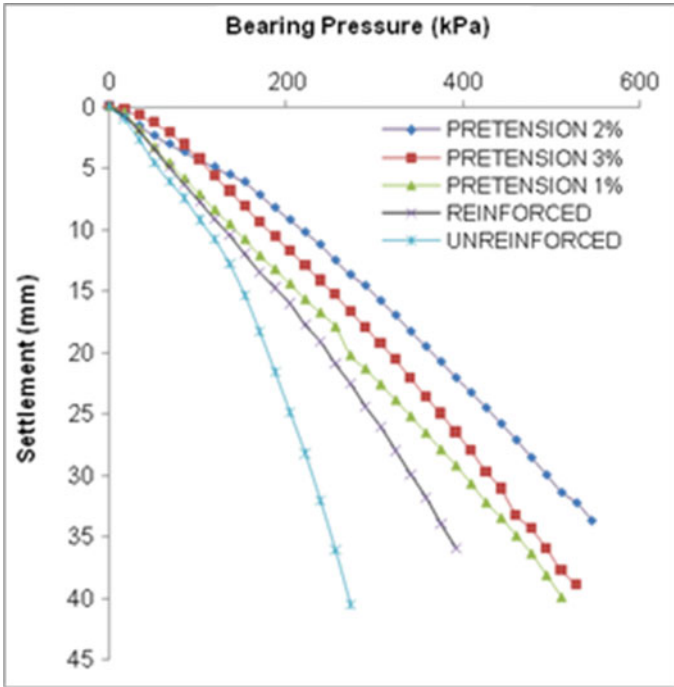


Fig. 12 Bearing pressure versus settlement curves for test series 1, 2 and 3

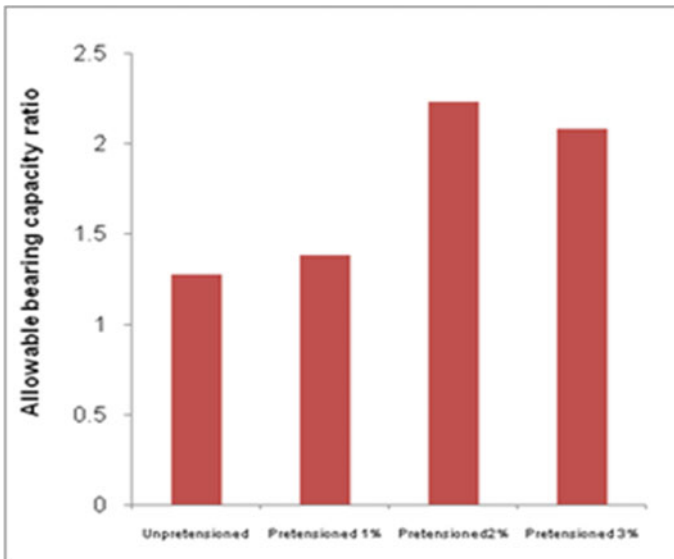


Fig. 13 Variation in allowable bearing capacity ratio corresponding to 5 mm settlement for loosely filled ferrochrome slag

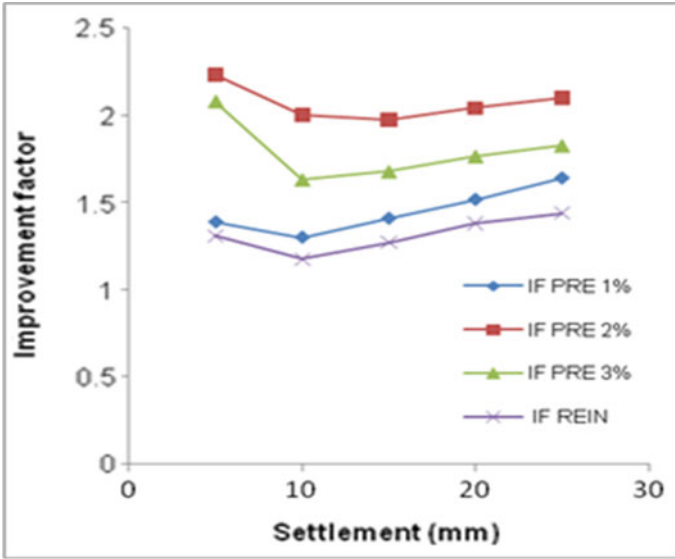


Fig. 14 Improvement factor curve for loosely filled ferrochrome slag

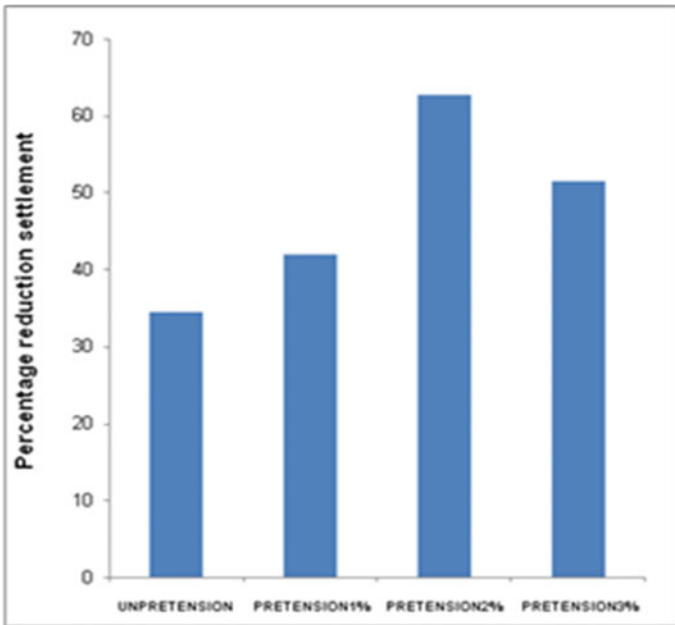


Fig. 15 Percentage reduction in settlement of footing for test series 2 and 3

5 Conclusions

Based on the experimental results, the following conclusion can be drawn.

1. The optimum depth of geogrid(u/B) is found to be 0.4.
2. It is found that pretensioning is effective in comparison to simply reinforcement of both density of ferrochrome slag because the addition of pretension to the geogrid reinforcement significantly enhances the settlement response and load-bearing capacity of the soil.
3. 2% pretensioning is most effective for both medium dense and loosely filled ferrochrome slag.
4. When we compare the allowable bearing capacity ratio corresponding to 5 mm settlement for 2% pretensioning, it is found that improvement in the allowable bearing capacity ratio for medium densely filled is more in comparison to loosely filled ferrochrome slag.
5. PRS(%) for the medium densely filled ferrochrome slag is more than the loosely filled ferrochrome slag. For 2% pretensioning, the PRS(%) value was obtained as 66.2% which is the maximum value for all the cases.
6. In unpretensioned condition, the amount of improvement is less even at higher settlement whereas in the case of pretensioned condition the improvement is much higher at lower settlement.

References

- Guido VA, Biesiadecki GL, Sullivan MJ (1985) Bearing capacity of a geotextile reinforced foundation. In: Proceedings of 11th international conference on soil mechanics and foundation engineering, pp 1777–1780. San Francisco, USA
- Konnur, Rakaraddi (2017) Behaviour of prestressed geotextile and geogrid reinforced granular bed which supports square footing at different depth on soil
- Lovisa J, Shukla SK, Sivakugan N (2010) Behaviour of prestressed geotextile-reinforced sand bed supporting a loaded circular footing. *Geotex Geomembr* 28, 23–32
- Shukla SK, Chandra S (1994) The effect of prestressing on the settlement characteristics of geosynthetic reinforced soil. *Geotex Geomembr* 13, 531–543

Dynamic Response of Tall Chimneys on Pile–Raft Foundation Subjected to Wind Load



L. Lakshmi, Monu Lal Burnwal, Samit Ray Chaudhuri,
and Prishati Raychowdhury

Abstract Tall and slender structures like chimney and towers are used generally in the power plants and telecommunication industry, respectively. For such structures with extreme heights and dynamic performance, the effect of wind load will have an important role in the design. The present paper evaluates the effect of deterministic wind load on the dynamic response of chimney. For depicting the restraint conditions of the structure in a realistic manner, soil flexibility (soil–structure interaction effect) has been considered while performing the analysis. For the wind analysis, along-wind effect has been considered. This paper explores the chimney considering nonlinear Soil–Structure Interaction (SSI) effects using Beam-On-Nonlinear-Winkler-Foundation (BNWF) approach. A 220-m-high RCC chimney of truncated hollow cone shape has been taken from the case study. The chimney is supported by a pile–raft foundation consisting of 332 bored cast in situ piles on a clayey silt deposit. The chimney has been assumed to be located in open terrain and subjected to a maximum wind speed of 50 m/s. The along-wind loads were computed according to IS: 875(Part 3) and applied along with the height of the chimney. Two-dimensional finite element (FEM) analysis is performed using OpenSees based on the direct method of SSI. Theoretical evaluation of the response considering beam elements for the chimney, pile, pile cap, and spring elements for SSI has also been a part of the study. Displacement responses of the chimney have been considered with both fixed base and flexible base conditions. The study demonstrates the influence and need for consideration of SSI which will properly estimate the response of a structure.

Keywords Chimney · SSI · OpenSees · BNWF · Dynamic analysis

L. Lakshmi · M. L. Burnwal (✉) · S. Ray Chaudhuri · P. Raychowdhury
Department of Civil Engineering, Indian Institute of Technology, Kanpur, India
e-mail: monulal@iitk.ac.in

© Springer Nature Singapore Pte Ltd. 2020
M. Latha Gali and P. Raghuvver Rao (eds.), *Construction in Geotechnical Engineering*, Lecture Notes in Civil Engineering 84,
https://doi.org/10.1007/978-981-15-6090-3_38

1 Introduction

The era of the industrial revolution is all marked by growth and advancement of the economy of a country where the power sector, also has a substantial role which indicates all the characteristics to be considered cautiously to help our environment. There is a remarkable rise in the demand for setting up of industrial chimneys due to the emerging requirement for power all over the world. Chimneys are tall and slender structures that are used to discharge waste/flue gases at a higher elevation so that environmental hazards can be minimized, i.e. caused when not appropriately dispersed. Industrial chimneys may have varying size and shape like for reinforced concrete chimney vents can be above 200 m in height and more than 20 m in diameter, and for steel chimneys, it can be few tens of meters high and less than 1 meter in diameter. They will be exposed to wind flow due to their large height and will be experiencing extreme wind loads which form the primary design load for this structure.

Failure of vents caused a tremendous loss to the power production in the past few decades due to design and construction problems. Significant incidents of such types have reported in central India recently which includes Balco Chimney collapse in Korba which is 200 km from Raipur, failure of two chimneys of factories in Rudrapur, and chimney collapse of Parichha thermal power plant in Jhansi which were mainly due to severe storms. Most of the chimney structures are constructed in less seismic-prone areas and hence are primarily designed for wind loads.

Analytical procedures to quantify dynamic wind effects are complicated and time-consuming. Manohar (1985) explained simplified static or quasi-static methods that considered the wind effect of chimney. Wind loads can be calculated using most of the design codes for a chimney; IS 4998(Part 1) 1992; CICIND (2001), ACI 307-08 (2008). T. Chmielewski et al. (2005) considered the influence of soil flexibility under the foundation of the chimney and the need to consider it. Foundation flexibility and its effect on the ductile behavior of tall and slender structures like chimneys or towers should be considered for the proper estimation of response and further ends into appropriate design considerations of such structures.

Due to the importance of chimney structure in the development of the economy of a country, the realization about this devastating wind force requires more revealing or sophisticated modeling techniques besides the consideration of static loads and load factors. Since codes discourage designs that allow mobilization of the foundation capacity, there is a need for the development of a well-calibrated simplified modeling tool. OpenSees' (2008) framework is a set of inter-related classes that includes domains, models, elements, solution algorithms, integrators, equation solvers, and databases. It allows great flexibility in solving simulation problems by combining modules like structural and geotechnical problems that enable us to consider soil and soil–structure–foundation interaction efficiently. The study focusses on the influence and need for consideration of soil–structure interaction by appropriate modeling which will adequately estimate the response of chimney structure subjected to wind loads.

2 Wind Force Computation

2.1 Deterministic Wind Field Simulation

Aerodynamic forces are those which are experienced by structures that are subjected to the wind which can be drag forces or lift forces. Drag forces act parallel to the direction of the wind and lift forces act perpendicular to the wind direction. The wind profile along the height of the structure, the wind velocity, and the characteristics of the structure are the factors on which these forces depend. Turbulence affects winds close to the surface of the earth which will hence vary with time. Thus, the response of a structure to the wind is dynamic in nature and it can be estimated properly by dynamic analysis. However, Wind forces can be obtained as equivalent static forces.

The response of chimney is estimated for along wind loads that act on the chimney. The loads calculated based on the IS simplified method is a vast simplification of the practice, stated in IS:875. It determines the wind pressure acting on the chimney and denotes the distribution of the value of the drag coefficient around the periphery of the chimney. The dynamic quality of the incident wind will cause a significant change in the applied load due to the inherent fluctuating nature of it. It is, however, not possible to consider the maximum wind load that the structure will be subjected to during its lifetime and then further proceed with the design. Quantification of the dynamic effect of wind is also tedious and time-consuming. A simplified method of IS code takes care of the dynamic nature of the loading by amplifying the incident load due to the mean wind load using the gust factor. Gust factor is given by the expected maximum response to the mean response of the structure. Either mean wind field or gust factor method can be used to compute the wind loading as per different codes but may not provide an accurate estimation of responses for tall structures like a chimney.

Basic wind speed is the peak gust velocity averaged over a short time interval of about 3 s and corresponds to mean heights of 10 m above ground level in open terrain(category-2) for a 50-year return period. The basic wind speed (V_b), as per IS: 875 (Part 3)-1987, is 50 m/s for Jhansi. The basic wind speed is improved to include the following effects to obtain the design velocity (V_z) for the structure: risk level; terrain roughness, height and size of the structure; and local topography. It is expressed as follows:

$$V_d = V_b k_1 k_2 k_3 \quad (1)$$

where V_b = basic wind speed = 50 m/s, k_1 = probability factor (risk coefficient) = 1.08, k_2 = terrain, height and structure size factor = 1.186, k_3 = topography factor = 1. Thus, the design wind speed, V_z at 204.9 m height is 67.1 m/s.

Design wind pressure is given by

$$p_z = 0.6 * V_z^2 \quad (2)$$

Equivalent static wind load has been calculated by multiplying design wind pressure with the projected area to obtain wind load at different heights.

2.2 Gust Factor Method

A gust is an abrupt upsurge in wind speed which lasts not more than 20 s. Wind gust is the maximum speed that exceeds the lowest wind speed measured during a time interval of 10 min. Wind speed contains two components one, static (mean) component, and a fluctuating component which varies with time interval on which the averaging of the gust is done.

Fluctuating wind speed would increase with a decrease in averaging time. The fluctuation rate is normally expressed in terms of intensity of turbulence which is the ratio of the standard deviation and the average speed of the wind and is expressed as a percentage. Chimney or other structures will experience dynamic oscillations due to the fluctuating wind (gust) component. Oscillations are insignificant in short rigid structures and can be properly dealt with as having an equivalent static pressure (IS 875-Part 3). More flexible systems such as tall buildings undergo a dynamic response to the gustiness of wind.

Short-period gusts may not cause any appreciable increase in stress in main components of structure but walls, glass panels, and roof sheets, sheeting rails, glazing bars, and purlins may be severely damaged. Consideration of gusts is important for the design of structures with high slenderness ratios.

An analysis procedure for evaluating the dynamic response of flexible structures under wind loading using the gust response factor is included. Along-wind load on chimney for the exposed area of wind (A_e , Elemental area) at any height (h_e) is expressed as follows:

$$F_z = C_i A_e p_z G \quad (3)$$

where C_i is the force coefficient of the building, G is the gust factor defined as peak load by mean load defined as follows:

$$G = 1 + g_r r \sqrt{B(1 + \varphi)^2 + \frac{SE}{\beta}} \quad (4)$$

where g_r is the peak factor defined as the ratio of the expected value to the root mean value of fluctuating load, r is the roughness factor which depends on the size of structure concerning the ground roughness, B is the background factor indicating a measure of a slowly varying component of fluctuating wind load, $\frac{SE}{\beta}$ is the measure of the resonant component of the fluctuating wind load, S is the size reduction factor,

E is the measure of available energy in the wind stream at a natural frequency of the structure, β is the damping coefficient, and φ is zero for height greater than 75 m. However, a load factor of 1.6 can be considered for along wind loads for the equivalent static load as per the British Standards.

3 Numerical Modeling

The freely available software platform OpenSees (OpenSees 2008) is used for studying chimney–pile–soil system for the two-dimensional finite element analysis. The detailed description of the chimney and pile, soil characteristics, analysis methods, and numerical modeling approach for the overall system is provided herein.

3.1 Modeling of Chimney

Chimneys generally have tall slender structures with circular cross sections. A representative of Parichha thermal power plant fireplace built by NBCC for 250 MW for UPRVUNL project at Jhansi district of Uttar Pradesh is considered for the study. Often chimney is more susceptible to large lateral dynamic loading like wind load, earthquake load, etc., and can have adverse effects due to weakening of the structure.

Structural behavior under lateral dynamic loading which affects the stiffness of chimney mainly depends on its shape and geometry. The modeled RCC chimney, 220 m high is of a truncated hollow cone in shape with segments having varying cross-sectional areas and moments of inertia. Geometry details of each element, outer diameter, and wall thickness of chimney are presented in Table 1.

Twenty non-linear beam–column elements of various lengths and cross sections represent the varying geometry of chimney as described. For soil–structure interaction study which considers the foundation flexibility, stack is modeled similar to fixed base, and piles are modeled with 11 elastic beam–column elements. Inelastic uniaxial materials are introduced, which are assigned to each fiber, or patch of fibers, in the section. The axial and flexural behaviors are coupled which is a characteristic of the fiber section. So, uniaxial Kent–Scott–Park concrete material model (Scott et al. 1982) is used to represent concrete and uniaxial bilinear steel material model with kinematic hardening and optional isotropic hardening (Steel01Material in OpenSees) is used for reinforcement.

Table 1 Details of Chimney's Geometry

Cross section	Position along the vertical axis, z (m)	Outer diameter \varnothing_{out} (m)	Wall thickness (m)
S1	0	25.6	0.68
S2	6.9	25.17	0.66
S3	13	24.53	0.63
S4	16.9	24.27	0.60
S5	20.8	23.62	0.58
S6	30.9	22.97	0.53
S7	40.9	22.32	0.52
S8	50.9	21.68	0.51
S9	60.9	21.03	0.5
S10	70.9	20.70	0.49
S11	75.9	20.06	0.48
S12	85.9	19.41	0.47
S13	95.9	18.75	0.46
S14	105.9	18.16	0.45
S15	115.9	17.14	0.44
S16	130.9	16.49	0.43
S17	140.9	15.84	0.42
S18	150.9	15.84	0.41
S19	160.9	15.2	0.4
S20	165.9	15.2	0.4
S21	204.9	15.2	0.4

3.2 Piles and Pile–Soil Interface

Chimney is located on the circular pile–raft foundation with 36.4 m outer diameter and 19.4 m inner diameter (Fig. 1).

The loads from the stacks are transferred to the pile cap which is further shifted to piles. A total of 332 piles are located in an arrangement of concentric circles throughout the chimney width (Fig. 2).

The raft is modeled assuming the beam element with prismatic section property. Pile group is substituted by a single pile with an equivalent diameter of 14.26 m. BNWF modeling is considered in order to consider the effect of soil–structure interaction.

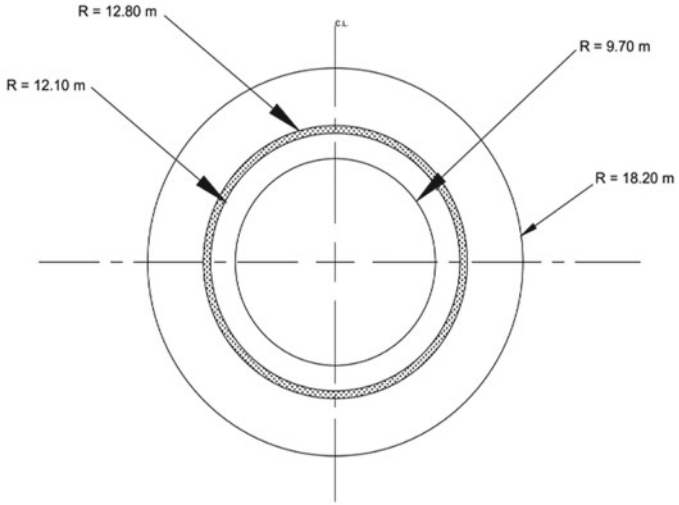


Fig. 1 Plan of the pile cap

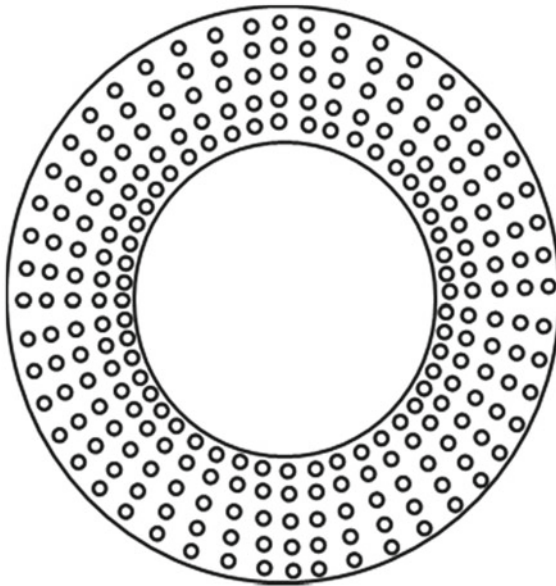


Fig. 2 Pile layout of the chimney

3.3 Soil–Foundation Interface Modeling

The behavior of soils is complicated in nature, because of its heterogeneous, anisotropic, and nonlinear force–displacement characteristics. The variability of the water table throughout the year at different seasons makes the soil more complex. The behavior of the soil is also influenced by consolidation and variable distribution of the pressure at the interface of soil and foundation (Dutta and Roy 2002) Therefore, it is very important to model and represent accurately the soil–foundation Interface.

Soil–structure interaction is modeled by using Beam-on-Nonlinear-Winkler-Foundation (BNWF) approach (Boulanger et al. 1999) that captures material and geometric non-linearity (Raychowdhury and Singh 2012). Soil yielding and degradation symbolize Material nonlinearity while uplifting, gapping, and sliding of the foundation is represented by geometric nonlinearity.

Soil–foundation interface modeling in BNWF model considers the displacement-based beam elements and zero-length elements to represent the soil respectively. Zero-length elements are assigned separate uniaxial material objects in the lateral and vertical directions for the soil springs. Two sets of nodes in zero-length element for springs have the identical location coordinates.

One set of spring nodes, the fixed nodes, are initially fixed in all three degrees-of-freedom (DOF). The other set of spring nodes, the slave nodes, are primarily fixed in only two DOFs, and are later given equal DOF with the pile nodes. The pile nodes are created with three dimensions and six DOF (3 translational, 3 rotational).

Springs, provided in the lateral direction represents P–y Springs and the vertical springs represent t–z and Q–z springs for the pile shaft and tip. P–y spring elements represent the lateral resistance of the soil–pile interface, T–z springs represent, respectively, resistance of friction along with the pile and q–z spring represents tip resistance at the base of the pile. PySimple1 material objects are incorporated in the direction x (loading direction), while the TzSimple1 and advanced, QzSimple1, pile material objects are embedded in the z (vertical) direction to simulate the behavior of OpenSees. These models are well-calibrated and widely accepted for the design and analysis of the deep foundations.

The details of these spring elements including their backbone equations, validation, and applications can be found in Boulanger et al. (1999) and Boulanger (2000).

The parameters to define the backbone curves for each spring is derived based on the properties of each layer of the deposit, as discussed in the following subsection. Here, T–z springs to represent frictional resistance are neglected due to the consideration of the effect of group pile while constitutive modeling of P–y and Q–z springs are considered for lateral and tip resistance. API procedure explains P–y curves for cohesionless soils and is given by Reese et al. (1974) and is represented as follows,

$$p = 0.9p_u \tanh \left[\frac{kz}{0.9p_u} y \right] \quad (5)$$

where p = lateral load, p_u = ultimate bearing capacity, z = depth, k = initial modulus of subgrade reaction, and y = lateral deflection. Ultimate bearing capacity, p_u , and the displacement at which 50% of p_u is mobilized are needed to be implemented for OpenSees uniaxial material PySimple1 which is determined using API procedures and graphs.

3.4 Selection of Soil Properties

The soils at the site consist of primarily of clayey silt/silty clay to about 18 m depth with some silty sand/sandy silt layers at 4.5–9 m depth. This is underlain by silty fine to coarse sand layer to about 18 m depth. Details regarding soil properties are given in Table 2.

Pinched hysteretic behavior to suitably account for the phenomena of gapping can be suitably simulated by P–y springs (PySimple1). Figure 3. P–y spring material model response shows normalized load vs horizontal displacement for a typical P–y spring material model. Similarly, asymmetric hysteretic response to account for soil’s weak strength is represented by vertical q–z springs (QzSimple2 material model).

Table 2 Details of soil profile and their properties

Soil Profile	Depth (m)	Φ (°)	γ (kN/m ³)	p_u (MN/m)	$y_{50} \times 10^{-3}$ (m)
Medium dense brown silty fine sand (SM)	0.00	28.8	7.06	111.4	3.30
	1.82	34.0	7.75	182.1	0.45
	3.64	34.0	8.34	196.0	0.45
Medium sand (SM)	5.46	28.8	8.34	131.5	3.90
	7.28	28.8	8.93	140.8	4.18
	9.10	28.8	8.93	140.8	4.18
	10.91	28.8	8.93	140.8	4.18
Very dense brown silty fine to coarse sand	12.73	38.0	7.46	239.1	0.33
	14.55	38.0	7.46	239.1	0.33
	16.37	38.0	7.46	239.1	0.33
Severely weathered granite	18.19	40.0	14.19	702.2	3.30
	20.01	40.0	14.19	702.2	3.30

Note γ = effective unit weight, ϕ = friction angle

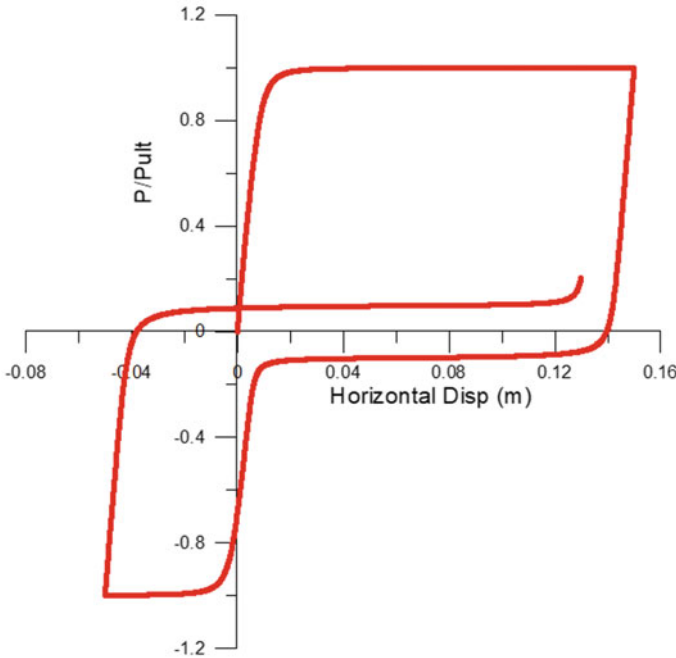


Fig. 3 P-y spring material model response

4 Results and Discussions

The behavior of chimney with SSI has been understood by various analysis methods including eigen value analysis and deterministic analysis.

Eigenvalue analysis is performed to obtain the fixed base and flexible base period which will give an estimate of the effect of SSI. The effect of SSI on the fundamental period is significant. It has been observed that there has been a shift of fundamental period from 2.47 s for a fixed base to 3.03 s for a flexible base. Thus, a reduction of about 18% is noted in the fundamental period for a fixed base than when foundation flexibility is introduced. This period elongation due to the influence of the rocking motion of the foundation is significant. The periods for different modes of the structure are listed in Table 3.

Table 3 Comparison of time period and frequency for flexible and fixed bases

Mode	Fixed base	Flexible base	% reduction with flexible base for T
	Time period (T) (secs)	Time period (secs)	
1	2.47	3.03	0.18
2	0.58	0.79	0.26
3	0.24	0.46	0.48

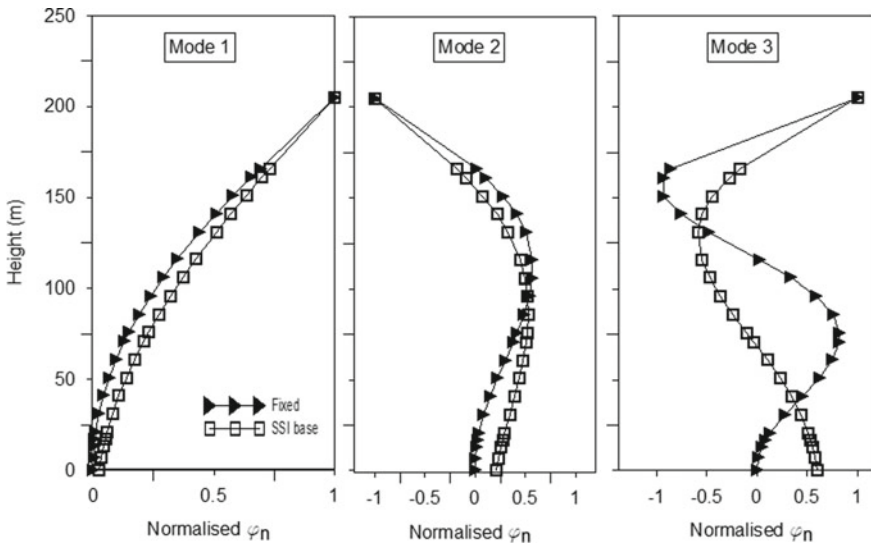


Fig. 4 Mode shapes of chimney considering fixed and flexible base conditions

Mode shapes for both fixed and flexible base are obtained and there is significant variation due to foundation flexibility induced by soil stratum (Fig. 4).

Deterministic analysis is performed with equivalent wind load and displacement responses are recorded for both fixed and flexible base along with the height of the chimney. The deformation response at the top of the respective fixed and flexible base chimney structure is found to be 39 cm and 56 cm, respectively. It is observed that the tip deformation response of chimney from the analysis of chimney with a fixed base is lower than that for the flexible base.

The effect of foundation flexibility came out to be significant which enhanced flexible base deformation response compared to fixed base with a percentage increase of 43.5% (Fig. 5).

As the base conditions are changed from fixed to flexible base, displacement increases. Inter-story drift ratio (IDR) is the response to evaluate the performance level of a structure based on various hazard levels. It is the relative displacement between two consecutive floors normalized with respect to the story height. A normalized height vs Inter-story drift ratio for fixed and flexible bases is plotted in Fig. 6. Inter-story drift response of chimney considering fixed and flexible base. Tall structures like chimney shows an increase in Inter-story drift ratio for a flexible base from a fixed base. It may be due to an increase in deformation and greater rocking behavior of chimney with SSI.

Pile deflection pattern is shown in Fig. 7. P–y spring response for medium dense, medium, and very dense sand layer. The displacement demand is found to increase at the base of the chimney. Foundation compliance in the case of nonlinear modeling of the SSI caused an increase in displacement demand.

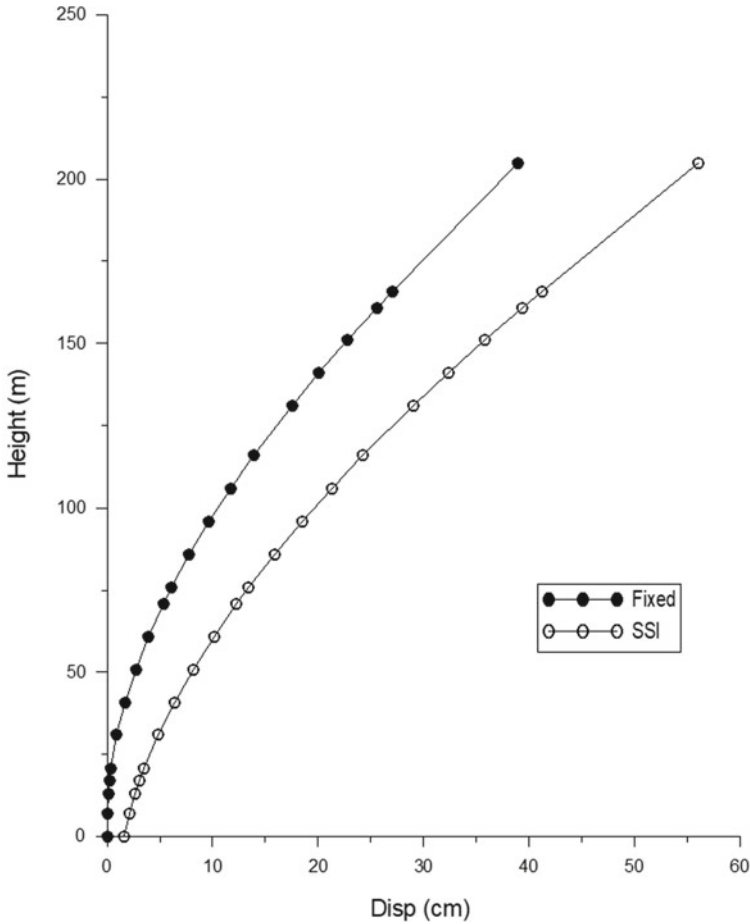


Fig. 5 Lateral displacement response of chimney considering fixed and flexible bases

The responses of P–y springs representing the behavior of the soil–pile interface is given in Fig. 8. Lateral displacement profile of Pile. Thus, the response of soil–pile interface is found to be significant and should be taken into consideration.

Generally, fixed base models are adopted for practical purposes. Estimation of actual response is difficult without proper modeling and quantification of the non-linear SSI effect. BNWF modeling in OpenSees could provide a better approximation of SSI effect. Here, amplification in deformation response of the structure with foundation flexibility is observed which can affect the performance of the system. Thus, the generalization of a structure without considering SSI may not be always conservative and cannot be neglected for a safe design.

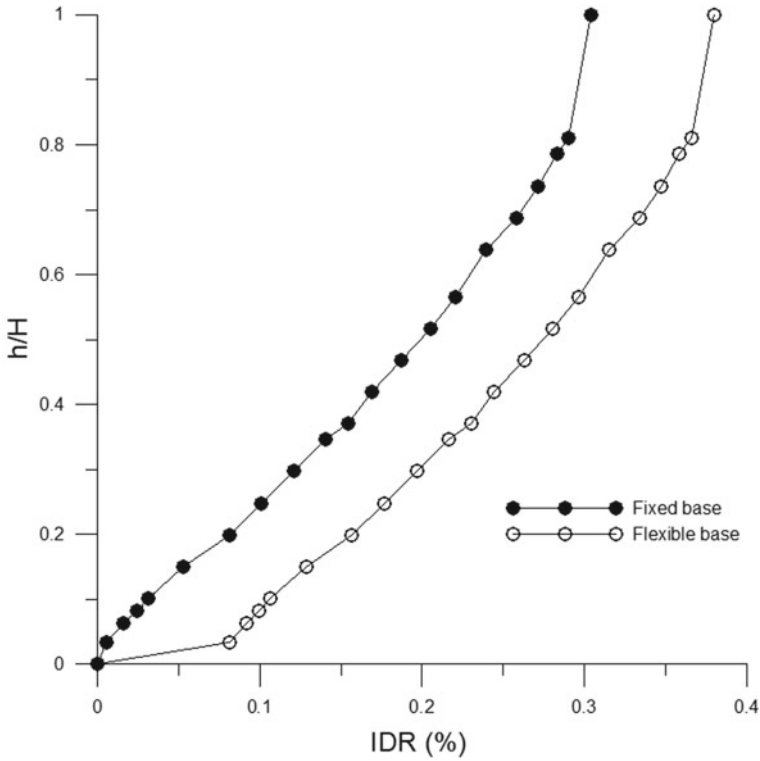


Fig. 6 Inter-story drift response of chimney considering fixed and flexible bases

5 Conclusions

The study explores the response of chimney structure with a piled raft foundation founded on four different types of soil using BNWF concept. Usually, structures are designed with a supposition that they are fixed at their foundation levels owing to the fact that SSI may lead to the conservative design and thus can be neglected safely. The present study focusses on this issue mainly by following suitable modeling and analysis procedures. Eigenvalue and deterministic analysis have been carried out and the following observations have been listed from the investigations:

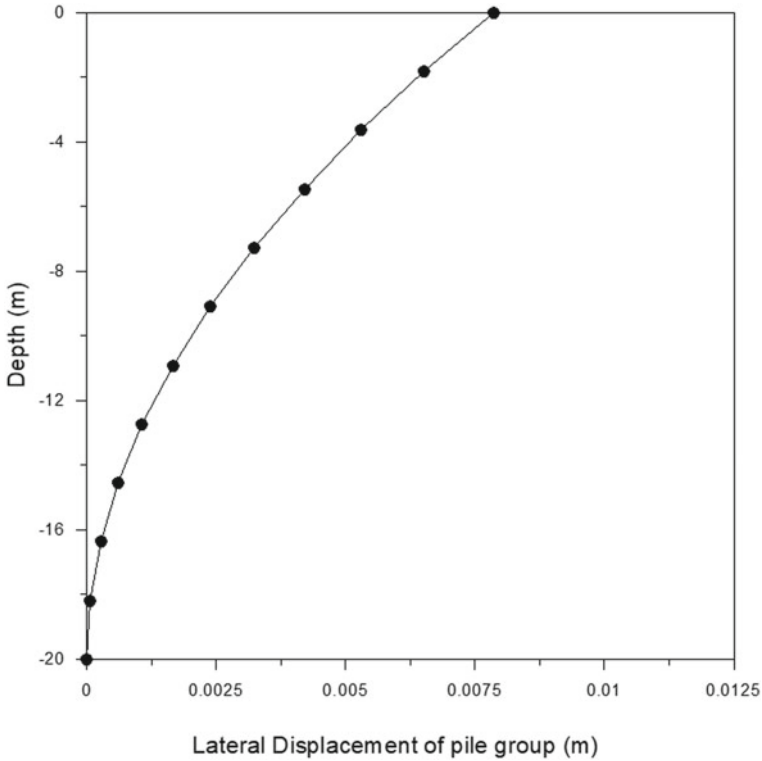


Fig. 7 Lateral displacement profile of Pile

- Effect of SSI is predominant at the base of the chimney
- Substantial rise in the deformation response in a lateral direction due to interaction with soil compared to the conventional method and further increase in displacement demand
- Modeling approach provides comparable response quantities
- Estimation of actual response of chimney subjected to wind load requires the consideration of SSI effect
- The comparison of IDR shows an average reduction of 41.03% from flexible base to fixed base. This show a detrimental effect of SSI for tall structures.
- Effect of SSI is significant which increased displacement demand
- Importance of considering SSI through proper modeling for achieving economic and safe design is identified.

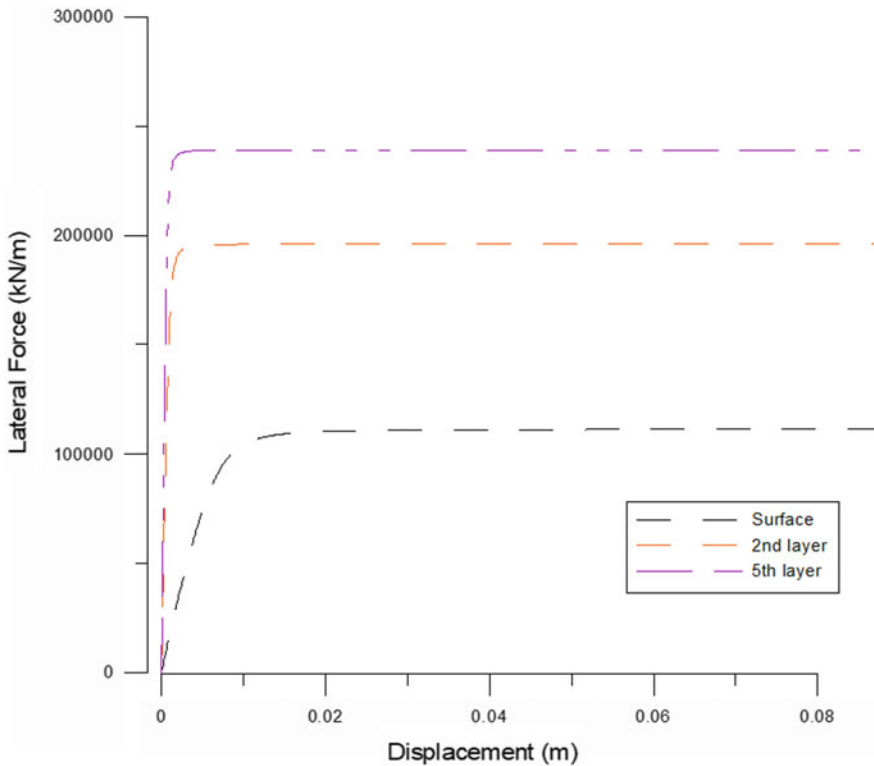


Fig. 8 P-y spring response for medium dense, medium, and very dense sand layers

References

Boulanger RW, Curras CJ, Kutter BL, Wilson DW, Abghari A (1999) Seismic soil-pile-structure interaction experiments and analyses. *J Geotech Geoenvironmen Eng* 125:750–759. [https://doi.org/10.1061/\(ASCE\)1090-0241\(1999\)125:9\(750\)](https://doi.org/10.1061/(ASCE)1090-0241(1999)125:9(750))

Boulanger RW (2000) The PySimple1, TzSimple1, and QzSimple1 material models. Documentation for the OpenSees platform

Chmielewski T, Gorski P, Beirou B, Kretzschmar J (2005) Theoretical and experimental free vibrations of tall industrial chimney with flexibility of soil. *Eng Struct* 27:25–34

CICIND (2001) Model code for concrete chimneys—Part A: the shell (Second edition, Revision 1). Zurich, Switzerland

Committee, A.C.I. (2008) Code requirements for reinforced concrete chimneys and commentary. Am. Concr. Institute, USA, 1–34 (2008)

Dutta SC, Roy R (2002) A critical review on idealization and modeling for interaction among soil—foundation—structure system. *Science* 80:1579–1594. [https://doi.org/10.1016/S0045-7949\(02\)00115-3](https://doi.org/10.1016/S0045-7949(02)00115-3)

Federal Emergency Management Agency (FEMA) (2000) Pre-standard and commentary for the seismic rehabilitation of buildings, FEMA-356, Washington, D.C

IS 875 (1987) Code of Practice for Design Loads (Other Than Earthquake) for Building and Structures—Part 3: Wind Loads (Second Revision). Bur. Indian Stand. New Delhi. (1987)

- Indian Standards, B.: IS 4998-1: Criteria for design of reinforced concrete chimneys, Part 1: Assessment of loads (1992)
- Manohar SN, Tall-Chimneys-.pdf (1985) Tata McGraw-Hill New Delhi, Bangalore
- OpenSees, OpenSees (Open System for Earthquake Engineering Simulation) (2008) Pacific Earthquake Engineering Research Center (PEER). University of California, Berkeley
- Raychowdhury P, Singh P (2012) Effect of nonlinear soil-structure interaction on seismic response of low-rise SMRF buildings. *Earthq Eng Eng Vib (Springer)* 11(4):541–551
- Reese LC, Cox WR, Koop FD (1974) Analysis of laterally loaded piles in sand. *Proc VI Ann Offshore Technol Conf Houston Texas* 2:473–485
- Scott BD, Park R, Priestley MJN (1982) Stress-Strain behavior of concrete confined by overlapping hoops at low and high strain rates. *J Am Concrete Inst* 79(1):13–27

Construction Dewatering for Underground Station in Urban Environment



K. Raja Rajan, D. Nagarajan, and T. Vijayakumar

Abstract Metro is seen as the only solution for mass rapid transit system in the urban areas. For an underground metro station, deep excavations in densely populated areas impose specific challenges to the contractor. Based on the type of soil or rock, excavation procedure, method, and time shall be adopted. The control of groundwater is one of the most common and complicated problems encountered on a deep excavation. The contractor selects the dewatering method, and the contractor is solely responsible for its design and operation. Many dewatering techniques like multiple wells, sump pumps, vacuum pumps, and deep wells are available to control groundwater. In this paper, the author explains the usage of MODFLOW software for dewatering analysis in the underground metro station and also about the dewatering system which has been adopted in the site. Pump out test is an accurate method of determining the safe yield of the well and also for assessing the actual site condition.

Keywords Dewatering · Deep excavation · Dewatering systems · Groundwater · Pump out test

1 Introduction

Urban transportation infrastructure in India needs big investment and a massive upgradation. Metro is seen as the only solution for the mass rapid transit system. After the success of Delhi Metro, lots of Indian cities are exploring the option to implement a metro rail project across the country.

K. Raja Rajan (✉) · D. Nagarajan · T. Vijayakumar
CMPC Division, EDRC, HCL, L&T Construction, Chennai, India
e-mail: k-raja@intecc.com

D. Nagarajan
e-mail: nagarajan-d@intecc.com

T. Vijayakumar
e-mail: tvk@intecc.com

For underground metro stations, deep excavations in densely populated urban areas impose specific challenges, especially to the safety and impact on adjacent structures. Effective risk management in the design and construction of deep excavations in the urban environment must consider a range of issues such as the design of excavation support, groundwater control system, pre-construction surveys of adjacent properties and utilities, and the implementation of effective monitoring systems. For constructing metro station which may be on an average of 20 m deep excavation to be carried out below ground. In order to perform excavation in the dry zone, the dewatering system to be well planned and executed. The contractor selects the dewatering method and the contractor is solely responsible for its design and operation. The authors of this paper had taken the role of designing the dewatering system for all four stations of Mumbai Metro Line 3 package 1 based on the site geologic condition.

2 Location and Site Details

Mumbai Metro Line 3 (MML3) Project is proposed from Colaba in South Mumbai to SEEPZ via Bandra Kurla Complex. Package UGC-01 is one of the seven packages of MML3 and it consists of four stations (Cuffe Parade, Vidhan Bhavan, Church gate, and Hutatma Chowk Station) and associated tunnels. MML3 UGC-01 was awarded to Larsen & Toubro and STEC Joint Venture (L&T STEC JV) Contractor to design and build.

3 Generalized Sub-soil Profile

Geotechnical Strata for each station have been classified into different units which are tabulated in Table 1. Predefined soil parameters are provided in the *Geotechnical Interceptive report*.

4 Retaining System and Method of Construction

For deep excavation, the earth has to be retained by a suitable shoring system in order to avoid disturbance to the adjacent structures. Since the excavation depth is very deep and location of the station in urban areas, open-cut excavation is not feasible. Earth retaining systems like diaphragm walls, secant piles, soldier piles, contiguous piles, and sheet piles were available for retaining system. A suitable structure shall be chosen based on the client's requirement, site geology, construction methods, groundwater, and soil/rock properties.

Table 1 Sub-soil classification with description

Soil Type	Description
Unit 1-Filled up material	Reddish brown dry clayey sand with gravel/clayey gravelly sand
Unit 2a: Soil	Silty sand, sandy silty, sandy clay, clayey sand
Unit 2b: Residual Soils	Very dense dark brownish yellow moist sand with gravel, boulders
Unit 3a: Basalt—WG V	Weak to very weak completely weathered
Unit 3b: Basalt—WG IV	Strong highly weathered to moderately weathered grey basalt with closely spaced horizontal fractures
Unit 3c: Basalt—WG III	Strong moderately weathered grey basalt with closely spaced horizontal fractures
Unit 3d: Basalt—WG I & II	Very strong moderately to slightly weathered basalt with widely spaced horizontal fractures
Unit 4a1: Shale/Breccia—WG V	Weak to moderately strong moderately weathered light brownish grey shale
Unit 4a2: Shale/Breccia—WG IV	Moderately strong slightly weathered dark grey shale with very closely spaced horizontal fractures

4.1 Method of Construction

For constructing underground metro stations many methods been widely followed by the contractors. Top-down and bottom-up methods were the conventional methods adopted by global contractors.

Bottom-up method: This method is applicable only when the traffic diversion is not possible. The principle of bottom-up method is to isolate the excavation area by proper earth retaining system and then to proceed with stages of excavation. After each stage of excavation, temporary strut shall be installed and activated before advancing to the next stage of excavation. A similar procedure is adopted till excavation reaches the final excavation level as shown in Fig. 1. Upon reaching the toe level, the base slab is constructed along with sidewalls. The gap between walls and excavated profile shall be filled with suitable material. As sidewall construction proceeds, bottom-most strut is deactivated and removed. Intermediate slabs shall be constructed as per levels and specifications. Similarly, the procedure is followed till top slab construction and the remaining portion is filled with soil and road laid for public traffic

Top-down method: This method is applicable only when the traffic diversion is possible. In some places, decking panel is used for traffic movement over the excavated portion as shown in Fig. 2. Earth retaining system is constructed and excavation shall be done up to top slab level. Once the top construction is completed, a filling is done above the top slab and then open to traffic. Through the openings in the top

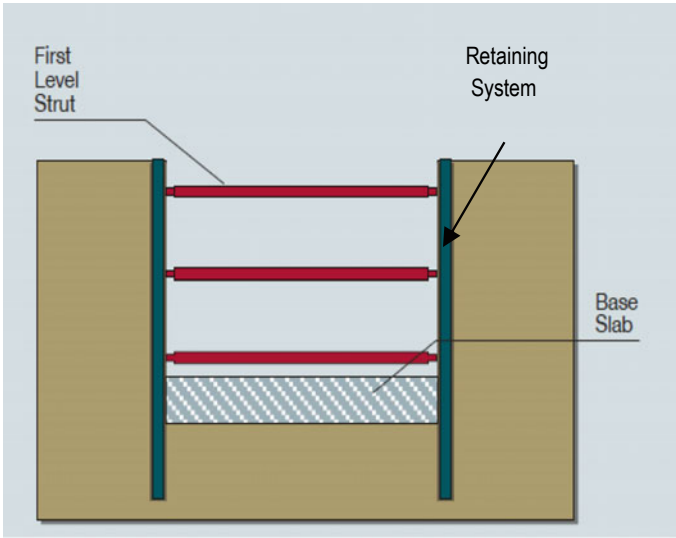


Fig. 1 Typical Bottom up construction method

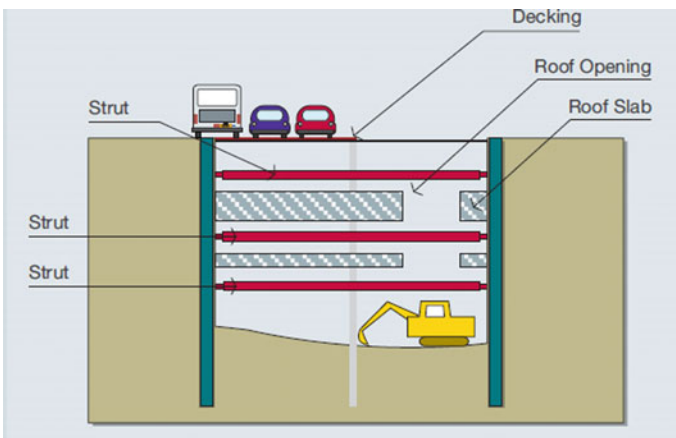


Fig. 2 Typical Top Down construction method

slab, further excavation and construction proceed. As construction moves from top to down, there is no requirement of temporary strut. Intermediate slabs itself act as strut members. Comparatively, this method has less working space and vehicle movement inside the excavated area.

5 Dewatering

Dewatering means “the separation of water from the soil,” Construction dewatering means lowering the groundwater table temporarily till the construction phase. This enables the contractor to have dry surface during excavation which will enhance the excavation productivity and also it is easy for construction equipment movement if the surface is dry. Some of the parameters like geology of the soil strata, type of retaining system adopted, groundwater condition, etc., may affect the process of dewatering. Many specialized dewatering agencies are available in the industry to cater to the issue of dewatering. At the same time, well-developed methods are readily available to implement the dewatering system (Fig. 3).

Exclusion techniques and dewatering techniques were the two major dewatering systems available to control the groundwater.

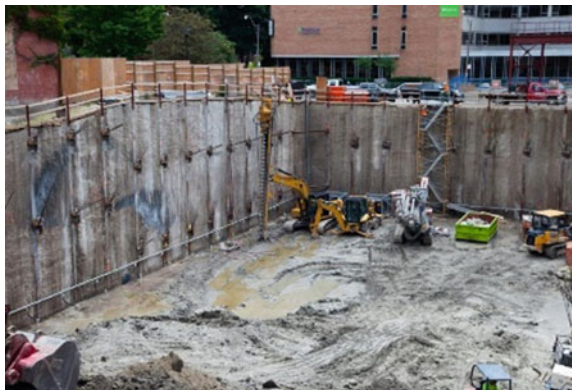
5.1 Exclusion Techniques

This technique is to exclude water from the excavation. The aim of groundwater control by exclusion techniques is to prevent groundwater from entering the working area. A region which has a very low permeability wall like sheet pile or diaphragm walls were physically constructed or inserted in the ground.

5.2 Dewatering Techniques

This technique is to temporarily lower the groundwater table until the construction period. There are many methods available to lower the groundwater table like well point method, sump system, deep well system, etc., were the common system

Fig. 3 Typical Underground metro station construction



adopted in most of the construction sites. But some advanced techniques like electro-osmosis, vacuum method also available for dewatering in critical ground cases. For deep excavation like underground metro station, basement construction, power plant foundation construction, the above dewatering techniques are essential to cater to the groundwater issues. In fact, before the excavation itself, dewatering should be commenced so that excavation work will not be hampered. Choosing a dewatering technique based on ground strata and depth of excavation is a critical task that has to be carried out with some engineering approach.

Well point method: A series of wells of required depth are created in the vicinity of the excavated area from where the water has to be pumped out as shown in Fig. 4. Riser pipes or dewatering pipes are then installed into those closely spaced wells which on the surface are connected to a flexible swing pipe which is ultimately appended to a common header pipe that is responsible for discharging the water away from the site. One end of the header pipe is connected to a vacuum pump which draws water through notches in the well point. The drawdown using this method is restricted to around 5–6 m below the well point pump level. If a deeper drawdown is required, multiple stages of well points must be used.

Open Sump Pumping Method: This is the most common and economical method of dewatering as gravity is the main playing force. Sump is created in the excavated area into which the surrounding water converges and accumulates facilitating easy discharge of water through robust solid handling pumps.

Since the bottom of the sump is situated at a level lower than that of the excavation bottom, it will abridge the seepage way along which groundwater from outside seeps into the excavation zone and, as a result, the exit gradient of the sump bottom will be larger than that on the excavation surface. Typical sump system is shown in Fig. 5.

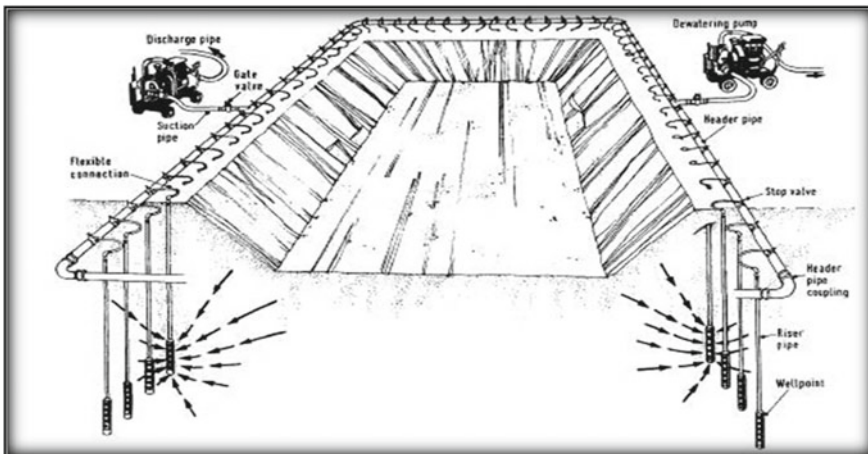


Fig. 4 Multiple Well system—Dewatering technique

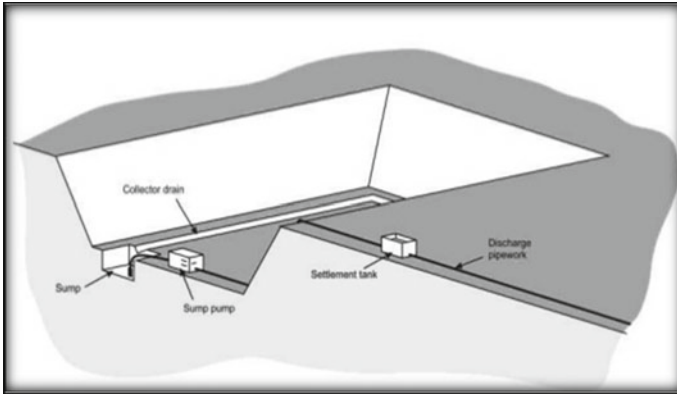


Fig. 5 Sump pump system—Dewatering technique

Deep Well method: A deep well system consists of an array of bored wells pumped by submersible pumps. Pumping from each well lowers the groundwater level and creates a cone of depression or drawdown around itself as shown in Fig. 6. Several wells acting in combination can lower groundwater level over a wide area beneath an excavation. Because the technique does not operate on a suction principle, large drawdown can be achieved, limited only by the depth of the wells, and the hydrogeological conditions. The wells are generally sited just outside the area of the proposed excavation and are pumped by electric submersible pumps near the base of each well. Water collection pipes, power supply generators, electrical controls, and monitoring systems are located at the surface

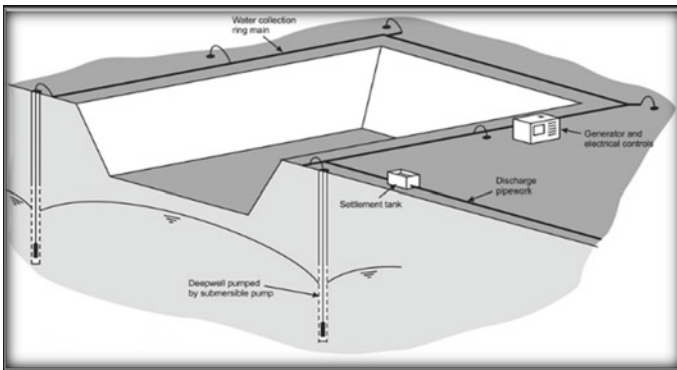


Fig. 6 Deep well system—Dewatering technique

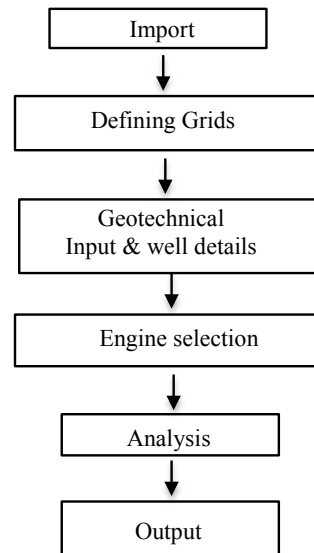
6 MODFLOWS

Due to the complex nature of hydraulic boundary conditions (flow barriers), caused by secant piles at this site, dewatering analysis using a theoretical approach is not adequate and requiring numerical simulations. Dewatering analysis using Visual MODFLOW v.2010.1 is employed to design the deep well design in underground metro stations. MODFLOW is a modular 3D finite difference groundwater flow model where similar program functions are grouped together and scientific computational and hydrologic options are constructed in such a manner that each option is independent of other options. It has provision for barrier flow conditions to be modeled.

The model is applicable for transient as well as steady-state model. The interface is divided into three separate modules, the Input Module, the Run Module, and the Output Module. When you open or create a file, you will be able to seamlessly switch between these modules to build or modify the model input parameters, run the simulations, calibrate the model, and display results (in plan view or cross section). The workflow of MODFLOW software is explained in Fig. 7 as a flowchart. Software works from importing the model from drawing or picture, providing adequate inputs, selecting the proper engine for analysis, and then the output is displayed.

The Input Module allows the user to graphically assign all of the necessary input parameters building a three-dimensional groundwater flow and contaminant transport model. The input menus represent the basic “model building blocks” for assembling a data set for MODFLOW. These menus are displayed in the logical order to guide the modeler through the steps necessary to design a groundwater flow and contaminant transport model.

Fig. 7 Flowchart of MODFLOW workflow



The Run Module allows the user to modify the various MODFLOW parameters and options which are run-specific. These include selecting initial head estimates, setting solver parameters, activating the re-wetting package, specifying the output controls, etc. The Output Module allows the user to display all of the modeling and calibration results for MODFLOW. The output menus allow you to select, customize, and overlay the various display options for presenting the modeling results.

7 Dewatering for Cuffe Parade Station

The contractor is solely responsible for adopting a suitable dewatering system to enhance the dry excavation in the station. Many dewatering techniques are readily available but as a pioneered contractor the most efficient and most economical system to be selected. This paper explains the dewatering design adopted for Cuffe Parade station using MODFLOW software.

In contract document, client has provided some contract requirements to be fulfilled while designing the dewatering system.

- The groundwater within the excavations shall be maintained at a level that permits achievement of undisturbed, stable and dry subgrade to permit construction and backfilling of the permanent works and avoids heave, piping or base failure of the excavation.
- The groundwater drawdown (a drop of the water table during dewatering/construction) outside the excavation/adjacent to works, shall be controlled such that the water table doesn't get lowered by more than 1 m below the lowest recorded groundwater table. For ensuring this, the recharging well system shall be provided if required.
- Wherever water-bearing seams, fissures, or broken ground yielding undesirably large quantities of water is encountered, it shall be grouted Cuffe Parade station extends to a length of about 407 m with cross width of 37 m. Station details have been tabulated in below Table 2 with other details.

Design consultant has predefined each excavation stage till the bottom of excavation which has been tabulated in Table 3. Excavation has to reach the depth of about 24 m below the existing ground level.

As per client requirement, dewatering to be done 1 m below each excavation stages, i.e. if first excavation stage is +0.59 m, then level of water by dewatering to be at -0.59 m. Similarly, for each stage, dewatering to be done at least 1 m below the proposed excavation level as shown in Fig. 8. Setting the above criteria as a

Table 2 Cuffe Parade station details

Length of station	Width of station	Ground level	Base slab bottom	Total depth of station
407 m	37 m	+3.84 m, CD	-21.24 m, CD	25 m

Table 3 Excavation stages of Cuffe Parade station

Description	Reduced Level	Depth below GL (m)
Natural ground level	+3.84	0.0
Initial ground water level	+2.84	1.0
First excavation level	+0.59	3.25
Second excavation level	-3.41	7.25
Third excavation level	-7.41	11.25
Max. Toe level of Secant Pile wall (3a)	-3.87	7.71
Max. Toe level of secant pile wall (3b)	-12.66	16.5
Fourth excavation level	-12.65	16.49
Final excavation level	-20.245	24.08

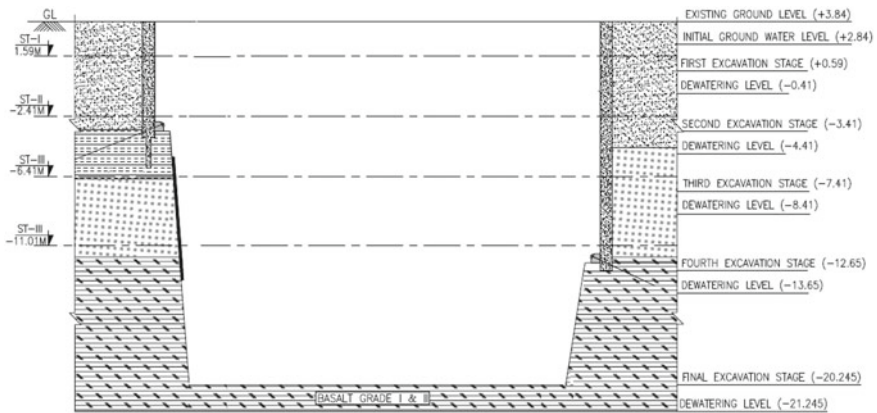


Fig. 8 Excavation and Strut Level details of Cuffe Parade station

benchmark, suitable dewatering design been adopted. Secant piles proposed as a temporary retaining system. Soft pile and hard piles form the combination of secant pile design. Reinforcement is provided in a hard pile whereas soft pile is filled only with concrete. The toe of secant pile is determined based on the encountering of rock level. Based on the type of rock grade, pile embedment is predefined by the consultant. During execution for each pile, geologist confirms the grade of rock and executes the proposed embedment of pile in rock. Below, Fig. 8 shows a typical cross section of Cuffe Parade station with secant piles as a retaining system and pile termination on either side based on rock grade with excavation sequence till base

slab level. Among the available dewatering system deep well system is found to be efficient and more suitable for the ground condition.

In rocky strata, open sump pumping is the only available dewatering system. MODFLOW software works based on certain assumptions. Faults or fissures present in the rocks are completely ignored in analysis, if encountered in execution, same to be closed by grouting.

Geotechnical inputs like soil strata, the permeability of each stratum (both vertical and horizontal), retaining system layout and depth, etc., to be defined as input parameters. In order to start the analysis, plan layout of the station is imported. Import files shall be PDF format, JPEG format, or it can be directly imported from Google maps. The figure below shows the imported plan of Cuffe Parade station in MODFLOW software.

After importing the plan, grids to be defined for ease of bifurcation of the station for analysis. Grids to be defined in both vertical and horizontal directions will help to cut the section anywhere in grid location as per the user's requirement. In this grid, spacing is taken as 1-m interval in both directions as shown in Fig. 9. Apart from grid, layers also can be defined so that output can be viewed as per the desired layer. For instance, if the user desired to view dewatering stage 10 m below ground level, simply the tenth layer shall be viewed so that corresponding drawdown can be

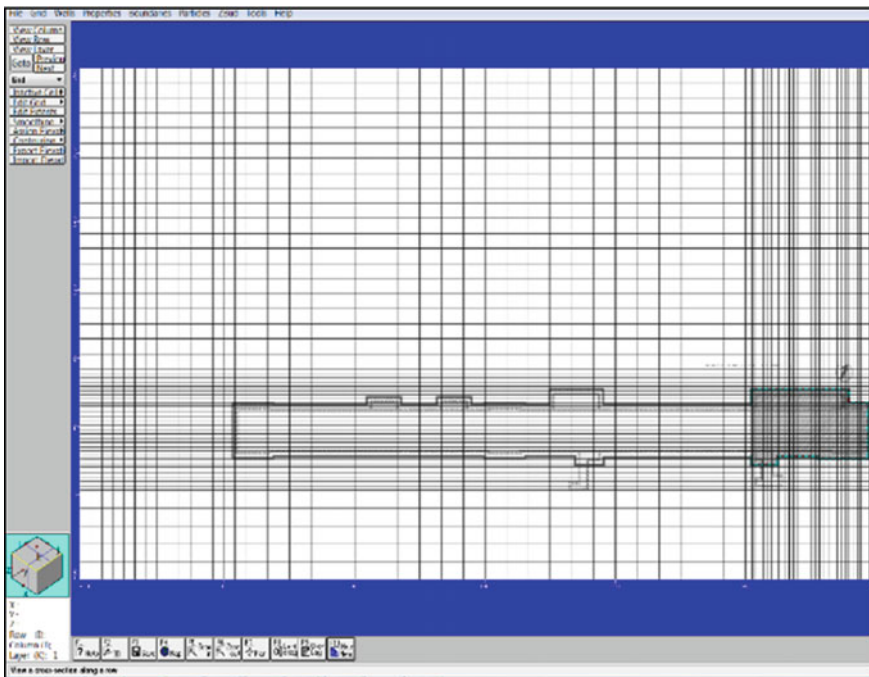


Fig. 9 Plan of Cuffe Parade station imported for analysis from PDF file

witnessed in the corresponding layers which is an effective tool for monitoring the dewatering analysis.

7.1 Input Data for Analysis

In this analysis, the aquifer is considered as unconfined. Groundwater table is considered at groundwater itself as per client requirement. Secant piles that act as a retaining system been modeled as dead cells which mean no water from outside station area is allowed to pass through the secant piles. Layout of the secant piles and depth of secant pile also modeled as per consultant drawings. In this model, the effect of secant pile is considered in the design, so it is assumed that the secant pile will be in position before the start of dewatering works. In MODFLOW software, water sources like sea, river, well, pond, etc., shall be modeled which will act as a source of water to groundwater which will be influenced in dewatering analysis inside the station area. In this station, sea is present 250 m away from the station area which is included in the model. Geotechnical details are taken from approved Geological Intercept Report of Cuffe Parade station area and modeled it as shown in Table 4 in MODFLOW software.

The permeability of each stratum is taken from GIR as the primary input for MODFLOW analysis. To be on the conservative side, vertical permeability is taken as half of the horizontal permeability. Permeability in rock strata is very low and considered as an impervious layer. Permeability of soil is considered much on the conservative side in order to design the system for adverse conditions. As a prudent contractor, L&T wants to design a safe dewatering system in order to meet any unpredictable situation like high ingress of water during excavation which may affect the excavation work to proceed further (Table 5).

Pumping wells used to pump out water from the excavation area. The diameter of wells varies from 200 to 300 mm in diameter. Perforated PVC pipe of 150 mm diameter is inserted in the well and the remaining area is filled with filter material which used to allow water inside the well without any clot at perforations. In this station total of 19 pumping wells been planned with a total depth of 20 m from ground level. Recharge wells which used to pump water in the ground in order to

Table 4 Sub soil data profile for Cuffe Parade station

Layer No.	Subsoil profile	Max depth (m)	
		From	To
1	Fill (Top Layer)	0.0	3–4.9
2	Residual Soil	4.9	3.0–6.0
3	Completely weathered Basalt	3.0–6.0	6–12
4	Highly weathered to Moderately weathered Shale/Basalt	12–13.5	15.0
5	Fresh to slightly weathered Amygdaloidal Basalt	Below 15.0	

Table 5 Soil permeability for Cuffe Parade station

Layer No.	Depth (m)		Horizontal conductivity k_x or k_y (m/sec)	Vertical conductivity k_z (m/sec)
	From	To		
1	0.0	4.5	5E-04	2.50E-04
2	4.5	12.0	1.13E-05	5.65E-06
4	Below 12.0		4.12E-06	2.06E-06

maintain the groundwater table outside the station area. As per contract condition, the groundwater table outside the station area shall not be lowered more than 1 m from the existing level. In order to maintain, constant recharge shall be done using recharge wells.

The pumping capacity of pumping well to be defined as input in order to calculate the number of days required to achieve the desired drawdown. In the present analysis 600 cum/day given as pumping capacity and 80 cum/day as recharge quantity for recharge wells which is positioned outside the station area. In order to know the exact ground permeability, it is recommended to conduct a pump out test in the station (Fig. 10).

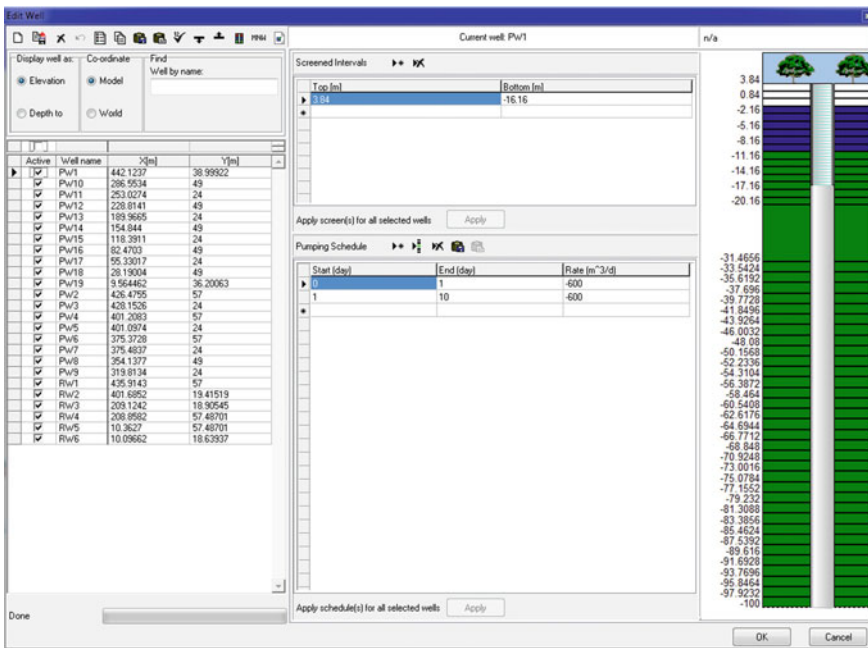


Fig. 10 Co-ordinates input for pumping and recharge wells

7.2 Pump Out Test

Pumping test is a field method to determine the actual permeability of strata and also the well yield. For conducting pump out test, one pumping well is used to check the yield of well and 2 or 3 observation wells are required to measure the drawdown of the strata. This helps to identify the effective well spacing. Pump out test permeability value may be compared with theoretical or laboratory permeability value to sense the difference in the actual field test. Pump out test needs minimum 2 days testing period in order to evaluate the actual field permeability value.

Pumping test is conducted to evaluate an aquifer by “stimulating” the aquifer through constant pumping, and observing the aquifer’s “response” (drawdown) in observation wells on the well in the area is the only method for computing the aquifer parameters. A long-duration pump test for 2160 min was conducted to observe the effect of pumping in pumping well and nearby observation wells. The pumping well and observation wells were of identical design.

From the long-duration pump test conducted in the study area, the following parameters have been computed

- Transmissivity (T)
- Field Permeability/Hydraulic Conductivity (k)
- Specific yield (Sy)
- Specific Capacity (C).

Though different methods are available for estimating the above parameters, most suitable methods chosen for computation are given in (Fig. 11).

The pumping test data were analyzed by Theis’s recovery and Jacob’s Methods in order to determine the above-said parameters. The transmissivity ‘T’ values are



Fig. 11 Pump out test at Cuffe Parade station area

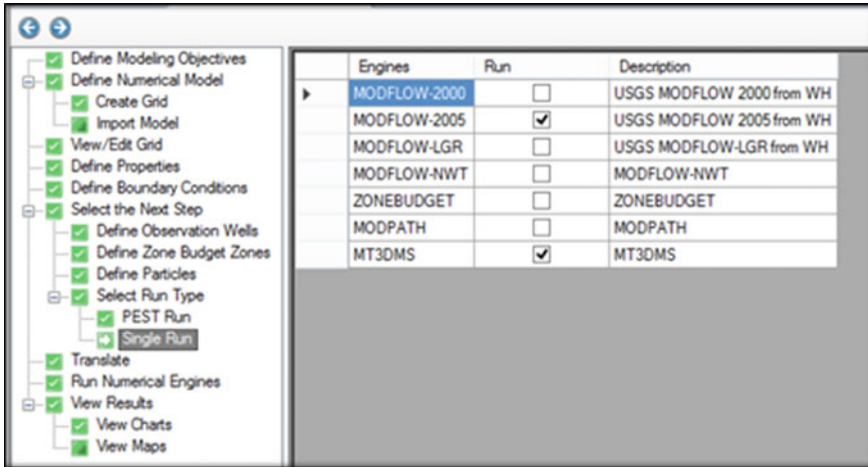


Fig. 12 Engine selection for MODFLOW analysis

1.44 m²/day and 0.81 m²/day, respectively. Permeability ‘k’ value in the pumping well (MW) is derived to be 0.93×10^{-5} cm/sec and 5.20×10^{-5} cm/sec, respectively. Specific yield (sy) in the pumping well MW is derived to be 0.13% and 0.05%, respectively. This indicates a lack of very fine interconnecting zones among fracture zones that are weak, and due to which groundwater movement is very slow in the station area.

7.3 Engine Selection for Analysis

After providing the required inputs, engine selection shall be made in order to analyze the dewatering design. Various engines have been enlisted in software for different usage (Figs. 12 and 13).

MODFLOW user manual provides a clear idea for the selection of appropriate engine based on the type of design. Once the engine is selected, the analysis starts for computing drawdown, water flow path, influence area of well, time is taken to achieve dewatering, etc., and the output window is used to view the desired output.

7.4 Output Window of MODFLOW Analysis

Many trials to be carried out by adjusting the number of days of dewatering, location of pump wells, depth of pump wells in order to achieve a more economical desired output. Software has a unique feature to make cross section at any grid and also to view drawdown at any depth. Some of the output window images are shown below

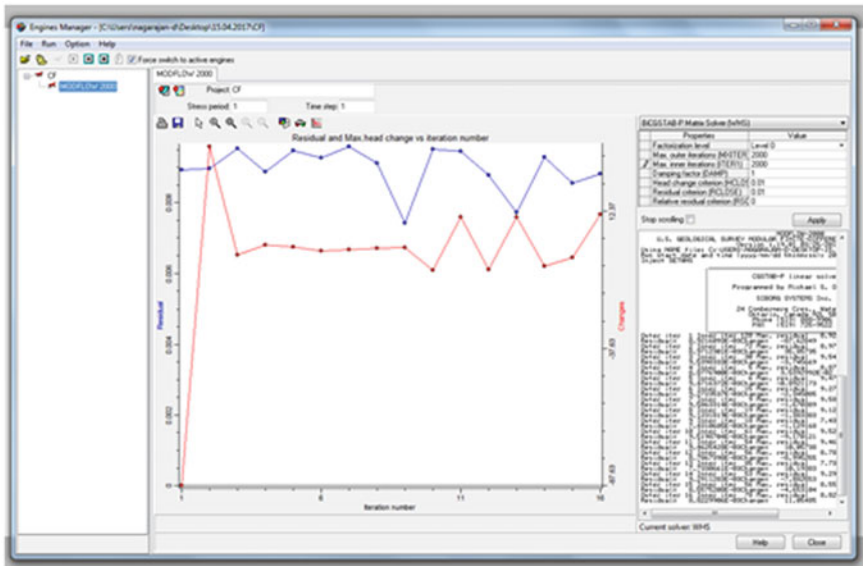


Fig. 13 Analysis in MODFLOW software for the selected engines

for better understanding. Typical drawdown achieved all along the length of station in plan view is shown below. Based on drawdown depth, different color legends assigned (Figs. 14, 15 and 16).

For the plan shown above, two cross sections been chosen in order to view the drawdown for cross section and longitudinal section of the station.

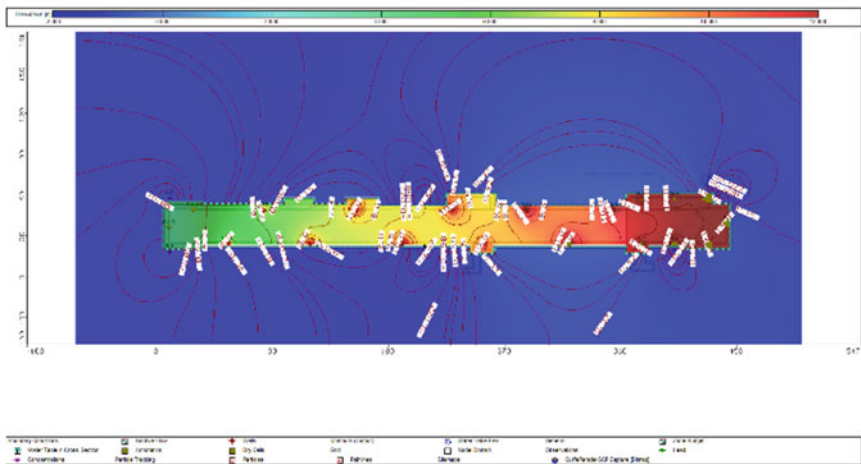


Fig. 14 Plan showing drawdown of Cuffe Parade station

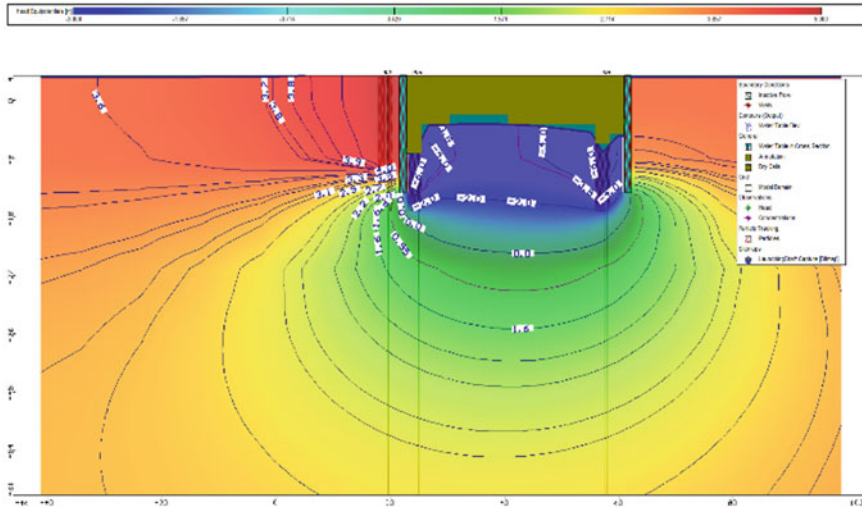


Fig. 15 Cross section showing drawdown of Cuffe Parade station

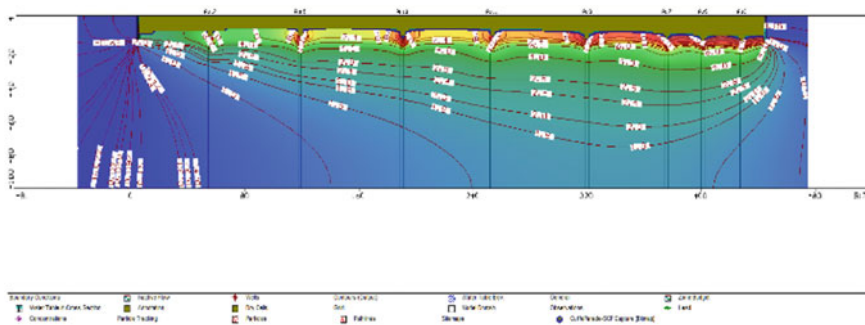


Fig. 16 Longitudinal section showing drawdown of Cuffe Parade station

Apart from drawdown, the water flow path shall be seen in the plan view which gives a clear direction of the water movement path. The maximum drawdown achieved in this station is 14 m below ground level, i.e. till the top of the rock strata.

7.5 Sump Pump System

If excavation reaches the rocky strata, then deep well is inefficient and for the dewatering sump pump system to be adopted. A total of six sump systems been deployed

for this station. Sump size is $1.5 \text{ m} \times 1 \text{ m} \times 1 \text{ m}$ which will be taken down as excavation proceeds. The sump is positioned 3 m inside secant pile such that it will not affect berm of secant pile. The water collected in the sump shall be pumped out periodically using a submersible pump. Apart from this, the sump requirement for monsoon is also calculated by the analytical method, and recommendation is provided to use of extra sump in the monsoon period. Maximum recorded rainwater is taken and compared with the area of excavation to arrive at sump pump requirements. Two extra pumps are kept in reserve for monsoon period.

7.6 Dewatering Layout

Apart from the deep well arrangement and sump system, dewatering layout is provided for the entire station. The capacity of pumps is decided based on the rate of pumping, required vertical lift, amount, and type of suspended solids. Suitable electrical submersible pumps shall be installed within each deep well. The pumps shall be connected to discharge pipes, cables, and ropes prior to lowering. The system can be fitted with an external control to automatically start and stop pumping at predetermined levels.

The units shall be lowered with the pipe and cable strapped to the lifting rope into the PVC screen casing. The lifting rope shall be secured at the top of well for removal of the pump in case of repair and maintenance. Discharge from pumping wells shall be measured and recorded at least twice a day during dewatering. Discharge from both deep wells and sump pumps to be connected to a common discharge pipeline which shall be provided along the periphery of the station. Water discharge is collected in a sedimentation tank before discharging into drainage. Water is allowed to stagnate in sedimentation tank so that sediments carried along water shall get settled in sedimentation tank and after some time water is allowed to discharge in drainage pipelines. Sedimentation tank is frequently cleaned in order to remove the settled sediments from the tank.

8 Protection of Adjacent Structures

Due to the lowering of groundwater, there may be an impact on the adjacent structures. The condition of the existing buildings is taken from the Mumbai Metro Line 3 Tender Documents—Building Condition Survey. The surveyed buildings are located within a bandwidth of about 60 m along the corridor defined as the “influence zone. Category of building given as per contract recommendation and suitable instrumentation has been planned all-around buildings located near the station. Building settlement and cracks have been monitored continuously during the time of excavation

and dewatering. If cracks and settlement exceed, the permissible level then excavation to be stopped. Observation wells located outside the station helps to monitor the groundwater table outside the station area.

9 Conclusions

Some of the key points to be noted while designing the dewatering techniques for underground metro station

- Many dewatering techniques like multiple wells, sump pumps, vacuum well, and deep wells are available to control the groundwater. The contractor has to choose a suitable technique based on sub-surface, permeability of strata, depth of excavation, and excavation area.
- Pumping wells used to pump water from the excavated zone, Recharge wells present outside the station used for pump in water to maintain the ground level outside station area, and observation well used to monitor the groundwater during the entire process.
- MODFLOW software works from importing the layout, providing required geotechnical inputs, choosing the engine to analyze, and output for the desired drawdown is obtained.
- Using MODFLOW software, well spacing, well depth, and influence of retaining structure shall be clearly pictured.
- Pump out test reveals the yield capacity of well and the actual permeability of the ground stratum. Pumping test conducted for 72 h continuously in order to determine transmissivity and permeability by Theis's Recovery Method and Jacob's Method.
- A total of 19 pumping wells, 6 recharge wells, and 2 observations wells were provided to dewater the entire Cuffe Parade station area.
- Pumping well diameter is 200 mm with a perforated pipe of 150 mm to encase the submersible pump with 50 mm of filter layer all around the perforation.
- Perforations to the well to be provided as per the specifications. Improper filter criteria shall affect the specific yield of well which ultimately reduce the efficiency of the well.
- Depth of pumping well terminated based on rock depth, the bottom of well is provided 2 m below the rock surface without any perforations in order to provide sufficient head for the efficiency of pump.
- Deep wells found to be inefficient in rock strata, dewatering in rocky layer depends only on sump pumping system.
- Sump shall be provided 3 m away from the secant pile wall in order to protect the berm of the wall.
- Surface water control due to monsoon been calculated separately by analytical method for which four 5HP pumps were provided in order to dewater the accumulated water due to rain.

- Flood protection wall of 1 m height been provided all along the periphery of the station in order to stop the inflow of water to the excavated area from the surroundings.
- Shotcrete been provided along the surface of the excavated rock in order to stop the seepage of water from the sides of the rock.
- If any local faults or fissures encountered during rock excavation, same has to be grouted completely.
- In Cuffe Parade station, rock encountered approximately 12 m below ground level, if no rock surface encounters, then depth of pumping well has to go below base slab level.
- Observation wells to be monitored continuously for the depth of ground water table outside the station area. Fluctuation of ground water shall be allowed maximum for 1 m.
- All discharges from deep wells and sump system shall be connected to the common discharge pipeline which flows to the sedimentation tank and followed to drainage outlet.
- Sedimentation tank used to remove the sludge which is mixed in the water which is helpful to avoid clot in the drainage system.
- Instrumentation is to be fixed in the adjacent buildings in order to monitor the cracks of the building during the time of dewatering and excavation of station building. Prior to dewatering, category of existing building condition to be identified and labeled.
- Inclinometer fixed on secant piles in order to monitor the pile deflection due to earth pressure during the process of excavation.

Acknowledgments I would like to convey my thanks to the management for allowing me to present this paper and my heartfelt regards to my colleagues and site team for their valuable contribution.

References

- Bureau of Indian Standards IS 9759 (1981, reaffirmed 2003): Guidelines for Dewatering during Construction
- Cashman PM, Preene M (2001) Ground water lowering in construction—a practical guide
- CIRIA C515 (2000), Groundwater Control: Design and Practice. Prepared by Preene M, Roberts T O L, Powrie W, Dyer M. CIRIA London
- Ground Water Information Greater Mumbai District Maharashtra—Govt. of India Ministry of Water Resources Central Ground Water Board
- Mumbai Metro—Package 1—Project contract & technical documents
- Paul K, Singh R (2017) Comparative study of construction technologies for underground metro station. *Int J Res Eng Technol* 6(3)
- Sadhegpour, Ghanbari and Fadee (2008) Groundwater lowering in deep excavation, International conference on case histories in Geotechnical engineering
- Visual MODFLOW, version 2010.1, Waterloo Hydro geologic, Ontario, Canada

Investigations On the Impact of Sub-Structures on Groundwater Flow



Rohitha P. Kamath and N. Unnikrishnan

Abstract Underground structures act as impervious obstacles and modify the groundwater flow pattern. Such structures below the groundwater table affect the hydrodynamic parameters of the aquifers and they disturb the mass balance of the flow system. The main adverse effects change in groundwater level, flow path, and flow velocity. The altered flow velocity leads to re-arrangement of soil particles and variation in the groundwater table. The effect of pile foundations on the groundwater flow pattern was investigated. Numerical simulations using the finite element method were undertaken to this effect. Using the data from the laboratory tests, the finite element model was validated. With the validated finite element model, the influence of various participating parameters was studied. Remedial measures to mitigate the effect of underground structures on the groundwater flow pattern are suggested.

Keywords Underground structure · Groundwater flow · Pile foundations · Numerical study · Finite element analysis

1 Introduction

Rapid urbanization has resulted in structures with ever-increasing height. Most of these structures are supported on deep foundations such as piles. The presence of underground structures below the groundwater table affects the hydrodynamic parameters of the aquifers and they disturb the mass balance of the flow system. These structures can bring about hydrogeological hazards, especially in the areas characterized by a regional rising trend of the water table. The impacts are also inflow path, flow velocity, and quality of water. When a linear underground structure is constructed in the ground where the groundwater level is extremely close to the surface, it blocks the flow of groundwater. Piles are generally made of very low-permeability materials such as concrete and steel. The existence of piles may change the overall behavior of flow in an aquifer. Long-term effects such as mixing

R. P. Kamath · N. Unnikrishnan (✉)
Government Engineering College Thrissur, Thrissur, Kerala, India
e-mail: unnikrishnan_n@yahoo.com

© Springer Nature Singapore Pte Ltd. 2020
M. Latha Gali and P. Raghuvver Rao (eds.), *Construction in Geotechnical Engineering*, Lecture Notes in Civil Engineering 84,
https://doi.org/10.1007/978-981-15-6090-3_40

of contaminants in the underground aquifer may take place. The rise of groundwater level may cause a flood on the upstream side of a structure, promote soil salinization, affect flora by rotting the roots of the plants, reduction of the bearing capacity of the soil, expansion of heavily compacted fills upon wetting, increase in loads on retaining systems or basement walls of buildings, development of uplift water pressure under foundations and floor slabs, ground heave due to the reduction of the effective stresses caused by the increasing pore water pressure, ground collapse in the soil with high collapse potential in the zone which become saturated by the rising water table, etc. Lowering of heads on the downstream side may cause ground subsidence, drying of springs and wells, seawater intrusion in coastal aquifers, death of phreatophytes, root withering of vegetations, consolidation settlement of underground utilities, etc.

The influence of underground structures is long-lasting and cumulative in nature. The influence may happen during the construction process also. The construction of basements may require dewatering in huge quantities which may seriously affect the environment and also the stability of structures in the vicinity. Usually, the shallow groundwater is more contaminated than deep groundwater. Underground structures are responsible for the mixing process between shallow and deep groundwater. The contaminants present within shallow depths get mixed with deep groundwater. The total mixing affected zone area increases linearly with underground structures density.

Several investigations on the influence of underground structures were reported in the past (Colombo et al. 2016; Ma et al. 2014; Pujades et al. 2012; Gattinoni and Scesi 2017). Yihdego et al. (2016) simulated the application of engineered subsurface barriers in the form of sheet piles to divert contaminated groundwater flow and determined the optimum depth of such barriers. Interestingly, a beneficial application of underground structures was thus brought out. Underground tunnels were found to influence the groundwater table (Marinos and Kavvas 1997). The cumulative impact of underground structures was also investigated (Attard et al. 2016). In the investigation reported herein, an attempt has been made to investigate the effect of pile foundations on the groundwater flow through finite element analysis. FEFLOW software used is a three-dimensional finite element code used for modeling flow and transport processes in porous media under saturated and unsaturated conditions. The software is suitable for simulating different conditions such as transient or steady-state flow, saturated or unsaturated flow, density-dependent flow, multiple water table, mass and heat transport, multi-species reactive transport, and fracture flow. FEFLOW has been widely used in the modeling of groundwater flow for similar cases as dealt with herein (Attard et al. 2016; Ding et al. 2008; Koskinen et al. 1996). The finite element model was validated using results from the experimental study. An experimental setup was developed for the purpose. It was found that the pile foundations influence the groundwater flow to a large extent. Remedial measures are also proposed for mitigating the effect of such underground structures.

2 Experimental Program

The experimental investigations were conducted in a sand bed placed inside a rectangular box of dimension 0.6*0.6*0.6 m. The test box was made up of fiber-reinforced plastic material. The box was filled with sand at a constant relative density to simulate an aquifer. Pluviation technique was used to maintain the relative density from experiment to experiment. The sand was filled up to a height of 0.45 m. Polyvinyl chloride (PVC) pipes of 25.4 mm diameter were buried vertically into the sand in the box to represent impermeable piles. The number of piles was altered to investigate the blocking effect of the piles. Provisions were provided at inlet and outlet for the uniform horizontal distribution of water. The flow was considered as steady. Piezometric tubes were installed to measure the head at the upstream and downstream side of the pile. Constant head of 500 mm was maintained using an overhead tank. Figure 1 gives a sketch of the experimental setup.

The experiments were conducted with and without piles. The numbers of piles used were 5, 6, 7, 8, and 9. The corresponding volume replacement ratios were 0.012169, 0.014603, 0.01704, 0.01947, and 0.02190. Hydraulic head at upstream and downstream sides of the pile area was measured (Table 1).

Fig. 1 Experimental setup

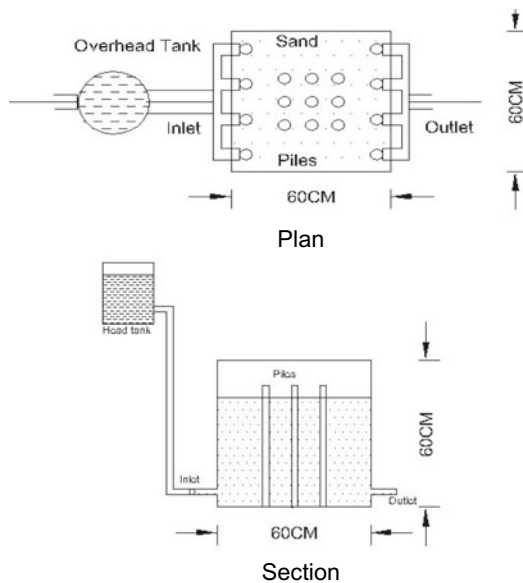


Table 1 Properties of sand

Parameter	Value
Specific gravity (Gs)	2.54
Density (kg/m ³)	2.532
Mass of sand (kg)	410.24
Permeability (m/s)	3.4722×10^{-5}
Porosity	0.3

3 Numerical Modeling

Finite element modeling of the problem was undertaken using the code FEFLOW 7.1. Results from the experiment were used for validating the model. Bulk soil and piles were modeled in three dimensions. The automatic mesh generation facility was used with refinement near the pile–soil interface. Figure 2 shows the finite element mesh. The flow system was solved by considering steady state. Phreatic surface is considered using the phreatic mode. Darcy’s equation is applied by selecting standard (saturated) groundwater flow equation. The flow direction is provided as a positive-x direction.

To calculate the hydraulic head distribution between the upstream and downstream sides of the pile area, appropriate boundary conditions are applied. Hydraulic heads equal to 0.5 m (upstream side) and 0.45 m (Downstream side) are used as the value for the first kind (Dirichlet) hydraulic head boundary condition to simulate the conditions in the experiment. Fluid transfer rate is assumed as zero at the outer sides of the model

Fig. 2 Finite element mesh for the pile–soil system (five pile case)

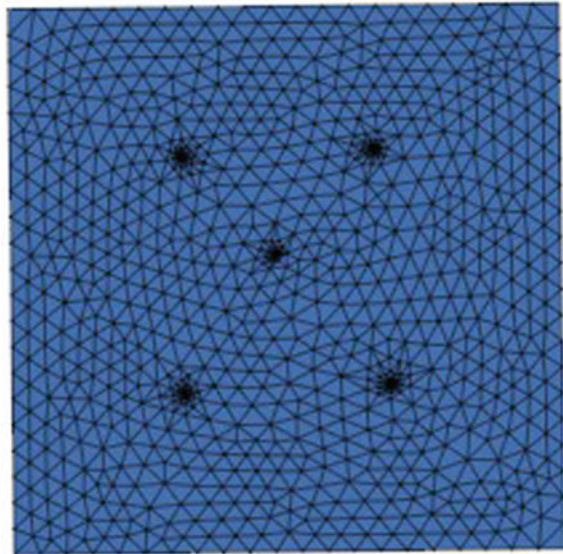


Table 2 Parameters varied

Parameters	Different conditions
No of piles	0, 5, 6, 7, 8, 9
Flow medium	Sand, Gravel
Radius of pile	R = 1.33 cm, 1.67 cm, 2.108 cm
Depth of pile	D = 50 cm, 40 cm, 35 cm
Pile spacing	5d, 4d, 3d

except for inlet, outlet, and top portions. A source was provided as 0.5 l/s and the out-transfer rate was also 0.5 l/s.

The hydraulic conductivity, porosity, source, and outflow rate were assigned to the model. The material properties were assigned to the elements. Hydraulic conductivity value of $3.4722e-05$ m/s, assigned by assuming isotropic conditions, K_{xx} , K_{yy} , and K_{zz} are same. Drain/fillable porosity value is 0.3. Hydraulic head distribution will be computed by running the steady-state model. The correct value of hydraulic head at the observation points are obtained from the hydraulic head chart. The same procedure is repeated for different conditions.

The validated finite element model was used to study the influence of certain parameters (Table 2.)

4 Results and Discussions

Variation in head difference with the number of piles is shown in Fig. 3. Figure 4 presents the same data in terms of the volume of impervious material that replaces the porous media. Results from both, finite element model and experiments, are compared in Fig. 4. The relationship shows a near-linear proportion barring the condition without piles. It is to be noted that the configuration of the piles vis-à-vis flow direction will have a bearing on the behavior.

The numerical analysis was extended to a more porous medium. The soil bed was modeled with the properties of gravel. Nine piles were used. Hydraulic conductivity value of 3×10^{-3} m/s was assigned to the porous media by assuming isotropic conditions (K_{xx} , K_{yy} , and K_{zz} assumed same). Drain/fillable porosity value was taken as 0.35. The effect of hydraulic conductivity was found minimal for the range of values considered.

Effect of pile dimensions was studied by varying the diameter. Soil bed with nine piles was simulated. From the results, the head difference increases with an increase in the radius of pile. The blocking effect due to piles increases with an increase in the radius of piles. The effect of radius of pile on the head difference is given in Fig. 5. It can be noticed that as the pile diameter increases, the head difference assumes an asymptotic value as shown. This indicates that the variation of head difference is not linear with the increasing obstructing cross section.

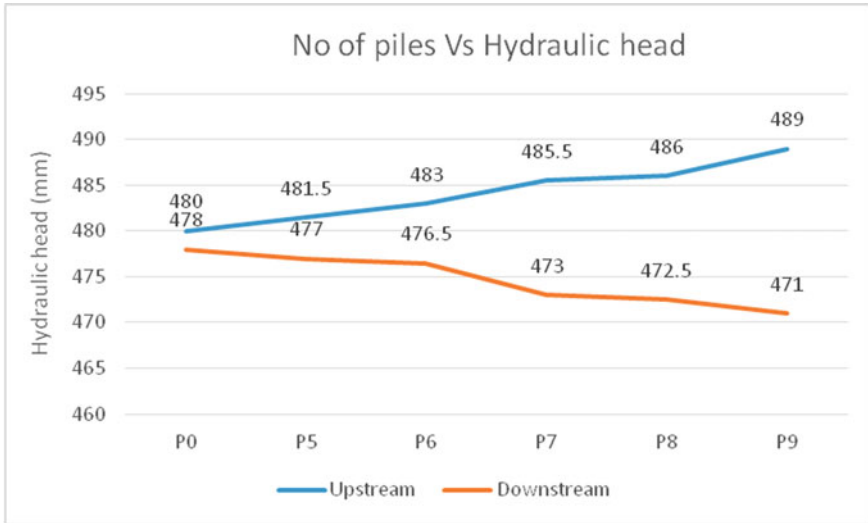


Fig. 3 Number of piles versus hydraulic head

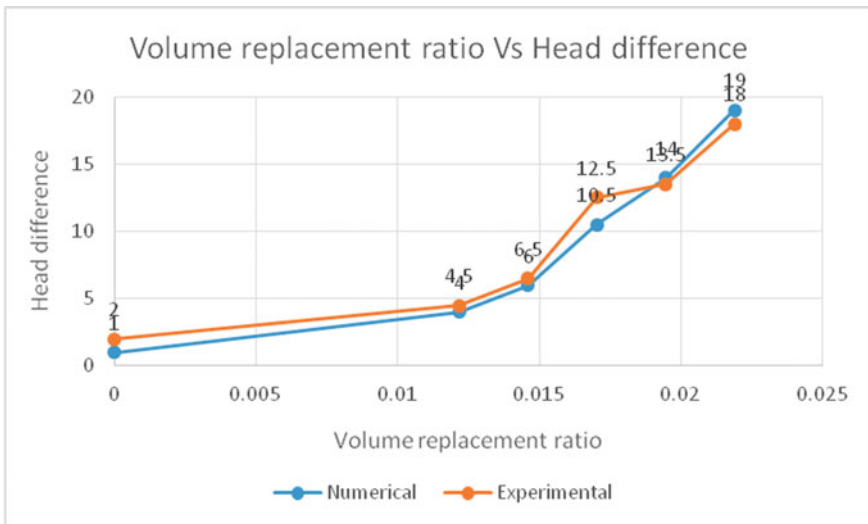


Fig. 4 Volume replacement ratio versus Head difference graph

To understand the effect of pile depth, three different pile depths were simulated. These were 0.35 m, 0.4 m, and 0.5 m, respectively. The head difference increases with an increase in the depth of pile (Fig. 6). The influence is higher at shorter depths. Very deep pile foundations may not make much difference in the case of head loss.

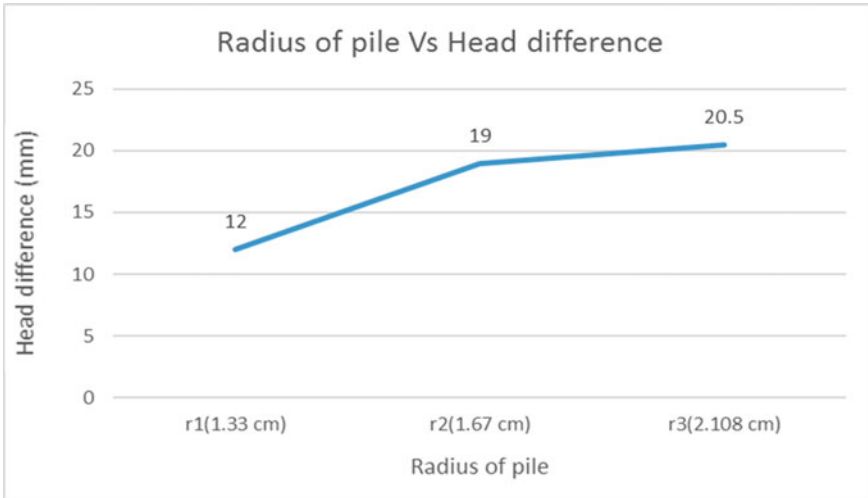


Fig. 5 Radius of pile versus head difference

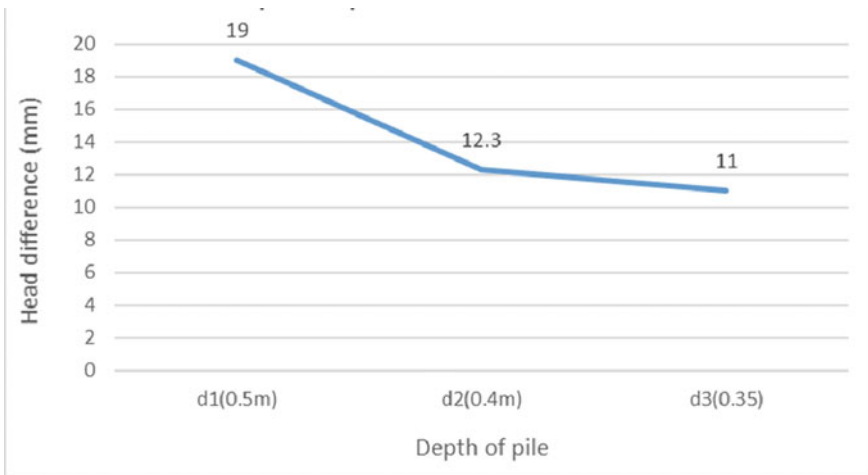


Fig. 6 Depth of pile versus head difference

5 Conclusions

Investigations on the influence of underground structures on the groundwater flow were presented. An experimental setup was fabricated for the purpose and laboratory model tests were conducted with and without embedded piles. As a part of the investigation, finite element analyses were conducted using the code FEFLOW. Results from the laboratory experiments were used to validate the finite element

model. Subsequently, finite element analyses were performed to study the influence of certain parameters. Based on the investigation, the following conclusions are drawn:

The existence of piles within the aquifer substantially reduces the head. As the number of pile increases, the head difference also increases.

When the flow medium is sand, there is considerable head difference between upstream and downstream of the pile area. When the flow is through the gravel, the blocking effect is less. As the porosity increases, the influence of substructures on groundwater flow is less.

Direction of flow is altered by the obstructing sub-structures. The hydraulic conductivity of aquifer reduces consequently. The influence of pile foundation is significant within shorter depths. Increasing depth beyond a certain value may not make much difference in the case of head loss. As the pile diameter increases, the head difference also increases. However, the incremental increase reduces at larger diameters.

References

- Attard G, Rossier Y, Winiarski T, Cuvillier L, Eisenlohr L (2016) Deterministic modelling of the cumulative impacts of underground structures on urban groundwater flow and the definition of a potential state of urban groundwater flow: example of Lyon, France. *Hydrogeol J* 24(5):1213–1229
- Colombo L, Gattinoni P, Scesi L (2016) Influence of underground structures and infrastructures on the groundwater level in the urban area of Milan, Italy. *Int J Sustain Develop Plan* 12(1):176–184
- Ding G, Jiao JJ, Zhang D (2008) Modelling study on the impact of deep building foundations on the groundwater system. *Hydrol Process Int J* 22(12):1857–1865
- Gattinoni P, Scesi L (2017) The groundwater rise in the urban area of Milan (Italy) and its interactions with underground structures and infrastructures. *Tunn Undergr Space Technol* 62:103–114
- Koskinen L, Laitinen M, Lofman J, Meling K, Mesz aro F (1996) FEFLOW: a finite element code for simulating groundwater flow, heat transfer and solute transport. *Trans Ecol Environ* 10:287–296
- Ma L, Xu YS, Shen SL, Sun WJ (2014) Evaluation of the hydraulic conductivity of aquifers with piles. *Hydrogeol J* 22(2):371–382
- Marinos P, Kavvas M (1997) Rise of Groundwater table when flow is obstructed by shallow tunnels. In: *Hydrogeology conference*, pp 49–54
- Pujades E, López A, Carrera J, Vázquez-Suñé E, Jurado A (2012) Barrier effect of underground structures on aquifers. *Eng Geol* 145:41–49
- Yihdego Y (2016) Evaluation of flow reduction due to hydraulic barrier engineering structure case of urban area flood, contamination and pollution risk assessment. *Geotech Geology Eng* 34:1643–1654

Application of Jet Grouting for Geotechnical Challenges



Akhila Manne, P. V. S. R. Prasad, and Madan Kumar Annam

Abstract Jet grouting employs the injection of a controlled amount of cement grout into the required volume of soil mass to improve the in situ ground. This ground improvement technique is applied for foundation modification and restoration works such as for waterproofing of dam foundations, confinement for excavations, underpinning of foundations, limiting subsidence over tunnels, etc. This technique can help improve the soil to support foundation loads with minimal settlement and function as excavation support or serve as both foundation and excavation support in a single operation. Such dual capability of the system increases the economic viability by saving time and cost. This paper briefly explains the limitations of various ground improvement methods, the applicability of jet grouting for various geotechnical engineering challenges, the importance of a field quality plan to achieve required design aspects. Case studies are presented that demonstrate the versatility of this emerging technology and its value as a cost-effective ground treatment tool.

Keywords Ground improvement · Jet grouting · Cement stabilization · Seepage control · Cut-off walls · Underpinning

1 Introduction

The application of ground improvement techniques to improve the bearing capacity and slope stability, limiting of settlement, to control permeability, for mitigation of liquefaction, stabilization of soils, etc., is widely known. Ground improvement techniques are classified based on the mechanism involved such as densification, consolidation, reinforcement, chemical treatment, etc.

Out of all the ground improvement methods, jet grouting is applicable for most of the geotechnical challenges such as for control of groundwater during construction, filling voids to prevent larger amounts of settlement, soil strengthening, stabilization

A. Manne (✉) · P. V. S. R. Prasad · M. K. Annam
Keller Ground Engineering, Centennial Square, Kodambakkam 600024, Chennai, India
e-mail: akhila@kellerindia.com

© Springer Nature Singapore Pte Ltd. 2020
M. Latha Gali and P. Raghuvver Rao (eds.), *Construction in Geotechnical Engineering*, Lecture Notes in Civil Engineering 84,
https://doi.org/10.1007/978-981-15-6090-3_41

of loose sands, foundation underpinning, filling voids in calcareous formations, and strengthening soils for protection during excavation.

Jet grouting technology is based on the injection of high-velocity fluids through small-diameter nozzles to erode the soil and mix it with injected grout to form a soil–cement column. The current paper focuses on the applications of jet grouting for various geotechnical challenges while discussing various case histories.

2 Ground Improvement: Challenges

One of the challenges of employing a ground improvement technique is the selection of a suitable technique. Selection of the most suitable method for ground improvement depends on the ground conditions (type of soil), project requirements (degree of improvement, depth, and extent of treatment required), and the cost involved. Various methods of ground improvement can be classified based on the mechanism as compaction/densification, consolidation, weight reduction, reinforcement, chemical treatment, thermal stabilization, and electro-treatment.

The application of compaction for ground improvement is dependent on the percent of fines in the soil, ability of the soil to dissipate excess pore water pressure, presence of boulders, utilities, and adjacent structures. Consolidation of soils is costly involving cost, time, laboratory tests, and is ineffective, if the moisture content of the soil is extremely low. Methods like reinforcement, thermal stabilization, and electric treatment are challenged by the presence of buried objects, utilities, degree of saturation of the soil, rate of groundwater movement, heat transfer in the melted soil, etc.

Effectiveness of chemical stabilization techniques is based on soil–grout compatibility and reactivity, operational parameters, column verticality, and weathering effects. Permeation grouting, jet grouting, deep soil mixing, lime columns, and fracture grouting are different types of chemical stabilization methods. Despite the challenges and limitations posed, grouting methods are applicable for most of the geotechnical challenges, various soil types, and for both new and existing structures.

3 Jet Grouting Applications

Different modes of grouting involve intrusion/penetration, displacement, permeation, and replacement (Fig. 1). Jet grouting is the most attractive of all the grouting methods due to its wide applications (Fig. 2). Jet grouting consists of disaggregation of soil and mixing it with a cementing agent or binder. This is achieved by high-pressure jets of grout comprising of a water/binder suspension injected through a nozzle, by which the soil around the drilled borehole is eroded

The eroded soil is brought into suspension and these particles are rearranged and mixed with the cement suspension, which subsequently sets and hardens to form

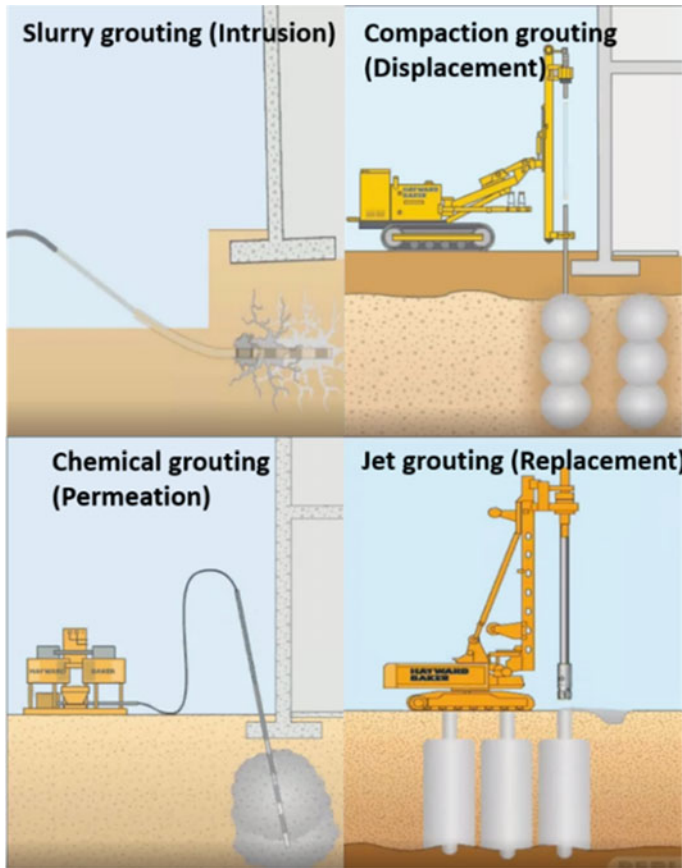


Fig. 1 Types of grouting and applications of jet grouting (credited to Hayward Baker Inc.)

a stabilized jet grout column. These columns are arranged in various patterns for different engineering challenges/applications (Fig. 2).

Jet grouting involves an injection of high-velocity fluids by different systems such as (1) single fluid: only grout, (2) double fluid: grout + air, and (3) triple fluid: water + grout + air. The choice of the system of jet grouting depends on the performance criteria required. The drilling depth and design diameter of the jet grout column are dependent on soil properties such as grain size distribution of the soil, silt and clay contents, water content, kind and amount of organics as well as types and content of the clay minerals. Apart from achieving the designed diameter, strength/stiffness of grout column, prevention of heaving, avoidance of high viscosities of the backflow material is also required.

The jet grout column characteristics such as diameter, permeability, and strength of the columns are dependent on the jetting parameters employed. These include



Fig. 2 Applications of jet grouting (credited to Hayward Baker Inc.)

rotation and extraction speeds, jetting pressure and grout flow rate, the grout mix, as well as soil type, grain size distribution, and consistency of the in situ soils.

3.1 Diameter of Jet Grout Column

Achievable column diameter can be predicted by theoretical or empirical approaches. As discussed, this is dependent on jetting parameters and in situ soil properties (Fig. 3). The column diameter can be predicted either by empirical approach or theoretical approaches. In the empirical methods, only certain operational parameters such as nozzle diameter, effect of air shroud, rotation speed, grout characteristics, and soil properties are ignored (Otterbein et al. 2008). Prediction of column diameter using empirical approaches that employ coefficients from case histories has their own

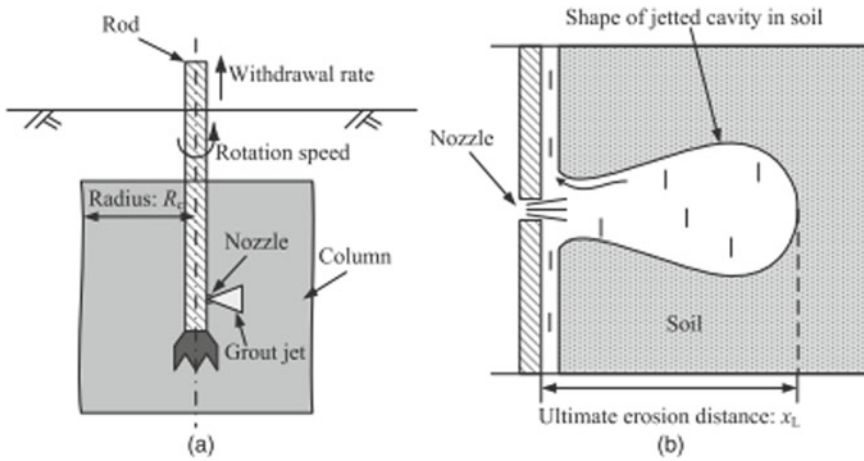


Fig. 3 Jet Grout column diameter (Shen et al. 2013)

limitations and it is necessary to confirm the predicted diameter with field tests. Tests commonly employed for confirmation of column diameter can be referred to in the quality control section.

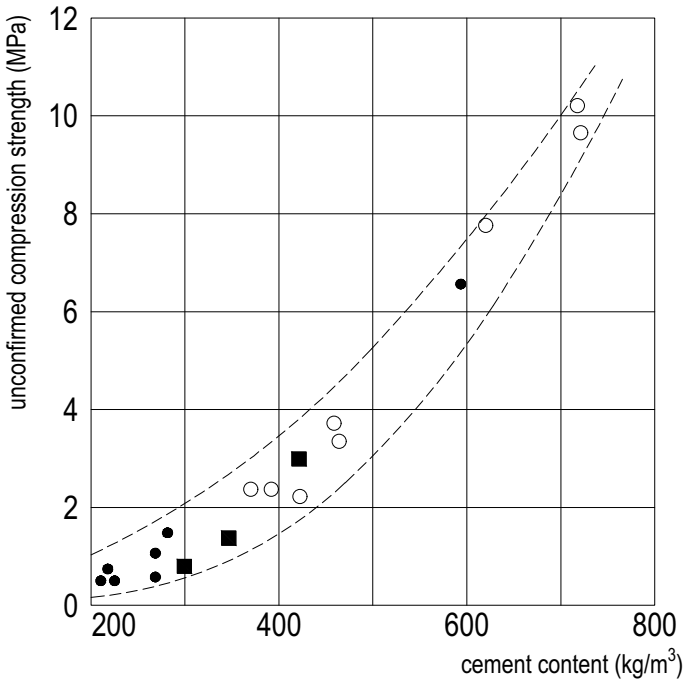
3.2 Strength

Apart from diameter, another crucial parameter is the strength of the jetted column. It is dependent on the water–cement ratio of the utilized grout and soil type. In practice, strength of the jet grout column is estimated from unconfined compression tests on samples taken from of the backflow material after a minimum of 28 days after construction. Another uncommon method is the wet sampling process where a sampler is installed on the jet grouting rig and is driven down into the fresh column to retrieve material from inside the column.

The cement content of the treated soil essentially influences its strength and is directly related to the cost. It is a trade-off between strength and project cost in design optimization. Gallavresi (1992) presented the strength of a jet grout column in correlation with cement content within the improved soil (Fig. 4).

4 Quality Control

The execution of a field trial prior to the main works is an appropriate solution to establish the jet grouting parameters, to check the diameter measurements, and, finally, to assess the strength/permeability of the treated soil. The ideal jetting parameters for



SINGLE FLUID SYSTEM:

- silty clays, clayey silts of medium low consistency
- sandy silts, silty sand of medium low consistency

THREE FLUID SYSTEM:

- peat

Fig. 4 Strength as a function of cement content (Gallavresi 1992)

a project site are established based on laboratory, field trials, and experience as well. Prior to starting production in a jet grouting project, a laboratory study and field trial are typically undertaken for the evaluation and refinement of the operational parameters and the assessment of the jet grout element considering geometric, mechanical, and permeability properties. The following are the quality control methods available (Figs. 5 and 6):

- Acoustic Column Inspector (ACI)
- Hydrophones
- Painted Bars
- Thermic Method
- Analytical Approach
- Theoretical Approach.



Fig. 5 Installed trial columns

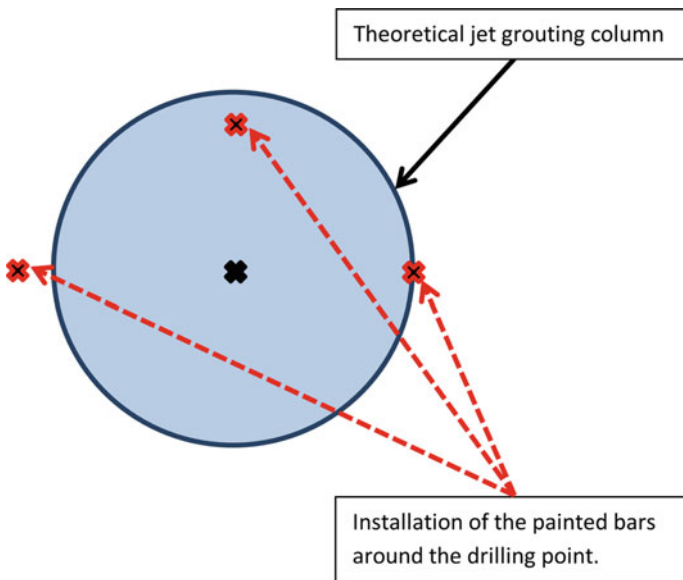


Fig. 6 Painted bars for diameter check

The predicted diameter can be confirmed on-site by measuring the diameter of the column by excavation, core drillings (vertical and inclined ones), thermic methods, painted bars, hydrophones, etc. Other uncommon methods are geophysical methods (electric cylinder method) and theoretical methods (wave analysis method, turbulent kinematic flow theory).

The grout properties such as viscosity, density, and bleed are initially tested in laboratory study before adopting the grout mix at the site. These properties are further tested at the site frequently to ensure consistency of the mix in the whole project. Jetting pressure and withdrawal rates can be monitored at the site with real time data acquisition systems (Fig. 7). Apart from these parameters, to ensure the formation of the diameter of jetted column including verticality, ACI (Acoustic column inspector) testing, Inclinometer test, painted bars (Fig. 6), and visual column inspection (Fig. 5) may appropriately be selected, based on availability. All these quality control methods are to be incorporated into the field testing plan. EN12716 provides various suggestions, recommendations, and requirements for a proper quality control plan.

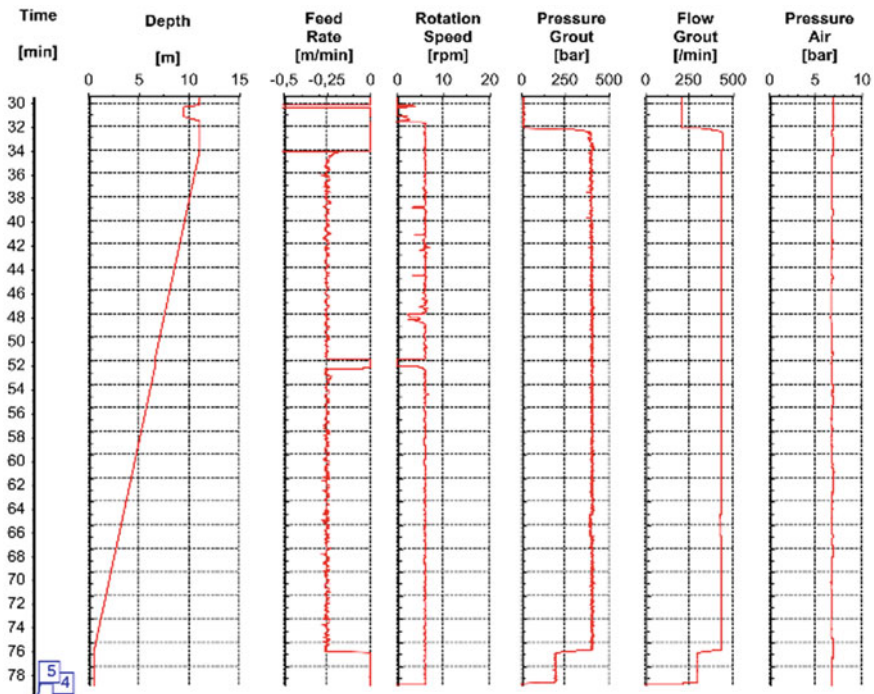


Fig. 7 Visualisation of operational parameters

5 Case Studies

Underpinning work adjacent to construction pits, foundation modification and restoration are the major applications of jet grouting. Jet grouting also facilitates tunnel constructions in loose soils. Building pit walls underpinned by grout elements and low permeable jet grout slabs enables the execution of deep building pits without the need for large scale groundwater lowering. Also, jet grouting is one of the chemical stabilization method in which environmentally safe mineral binder material can be used.

5.1 Jet Grouting for Stabilization

Underpinning. Jet grouting technology is an economic alternative to supplement conventional shoring methods such as bored pile walls, sheet pile walls. When the shoring methods are to be made in confined spaces or to carry out underpinning work in addition to the shoring, jet grouting technology is very useful. Underpinning by means of low deformation gravity walls is also used as a groundwater seepage barrier as it can be safely constructed even from confined working areas.

In Vienna, for construction of a new building of the Museum of Contemporary Art, an existing historical hall was used, and it required the excavation of ~8 m. This required the underpinning of the existing historical structure in soils with a clay content up to 23%. The project required strength of 4–5 MPa for the watertight excavation. In the lower part of the columns, cutting and grouting were performed in two steps to increase the diameter and to ensure the cement content in the columns (Fig. 8). The underpinning was created, with overcut columns from the outside and inside.

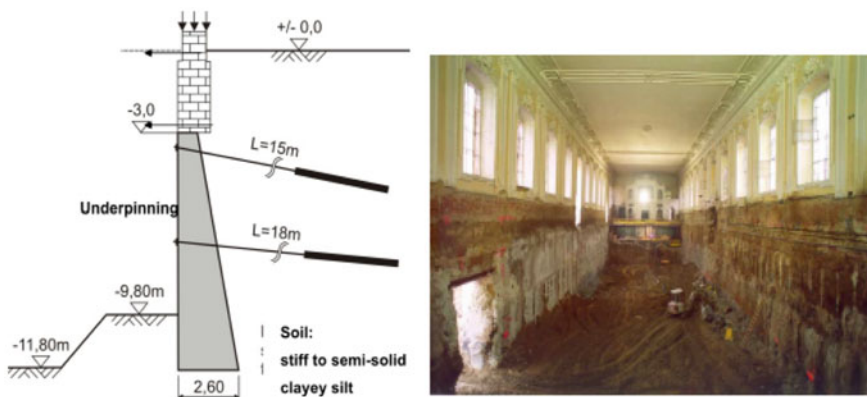


Fig. 8 Underpinning of an old hall for Museum of Contemporary Art, Vienna (Otterbein et al. 2008)

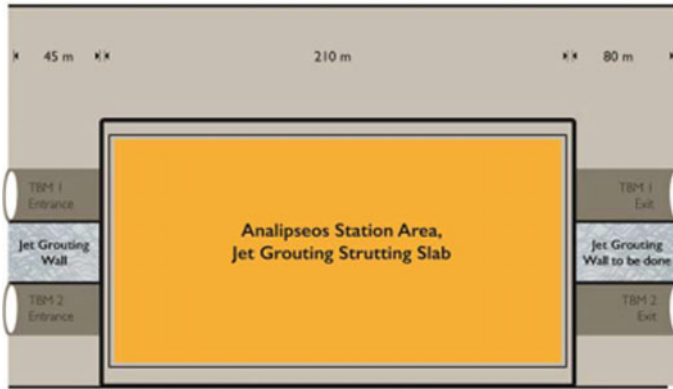


Fig. 9 Plan view of the solution proposed for Analipseos metro station

The required shape/diameter of the jet grout columns was created by optimizing the operational parameters.

Excavation Support. For the Analipseos metro station in Thessaloniki, Greece, jet grouting was used as one of the geotechnical solutions. Executional challenge is part of the project due to the presence of an adjacent road. For the safe passage of TBMs for tunnel construction, the area (45 m long and 8–25 m deep) between the TBMs required the improvement as the distance between the TBM tunnels was less than 3 m (Figs. 9 & 10). Jet grouting wall used with 190 elements for excavation support between the tunnels. About 50 of these columns were required to be installed at 40° inclinations in two directions due to the presence of adjacent road and existing service lines. Columns with diameters of 1.3–1.0 m were installed with characteristic strength of 0.9 MPa based on DIN 4093 criteria.

Jet grouting strutting slab was also installed in this project to eliminate the deformations of the diaphragm walls and neighboring buildings during the excavation phase. A total of 3,045 grout columns were installed in total (Fig. 10).

5.2 Jet Grouting for Sealing

Cut-off walls. The SMART tunnel project in Kuala Lumpur, Malaysia, was planned in a very challenging geological terrain located in public areas beneath sensitive structures like rail tracks. The terrain comprises of cavernous limestone, with highly permeable subterranean channels and cavities (Raju and Yee 2006). Such a ground profile posed a challenge for tunneling and retention works as it may lead to ground subsidence and damage to the structures above. For facilitating the tunneling and retention works, rock fissure grouting, compaction grouting, and jet grouting were carried out based on specific site conditions. Jet grouting was instituted behind some

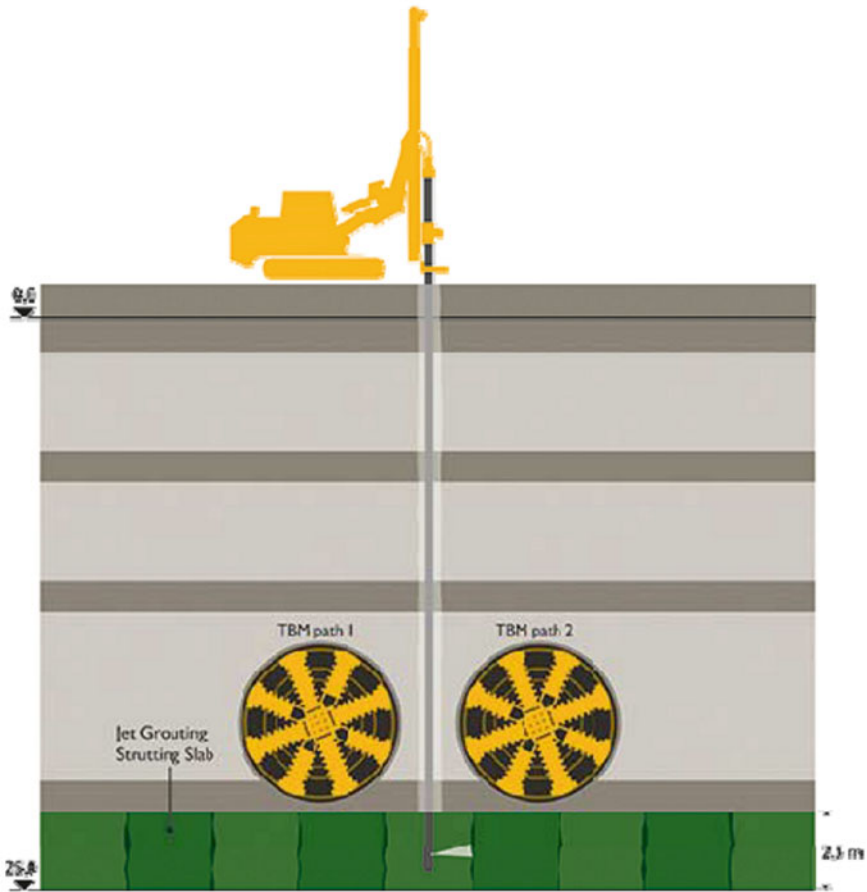


Fig. 10 Cross section of jet grouted strutting slab beneath the foundation of the metro station

of the retaining walls to minimize water seepage and to reduce lateral active earth pressures (Fig. 11). Jet grouting was effectively used for seepage control in this project.

6 Conclusion

Jet grouting technology can be used to install jet grouting elements in most soil types ranging from weak to soft marine sediments to dense sands for stabilization and sealing works of existing and new structures. The successful application of jet grouting works for various geotechnical problems depends on proper identification of the problem and subsequent implementation of appropriate mitigating measures

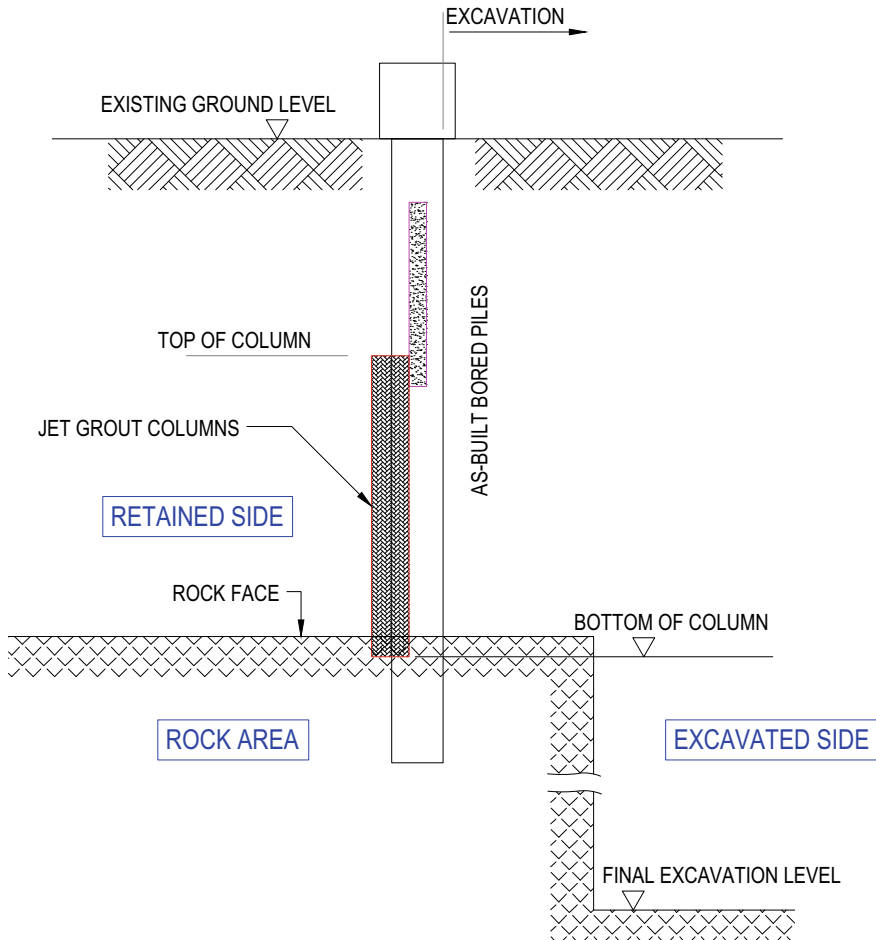


Fig. 11 Jet grouting treatment behind CBP wall (Raju and Yee 2006)

(using a suitable type of grout, grout parameters, etc.). The design must consider the possible diameters, strength, and deformability of jet grouting elements in the in situ soils. The importance of soil investigation, laboratory, field trials, and field quality plans was discussed. Since grouting works cannot be assessed visually, a strict quality control system ensures that the desired result is achieved. It is also understood from the case histories that jet grouting can be an effective solution for various applications such as foundation restoration, underpinning, tunnel protection, earth pressure relief, sealing covers/slabs, etc.

References

- Gallavresi F (1992) Grouting improvement of foundation soils. In: ASCE Conference Proceedings: Grouting, Soil Improvement and Geosynthetics, vol 1, New Orleans, pp 1–38, February 25–28
- Otterbein R, Pablick T, Trunk U (2008) Jet grouting solutions for excavations in marine sediments, In: 11th Baltic Sea geotechnical conference: geotechnics in maritime engineering, Gdansk, Poland
- Raju VR, Yee YW (2006) Grouting in limestone for SMART tunnel project in Kuala Lumpur. In: International conference and exhibition on tunneling and trenchless technology
- Shen SL, Wang ZF, Yang J, Ho CE (2013) Generalized approach for prediction of jet grout column diameter. *J Geotech Geo-environ Eng* 139(12):2060–2069

Optimal Foundation Solution for Residential Projects



B. Vani and Madan Kumar Annam

Abstract Ground improvement is an optimal foundation solution, especially for weak soils and it can be used as an alternative to complement deep foundations such as conventional piling methods. This paper presents a case history of a housing project located in Chennai, India, wherein the project site consists of soft silty clays underlain by loose to medium dense silty sands. To provide housing for the socio-economically poor, the owner decided to optimize the foundation cost. Ground improvement using vibro stone columns, dry bottom feed method was chosen to be the optimal solution and the solution saves construction time too. This technique helped to increase the bearing capacity and to reduce the total settlements and differential settlements within the acceptable limits. Various aspects of sub-soil conditions, design aspects, construction methodology, and quality control measures are discussed in detail, in this paper.

Keywords Stone columns · Ground improvement · Settlement monitoring · Vibro replacement

1 Introduction

Pile foundations are the inherent solution when shallow foundations do not satisfy the bearing capacity or performance requirements. Pile foundations are also required where ground conditions are poor and provide little capacity or stiffness to ensure short- or long-term serviceability requirements. This often occurs in urban areas where increasingly higher structures apply increasingly higher forces to the ground. Apart from deep foundations, ground improvement can be employed as an alternative optimal solution in foundations in weak soil conditions, whereby the properties

B. Vani (✉) · M. K. Annam
Keller Ground Engineering, Centennial Square, Kodambakkam 600024,, Chennai, India
e-mail: vani@kellerindia.com

M. K. Annam
e-mail: madankumar@kellerindia.com

of the ground are improved to allow structures to be founded on simple, shallow foundations.

Optimal foundation solution provides an alternative or an approach that best fits the situation, employs resources most effectively and efficiently, and yields the highest possible return under the given circumstances. The design of an optimal foundation considers the technical performance criteria to arrive at the most beneficial solution for structure under consideration. Also, optimal foundation accompanied by flexibility in design and time convenience can also provide cost-effective solution.

In the current paper, the optimal foundation solution is discussed for a low-cost housing project. The site consists of weak deposits of soils with top 6–10 m of silty clay of varying consistency and shallow groundwater table at EGL. Therefore, the intuitive foundation choice was pile foundations. However, when the cost, construction time, and environmental effects (noise pollution, ground vibrations, and carbon footprint) for pile foundations are assessed, application of ground improvement technique proved to be an optimal solution.

2 Project and Soil Conditions

Tamil Nadu Slum Clearance Board (TNSCB) proposed to construct a residential project (G + 3) at New Town, Manali in Chennai. The proposed development consists of seven blocks (block-1–block-7) which cover the total site area of 5400 m². The overall layout and elevation of the residential building are shown in Figs. 1 and 2.

The project site is underlain by 11 m of silty clay of medium to high plasticity with SPT 'N' < 10, followed by silty clay with 'N' 10–20 and then by silty sand up to the termination level (N > 30) up to 30 m. Typical soil profile for blocks 3 and 4 is shown in Fig. 3.

3 Design Approach

The performance criteria of the project necessitate the bearing capacity of the foundation soil to be ~90 kPa and settlements as per IS code (IS 1904:1986), i.e., < 100 mm. The buildings rest on rafts and when loading intensity of 90 kPa is imposed on weak ground (N < 10), they induce high settlements. From the settlement analysis, it is understood that the top 11 m soil contributed to ~90% (123 mm) of the total settlement.

Since the proposed residential building is located within the proximity of a well-developed residential locality and considering the project boundary conditions, vibro stone columns (dry bottom feed method) was selected as a viable method as an optimal foundation system.

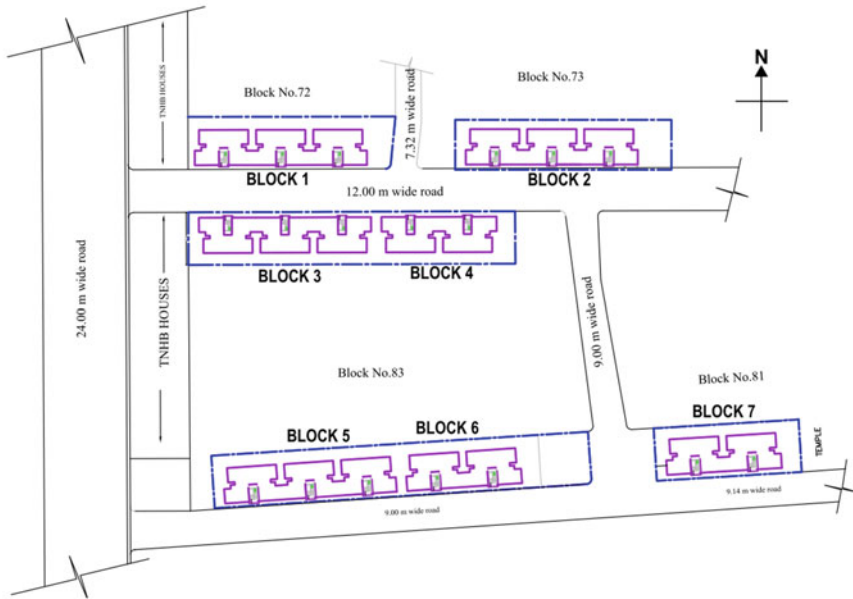


Fig. 1 Overall layout of the project site

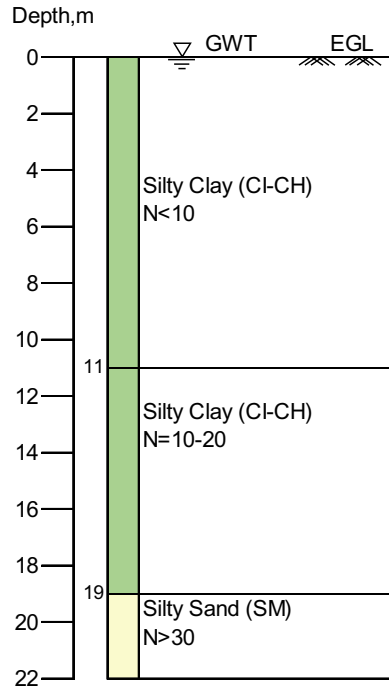


Fig. 2 Elevation view of the residential project

4 Ground Improvement as an Optimal Solution

Vibro replacement using stone columns acts as a drainage path allowing for rapid consolidation by faster dissipation of construction pore water pressure. The improved drainage capabilities of the stone column-treated ground provide

Fig. 3 Typical soil profile



much better resistance to liquefaction of the surrounding soil. Performance of this composite system consisting of stone columns as reinforcing elements and the weak soil mass that can be established theoretically and can also be established by full-size plate load tests. Priebe (1995) developed the design of vibro stone columns on a theoretical basis which can be adapted to different soil conditions.

Fig. 4 shows a schematic procedure of vibro stone column construction using the dry bottom feed method. Crushed stone aggregates according to specifications in BS EN 14731 are ejected from the tip of vibrator which accompanied by strong vibratory forces results in a compacted stone column. Stone columns are constructed from bottom to up and the diameter of stone column depends on the stiffness of surrounding soil and vibrator properties.

Ground treatment using stone columns improves the ground in the following ways:

- Stone columns are elements of greater stiffness than surrounding soil. As a result, the load-bearing capacity of stone column is greater than that of the surrounding soil. Thus, a uniformly spaced stone column arrangement will have higher bearing capacity and less settlement than that of natural ground.
- Stone columns being elements of greater permeability provides drainage path for the dissipation of excess pore water on the application of load. The vertical movement of water in soil deposit is converted to radial drainage thus increasing

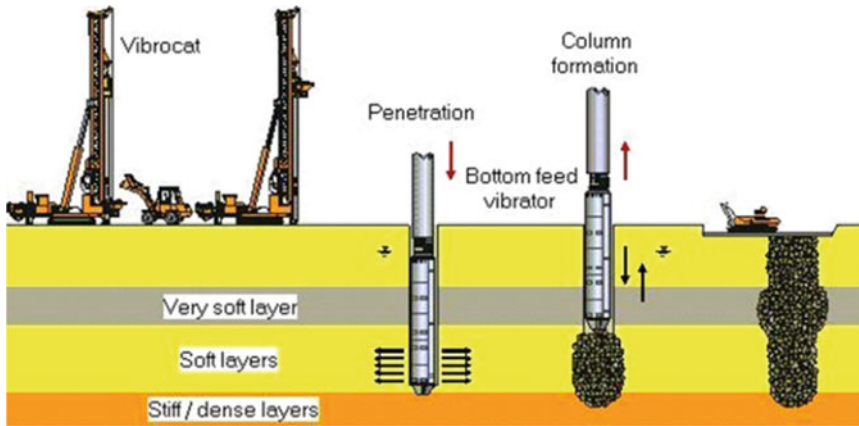


Fig. 4 Sequence of installation of dry vibro stone columns

the rate of settlement. This property of stone column is beneficial in reducing the long term settlement of footings founded on clayey soil.

Also, the installation of vibro stone columns imparts vibratory energy to soil thus densifying loose deposits of sands.

Vibro stone columns can be used most successfully where limited working space is available, especially in developed or urban areas or where no near water source can be found. It also has a built-in real-time computer monitoring system to provide quality control on compaction effort throughout the construction process. The typical cross section of the proposed project is shown in Fig. 5.



Fig. 5 Installation of vibro stone columns (dry bottom feed method)

5 Quality Control

5.1 During Construction of Stone Columns

The quality of stone columns during installation can be monitored by an automated computerized recording device fitted to the vibrocat. The recorder yields a computer record (M4 Graph) of the installation process in a continuous graphical mode, plotting depth versus time and power consumption (compaction effort) versus time for each column. The M4 record also contains details such as date of installation, start and finish times of installation, period of installation, maximum depth, compaction effort during penetration, and compaction process. These parameters allow monitoring of the quality of the stone columns being installed. Further, diameter of the stone column and consumption of backfill are continuously monitored to estimate the in situ achieved diameter. The typical cross section of the vibro stone column is shown in Fig. 6.

5.2 Post-construction of Stone Columns

Full-size field plate load testing is one of the methods to assess the performance of the improved soil treated with stone columns as per the Indian Standards IS 15284:

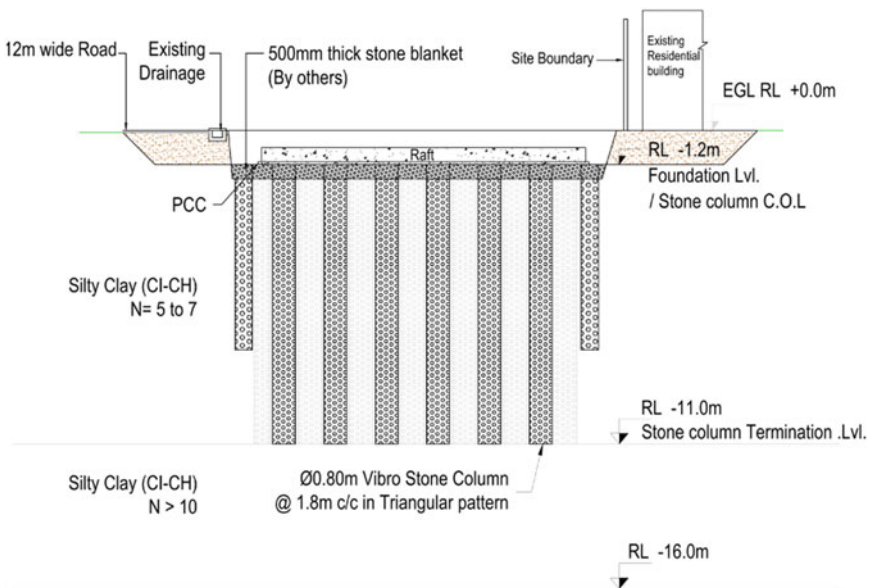


Fig. 6 Cross section of the stone column

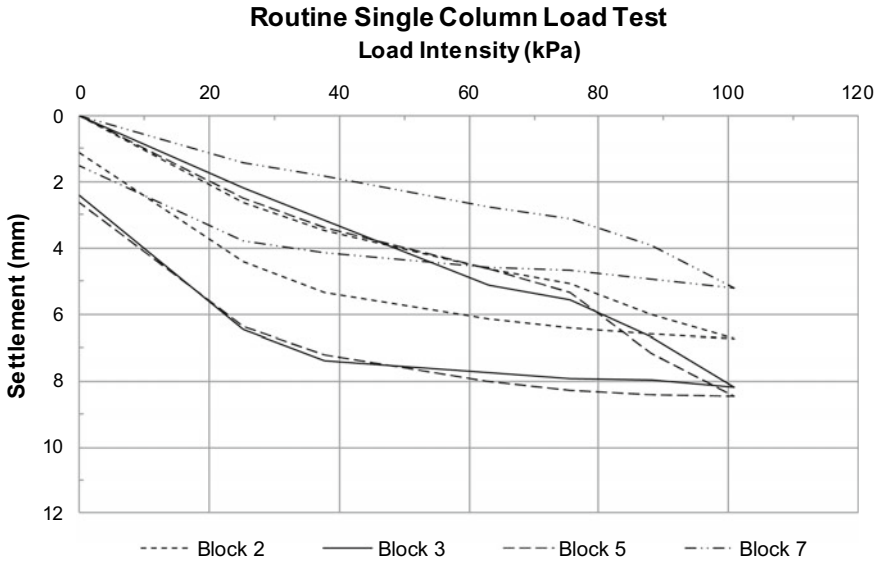


Fig. 7 Routine single-column load test summary

2003. The size of the test pad and the magnitude of the test load can vary according to the stone column layout, treatment depth, load, and type of structure.

In this project, routine single stone column load tests were performed to ascertain the effectiveness of design and performance of the ground improvement works. The observed settlements are within the acceptable limits of 75–100 mm for raft foundations according to the stipulations specified in the Indian Standard code of practice (IS 1904:1986) for the applied design load intensity of 90 kPa.

In addition to single-column load tests, group column load tests were performed. The observed settlements are within the acceptable limits for the applied design load intensity of 90 kPa. Load test results are presented Figs. 7 and 8.

To understand the post-construction performance of the structures, it is planned to conduct field settlement monitoring up to 2 years of the life of structures. The typical layout of settlement monitoring points for block 1 is shown in Fig. 9. About four locations were identified on each block to monitor settlements during and post-construction. The construction and settlement monitoring works are currently in progress.

6 Conclusion

Vibro stone columns are proved to be an optimal ground improvement solution to support residential buildings on varying weak soil deposits. It also helps in improving shear strength and reduces compressibility of the in situ soil. Vibro stone columns

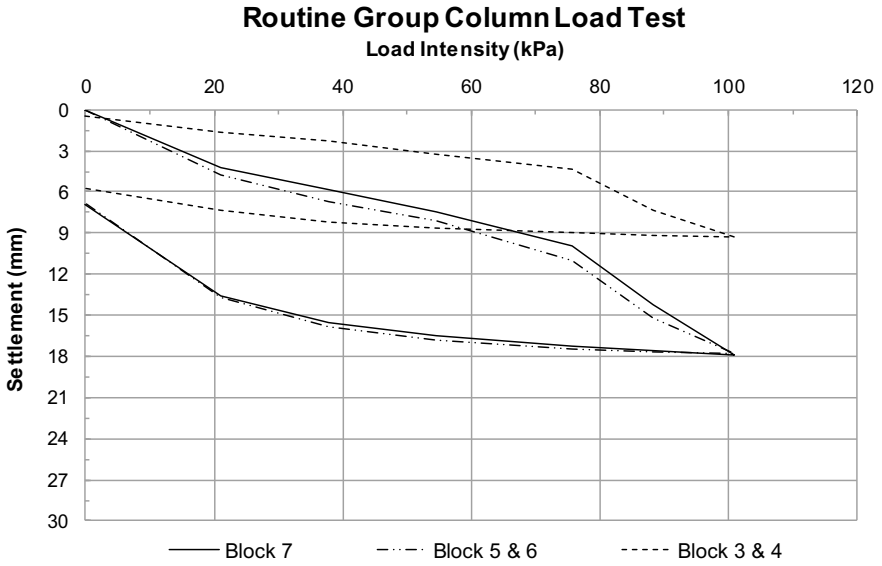


Fig. 8 Routine group column load test summary

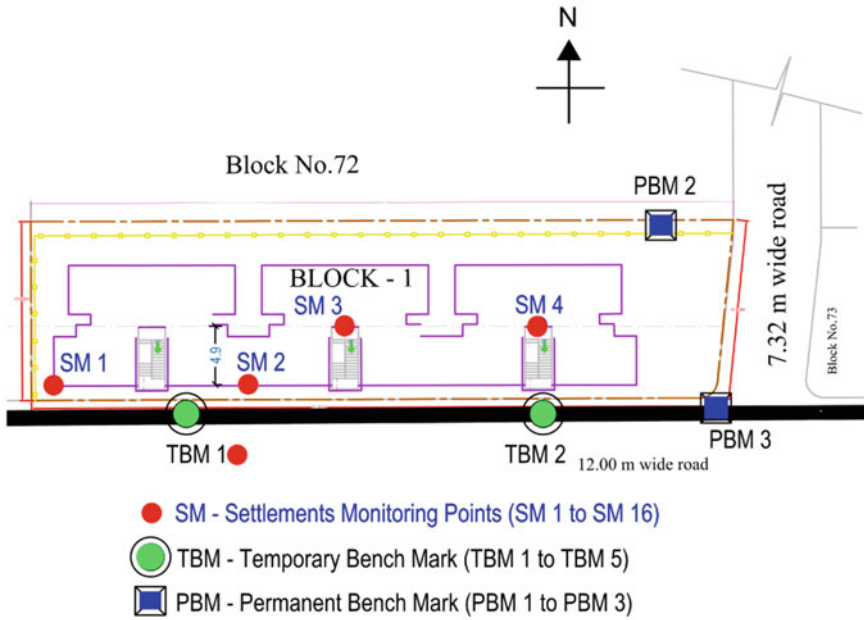


Fig. 9 Plan layout of settlement monitoring points for block 1

can accelerate the overall construction schedule and enable the completion of the project within stipulated duration.

The paper presents a case of ground improvement using vibro stone columns used for a low-cost housing project. The project site is underlain by weak and compressible soils resulting in low bearing capacity and high settlements. To match the performance criteria, pile foundations or ground improvement solutions are to be adopted. Ground improvement using vibro stone columns proved to be the optimal solution for this project. The project could be completed within 6 weeks against 6 months if pile foundations were adopted. In addition to improving the bearing capacity and reducing the settlements, the solution helped in economizing the foundation cost and optimizing construction time.

References

- BS EN 14731:2005 (2015) Execution of special geotechnical works—Ground treatment by deep vibration
- IS 15284 (Part 1) (2003) Indian standard for design and construction for ground improvement—guidelines, Part 1: stone columns
- IS 1904–1986 (2006) Code of Practice for design and construction of foundations in soils: general requirements
- IS 6403: 1981 (Reaffirmed 2002) Indian standard code of practice for determination of bearing capacity of shallow foundations
- Priebe HJ (1995) The Design of vibro replacement, Ground Engineering. GT 037-13 E

Reanalysis of Failure of Soil-Nailed Shoring System and Remedial Measures



S. Vibha, S. P. Srinivas, and G. L. Sivakumar Babu

Abstract Support systems in urban areas for temporary excavations are necessary to keep the sides of excavation nearly vertical, to minimize the excavation area and to ensure that the excavation is stable from stability as well as deformation criteria and will not lead to any damages in the surrounding area. In the present study, the paper discusses the cause for the failure of excavation of 11.65 m deep supported by nailing. The serviceability requirements and factors of safety are evaluated using finite element analysis. Further, it discusses the revised design for a temporary support system. The paper highlights the importance of pull out tests in the preliminary stage as well as during execution which are useful in design and performance assessment of the shoring system. The revised system is implemented in the field and is performing well.

Keywords Soil nailing · Failure analysis · Numerical analysis

1 Introduction

Temporary excavations are supported by various systems like retaining walls, sheet pile, micro-piling, soil nailing, bracing and many methods. Soil nailing is widely used to support temporary excavation in urban areas. Evaluation of the stability of the soil nail wall is an important aspect as the magnitude and consequence of failure can be significant.

S. Vibha (✉) · G. L. S. Babu
Department of Civil Engineering, Indian Institute of Science, Bangalore, Karnataka, India
e-mail: roshini.vibha@gmail.com

S. P. Srinivas
Wipro Limited, Bangalore, Karnataka, India

© Springer Nature Singapore Pte Ltd. 2020
M. Latha Gali and P. Raghuvier Rao (eds.), *Construction in Geotechnical Engineering*, Lecture Notes in Civil Engineering 84,
https://doi.org/10.1007/978-981-15-6090-3_43

1.1 Failure Modes of Soil Nail Walls

Failure of the soil nail wall is broadly classified into three distinct groups: external failure mode, internal failure mode and facing failure mode (FHWA 2003).

External failure modes. The development of potential failure surfaces is outside the soil-nailed region. Global failure mode, sliding failure mode and bearing failure mode are considered during the external stability analysis of the soil nail wall. Global stability refers to the overall stability of the reinforced soil nail wall mass. In this failure mode, the slip surface passes behind and beneath the soil nail wall system and the retained mass exceeds the resistance provided by the soil along the slip surface and the nails. Sliding mode of failure may occur when lateral earth pressure exceeds the sliding resistance along the base of the soil nail wall. Bearing mode of failure is triggered by an unbalanced load caused by excavation.

Internal failure modes. Important types of internal failure modes are pullout failure and tensile failure. Pullout failure occurs when bond strength between the soil and nail is mobilized or when the pullout length of the nail is insufficient. Tensile failure occurs when the axial force in the nail is greater than the tensile/rupture capacity of the nail.

Facing failure modes. Most common potential failure modes of facing failure are flexure failure and punching failure. Flexure failure is due to excessive bending of facings beyond its flexural capacity. Punching failure is due to the insufficient shearing capacity of facing elements around the nail head.

2 Literature

Pullout resistance and tensile strength of nails are important to assess the internal stability of soil nail walls. Ultimate shear strength between the nail and the surrounding soil and effective pullout length are important factors that influence the pullout resistance of nail in the soil nail wall. Field pullout tests are conducted to determine the pullout resistance of soil nails [FHWA 2003].

Pullout failure is particularly of critical importance in upper layers of the wall where the normal pressure on the reinforcement is low (Khedkar and Mandal 2009). Pullout tests are appropriate for studying the nail–soil interaction to assess the performance of the walls (Sivakumar Babu and Singh 2010).

It is found that the variability of cohesion and internal friction of soil influences the internal stability soil nail wall (Sivakumar Babu and Singh 2009a). The minimum factor of safety for the design of temporary soil nail wall [FHWA 200] is shown in Table 1.

The purpose of this paper is to highlight the importance of field pullout tests to be conducted as a preliminary test and during the execution. The importance of the pullout test is studied from analysing the failure of excavation supported by soil

Table 1 Minimum factor of safety recommended for temporary soil nail wall (FHWA 2003)

Failure mode		Symbol	Factor of safety
External stability	Global stability	FS _G	1.35
	Sliding stability	FS _{SL}	1.30
Internal stability	Pullout resistance	FS _P	2.00
	Tensile strength of nail	FS _T	1.80

nailing. Stability analysis of excavations is evaluated using finite element analysis. Pullout resistance of driven nails along with the depth of excavation were studied by simulating pullout. Further, the cause for failure of the soil nail support system and remedial measure is discussed.

3 Details of Failed Sections

It was proposed to build an office complex in Bangalore. According to the details given by the executors, the soil nail wall was designed to support excavation of 11.65 m deep. The soil nail support system is designed with driven nails of diameter 16 mm placed at 330 mm centre to centre for the first 4 m excavation depth. Twelve-metre-long grouted nails with 25 mm diameter were placed at 2 m centre to centre with excavation side supported by a micropile. Details of the section are as shown in Fig. 1. It was also noticed that Bangalore had received untimely rain during the month.

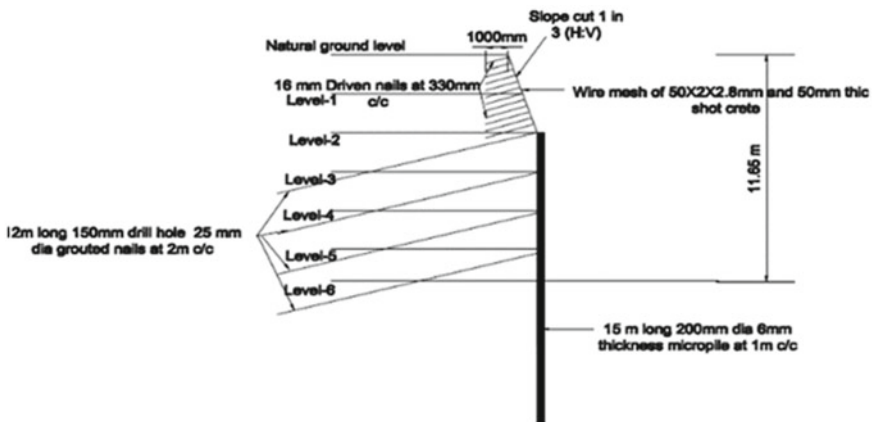


Fig. 1 Details of excavation and nails



Fig. 2 Photograph of the failed section

During the process of excavation and nailing, the soil nail support system collapsed. The depth of excavation had reached 4 m and it was found that the nails were pushed out from the soil. Figure 2 shows the photograph of the failed support system.

4 Analysis

4.1 *Maximum Pullout Capacity of Nail*

The force P (kN/m) to be mobilized along the interface of nail and soil for a unit length of the nail is given by,

$$P = \pi d(c + \sigma \tan \varphi) \quad (1)$$

where, P = pullout capacity per metre length of the nail (kN/m), d = diameter of the nail in m, l = length of the nail, C = cohesion in kPa, σ = overburden pressure in kPa and φ = angle of friction.

4.2 Numerical Analysis

In the present study, stability analysis of the section and pullout simulation is carried out by using a finite element software. Plaxis V 8 is used to evaluate displacements and global factor of safety of the sections.

Numerical Modelling. Plane state of stress is assumed for analysis. The 15-node triangular elements with medium mesh density are used for discretization. Mohr–Coulomb material model is adopted. The geometry of the section given in Fig. 1 is modelled to simulate the excavation in the field. The analysis is carried out for a cohesion value of 26 kPa, an average cohesion of 13 kPa and a reduced cohesion of 5 kPa. The properties of soil and nails used for the stability analysis and pullout simulation are shown in Table 2.

The pullout test is simulated for driven nails and grouted nails. Equal nail diameter, length and spacing are assumed for driven and grouted nails. Grout of diameter 150 mm and modulus of elasticity of 22 GPa is adopted. To simulate pullout, nodal force is applied and corresponding displacements are noted. Nodal force is increased from 5 to 75 kN. To study the variation of pullout resistance along with the depth of excavation, nodal force is applied at depths of 3, 6 and 10 m from natural ground surface. For grouted nails, equivalent modulus of elasticity (E_{eq}) is determined accounting for the contribution of elastic stiffness of both grout cover as well as reinforcement bar (Sivakumar Babu and Singh 2009b). E_{eq} is determined as follows:

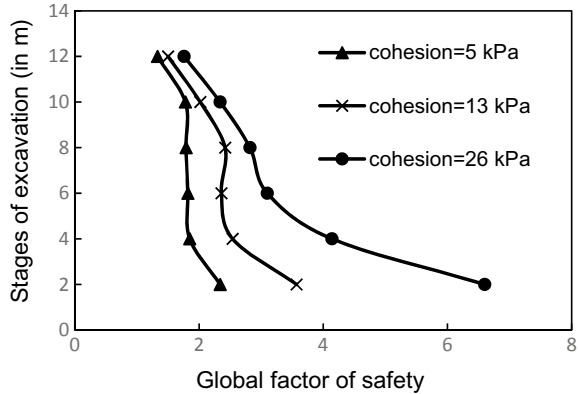
$$E_{eq} = E_n(A_n/A) + E_g(A_g/A) \tag{2}$$

where E_n is the modulus of elasticity of nails, A_n = cross-sectional area of the nail, E_g is the modulus of elasticity of grout, A = Area of cross section of grouted nails ($0.25 \cdot \pi \cdot DDH$, DDH is the drill hole diameter).

Table 2 Properties of soil and nails

Parameters	Value
Angle of friction, ϕ (Degree)	26
Cohesion, C (kPa)	10
Modulus of elasticity soil E_s (MPa)	20
Unit weight of soil γ (kN/m ³)	20
Poisson’s ratio ν	0.35
Diameter of driven nails, (mm) ¹	16
Diameter of grouted nails, (mm) ¹	25
Modulus of elasticity of nail (GPa)	200
Yield strength of nail (MPa)	415

Fig. 3 Global factor of safety



5 Results and Discussion

The stability analysis and pullout simulations for different cases as discussed above is carried out. The results and discussion is presented in the following sections

5.1 Stability Analysis of Section

Stability analysis of the section shown in Fig. 1 is carried out using Plaxis. Figure 3 shows the variation of the global factor of safety with the stages of excavation for the cohesion of 26, 13 and 5 kPa. It is evident from Fig. 3, that the global factor of safety reduces as the cohesion reduces.

5.2 Pullout Simulation

Pullout simulation is carried out at a depth 3, 6 and 10 m from the ground surface. The pullout force–displacement curve for driven nails along the depth is shown in Fig. 4. It is observed that the displacements for the corresponding pullout force are higher at shallow depth. Thus, displacement is higher at lower over-burden pressure. This is in good agreement with Khedkar (2009), that pullout resistance is lower at lower over-burden pressure. It can be concluded that pullout resistance increases at deeper depths.

Figure 5 shows the results of pullout simulations carried out for driven and grouted nails. It is noted that the pullout force required for corresponding displacements is higher in the case of grouted nails. The bond strength of the interface between the grout and soil is higher compared to the interface shear strength between nail and soil. It can be concluded that the pullout resistance of the grouted nail is higher than the driven nail.

Fig. 4 Force–displacement curve for driven nails for various depths

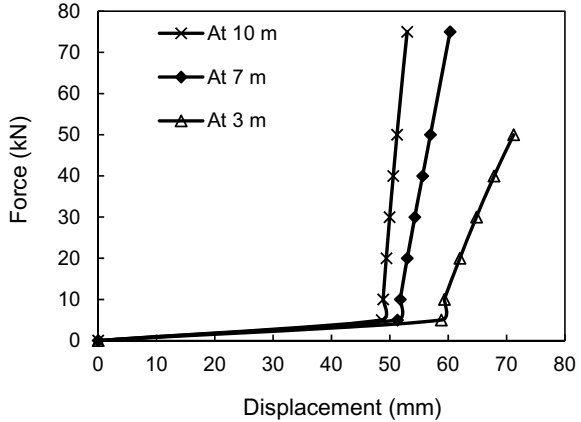
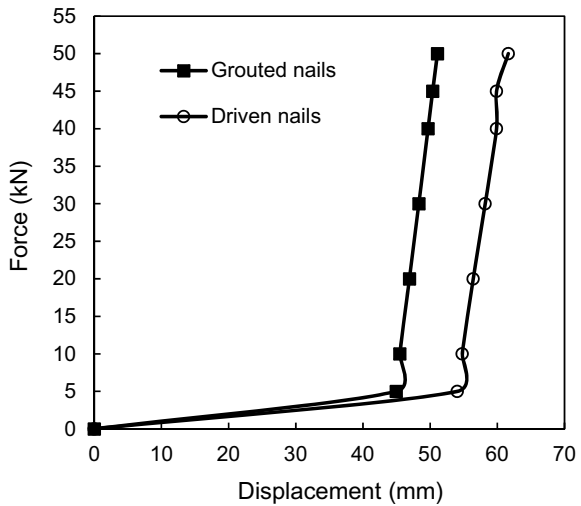


Fig. 5 Force–displacement curve for driven and grouted nails



5.3 Cause for the Failure

Minimum factor of safety against pullout (FSp) as recommended by FHWA-2003 is 2. The factor of safety against pullout is given by

$$F_{Sp} = \text{Maximum pullout capacity of nail} / \text{maximum tensile force in the nail} \quad (3)$$

The pullout capacity per unit length of the nail is calculated using equation [1]. The maximum tensile force per unit length of the nail is obtained from numerical simulations. Table 3 shows the factor of safety against pullout for driven nails at various depths.

Table 3 Factor of safety for driven nails

Depth (in m)	Maximum pullout capacity (in kN/m)		Tensile force developed (in kN/m)		Factor of safety against pullout	
	10	5	10	5	10	5
2	1.85	1.54	9.08	7.91	0.2	0.19
4	3.08	2.76	9.75	10.11	0.32	0.27

From Table 3, it can be concluded that the failure of driven nails in the field is due to a reduction in cohesion which has resulted in poor pullout resistance. The stress release during the excavation as well as rainfall is considered to contribute to the reduction in cohesion during the excavation. Thus, it is necessary to perform pullout tests as a preliminary test and during the execution.

6 Remedial Measure

As a remedial measure, the design was revised and the grouted nails were provided in place of driven nails.

6.1 Details of Revised Design

Details of the proposed nailing system are shown in Fig. 6. For the first 10 m depth of excavation, grouted nails of 20 mm nail diameter and 100 mm grout diameter and beyond 10 m depth of excavation, grouted nails of 28 mm nail diameter and 100 mm grout diameter of length 8 m is suggested. The grouted nails are placed at 1.5 m spacing. Summary of stability analysis of the revised section is given in Table 4.

From Fig. 5 and Table 4, it can be concluded that the grouted nails have a higher factor of safety against pullout and higher global factor of safety.

The revised design is implemented in the field and is performing well.

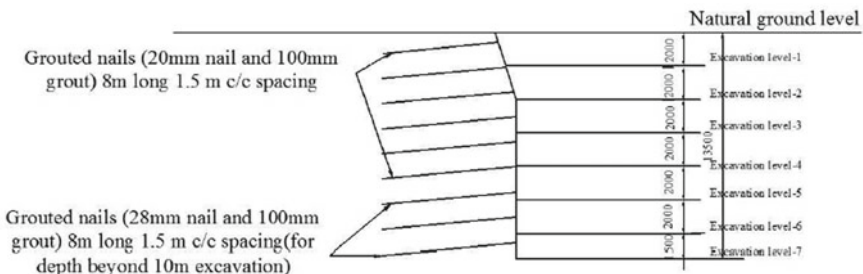


Fig. 6 Details of the revised design

Table 4 Summary of the revised section

Parameter	Value
Max. pullout capacity of nail, at 2 m (kN/m)	61.89
Max. pullout capacity of nail at, 3.5 m (kN/m)	91.11
Tensile force in nail, at 2 m (kN/m)	21.16
Tensile force in nail, at 3.5 m (kN/m)	30.67
Tensile force in nail, at 11.5 m (kN/m)	1038.48
Tensile capacity of nail (kN/m)	15393.8
Global factor of safety	1.35
Factor of safety against pullout, at 2 m	2.92
Factor of safety against pullout, at 3.5 m	2.97
Factor of safety against rupture, at 11.5 m	14.82

7 Conclusions

In the present study, stability analysis of a soil nail wall and remedial measure for failed soil wall is presented. The cause for the failure is ascertained. It is determined by carrying out stability analysis for the given section for three different cohesion values. The response to pullout is studied for driven nails and grouted nails by simulating pullout in a finite element software. From the above discussions, it can be noted that the field pullout tests are necessary as a primary test and during the execution. It is important to note that cohesion has a significant influence on the global factor of safety and pullout resistance. Pullout resistance increases at deeper depths. A higher factor of safety should be adopted in sites where the design relies on cohesion value and prone to change in the water table.

References

- Babu G, Singh V (2010) Soil nails field pullout testing: evaluation and applications. *Int J Geotech Eng* 4(1):13–21
- FHWA (2003) Geotechnical engineering circular No. 7—soil nail walls. Report FHWA0-IF-03-017, U.S. Department of Transportation. Federal Highway Administration, Washington D. C
- Khedkar M, Mandal J (2009) Pullout response of cellular reinforcement under low normal pressures. *Int J Geotech Eng* 3(1):75–87
- Sivakumar Babu GL, Singh VP (2009a) Reliability analysis of soil nail walls. *Georisk Assess Manag Risk Eng Syst Geohazard*, 3(1):44–54
- Sivakumar Babu GL, Singh V (2009b) Simulation of soil nail structures using PLAXIS 2D. *Plaxis Bulletin*, Spring issue
- Sivakumar Babu GL, Singh V (2010) Soil nails field pullout testing: evaluation and applications. *Int J Geotech Eng* 4(1):13–21

Determination of Compacted Dense Sand Layer Thickness on Loose Sand Using Odemark's Method for Design of Shallow Foundation



Partha Pratim Biswas, Manoj Kumar Sahis, and Agnimitra Sengupta

Abstract Bearing capacity of loose sand can be improved by replacing the soil with a suitable thickness of dense sand layer for laying shallow foundations. Present paper deals with a methodology for calculating the optimum depth of such compacted dense sand required for strip footing. In this paper, load on the foundation has been considered to act on a two-layered system. Primarily an imaginary depth of homogeneous loose sand has been determined at which its bearing capacity becomes equal to the vertical stress developed at the same depth using Terzaghi's theory and stress dispersion approach. The depth of loose sand thus obtained has been transformed into a two-layered system using Odemark's method to determine the thickness of the dense sand layer. It has been found that such depth of dense sand bed increases with the increase in foundation load and footing width but reduces with an increase in friction angle of the top layer.

Keywords Odemark's method · Terzaghi's method · Bearing capacity · Angle of friction · Dense sand

1 Introduction

Shallow foundation is often found to be cost effective for construction of low to medium storey building, provided the soil below the footing yields a better load-bearing capacity. Therefore, the geotechnical properties of subsoil on which the foundation rests are important to determine the bearing capacity. It is relevant to note that the bearing capacity of shallow foundation is largely governed by the shear

P. P. Biswas · M. K. Sahis (✉) · A. Sengupta
Jadavpur University, Kolkata 700098, India
e-mail: manojshahis@gmail.com

P. P. Biswas
e-mail: drppb@yahoo.in

A. Sengupta
e-mail: senguptaagni@gmail.com

strength parameters of soil lying within the influence zone of footing. Such influence zone below the base level of foundation has been analyzed by Prandtl (1920), Terzaghi (1943), and Meyerhof (Meyerhof 1963; Meyerhof 1974; Meyerhof and Hanna 1978) and Madhav and Sharma (1991). All such analysis reveal that the nature of the failure of the foundation in terms of shear failure was considered in respective research works to find out the extent of failure zone below the footing with the variations in soil properties with different boundary conditions. In this backdrop, the concept of influence zone of footing in the subsoil needs to be examined judiciously to understand the depth of active soil mass which takes part in the stability of the foundation system in terms of shear and settlement failure. Moreover, the factors which may affect the depth of the influence zone are also important for evaluation of the performance of shallow foundation during its service life.

2 Objective

Presence of weak and loose granular soil within the influence zone below shallow foundation affects adversely the load-carrying capacity of the soil. In order to increase the bearing capacity of such soil, filling of dense compacted layer of granular soil may be done after excavating and removing the loose granular soil up to a specific depth. Therefore, the determination of the optimum depth of dense compacted sand bed becomes an important factor to ensure the stability of the foundation system and the economy of the project. In this backdrop, present paper aims to find out a methodology for the determination of the optimum depth of compacted sand bed to be placed on the top of loose sand deposit as a platform for placing shallow foundation.

3 Proposed Model

In this paper, load on foundation has been assumed as uniformly distributed load acting on a strip footing which rests on a compacted sand bed followed by a loose sand layer in the form of a two-layered system. Primarily an imaginary depth of loose sand layer at which the bearing capacity of soil becomes equal to the vertical stress was developed using Terzaghi's method and stress dispersion approach as recommended by Biswas et al. (2017). The depth of loose sand thus obtained is the depth below which the stress due to foundation load becomes less than the bearing capacity of soil and above which the soil will be subjected at a larger stress than the bearing capacity, thereby indicating the zone of failure. The depth of loose sand within the zone of failure needs to be transformed to a suitable thickness of compacted sand with a better load carrying capacity. Odemark's method (Ullidtz et al. 1998) is generally used to transform a two-layered system into a homogenous system considering the elastic moduli of the layers and the thickness of the top layer. In the present analysis, the depth of homogenous loose sand layer has been transformed into a two-layered

system by reverse application of the Odemark’s approach. The mathematical model used in the present work has been illustrated below with relevant assumptions made in the model.

If B is the width of the footing and h is the imaginary depth at which the bearing capacity of loose sand layer with a friction angle of ϕ_2 becomes equal to the vertical stress due to the surface load intensity (q) on a strip footing resting at ground surface, the following correlations may be developed.

The vertical stress at a depth h below the base of the footing with q intensity using 2:1 method of stress dispersion may be expressed as in Eq. 1.

$$\sigma = \frac{qB}{B + h} \tag{1}$$

However, the bearing capacity of loose sand at a depth h may be determined using the dispersed width of foundation at depth h equal to $(B + h)$ and are as follows.

$$q_u = 0.5\gamma_2(B + h)N_{\gamma(2)} \tag{2}$$

Equating Eqs. 1 and 2, the following correlation can be established.

$$\frac{qB}{B + h} = 0.5\gamma_2(B + h)N_{\gamma(2)} \tag{3}$$

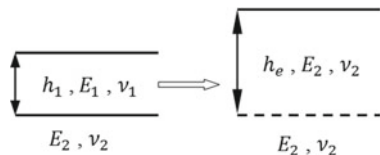
Now, the depth h thus obtained from Eq. 3 has to be transformed into a two-layer system using reverse Odemark’s approach.

4 Odemark’s Method for System Transformation

Odemark’s method assumes that the stress and strain below a layer depend on the stiffness of that layer only. If the thickness, elastic moduli, and Poisson ratio of the layers are changed but the stiffness remains unchanged, then the stress and strains below the layer should also remain unchanged. The transformation of layers can be done in the following manner as shown in Fig. 1 by Odemark’s approach.

In the two-layered system as proposed in the present model, the top layer is the compacted sand with modulus E_1 , thickness h_1 , and ν_1 as Poisson ratio resting on a

Fig. 1 Transformation of a layered system by Odemark’s Method



loose sand layer with modulus E_2 , and a Poisson ratio of ν_2 , which has been shown in Fig. 1.

Transformation of such two-layered system can be done with a concept of equivalent thickness (h_e) with a homogeneous modulus (E_2) and with a Poisson ratio of ν_2 , which can be expressed as

$$h_e = fh_1 \sqrt[3]{\frac{E_1(1 - \nu_2^2)}{E_2(1 - \nu_1^2)}} \quad (4)$$

$$h_1 = \frac{h_e}{f} \sqrt[3]{\frac{E_2(1 - \nu_1^2)}{E_1(1 - \nu_2^2)}} \quad (5)$$

If the Poisson ratio of soil of two layers are assumed same, then the equation may be expressed as

$$h_1 = \frac{h_e}{f} \sqrt[3]{\frac{E_2}{E_1}} \quad (6)$$

In the present problem, the thickness of the homogeneous loose sand (h_e) may be obtained by an analytical approach using Eq. 3.

Hence, the thickness of the top layer in a two-layered system, h_1 can be determined from Eq. 6 if the elastic moduli of compacted sand and loose sand layers are known.

In this paper, the ratio of elastic moduli of the compacted sand bed and the loose sand has been considered as the respective ratio of the ultimate bearing capacity (Bureau of Indian Standards IS: 6403 1981) of soil with strip footing, which means

$$\frac{E_1}{E_2} = \frac{0.5\gamma_1 BN_{\gamma(1)}}{0.5\gamma_2(B+h)N_{\gamma(2)}} \quad (7)$$

where N_{γ_1} and N_{γ_2} are the bearing capacity factors, and γ = unit weight of soil.

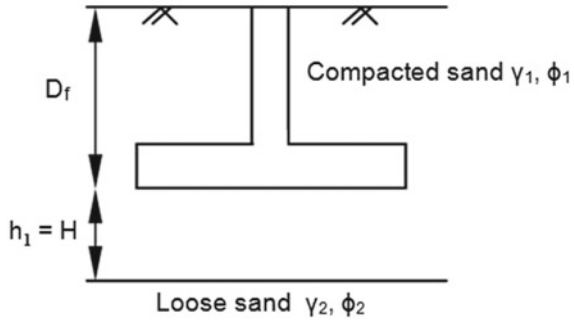
Therefore,

$$h_1 = \frac{h_e}{f} \sqrt[3]{\frac{0.5\gamma_2(B+h)N_{\gamma(2)}}{0.5\gamma_1 BN_{\gamma(1)}}} \quad (8)$$

5 Validation

The ultimate bearing capacity of shallow foundation as strip footing of width B placed on a stronger sand layer underlain by a weak loose sand that extends to great depth as shown in Fig. 2 was proposed by Meyerhof and Hanna (1978).

Fig. 2 Dense sand layer underlain by loose sand



The basic principle of this theory assumes if the top dense sand layer is relatively thick then the failure wedge is localized inside the dense sand. In such case,

$$q_{u(t)} = \gamma_1 D_f N_{q(1)} + \frac{1}{2} \gamma_1 B N_{\gamma(1)} \tag{9}$$

However, if the thickness of the dense sand layer (H) below the foundation is relatively thin, the theory assumes that the failure in soil would take place by punching in the dense sand layer followed by a general shear failure in the weaker loose sand layer. In such case, the ultimate bearing capacity for the foundation may be expressed as

$$q_u = q_{u(b)} + \gamma_1 H^2 \left(1 + \frac{2D_f}{H} \right) K_s \frac{\tan \phi'_1}{B} - \gamma_1 H \leq q_{u(t)} \tag{10}$$

$$\text{where } q_{u(b)} = \gamma_1 (D_f + H) N_{q(2)} + \frac{1}{2} \gamma_2 B N_{\gamma(2)} \tag{11}$$

Considering the footing to lie on top of the dense sand bed, i.e., $D_f = 0$, the ultimate bearing capacity can be obtained from Eq. 10 using Eqs. 9 and 11 as mandatory boundary conditions. From these equations the value of H can be determined if the friction angles of the dense and loose sand layers are known. The thickness thus obtained is the optimum thickness required to prevent punching shear failure of the top soil in a two-layered system and are presented in Table 1. In all the equations, N_{γ_1} and N_{γ_2} are the Meyerhof's bearing capacity factors for stronger and weaker sand layers respectively, and unit weight of the stronger and weaker soils are γ_1 and γ_2 , respectively. The punching shear coefficient K_s may be obtained from the correlation recommended by Meyerhof and Hanna for a ratio as shown in Eq. 12.

$$\frac{q_1}{q_2} = \frac{\gamma_1 N_{\gamma(1)}}{\gamma_2 N_{\gamma(2)}} \tag{12}$$

Table 1 Comparison with Meyerhof’s study

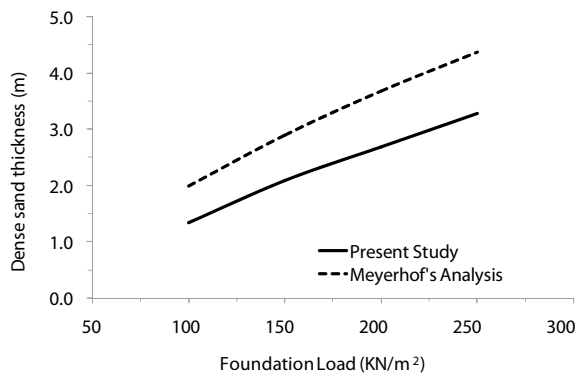
Angle of internal friction (ϕ)	Compacted sand layer thickness (m)	
	Meyerhof	Present study
25°	0.99	0.97
30°	2.48	2.09
35°	4.76	3.49
40°	7.67	5.36

6 Results and Discussions

It has been found that the thickness of the compacted sand layer required to prevent punching failure of the top soil increases with increase in its angle of internal friction as shown in Table 1. Higher angle of friction implies increased bearing capacity and hence the load required to induce its punching failure is higher, which in turn requires increased sand layer thickness to reduce its intensity to the bearing capacity of the lower loose sand. The data as output in Table 1 has been found with input data of friction angle and bulk density of loose soil as 20° and 18.5 kN/m³ whereas the friction angle of dense sand varied from 25 to 40° for a strip foundation with a width of 2.0 m, and load being equal to the bearing capacity of the top layer. But the comparison with the results of Meyerhof shows that the divergence of the required dense sand thickness on top increases with the increase in friction angle as evident in Table 1. However, when the friction angle is relatively small the results obtained in present work are comparable with Meyerhof’s estimate. Moreover, it is to be noted that the assumptions made by Meyerhof was from the concept of punching shear failure below footing if the dense sand thickness is comparatively small.

It is interesting to note that the required thickness of sand bed increases with the increase in foundation load intensity when other parameters remain unchanged. Figure 3 represents such comparison with a strip foundation of width of 2.0 m, the friction angle, and bulk density for loose soil as 10° and 18.5 kN/m³ and those for

Fig. 3 Variation of compacted sand layer thickness with foundation load intensity



the dense sand as 30° and 19.0 kN/m^3 , respectively. The load intensity on footing was considered from 100 to 250 kN/m^2 in present study. The required thickness of compacted dense sand for a footing is less than that needed using the approach suggested by Meyerhof.

It has been observed that the thickness of dense sand on loose sand deposit reduces with the increase in angle of internal friction of either of the sand layers where, the width of foundation remains constant as shown in Fig. 4. Higher angle of internal friction implies higher load-bearing capacity, hence reduced thickness of compacted sand will be required to prevent failure.

Similar trend has been observed in Fig. 5 for variation of dense sand layer thickness when the angle of friction for the loose sand was kept constant. It is also observed that the thickness of compacted sand on loose sand increases with increase in footing width and vice versa, since footing width influences the 20% stress contour depth from its base. The more is the width of footing; more will be depth of influence. The zone of soil within this depth contributes in shear and settlement failure. However, the effect of variation in foundation width on sand layer thickness reduces when the compaction of sand is better with an increased value of friction angle.

Fig. 4 Variation of compacted sand thickness with angle of internal friction (Foundation width = 2 m, Load = 300 kN/m^2)

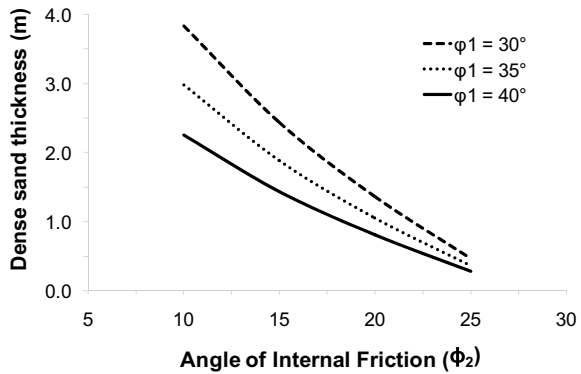
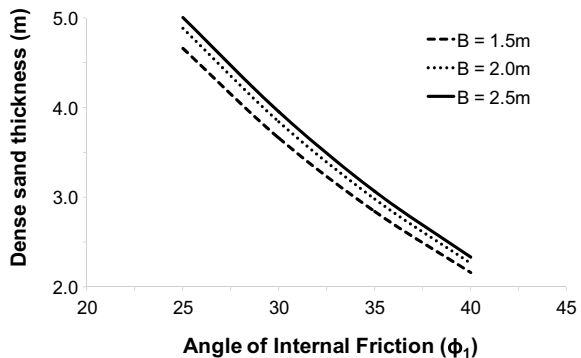


Fig. 5 Variation of compacted sand thickness with angle of internal friction ($\phi_2 = 10^\circ$, Load = 300 kN/m^2)



7 Conclusions

It has been found that the depth of sand bed increases with the increase in foundation load intensity provided the width of the footing and properties of loose sand remain unchanged. If the friction angle of loose soil increases then the requirement of dense sand layer on its top decreases. Moreover, it has been found that the thickness of compacted sand on weak loose sand deposit reduces with the increase in angle of internal friction of dense sand and vice versa. In the present work, the thickness of compacted sand has also been found to increase with the increase in foundation width. It is relevant to note that the requirement of dense sand layer thickness is comparatively less than the theoretical approach recommended by Meyerhof.

Keeping this in view, the proposed methodology may be considered as a useful tool in the area of ground improvement technique for replacement of soft soil below footing for laying shallow foundation using compacted sand bed.

References

- Biswas PP, Sahis MK, Sengupta A (2017) Determination of compacted granular layer thickness on soft clay using Odemark's method for design of shallow foundation, Indian Geotechnical Conference, IIT Guwahati, India
- Bureau of Indian Standards (1981) IS 6403: Code of practice for determination of bearing capacity of shallow foundations
- Meyerhof GG (1963) Some recent research on the bearing capacity of foundations. *Can Geotech J* 1:16–26
- Meyerhof GG (1974) Ultimate bearing capacity of footings on sand layer overlying clay. *Can Geotech J* 11:223–229
- Meyerhof GG, Hanna AM (1978) Ultimate bearing capacity of foundations on layered soil under inclined load. *Can Geotech J*, 565–572
- Madhav MR, Sharma JSN (1991) Bearing capacity of clay overlain by stiff soil. *J Geotech Eng ASCE* 117(12):1941–1948
- Prandtl (1920) Lecture at the international centre for theoretical physics. Trieste, Italy
- Terzaghi K (1943) Bearing capacity. *Theor Soil Mech*. John Wiley & Sons, New York
- Ullidtz P (1998) Modelling flexible pavement response and performance, pp 38–41

Reliability Analysis on Fatigue and Rutting Failures of Flexible Pavement with the Variation of Surrounding Atmospheric Condition and Mix Design of Bitumen



Sourav Mitra, Saurav Pal, and Pritam Aitch

Abstract Reliability is defined as the probability that the pavement's traffic load capacity exceeds the cumulative traffic loading on the pavement during a selected design life. Fatigue and rutting in flexible pavement are serious mode of failure in high-temperature areas including India and may lead to early failure in pavement. Performance of pavement depends upon various factors such as subgrade support, pavement composition and its thickness, traffic loading and environmental factors. So it is evident that reliability is very much affected by variation of selected temperature range which is shown in this study. The fatigue life decreases with the increase of temperature. It is noticed that slight changes in volume of air voids and volume of bitumen have huge influence on the fatigue life. Temperature variation also affect the rutting life significantly which is well proved in this study. The probability of exceeding the design value is determined and this Reliability is plotted with some parameters.

Keywords Reliability · Variation of surrounding temperature · Fatigue failure · Rutting failure · Resilient modulus

1 Introduction

Indian road network of 61 lakh km is second largest in the world. India and other developing countries have realized the importance for providing good transportation facilities. Due to rapid socioeconomic development and industrialization in India is

S. Mitra (✉) · S. Pal
MeghnadSaha Institute of Technology, Kolkata-700150, India
e-mail: mitra.sourav60@gmail.com

S. Pal
e-mail: saurav.pal@msit.edu.in

P. Aitch
Jadavpur University, Kolkata-700032, India
e-mail: pritamaitch@gmail.com

necessary to implement modern design techniques from time to time for smooth and safe network. In India highways are predominantly constructed using bituminous materials. During last decade significant studies were carried for better characterization of bituminous mixes in order to build long-lasting pavements. Fatigue occurs when a material is subjected to repeated loading and subsequent unloading. Fatigue is usually associated with tensile stresses but fatigue cracks have been reported due to compressive loads. Rutting in pavement is a serious mode of distress beside fatigue in bituminous pavement in high-temperature areas including India and may lead to premature failure in pavements and results in early and costly rehabilitation. The fatigue and rutting performances are very much uncertain due to many uncertainties related to pavement life parameters and traffic condition. Premature distress and related difficulties in pavement result in a financial burden on tax payer. Hence, these difficulties need to be properly addressed through evaluation.

Reliability is a measure of the probability that a pavement is expected to provide satisfactory service to the users throughout its design service life.

In this paper the predicted pavement life is considered as strain and stiffness function of bituminous pavement, which is related to surrounding temperature and environment. Since the temperature is variable, it follows that the pavement life would also exhibit variable nature. The Reliability may then be interpreted as a probability of the pavement structure exceeding some level of predicted pavement life. Therefore, incorporation of Reliability in the analysis of behavior of flexible pavement is the focus of this paper.

2 Definition of Reliability

The concept of reliability could be used to quantify the uncertainty associated with design predictions. The application of reliability in pavement design is to quantify the probability that a pavement structure will perform, as intended, for the duration of its design life. Reliability analysis allows for a rational accounting of the variability in the design parameters. Kulkarni (1994) defined reliability in terms of traffic:

“To provide uniformity, pavement design reliability is defined as the probability that the pavement’s traffic load capacity exceeds the cumulative traffic loading on the pavement during a selected design life.”

The above statement may be expressed mathematically as:

$$R = P[N > n] \quad (1)$$

where “ N ” is the traffic load capacity of the pavement structure and “ n ” is the actual number of load applications. Specifically, reliability is the probability that the number of allowable traffic loads exceeds the number of applied traffic loads.

3 Fatigue and Rutting Failure as Per IRC-37:2012

3.1 Fatigue Life

When load is repeated, the tensile strain developed at the bottom of the bituminous layer develops micro-cracks, which go on widening and expanding till the load repetitions are large enough for the cracks to propagate to the surface over an area of the surface. The phenomenon is called fatigue (or fracture) of the bituminous layer and the number of load repetitions in terms of standard axles that cause fatigue denotes the fatigue life of the pavement.

As per IRC: 37-2012 a flexible pavement is modeled as an elastic multilayer structure. Tensile strain, ϵ_t , at the bottom of the bituminous layer which causes fatigue failure and the vertical subgrade strain, ϵ_v , on the top of the subgrade which causes rutting failure which is shown in Fig. 1. According to IRC 37:2012 fatigue life is calculated from the equation given below,

$$N_f = 0.5161 \times C \times 10^{-04} \times \left[\frac{1}{\epsilon_t} \right]^{3.89} \times \left[\frac{1}{M_R} \right]^{0.854} \tag{2}$$

where

$$C = 10^M \tag{3}$$

$$M = 4.84 \left[\frac{V_B}{(V_A + V_B)} - 0.69 \right] \tag{4}$$

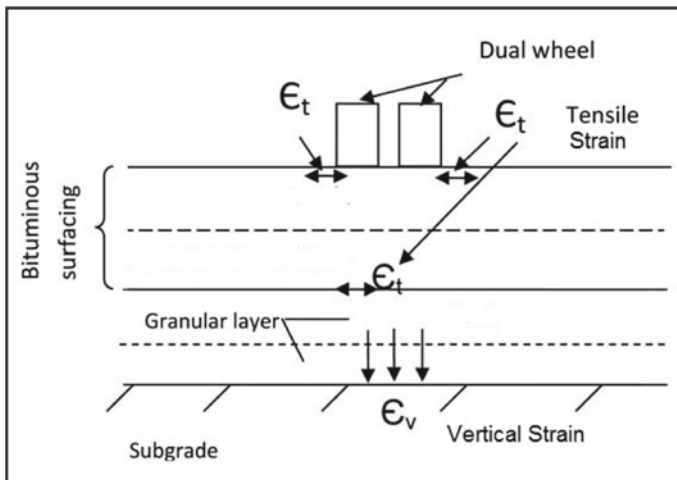


Fig. 1 Different layers of a flexible pavement

N_f = Fatigue life in a number of standard axles,

ε_t = Maximum Tensile strain at the bottom of the bituminous layer, and

M_R = Resilient modulus of the bituminous layer,.

V_A = Volume of Air voids in mix (in percentage).

V_B = Volume of bitumen in mix (in percentage).

Equation 2 is recommended for use for traffic greater than 30 msa where richer bituminous mixes with stiffer VG 40 binder should be used. The volume of stiffer grade bitumen is possible to be increased by slightly opening the grading. The Indian Roads Congress (IRC-37:2012) recommends that the designer should consider these aspects with a view to achieving a high fatigue life of bituminous mixes.

3.2 Rutting Life

Rutting is the permanent deformation in pavement generally takes place longitudinally along the wheel path. Like the fatigue model, rutting model also studies at 80 and 90% reliability levels. The two equations are given below, respectively:

$$N_R = 4.1656 \times 10^{-08} \left[\frac{1}{\varepsilon_v} \right]^{4.5337} \quad (5)$$

$$N_R = 1.41 \times 10^{-08} \left[\frac{1}{\varepsilon_v} \right]^{4.5337} \quad (6)$$

where,

N_R = rutting life in number of standard axles, and

ε_v = Vertical strain in the subgrade.

The model considers the vertical strain in subgrade as the only variable for rutting, which is a measure of bearing capacity of the subgrade.

4 Details of Mechanistic Empirical Method of Design

The method used in data analysis is mechanistic empirical method. IITPAVE software has been used for the computation of stresses and strains in flexible pavements. In this approach, the pavement is idealized as a layered elastic structure consisting of three to four layers made up of bituminous surfacing, base, sub-base, and the subgrade.

Table 1 Resilient modulus of VG 40 bitumen mix, MPa for different temperature

20 °C	25 °C	30 °C	35 °C	40 °C
6000	5000	4000	3000	2000

Each layer is characterized by its resilient modulus (M_R), Poisson’s ratio (ν), and thickness. All the reliability computations in this design methodology have been performed using the computer program. The detailed procedures are listed below,

Step-1: CBR Value

In real life CBR value is taken from soil investigation report but in this case any real-life example has not been considered and 3%, 6%, and 9% CBR values are taken for design purpose.

Step-2: Temperature

Five temperatures (20 °C, 25 °C, 30 °C, 35 °C, and 40 °C) as data and five cumulative standard axle load values (50, 75,100,125, and 150 msa) are taken into account for this study.

Step-3: Layer thickness

The purpose of M-E flexible pavement design is to determine the thickness of each pavement layer to withstand the traffic and environmental conditions during the design period. Design thickness of BC, DBM, Base, Sub-base, and Subgrade are calculated using design catalogue given in IRC: 37-2012.

Step-4: Resilient Modulus

Resilient Modulus of different grades of Bitumen varies with temperature drastically, which is given in Table 1. VG-40 bitumen is used in this paper for bituminous layer.

Resilient modulus (M_R) for granular sub-base and base is given by the following equation

$$M_R = 0.2h^{0.45} \times M_{Rsubgrade} \tag{7}$$

The relation between resilient modulus and the effective CBR is given as:

$$M_R(\text{MPa}) = 10 \times \text{CBR for CBR} \leq 5 \tag{8}$$

$$= 17.6 \times (\text{CBR})^{0.64} \text{ for CBR} > 5 \tag{9}$$

Step-5: Poisson’s Ratio

Poisson’s Ratio is different for different layers of pavement, according to IRC 37:2012 the Poisson’s Ratio is given below in Table 2.

Table 2 Poisson's ratio for different layers

Layer	Poisson's ratio
Bituminous layer	0.35 (For temperature up to 35 °C) 0.50 (Higher temperature)
Granular base and sub-base	0.35
Subgrade layer	0.40

Step-6: Strain

Tensile strain, ε_t and vertical subgrade strain, ε_v are calculated from IITPAVE software. A satisfactory pavement design can be achieved through iterative process by varying layer thickness (± 5 mm here). In this study Monte Carlo Simulation is used for Reliability analysis. The number of Monte Carlo cycles is used in design is 10,000.

Step-7: Fatigue and rutting life calculation

As discussed earlier, IRC 37:2012 has introduced fatigue model equation (Eq. 2) and a rutting model equation (Eq. 6). For fatigue life calculation bituminous mix design value is important. Here volume of air voids (V_A) is used as 4% and volume of bitumen (V_B) is used as 12.5%. Rutting variability is most affected by the stiffness of the subgrade material and the thicknesses of the overlying materials. By applying Monte Carlo Simulation fatigue life and rutting life values are calculated for different temperature, different CBR value, and different msa.

Step-8: Reliability calculation

According to the definition of reliability the number of times fatigue life or rutting life exceeds the design value (msa value) that is termed as Reliability of the pavement at a particular temperature. So, Fatigue and rutting Reliability of a particular pavement can be found out for different temperature conditions, allowing different limits of thickness. Finally, the probability of exceeding the design value is determined.

5 Results

Reliability value is calculated for fatigue and rutting deformation for flexible pavement by use of IITPAVE software which helps in the calculation of the tensile strain at the bottom of the bituminous layer and the compressive strain at the top of the subgrade soil. These computed strains are incorporated in the fatigue models and rutting models to estimate the pavement life for different temperatures. The results are discussed below.

5.1 Fatigue Reliability for Different Temperatures

Fatigue life (in standard axes) is determined from Eq. 2 for specified numbers of cycles (10,000 numbers of Monte Carlo cycles). The number of times, the fatigue life (in msa) exceeds the design life (in msa) expressed in percentage, is numerically defined as Reliability.

At 20 °C and 25 °C for different msa values (50, 75, 100, 125, and 150msa) fatigue reliability comes as 100%.

It is noticed that fatigue reliability is decreased when temperature value increased, for 30 °C temperature fatigue Reliability value is less than 50% and for 35 °C and 40 °C it remains zero. For different msa values fatigue Reliability value reduces drastically.

For 3, 6, and 9% CBR and different msa values fatigue Reliability values are taken and plotted.

Three figures (Figs. 2, 3, and 4) show fatigue Reliability variation for different temperature and CBR values. It shows nearly same results for these msa values. It is observed from Figs. 2, 3, and 4 for temperature of 20 °C and 25 °C the reliability value is 100% but when temperature is 35 °C and 40 °C Reliability value becomes zero. The properties of the bituminous mixtures used in flexible pavement are greatly influenced by environmental temperature.

Fig. 2 Variation of reliability with temperature for 50 msa value

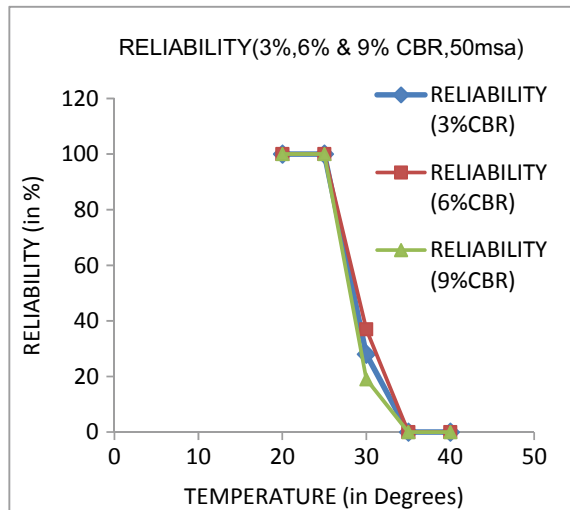


Fig. 3 Variation of reliability with temperature for 100 msa value

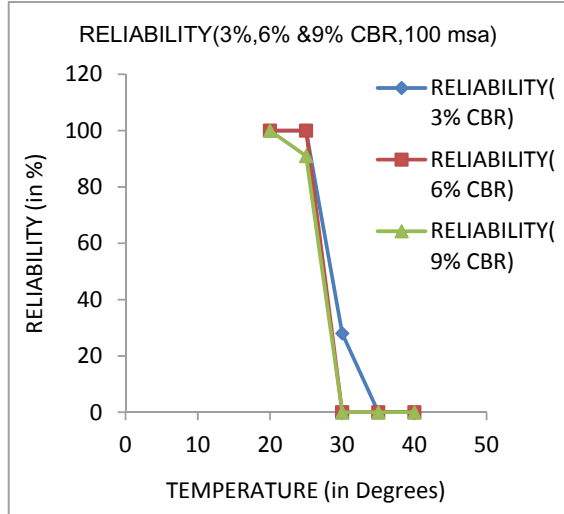
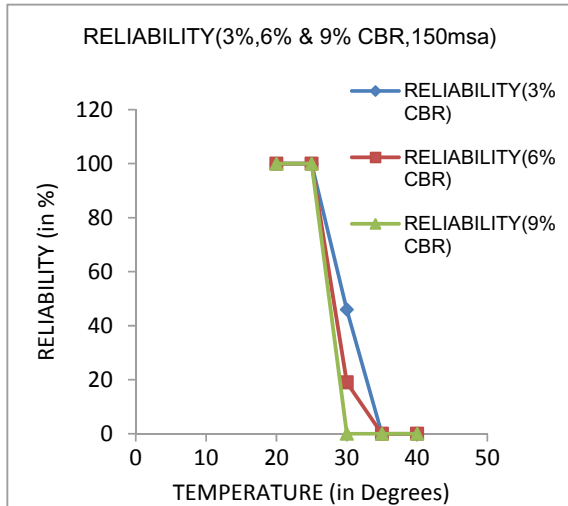


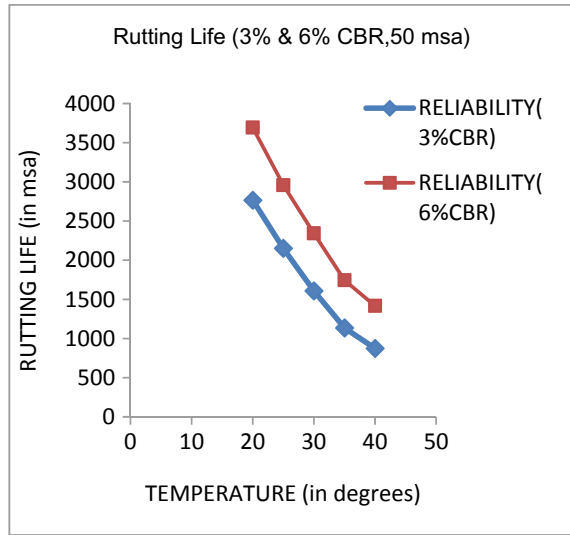
Fig. 4 Variation of reliability with temperature for 150 msa value



5.2 Rutting Reliability

Rutting Reliability value is also calculated for five different temperatures (20 °C, 25 °C, 30 °C, 35 °C, and 40 °C) and 3% CBR and 6% CBR value. It can be seen from Fig. 5 that rutting life is very much greater than the considered MSA value (50, 100, and 150 msa) and it is also decreased when temperature is increased. Rutting failure is mostly depended upon the stiffness of the subgrade material and the thicknesses of the overlying materials. So from above result it can be seen that

Fig. 5 Variation of rutting life with temperature for 50 msa value



for perfectly compacted subgrade rutting is not a major criterion for the selected temperature range.

6 Discussions

It is shown that the fatigue life decreases with the increase of temperature. Fatigue life can be increased by changing the mix design value. Mix design can be reformed by changing the values of Volume of Air Voids (V_A) and Volume of Bitumen (V_B) which is shown in Table 3. Specified range of V_A is 3–5% in India. In this study, 90% reliability is considered to be good fatigue reliability for all important roads.

Table 3 Recommended values of volume air voids (V_A) and volume of bitumen (V_B) for 90 to 100% reliability

CBR	20 °C and 25 °C	30 °C	35 °C	40 °C
3%	$V_A = 4\%$ and $V_B = 12.5\%$	$V_A = 3.5\%$ and $V_B = 13.5\%$	$V_A = 3\%$ and $V_B = 14\%$	$V_A = 3\%$ and $V_B = 17\%$
6%	$V_A = 4\%$ and $V_B = 12.5\%$	$V_A = 3.5\%$ and $V_B = 13.5\%$	$V_A = 3\%$ and $V_B = 14\%$	$V_A = 3\%$ and $V_B = 17\%$
9%	$V_A = 4\%$ and $V_B = 12.5\%$	$V_A = 3.5\%$ and $V_B = 13.5\%$	$V_A = 3\%$ and $V_B = 14\%$	$V_A = 3\%$ and $V_B = 17\%$

Table 3 shows that slight changes in volume of air voids (V_A) and volume of bitumen (V_B) have huge influence on the fatigue life. For example if bitumen content is increased from 0.5 to 0.6% above the optimum bitumen content obtained by Marshall Test and air void is reduced to the minimum acceptable level of 3% and volume of bitumen increased to the level of 17%, the fatigue life also increased which means that low air voids and higher bitumen content is necessary for the bituminous layer to obtain fatigue-resistant mix. Mix design is the key factor to enhance the fatigue life.

The rutting failure also affected with temperature and moisture condition, higher temperature leads to cause more rutting. If rutting failure occurs it is not possible to change the subgrade layer frequently so rutting life should be much higher than the considered design life to avoid early failure. However Rutting is dependent on strength of the subgrade, but for perfectly compacted subgrade, rutting is not found to be a major criterion for the selected temperature range.

7 Conclusions

Based upon the research findings presented in this report, the following conclusions and recommendations may be made:

1. For most practical design methodologies, the number of Monte Carlo cycles should be set at minimum 5,000 which were set at 10,000 in this study for better results.
2. The input parameters having the greatest influence on the fatigue performance variability are bituminous modulus and thickness.
3. Temperature variation also affects the rutting life. However rutting is dependent on subgrade strength of the soil, but for perfectly compacted subgrade, rutting is not found to be a major criterion for selected temperature range.
4. Indian maps are advised to split into some temperature zones for flexible pavement design as temperature variation can affect reliability analysis drastically. So it is recommended that design catalogue should have been different for different temperature zones.

It is difficult to make firm recommendations regarding acceptable levels of design reliability until the design procedure is applied on a wider basis. The recommendations made by AASHTO Guide (1993) may be used as points of reference. However, the designer must ultimately make the decision-based upon the available study results on design practices. One of the fundamental principles of M-E design is that it must be calibrated to local conditions. Further investigations and calibration are required to fine-tune the design procedure.

References

- AASHTO Guide (1993) For Design of Pavement Structures, American Association of State Highway and Transportation Officials
- IRC 37:2012 (2012) Guidelines for the design of flexible pavement
- Kulkari RB (1994) Rational approach in applying reliability theory to pavement structural design. Transportation Research Record No. 1449, Transportation Research Board, pp 13–17

Application of Under Sleeper Pads to Enhance the Sleeper-Ballast Interface Behaviors



Sinniah K. Navaratnarajah and Buddhima Indraratna

Abstract Railway industries are facing greater technical and economic challenges to increase the train speeds and hauling capacity of the trains to cope up with the growing population and increasing traffic problems. However, increasing dynamic stresses from the passage of faster and heavy haul trains progressively degrades the ballast layer and other track substructure layers which inevitably leads to excessive settlement and track instability. Nowadays, heavier concrete sleepers used in most of the ballasted tracks are subjected to even greater stresses and faster deterioration. Under Sleeper Pads (USPs) are resilient pads installed at the bottom face of concrete sleepers to increase the degree of vertical elasticity in the track structure and also with the intention of enhancing sleeper–ballast interaction to minimize dynamic stresses and subsequent track deterioration. In this study, cyclic loads from fast and heavy haul trains have been simulated using a large-scale Process Simulation Prismatic Triaxial Apparatus (PSPTA) to investigate the performance of ballast improved by the USPs. The laboratory results indicate that the inclusion of USP at the harder interface of concrete sleeper-ballast significantly curtails the stresses transmitted and minimizes the amount of plastic deformation and degradation of ballast.

Keywords Ballast · Cyclic load · USP · Deformation · Degradation

1 Introduction

The rail networks in many countries play a prominent role in the conveyance of commuter transport and bulk freight. Nowadays, the railway industries are placing greater emphasis on implementing fast and heavy haul corridors to deliver more

S. K. Navaratnarajah (✉)

Department of Civil Engineering, Faculty of Engineering, University of Peradeniya, Peradeniya 20400, Sri Lanka
e-mail: navask@eng.pdn.ac.lk

B. Indraratna

Centre for Geomechanics and Railway Engineering, University of Wollongong, Wollongong City, NSW 2522, Australia

© Springer Nature Singapore Pte Ltd. 2020

M. Latha Gali and P. Raghuvver Rao (eds.), *Construction in Geotechnical Engineering*, Lecture Notes in Civil Engineering 84,
https://doi.org/10.1007/978-981-15-6090-3_46

619

efficient and cost-effective services. However, the deterioration of a rail track due to large dynamic wheel loads is inevitable over the years and one that leads to more frequent high-cost maintenance. The degradation of the ballast layer in the rail track substructure contributes to a large percentage of maintenance costs, apart from affecting the longevity and stability of a track. Besides, this problem is more critical in isolated track locations where the ballast is in direct contact with much stiffer interfaces such as bridge decks and tunnel inverts and in locations where heavier concrete sleepers are used. One measure used to minimize track deterioration in these isolated places is the use of artificial inclusions such as resilient rubber elements at the aforesaid hard interface locations. The use of soft synthetic rubber pads in track foundations to alleviate track damage has become increasingly popular in recent times (Nimbalkar et al. 2012; Sol-Sanchez et al. 2015; Indraratna et al. 2014; Zhai et al. 2004; Navaratnarajah and Indraratna 2017; Navaratnarajah and Indraratna 2018). Among the wide range of mitigation techniques, one option could be to modify the vertical stiffness of track by attaching resilient rubber pads under the sleeper called Under Sleeper Pads (USPs) especially for heavy-duty precast concrete sleepers (Sol-Sanchez et al. 2015; Indraratna et al. 2012; Loy 2008; Navaratnarajah et al. 2016). Apart from bringing back the track resiliency, USPs increase the contact area between concrete sleeper and ballast which leads to a reduction in stress transmitted from the sleepers to the substructure layer and helps to distribute the wheel load uniformly to more numbers of adjacent sleepers (Abadi et al. 2015; Sol-Sanchez et al. 2014; Navaratnarajah et al. 2018). These sleeper pads also even out the differences in stiffness along transition zones and turnouts (Loy 2009).

Elastic elements in track have been used in European countries for various specific solutions. Swiss National Railways (SBB) and German Railway Company (DB) recommended increasing track flexibility using rubber elements such as USPs in tracks where the thickness of the ballast layer is less than 300 mm. At the beginning of the 1990s, the French National Railway Company (SNCF) started using a thin layer of polyurethane under the sleepers to reduce the contact stress between sleeper and ballast (Bolmsvik 2005). Since 2005, the Austrians have used USPs as a standard component in turnouts to improve the quality of the track and reduce the growth of rail corrugations on curves with small radii in category A tracks (Schneider et al. 2011). An LCC analysis on the Austrian Railway showed that USPs significantly reduced the depreciation, operational hindrance, and maintenance costs leading to a reduction of the average annual cost of the track (Schilder 2013). When soft USPs were installed under hard concrete sleepers, it reduced the ballast degradation and extended the intervals needed to tamp the ballast, and increased the service life of ballast by at least 100%, both of which resulted in enormous savings in maintenance expenditure (Marschnig and Veit 2011). Lakuši, et al. (2010) also stated that ballast tamping intervals can be 2–2.5 times longer when USPs are used in heavy haul rail tracks.

Only limited studies have been carried out to investigate geotechnical behaviors such as stress-strain and the degradation aspects of ballast under dynamic loads when the ballast is stabilized with rubber mats (Nimbalkar et al. 2012; Indraratna et al. 2014; Sol-Sanchez et al. 2014; Johansson et al. 2008; Nimbalkar and Indraratna

2016). Therefore, this study aims to evaluate the geotechnical behaviors and the benefits of ballast stabilized with USPs on concrete sleepers under repeated cyclic loading. The large-scale laboratory testing program in this current study consisted of two loading frequencies of 15 and 20 Hz (approximate train speeds of 110 and 145 km/h, respectively) and two-axle loads of 25 and 35 t (simulating a passenger and a heavy haul freight trains, respectively) to examine how USPs would help to mitigate the excessive irrecoverable ballast deformation, ballast stresses, and particle breakage.

2 Prototype Process Simulation Apparatus

Large-scale testing apparatus with a specimen of actual particle size provides more insightful and tangible practical outcomes to geomechanical problems. In this study, laboratory simulation of a prototype track substructure using a novel Process Simulation Prismoidal Triaxial Apparatus (PSPTA) was used to understand and assess the stress-strain and degradation behavior of ballast, and how USPs influence these behaviors. This unique facility was designed and built at the University of Wollongong to examine the integrated behavior of actual track materials such as rail, sleeper (i.e., concrete sleeper in this study), ballast, subballast, subgrade, and any geosynthetic inclusions (i.e., the USP in this study) used in a ballasted track foundation diagrammatically represented in Fig. 1a (modified from (Navaratnarajah and Indraratna 2017)). This prototype apparatus shown in Fig. 1b has special features; (i) it can replicate the influence zone or the unit cell area of an Australian standard gauge heavy haul track, (ii) it has a true triaxial chamber where three mutually orthogonal independent principal stresses can be applied, (iii) it has four independent moveable vertical walls which simulate the lateral movement of ballast in a real track, and (iv) the vertical actuator capacity is 100 kN and can apply cyclic loads up to 60 Hz is capable to simulate fast and heavy haul trains.

The same prototype width of a sleeper with rail assembly was used to generate a comparable pressure beneath the sleeper at similar train axle loads simulated by the loading actuator of PSPTA. The plan dimensions of the PSPTA cubical cell are 800 mm by 600 mm as shown in Fig. 1b. The depth of the test chamber is sufficient to accommodate the typical depth of ballast in track (i.e., 250–300 mm) followed by the underlying substructure layers (Figs. 1a and b). It is noteworthy that no laboratory equipment is able to represent the actual depth of stratified ground beneath the track, so in this study, the non-displacement boundary of the PSPTA was fixed at a depth of 600 mm.

In this study, a plane strain condition was simulated by ensuring a near-zero lateral strain in the longitudinal direction (train passage direction which is perpendicular to the sleepers). This means its use is limited to a long straight section of track where the assumption of a plane strain condition (i.e., $\epsilon_2 = 0$) is often reasonable. Since the longitudinal side walls were kept restrained by a hydraulic jack connected to the wall, the confining pressure exerted by the walls in the longitudinal direction (σ_2)

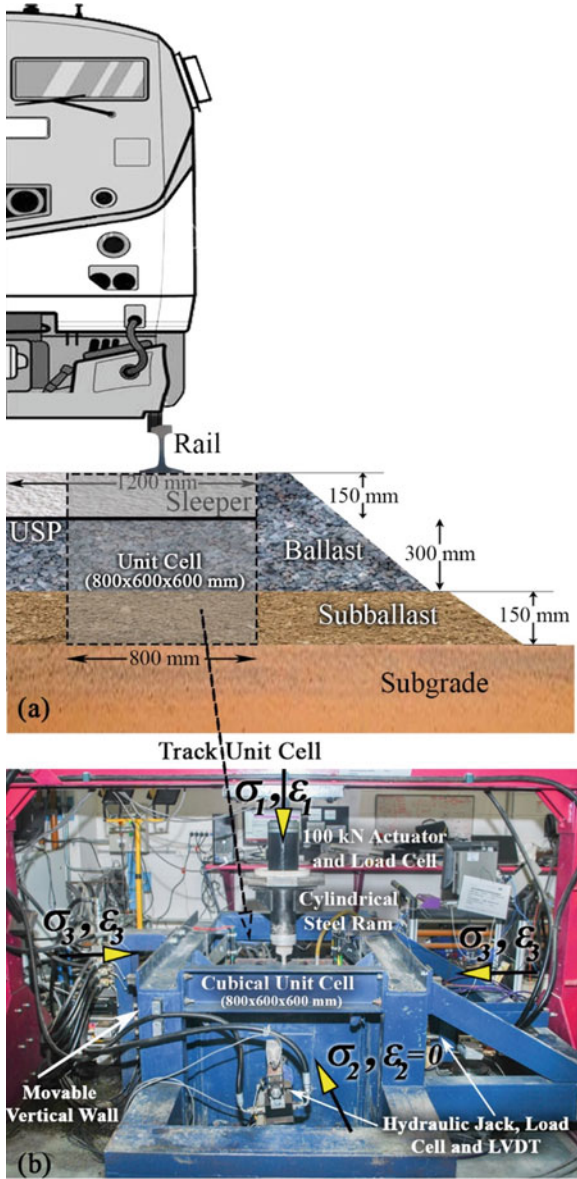


Fig. 1 a Diagrammatic representation of a ballasted railway track and b Prototype PSPTA (modified from Navaratnarajah and Indraratna (2017))

would vary during the test and it was measured by the load cell attached in line with the hydraulic jack (Fig. 1b).

3 Large-Scale Laboratory Test Materials

The integrated substructure layers built inside the cubical chamber of the PSPTA consisted of rail, concrete sleeper, ballast, and subballast. The performance of this integrated track was investigated with and without placing the USP at the bottom face of the concrete sleeper. The test materials used in this study are discussed below.

3.1 *Fresh Ballast*

The fresh ballast material commonly used in NSW rail tracks was used for laboratory tests. It was obtained from Bombo quarry near Wollongong City and is predominantly latite (volcanic) basalt, a common igneous rock that can be found along the south coast of NSW, Australia. These basalt aggregates are dark, fine-grained, and very dense, and have sharp angular corners when blasted and quarried. The fresh ballast obtained from the quarry was prepared for testing in accordance with AS 2758.7 (2015); the laboratory samples were cleaned with water and dried before screening through selected sieve sizes and then mixed in the desired proportions to obtain the required particle size distribution (PSD). The PSD and grain size characteristics of the ballast are shown in Fig. 2a.

3.2 *Subballast*

The laboratory testing was conducted by simulating a regular open track where the ballast is placed on top of the subballast or subgrade. In this study, a 150 mm thick layer of subballast was placed beneath the ballast layer. This subballast was also obtained from Bombo quarry, NSW. The maximum dry density ($\gamma_{d, \max}$) and optimum moisture content (w_{omc}) of the subballast are 2115 kg/m³ and 10%, respectively. Prior to testing, the raw granular subballast was sieved to meet the Australian standards (AS 2758.7 2015). The PSD and the grain size characteristics of the subballast are also shown in Fig. 2a.

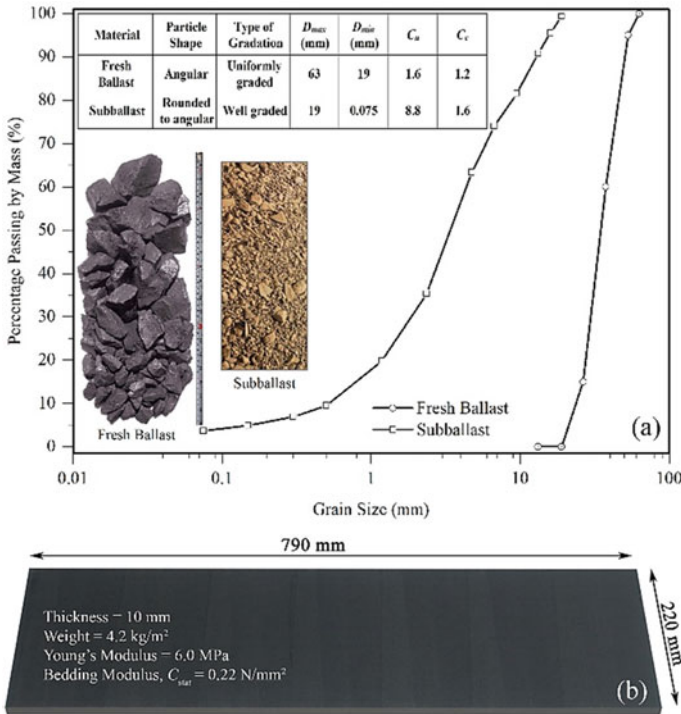


Fig. 2 a The Particle Size Distribution (PSD) and grain size characteristics of the ballast and subballast and b Sample of an Under Sleeper Pad (USP)

3.3 Under Sleeper Pad (USP)

The USPs used in this study shown in Fig. 2b was a 10 mm thick elastoplastic synthetic material made from polyurethane elastomers. This USP (790 × 220 mm) was glued tightly to the base of the concrete sleeper (at the sleeper-ballast interface) when testing with the pad. The mechanical properties of the USP are also shown in Fig. 2b.

4 Cyclic Load Testing

4.1 Specimen Preparation

The laboratory test specimen preparation procedures are shown in Figs. 3a–d. The bottom layer of the test specimen consisted of a 150 mm thick subballast overlain by a 300 mm thick layer of ballast. The subballast was compacted to around 95% of

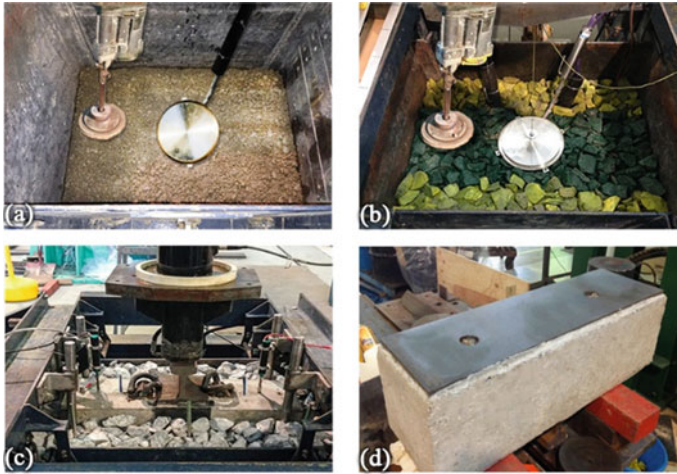


Fig. 3 Compaction of **a** Subballast; and **b** Ballast layers using a rubber-padded vibratory hammer and pressure cells placed at the interfaces; **c** Rail-sleeper assembly placed on top of the ballast layer; **d** USP attached to the concrete sleeper

$\gamma_{d, \max}$ at 10% moisture content using a vibratory hammer, before placing the ballast layer (Fig. 3a). Fresh ballast was placed as three 100 mm thick layers and each layer was compacted to a typical field density of 1560 kg/m^3 (initial void ratio, $e_0 = 0.73$) by using a rubber-padded vibratory compactor to minimize any ballast damage during tamping (Fig. 3b). The representative ballast aggregates directly under the sleeper in each of the three layers (top, middle and bottom layers) were color-coded as red, green, and blue to differentiate and better assess the degradation of ballast with the depth. The other aggregates below the sleeper (which are not directly under the sleeper) were painted yellow (Fig. 3b). The rail-sleeper assembly was then placed at the center and the space around the sleeper was filled with white color coated 150 mm thick compacted crib ballast (Fig. 3c). When testing with USP, the pad was tightly glued to the base of the concrete sleeper (Fig. 3d). Due to the height limitation of the PSPTA (600 mm height), the effect of subgrade was not considered in this study. Given that the bottom steel boundary is rigid and sitting on a strong laboratory floor (steel and concrete), this equipment is sufficient to mimic to some extent very stiff subgrade, but in situations where deep soft clays exist as subgrade, the measured settlements will be underestimated by PSPTA as explained elsewhere by Indraratna, et al. (2011).

4.2 Vertical Cyclic Stress

The typical cyclic loading experienced by rail track foundations was simulated in the PSPTA. The vertical cyclic stress applied by the servo-hydraulic actuator (Fig. 1b)

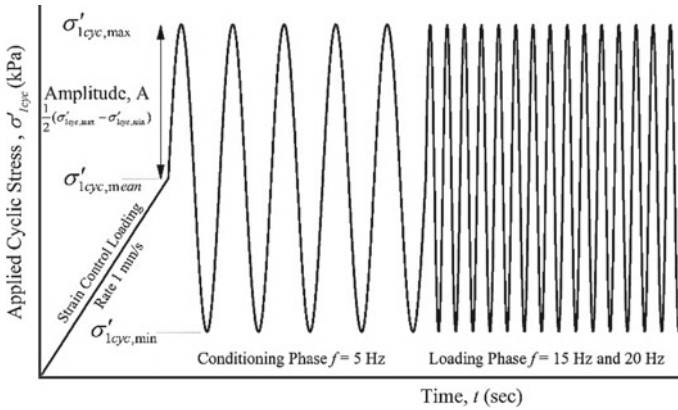


Fig. 4 Applied Cyclic Load

through cylindrical steel ram was transmitted to the ballast layer by a rail-sleeper assembly (Fig. 3c). The harmonic sinusoidal loading (cyclic major principal stress, σ'_{1cyc}) applied is shown in Fig. 4. The minimum ($\sigma'_{1cyc,min} = 30$ kPa), maximum ($\sigma'_{1cyc,max} = 230$ and 320 kPa), mean stress ($\sigma'_{1cyc,mean} = 130$ and 175 kPa), and amplitude ($A = 100$ and 145 kPa) of the applied cyclic loading were corresponding to 25 and 35 t axle loads, respectively. These pressures were determined using the American Railway Engineering (AREA) method (Li and Selig 1998). Initially, a strain-controlled loading at a rate of 1 mm/s was applied to bring the ballast-sleeper interface stress up to the mean cyclic deviator stress ($\sigma'_{1cyc,mean}$), and then a stress-controlled loading was applied by selecting loading amplitude (A) of $1/2(\sigma'_{1cyc,max} - \sigma'_{1cyc,min})$. A stress-controlled load was applied in two stages: a conditioning phase where a reduced loading frequency (f) of 5 Hz was used for 100 load cycles (N) to improve contact at the sleeper-ballast interface and avoid losing actuator contact with the rail top surface. This ensures that the different components are seated properly at their interfaces. Subsequently, a loading phase with an actual test frequency ($f = 15$ and 20 Hz) was applied for the remaining 500,000 cycles.

4.3 Lateral Confining Stress

Lateral confinement provided by the weight of the crib and shoulder ballast in a real rail track was simulated by the vertical walls (Fig. 1b) of the PSPTA cubical chamber. In an actual rail track, longitudinal ballast strain (intermediate principal strain, ϵ_2) is negligible (for a long straight rail track), but transverse strain (minor principal strain, ϵ_3) is significant due to low confinement (Indraratna et al. 2015; Ishikawa et al. 2011), therefore the vertical walls in the longitudinal direction were locked in position (i.e., $\epsilon_2 = 0$) and the corresponding stress exerted by the wall (intermediate principal stress, σ_2) was measured. The ballast aggregates were allowed to spread laterally along the direction parallel to the sleeper under the applied cyclic load, therefore the vertical

walls in the transverse direction were allowed to move in the lateral direction with an applied confining stress (minor principal stress, σ_3) of 15 kPa. The accompanying lateral movement (ε_3) was measured during testing.

4.4 Instrumentation and Data Acquisition

The performance of integrated layered track simulated in the laboratory was monitored accurately in real-time with robust and high-precision instruments and data acquisition units built and coupled along with PSPTA. The instrumentation used in this study consists of load cells, Linear Variable Differential Transformers (LVDTs), potentiometers, pressure cells, and settlement plates. The vertical and lateral loads were measured using in-built load cells attached to the main actuator and hydraulic jack, respectively (Fig. 1b). Lateral deformation in the direction parallel to the sleeper is based on the movement of vertical walls where LVDTs are connected between the vertical walls and the external frame. Rapid response hydraulic pressure cells (230 mm in diameter by 25 mm high, and with a capacity of 1 Mpa shown in Fig. 3a and b) specifically made for granular soil type were placed at each of the following interfaces to measure variations in pressure with depth: (i) at the sleeper-ballast interface; (ii) at the middle of the load-bearing ballast layer; and (iii) at the ballast-subballast interface. The pressure cells were placed with care to ensure they are in full contact with the concrete sleeper, ballast layers, and the subballast to avoid any erroneous data being recorded during testing.

The vertical deformation of ballast and subballast were measured using the potentiometers (stroke 100 mm) and stainless steel settlement plates with a base of $100 \times 100 \times 6$ mm attached to 10 mm diameter rods with lengths that match the depth of the embedded layer inside the cubical chamber (Fig. 3c). The settlement plates were installed at the ballast-subballast and sleeper-ballast interfaces. Every instrument was calibrated and the calibration factors were inserted into the host computer which is supported by LabVIEW software to record all associated load, stress and deformation data against time and the number of loading cycles (N) during testing. The transducer housings and the cable leads of the instruments were encased in flexible rubber conduits to protect them from damage due to vibratory compaction of the ballast sample during preparation and during the cyclic loadings.

The initial readings of all the instruments were taken before starting the cyclic loading test phase. A total of 500,000 load cycles were applied in each test but was interrupted at specific cycles (100, 500, 1,000, 5,000, 10,000, 50,000, 100,000,, 500,000) to take manual readings from settlement pegs and to capture the resilience of ballast material at the end of these cycles. At the completion of each test, the ballast layers were separated based on colors and the final weights of each of the three ballast layers (top, middle, and bottom) were carefully measured by screening through selected sieves (as per the PSD) for the ballast breakage estimation.

5 Laboratory Test Results and Discussion

A total of eight large-scale cyclic load tests were carried out to verify the performance of USP in the attenuation of stress-strain and degradation responses of ballast. When a track transmits a more concentrated rail seat load to sleepers, the sleeper-ballast interface distributes the load over a larger area. However, the sleeper only transmits stresses through a finite number of small discrete contacts at the ballast-sleeper interface (Le Pen 2008). Compared to timber sleepers, when concrete sleepers are used in rail track, the contact areas of these discrete points further reduce and increase the interface contact stresses. In this study, to increase the interface contact area, a resilient rubber pad (USP) was used with the concrete sleeper. As per the visual observations are shown in Fig. 5a (USP before the test) and Fig. 5b (USP after the test) revealed that the ballast particles bedded uniformly with the concrete sleeper when a USP is placed on the bottom face of the sleeper. The contact area between the ballast and the sleeper is then increased because the resilient layer allows the ballast aggregates to be partially pressed (indented) at the surface of USP as shown in Fig. 5b. This resulted in a more uniform distribution of pressure than without USP on the bottom face of the concrete sleeper.

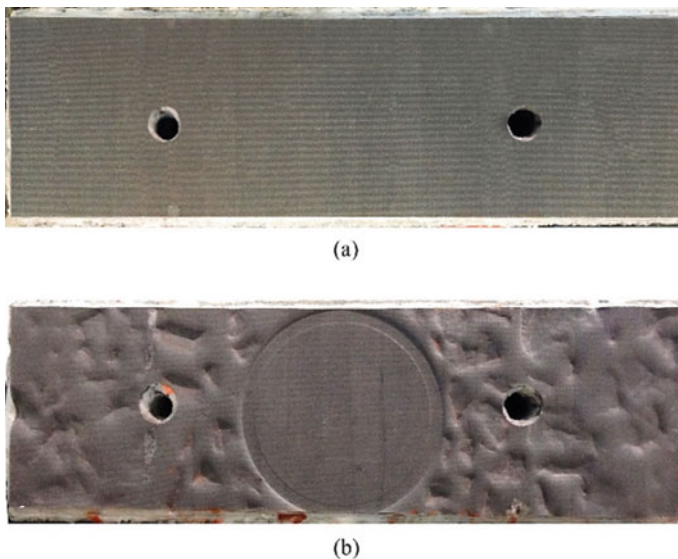


Fig. 5 a USP before the test and b USP after the test (modified from (Navaratnarajah et al. 2018))

5.1 Vertical and Lateral Deformation

The vertical residual plastic deformation of the ballast was measured at the end of each selected cycle (N) by taking the average value of the difference between the readings from the settlement plates placed at the sleeper-ballast interface and the ballast-subballast interface, to exclude any plastic deformation of the subballast layer. The lateral residual plastic deformation is calculated by taking the average lateral movement of the vertical walls in the direction parallel to the sleeper. The vertical and lateral plastic deformation with and without USP for 25 and 35 t axle loads are shown in Figs. 6 and 7, respectively. Based on the results, the plastic deformation of the ballast increasing with the axle load and train speed (loading frequency). The test results indicated that the ballast deformed rapidly up to around 10,000 cycles due to its initial densification and further packing after the corners of the sharp angular aggregates began to break. However, once the ballast started to stabilize, the rate of deformation gradually decreased and then remained relatively constant after around 100,000 cycles. This showed that the ballast aggregates undergo considerable particle rearrangement and densification during the initial cycles, but after reaching a threshold compression, any subsequent load cycles would resist further deformation.

It is evident that the ballast deformation (vertical and lateral) has decreased significantly by using USP. The increased contact area of ballast by the USP at the sleeper-ballast interface reduced the induced stresses at the interface and at the particle-particle contact, allowing for a more uniform distribution of stress which in turn decreased the overall deformation. The indentation of the ballast particle on the rubber inclusion (Fig. 5b) influences the interface friction between the ballast and rubber pad which also contributes to the reduction of lateral deformation.

Based on the loading frequencies of 15 and 20 Hz tested in this study, the vertical deformation decreased up to about 29% for a 25 t axle load, and up to about 21% for a 35 t axle load when USP was used with the concrete sleeper. Lateral deformation decreased in up to about 14% for a 25 t axle load and up to about 11% for a 35 t axle load. This shows attaching USPs at the bottom face of the concrete sleepers is an ideal technique to reduce the long-term plastic settlement of a track subjected to repetitive cyclic loading.

5.2 Vertical Stress Distribution

Ballast in the rail track provides stability for the track substructure by distributing the dynamic stresses exerted by moving trains. By distributing the stresses within the depth of the ballast layer, it also significantly reduces the stress transmitted to the underlying layers such as subballast and subgrade layers. To measure the dynamically induced pressure variation along the depth of the ballast layer, pressure cells were placed at the sleeper-ballast interface, in the middle of the ballast layer, and at the ballast-subballast interface. Figure 8 shows the variations in pressure with

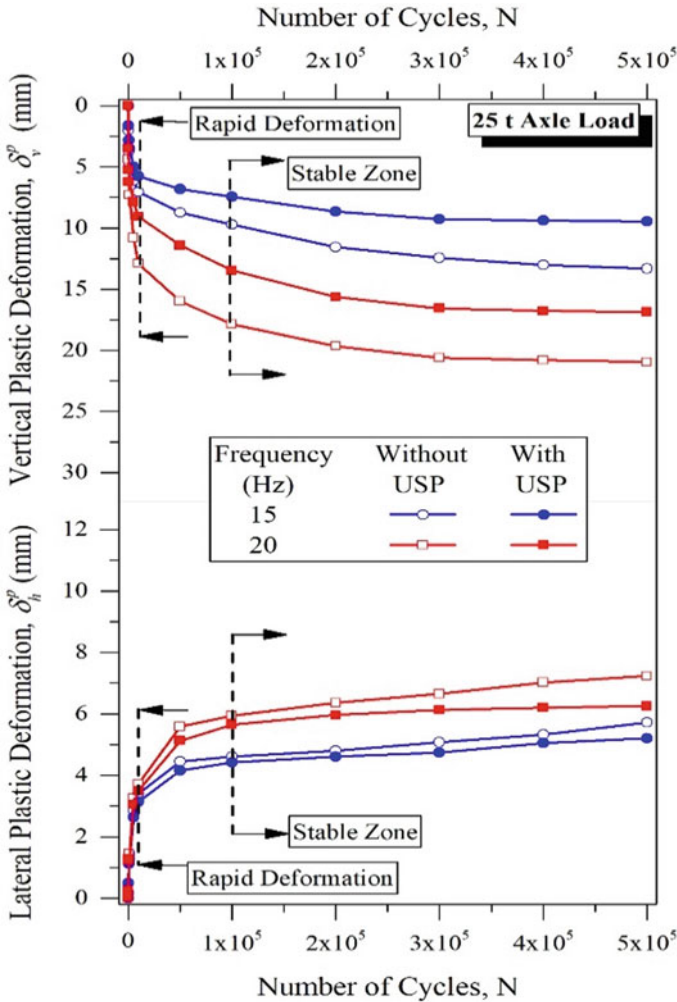


Fig. 6 Variation of Vertical and Lateral plastic deformation with the number of cycles (N) with and without USP for 25 t axle load (data sourced from Navaratnarajah et al. (2018))

and without USP along the depth of the ballast layer. It is evident from this study, that the dynamically induced stresses in the ballast increased with the axle load and train speed (loading frequency). When USP was placed under the concrete sleeper, there was a definite reduction in stress within the ballast mass because the dynamically induced stress is now reduced by the softer interface between ballast and concrete sleeper by the USP.

Based on Fig. 8, the average reduction of stress is varying from about 12 and 10% at the sleeper-ballast interface, 10 and 8.5% in the middle of the ballast layer and about 9.5 and 8% at the ballast-subballast interface for 25 and 35 t axle loads,

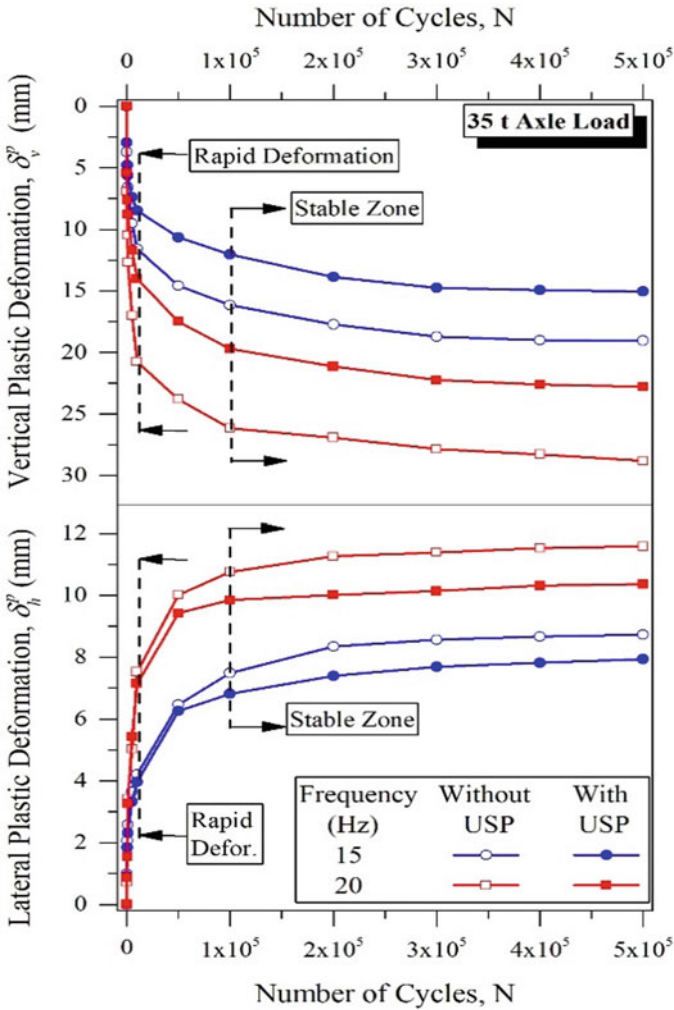


Fig. 7 Variation of Vertical and Lateral plastic deformation with the number of cycles (N) with and without USP for 35 t axle load (data sourced from Navaratnarajah et al. (2018))

respectively. It is evident from the values that the reduction in stress is higher in the zone near the USP-ballast interface. When a USP is used with the concrete sleeper, the ballast aggregates made a more uniform and increased area of contact at the sleeper-ballast interface that leads to a reduction in ballast stress. These outcomes are in line with the findings by Dahlberg (2010) and Le et al. (1999).

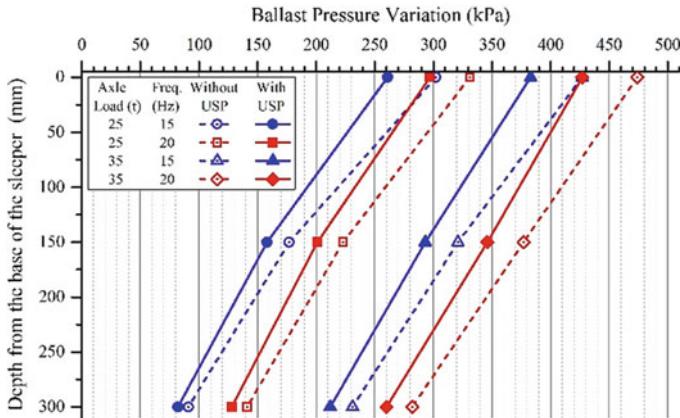


Fig. 8 Variation of ballast pressure with and without USP (data sourced from Navaratnarajah et al. (2018))

5.3 Ballast Breakage

Ballast particles undergo three different types of particle degradation (i) grinding (abrasion), (ii) angular corner breakage (attrition), and (iii) distinct splitting across the body of particles (fracture) under the application of a repetitive cyclic load. As the induced stresses from moving train directly transmitted to the ballast layer through rail and sleeper, the ballast layers undergo significant damage during the passage of a train. In this study, the Ballast Breakage Index (BBI) method proposed specifically for railway ballast by Indraratna et al. (2005) was used to evaluate ballast degradation. As explained previously, the ballast breakage potential varies with depth due to changes in stress along the depth of the ballast layer. Therefore, the ballast mass was divided into three layers top, middle, and bottom and analyzed separately. These layers correspond to ballast breakage governed by variations in stress and the three different types of interfaces. The top is the sleeper-ballast zone, the middle is the ballast-ballast-zone, and the bottom is the ballast-subballast zone. To better quantify degradation in these zones, the representative fresh ballast (Fig. 9a) directly under the sleeper was color-coded in each test, after which each layer of degraded ballast (Fig. 9b) was separated according to their colors. Subsequently, the PSD was carried out and plotted to evaluate their BBI as per the method proposed in Indraratna et al. (2005).

The BBI for the top, middle, and bottom layers are presented in Fig. 10a and b for ballast tested with and without USP for 25 and 35 t axle loads, respectively. As expected, ballast breakage was greater at the top layer due to having a higher interface and inter-particle contact stress at the top, followed by the middle, and then the bottom layers. It is also evident from this study, the ballast degradation increased with the axle load and train speed (loading frequency). However, the results indicate that ballast degradation was significantly reduced by the USP used under the concrete



Fig. 9 **a** Fresh ballast before the test and **b** Degraded ballast after the test (modified from Navaratnarajah (2017))

sleeper. The increased contact area due to USP and the subsequent reduction in the interface and inter-particle ballast stress is probably the main reason behind this substantial reduction of ballast breakage. Considering each ballast layer separately, the reduction for the 25 and 35 t axle loads tested with 15 and 20 Hz frequency was in the order of 53–63% for the top layer, 51–59% for the middle layer, and 48–62% for the bottom layer. When all three layers are considered, on average, the USP reduced degradation by more than 50%.

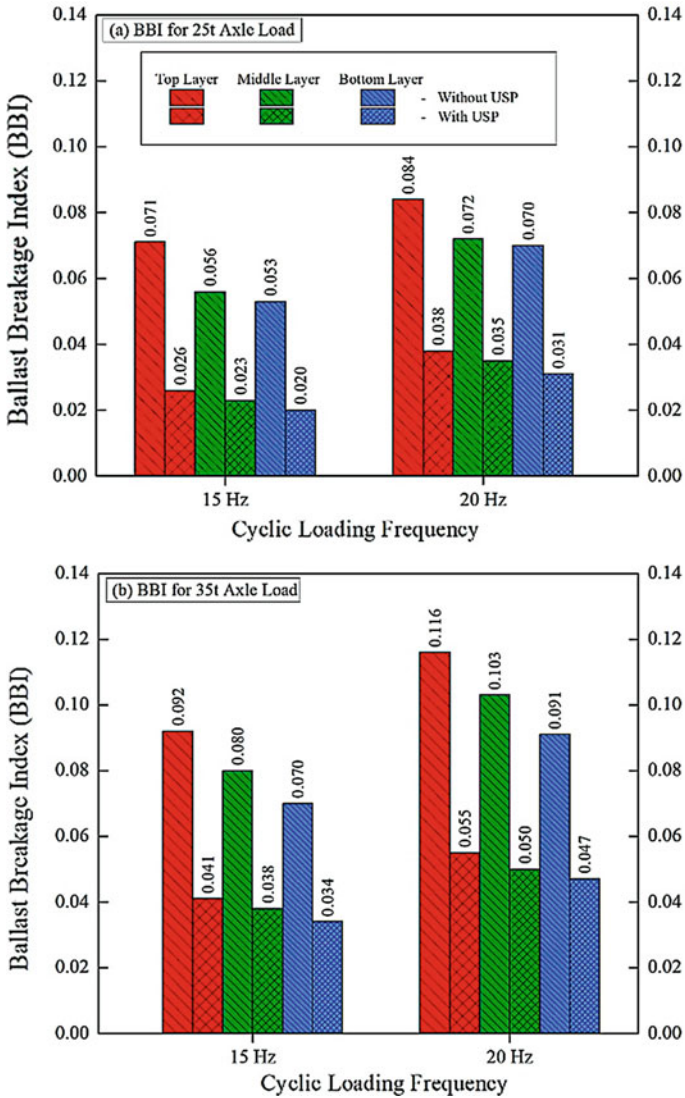


Fig. 10 Ballast Breakage Index (BBI): **a** 25 t axle load and **b** 35 t axle load (data sourced from Navaratnarajah et al. (2018))

6 Conclusion

A series of large-scale cyclic loading tests using the Process Simulation Prismoïdal Triaxial Apparatus (PSPTA) were carried out with axle loads of 25 and 35 t and at varying loading frequencies of 10 and 15 Hz to investigate the performance of USP stabilized at the harder interface (concrete sleeper-ballast interface). An open track

simulated by placing subballast underneath the ballast layer and a USP attached on the bottom face of a concrete sleeper showed promising outcomes in the reduction of vertical and lateral deformations, stress, and degradation of ballast. Generally, concrete sleepers transmit stress to the ballast through a finite number of small discrete contacts at the sleeper-ballast interface. However, it is evident from the imprints of ballast on the USP, that when a USP is inserted at the sleeper-ballast interface, the ballast particles bed uniformly with the concrete sleeper and enhance the interface contacts and markedly reduces the stresses in the ballast especially at the top zone which leads to reduction in ballast deformation (vertical and lateral) and degradation. Based on this study, using USPs on concrete sleepers is a favorable solution to reduce the stress-strain and degradation of ballast, and in a practical sense to minimize the maintenance costs of ballasted rail tracks.

Acknowledgments The financial support provided by the Australian Research Council (ARC) and University Postgraduate Award (UPA) by the University of Wollongong to conduct this research study is gratefully appreciated. The assistance provided by senior technical officers Alan Grant, Cameron Neilson, and Ritchie McLean in the School of Civil and Environmental Engineering, University of Wollongong, Australia is also appreciated.

References

- Abadi T, Le Pen L, Zervos A, Powrie W (2015) Measuring the area and number of ballast particle contacts at sleeper/ballast and ballast/subgrade interfaces. *Int J Railw Technol* 4:45–72
- AS 2758.7 (2015) Aggregates and rock for engineering purposes, Part 7: Railway ballast, Standard Australia, Sydney, New South Wales, Australia
- Bolmsvik R (2005) Influence of USP on track response—a literature survey. Abetong Teknik AB Växjö, Sweden
- Dahlberg T (2010) Railway track stiffness variations—consequences and countermeasures. *Int J Civ Eng* 8:1–12
- Indraratna B, Lackenby J, Christie D (2005) Effect of confining pressure on the degradation of ballast under cyclic loading. *Géotechnique* 55:325–328
- Indraratna B, Salim W, Rujikiatkamjorn C (2011) Advanced rail geotechnology: ballasted track. CRC Press/Balkema, Rotterdam, Netherlands
- Indraratna B, Nimbalkar S, Rujikiatkamjorn C (2012) Performance evaluation of shock mats and synthetic grids in the improvement of rail ballast. In: 2nd International Conference on Transportation Geotechnics (ICTG). Sapporo, Japan, pp 47–62
- Indraratna B, Navaratnarajah SK, Nimbalkar S, Rujikiatkamjorn C (2014) Use of shock mats for enhanced stability of railroad track foundation. *Aust Geomech J Spec Ed ARC Cent Excell Geotech Sci Eng* 49:101–111
- Indraratna B, Biabani M, Nimbalkar S (2015) Behavior of geocell-reinforced subballast subjected to cyclic loading in plane-strain condition. *J Geotech Geoenviron Eng* 141:1–16
- Ishikawa T, Sekine E, Miura S (2011) Cyclic deformation of granular material subjected to moving-wheel loads. *Can Geotech J* 48:691–703
- Johansson A, Nielsen JCO, Bolmsvik R, Karlström A, Lundén R (2008) Under sleeper pads—Influence on dynamic train-track interaction. *Wear* 265:1479–1487
- Lakuši S, Ahac M, Haladin I (2010) Experimental investigation of railway track with under sleeper pad. In: 10th Slovenian road and transportation congress. Portoroz, Slovenija, pp 386–393

- Le Pen L (2008) Track behaviour: the importance of the sleeper to ballast interface. PhD Thesis, University of Southampton
- Le R, Ripke B, Zacher M (1999) Ballast mats on high speed bridges. In: Fourth European Conference on Structural Dynamics: EURO-DYN'99. A.A. Balkema, Rotterdam, Prague, Czech Republic, pp 699–703
- Li D, Selig E (1998) Method for railroad track foundation design. I: development. *J Geotech Geoenviron Eng* 124(4):316–322
- Loy H (2008) Under sleeper pads: improving track quality while reducing operational costs. *Eur Railw Rev* 1–8
- Loy H (2009) Under sleeper pads in turnouts. *Railw Tech Rev* 2:35–38
- Marschnig S, Veit P (2011) Making a case for under-sleeper pads. *Int Railw J* 51:27–29
- Navaratnarajah SK (2017) Application of rubber inclusions to enhance the stability of ballasted rail track under cyclic loading. PhD Thesis, University of Wollongong, Australia
- Navaratnarajah SK, Indraratna B (2017) Use of rubber mats to improve the deformation and degradation behavior of rail ballast under cyclic loading. *ASCE J Geotech Geoenviron Eng* 143:04017015
- Navaratnarajah SK, Indraratna B (2018) Closure to “Use of rubber mats to improve the deformation and degradation behavior of rail ballast under cyclic loading” by Sinniah K. Navaratnarajah and Buddhima Indraratna. *ASCE J Geotech Geoenviron Eng* 144:07018014
- Navaratnarajah SK, Indraratna B, Nimbalkar S (2016) Application of shock mats in rail track foundation subjected to dynamic loads. *Proced Eng* 143:1108–1119
- Navaratnarajah SK, Indraratna B, Ngo NT (2018) Influence of under sleeper pads on ballast behavior under cyclic loading: experimental and numerical studies. *ASCE J Geotech Geoenviron Eng* (Accepted-in production)
- Nimbalkar S, Indraratna B (2016) Improved performance of ballasted rail track using geosynthetics and rubber shockmat. *J Geotech Geoenviron Eng* 142:04016031
- Nimbalkar S, Indraratna B, Dash S, Christie D (2012) Improved performance of railway ballast under impact loads using shock mats. *J Geotech Geoenviron Eng* 138:281–294
- Schilder R (2013) Track innovations by Austrian railways. In: Proceedings of the AREMA 2013 annual conference. Indianapolis, IN, pp 1332–1347
- Schneider P, Bolmsvik R, Nielsen JCO (2011) In situ performance of a ballasted railway track with under sleeper pads. *Proc Inst Mech Eng Part F J Rail Rapid Transit* 225:299–309
- Sol-Sanchez M, Moreno-Navarro F, Rubio-Gómez MC (2014) Viability of using end-of-life tire pads as under sleeper pads in railway. *Constr Build Mater* 64:150–156
- Sol-Sanchez M, Moreno-Navarro F, Rubio-Gómez MC (2015) The use of elastic elements in railway tracks: a state of the art review. *Constr Build Mater* 75:293–305
- Zhai WM, Wang KY, Lin JH (2004) Modelling and experiment of railway ballast vibrations. *J Sound Vib* 270:673–683

Strengthening of Weak Subgrade Using Geocell



G. Sridevi , G. Sudarshan , and A. Shivaraj 

Abstract Infra structure projects require bulk quantities of construction materials to build and maintain. Use of locally available materials, which possesses very low shear strength and stiffness, suffers premature failure. Use of inferior quality of materials, in the base and sub base causes excessive lateral spreading that leads to severe distress and costly maintenance. Researchers are in search of alternative materials in order to minimize the construction cost and maintenance cost. Present work focuses on the behavior of flexible pavement reinforced with and without Geocell. Geocell is cellular confinement system made from a polymer material that enhances the stiffness of layer when it is encased. The effectiveness of a Geocell when it is used to reinforce conventional flexible pavements depends on several factors such as thickness of the Geocell, infill material, and placement depth. Reinforced flexible pavement is designed as per the IRC 37-2012 standards. Further influence of geocell is studied by placing geocell at different levels of pavement. Parameters like maximum principal stress developed, distribution, and propagation of stress through subgrade layers, deformation of layers, and maximum deformation of pavement under vehicle load are compared for both reinforced and unreinforced flexible pavement.

Keywords Flexible pavement · Finite element method · Principal stress

G. Sridevi · G. Sudarshan · A. Shivaraj (✉)
B V Raju Institute of Technology, Narsapur, India
e-mail: shivaraj.a@bvrit.ac.in

G. Sridevi
e-mail: sridevi.g@bvrit.ac.in

G. Sudarshan
e-mail: sudarshan.g@bvrit.ac.in

1 Introduction

A flexible pavement is a structure comprising of different layers consisting of different materials. The longevity of flexible pavement depends on various parameters such as thickness of various layers comprising of the pavement, the properties materials used, environmental and climatic factors. The primary function of the pavement is to prevent excessive deformation of the pavement structure. Many times the pavements fail either structurally or functionally because of inadequate thickness or increased traffic loads. The demand for good quality raw materials in pavement construction projects is increasing day by day. The scarcity of natural resources and increase in demand for construction materials is driving pavement engineers to look alternate new materials in place of natural material. Use of Geosynthetics to reinforce the flexible pavement is one of the alternatives to address the problem of scarcity of resources, poor quality subgrade soil, and durability. The aggregate layer provided above the subgrade distributes the load in order to prevent excess deformation of the subgrade soil. Pavements on weak subgrades will undergo excessive deformations when loads are applied due to lateral flow of soil. Any effort made to confine soil which prevents lateral flow of soil would be a promising solution to ensure better performance of subgrade soil. Geocells are one of the novel methods adopted to confine the soil to prevent lateral deformations. The high hoop stress developed by Geocell prevents lateral spreading of infill soil. The enhanced interface friction along the cell walls also helps in reducing the stress transmission to the subgrade soil.

The geocell reinforcement is a three-dimensional honeycomb-like structure of cells that contains and confines the soil within, which leads to substantial performance improvement (Webster and Watkins 1977; Rea and Mitchell 1978; Bush et al. 1990; Schimizu and Inui 1990; Cowland and Wong 1993; Mandal and Gupta 1994; Dash et al. 2001; Sitharam et al. 2005; Sitharam and Dash 2007; Madhavi Latha et al. 2006; Madhavi Latha and Murthy 2007; Zhou and Wen 2008; Emersleben and Meyer 2008; Pokharel et al. 2010; Dash 2012; Tanyu et al. 2013; Hegde and Sitharam 2015). Krishna Swami et al (2000) concluded that geocell base improved the performance of the embankment in terms of the maximum surcharge load and the deformations. The properties like tensile strength and aspect ratio of the geocell influence the overall performance of the geocell reinforced pavement.

Geocells not only provide a lateral confinement to the fill but also workability and serviceability. Geocells are extensively used in various geotechnical applications by reinforcing soft soil strata and stabilizing slopes and embankments (Chen et al. 2013).

The Geocell imparts stiffness to the soil layer and distributes the loads over a wider area and, results in lower settlement of the underlying layer (Huang et al. 2013). Triaxial tests carried out on granular soil samples reinforced by single cell of geocell and two, three, and four cells of geocell suggest that geocell strengthens the granular soil by developing apparent cohesion (Cr) and making a negligible change in internal friction angle (Bathurst et al. 1993).

2 Objectives of the Study

- To study the influence and effect of Geocell layer, when placed between different layers of flexible pavement.
- To compare and study the behavior and maximum stress developed in unreinforced and reinforced pavement.
- To compare and study maximum deformation of unreinforced and reinforced pavement.

3 Methodology

Unreinforced Flexible pavement is designed as per IRC: 37-2012. IRC-37-2012 deals with 5 design of alternate pavement compositions. In the present study, 2 alternatives are considered.

1. GSB + WMM + DBM + BC (as in 2001 Guide)
2. Cement treated Sub base + CTB + WMM + DBM + BC. The cross section of the pavement is given in Fig. 1 and material properties are shown Table 1.

The reinforced flexible pavement is designed based on Giroud and Han method. This method considers the effects of the aggregate base layer stiffness, which has relationship with the CBR of the aggregate base material. In Giroud and Han method,

Fig. 1 Cross section of flexible pavement

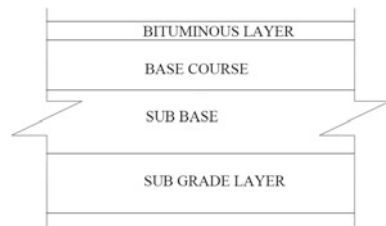


Table 1 Material properties of sub structure layers

	E (Mpa)	Poisson’s ratio (μ)	Unit weight (kN/m ³)	α/c
Bituminous layer	3000	0.35	24.15	
Granular base	100	0.4	22	
Sub base	50	0.4	20	
Sub grade	50	0.4	16	
Cement treated base	31.62	0.15	24	10×10^{-6}
Cement treated sub base	19.36	0.2	23	10×10^{-6}

the stress distribution angle varies based on the number of loading cycles, the aggregate base layer thickness, the radius of the contact area, and the type and properties of geosynthetics. These features make this design approach more exact and realistic.

Total four models are considered for the analysis out of which two are unreinforced and two are reinforced flexible pavement. In the case of reinforced flexible pavement the Geocell position is changed keeping the thickness of the pavement same.

4 Model Description

Finite Element method is appropriate structural method for analysis of flexible pavements. Modeling in ANSYS software includes creation of geometrical model, assignment of material properties, discretization, contact between the layers, and assignment of loads.

Three 3D models of pavement with Geocell are modeled in ANSYS software. 8-Noded constant stress solid elements were used to model sub structure layers. The flexible pavement modeled in ANSYS is shown Fig. 2.

Model—I Flexible pavement with Granular base and granular sub base.

Thickness of Bituminous layer = 180 mm.

Thickness of Granular Base course layer = 250 mm.

Thickness of Granular Sub base layer = 315 mm.

Thickness of Sub grade layer = 300 mm.

Model—II Bituminous pavement with cemented base and sub base with crack relief interlayer of aggregate.

Thickness of Bituminous layer = 100 mm.

Thickness of Aggregate layer = 100 mm

Thickness of cemented Base course layer = 111 mm.

Fig. 2 Flexible pavement model in Ansys

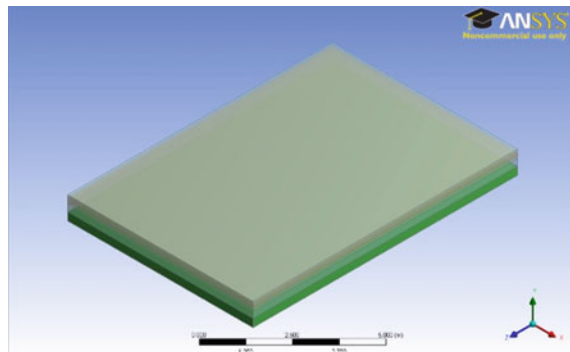


Table 2 Material properties of Geocell layer

Density (kg/m ³)	1809.2
Modulus of elasticity (N/mm ²)	1.1 × 10 ⁹
Poisson’s ratio (μ)	0.42
Thickness of layer (mm)	150

Thickness of cemented Sub base layer = 250 mm.

Thickness of Sub grade layer = 300 mm.

Model—III Bituminous pavement with Geocell between subgrade and base course.

Thickness of Bituminous layer = 50 mm.

Thickness of Base course layer = 172 mm.

Thickness of GEOCELL = 150 mm

Thickness of Sub grade layer = 300 mm

Model—IV Bituminous pavement with Geocell between bituminous layer and base course.

Thickness of Bituminous layer = 50 mm.

Thickness of Base course layer = 172 mm.

Thickness of GEOCELL = 150 mm

Thickness of Sub grade layer = 300 mm

Geocell properties used in study are shown in Table 2. The properties shown correspond to a presto GW20V geocell type.

5 Results and Discussions

Analysis of models are done in ANSYS Software and compared for Principal stress and Deformation results with geocell of thickness 150 mm placed between Sub base and base course and between Base course and Bituminous layer. Developed principal stress in cement-treated base flexible pavement without geocell can be seen in Fig. 3. Figures 4 and 5 shows principal stress developed and maximum deformation in pavements. Tables 3 and 4 shows principal stress developed and maximum deformation values in pavements.

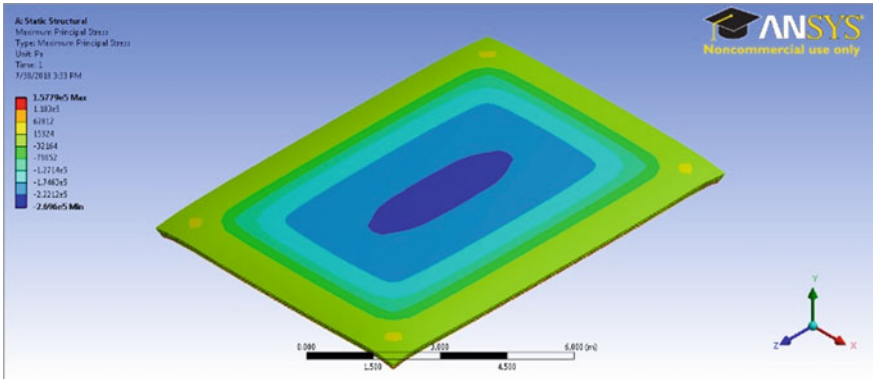


Fig. 3 Principal stress developed in cement-treated base flexible pavement without geocell

Fig. 4 Principal stress graph

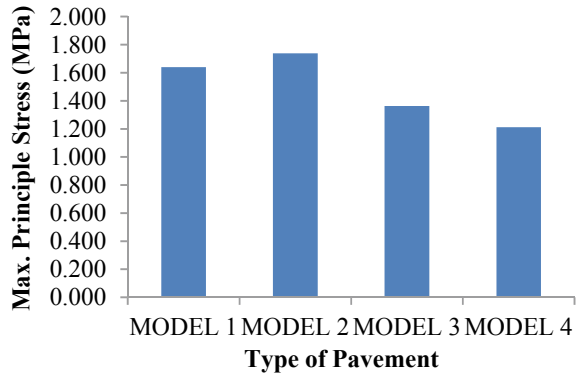


Fig. 5 Maximum deformation graph

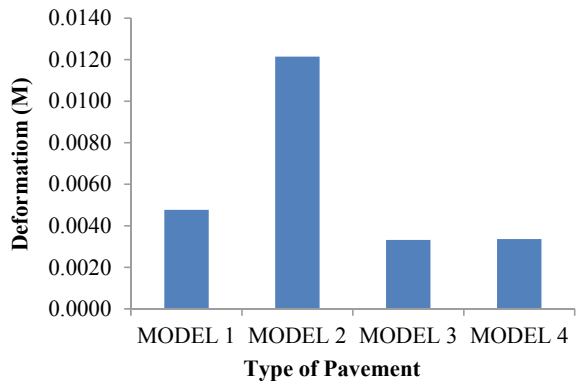


Table 3 Principal stresses in models

Flexible Pavement without Geocell, MPa	Flexible Pavement Cement treated without Geocell, MPa	Flexible Pavement with Geocell between base course and Bituminous layer, MPa	Flexible Pavement with Geocell between base course and subgrade, MPa
1.640	1.739	1.363	1.212

Table 4 Maximum deformation in different pavements

Flexible Pavement without Geocell, m	Flexible Pavement Cement treated without Geocell, m	Flexible Pavement with Geocell between base course and Bituminous layer, m	Flexible Pavement with Geocell between base course and subgrade, m
0.00478	0.01215	0.00333	0.00336

6 Conclusions

- Considerable reduction in pavement thickness is observed in Geocell reinforced pavement. Apart from saving the cost of construction, it also reduces the resource consumption.
- Significant reduction in deformation of the pavement is observed in the case of geocell reinforced flexible pavement. 30.33% reduction is observed in model 3 and 29.70% reduction Model 4.
- The reduction in Principal stress of the pavement is observed in the case of geocell reinforced flexible pavement. 16.89% reduction is observed in model 3 and 26.09% reduction Model 4.
- It can be concluded from the results is that the potential for reduction is pronounced in the case of soils with lower CBR, and also the sections designed for higher traffic. This study suggests that the base course aggregate thickness can be reduced by providing geocell reinforcement in the top of sub base layer or at the base layer.
- The geocell provides a sustainable solution for the roads using materials with low environmental impact and reduction in utilization of broken aggregates.

References

- Bathurst RJ, Karpurapu R (1993) Large scale triaxial compression testing of geocell reinforced granular soils. *Geotech Test J* 16:296–303
- Bush DI, Jenner CG, Bassett RH (1990) The design and construction of geocell foundation mattress supporting embankments over soft ground. *Geotext Geomembr* 9:83–98
- Chen RH, Huang YW, Huang FC (2013) Confinement effect of geocells on sand samples under triaxial compression. *Geotext Geomembr* 37:35–44

- Cowland JW, Wong SCK (1993) Performance of a road embankment on soft clay supported on a geocell mattress foundation. *Geotext Geomembr* 12:687–705
- Dash SK (2012) Effect of geocell type on load carrying mechanism of geocell reinforced sand foundations. *Int J Geomech, ASCE* 12:537–548
- Dash SK, Krishnaswamy NR, Rajagopal K (2001) Bearing capacity of strip footings supported on geocell-reinforced sand. *Geotext Geomembr* 19(4):235–256
- Dash SK, Sireesh S, Sitharam TG (2003) Model studies on circular footing supported on geocell reinforced sand underlain by soft clay. *Geotext Geomembr* 21:197–219
- Emersleben A, Meyer M (2008) Bearing capacity improvement of asphalt paved road construction due to the use of geocells - falling weight deflector and vertical stress measurements. *Geosynthetics Asia 2008 Geosynthetics in civil and environmental engineering*, In: Proceedings of the 4th Asian Regional Conference in Geosynthetics, Shanghai, China, pp 474–753
- Hegde TG, Sitharam (2015) Experimental and numerical studies on protection of buried pipelines and underground utilities using geocells. *Geotext Geomembr* 43:372–381
- Huang X, Han J (2013) Geocell-reinforced granular under static and cyclic loading: a synthesis of analysis. *Geotech Eng J SEAGS AGSSEA* 44(4):17–23
- Krishnaswamy NR, Rajagopal K, MadhaviLatha G (2000) Model studies on geocell supported embankments constructed over a soft clay foundation. *Geotech Test J* 23(1):45–54
- Madhavi Latha G, Murthy VS (2007) Effects of reinforcement form on the behaviour of geosynthetic reinforced sand. *Geotext Geomembr* 25:23–32
- Madhavi Latha G, Rajagopal K, Krishnaswamy NR (2006) Experimental and theoretical investigations on geocell supported embankments. *Int J Geomech* 6(1):30–35
- Mandal JN, Gupta P (1994) Stability of geocell-reinforced soil. *Constr Build Mater* 8(1):55–62
- Pokharel SK, Han J, Leshchinsky D, Parsons RL, Halahmi I (2010) Investigation of factors influencing behavior of single geocell-reinforced bases under static loading. *J Geotextile Geomembr* 28:570–578
- Rea C, Mitchell K (1978) Sand reinforcement using paper grid cells. In: Proceedings, Symposium on Earth Reinforcement, ASCE Annual Convention, Pittsburgh, PA, pp 644–663
- Schimizu, Inui (1990) *Geotextiles, geomembranes and related products* Den Hoedt. 1990 Balkema, Rotterdam, ISBN9061911192
- Sitharam TG, Sireesh S, Dash SK (2005) Model studies of a circular footing supported on geocell-reinforced clay. *Can Geotech J* 42(2):693–703
- Tanyu BF, Aydilek AH, Lau AW, Edil TB, Benson CH (2013) Laboratory evaluation of geocell-reinforced gravel subbase over poor subgrades. *Geosynthetics Int* 20:47–61
- Webster SL, Watkins JE (1977) Investigation of construction techniques for tactical bridge approach roads across soft ground. Technical Rep S-77-1, U.S. Army Engineers Waterway Experiment Station, Vicksburg, MS
- Zhou H, Wen X (2008) Model studies on geogrid- or geocell-reinforced sand cushion on soft soil. *Geotext Geomembr* 26(3):231–238

Stresses Induced on Existing Pipeline Due to Laying of New Pipeline



Seema Gurnani, Altaf Usmani, and Charanjit Singh

Abstract In recent times, increasing demand for energy has led to rapid development of subsea and offshore assets for oil and gas transportation. Cross-country pipelines are laid to connect and transport hydrocarbons from different source stations to its consumers across the countries. Case study of a new subsea pipeline proposed to be laid on seabed and routed through cross existing pipelines is discussed in this paper. Numerical modeling using Finite Element Analysis (FEA) is carried out to analyze present stress level on existing pipelines, i.e., stress due to backfill and increment in vertical stresses in the soil just above the existing pipeline due to proposed new pipeline. Different pipeline loading conditions along with methodology and assumptions of static analysis are presented. Maximum vertical stress in the soil at the top of existing pipelines due to laying of proposed pipeline is computed. These induced stresses are also compared with the initial stresses on the existing pipeline.

Keywords Subsea pipeline · Stress analysis · Third keyword

1 Introduction

India is a vast country and it has a huge network of cross-country oil and gas pipelines. These pipelines transport oil and gas from source to refineries/terminals and from there on to consumers after processing. The cross-country pipeline crosses land and seas to serve the purpose. These pipelines may run parallel to each other and may be laid such that to cross each other at different levels. This paper presents brief methodology on pipeline laying in marine environment and describes a case study of stresses induced over existing pipelines due to laying of new subsea pipeline.

Existing three numbers subsea pipelines of 24" diameter are laid in a trench covered with engineered backfill of thickness varying from 2.5 to 3.5 m. New subsea pipeline of 20" diameter is proposed to be laid on seabed and routed to cross existing

S. Gurnani (✉) · A. Usmani · C. Singh
Engineers India Limited, New Delhi, India
e-mail: seema.gurnani@eil.co.in

© Springer Nature Singapore Pte Ltd. 2020
M. Latha Gali and P. Raghuvver Rao (eds.), *Construction in Geotechnical Engineering*, Lecture Notes in Civil Engineering 84,
https://doi.org/10.1007/978-981-15-6090-3_48

pipelines. Stress generated on existing pipeline due to existing backfill and increment in vertical stresses in the soil just above the existing pipeline due to proposed pipeline are calculated. Four pipeline loading conditions, namely, as-laid, flooded, hydro-test, and operating are considered.

Methodology and assumptions of static analysis is presented. The stresses induced due to laying of pipeline are computed and compared with the initial stresses on the existing pipeline due to backfill.

2 Literature Survey

Pipeline laying in marine environment is complicated task owing to underwater environment, failures caused by varying loads (Xiaonan et al. 2014; Huang et al. 2012; Shijuan et al. 2014), and any incorrect estimation and manipulation of stresses and deformations tends to produce irreparable damage as well as the delay in completion of projects. The structural behavior of the pipe system during installation operation is dependent on both the overall behavior of the pipeline system and the mechanism of load transfer between the installation vessel and pipe as well as soil–pipe interaction and seabed–pipe interaction (Yong and Qiang 2005; Gary et al. 1997).

In this paper, a case study of proposed new 20” pipeline which is to be laid perpendicular to existing pipeline of 24” is analyzed for stress–deformation studies. Popularly available classical solutions utilize only one type of external loading, i.e., either the pipe load or the backfill loading. In the present case study, combined effect of both types of the loadings is studied by carrying out 2-D Finite element analysis. 2-D analysis is performed as the length of pipe is infinitely long as compared with the cross-sectional dimension of pipeline.

3 Project Site and Pipeline Laying Methodology

Project site is located in the seas off east coast of India. 21.5 km long, 20” multiphase pipeline was laid in sea with the pipelay barge. Pipeline is laid in trenching and backfilled. Pipeline laid in trenching and backfilled provides protection to pipeline from anchoring or any accidental damage. It also helps in avoiding the uplift or upheaval of pipeline due to buoyancy. Typical Backfilling details of proposed 20” pipeline are provided in Fig. 1.

Following are the broad pipeline laying steps:

- (i) Pre-engineering Survey assess seabed level and seabed features
- (ii) Pipeline Design
- (iii) Preconstruction survey to reconfirm seabed level and seabed features

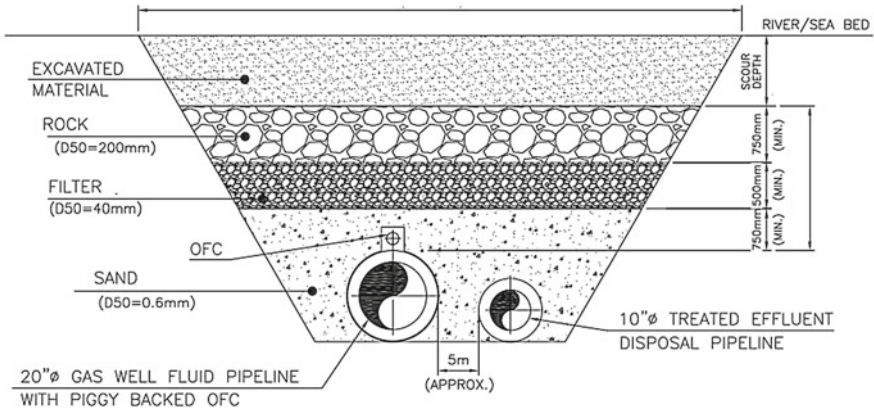


Fig. 1 Typical subsea pipeline trenching detail of 20" proposed pipeline from KP9.5 to KP21.5

- (iv) Barge positioning, Barge track control, Anchoring, Trenching, Touchdown monitoring, etc.
- (v) Pipeline handling from separate transportation barge
- (vi) Pipeline welding and laying with S-lay method
- (vii) Backfilling.

During the pre-engineering survey, it was found that proposed 20" pipeline is to be laid perpendicular to three numbers 24" diameter existing pipeline, and thus it has to cross the 131 m long trench. Typical trenching details of existing pipeline are indicated in Fig. 2. The stress induced due to laying of new pipeline on the existing pipeline is studied.

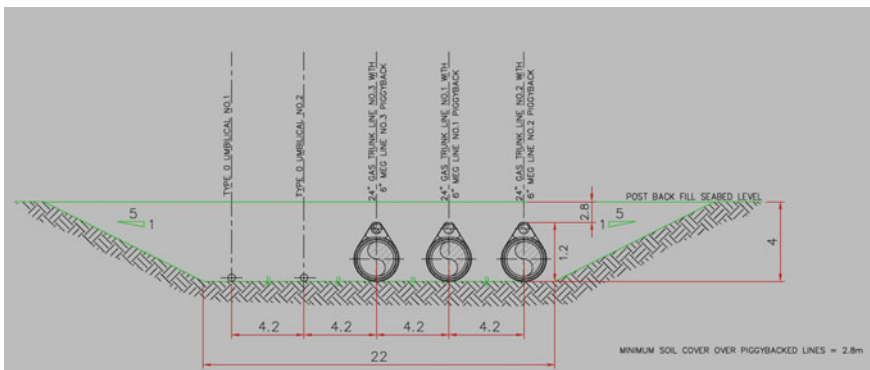


Fig. 2 Typical submarine pipeline trenching detail of 24" existing pipelines

4 Analysis Methodology

The Fig. 3 is an indicative figure showing crossing over of pipelines. There exists a graded sand backfill above existing pipelines with thickness of backfill varying from 2.5 to 3.5 m. Seabed level is considered to be flushing with the backfill level, and the proposed pipeline is planned to be laid directly on the existing bed level, i.e., just above the backfill.

Refer Table 1 for backfill layers properties. Plane A-A indicates plane just above the top of existing pipeline and the level corresponding to this plane is called as existing pipeline level. The reference for computation of vertical stress increment in this existing condition and stress increments in the soil at this level due to laying of new pipeline are studied.

With regard to the loading conditions of the proposed pipeline, all four loading conditions, namely, as-laid, flooded, hydro-test, and operating are considered. Flooded and hydro-test loading are grouped together due to the similar load values. The loading considered in the analysis is presented in Table 2.

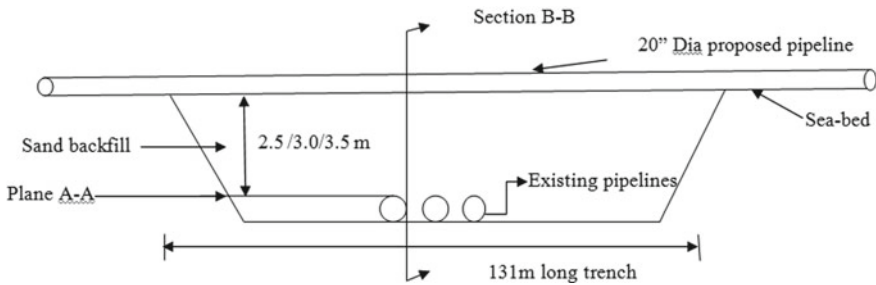


Fig. 3 Section indicating cross-over of Pipelines

Table 1 Characteristics of backfill soil

Denomination	Characteristic
Type	Graded sand
Grain size (D ₅₀)	150 μm
Backfill thickness (m)	2.5/3.0/3.5
Submerged unit weight (kN/m ³)	4
Poisson's ratio	0.40
Modulus of elasticity (N/mm ²)	40000

Table 2 Pipeline loading condition

Loading condition	Submerged pipeline load (kg/m)
As-laid	200
Flooded/Hydro-test	380
Operating	230

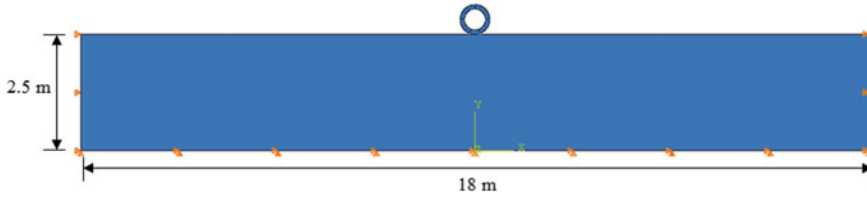


Fig. 4 Typical boundary condition used in the model

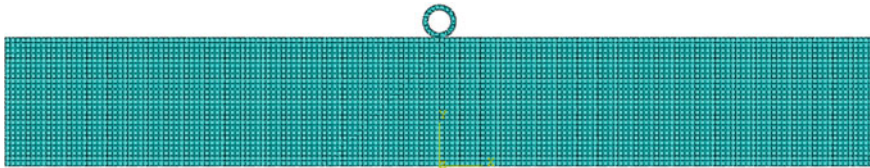


Fig. 5 Typical meshing used in the analysis

Finite Element Modeling (FEM) and Analysis (FEA) are carried out in general purpose finite element software ABAQUS version 6.11 to analyze the present stress level, i.e., stress corresponding to existing conditions and increment in vertical stresses in the soil just above the existing pipeline due to proposed pipeline. The semi-infinite soil medium is modeled using the plain strain elements CPS8R in ABAQUS. The soil domain consists of a single layer of Graded Sand (refer Table 1). In addition to the soil layer, pipeline with concrete coating is also included in the model, and stress analysis has been carried out using plain strain condition for three loading conditions as provided in Table 2. For the analysis, the soil domain boundaries are modeled at far distance from the location of pipeline in lateral direction to avoid the effect of boundary on the stress results. The bottom of the soil domain is vertically and laterally restrained at the top of existing pipelines and the lateral boundaries are provided with only lateral restraints. The boundary conditions and mesh generation for the FE model with 2.5 m backfill thickness are shown in Fig. 4 and Fig. 5, respectively.

5 Analysis Results

Incremental stresses due to proposed 20" pipeline (i.e., considering $B = 508$ mm) with loading conditions as-laid, hydro-test, and operating condition are shown in Figs. 6, 7, 8, 9, 10, 11, 12, 13, and 14, and maximum stress values are presented in Tables 3, 4, and 5. Existing condition vertical stress just above the existing pipeline due to 2.5 m ($\approx 5B$), 3.0 m ($\approx 6B$), and 3.5 m ($\approx 7B$) thick backfill material only is tabulated in Table 3, Table 4, and Table 5, respectively. Increment in vertical stresses in the soil at the top of existing pipeline due to different pipeline loadings with respect to existing conditions is also tabulated in these tables. Effect of loading intensity on

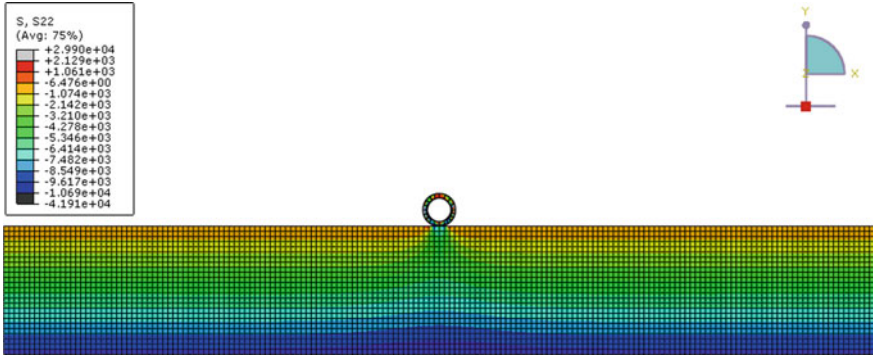


Fig. 6 Stress above existing pipeline level with proposed pipeline for as-laid condition (2.5 m backfill)

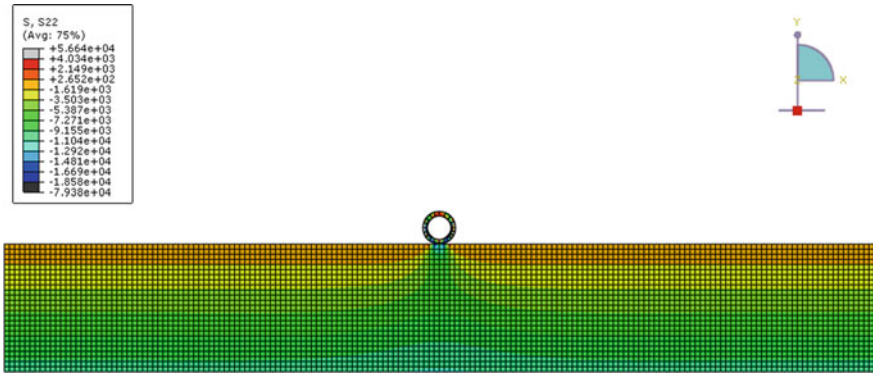


Fig. 7 Stress above existing pipeline with proposed pipeline for hydro-test condition (2.5 m backfill)

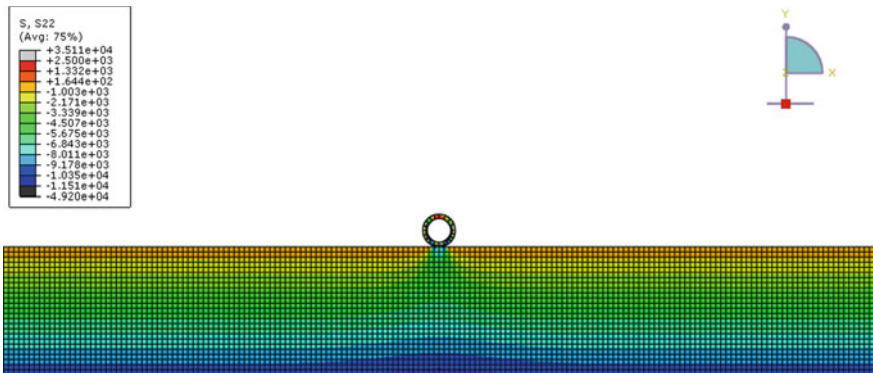


Fig. 8 Stress above existing pipeline with proposed pipeline for operating condition (2.5 m backfill)

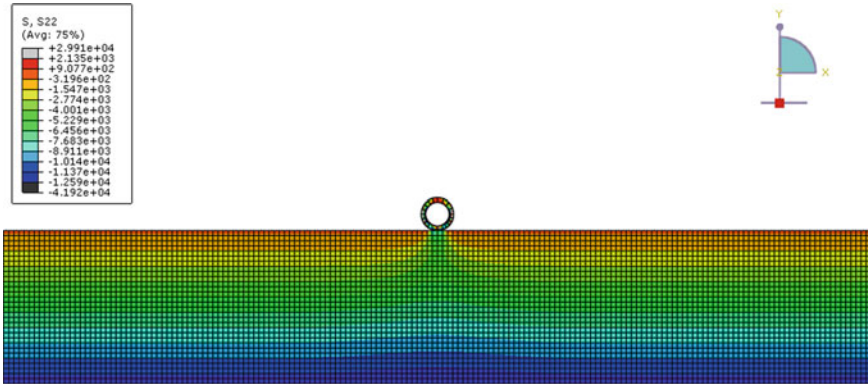


Fig. 9 Stress above existing pipeline level with proposed pipeline for as-laid condition (3.0 m backfill)

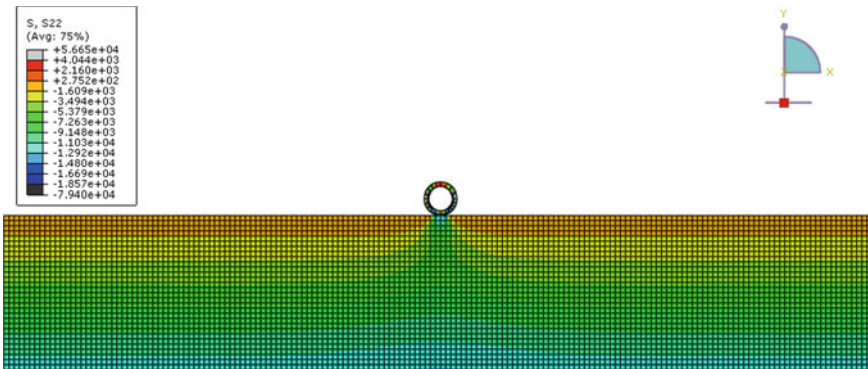


Fig. 10 Stress above existing pipeline with proposed pipeline for hydro-test condition (3.0 m backfill)

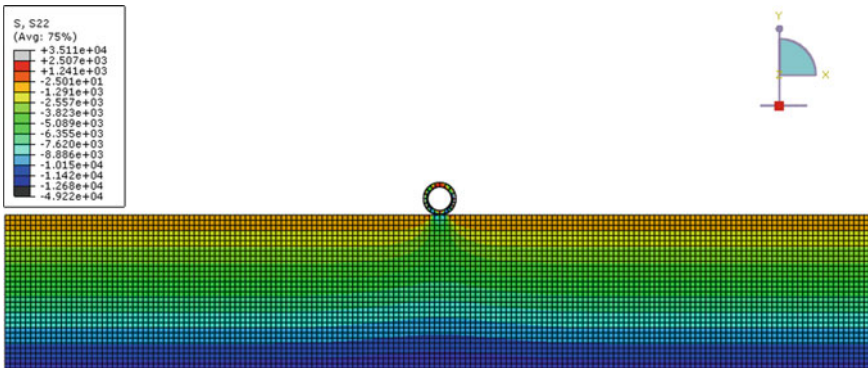


Fig. 11 Stress above existing pipeline with proposed pipeline for operating condition (3.0 m backfill)

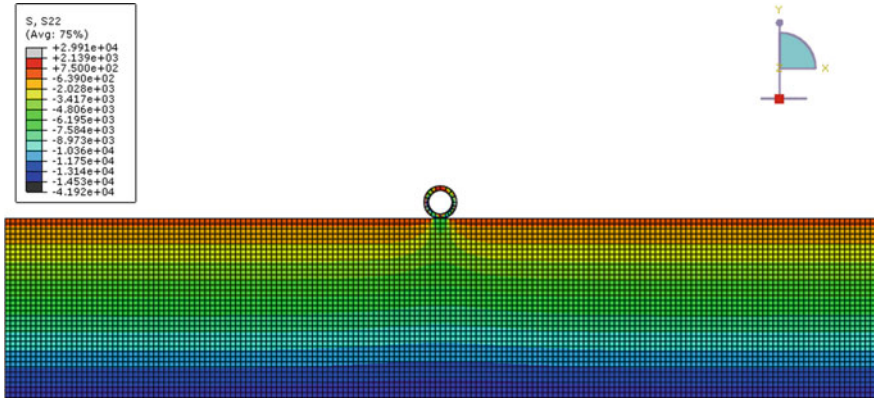


Fig. 12 Stress above existing pipeline level with proposed pipeline for as-laid condition (3.5 m backfill)

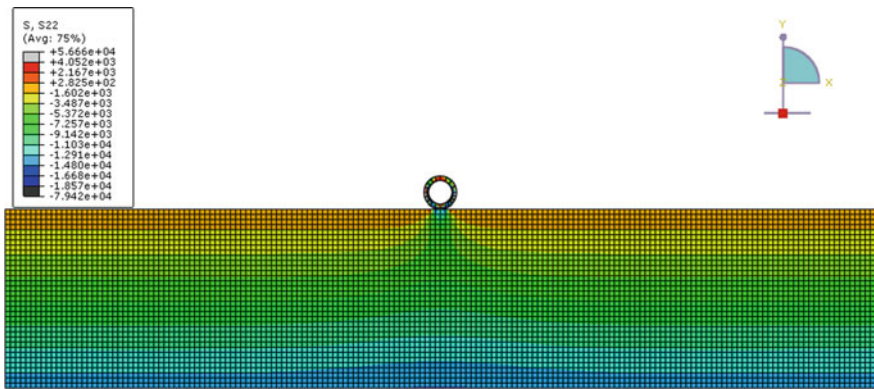


Fig. 13 Stress above existing pipeline with proposed pipeline for hydro-test condition (3.5 m backfill)

stress increment, i.e., extent of pressure bulb, is studied. It is further observed from the analysis that influence on vertical stress due to proposed pipeline is found to be limited to a depth of $\approx 2B$ below proposed pipeline level. Beyond this depth, the stress pattern is found to be dominated by the soil/backfill.

6 Discussions

Increment in vertical stresses at the existing pipelines (3 nos.-24” dia) level due to crossing over of proposed 20” diameter new pipeline with different backfill thicknesses and loading conditions is analyzed in this study. Results of maximum vertical

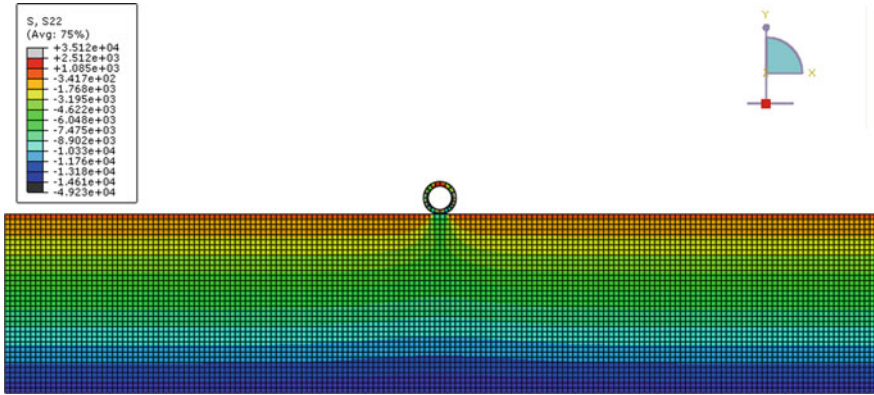


Fig. 14 Stress above existing pipeline with proposed pipeline for operating condition (3.5 m backfill)

Table 3 Maximum stress values with 2.5 m depth of backfill

Loading condition	Max. vertical stress in the soil at existing pipeline level (kPa)	Vertical stress increment in the soil at existing pipeline level (kPa)	% age increment in stress
Existing	10.06	–	–
As-laid	10.66	0.6	5.96
Hydro-test	11.3	1.24	12.32
Operating	10.7	0.64	6.36

Table 4 Maximum stress values with 3.0 m depth of backfill

Loading condition	Max. vertical stress in the soil at existing pipeline level (kPa)	Vertical stress increment in the soil at existing pipeline level (kPa)	% age increment in stress
Existing	12.08	–	–
As-laid	12.6	0.52	4.30
Hydro-test	13.1	1.02	8.44
Operating	12.7	0.62	5.13

Table 5 Maximum stress values with 3.5 m depth of backfill

Loading condition	Max. vertical stress in the soil at existing pipeline level (kPa)	Vertical stress increment in the soil at existing pipeline level (kPa)	% age increment in stress
Existing	14.09	–	–
As-laid	14.53	0.44	3.12
Hydro-test	14.9	0.81	5.74
Operating	14.6	0.51	3.62

stresses in the soil at the existing pipeline level are tabulated in Tables 3, 4, and 5. Stress conditions for different cases are illustrated in Figs. 6, 7, 8, 9, 10, 11, 12, 13, and 14. It is found that vertical stresses just above the pipeline level for existing backfill loading only are highest in case of 3.5 m backfill and lowest in case of 2.5 m backfill.

It is evident from the obtained results that for the different loading conditions of pipeline increment in vertical stresses is highest for hydro-test condition, lowest for the as-laid conditions, and for operating condition increment values are found to be between these two extremes.

Following are main conclusions:

1. Loading intensity influences pressure bulb, i.e., higher is the loading intensity, more will be the effect of stress, and this effect of stress will be up to a deeper depth.
2. From the analysis, it is observed that for all the loading conditions the impact of proposed pipeline is limited to twice the diameter of pipeline. Beyond this depth, the stress pattern is found to be dominated by the soil/backfill.
3. Effect of increase in vertical stress decreases with the increase in depth below the level of loading.
4. There is marginal increase in stress on the existing pipelines due to laying of new proposed pipeline as the existing pipeline has sufficient backfill cover. Hence, trenching and backfilling is more suitable method of pipeline laying for its protection.

Acknowledgments Authors express gratitude to their organization Engineers India Limited for giving them the opportunity to work on this task. Credit is given to the teams from Offshore and Pipeline Engineering and ETD departments for their valuable suggestions and contribution toward completion of this study.

References

- Gary H, Nauru K, Han C (1997) Expansion analysis of subsea pipe-in-pipe flowline. In: Proceedings international offshore and polar engineering conference, Honolulu
- Huang K, Shijuan WU, Hongfang LU (2012) Stress analysis of the pipeline along the slopes. *Nat Gas Oil* 30(4):1–4
- Shijuan W, Liqiong C, Hongfang L, Xiaonan W (2014) Stress analysis of submarine pipeline laying by j type. *Adv Ind Eng Manag* 3(3):49–52
- Xiaonan WU, Hongfang LU, Shijuan WU (2014) Analysis of suspended pipeline stress sensitivity. *Appl Mech Mater* 501:2331–2334
- Yong B, Qiang B (2005) Chapter 34, Installation design: subsea pipelines and risers. Elsevier, Oxford, p 607

Some Studies on Pavements on Flyash-Stabilized Expansive Subgrades



D. Nigade-Saha Sanjivani and B. V. S. Viswanadham

Abstract Construction of roads over expansive soils is associated with huge construction and maintenance costs. Stabilization of such subgrades with flyash is a cost-effective alternative to replacing the expansive subgrade with good quality borrow materials. Performance of stabilized pavements can be assessed and predicted on the basis of laboratory tests, full-scale field tests and numerical analyses. Numerical studies can simulate field and laboratory tests at very minimal costs and within a short duration. Hence, numerical analysis can be used for parametric studies to optimize the thickness of the stabilized subgrade. Engineering parameters of the untreated and treated expansive subgrade were found in a laboratory program. Static and dynamic analysis of axisymmetric models of pavement was conducted using Plaxis-2D. Improvement in parameters like vertical strain at top of subgrade and vertical displacement at top of pavement was found. The thickness of the granular layer and the treated subgrade layer was varied. The static analysis indicates that with the stabilization of the top 0.5 and 1.0 m thickness of subgrade layer, the design life of the pavement can be increased by 4–6 times and 30–70 times, respectively.

Keywords Expansive soil · Flyash-stabilized subgrade · Static analysis · Dynamic analysis · Axisymmetric model · Vertical strain

1 Introduction

Soils exhibiting significant increase in volume on exposure to water are called expansive soils. As per IS 1498-1997, soils with high degree of expansion exhibit a free swell index of 100–200%, a liquid limit of about 50–70%, a plastic limit of about 23–32% and a shrinkage limit of about 30–60%. Soils with very high degree of expansion show a liquid limit in the range of 70–90%. The plastic limit and shrinkage limit of very highly expansive soils exceed 32% and 60%, respectively, whereas the free

D. Nigade-Saha Sanjivani · B. V. S. Viswanadham (✉)
Department of Civil Engineering, Indian Institute of Technology Bombay, 400076 Mumbai,
Maharashtra, India
e-mail: bvsb228@gmail.com; viswam@civil.iitb.ac.in

© Springer Nature Singapore Pte Ltd. 2020
M. Latha Gali and P. Raghuvver Rao (eds.), *Construction in Geotechnical Engineering*, Lecture Notes in Civil Engineering 84,
https://doi.org/10.1007/978-981-15-6090-3_49

swell index exceeds 200%. In India, expansive soils which are locally called as 'Black cotton soils' are spread over 5.46 lakh sq km, i.e. 16.6 per cent of the total geographical area of the country. Entire Maharashtra except a narrow stretch along its coast and more than 90% of Madhya Pradesh are covered by these soils. Black cotton soils are also found in central parts of Gujarat, southern parts of Rajasthan, some districts of Uttar Pradesh and significant parts of southern India including some districts of Karnataka, Andhra Pradesh and Telangana.

1.1 Necessity of Stabilizing Expansive Subgrade

The black cotton soil has very good strength when in dry condition. However, on contact with water, the soil becomes very soft, thereby losing its strength. This soil, when in the soft condition, shows a lot of heave and penetrates into the voids of the granular base/sub-base layers of the pavement. Due to vehicular loading also, the expansive subgrade soil gradually intrudes into the base and sub-base courses, ultimately leading to upheaval, cracking and failure of the pavement.

The weak subgrade also undergoes significant deformation under the action of vertical compressive loads and causes rutting, corrugation, shoving, depressions and potholing in the pavement. These distresses lead to reduction in riding quality of the pavement and eventually lead to structural failure of the pavement. This results in high maintenance costs. The low strength of these soils in the presence of water necessitates thick pavement crusts, thereby increasing the capital costs of the roads.

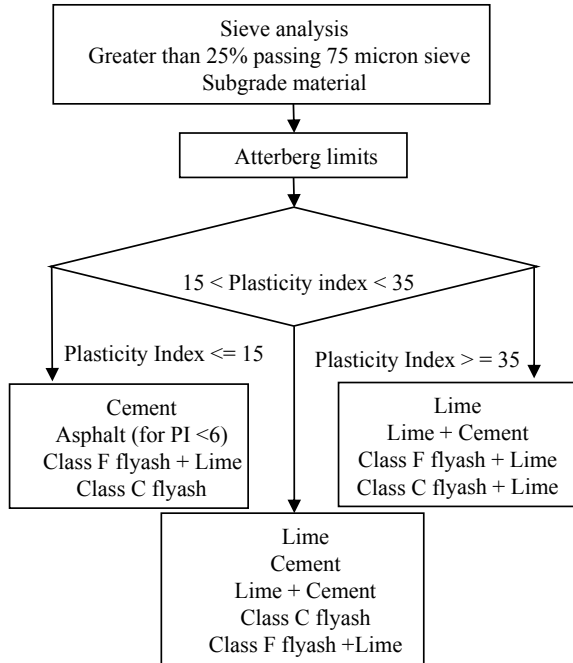
1.2 Methods of Improving Subgrade Soils

The capacity of weak soils can be improved by soil modification or soil stabilization. Soil modification aims at providing a working platform for construction equipment. A minimum strength gain of 210 kPa above natural soils is specified. The increased strength of modified subgrade is not considered in pavement design. Soil stabilization aims at increasing the subgrade strength to an extent such that its effect is accounted in pavement design. A minimum strength gain of about 350 and 700 kPa is recommended for stabilization with lime and cement, respectively.

The subgrade can be modified or stabilized through a variety of electrical, thermal, physical and chemical processes. The physical/mechanical stabilization includes soil removal and replacement, soil densification, soil blending and soil reinforcements with geosynthetics, etc. The chemical processes include mixing with cement, lime, cement byproducts, flyash, asphalt, etc. Typical recommendations regarding additives for subgrade stabilization are presented in Fig. 1.

Cement stabilization can be achieved by adding 5% cement to well-graded soil, 9% cement to poorly graded sand, 10% cement to non-plastic silts and 13% cement

Fig. 1 Decision tree for selection of stabilizers for subgrade (Source: Little and Nair (Little and Nair 2009))



to plastic clays. Generally, for clayey soils, 2–10% of lime is added. Depending on the soil type, about 15–30% of flyash has been reported to be used.

Class C flyash, which is produced from sub-bituminous and lignite coals, has high concentrations of calcium carbonate. It is self-cementing and requires no addition of lime and/or cement. Class F flyash, which is produced from bituminous and anthracite coals, has low concentration of calcium compounds. As it is not self-cementing, it is used in conjunction with lime for soil stabilization. Generally, 2–8% by weight of lime and 8–15% by weight of flyash is used with 0.5–1.5% of Portland cement (if necessary for initial strength gain).

The increased demands of electrical energy and availability of sufficient coal reserves has led to rise in number of coal-fired thermal power plants in the country. Indian coal is of low grade in comparison to imported coals and has ash content of the order of 30–45% as against 10–15% of the imported coal. This results in generation of a huge amount of flyash.

The level of utilization of flyash in India is low in comparison with countries like Germany, Belgium and the Netherlands where more than 95% of flyash generated is reportedly used. As per report of Central Electrical Authority, New Delhi (2016), the highest level of flyash utilization of about 62.6% was achieved in the year 2009–2010. During the first half of the year 2015–2016, utilization of flyash is 56.04% which is behind the stipulated target and hence leading to large-scale accumulation of flyash. The unutilized flyash not only causes pollution of water and air, but also requires large areas of land for its disposal. It has also been reported that the utilization of

flyash is in the range of 42% for manufacture of cement. About 10–12% utilization is seen in flyash-based building products, land reclamation, mine filling, etc. Only 5% utilization of flyash is seen in the construction of roads and embankments. Utilization of flyash in the road sector has a large potential and shall lead to savings of precious natural resources.

For increasing the utilization of flyash, the Indian government is promoting the utilization of flyash in the road sector. The latest MoEF&CC's Notification of 25th January 2016 (Ministry of Environment 2016) stipulates clauses vide which, the cost of transportation of ash for road construction shall be borne entirely/partially by the coal/lignite-based thermal power plants, for road projects under Pradhan Mantri Gramin Sadak Yojna and other asset creation programmes. Beeghly (2003) has reported that use of lime–flyash stabilization of subgrade soils can reduce construction cost by more than 20% due to permanent improvement in strength of pavement subgrade. Also, more than 100% savings can be achieved by lime–flyash stabilization in comparison with the alternative of removal and replacement of poor quality subgrades. Thus, stabilizing of weak subgrades with flyash is a promising and eco-friendly solution to several problems faced by the Power sector and the Highway sector.

1.3 Motivation Behind the Present Study

IRC 36-2010, 'Recommended practice for the construction of earth embankments and subgrade for road works' specifies the acceptance criteria/physical requirements for materials used in embankments, subgrades, etc. As per clause 4.4.1 of IRC 36-2010

Expansive clay exhibiting marked swell and shrinkage properties, and "free swelling index" exceeding 50% {when tested as per IS 2720 (Part 40)} shall not be used as a fill material. Where an expansive clay having "free swelling index" less than 50% is used as a fill material, subgrade and top 500 mm portion of the embankment just below subgrade shall be non-expansive in nature.

Thus, for embankments on expansive soils, the top 500 mm thick portion of the embankment below subgrade along with another 300 mm (for other/major district roads) to 500 mm (for state/national highways) thick portion of the subgrade needs to be of non-expansive type. Figure 2 shows a typical cross section of a two-lane National highway on expansive subgrade.

Table 1 presents the quantity of expansive soil to be replaced with non-expansive material, in order to satisfy above criteria for a two-lane NH road. It can be seen that, for a two-lane NH road on an expansive subgrade, the construction costs will be inflated by Rs. 35.85 lakhs/km for embankment in fill sections, and by Rs. 50.19 lakhs/km for embankment in cut sections.

Stabilizing of weak subgrades with flyash is a feasible solution when the cost of removal and replacement of the poor quality subgrade material exceeds the cost of

Fig. 2 Typical cross section of two-lane NH road over expansive soil

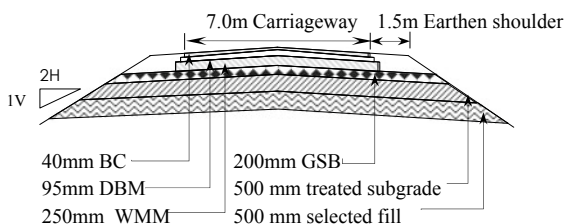


Table 1 Quantity of expansive founding soil to be replaced (For a two-lane NH with design traffic 30 MSA and design CBR of 10%)

Parameter	Details
Pavement block as per IRC 37, 2014	40 Bituminous concrete +95 Dense Bituminous Macadam +250 Wet Mix Macadam +200 Granular sub-base (total thickness = 585 mm)
Thickness of soil layer to be replaced	500 (subgrade) + 500 (fill) = 1000 mm
Average width of layer to be replaced	$10 + [2 \times (2 \times 0.585)] + \{2 \times [2 \times (1.0/2)]\} = 14.34$ m
Volume of soil to be replaced	$14.34 \times 1000 = 14340$ cum/km
Cost of providing good quality material	$14340 \times 250 =$ Rs. 35,85,000/km (@ Rs 250/cum)
Cost of removing and disposing unsuitable material	$14340 \times 100 =$ Rs. 14,34,000/km (@ Rs. 100/cum)

stabilizing the subgrade. IRC: 37-2012 offers guidelines regarding flyash-stabilized base course and sub-base course; however, clear guidelines/information regarding the mix proportions or engineering properties of flyash-stabilized subgrades in the Indian context are not available.

Performance of stabilized pavements can be assessed and predicted on the basis of full-scale field tests, laboratory tests and numerical simulations. Full-scale tests include long-term performance field studies and accelerated pavement tests. They can accurately simulate actual pavement behaviour, but are costly and hence limited to research schemes. Laboratory tests are cheaper than field tests and can be performed under controlled conditions and hence can be used to supplement field tests for research schemes. However, it has been difficult to replicate the actual behaviour of the pavement system under laboratory tests. Numerical studies are cost-effective in comparison with the laboratory and field tests and can be conducted to simulate both field and laboratory tests. They can be used for parametric studies. Numerical analysis can reflect the time-dependent behaviour. Also, they can be used to easily predict the long-term behaviour of a pavement system.

1.4 Literature Review

In case of a treated soil, the extent of stabilization achieved is a function of several parameters. The stabilizing effect depends largely on soil type, type and amount of stabilizer, amount of water used for compaction, time gap between stabilizing and compaction of blended soil and also on the conditions/duration of curing.

Lime, cement and other chemicals have been used individually or in combination with flyash as a stabilizer. A combination of flyash with lime or combination of flyash with lime and cement has been reported to be a better and economical alternative to using only flyash as an additive.

Sivapullaiah et al. (1996) observed that the addition of 1–3% lime along with flyash was found to be more effective in improving the Atterberg limits and plasticity index of highly plastic soils, than addition of flyash alone. Zha et al. (2008) have also reported that addition of about 1% lime was found to improve the swelling characteristics of a highly plastic clayey soil, stabilized with flyash. Lav et al. (2005) have highlighted the absence of puzzolanic action in case of stabilization with class F flyash, which could be improved considerably by addition of lime and/or cement.

The amount of stabilizing agent used has varied considerably. It was found that the effect of stabilization increased with content of flyash. However, the general trend is to use about 15–20% flyash. Cokca (2001) and Bose (2012) have reported the optimum percentage of flyash as 20%.

Laboratory investigations were undertaken by Nigade-Saha and Viswanadham (2018), to study the effect of combination of locally available class F type flyashes with lime, in stabilizing expansive soils. Index tests to determine free swell index and linear shrinkage along with detailed tests to determine Unconfined Compressive strength (UCS), CBR and heave were performed. The mix of expansive soil, class F flyash and lime in the proportion of 78:20:2 was effective in increasing the UCS and CBR manifold. The volume change in terms of heave, free swell and linear shrinkage was also significantly reduced.

Several numerical analyses of stabilized and unstabilized pavements have been conducted and found to agree with the laboratory and field performances. Ling and Liu (2003) used the software Plaxis-2D to conduct a FEM analysis of a pavement system, assuming plane strain conditions. The results were validated with well-controlled laboratory loading tests.

Howard and Warren (2009) have presented an axisymmetric finite element modelling of thin flexible pavement over weak soils using the software Plaxis. Axisymmetric modelling with six-noded triangular elements was used. Linear elastic model was chosen for wearing course. Mohr–Coulomb model was used for subgrade soil and the natural ground. A haversine transient load was applied to an area of 150 mm radius.

Kazemian et al. (2010) conducted a two-dimensional finite element analysis to model a rehabilitated pavement above a backfilled trench. All materials were modelled as 15-noded triangular elements following the Mohr–Coulomb criteria. Dynamic analysis was conducted with a peak load of 707 kPa and 0.025 s duration

applied on a loaded area of 150 mm radius. Rayleigh damping parameters available in the literature were adopted.

Pandey et al. (2012) conducted two-dimensional axisymmetric analysis using the Plaxis software. Both static and dynamic analyses were conducted. A pavement designed for a CBR of 7% as per IRC 37-2001 was analysed. The width of the model was assumed to be 5 m, whereas the radius of the loaded area was assumed as 200 mm. All materials were assumed to have isotropic linear elastic behaviour. The pavement materials were modelled as 15-noded triangular elements. Loading of 550 kPa was applied on loaded area for static case, whereas, for the dynamic case, a haversine pulse load of peak pressure 550 kPa and 0.1 s duration was applied. Fatigue strain at bottom of asphalt layer and rutting strain at the top of subgrade layer were predicted.

Saad et al. (2006) used a finite element program ADINA for conducting three-dimensional, dynamic analysis of a pavement. The wearing course, base and subgrade were modelled as eight-noded isoparametric elements. The wearing course was treated as linear elastic. The base was modelled as an elasto-plastic Drucker–Prager material. The subgrade was simulated by the Modified CamClay model. A dynamic load of 40 kN with tyre contact pressure of 550 kPa was simulated with a triangular wave of 0.1 s duration corresponding to an average vehicle speed of 32.18 km/s. Performance was measured in terms of horizontal strain at the bottom of the wearing course and vertical displacement at the top of subgrade.

1.5 Methodology

In the present study, an expansive soil subgrade and different stabilizers were characterized in the laboratory. Different mix types for stabilizing weak subgrades were formulated and their performance was compared through unconfined compression tests. Numerical analysis using static/dynamic loading was conducted to compare the performances of the untreated and treated subgrades. Plaxis software was used for analysing an axisymmetric model. Improvement factors to quantify the benefits of stabilization were computed.

2 Materials

The physical and chemical properties of the untreated subgrade soil, various flyashes and activators used are presented in the following paragraphs.

2.1 Expansive Soil

A black cotton soil from a locality near Pune in the state of Maharashtra has been tested. The soil showed a specific gravity of 2.685, activity of 0.6 and a free swell index of 110%. The soil exhibited a liquid limit of 80%, a plastic limit of 35% and a plasticity index of 45%. The soil has about 60.5% finer than 2μ and about 32.6% finer than 75μ . The soil is classified as a clayey soil with very high plasticity (CH). The untreated soil has OMC and MDD values of 35.5% and 12.66 kN/m^3 , respectively. The soil has an unsoaked CBR value of 6.1% and a soaked CBR value of 1.5%. It can be concluded that the soil is weak and highly expansive, thereby is unsuitable as a subgrade.

2.2 Flyash

Class F flyash contains less than 10% of CaO and hence possesses only pozzolanic properties. The flyashes available from the plants at Nashik, Dahanu, Ratnagiri and Surat were procured for the present study and are denoted as Flyash N, Flyash D, Flyash R and Flyash S, respectively. The grain size distribution curves of the untreated soil and the flyashes are presented in Fig. 3.

The Flyash D is a well-graded silty clay, light in colour and with small-sized soft lumps. The Flyash N is a gap-graded sandy silt, grey in colour, with significant amount of black particles of unburnt coal, but without any lumps. The Flyash R is light in colour and without any lumps. The Flyash S is very dark in colour, with large-sized hard lumps. Both Flyash R and Flyash S are uniformly graded silty soils. The physical and chemical characteristics of these flyashes are summarized in Table 2.

It can be seen that the specific gravity of the flyashes is low, except for flyash S. The CaO content is also less than 10%. All the flyashes used for the present study can thus be classified as class F type of flyashes. The silica content, alumina content and content of iron oxide for all flyashes are comparable.

Fig. 3 Grain size distribution

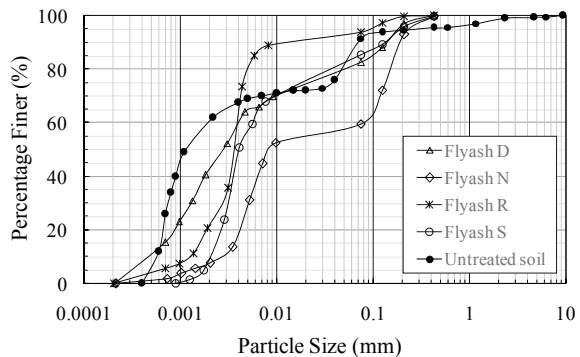


Table 2 Physical and chemical properties of flyashes

Parameter	Flyash D	Flyash N	Flyash R	Flyash S
G _s	2.065	2.054	2.125	2.430
Fine sand (%)	17.40	40.20	6.00	14.2
Silt (%)	40.60	51.80	73.10	75.5
Clay (%)	42.00	7.80	20.80	10.0
CaO (%)	0.14	0.37	1.35	1.18
SiO ₂ (%)	54.80	58.12	43.56	48.44
Al ₂ O ₃ (%)	22.00	12.52	20.51	21.44
Fe ₂ O ₃ (%)	10.80	13.22	12.50	12.18
MgO (%)	0.01	0.03	0.24	0.14

2.3 Lime

Laboratory grade quicklime available in a fine powdered form was used. The specific gravity of lime was 2.070.

3 Laboratory Tests

Details of the laboratory tests like formulation of sample mix, procedure for preparing, curing and testing of samples are presented in following paragraphs. The findings of the tests are also discussed.

3.1 Mix Design

The optimum percentage of flyash has generally been found to be 20% and hence has been adopted in the present study. The optimum lime content, which is the lowest percentage of lime in soil that gives a pH of 12.4, was found on the basis of the pH procedure developed by Eades and Grim and included in ASTM D 6276-99a. The results indicate an optimum lime content of 4%. Four trial combinations with different flyashes and 2% of lime were formulated and tested. Table 3 indicates the nomenclature for the various lime + flyash (LFA) mix.

Table 3 Nomenclature for trial mix for laboratory tests

Proportion of Soil:Flyash:Lime	Flyash D	Flyash N	Flyash R	Flyash S
78:20:2	D20L2	N20L2	R20L2	S20L2

For preparation of samples, oven-dried expansive soil passing appropriate sieve was mixed with required amount of water and kept for 24 h to ensure uniform distribution of water in the samples. The additives in required quantities in dry form were then hand mixed with the wet soil, and samples were prepared. A uniform time gap between mixing of additives with soil and compaction of the sample was maintained.

3.2 Compaction Characteristics

The compaction characteristics of the treated and the untreated soil samples were determined as per IS: 4332 (Part III). The untreated soil has OMC and MDD values of 35.5% and 12.66 kN/m³, respectively. The soil treated with LFA showed a reduction in both MDD and OMC. The OMC and MDD of the LFA-treated soil were found to be 33.0% and 12.2 kN/m³, respectively.

3.3 Unconfined Compressive Strength

To assess the effectiveness of a stabilizer, various agencies have notified the unconfined compressive strength criteria. UCS samples of size 50 mm in diameter and 100 mm in height were cast at the optimum moisture content and maximum dry density using compression device. The samples were allowed to cure for duration of 7, 14 and 28 days. Three samples each of every soil mix for each duration of curing were tested in a UTM at a strain rate of 1.25 mm/min. Figure 4 shows the improvement in the UCS values of the soil treated with Flyash R and lime.

A consistent increase in the failure stress values as well as the initial tangent modulus with increase in duration of curing was observed for all combinations. Table 4 compares the elastic parameters of the LFA-treated soil after 28 days of

Fig. 4 Improvement in UCS of soil treated with lime and Flyash R (Source: Nigade-Saha and Viswanadham (2018))

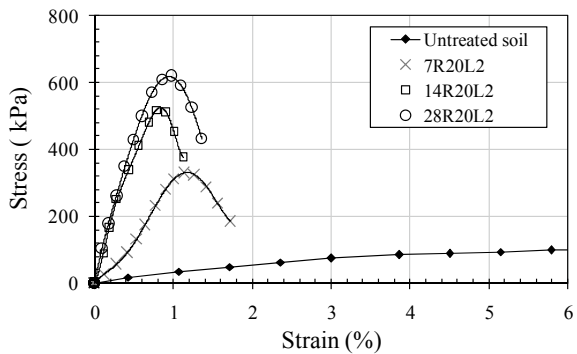


Table 4 Elastic parameters in compression of untreated/LFA-treated expansive soil

Mix	Failure stress (MPa)	Failure strain (%)	Modulus (MPa)		
			Initial tangent	1% Secant	Failure
Untreated soil	0.10	6.21	3.29	3.18	1.58
D20L2	0.51	0.93	74.27	48.91	55.25
N20L2	0.56	1.06	93.15	55.67	52.62
R20L2	0.63	0.98	82.04	62.26	63.90
S20L2	0.80	1.55	81.39	55.15	51.80

curing.

The expansive soil having a UCS of 0.1 MPa, on treatment with LFA and after curing for 28 days, exhibited unconfined compressive strength in the range of 0.5–0.80 MPa. The failure strain for LFA-treated soils varied in the range of 0.90–1.55% as against 6.2% for the untreated soil. The initial tangent modulus and the 1% secant modulus of the untreated soil were 3.29 MPa and 3.18 MPa, respectively. After 28 days of curing, the initial tangent modulus of treated soil was found to be in the range of 75–95 MPa. The 1% secant modulus was obtained in the range of 45–65 MPa.

4 Numerical Analysis

To understand the response of the stabilized subgrades to vehicular traffic, cyclic plate-load tests need to be conducted. To avoid boundary effects, these tests need to be conducted on large size models, thereby requiring large quantity of material. A lot of expenditure and effort is required for preparation of the test samples. Also, preparation of samples of stabilized subgrade is very time-consuming due to the time required for curing the subgrades. To achieve an optimum combination of various pavement layers, it is necessary to conduct parametric studies by varying the parameters like the strength and thickness of the base course and/or the treated subgrade layer. As mentioned earlier, cyclic plate-load tests are costly and time-consuming, and hence cannot be used for parametric studies. Numerical analysis can instead be used for the parametric studies.

4.1 Problem Definition

The effectiveness of the stabilization program will depend on the strength and thickness of the untreated/treated subgrade layer and the base course. Numerical analysis using the software Plaxis-2D is conducted on models with varying thickness of the

base course/treated subgrade. The effect of the thickness of stabilized layer/base course on vertical strain and settlement of the pavement has been studied.

4.2 General Parameters

An axisymmetric model was created in Plaxis-2D. The width and the depth of the formulation are adopted as 20 m and 16 m, respectively, to avoid boundary effects in dynamic analysis. 15-noded triangular elements are used to model the pavement layers. The asphaltic concrete and dense bituminous macadam layers are modelled as a single layer. Similarly, the granular base and granular sub-base are modelled as a single layer.

4.3 Material Properties for Numerical Analysis

The elastic modulus of the bituminous layer is considered as 1700 MPa, as per Table 7.1 of IRC: 37-2012. The elastic modulus of the granular layer is adopted as 300 MPa as recommended in Annexure VII of IRC: 37-2012. The properties of the untreated and the treated subgrade soil are adopted on the basis of the properties listed in Table 5. The design elastic modulus is assumed as approximately equal to half of the failure modulus. For the untreated soil, the elastic modulus of 0.8 MPa is adopted corresponding to failure modulus of 1.58 MPa. For the LFA-treated soils, the failure modulus varies from 51.8 to 63.9 MPa. Assuming a failure modulus of 50 MPa, the design elastic modulus of 25 MPa has been adopted. The values of Poisson's ratio of 0.25 for the treated layer and 0.35 for other layers are adopted from literature.

Table 5 Details of different pavement crusts analysed

Pavement layer	Thickness (mm)	E (MPa)	ν	γ (kN/m ³)
Bituminous layer	110	1700	0.35	22.8
Granular layer	325/450	300	0.35	21.2
Treated subgrade	0/500/1000	25	0.25	18.0
Natural subgrade	Variable	0.8	0.35	17.5

4.4 Thickness of Soil Layers for Parametric Study

The thicknesses of the wearing course and the base course have been decided as per the pavement blocks included in IRC: 37-2012. The cases for CBR varying from 3 to 15% and a design traffic of 10 Million Standard Axles (MSA) are considered.

The thickness of the bituminous course including the thickness of BC and DBM varies from 130 to 80 mm for CBR varying from 3 to 15%. An average value of 110 mm is adopted as thickness of the bituminous layer.

For the thickness of granular layer, two options of 325 and 450 mm are considered. As per the pavement block suggested in IRC: 37-2012, the thickness of the granular course including the thickness of granular base and GSB varies from 630 to 450 mm for CBR varying from 3 to 15%. The parametric study is therefore carried out for a thickness of granular layer of 450 mm as the first alternative. Since the minimum specified thickness of granular base and GSB is 225 mm and 100 mm, respectively, (as per plate 7 and 8 of IRC: 37-2012), the thickness of the granular layer is selected as 325 mm (which is the minimum possible thickness from construction point of view) as the second alternative.

The stabilization of top 0, 0.5 and 1.0 m of the weak subgrade is modelled in this study. Thus, there are three alternatives for thickness of treated layer. A total of six models (2 different thickness of base course \times 3 different thickness of treated layer = 6 pavement crust combinations) as given in Table 5 were analysed.

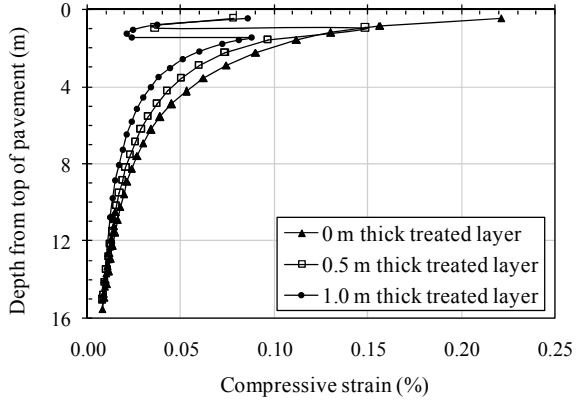
4.5 Static Analysis

For static analysis, the vertical boundaries are fixed horizontally, but allow vertical movement. The lower horizontal boundary is completely fixed, whereas the upper boundary is free. A constant loading of 560 kPa is applied on an area of radius of 150 mm. Initially, only two basic cases with 110 mm thick bituminous layer and no LFA layer were analysed. At a depth of 15 m from the top of pavement, the vertical strain due to static loading was found to reduce to about 10% of the vertical strain at the subgrade top. The depth of the lower boundary kept at 16 m is thus adequate. The variation of vertical strain with depth along centre line of loaded area is shown in Fig. 5a, b, respectively.

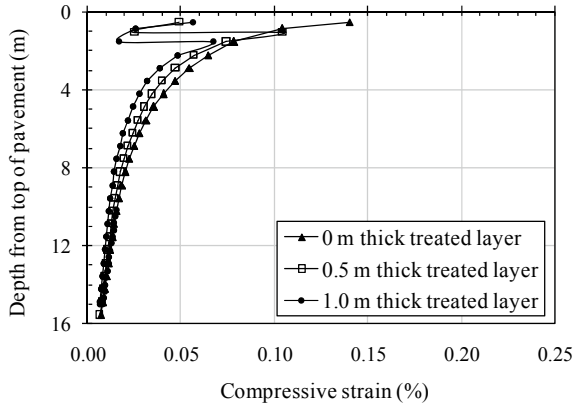
The vertical compressive strain (in percentage) at top of subgrade (ϵ_z) for the pavement with 325 mm thick base over untreated subgrade is 0.221, which is reduced to 0.149 and 0.087, as the thickness of treated layer increased to 0.5 m and 1.0 m, respectively. For the pavement with 450 mm thick base over untreated subgrade, ϵ_z reduced from 0.141 to 0.104 and 0.067, as the thickness of treated layer increased to 0.5 m and 1.0 m, respectively.

The variation of vertical displacement 's' at top of pavement with radial distance from centre of loaded area is shown in Fig. 6a, b, respectively. The vertical displacement at top of pavement for the pavement with 325 mm thick base is reduced from

Fig. 5 Variation of vertical compressive strain along centre line of loaded area



a) 325 mm thick granular base

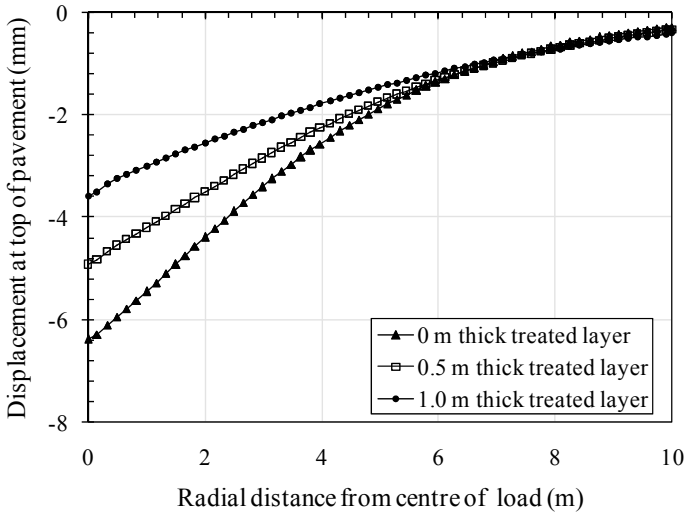


b) 450 mm thick granular base

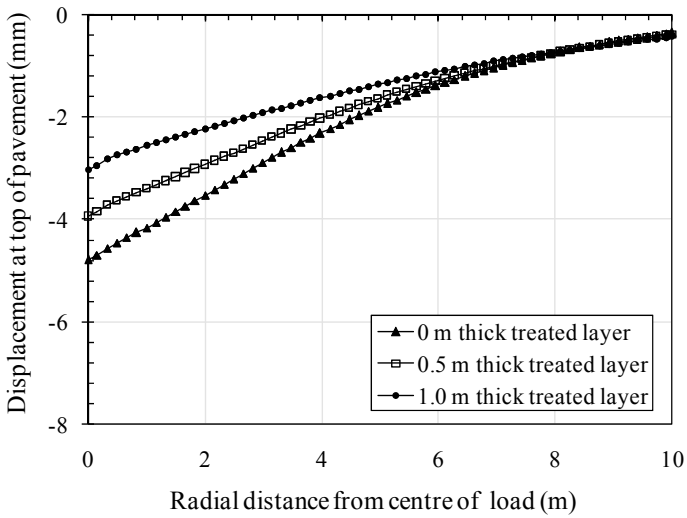
6.378 mm to 4.916 mm and 3.589 mm, as the thickness of treated layer increased from 0 m to 0.5 m and 1.0 m, respectively.

In case of pavement with 450 mm thick base, the settlement at top of pavement is reduced from 4.787 mm to 3.934 mm and 3.037 mm as the thickness of treated layer increased from 0 m to 0.5 m and 1.0 m, respectively. Table 6 lists the values of vertical strain at top of subgrade and the vertical displacement at top of pavement for the six pavement crusts.

The improvement factor due to stabilization of subgrade is computed as the ratio of the response of the untreated soil to that of the treated soil in terms of parameters like vertical strain at the top of subgrade or the settlement at top of pavement.



a) 325mm thick granular base



b) 450 mm thick granular base

Fig. 6 Variation of vertical displacement at top of pavement with radial distance from centre of static load

Table 6 Vertical strain at top of subgrade and vertical displacement at top of pavement (static analysis)

Thickness of treated layer (mm)	Vertical strain at top of subgrade (%)		Settlement at top of pavement (mm)	
	Thickness of base		Thickness of base	
	325	450	325	450
0.0	0.221	0.140	6.378	4.787
0.5	0.149	0.104	4.916	3.934
1.0	0.087	0.067	3.589	3.037

The design traffic (in cumulative standard axles) is computed by the rutting criteria specified in IRC: 37-2012, as per Eq. 1, based on the vertical strain at the top of subgrade. The equation is based on 80% reliability.

$$N_R = 4.1656 \times 10 \left(\frac{1}{\epsilon_z} \right)^{4.5337} \tag{1}$$

In this equation, ‘ N_R ’ is the cumulative standard axles causing a rutting of 20 mm. Therefore, the improvement in the life of the treated pavement can be calculated on the basis of Eq. 2 where the bracketed term on the right hand side is the improvement factor in the vertical compressive strain at the top of subgrade. The bracketed term on the left hand side of Eq. 2 is the improvement factor in design traffic, based on the rutting criteria.

$$\left(\frac{N_{R \text{ treated soil}}}{N_{R \text{ untreated soil}}} \right)^{\square} = \left(\frac{\epsilon_{z \text{ untreated soil}}}{\epsilon_{z \text{ treated soil}}} \right)^{4.5337} \tag{2}$$

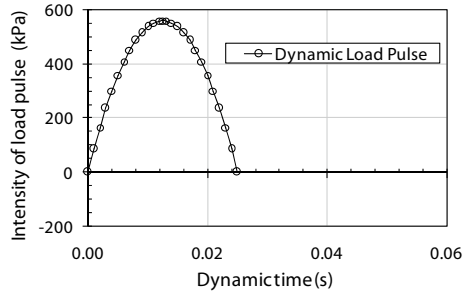
The improvement factors for the parameters like vertical compressive strain at the top of the subgrade and the rutting life of the pavement are listed in Table 7.

Thus, as per the rutting criteria specified in IRC: 37-2012, the rutting life for the pavements with 325 mm thick base will increase to 5.97 and 68.45 times by LFA treatment of the top 0.5 m and 1.0 m thick layers of the expansive subgrade,

Table 7 Improvement factors for different thickness of treated subgrade layer

Thickness of LFA-treated subgrade layer (mm)	Improvement factor ϵ_z		Improvement factor for design traffic (Rutting)	
	Thickness of base		Thickness of base	
	325	450	325	450
0.0	1.00	1.00	1.00	1.00
0.5	1.48	1.35	5.97	3.85
1.0	2.54	2.09	68.45	28.25

Fig. 7 Haversine load pulse for dynamic analysis



respectively. Similarly, the rutting life for the pavements with 450 mm thick base will increase to 3.85 and 28.25 times by treating the top 0.5 m and 1.0 m thick layers, respectively.

4.6 Dynamic Analysis

To understand the response to transient loading, dynamic analysis was also conducted. The vertical boundary below the load is fixed horizontally, but allows vertical movement. The upper boundary is free. The vertical boundary away from the load and the lowest horizontal boundary are specified as viscous.

A haversine load pulse of peak value of 560 kPa and duration of 0.025 s as shown in Fig. 7 were used. The number of calculation steps during the loading was kept as 25 since there was not much loss of accuracy.

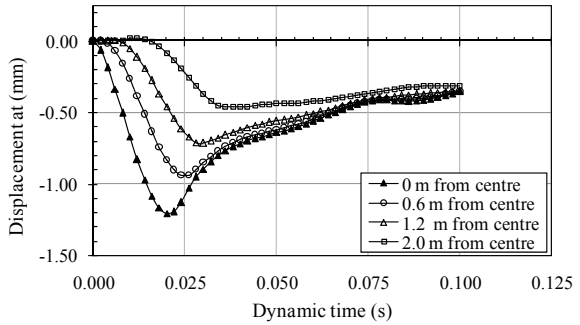
At different instances of dynamic time, the vertical displacements at points on the top of pavement at radial distance of 0, 0.3, 0.6, 0.9, 1.2, 1.5 and 2.0 m from centre of loaded area were found. Figure 8a–c show the results for the cases of 0, 0.5 and 1.0 m thick treated layers below 325 mm thick base layer.

For purpose of clarity, the results for points at a distance of 0.3, 0.9 and 1.5 m are not shown in above figures. The maximum value of peak settlement is seen below the centre of loaded area and decreases with increased radial distance. Also, with the increase in thickness of the treated layer, a marked decrease in the amount of peak as well as the residual settlement is observed.

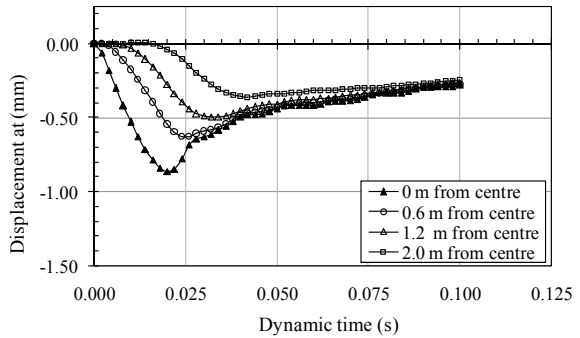
With the increase in thickness of the treated subgrade layer, the time for which the pavement system remains deformed under the load impulse is reduced due to the increase in stiffness of the pavement system. Thus, with the increase in thickness of the treated layer, the overlapping of the stresses and deformations caused due to subsequent load cycles is reduced, thereby reducing the cumulative distress caused.

The peak displacements occurring during single application of dynamic load, at points on the top of pavement, at different radial distances from centre of loaded area, are plotted to obtain the settlement profile. Figure 9a shows the settlement profiles in case of 325 mm thick base.

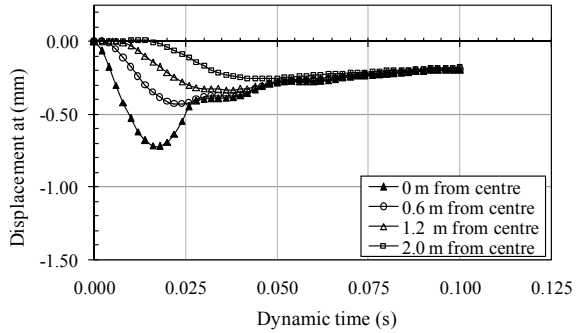
Fig. 8 Variation of vertical displacement at pavement top with time (325 mm thick granular base)



a) 0m thick treated layer



b) 0.5m thick treated layer

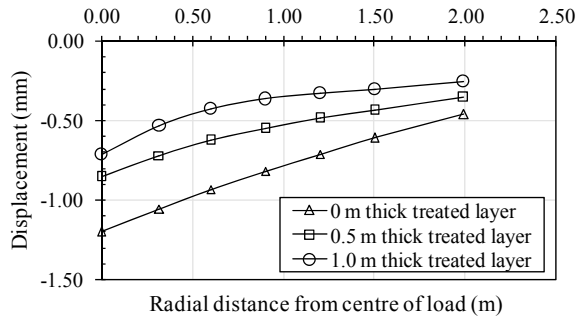


c) 1.0m thick treated layer

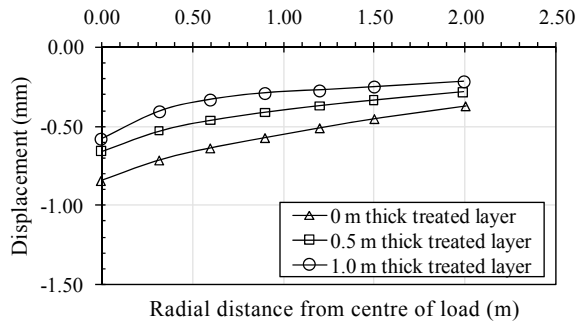
The maximum peak settlement has reduced from 1.204 mm to 0.859 mm and 0.717 mm, respectively, for 0.5 m and 1.0 m thick treated layers. Thus, about 40 and 68% reduction in maximum peak settlement is seen when the top 0.5 m thick layer and top 1.0 m thick layer of the subgrade below 325 mm thick base is treated.

The settlement profiles for the three cases of 450 mm thick granular base are presented in Fig. 9b. The maximum peak settlement has reduced from 0.846 mm to

Fig. 9 Variation of peak vertical displacement at top of pavement with radial distance from centre of dynamic load



a) 325mm thick granular base

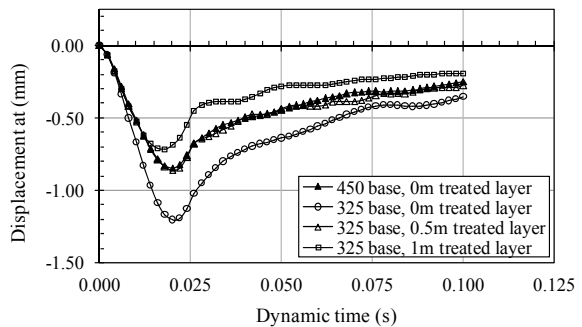


b) 450mm thick granular base

0.659 mm and 0.581 mm, respectively, for 0.5 m and 1.0 m thick treated layers. Thus, about 28% and 45% reduction in maximum peak settlement is seen when the top 0.5 m thick layer and top 1.0 m thick layer of the expansive subgrade below 450 mm thick base is treated with LFA.

The graphs of vertical displacement versus dynamic time, for a point at top of pavement below centre of loaded area, for the cases of 0 m, 0.5 m and 1 m thick LFA-treated subgrade layers, laid below a 325 mm thick base are presented in Fig. 10.

Fig. 10 Vertical displacement below centre of loaded area for different pavement blocks



These curves are compared with that of 450 mm thick base laid directly over the untreated subgrade.

It is observed that the response of 325 mm thick base over 0.5 m thick LFA-stabilized subgrade is exactly similar to that of 450 mm thick base over untreated subgrade. This indicates that the pavement comprising 325 mm thick base course laid over 0.5 m thick LFA-treated subgrade is equivalent to a pavement comprising 450 mm thick base course laid directly over the untreated subgrade.

It can be concluded that, with the present mix proportion of 20% class F flyash and 2% of lime as activator, treatment of the top 500 mm thick subgrade soil can lead to a reduction of $450 - 325 = 125$ mm thickness of the granular layer, which is $125/450 = 28\%$ reduction in the quantity of granular layer. Thus, stabilization of the subgrade results in significant savings in scarce raw materials required for constructing pavements on expansive soils.

5 Conclusions

Stabilization of expansive soils in lieu of their removal and replacement is highly cost-effective due to significant reduction in construction and maintenance costs. Laboratory test program on a highly expansive black cotton soil treated with a mix of 20% class F flyash and 2% lime indicated considerable improvement in the strength parameters. From the results of the laboratory tests, it can be concluded that, with LFA treatment of expansive soil, the UCS can be improved from 100 kPa to the range of 500–800 kPa, whereas the failure modulus can be improved from 1.6 MPa to the range of 50–65 MPa.

Numerical analysis was conducted on six pavement compositions. Parameters like vertical strain at top of subgrade and vertical displacement at the top of pavement were studied in the static analysis. In the dynamic analysis, variation of vertical displacement at top of pavement with dynamic time was studied. Variation of maximum vertical displacement at top of pavement with radial distance from loaded area was also observed in dynamic analysis. Following conclusions were drawn from the numerical analysis:

1. For pavements on expansive subgrades and having 325–450 mm thick granular courses, the results of static analysis indicate that when the top 0.5 m thick layer of expansive subgrade is stabilized by LFA treatment, the vertical strain at top of subgrade is reduced by 1.35–1.5 times. On treatment of the top 1.0 m thick layer, the reduction in vertical strain is of the order of 2.1–2.5 times. The corresponding design axles of the stabilized pavements, calculated on the basis of rutting criterion, are of the order of 4–6 times of that for the untreated pavement in case of stabilization of top 0.5 m layer and 30–70 times for stabilization of the top 1.0 m layer.
2. The reduction in the maximum settlement at the top of pavement, as per static analysis, is in the range of 22–30% and 58–78% for stabilization of the top 0.5 m

and 1.0 m thick layers of the subgrade, respectively. As per dynamic analysis, the reduction in the maximum settlement (at top of pavement) due to LFA treatment of the top 0.5 m and 1.0 m thick layer of the expansive subgrade is in the range of 28–40% and 45–68%, respectively.

3. Results of the dynamic analysis indicate that with the increase in thickness of the treated subgrade layer, there is a marked decrease in the amount of peak settlement as well as the residual settlement. Also with the increase in thickness of the treated layer, the overlapping of the stresses due to subsequent load cycles is reduced, thereby reducing the cumulative distress.
4. The static as well as dynamic analysis indicate that treatment with 20% class F flyash + 2% lime causes tremendous improvement in performance of a pavement over an expansive subgrade. The improvement factors obtained from static and dynamic analysis are comparable.
5. The treatment of only the top 500 mm thick subgrade soil with LFA treatment (20% class F flyash + 2% of lime) was found to reduce the thickness of granular layer by 125 mm. The effects of stabilization of subgrade are more prominent in case of lesser thickness of base course.

Thus, from the results of both laboratory studies as well as numerical studies, it can be concluded that the LFA treatment is highly effective in stabilizing expansive subgrades.

References

- ASTM D 6276-99a: Standard test method for using pH to estimate the soil-lime proportion requirement for soil stabilization
- Beeghly J (2003) Recent experiences with lime-flyash stabilization of pavement subgrade soils, base and recycled asphalt. In: Proceedings of international ash symposium, vol 46. University of Kentucky, pp 1–18
- Central Electrical Authority, New Delhi (2016) Report on flyash generation at coal/lignite based thermal power stations and its utilization in the country for 2014–15 and 2015–16. New Delhi, India
- Cokca E (2001) Use of Class C fly ashes for the stabilization of an expansive soil. *J Geotech Geo-environ Eng* 127(7):568–573
- Howard I, Warren K (2009) Finite element modeling of instrumented flexible pavements under stationary transient loading. *J Trans Eng* 135(2):53–61
- IRC: 36 (2010) Recommended practice for the construction of earth embankments and subgrade for road works, New Delhi, India
- IRC: 37 (2012) Guidelines for the design of flexible pavements, New Delhi, India
- IS 2720(Part 40) (1977) Methods of test for soils: determination of free swell index of soils. Bureau of Indian standards, New Delhi
- IS 4332(Part 3) (1967) Methods of test for stabilized soils: test for determination of moisture content-dry density relation for stabilized soil mixtures. Bureau of Indian standards, New Delhi
- Kazemian S, Barghchi M, Prasad A, Maydi H, Huat B (2010) Reinforced pavement above trench under urban traffic load: Case study and finite element (FE) analysis. *J Sci Res Essays* 5(21):3313–3328

- Lav A, Lav M, Goktepe A (2005) Analysis and design of a stabilized flyash as a pavement base material. In: Proceedings of international conference of world of coal ash, vol 85, Kentucky, pp 2359–2370
- Ling H, Liu K (2003) Finite element studies of asphalt concrete pavement reinforced with geogrid. *J Eng Mech* 129(7):801–811
- Little D, Nair S (2009) Recommended practice for stabilization of subgrade soils and base material. NCHRP Project 20-07 Final report, Transportation research board, pp 1–57
- Ministry of Environments (2016) Forests and Climate Notification published in The Gazette of India, Extraordinary, Part II, section 3, Sub-section (ii), vide S.O. 254(E), dated the 25th January, 2016
- Nigade-Saha S, Viswanadham B (2018) Experimental study of flyash-stabilized expansive soil. In: Proceedings of the international symposium on geotechnics for transportation infrastructure, ISGTI-2018, vol 1. Springer, New Delhi, India, pp 634–639
- Pandey S, Rao K, Tiwari D (2012) Effect of geogrid reinforcement on critical responses of bituminous pavements. In: Proceedings of 25th ARRB conference—shaping the future: linking policy, research and outcomes, Perth, Australia, pp 1–16
- Saad B, Mitri H, Poorooshasb H (2006) 3D FE analysis of flexible pavement with geosynthetic reinforcement. *J Trans Eng ASCE* 132(5):402–415
- Sivapullaiah P, Prashanth J, Sridharan A (1996) Effect of fly ash on the index properties of black cotton soil. *Soils Found* 36(1):97–103
- Zha F, Liu S, Du Y, Cui K (2008) Behavior of expansive soils stabilized with fly ash. *Nat Hazards* 47(3):509–523

Comparison of Geostatistical Technique to Assess the Safe Zones of Water Storage



Sunayana, Vikas Kumar, and Komal Kalawapudi

Abstract The quality of water leaching through chemically contaminated soil has affected underground storage. This study aims to find the region of permissible groundwater quality for domestic purposes existing near landfill. This was done by using ArcGIS, and different interpolation methods were used to know the area lying under permissible standards of water usage. It was found that for year 2014 IDW was the best spatial interpolation method, while for 2016 RBF was best with least Root Mean Square error (RMSE) and high value of coefficient of determination (R^2). The results of the analysis were helpful in identifying safe zone of groundwater storage and also show that sampling locations are under tidal effect. While assessing zones, it has been found that certain zone has exceeded concentration compared to previous year. This may be attributed to leachate percolation or mixing of high TDS water.

Keywords Interpolation · Landfill · Contamination sources · Groundwater · Deterministic methods

1 Introduction

Soil and its interaction with water is a natural process, and during this process, individual behavior of both components should not be compromised. But with the time and added pressure on natural resources, their quality in isolation has been impacted. Groundwater resources are one such resource of water where earth material acts as a natural filter compared to surface water sources, which are directly exposed and more prone to pollution. The sources of pollution in surface water are numerous but groundwater sources are also getting polluted in the form of surface runoff from contaminated areas, which in turn is joining groundwater storage. Even after

Sunayana (✉) · K. Kalawapudi
Mumbai Zonal Centre, CSIR-NEERI, Mumbai, India
e-mail: sunayana@neeri.res.in; sunayana21iitk@gmail.com

V. Kumar
CE Department, MMMUT, Gorakhpur, U.P, India

© Springer Nature Singapore Pte Ltd. 2020
M. Latha Gali and P. Raghuvver Rao (eds.), *Construction in Geotechnical Engineering*, Lecture Notes in Civil Engineering 84,
https://doi.org/10.1007/978-981-15-6090-3_50

multiple stages of movement through void spaces, groundwater is getting polluted. It includes industrial wastes, municipal landfills, agricultural chemicals, septic system and cesspool effluents, leaks from system, petroleum pipelines and storage tanks, animal wastes, acid mine drainage, oil field brines, saltwater intrusion and irrigation return flow, etc., (Morales et al. 2000) which are some of the anthropogenic activities that are polluting aquifers, i.e., stored groundwater.

In such scenario, the quality of groundwater which exists becomes important, and also because of tremendous population load on every natural resource, the dependency on one of the natural resources, i.e., groundwater resource for domestic uses, is quite high in many areas of country (Vijay et al. 2011). The unsustainable usage of groundwater in developing countries poses an issue of sustainable yield from aquifer in near future (Mohanty et al. 2010) and also a threat to the degradation of its water quality. Thus, assessment of safe zones for ground water storage becomes important with reference to use as well as preventing them from any further deterioration via any activity. Researchers in field of groundwater quality and modeling had used GIS for many decision-making processes. For many groundwater long-time monitoring projects, geospatial techniques had been used to optimize monitoring locations (Ling et al. 2005). Spatial distribution for hillside groundwater level had been done by hydrologists by making contour maps (Sherlock and McDonnell 2003). Effect of landfill seepage on groundwater has been studied (Atekwana and Krishnamurthy 2004). Evaluation of processes governing groundwater quality has been done using GIS for Gujarat (Rina et al. 2011). Geostatistical assessment of nitrate in groundwater of Puri city has been done (Varma et al. 2012). GIS has been efficiently used as a spatial interpolation tool for groundwater characterization and quality analysis. In this study, groundwater quality with total dissolved solids as the parameter has been spatially interpolated using different methods such as IDW, LPI, and RBF. Based on these results, safe zones of groundwater storage have been identified for the study area.

2 Study Area

The area selected for finding the safe zones of ground water storage for domestic use is near landfill site in Mumbai. The site is located in the eastern suburbs of Mumbai between Thane and Mumbai off the Eastern Express Highway (No. 3) among a mangrove swamp area as depicted in Fig. 1 with latitudes 19°7'16.15"N and 19°7'38.67"N and longitudes 72°57'01.89"E and 72°57'02.55"E and elevation above mean sea level of 1 m. The people are residing within 500 m vicinity on one side of the site, and on the other side, there are mangroves and creek area which has offshoots and via those saline water is reaching to the mangroves.



Fig. 1 Study site with sampling locations marked

3 Materials and Methods

The groundwater quality analysis for various parameters at ten different locations of the site as shown in Fig. 1 was done. In year 2014, monitoring of these locations was done to establish baseline concentrations, and again in year 2016 analysis was conducted. The study area is a dumping site and has vicinity to human inhabitation. Therefore, anticipating any impact on human population and also as per the Municipal Solid Waste Management Rules (2016), the physicochemical parameters were selected to understand the groundwater quality. The parameters analyzed were pH, Total Dissolved Solids (TDS), Total Hardness, Chlorides, Sulfate, Nitrates, Dissolved Oxygen, Total suspended Solids, and Heavy metals. Onsite measurement for certain parameters like temperature, pH, and conductivity was carried out immediately after sample collection at the spot using hand-held meters. For physicochemical analysis, sample was collected separately in two-liter jerry cans and preserved at the site and transported to laboratory for analysis. All the water parameters were carried out using standard protocol “Standard Methods for the Examination of Water and Wastewater (APHA)” 21st Edition. In this study, only the spatial variation for Total Dissolved Solids (TDS) for years 2014 and 2016 was taken to find and assess suitable zones for groundwater domestic usage. Further, geostatistical deterministic methods like Inverse Distance Weighting (IDW), Local Polynomial Interpolation (LPI), and Radial Basis Function (RBF) were used to do the spatial analyst for existing safe and portable groundwater storage zones.

3.1 Interpolation Methods

Researchers have been using different interpolation methods for different mapping scenarios: be it spatial interpolation method based on collected depth samples (Merwade 2009), topographic data-based methods (Alcântara et al. 2010), and remote sensing methods (Gholamalifard et al. 2013; Abileah and Vignudelli 2011). Presently, there are more than 40 spatial interpolation methods described in the literature, which are classified into deterministic, geostatistical, and combined types (Curtarelli et al. 2015). The best performance of model depends upon many factors (e.g., sample size and the nature of the data), which affect the estimation of a spatial interpolator, and the performance of different model is on case-to-case basis. Thus, explicitly one cannot be said as the best performing model. In this study as mentioned earlier only the deterministic interpolation techniques were used to find safe zones of water storage in the study area. The IDW method used is based on extent of similarity, RBF on degree of smoothing, and LPI, which were the three different methods that had been adopted.

3.1.1 IDW Method

This is one of the most used deterministic spatial interpolation methods in various disciplines of engineering and science. The estimated values in this method are based on values of nearby known locations. The weights for different interpolating points are the inverse of the distance from the interpolation point. This signifies that points which are near have high values of weights compared to points which are at distant (Robinson and Metternicht 2006; Bhunia et al. 2018).

$$Z(x_0) = \frac{\sum_{i=1}^n \frac{x_i}{d_{ij}^\alpha}}{\sum_{i=1}^n \frac{1}{d_{ij}^\alpha}} \quad (1)$$

where $Z(x_0)$ is the final interpolated value, n is the total number of sample data values, x_i is the i th data value, d_{ij} is the separation distance between interpolated value and the sample data value, and α is the weighting power.

3.1.2 LPI Method

This method uses local polynomial by using points in the specified neighborhood instead of all data (Hani and Abari 2011). Using this method, neighborhoods can overlap, and surface value at the center of neighborhood is the predicted value. This method is suitable for surfaces that have short-range variation (ESRI 2001).

Table 1 Summary of statistical parameters for TDS in study area

Year	Total no. of samples	Min	Max	Avg.	SD	CV
2014	105	890	55249	10186	16498	161.96
2016	124	321	5353	2733	1466	53.67

SD = Standard Deviation, CV = Coefficient of Variation

3.1.3 RBF Method

This method of generating interpolation surfaces predicts values near to measured values at the same point, and the surface which is generated should pass through each measured point. This method has been derived from algorithm developed for artificial neural networks and thus uses same algorithm (Sun 2009). When using this method, ArcGIS tool has option of choosing Thin-Plate Spline (TPS), Spline with Tension (SPT), Completely Regularized Spline (CRS), Multi-Quadratic function (MQ), and Inverse Multi-Quadratic function (IMQ) as one of the techniques under this method. It has been highlighted that RBF should not be chosen for those datasets where there is a significant change in surface values even in short distances (ESRI 2001). The most extensively used RBF is Completely Regularized Spline, which has been used in this study as well.

3.2 Monitoring Data

As highlighted earlier, monitoring data for years 2014 and 2016 was used for the spatial analysis in this study. The annual average of values for total dissolved solids was taken for both the years separately at all sampling locations. The statistics for total dissolved solids (mg/l) as annual average for years 2014 and 2016 is mentioned in Table 1.

From Table 1, it can be inferred that in year 2014 there were very high concentrations of total dissolved solids in groundwater, but on the contrary in year 2016 the values had come down significantly. The high TDS values may be attributed to mixing of different water sources such as freshwater whose TDS is less than 1500 mg/l, brackish water 1500–5000 mg/l, saline water greater than 5000 mg/l, and seawater between 34,000 and 38,000 mg/l (Wilson et al. 2014). The analysis of samples for years 2014 and 2016 was interpolated separately using deterministic methods to visualize changes on year-to-year basis. Table 2 presents the statistics for different interpolation methods comparing Root Mean Square Error (RMSE), Mean Absolute Error, and coefficient of determination (R^2).

From Table 2, it can be inferred that for year 2014 in interpolating TDS concentration for the study site IDW method was best among all three methods, while for year 2016 RBF was best in spatial interpolating because RMSE values were least

Table 2 Comparison of statistical parameter between observed value of total dissolved solids and predicted value by three interpolation methods for years 2014 and 2016

Method	RMSE	MAE	R ²
<i>2014</i>			
IDW	0.2593	0.2098	0.94
LPI	0.3045	0.2591	0.87
RBF	0.2717	0.2295	0.92
<i>2016</i>			
IDW	0.2918	0.2343	0.96
LPI	0.3218	0.2486	0.89
RBF	0.2874	0.2233	0.98

and gave high values of R² also. The order of best performance method based on least RMSE for 2014 is IDW < RBF < LPI and for year 2016 is RBF < IDW < LPI.

In Figs. 2 and 3, the difference between experimental value and predicted value has been shown at all locations for both the years.

On seeing Fig. 2, it can be said that MW6, MW8, and MW10 showed high values of error; this can be because of rapid change in quality of water existing near those points as can be confirmed from year 2016 results that at point MW6 the concentration of TDS has gone up significantly as in Fig. 9. For point MW8, the concentrations are reduced in year 2016 compared to year 2014. Since these resultant TDS results are annual average, it can be said that because of monsoon and seawater ingress there is a rapid change in some groundwater existing safe zones for points which are

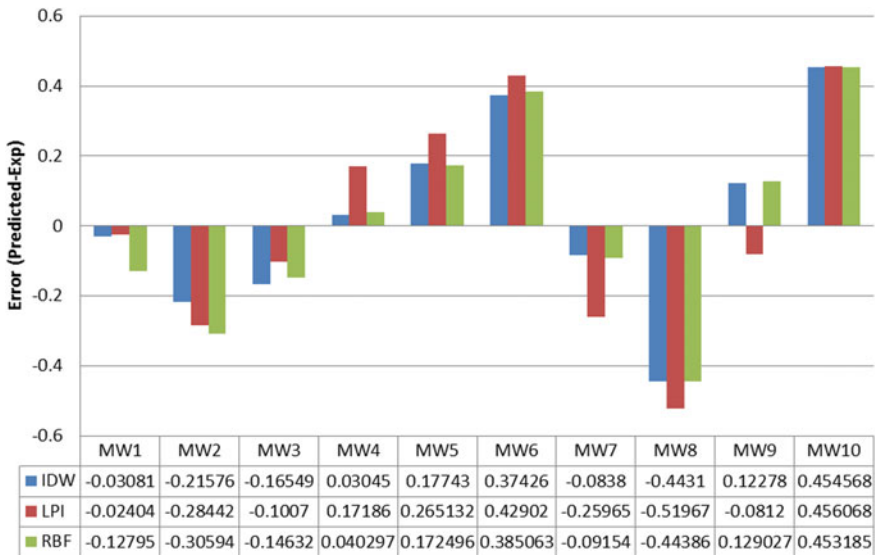


Fig. 2 Difference between predicted and experimental value for all the three methods for year 2014 at all the sampling locations

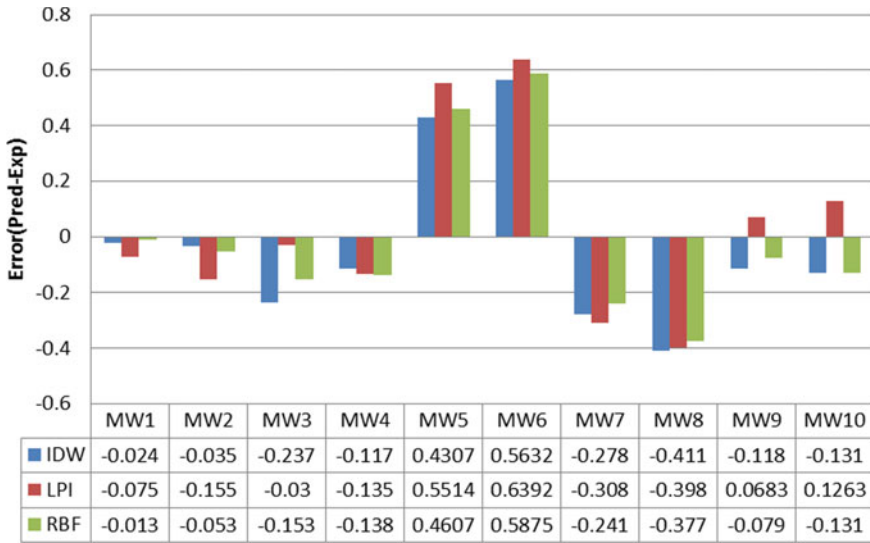


Fig. 3 Difference between predicted and experimental value for all the three methods for year 2016 at all the sampling locations

affected either by leachate percolation or through seawater ingress from the creek. Point MW6 region initially in year 2014 was one of the safe zones as per TDS concentration, i.e., concentration varied from 300–1000 mg/l, while in year 2016 this point with RBF interpolation maps (Fig. 9) came under unsafe zone of water as concentrations were above 2000 mg/l. The marking of safe zones is done on the fact that desirable limit for drinking water is 500 mg/l and permissible limit is 2000 mg/l; as per Indian Standards for drinking water, any zone showing values higher than these values would be marked as unsafe zone for groundwater usage for drinking purpose.

4 Results

The spatial interpolation maps using deterministic methods had been made in ArcGIS for years 2014 and 2016 separately using IDW, LPI, and RBF method. The Figs. 4, 5, and 6 are for year 2014, and on comparing these figures it can be interpreted that zone near point MW7, MW9, and MW 10 falls under the category of unsafe zones, while all other zones are safe to use as per total dissolved solids norms and standards.

As the monitoring was carried out in 2016 as well for TDS concentrations, the interpolation maps are quite different from year 2014 at the same monitoring locations. After comparing the statistics of different interpolation methods for year 2016, RBF was the best performing method, and it was seen that zone near MW6 has

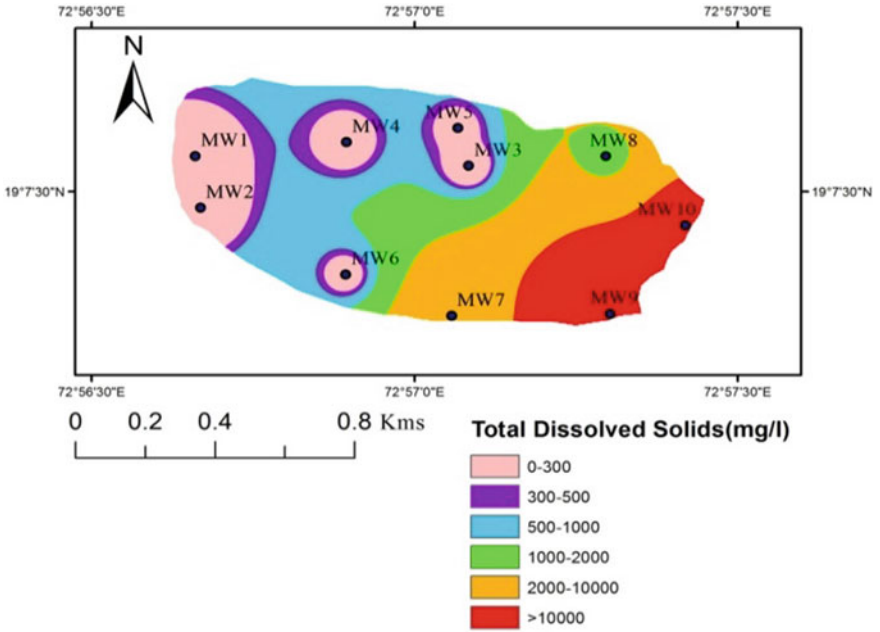


Fig. 4 Spatial Interpolation map using all sampling locations for 2014 by IDW method

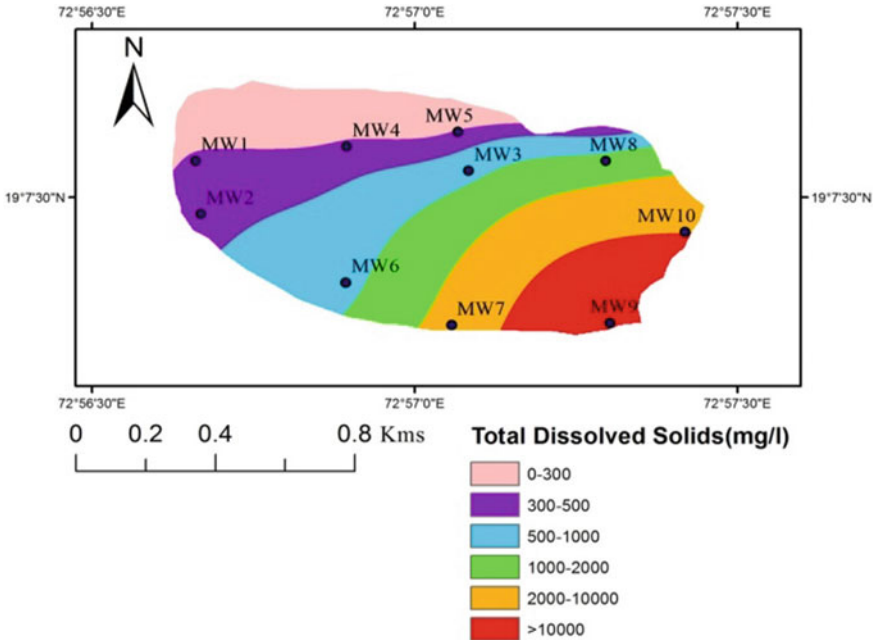


Fig. 5 Spatial Interpolation map using all sampling locations for 2014 by LPI method

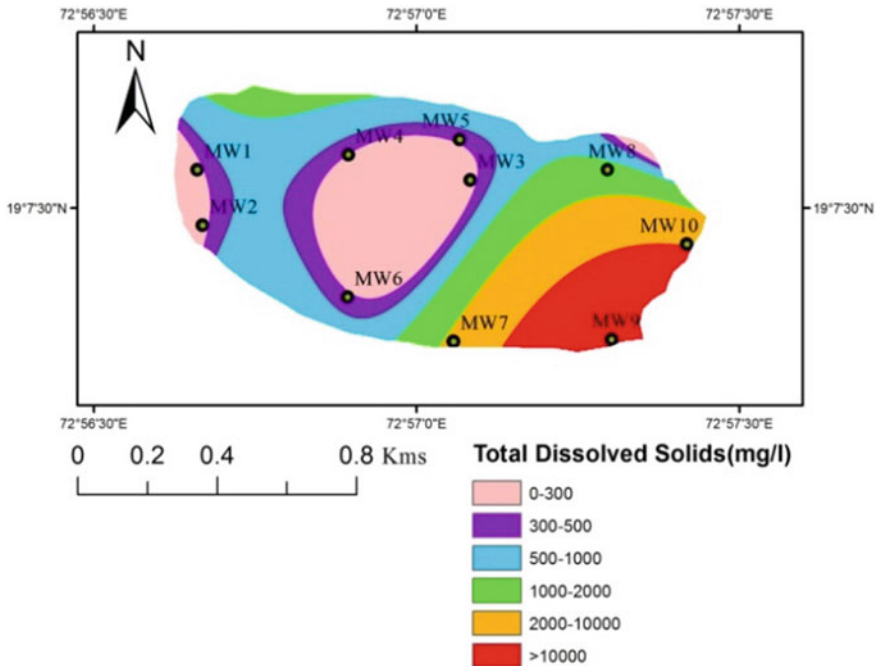


Fig. 6 Spatial Interpolation map using all sampling locations for 2014 by RBF method

got high TDS concentrations for year 2016 and has become an unsafe zone of groundwater storage.

The maps shown in Figs. 7, 8, and 9 were used to understand the extent of safe and unsafe zones of groundwater storage.

From Figs. 7, 8, and 9, it can be said that zones near MW9 and MW10 are still unsafe, while MW6 has become unsafe and zone near MW7 shows improved water quality. This can be due to fresh water, which has TDS less than 1500 mg/l (Wilson et al. 2014), that could be finding its way to the groundwater and hence reducing the concentrations of TDS near to the zone of MW7. Further, zones near MW9 and MW10 were necessarily under seawater ingress as the concentrations are quite high. Seawater had TDS concentration between 34,000 and 38,000 mg/l (Wilson et al. 2014); any small dilution by seawater would impart high TDS to the mixing water. The placement of monitoring wells could also be subjected to such that there are intermixing zones of different types of water sources.

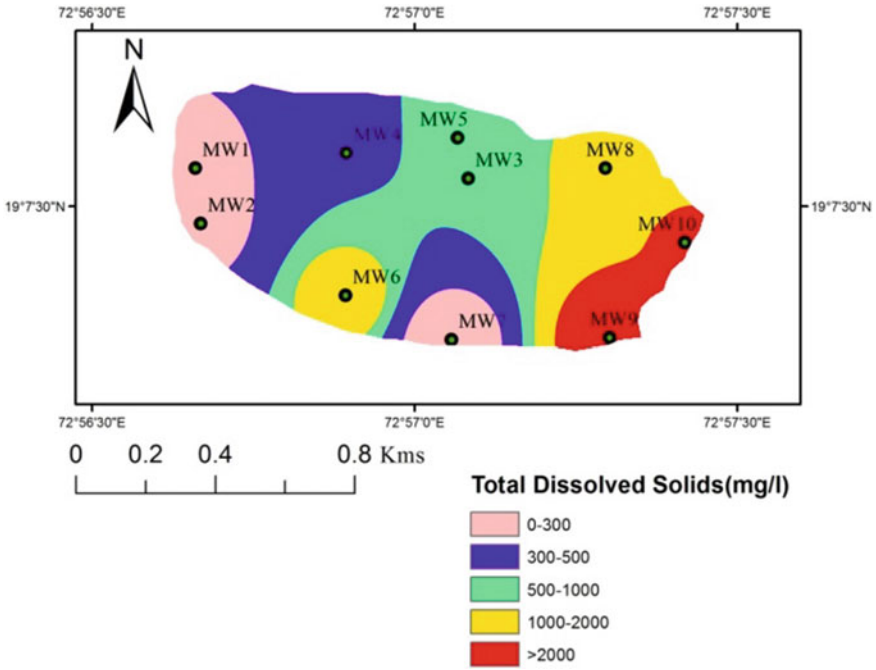


Fig. 7 Spatial Interpolation map using all sampling locations for 2016 by IDW method

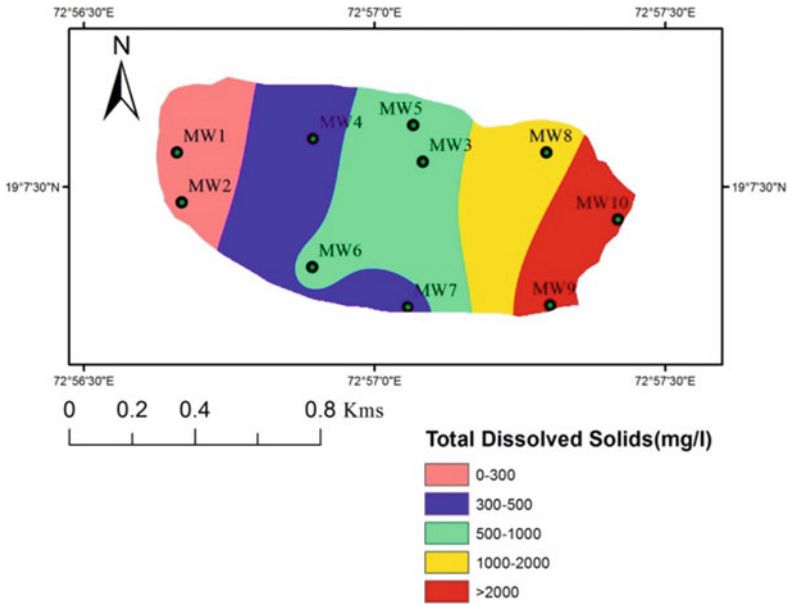


Fig. 8 Spatial Interpolation map using all sampling locations for 2016 by LPI

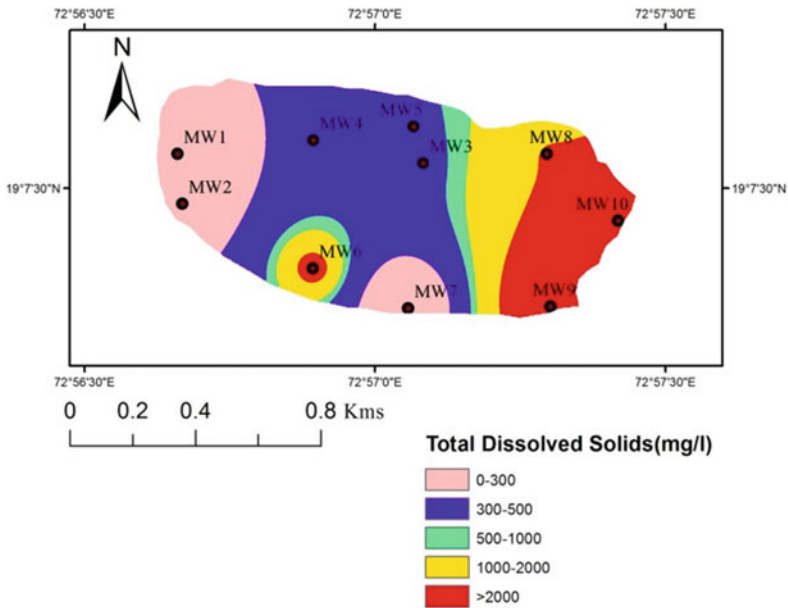


Fig. 9 Spatial Interpolation map using all sampling locations for 2016 by RBF

5 Conclusions

From this study, it was concluded that deterministic methods are good to do spatial interpolation for an area; but depending upon parameter and changes in values with time and location rapidly, these methods should be chosen wisely. It was found that zones near MW9 and MW10 are unsafe zone as per TDS permissible standard of 2000 mg/l and therefore are not a viable source of water for domestic usage. Zone near MW6 showed changes in TDS norms, and this can be attributed to percolation from landfill site or due to inflow of some another high TDS water. The IDW and RBF were best performing geostatistical interpolation methods for years 2014 and 2016, respectively, based on least RMSE and high R^2 .

Further, while working with different methods like IDW, LPI, and RBF, it was seen that they will produce different error for same parameter, and hence producing different RMSE, MSE, and R^2 values as can be seen in this study also in Table 2. The spatial interpolation analysis for different parameters in same year produces different values for different parameters which means that a method has to be optimized as per the parameter of groundwater quality (e.g., pH and TDS as the different units of measurement), then as per the year (2014 or 2016 for this case), and finally the choice of method IDW, LPI, or RBF.

References

- Abileah R, Vignudelli S (2011) A completely remote sensing approach to monitoring reservoirs water volume. *Int Water Technol J* 1:63–77
- Alcântara E, Novo E, Stech J, Assireu A, Nascimento R, Lorenzetti J, Souza A (2010) Integrating historical topographic maps and SRTM data to derive the bathymetry of a tropical reservoir. *J Hydrol* 389:311–316
- Atekwana EA, Krishnamurthy RV (2004) Investigating landfill-impacted groundwater seepage into headwater streams using stable carbon isotopes. *Hydrological Process* 18:1915–1926. <https://doi.org/10.1002/hyp.1457>
- Bhunia GS, Shit PK, Maiti R (2018) Comparison of GIS-based interpolation methods for spatial distribution of soil organic carbon (SOC). *J Saudi Soc Agric Sci* 17:114–126
- Curtarelli M, Leao J, Ogashawara I, Lorenzetti J, Stech J (2015) Assessment of spatial interpolation methods to map the bathymetry of an Amazonian Hydroelectric Reservoir To Aid In Decision Making For Water Management. *ISPRS Int J Geo-Inf* 4:220–235. <https://doi.org/10.3390/ijgi4010220>
- ESRI (2001) *Using ArcGIS Geostatistical Analyst*. ESRI Press, Redlands, CA
- Gholamalifard M, Kutsler T, Esmaili-Sari A, Abkar AA, Naimi B (2013) Remotely sensed empirical modeling of bathymetry in the Southeastern Caspian Sea. *Remote Sens* 5:2746–2762
- Hani A, Abari SAH (2011) Determination of Cd, Zn, K, pH, TNV, organic material and electrical conductivity (EC) distribution in agricultural soils using geostatistics and GIS (case study: South Western of Natanz–Iran). *World Acad Sci Eng Technol* 5(12):22–25
- Ling M, Rifai HS, Newell CJ (2005) Optimizing groundwater long-term monitoring networks using Delaunay triangulation spatial analysis techniques”. *Environmetrics* 16:635–657. <https://doi.org/10.1002/env.727>
- Merwade V (2009) Effect of spatial trends on interpolation of river bathymetry. *J Hydrol* 371:169–181
- Mohanty S, Jha MK, Kumar A, Sudheer KP (2010) Artificial neural network modeling for groundwater level forecasting in a River Island of Eastern India. *Water Resour Manag* 24:1845–1865. <https://doi.org/10.1007/s11269-009-9527-x>
- Morales JA, Graterol LS, Mesa J (2000) Determination of chloride, sulfate and nitrate in groundwater samples by ion chromatography. *J Chromatogr A* 884:185–190
- Rina K, Datta PS, Singh CK, Mukherjee S (2011) Characterization and evaluation of processes governing the groundwater quality in parts of the Sabarmati basin, Gujarat using hydrochemistry integrated with GIS. *Hydrological Process* 1–14. <https://doi.org/10.1002/hyp.8284>
- Robinson TP, Metternicht GM (2006) Testing the performance of spatial interpolation techniques for mapping soil properties. *Comput Electron Agric* 50:97–108
- Sherlock MD, McDonnell JJ (2003) A new tool for hillslope hydrologists: spatially distributed groundwater level and soilwater content measured using electromagnetic induction. *Hydrological Process* 17:1965–1977. <https://doi.org/10.1002/hyp.1221>
- Sun, Y, Kang S, Li F, Zhang L (2009) Comparison of interpolation methods for depth to groundwater and its temporal and spatial variations in the Minqin oasis of northwest China. *Environ Model Softw* 24:1163–1170
- Varma KN, Vijay R, Sohony RA (2012) Geostatistical assessment of nitrate in groundwater of Puri City, India. *J Environ Sci Eng* 54(2):227–233
- Vijay R, Sharma A, Ramya SS, Gupta A (2011) Fluctuation of groundwater in an urban coastal city of India: a GIS-based approach. *Hydrol Process* 25:1479–1485. <https://doi.org/10.1002/hyp.7914>

Wilson JM, Wang Y, VanBriesen JM (2014) Sources of high total dissolved solids to drinking water supply in southwestern Pennsylvania. *J Environ Eng* 140(5):B4014003. [https://doi.org/10.1061/\(ASCE\)EE.1943-7870.0000733](https://doi.org/10.1061/(ASCE)EE.1943-7870.0000733)

Pullout Capacity of Ground Anchors in Non-homogeneous Cohesive–Frictional Soil



Soumya Sadhukhan and Paramita Bhattacharya

Abstract Anchors are widely applied as the foundation of structures where significant pullout load is expected. Among various kinds of anchors, plate anchors are frequently employed in practice. The vast majority of the previous works have focused on the pullout capacity of the plate anchors either in undrained homogeneous and non-homogeneous clay or in drained homogeneous sand. The present work has studied the holding capacity of a horizontal anchor plate, subjected to pure vertical pull in homogeneous as well as non-homogeneous cohesive–frictional soil for different combinations of (i) normalized cohesion ($c_0/\gamma B$), (ii) soil frictional angle (ϕ), and (iii) normalized increment factor of cohesion below ground level (r_c), where c_0 represents the cohesion of soil at the ground level, γ represents the soil unit weight, and B represents the width of the plate. The vertical pullout load (Q_u) of the horizontal strip anchor plate is computed using lower bound limit analysis, in conjunction with finite element discretization. The results have been exhibited in a non-dimensional form as Q_u/c_0B . It has been observed that the non-dimensional pullout capacity (Q_u/c_0B) increases almost linearly with H/B as long as the measure of ϕ is low; whereas, in case of larger values of ϕ , the increment is non-linear. In addition, the non-dimensional pullout capacity Q_u/c_0B has been observed to increase considerably with an increment in r_c . Although lower bound limit analysis is appropriate for associated flow rule materials, the present analysis has been extended considering non-associated flow rule materials for a few cases by utilizing reduced shear strength parameters. The non-dimensional pullout capacity has been observed to reduce slightly in the case of non-associated flow rule materials, especially for higher values of ϕ . Since the lower bound limit analysis gives the conservative estimation of the ultimate load; therefore, the results computed in this analysis can be used safely for the designing purpose.

S. Sadhukhan (✉) · P. Bhattacharya
Department of Civil Engineering, Indian Institute of Technology Kharagpur, Kharagpur, West Bengal, India
e-mail: soumyasadhukhan@iitkgp.ac.in

P. Bhattacharya
e-mail: paramita@civil.iitkgp.ac.in

Keywords Pullout capacity · Cohesive–frictional · Non-homogeneous

1 Introduction

Anchors are generally used to resist outwardly directed force or overturning moment in structures like transmission towers, radar towers, submerged pipelines, dry docs, etc. Previously, a noteworthy number of researches to quantify the pullout capacity of anchors in cohesive (Rowe and Davis 1982a; Das 1978; Rao and Prasad 1992; Merifield et al. 2001, 2005; Song et al. 2008; Wang et al. 2010) and cohesionless (Rowe and Davis 1982b; Murray and Geddes 1987; Kumar 1997; Ilamparuthi and Muthukrishnaiah 1999; Merifield and Sloan 2006; Bhattacharya and Kumar 2014a, b, 2016; Yu et al. 2014; Giampa et al. 2016) soil have been reported in the literature. These research works are focused to figure out the pullout capacity of ground anchors either in cohesionless soil or in cohesive soil. Very few analytical solutions (Meyerhof and Adams 1968; Vesic 1971; Rao and Kumar 1994) are available to find out the pullout capacity of anchors in cohesive–frictional soil. A few works have been performed to consider the impact of non-homogeneity and anisotropy (Bhattacharya 2017, 2018) on anchor's pullout behavior. Nonetheless, just a couple of numerical investigations have been led to figure the pullout capacity of ground anchors in cohesive–frictional soil (Perazzelli and Anagnostou 2017). In practice, often anchors are required to be introduced in the ground where both cohesion and friction will be present. It is additionally noted that the value of cohesion keeps on increasing in the downward direction in case of normally consolidated as well as lightly over-consolidated clay (Bishop 1966). Thus, the capacity of an anchor plate buried in such non-homogenous cohesive–frictional soil is required to be addressed.

The present investigation is aimed to estimate the pullout capacity of horizontally placed strip anchor plate embedded in non-homogeneous cohesive–frictional soil using lower bound limit analysis with finite element discretization and linear optimization technique. The analysis has been performed for different combinations of $c_0/\gamma B$, ϕ , and r_c , where c_0 represents the cohesion of soil at ground surface, γ represents the soil unit weight, ϕ represents the friction angle of soil, B represents the width of the plate, and r_c represents the normalized rate of increment of cohesion below ground surface. The majority of the analysis has been performed considering the associated flow rule. However, it has been extended considering non-associated flow rule for a few cases.

2 Description of Problem

A horizontal strip anchor plate of width B is installed below the ground level at a distance H as appeared in Fig. 1. It is assumed that the plate is fully rigid. The plate has negligible thickness comparing to its width. The soil domain is assumed to follow Mohr–Coulomb yield criteria. The cohesion below ground surface increases

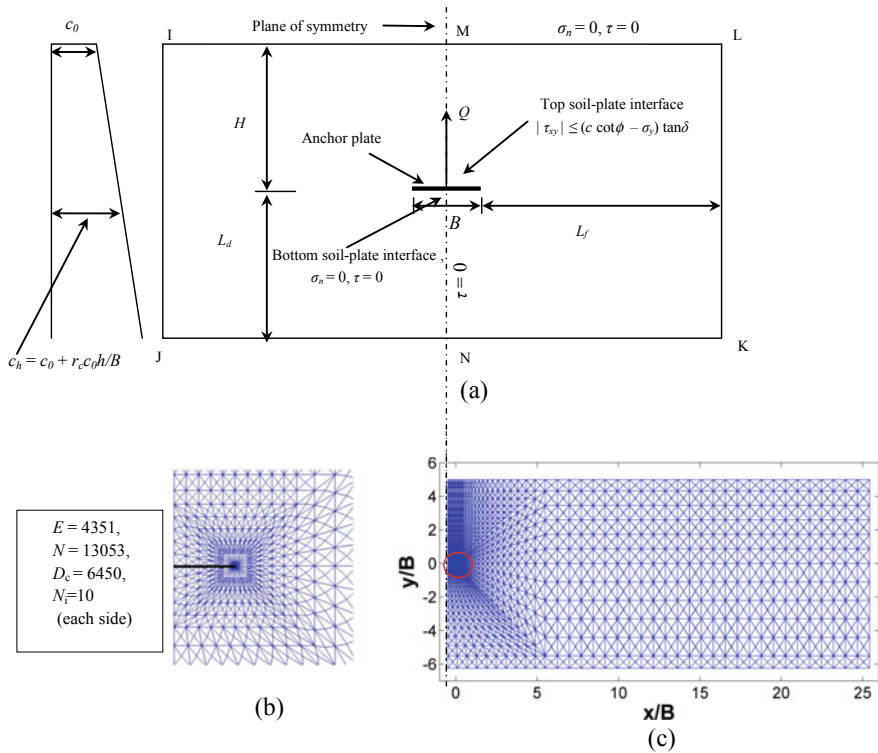


Fig. 1 a Outline of the domain, b detailing of the mesh near the anchor plate and c typical finite element mesh

at a constant rate in the case of non-homogeneous soil. The uplift resistance of the anchor plate is required to be determined for various combinations of H/B , $c_0/\gamma B$, ϕ , and r_c .

3 Problem Domain, Stress Boundary Conditions, and Finite Element Mesh

Figure. 1a demonstrates the schematic diagram of the problem domain. A rectangular domain, IJKL, has been considered for this analysis. The vertical line MN bisects the problem domain symmetrically. Thus, exploiting the symmetry, half of the domain (MNKL) has been chosen for this study. To eliminate the boundary effect, the clear distance (L_f) from the right edge anchor plate to the boundary line KL has been kept as $5B-40B$ depending upon the material property of the soil and the embedment ratio (H/B). The distance between the bottom-most boundary of the domain NK and anchor plate (L_d) has been kept equal to $3B-9B$ depending on the soil parameters and

embedment ratio. The value of L_f and L_d has been decided based upon two criteria: (i) The yielded element or the fully plastic zone should not touch the boundary lines KL and NK, and (ii) by further expanding the domain boundaries, there should not be any noteworthy differences in the failure load.

Fig. 1a also demonstrates the different stress boundary conditions which have been imposed on different domain boundaries. The value of the normal and shear stress has been assigned to 0 along with the boundary line ML, which represents the ground surface. At the nodes lying on the boundary MN, the value of shear stress is kept as 0. Since the yield condition has been checked at each node, no boundary condition is required to be imposed along the boundaries NK and KL.

A no-tension criterion has been employed at the contact boundary between the base of the anchor plate and the soil underneath. This is required because suction will develop beneath the anchor plate in the presence of the cohesion of soil. Therefore, when the plate is lifted up, there will be no connection between the plate and the soil underneath. This assumption will provide a conservative estimation of the failure load and eliminate the uncertainties associated with the suction force. To model this no-tension criterion, the values of the normal and shear stresses acting on the nodes lying at the bottom plane of the plate have been assigned to 0.

A shear slip has been allowed among the nodes lying along the top plane of the plate and the boundary of the soil in contact. This has been incorporated by imposing the following boundary condition at the nodes along the top plane of the plate

$$|\tau_{xy}| \leq (c \cot\phi - \sigma_y) \tan\delta \quad (1)$$

In the above equation, c represents the cohesion of the ground, ϕ represents the friction angle of soil, and δ represents the angle of friction between the anchor plate and the soil. It is worth mentioning that in the present analysis, the tensile stress is considered as positive. Thus, negative sign is attached to σ_y in Eq. 1. In this paper, δ has been adopted equal to ϕ .

Linear triangular elements have been used to discretize the domain. The mesh has been framed in a way so that the number of elements increases continuously close to the tip of the plate. Also, the area near the anchor plate has been meshed more finely compared to the rest of the domain. One such mesh having an embedment ratio of 5 is demonstrated in Fig. 1c. The detailed view of the mesh near the anchor plate is demonstrated in Fig. 1b. The overall count of elements (E) in the particular mesh is 4351. In Fig. 1b, the other terms such as N , D_e , and N_e represent the total count of nodes, the number of edge discontinuities, and the number of nodes lying anchor–soil interface, respectively.

4 Methodology

The lower bound limit analysis formulation in amalgamation with finite element discretization proposed by Sloan (1988) has been used in the present study. In this formulation, the nodal normal and shear stresses (σ_x , σ_y , and τ_{xy}) are the fundamental

unknown variables. To solve the problem, firstly, the equilibrium of each element has been established. For a plane strain problem, the equilibrium equations are as follows

$$\frac{\partial \sigma_x}{\partial x} + \frac{\partial \tau_{xy}}{\partial y} = 0 \quad (2)$$

$$\frac{\partial \tau_{xy}}{\partial x} + \frac{\partial \sigma_y}{\partial y} = \gamma \quad (3)$$

In addition, statically adoptable stress discontinuities have been ascribed at each of the adjacent boundaries of the elements. To impose this condition, the normal and shear stresses have been made continuous along all the lines of discontinuity of the entire mesh. Finally, the yield condition has been satisfied at all the nodes.

The expression for the collapse load has been formulated by numerically integrating of the normal stresses acting at the nodes lying at the upper face of the plate flowing the expression:

$$Q_u = \int_0^B \text{for top surface} (-\sigma_y dA) \quad (4)$$

where σ_y represents the normal stress acting along the upper plane of the plate. dA is the area of that element on which σ_y is acting. The integration points have been chosen at the location of the nodes.

The element equilibrium, edge discontinuity, and stress boundary conditions will form a set of equality constraints. Conversely, the yield criterion and the stress boundary condition at the anchor–soil interface will form a set of the inequality constraints. Finally, the maximum value of the collapse load (Q_u) which will satisfy the above-mentioned constraints will be the lower bound of the true collapse load. In this analysis, a linear optimization strategy has been employed. Thus, the Mohr–Coulomb yield function has been replaced with a polygon having sides p , following the method of Bottero et al. (1980). A typical value of p equal to 22 has been adopted in the current study, which gave quite satisfactory results. The optimization has been performed using the LINPROG function available in MATLAB.

5 Results and Discussion

5.1 Comparison

To validate the present numerical model, firstly, the values of the non-dimensional pullout capacity factor F_c have been calculated using the Eq. 5 as follows:

$$\text{For } c_0 \neq 0 \text{ and } \gamma = 0; F_c = \frac{Q_u}{c_0 B} \quad (5)$$

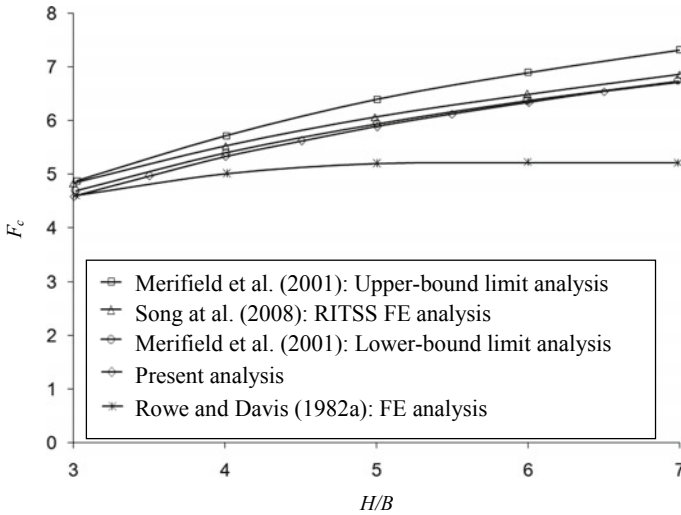


Fig. 2 Comparison of present lower bound solution with available works in literature

It should be noted that the contribution from the unit weight of soil has not been taken into account while estimating the values of F_c . Thus, the resistance offered by the soil against uplifting is provided solely by the cohesion of the soil. Fig. 2 demonstrates the plot of F_c versus H/B .

The values of F_c computed using the current analysis have been compared with the lower bound and upper bound solution reported by Merifield et al. (2001); large strain FE solution reported by Song et al. (2008); and small strain FE solution reported by Rowe and Davis (1982a). Fig. 2 demonstrates the comparison. It is observed from Fig. 2 that the current estimates of F_c are in great concurrence with the results given by the prior analysts.

5.2 Variation of Non-dimensional Pullout Capacity

The pullout resistance of the anchor plate has been presented as a non-dimensional form Q_u/c_0B , where Q_u is the ultimate pullout resistance against uplifting per unit length of the strip. It has been noted from the literature that the cohesion of clay often increases continuously below the ground surface. This phenomenon is mostly observed in the case of normally consolidated and lightly over-consolidated clay (Bishop 1966). Thus, in the current study, the influence of material non-homogeneity is incorporated by considering the linear variation of cohesion below ground surface following Eq. 6.

$$c_h = c_0 + r_c c_0 h/B \tag{6}$$

In the above equation, the cohesion at ground level is termed as c_0 , the cohesion at a particular depth h from the ground level is termed as c_h and the normalized rate of increment of cohesion below ground surface is termed as r_c .

The non-dimensional pullout capacity Q_u/c_0B has been calculated for five different H/B ratio (3, 4, 5, 6, and 7), three different values of $c_0/\gamma B$ (1, 2.5, 5), three different values of ϕ (5° , 15° , 30°), and three different values of r_c (0, 1/8, 1/4). The variation of Q_u/c_0B with the H/B ratio for the above-mentioned values of ϕ , r_c , and $c_0/\gamma B$ has been presented in Figs. 3 and 4.

It has been observed from Figs. 3 and 4 that the non-dimensional pullout capacity Q_u/c_0B increases almost linearly with the embedment ratio (H/B) for $\phi = 5^\circ$ but, as the value of ϕ increases, the increment of pullout capacity with H/B becomes non-linear. In other words, the rate of increment of the non-dimensional pullout capacity with H/B increases for higher values of ϕ . It is obvious that the higher value of c_0 will result in greater pullout capacity. However, when the pullout capacity is expressed in non-dimensional term (Q_u/c_0B), it is observed to decrease with an increment of the normalized cohesion $c_0/\gamma_{clay}B$. Finally, due to the non-homogeneous nature of the soil, the non-dimensional pullout capacity (Q_u/c_0B) increases significantly with an increment of r_c , while other parameters such as ϕ and Q_u/c_0B are constant.

5.3 Inclusion of Non-associated Flow Rule

The analysis has been extended considering non-associated flow rule for $\phi = 30^\circ$, $r_c = 1/4$, and $c_0/\gamma_{clay} B = 1, 2.5, \text{ and } 5$. Three different values of dilative coefficient $\eta = 1, 0.5, \text{ and } 0$ have been considered in this analysis, where $\eta = \psi/\phi$ and ψ is the dilation angle for a frictional material. Thus, $\eta = 0$ represents the state of $\psi = 0$ and $\eta = 1$ represents the state of $\psi = \phi$, the later is analogous to the state of associated flow rule. In the current analysis, the effect of dilation has been incorporated using the following expressions (Drescher and Detournay 1993)

$$\tan \phi^* = \tan \frac{\cos \phi \cos \psi}{1 - \sin \phi \sin \psi} \tag{7}$$

$$c^* = c \frac{\cos \phi \cos \psi}{1 - \sin \phi \sin \psi} \tag{8}$$

These modified values of ϕ^* and c^* has been used to impose the non-associated flow rule in the current analysis. The results have been plotted in Fig. 5. A slight reduction can be observed in Fig. 5 due to the change in η from 1 to 0, especially for higher values of ϕ .

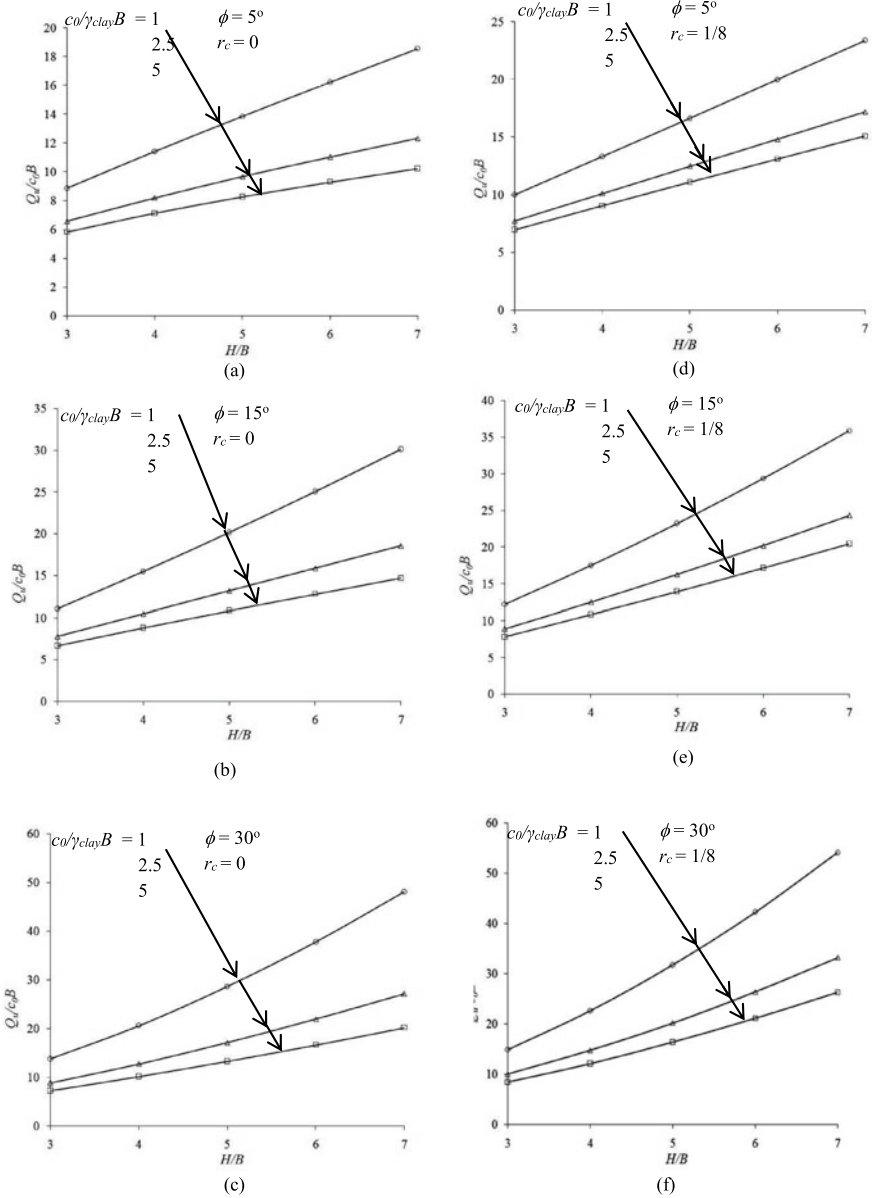


Fig. 3 Variation of non-dimensional pullout capacity Q_u/c_0B with H/B for **a** $\phi = 5^\circ, r_c = 0$; **b** $\phi = 15^\circ, r_c = 0$; **c** $\phi = 30^\circ, r_c = 0$; **d** $\phi = 5^\circ, r_c = 1/8$; **e** $\phi = 15^\circ, r_c = 1/8$; **f** $\phi = 30^\circ, r_c = 1/8$

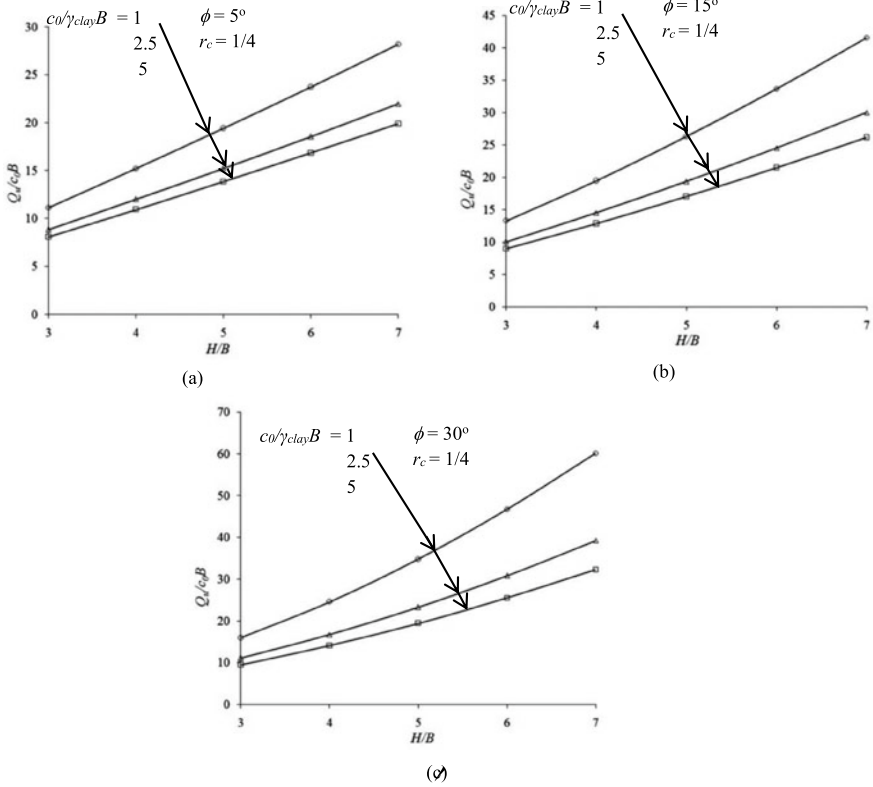
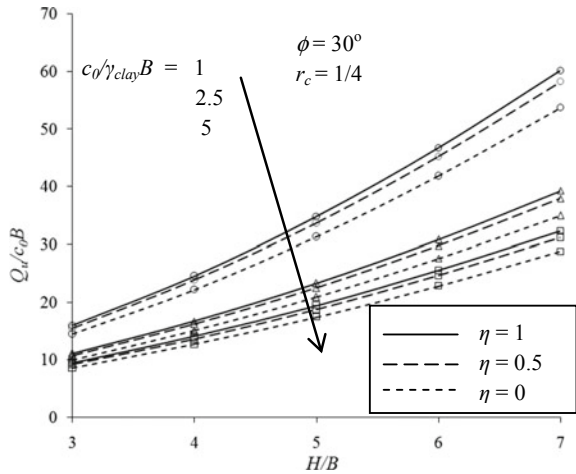


Fig. 4 Variation of non-dimensional pullout capacity Q_u/c_0B with H/B for **a** $\phi = 5^\circ$, $r_c = 1/4$; **b** $\phi = 15^\circ$, $r_c = 1/4$; **c** $\phi = 30^\circ$, $r_c = 1/4$

Fig. 5 Variation of non-dimensional pullout capacity Q_u/c_0B with H/B for $\phi = 30^\circ$, $r_c = 1/4$ considering non-associated flow rule



6 Stress Contour

After optimizing the objective function, the values of the stress variables at each node are known and the stress state has been expressed as a non-dimensional number a/d , where $a = (\sigma_x - \sigma_y)^2 + (2\tau_{xy})^2$ and $d = [2c \cos \phi - (\sigma_x + \sigma_y) \sin \phi]^2$. The stress contour plots for some selected cases have been shown in Fig. 6. This representation reveals which elements of the domain have reached the yield state. The area marked by dark red color in the stress contour plot represents the regions, where the stress state has reached the yield point ($a/d = 1$). Conversely, the area having a/d ratio <1 represents the regions where the stress state has not reached the yield point. The stress contour has been plotted in Fig. 6 for four different cases. It can be observed from Fig. 6a and c that the yielded zone arises from the initial position of the anchor plate and approaches to the ground level and as the friction angle is low (5°) the failure zone has not distributed too far from the anchor plate. On the other hand, in Fig. 6b and d for both vale of H/B , the failure zone is distributed over a larger area as the value of ϕ is high (30°).

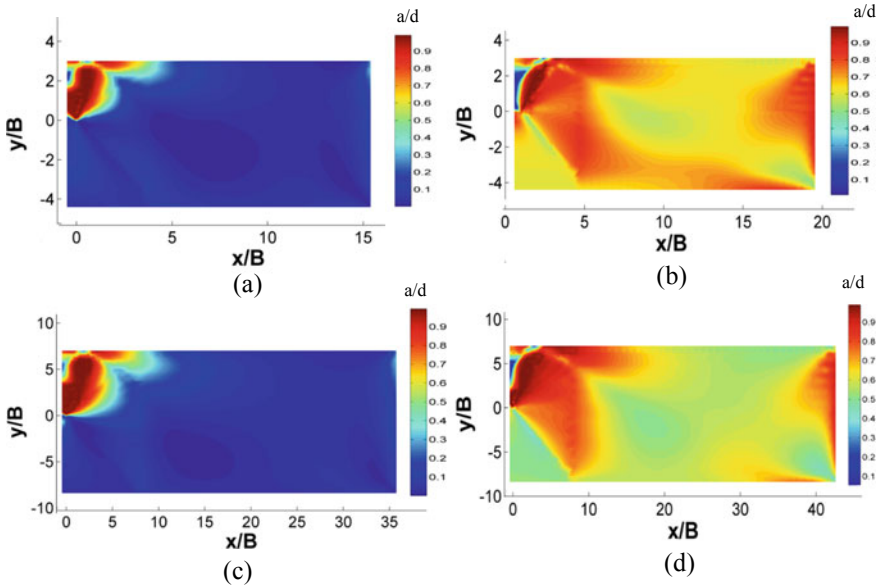


Fig. 6 Proximity of stress state to failure **a** $H/B = 3, c_0/\gamma_{clay} B = 5, \phi = 5^\circ, r_c = 1/4$; **b** $H/B = 3, c_0/\gamma_{clay} B = 5, \phi = 30^\circ, r_c = 1/4$; **c** $H/B = 7, c_0/\gamma_{clay} B = 5, \phi = 5^\circ, r_c = 1/4$; **d** $H/B = 7, c_0/\gamma_{clay} B = 5, \phi = 30^\circ, r_c = 1/4$

7 Conclusions

The present investigation has been focused on the estimation of the vertical pullout limit of horizontal strip anchor plate buried in non-homogeneous cohesive–frictional soil using lower bound limit analysis with finite element discretization and linear optimization algorithm. The analysis has been extended considering non-associated flow rule utilizing reduced shear strength parameters. It has been noticed from the results that as long as the value of ϕ remains low, the non-dimensional pullout capacity Q_u/c_0B increases almost linearly with the embedment ratio (H/B). Conversely, for materials having a greater value of ϕ , the value of non-dimensional pullout capacity increase at a greater rate with H/B , and the nature of the graphs becomes non-linear. The non-dimensional pullout capacity (Q_u/c_0B) increases quite significantly with an increase in r_c . Finally, a slightly lower value of Q_u/c_0B was observed in the case of non-associated flow rule, i.e. the non-dimensional pullout capacity decrease with a decrease in the value of η . The lower bound limit analysis provides a conservative value of the ultimate load; thus, it is expected that the results will be helpful for the practicing engineers.

References

- Bhattacharya P (2017) Pullout capacity of shallow inclined anchor in anisotropic and nonhomogeneous undrained clay. *Geomech Eng* 13(5):825–844
- Bhattacharya P (2018) Undrained uplift capacity of strip plate anchor nearby clayey slope. *Geotech Geol Eng* 36:1393–1407
- Bhattacharya P, Kumar J (2014a) Pullout capacity of inclined plate anchors embedded in sand. *Can Geotech J* 51(11):1365–1370
- Bhattacharya P, Kumar J (2014b) Vertical pullout capacity of horizontal anchor plates in the presence of seismic and seepage forces. *Geomech Geoeng* 9(4):294–302
- Bhattacharya P, Kumar J (2016) Uplift capacity of anchors in layered sand using finite element limit analysis: formulation and results. *Int J Geomech* 16(3):04015078
- Bishop AW (1966) The strength of soils as engineering materials. *Géotechnique* 16(2):89–128
- Bottero A, Negre R, Pastor J, Turgeman S (1980) Finite element method and limit analysis theory for soil mechanics problems. *Comput Methods Appl Mech Eng* 22(1):131–149
- Das BM (1978) Model tests for uplift capacity of foundations in clay. *Soils Found* 18(2):17–24
- Drescher A, Detournay E (1993) Limit load in translational failure mechanisms for associative and non-associative materials. *Geotechnique* 43(3):443–456
- Giampa JR, Bradshaw AS, Schneider JA (2016) Influence of dilation angle on drained shallow circular anchor uplift capacity. *Int J Geomech* 17(2):04016056
- Ilamparuthi K, Muthukrishnaiah K (1999) Anchors in sand bed: delineation of rupture surface. *Ocean Eng* 26(12):1249–1273
- Kumar J (1997) Upper bound solution for pullout capacity of anchors on sandy slopes. *Int J Numer Anal Meth Geomech* 21(7):477–484
- Merifield RS, Sloan SW (2006) The ultimate pullout capacity of anchors in frictional soil. *Can Geotech J* 43(8):852–868
- Merifield RS, Lyamin AV, Sloan SW (2005) Stability of inclined plate anchors in cohesive soil. *J Geotech Geoenvironmental Eng* 131(6):792–799

- Merifield RS, Sloan SW, Yu HS (2001) Stability of plate anchors in undrained clay. *Geotechnique* 51(2):141–154
- Meyerhof GG, Adams J (1968) The ultimate uplift capacity of foundations. *Can Geotech J* 5(4):225–244
- Murray EJ, Geddes JD (1987) Uplift of anchor plates in sand. *J Geotech Eng* 113(3):202–215
- Perazzelli P, Anagnostou G (2017) Uplift resistance of strip anchors in cohesive frictional mediums of limited tensile strength. *Int J Geomech* 17(9):04017042
- Rao KSS, Kumar J (1994) Vertical uplift capacity of horizontal anchors. *J Geotech Eng* 120(7):1134–1147
- Rao SN, Prasad YVSN (1992) Uplift capacity of plate anchors in sloped clayey ground. *Soils Found* 32(4):164–170
- Rowe RK, Davis EH (1982a) The behaviour of anchor plates in clay. *Geotechnique* 32(1):9–23
- Rowe RK, Davis EH (1982b) The behaviour of anchor plates in sand. *Géotechnique* 32(1):25–41
- Sloan SW (1988) Lower bound limit analysis using finite elements and linear programming. *Int J Numer Anal Methods Geomech* 12(1):61–77
- Song Z, Hu Y, Randolph MF (2008) Numerical simulation of vertical pullout of plate anchors in clay. *J Geotech Geoenvironmental Eng* 134(6):866–875
- Vesic AS (1971) Breakout resistance of objects embedded in ocean bottom. *J Soil Mech Found Div* 97(9):1183–1205
- Wang D, Hu Y, Randolph MF (2010) Three-dimensional large deformation finite-element analysis of plate anchors in uniform clay. *J Geotechn Geoenvironmental Eng* 136(2):355–365
- Yu SB, Merifield RS, Lyamin AV, Fu XD, Fu D (2014) Kinematic limit analysis of pullout capacity for plate anchors in sandy slopes. *Struct Eng Mech* 51(4):565–579

Settlement Analysis of Single Circular Hollow Pile



Ravikant S. Sathe, Jitendra Kumar Sharma, and Bharat P. Suneja

Abstract Piles are designed to transfer a load of superstructure to the deep hard soil strata crossing the upper weaker strata through frictional or end bearing action. Settlement analyses for single or group of the solid pile are available in literature based on analytical or empirical approaches. The present study deals with the settlement analysis of single circular hollow and single conventional pile using Plaxis-3D foundation. Effect of diameter, length and position of hollow portion filled with different granular materials of moduli of elasticity is evaluated and studied in terms of the load settlement curve. Results of floating conventional circular pile and floating circular hollow pile are compared in terms of parameters as mentioned above by keeping the same conditions and properties of surrounding soil and pile. Floating circular hollow pile gives optimum and economical results as compared to the single circular conventional pile in respect of settlement up to a certain percentage of varying hollow portion.

Keywords Circular hollow pile · Settlement · Granular material · Floating pile

1 Introduction

Pile foundation is utilized when the soil close to the surface can't support structural foundation loads because of either the probability of extreme settlement or low bearing limit. The essential capacity of a pile is to move the foundation load to more profound soil strata that are more grounded or load-bearing limit is more and less

R. S. Sathe (✉) · J. K. Sharma · B. P. Suneja
Civil Engineering Department, University Department,
Rajasthan Technical University, Kota, India
e-mail: ravikant.sathe07@gmail.com

J. K. Sharma
e-mail: jksharma@rtu.ac.in

B. P. Suneja
e-mail: bpsuneja@gmail.com

compressible. Pile foundation is viewed as progressively costly comparative with the shallow foundation. So, it should be only selected when shallow foundations cannot satisfy an acceptable factor of safety against the bearing failure in the foundation soil or acceptable settlement during the life of the structure. These two independent design criteria can arise due to several reasons among them nature and magnitude of structural loads, settlement sensitive structures and type of soil. Hence, the goal of the pile is to achieve the design criteria by transferring structural loads to the deep, stable and strong soil strata. Sometimes, the case can be more complicated when the stronger soil layers with relatively small thickness exist above weak soil that extended to great depths. In this case, the methodology of using pile foundations includes some uncertainties, and the behaviour of piles cannot be certainly expected. The vulnerabilities of pile conduct emerge from non-homogeneity of soil and change of soil properties after pile installation. In addition, the greater part of the standards or approaches for assessing the bearing limit and distortion of pile contemplated the general case that weak soil is overlying solid soil. As pile behaviour depends, for the most part, on soil properties and technique for pile installation, incredible endeavours ought to be taken to decide soil properties all through lab and field tests.

Most of the researcher has worked on settlement analysis of axially loaded single circular pile Pooja and Sharma (2017a, b), Seo et al. (2008) by using various methods and approaches in homogeneous and non-homogeneous soils, Polous (1979). Available settlement analysis either assumes that the soil resistance can be represented by a series of disjointed spring or that of the soil is a continuum (Salgado et al. 2011). The continuum approach Fawad and Paul (2015) has traditionally required expensive numerical techniques, such as the boundary integral method or the finite element method to obtain solutions. The advantage of this continuum-based analysis is that it captures the three-dimensional nature of the pile–soil interaction and produces the pile load–settlement response in seconds.

In the present study, the analysis is done for single circular conventional pile and single circular hollow pile with a hollow portion filled by granular material as well as varying the position of the hollow portion within the pile for the load–settlement curve and stress.

1.1 Finite Element Methods

The FEM is one of the most famous numerical techniques utilized for calculating and designing all sorts of convoluted structures in different fields of engineering. At the underlying stage, the strategy is created as an expansion of a matrix method for the analysis of structural engineering problems. Nonetheless, later it has been perceived as the more dominant technique for breaking down the issues in different fields of engineering, for example, heat stream, soil mechanics, liquid mechanics, rock mechanics and so forth. In FEM, a continuum is partitioned into various components. Every component comprises of various hubs and every hub has various degrees of

opportunity that compare to discrete estimations of questions in the limit esteem issue to be illuminated.

1.2 *Plaxis-3D Foundation*

The Plaxis-3D foundation program is predicated on the FEM, to perform deformation and stability analysis for varied forms of foundations and excavations in soil and rock. And, it can even be used for alternative forms of geotechnical structures.

2 Literature Review

Butterfield and Banerjee (1971) displayed the reaction of unbending and compressible single pile inserted in a homogeneous, isotropic and straight versatile soil medium. It has been acquired by utilizing thorough investigation dependent on Mindlin's solution for a point load in the inside of a thought versatile medium.

Armaleh and Desai (1987) examined another experimental strategy for simulating the non-linear point resistance response of single piles in cohesionless soil. Additionally, the shear resistance reactions along the pile shaft were found by utilizing the idea of the $t-z$ curve.

Guo et al. (1997) presented new closed-form solutions for the axial response of piles in elastic-plastic, non-homogeneous media. The effect of non-homogeneity and partial slip on the load and displacement profiles along the pile shaft were explored.

Kirzhner and Rosenhouse (2001) discussed the bearing capacity and load-deformation of a single pile in granular soil analysed piles under vertical loads in the study of the mechanism of shaft friction as well as the effect of deformation modulus on bearing capacity of single pile in granular materials by using FLAC program.

Neves et al. (2001) presented soil behaviour of a perfectly plastic elastic model (Mohr-Coulomb) and an elastoplastic model with strain hardening, Nova in terms of load-settlement and force distribution long pile surface. Also, numerical results were compared with experimental results.

Reddy et al. (2015) displayed a numerical investigation of pile-soil interaction issue, considering the parameter affecting the axial load-deformation behaviour of pile inserted in a multilayered soil medium.

Vijay et al. (2015) discussed the settlement behaviour of the single granular pile under axial loading at various depths along its length. The effects of different parameters on settlement reduction at different depths were quantified to arrive at a rational design. Results of the study on floating and end bearing granular piles constructed in soft soil were presented.

Pooja and Sharma (2017a, b) studied the response of non-homogeneous floating granular pile in homogeneous soil medium based on the elastic continuum approach.

3 Analysis

The results of the loading tests were performed in Brazil. During a full-scale field test, six piles were tested (Neves et al. 2001). The diameter of piles ranged from 0.35 to 0.5 m, and they were loaded in compression as well as tension condition. Lengths of piles were considered as 10 m. The piles were monitored using extensometer and load cells to getting accurate results. In that, one of the pile was of 0.4 m diameter pile with a length of 10 m ultimately loaded to failure in compression. It has been constructed in clayey sand and silty which divided into several layers.

For the analysis, the general set-up of a 3D model, including pile modelled as volumetric elements.

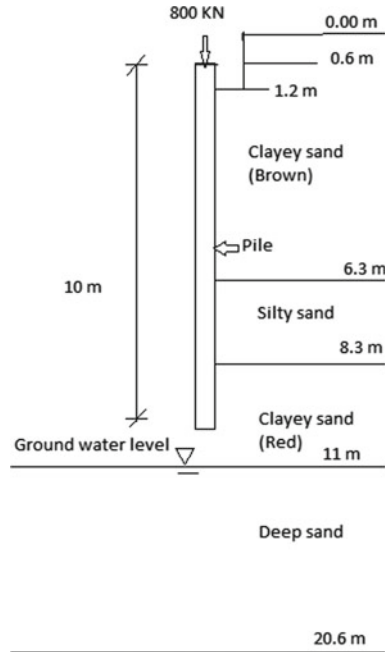
3.1 Assumptions

- The soil medium is continuous, non-homogeneous and isotropic.
- An axisymmetric configuration has been implemented, with the axis of symmetry aligned with the axis of the pile.
- No-slip or yield at the pile–soil interface.
- The sides of the Pile are perfectly rough and rigid.
- The analysis is performed for the no-tension condition in the soil as well.

3.2 Geometry Model

In this study, the length and diameter of the conventional floating circular pile and the hollow floating circular pile was considered as 10 m and 0.4 m, respectively. But, in the case of hollow floating circular pile, the inner diameter of the hollow portion is kept 0.2 m and thickness as 0.1 m, i.e. the outer diameter of the pile 0.4 m. The position of hollow portion is varied from 2 to 8 m from a top surface of the pile as per cases. The point load of 800 kN was applied to the centre of the pile. The embedded pile is considered cast in situ in multilayered granular soil. In the present analysis, the horizontal range of dummy soil is considered as 60R (60 times radius of pile) to both the x- and z-directions from the centre of the pile. And, its depth (two times length of the pile) as 20.6 m from a top surface of the soil. The water level was considered just below the tip of the pile, i.e. at 11 m from the top surface of the soil (Neves et al. 2001) as shown in Fig. 1.

Fig. 1 Geometry of pile–soil system



3.3 Properties of Soil and Pile

The properties are used for the analysis of the load–settlement curve for all the cases, as mentioned in Table 1. The thickness of the first soil layer considered as 0.00–6.3 m,

Table 1 Properties of soil and pile (Neves et al. 2001)

Parameter	Clayey sand (Brown)	Silty sand	Clayey sand (Red)	Deep sand	Pile	Unit
Unsaturated soil weight (γ_{unsat})	16.7	18.8	19.8	17.6	24	kN/m ³
Saturated soil weight (γ_{sat})	16.7	18.8	19.8	20	–	kN/m ³
Young’s modulus (E)	9150	13,510	13,570	19,300	29.2×106	kN/m ²
Poisson’s ratio (ν)	0.3	0.3	0.3	0.3	0.15	–
Cohesion (c)	13	12	14	17	–	kN/m ²
Friction angle (Φ)	26	23	23	23	–	°

second layer 6.3–8.3 m, third layer 8.3–11.0 m and fourth layer 11.0–20.6 m. For each layer of soil Mohr–Columb and the drained condition is used, and for pile, the linear elastic and non-porous condition is used.

4 Result and Discussion

Validation of results is done with (Naves 2001)

The results match very closely with the present study analysis, as shown in Table 2.

From Table 3 and Fig. 2, it is observed that the settlement of 2-m hollow circular floating pile is increasing with changing the position of the hollow portion within the pile from top to bottom. When the position of the hollow portion is kept at 2, 3 and 4 m below from top of the pile, then a top settlement of pile is similar to the conventional floating circular pile. But, when it is kept at 5 and 6 m from top of the pile, the top settlement of floating circular hollow pile is increasing as compared to conventional floating circular pile due to less stress is generated at the top of the pile. In the top settlement of floating circular hollow pile is not more different from as conventional floating circular pile because the hollow portion is get filled with granular material such as sand. Generally, in floating circular pile friction is developed on the outer surface of the pile but in this case, friction is developed on outer as well as the inner surface of the pile due to filled material in the hollow portion.

From Figs. 3 and 4, it is observed that top settlement of 3 and 4 m floating circular hollow pile is the same as compared to the conventional circular pile when the position of the hollow portion is kept below 2 and 3 m from a top surface of pile, and it is increased when the position of the hollow portion is kept below more than 3 m from the top surface of the pile as mentioned in Tables 4 and 5.

Table 2 Validation of load–settlement curve

Parameters	Settlement of conventional circular pile (mm)	
	Neves et al. (2001)	Present study
L = 10 m, D = 0.4 m, Q = 600 kN	14.12	14.1

Table 3 Top settlement of pile when 2-m hollow portion with varying its position

Sr. no.	Parameters of pile	Load (kN)	Settlement (mm)
1	Conventional	800	118
2	2M 2.6–4.6		118
3	2M 3.6–5.6		118
4	2M 4.6–6.6		119
5	2M 5.6–7.6		130
6	2M 6.6–8.6		131

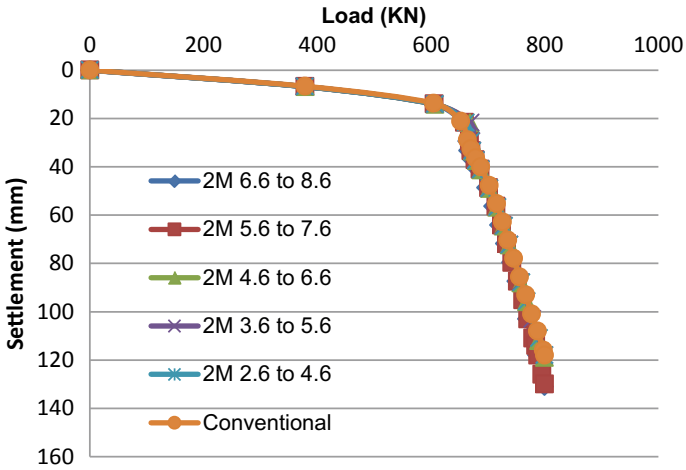


Fig. 2 Load–settlement curve for the 2-m hollow portion

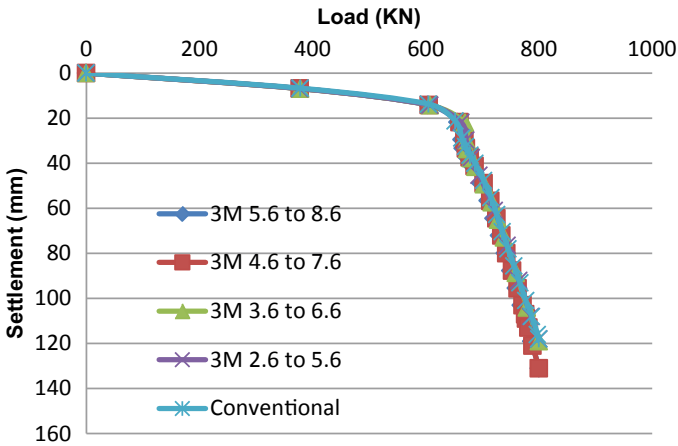


Fig. 3 Load–settlement curve for a 3-m hollow portion

From Figs. 5 and 6, it is observed that the top settlement of hollow floating circular pile is increasing because the position of the hollow portion is below than mid-length of the pile as mentioned in Tables 6 and 7, respectively.

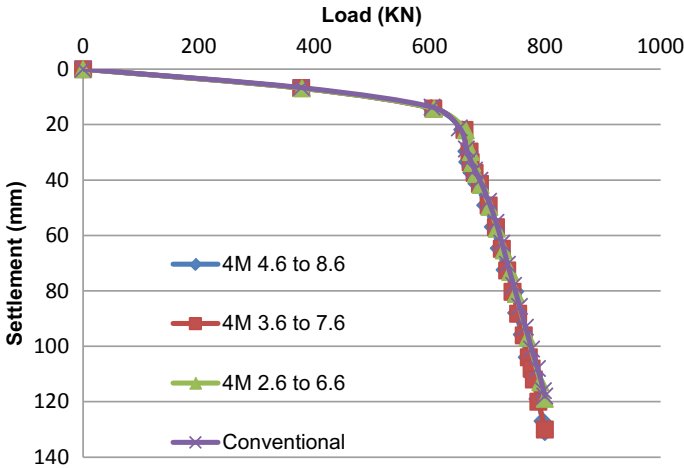


Fig. 4 Load–settlement curve for a 4-m hollow portion

Table 4 Top settlement of pile when 3-m hollow portion with varying its position

Sr. no.	Parameters of pile	Load (kN)	Settlement (mm)
1	Conventional	800	118
2	2M 2.6–5.6		118
3	2M 3.6–6.6		119
4	2M 4.6–7.6		131
5	2M 5.6–8.6		131

Table 5 Top settlement of pile when 4-m hollow portion with varying its position

Sr. no.	Parameters of pile	Load (kN)	Settlement (mm)
1	Conventional	800	118
2	2M 2.6–6.6		119
3	2M 3.6–7.6		131
4	2M 4.6–8.6		131

5 Conclusion

The effect of the hollow portion on floating circular pile was examined, and it was found that if the position of hollow portion kept in between 2 and 6 m from the top surface of pile below, then hollow floating circular pile gives almost in the range of solid pile results in terms of top settlement of pile. If it kept below 6 m from the top surface of the pile, then the top settlement of the hollow floating circular pile goes increases with an increase in the hollow portion. Thus, it is reasonable to provide a hollow portion between 2 and 6 m from the top surface of the pile.

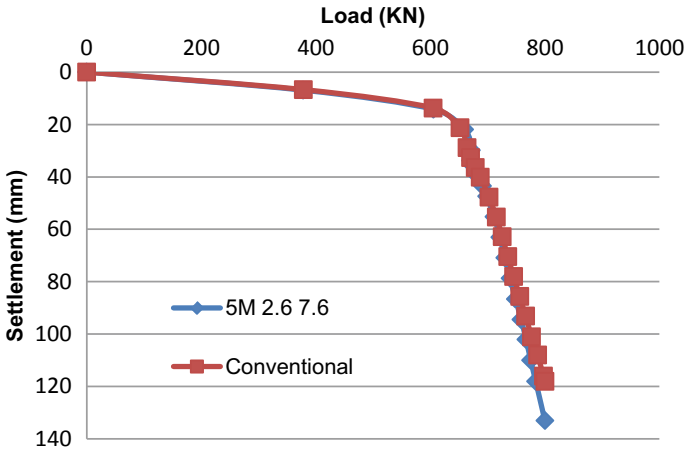


Fig. 5 Load–settlement curve for a 5-m hollow portion

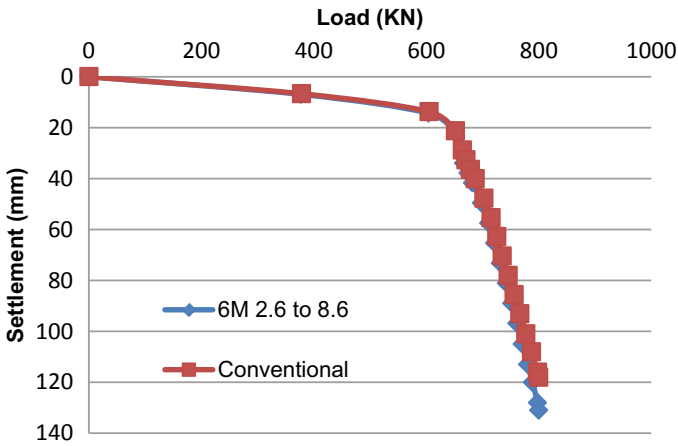


Fig. 6 Load–settlement curve for a 6-m hollow portion

Table 6 Top settlement of pile when 5-m hollow portion with varying its position

Sr. no.	Parameters of pile	Load (kN)	Settlement (mm)
1	Conventional	800	118
2	2M 2.6–7.6		131

Table 7 Top settlement of pile when 6-m hollow portion with varying its position

Sr. no.	Parameters of pile	Load (kN)	Settlement (mm)
1	Conventional	800	118
2	2M 2.6–8.6		131

It should be noted that the top settlement of a 4-m hollow floating circular pile shows better results. When its position kept below 2 m from the top surface of the pile as compare to other cases discussed in the present study.

References

- Armaleh S, Desai CS (1987) Load deformation response of axially loaded piles. *J Geotech Eng* 113(12):1483. [https://doi.org/10.1061/\(ASCE\)0733-9410](https://doi.org/10.1061/(ASCE)0733-9410)
- Butterfield R, Banerjee PK (1971) The elastic analysis of compressible piles and pile groups. *Geotechnique* 21:43–60
- Fawad NS, Paul M (2015) Elastic continuum solution of stacked pile model for axial load displacement analysis. *Geotech Eng J SEAGS & AGSSEA* 46:20–28
- Guo WD et al (1997) Vertically loaded piles in non homogeneous media. *Int J Numer Anal Meth Geomech* 21:507–532
- Kirzhner F, Rosenhouse K (2001) Analysis of the ultimate bearing capacity of a single pile in granular soils. *Trans Eng Sci ASCE* 32:207–214
- Neves MD et al (2001) Behavioral study of bored piles. *Bulletin des laboratoires des ponts et chaussées* 231, 55–67
- Polous HG (1979) Settlement of single piles in non homogeneous soil. *J Geotech Eng Div ASCE* 105
- Pooja G, Sharma JK (2017a) Settlement analysis of non homogeneous single granular pile. *Indian Geotech J* 48:92–101. <https://doi.org/10.1007/s40098-017-0240-z>
- Pooja G, Sharma JK (2017b) Non linear analysis of single floating granular pile. *IJRTER* 3:103–111
- Reddy RK et al (2015) Numerical analysis of piles in layered soils. *IJET* 7:482–489
- Salgado R et al (2011) Variational elastic solution for axially loaded piles in multilayered soil. *Int J Numer Anal Meth Geomech*. <https://doi.org/10.1002/nag.1110>
- Seo H et al (2008) Settlement analysis of axially loaded piles. In: *Case histories in geotechnical engineering*, Arlington
- Vijay K et al (2015) Settlement of single granular pile at different depths. In: *Indian geotechnical conference*, 2015

Effect of Excavation on the Settlement of Adjacent Structures



M. S. Aswathy, Achal Mittal, and Sidharth Behera

Abstract The requirement of increased infrastructure and limitation of space due to urbanization has resulted in the use of subsurface structures to meet the demands. There are many challenges in performing construction activities such as excavation adjacent to existing buildings and settlement is perhaps the most challenging among them. This paper studies the effect of excavation adjacent to existing buildings in the Delhi region for DMRC site carried out by CSIR—Central Building Research Institute. The excavation was carried out for a shaft opening of size 20 m × 20 m and the depth of excavation was around 18 m. The offset distance from the adjacent buildings varied from 4 to 15 m. The analysis was carried out using PLAXIS 3D software. The actual soil data of the site with realistic loadings of the buildings were considered. The results revealed that the settlement of the existing buildings doubled due to the adjacent construction activity as compared to the case of static load due to buildings. Post-excavation settlement was found to be more than the permissible limit indicating the need for improvement measures to be undertaken to minimize the damage to existing structures.

Keywords Deep excavation · Diaphragm wall · Settlement

1 Introduction

Urbanization in developing countries, like India, has caused an increase in demand for infrastructure facilities. In metro cities like Delhi where space constraints are a major issue, this requirement of infrastructure can be met by the utilization of underground spaces. The construction of underground tunnels changes the in situ soil stresses due to excavation of soil which could in turn result in subsurface/surface deformation of the ground (Ocak 2008). In urban areas, such ground deformations could induce minor to major damage to the overlying structures/utilities. Hence, it is essential to

M. S. Aswathy (✉) · A. Mittal · S. Behera
CSIR—Central Building Research Institute, Roorkee, Uttarakhand, India
e-mail: aswathy@cbri.res.in; achuscorpio24@gmail.com

© Springer Nature Singapore Pte Ltd. 2020
M. Latha Gali and P. Raghuvver Rao (eds.), *Construction in Geotechnical Engineering*, Lecture Notes in Civil Engineering 84,
https://doi.org/10.1007/978-981-15-6090-3_53

713

analyze/predict the settlement caused due to any such underground construction, so that necessary measures can be adopted to assure the safety of adjacent utilities.

Erin and Charles (2007) Leung analyzed the field monitoring data obtained from 14 deep excavation case histories in mixed ground conditions in Hong Kong. It was observed that the measured wall deflection and settlement are relatively independent of the stiffness of the retention system and the settlement influence zone of the excavations extends to a distance of 2.5 H. Laboratory model tests revealed that the addition of geosynthetic reinforcement below footing resting on sand significantly decreases vertical settlements and the tilts of the footings due to the adjacent deep excavation. When the footing is located very close to excavation the effect of reinforcement was found to be appreciable, while the effect can be neglected for footings at a distance more than 3B from excavation, where B is the width of footing (El Sawwaf and Nazir 2012). From the numerical studies by Suched et al. (2013), it was stated that simulation process and selection of relevant parameters play a major role in numerical analysis. Bhatkar et al. (2017) compared the site monitoring data of underground metro construction with numerical results. Though the deformations predicted from numerical methods were found to be higher than the actual field values, through back-calculation and proper estimation of material properties, the numerical simulation method is recommended as an efficient tool to assure the safety of adjacent structures.

A tunnel-boring machine (TBM) retrieval shaft was constructed near the thickly populated Rameswar Nagar region as part of tunneling works for Delhi Metro Rail Corporation (DMRC) project. In this paper, the settlement behavior of adjacent buildings due to shaft excavation is studied using finite element software PLAXIS 3D.

2 Subsoil Profile

The subsoil profile at the project site consists of five layers. The topmost layer is man-made fill followed by brown silty clay or clayey silt with small kankar/gravel of low plasticity. The third layer comprises of gray silty sand or fine to medium sand and/or sandy silt, clayey sandy silt, or silty sand with small kankar/gravel. Brown clayey silt or silty clay with small kankar/gravel of medium plasticity constitutes the fourth layer. The bottommost layer consists of gray silty sand or fine to medium sand and/or sandy silt, clayey sandy silt, or silty sand with small kankar/gravel. The groundwater table was located at a depth of 4.7 m below the ground level.

2.1 Soil Parameters for Analysis

The average standard penetration test values for each soil layer are given in Table 1.

Table 1 Soil type and SPT N values

Layer	Thickness	SPT N
Manmade fill	1.5	11
Sandy silt	3	9
Silty sand	3	20
Silty sand	4.5	34
Sandy silt	4.5	10
Silty sand	3.5	43
Silty sand	10	>50

Table 2 Soil parameters

Layer	Cohesion/Angle of internal friction	Modulus of elasticity (kPa)
Manmade fill	28°	10,330
Sandy silt	45 kPa	10,800
Silty sand	29°	15,100
Silty sand	33°	22,520
Sandy silt	50 kPa	12,000
Silty sand	33°	45,900
Silty sand	33°	55,000

The strength parameters of the soil are analyzed based on the laboratory test results and general correlations with SPT N values. The modulus of elasticity of soil is obtained using Eqs. (1)–(3) (Schultze and Menzenbach 1961; CIRIA 1995).

$$E = 2400 + 530 * N + 2100 \text{ kPa, for Silty sands} \tag{1}$$

$$E = 1.2N * 1000 \text{ kPa, for Sandy Silts} \tag{2}$$

$$E = 7000\sqrt{N} \text{ kPa, for dense sands} \tag{3}$$

The soil properties used for the analysis are summarized in Table 2.

3 Excavation Scheme

The excavation scheme consisted of contiguous piles and secant piles of diameter 1000 mm. The contiguous piles are placed at a spacing of 1.1 m center to center. The piles were embedded to a depth of 2.5 times diameter below the excavation level. Five levels of struts were provided as a support system and waler beams were used

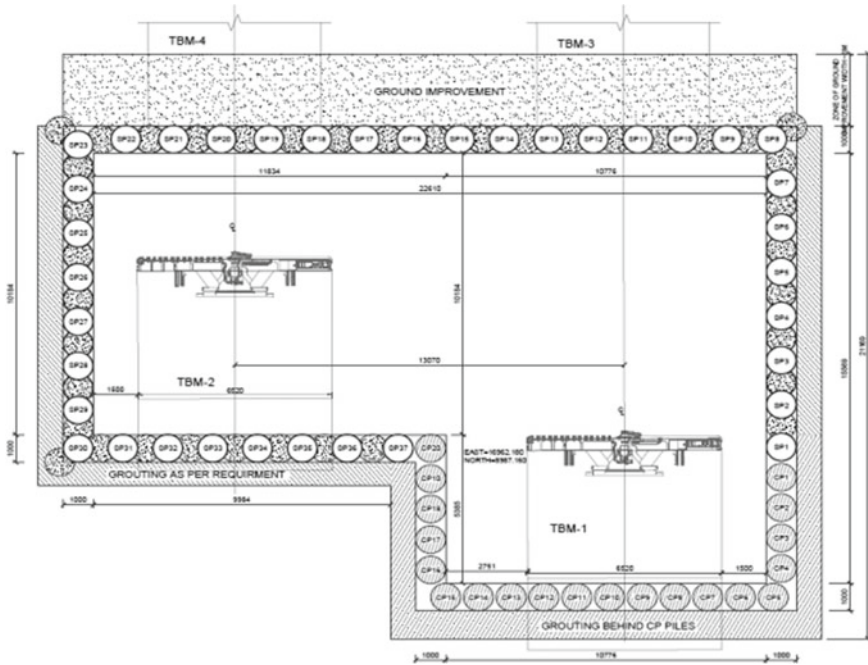


Fig. 1 Plan view of excavation shaft

for connecting the strut and transferring the load. Universal beam (UB) sections of size 457 mm × 152 mm × 74 mm were used for straight and diagonal struts and UB 610 mm × 229 mm × 101 mm sections were used for waler beams. A plan and typical section of the excavation scheme are shown in Figs. 1 and 2, respectively.

4 Numerical Modeling

Numerical modeling was done using PLAXIS 3D (2012) finite element software. In PLAXIS, the basic equations of static deformation of soil are formulated within the framework of continuum mechanics. The model is 100 m × 100 m extending to a depth of 40 m as shown in Fig. 3.

The contiguous piles and secant piles are modeled as embedded pile elements and struts and walers as beam elements. Embedded pile elements consist of beam elements with special interface elements that provide soil–beam interaction. The contiguous piles are of grade M40 and the secant pile–wall system consists of primary piles of M20 grade and secondary piles of M40 grade. The modulus of elasticity of the contiguous piles and secant piles were obtained using the Eq. (4).

$$E = 5000\sqrt{f_{ck}} \tag{4}$$

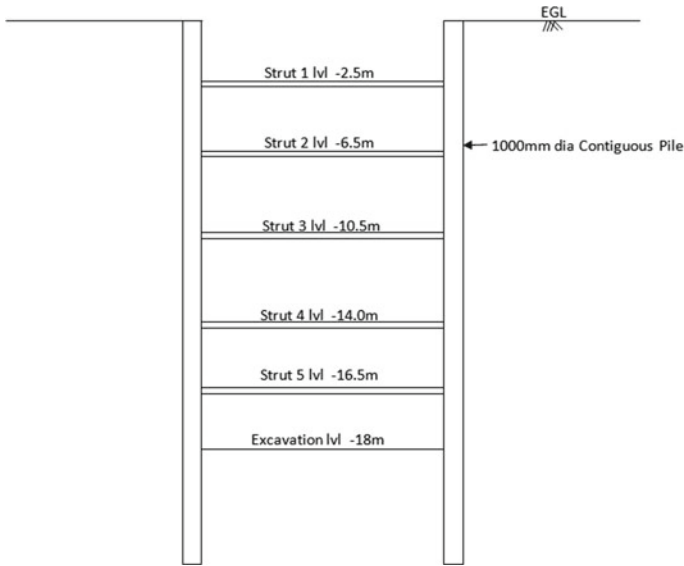


Fig. 2 Typical section of excavation scheme

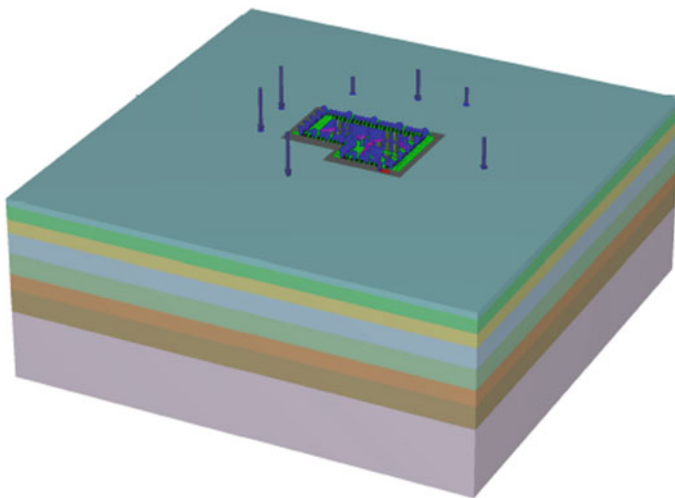


Fig. 3 Geometry model

The material properties of the contiguous pile, secant pile (primary), struts, and water beam are shown in Tables 3 and 4.

After modeling geometry, the generation of finite element mesh is carried out. The mesh generation is fully automatic wherein the geometry is divided into volume elements and compatible structural elements. The soil elements of 3D finite element

Table 3 Contiguous pile and secant pile material properties

Property	Contiguous pile/Secondary secant pile	Primary secant pile
Modulus of elasticity (kN/m ²)	31.62E6	22.36E6
Density (kN/m ³)	25	24
Diameter (m)	1.0	1.0
Area (m ²)	0.7854	0.7854

Table 4 Strut and Waler beam material properties

Property	Strut	Waler beam
Modulus of elasticity (kN/m ²)	2.1E6	2.1E6
Density (kN/m ³)	78.5	78.5
Area (m ²)	0.0189	0.02580

mesh are ten-node tetrahedral elements and beam elements are composed of three-node line elements. In locations expecting larger deformation gradients, an accurate finer mesh is desirable, which could be done using local fineness factor. The fineness factor is set to 1.0 for geometry entities and 0.5 for loads and structural objects.

The staged construction follows the mesh generation. The building loads are applied as UDL in the first phase followed by activation of contiguous piles and soldier piles. The excavation is carried out in stages wherein each excavation is done up to 0.6 m below the strut level until the final excavation level is reached.

5 Results and Discussion

The maximum settlement of the existing buildings prior to excavation was found to be 35 mm as shown in Fig. 4. The post-excavation settlement of the buildings increased to 69 mm (shown in Fig. 5) which is more than the permissible limit of 60 mm for isolated foundations in sand. This indicates that the surface settlement due to excavation under Greenfield conditions is 34 mm, which 0.2% of the depth of excavation. This is validated by the empirical work by Clough and O'Rourke (1990) where the maximum soil settlement behind the wall is about 0.15–0.3% of excavation depth in sands.

A plot of maximum settlement at each stage is given in Fig. 6. The maximum settlement is found to be at a distance of 10 m from the bottom excavation boundary line at all the stages. The settlement was found to be 0.1% depth of excavation immediately behind the contiguous pile wall. The settlement gradually increases and reaches a maximum value almost at the mid of the building and then reducing beyond that and reaching negligible value at two times depth of excavation from the boundary (shown in Fig. 7) which is similar to results presented by Peck (1969).

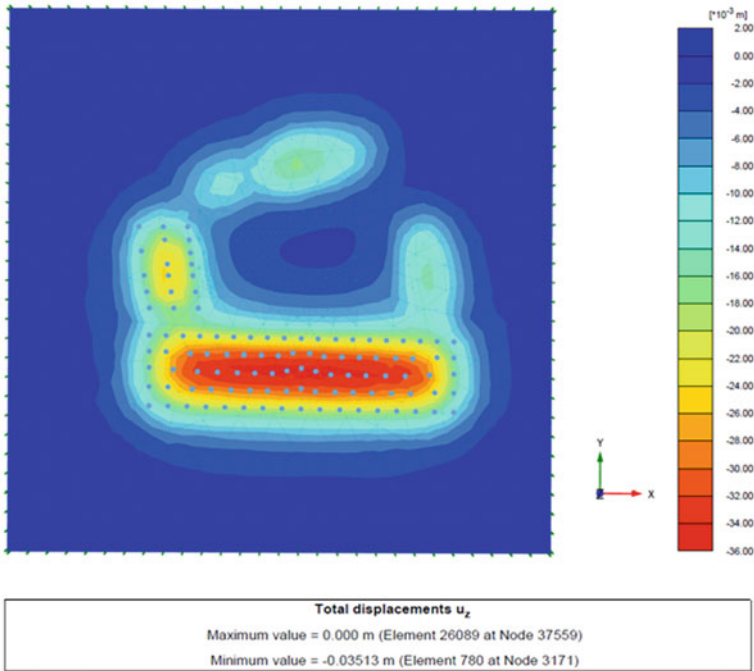


Fig. 4 Vertical displacement before excavation

Hsieh and Ou (1998) suggested that the soil settlement profile (in the horizontal direction) behind the wall depends on the shape of the wall deflection. A concave type of soil deformation, in which maximum settlement occurs at a distance away from the wall (as in the present case), is expected if the wall shows deep inward movement (Figs. 7 and 8).

The above research data indicates that the observation of maximum settlement at some distance (approximately equal to half the excavated depth) away from the wall could not only be due to the presence of building loads but also has a relation with the shape of the wall deflection.

6 Conclusions

The following conclusions could be drawn from the current study:

1. The maximum surface settlement due to excavation is in the range of 0.2% of the depth of excavation in the case of sandy soil.
2. The settlement profile around the excavation site depends on the shape of wall deflection; if the wall shows deep inward movement, then maximum displacement occurs at some distance away from the wall.

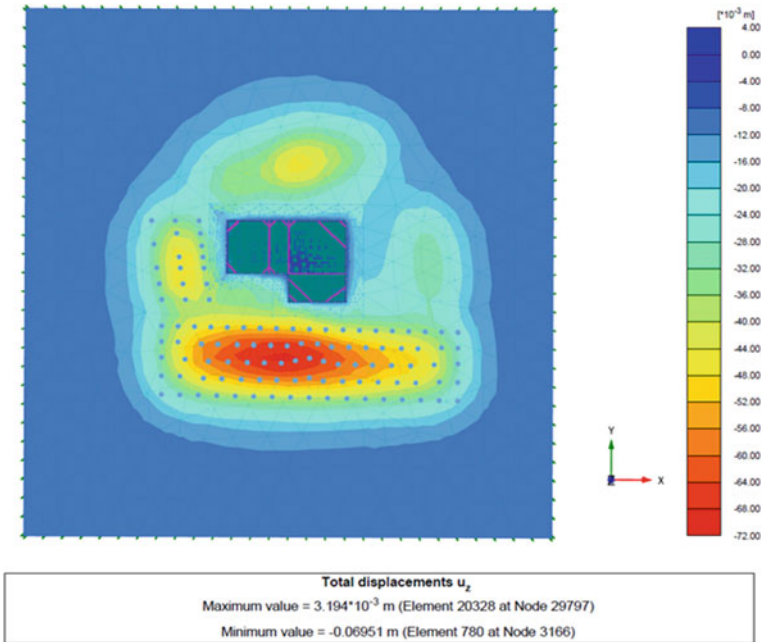
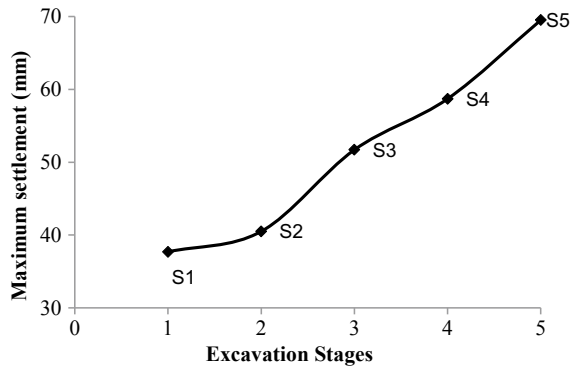


Fig. 5 Vertical displacement after excavation

Fig. 6 Maximum settlement in each excavation stage



3. The settlement of the surface becomes negligible beyond a distance of twice the depth of excavation from the excavation boundary.

Fig. 7 Surface settlement plot

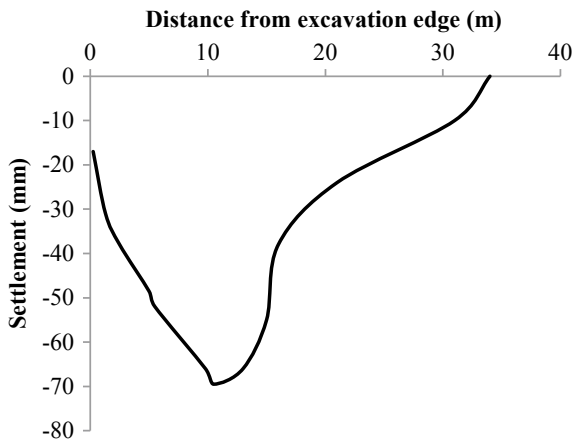
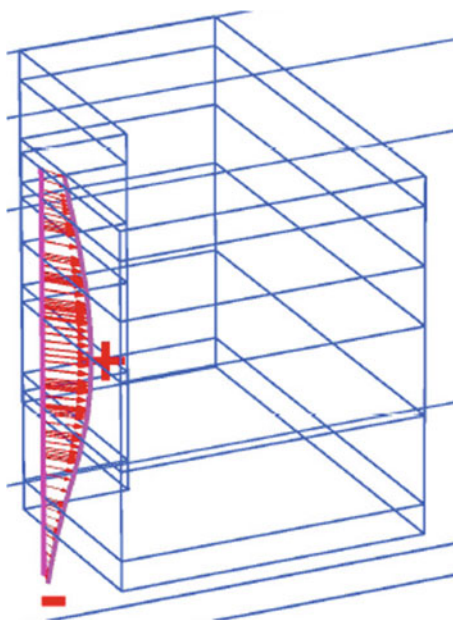


Fig. 8 Typical shape of wall deflection



References

- Bhatkar T, Barman D, Mandal A, Usmani A (2017) Prediction of behaviour of a deep excavation in soft soil: a case study. *Int J Geotech Eng* 11:10–19
- Clayton CRI (1995) The standard penetration test (SPT): methods and use. CIRIA report 143
- Clough GW, O'Rourke TD (1990) Construction induced movements of in situ walls. In: Proceedings, ASCE conference on design and performance of earth retaining structures, geotechnical special publication, ASCE, vol 25, pp 439–470

- El Sawwaf M, Nazir AK (2012) The effect of deep excavation-induced lateral soil movements on the behavior of strip footing supported on reinforced sand. *J Adv Res* 3:337–344
- Erin HYL, Charles WVN (2007) Wall and ground movements associated with deep excavations supported by cast in situ wall in mixed ground conditions. *J Geotech Geoenviron Eng* 133(2):129–143
- Hsieh PG, Ou CY (1998) Shape of ground surface settlement profiles caused by excavation. *Can Geotech J* 35(6):1004–1017
- Ocak I (2008) Control of surface settlements with umbrella arch method in second stage excavations of Istanbul Metro. *Tunn Undergr Space Technol* 23(6):674–681
- Peck RB (1969) Deep excavations and tunnelling in soft ground. In: *Proceeding of the 7th international conference on soil mechanics and foundations engineering, Mexico City, State of the Art Volume*, pp 225–290
- RBJ Brinkgreve, E Engin, WM Swolfs (2012) *PLAXIS 3D Manual* Plaxis bv, the Netherlands
- Schultze E, Menzenbach E (1961) Standard penetration test and compressibility of soils. In: *Proceedings of the fifth international conference on soil mechanics and foundation engineering, Paris, vol 1*, p 527
- Suched L, Chanaton S, Wanatowski D, Erwin O, Balasubramaniam A (2013) Finite element analysis of a deep excavation: a case study from the Bangkok MRT. *Soils Found* 53(5):756–773

Full-Scale Load Test on Bored Cast in situ Piles—A Case Study



B. V. S. Viswanadham and Pankaj Kumar

Abstract This paper presents a case study on two full-scale pile load tests on the bored cast in situ piles of 800 mm diameter having 10 m length. These piles are intended to be used as foundations for a 20-storeyed residential building in Mumbai. For determining the allowable load carrying capacity of piles, it was decided to carry out initial load tests and gain insight on the behaviour of piles. Further, to verify conformity with the design load obtained from static calculations. A novel method of loading the piles has been used and introduced, as conventional static pile load testing methods require enormous temporary infrastructure for applying larger loads. In this method, a reaction system has been used that derives reaction from the rock anchors using a hydraulic jack to impose the 2–2.5 times the design load on test piles. In this paper, the reaction method was described along with the design of rock anchors. This paper presents a method to predict a safe load from the pile load test data for adopting in the design.

Keywords Full-scale load test · Static load test · Pile load test set-up · Bored cast in situ piles

1 Introduction

Design and construction of pile foundations for multi-storeyed buildings by considering safe loads beyond theoretical values as recommended by empirical equations and design standards should be supplemented by an actual load-bearing capacity of individual piles. There are various methods viz. empirical, numerical and analytical, to predict safe load-bearing capacity and settlements in individual piles. Several researchers in the past have also conducted in situ full-scale initial pile load tests to measure pile resistance and settlements for estimating the load-bearing capacity of piles. Such tests are expensive and time-consuming but ensure a safe and economical design of the overall foundation system. In the present study, two full-scale

B. V. S. Viswanadham (✉) · P. Kumar
Department of Civil Engineering, IIT Bombay, Mumbai, Maharashtra, India
e-mail: viswam@civil.iitb.ac.in; bvsb228@gmail.com

© Springer Nature Singapore Pte Ltd. 2020
M. Latha Gali and P. Raghuvver Rao (eds.), *Construction in Geotechnical Engineering*, Lecture Notes in Civil Engineering 84,
https://doi.org/10.1007/978-981-15-6090-3_54

723

pile load tests were conducted to estimate the safe load on a single test pile and to predict settlements under working load conditions. A novel method of loading the piles has been used and introduced. In this method, a reaction system has been used that derives reaction from the rock anchors using a hydraulic pump hydraulic jack system to impose 2–2.5 times the design load on the test piles. The load and settlement observations were recorded for both the tests and safe load results were interpreted through load–settlement curves by applying different methods viz. IS 2911 (Part-4), Double tangent, Mazurkiewicz’s and De Beer’s.

2 Project Description and Geotechnical Conditions

It is planned to construct a residential building in Mumbai, which will consist of stilt + 20 upper floors. Four boreholes (BH-1–BH-4) and two trial pits were made to explore ground stratification and for geotechnical observations.

Sub-surface profile at this site consists of fill overlying residual soils underlain by completely weathered rock and then by basalt bedrock as shown in Fig. 1. The sub-surface investigation was completed generally as per “IS: 1892-1979”. The field investigation was carried out using a rotary machine. The casing was used to support

Fig. 1 Typical sub-surface soil profile at the site

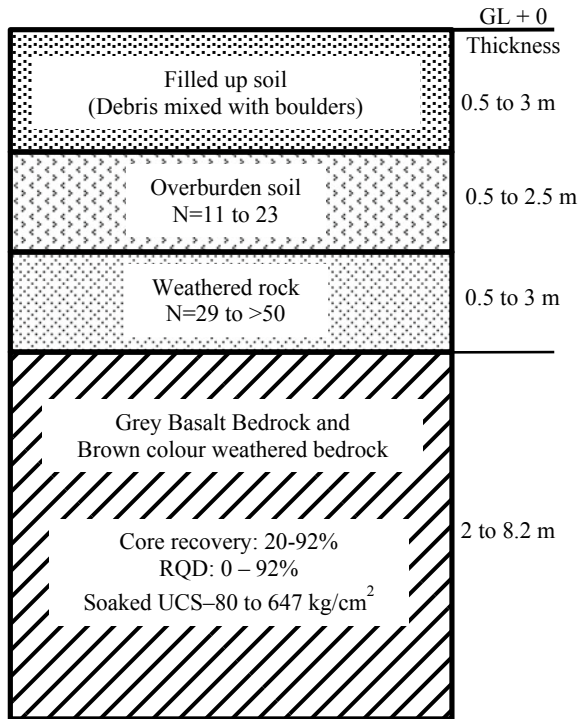


Table 1 Pile geometry and installation type

Pile designation	Length (m)	Diameter (mm)	Installation
Pile 1	10.15	800	Bored, Cast in situ
Pile 2	10.15	800	Bored, Cast in situ

sides of borehole until sufficiently stiff strata were encountered. Standard Penetration Tests (SPT) were carried out in soil in accordance with “IS 2131-1981”. Based on SPT tests conducted within these layers, the consistency of cohesive soils (clay) varies from stiff to very stiff. When SPT refusal was obtained in hard strata, rock coring was done using a diamond bit and double tube core barrel to obtain rock samples and then rock core recovery and RQD were determined. Core recoveries varied typically between 11 and 98%, while rock quality designation (RQD) ranged between 0 and 98%. The compressive strength of rock core samples varies from 9 to 600 kg/cm². The boreholes were terminated on this bedrock layer at depths of 11–17 m below the ground surface. Groundwater was observed in boreholes at a depth of 4 m below the ground surface. Seasonal and annual fluctuations in groundwater levels can be expected.

For foundation, it was decided to provide 800 mm diameter and 10 m long bored cast in situ piles to support the multi-storeyed building. As per static pile load capacity, analysis for an 800-mm-diameter pile, the safe vertical and lateral pile capacities adopted were 250 t and 17 t, respectively. The characteristics of the test piles are shown in Table 1.

3 Static Pile Load Test Program and Setup

The pile testing program consisted of two static initial pile load tests carried out in accordance with “IS: 2911 (Part 4)-1985”. The 10 m long test piles were constructed to estimate the safe load-carrying capacity of individual piles. As the majority of the strata consisted of cohesive soils, load tests on the piles were carried out after 15 days of driving to ensure uniform dissipation of pore water pressure and linear rate of settlements during testing. The static pile load test set-up is shown in Fig. 2. Various components of the test set-up consist of rock anchors, anchor strands, reaction girder, hydraulic jack, hydraulic pump, supporting stool, steel bearing plate and dial gauges. Details of both the load tests are given in Table 2.

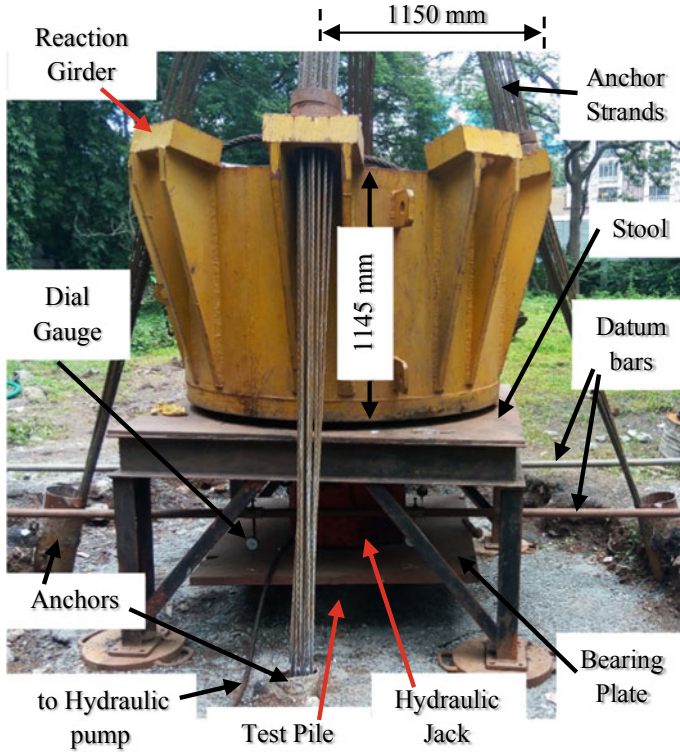


Fig. 2 Static pile load test setup

Table 2 Description of loads for test piles

Pile designation	Design load (T)	Test load (T)
Pile 1	265	530
Pile 2	265	530

3.1 Anchor Design

Temporary ground anchors were designed and constructed as per “IS 10270 (1982)” for the loading system to test an 800-mm-diameter pile with design load capacity as 265 t. The test load to be applied on the pile head was taken as twice the design load capacity, i.e. 530 t. It was assumed that shaft friction available was 30 t/m². The diameter of the anchor drill hole was 200 mm and the shaft area of anchor bore was 0.628 m² per metre. Now, the total shaft friction available was 18.852 t per metre. The length of the shaft (L) required is given by Eq. (1).

$$L = \frac{\text{working load}}{\pi \times \text{hole dia} \times \text{shaft friction}} \tag{1}$$

The anchor strands were designed as per “IS 1343 (2012)/BS 8081 (1989)”, with seven pre-stressed wires having a nominal diameter of 15.2 mm and ultimate strength of 30 t. Accordingly, the number of strands (N) as given by Eq. (2) required for anchor capacity of 150 t were taken as 12 considering the factor of safety value of 2. The pre-stressing force was assumed to be in a range of 0.6–0.8 times the ultimate strength of strand.

$$N = \frac{\text{working load} \times FoS}{\text{Ultimate strength of strand}} \quad (2)$$

The designed anchor of capacity 175 T was having 11 m of fixed length and 7 m of free length. Anchor strands that were used could be either 16 nos. of 12.7 mm diameter or 12 nos. of 15.2 mm diameter with GP2 grout. A total of four anchors were used for reaction loading and to provide support for the reaction girder in the test assembly. The combined ultimate capacity of the reaction anchors was 30% more than the test pile load.

3.2 Other Components

A hydraulic pump was used to apply pressure on the pile head through a hydraulic jack to load the test piles to desired loading conditions at fixed intervals of time. It had a capacity of 1500 t and a ram diameter of 0.525 m. The pressure gauge reading on the hydraulic pump for 10 t of load on the pile head was observed as 4.62 kg/cm². Dial gauges were used to record average settlements of pile head for both the piles. A total of four dial gauges of 0.01-mm sensitivity were positioned at each corner on top of a steel bearing plate and firmly held by datum bars. The bearing plate was centered on top of the test pile and bears against the test frame.

4 Load Test Methodology

The pile on which the test was carried out was chipped to and dressed perfectly. Rock anchors of approximately 175 t capacity were drilled at fixed locations at 15° to the vertical. The anchor length constituted 11 m of fixed grouted length and 7 m of free length. After the pile had achieved its strength, a steel bearing plate was placed on top of the pile head block. A 1500 t capacity hydraulic jack was then placed at the centre of the bearing plate. On top of this hydraulic jack was placed a mild steel stool which was used for temporarily supporting the reaction girder. The anchor strands were then homed into the lugs of the reaction girder and locked. The dial gauges were housed on two datum bars at each of the four corners of the steel bearing plate. The hydraulic jack was then connected to the hydraulic pump which was fitted with a pressure gauge for reading the load. The test was then commenced at

20% increments of the design load. As the test progressed, dial gauge readings were recorded for settlements of the pile head. On reaching the test load, it was maintained for more than 12 h before recording the final settlement. The load was then released in three equal unloading stages and the rebound was recorded.

5 Result Interpretation and Discussion

The load–settlement curves obtained for both the test piles are shown in Fig. 3. It is noted from curves for both the piles that the load–settlement relationship is approximately linear in the loading stage (initial part of the curve) and non-linear in the unloading stage. The non-linear portion is also observed during the final increment of loading. Both the test piles continue to settle with an increase in load which means that none of the test piles were loaded to their ultimate capacity. The pile head settlements observed are shown in Table 3.

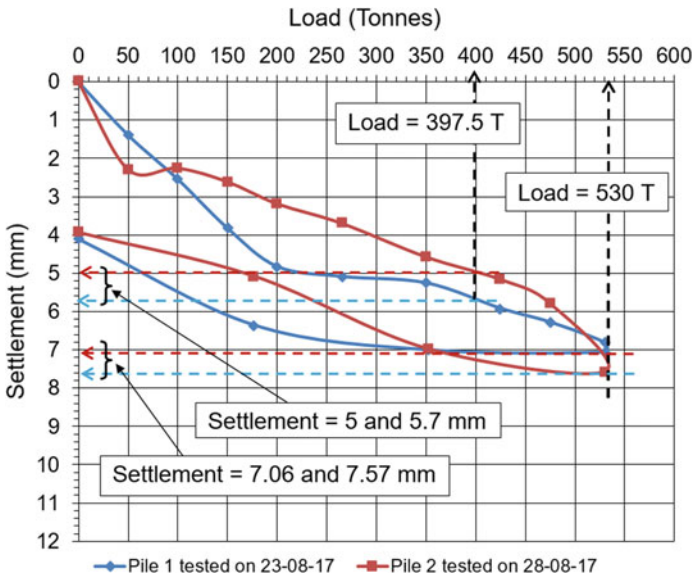


Fig. 3 Variation of settlement with applied load for a concrete pile during the vertical load test

Table 3 Pile head settlements from initial pile load tests

Observations	Pile 1	Pile 2
Temporary settlement (mm)	7.06	7.57
Permanent settlement (mm)	4.11	3.93
Rebound (mm)	2.96	3.64

Table 4 Safe loads from initial pile load tests

Criteria	Pile 1	Pile 2
IS 2911 (Part 4)	353 T	353 T

As per “IS: 2911 (Part 4) (1985) (reaffirmed 2010), Clause 6”, for vertical load test (compression) the safe load on the single pile as shown in Table 4, should be least of the following criteria:

- (a) Safe load on a single pile should be two-third of the final load at which total displacement attains a value of 12 mm unless otherwise required in a given case on the basis of nature and type of structure in which case, the safe load should be corresponding to the stated total displacement. In the present case, both the test piles are loaded to 530 T and corresponding temporary settlements observed, from Fig. 3, are 7.06 and 7.57 mm, respectively. The above settlement values are less than the 12 mm requirement. Therefore, considering 530 T as the final load, two-third of this final load can be adopted as a safe load.

$$\begin{aligned} \text{Safe load} &= (2/3) \times 530 \\ &= 353 \text{ T} \end{aligned}$$

- (b) Safe load should be 50% of the final load at which the total displacement equals 10% of the pile diameter in case of uniform diameter piles.

$$\begin{aligned} \text{Diameter of the pile} &= 800 \text{ mm} \\ 10\% \text{ of pile diameter} &= 80 \text{ mm} \end{aligned}$$

Load corresponding to settlement equalling 10% of pile diameter i.e. 80 mm cannot be deduced from Fig. 3, therefore clause not applicable.

- (c) During a routine test carried out for a test load of at least 1.5 times working load, the maximum settlement of test loading being in position should not exceed 12 mm.

$$\begin{aligned} \text{Working load} &= 265 \text{ T (design load)} \\ \text{Test load} &= 1.5 \times 265 \\ &= 397.5 \text{ T} \end{aligned}$$

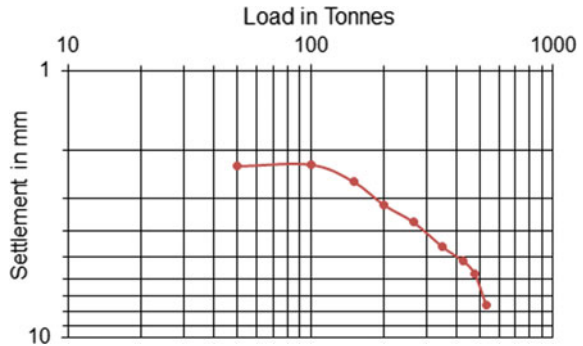
Considering this test load of 397.5 T and referring to Fig. 3, the settlements observed for pile tests 1 and 2 are nearly 5 mm and 5.7 mm, respectively, which are less than the maximum permissible limit of 12 mm.

The ultimate loads for the test piles are predicted from load–settlement observations using different interpretation methods, viz. IS 2911 (Part-4), Double tangent, Mazurkiewicz’s and De Beer’s as shown in Table 5. Mostly, these methods are suitable for load–settlement observations for Pile 2 only. Other methods like Davisson’s,

Table 5 Ultimate loads from initial pile load tests

Criteria	Ultimate load (T)
IS 2911 (Part 4)	530
Double tangent	490
De Beer (1968)	>500
Mazurkiewicz’s	>520

Fig. 4 Yield load according to De Beer’s method for Pile 2



Chin-Kondner, Decourt’s extrapolation and Brinch Hansen’s 80% criteria also exist but were not applicable to the test piles considered herein.

The safe load obtained as per “IS 2911 (Part-4)” for the test piles was converted to ultimate load by considering a factor of safety of 1.5. As per “Double tangent criterion”, the ultimate load corresponds to the intersection of the tangents from the initial straightline portion and the latter non-linear portion of the load–settlement curve. As per “De Beer’s method”, load–settlement observations are plotted on a double logarithmic chart as shown in Fig. 4. The intersection of two approximately straight lines depicts the pile-yielding load. According to “Mazurkiewicz’s method, as suggested by Fellenius (1980)”, settlement axis is divided into the number of equally spaced horizontal lines on the load–settlement curve and corresponding loads are marked with vertical lines on the load axis as shown in Fig. 5. For the marked loads, a 45° line is drawn to intersect the next vertical line of the marked load. All these intersection points are then joined through an approximately straight line to intersect the load axis at the ultimate failure load.

6 Conclusions

Full-scale static pile load tests were carried out on two bored cast in situ test piles of 800 mm diameter and length 10 m constructed in cohesive soils. Static pile load tests were carried out to ascertain safe design load on individual piles, which will act as foundations for the multi-storeyed building at Mumbai. Based on test results obtained

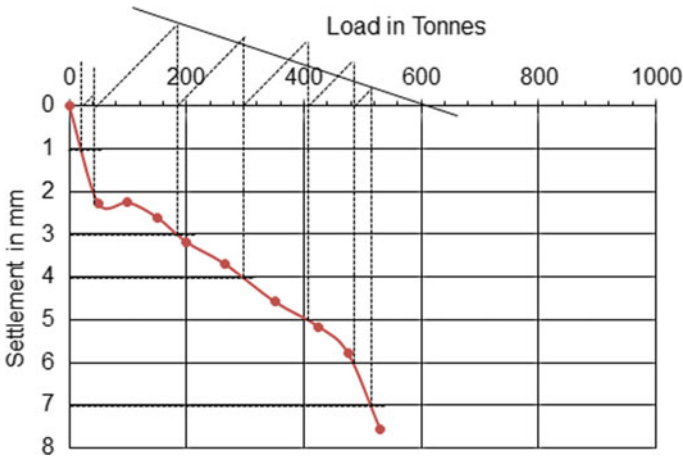


Fig. 5 Ultimate load according to Mazurkiewicz’s method for Pile 2

after the interpretation of load–settlement curves, the safe load to be considered on the single pile should be 353 T for the design (as per IS 2911 Part-4). The ultimate failure load to be considered on the test piles should be 490 T as obtained from the double tangent method.

References

De Beer EE (1968) Proefondervindlijke bijdrage tot de studie van het grensdrag vermogen van zand onder funderingen op staal. Tijdschrift der Openbar Verken van België, No. 6, 1967 and No. 4, 5, and 6

Fellenius BH (1980) The analysis of results from routine pile load tests. *Ground Eng* 13(6):19–31

IS: 10270 (1982) Guidelines for design and construction of prestressed rock anchors

IS: 1892 (1979) Code of practice for subsurface investigation for foundations

IS: 2131-1981. Method for standard penetration test for soils

IS: 2911 (Part 4)-1985. Code of practice for design and construction of pile foundations

Review of Historic Forensic Geotechnical Engineering



Leonardo Souza and Purnanand Savoikar

Abstract We need to preserve our ancient but fast disappearing culture through its structures and substructures. For instance, the ancient people notably built seismic-resistant footings and foundations as well as structures of the earth. In ancient India, engineers had already incorporated many important geotechnical techniques in embankment building as are still observed in the Bunds seen in Goa. Conservation poses an important engineering challenge. Historic Forensic Geotechnical Engineering studies play a vital role in such preservation of traditional architecture. This paper examines various types of Forensic Geotechnical Research and the rationale for further research of historic geotechnical substructures and superstructures and their building techniques and variability. It attempts to overview these important architectural remains and the need for actions. This paper explores the need to study Historic Geotechnical Structures as an important sub-branch of Forensic Geotechnical Engineering Studies by forensic review of different ancient Geotechnical structures and the possibility of making it part of mainstream studies.

Keywords Forensic geotechnical investigations · Historic geotechnical · Structures

1 Introduction

Preservation of our ancient but fast disappearing culture through its structures and substructures is an important engineering challenge. The popular opinion usually is that it is more beneficial, technically simple, and economical to construct new buildings instead of preserving the old ones, demolish the old shacks to construct modern gleaming skyscrapers. Nevertheless, in this age, a sizeable growing segment of the population has realized the significance of preserving our past. Moreover, these interventions have to guarantee the performance of the structure for durability, structural conformity, and sustainability. Historically, the buildings were placed on strategic locations whose supporting soil had hidden unconformities which in time

L. Souza (✉) · P. Savoikar
Civil Engineering Department, Goa Engineering College, Farmagudi 403401, Goa, India
e-mail: lrds@rediffmail.com

© Springer Nature Singapore Pte Ltd. 2020
M. Latha Gali and P. Raghuvver Rao (eds.), *Construction in Geotechnical Engineering*, Lecture Notes in Civil Engineering 84,
https://doi.org/10.1007/978-981-15-6090-3_55

733

led to the alteration of the physico-mechanical characteristics of the underlying layers (XVIII EYGEC—Portonovo et al. 2007).

1.1 Role of Geotechnical Engineering in Preservation

Earth construction techniques have been around for over 9000 years (Minke 2006). Many aspects of the use and significance of Historic Forensic Geotechnical Engineering studies are considered vital to the preservation of such traditional architecture. Conservation efforts involve a number of factors belonging to different fields: technical, cultural, humanistic, social, economical, and administrative. From a pure engineering point of view, the peculiarity of these types of interventions consists of the necessity of preserving the entire entity, maintaining its integrity, besides guaranteeing the secure utility of the structures and substructures. Over the years, the ever-increasing developmental pressures led to a neglect of monuments and heritage areas and resulted in their decay, which called for evolving harmonious strategies and conservation measures of their environs that, if taken in time, it will save them from gradual but imminent destruction (Shankar and Uma 2012).

To achieve this, we start from the technical analysis of historical documents and collection of all information related to the case studied. Subsequently, on the base of such information in situ investigations and monitoring on the foundation structure and on the subsoil must be carried out. Once all data have been collected, advanced analysis methodologies can be applied to the detailed geotechnical model of the historical structures and substructures. The geotechnical response of such edifices, subjected to general loading conditions, has been studied by various research groups for the last many decades. The poor preservation of most archeological architecture is a severely limiting factor in historical restoration and research. The ground plan, the foundation works, and, possibly, the lower part of the superstructure is generally all that remains of a building on an archeological site. These geotechnical remains thus form the basis for any reconstructions of the missing upper parts of the superstructure including the roof (Tringham 1991). This focuses on the importance of historical geotechnical investigations.

1.2 Benefits of Conservation of Historic Structures

One cannot escape the progress, but history must not be sacrificed at the altar of development. We must tackle this topic head-on and remind others of the often forgotten benefits of keeping our heritage intact. Preservation and restoration play a cultural role—they teach us about the history that happened before we were born and promote respect for those who lived in different times and different societies. Historical structures also introduce a certain charm and character to the neighborhood that people reside in.

Many times restoring an old building is often much more economical than building the new one. Restoration works require more skills and knowledge than a simple building. This leads to a vast improvement in applied technical expertise and awareness. While building new green buildings and energy-saving houses is important, restoring the old ones is as “green” as possible. Preservation and restoration is the ultimate form of recycling. It’s also good for the environment. It reduces construction waste and saves the energy usually spent on manufacturing and transporting new building materials and tools. Fewer building materials are required to refurbish old buildings, which reduces waste headed to landfills and the demand for aggregates gouging holes in the countryside to supply the materials for new stones, bricks, concrete, and mortar.

Neuroesthetics, a relatively new branch of neuroscience suggests the theory that beauty in art and design (which we usually find in historic structures) makes one happy. Historically significant buildings contribute to our countries cultural and economic well-being through tourism—not to mention the vibrancy of life. In fact, it is the major reason for people to visit distant places. Historic structures create heritage designations that boost property values. Preservation of Heritage structures being more labor-intensive means more technical jobs—both skilled and unskilled. Most importantly, historic structures are physical links to our past culturally and technically.

1.3 Technical Benefits of Conservation of Historic Structures

There are many questions which when asked can contribute to the general pool of technical knowledge:

1. Construction Technology—how they were built, and later modified, (e.g. ancient construction equipment and tools)
2. Material Technology—with what they were built, and later modified.
3. Design Technology—principles on which they were built, and later modified. (e.g. load transfer by arching and vaulting)
4. Technology Transfer—how much was transferred to modern science, why it was successful in some cases, less so in others. (e.g. Coulomb’s earth pressure principal for fort walls)
5. Technology Assimilation—how these techniques were eventually assimilated into the cultures where they were introduced sometime by mixing religion and rituals into it. (e.g. Vaastu Shastra and Feng Shui)

2 Types of Geotechnical Investigations

Geotechnical Engineering is the branch of Civil Engineering (Fig. 1) which deals with the performance of earthen materials and their interaction with man-made elements: foundations, substructures, and superstructures. Geotechnical Engineers are commonly called upon to evaluate the feasibility of construction sites, behavior of soils at the site in their natural or reworked state, the ease of soil and/or rock excavation, or bearing capacity for the proposed construction. These investigations can be broadly classified as pre-construction and forensic investigations. Forensic investigations can further be classed as Ex post facto (geotechnical investigation after the incident has occurred), pre facto (geotechnical monitoring for incident prevention), and historic investigations (geotechnical investigations for the older structures) (Table 1).

Geotechnical investigations and testing methods (Table 2) are usually done through the macro-element approach, which enables to consider the external resultant forces applied to the geo-structure (V, H, M) and the corresponding displacements (u, v, θ) as generalized stress and strain variables and then analyzed. Nowadays, this is done by computerized simulation or lab studies.

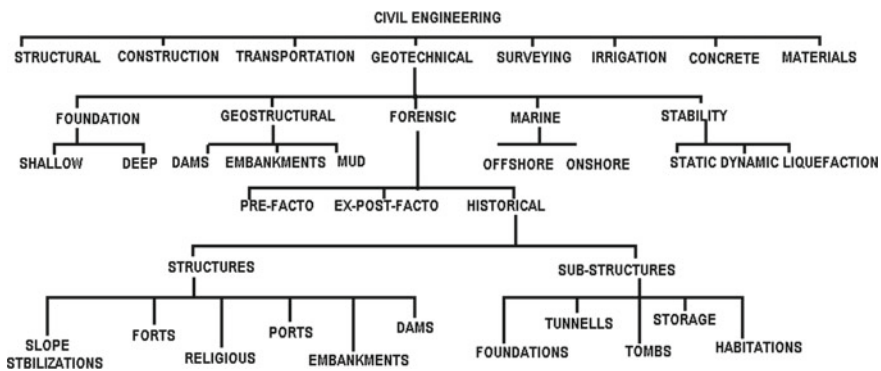


Fig. 1 Branches of civil engineering

Table 1 Geotechnical investigations

No.	Investigation type
1	Site investigations for the individual house
2	Site investigations for commercial engineering
3	Site investigations for the linear infrastructure
4	Fill compaction investigations
5	Geotechnical investigations for the older structures
6	Geotechnical investigation after the incident
7	Geotechnical monitoring for incident prevention

Table 2 Geotechnical testing methods

No.	Testing methods
1	Soil classification testing
2	Soil basic properties and Atterberg limits
3	Shear testing—static and cyclic
4	Permeability testing
5	Piezometer installations
6	Cone penetration test (CPT) Standard penetration test (SPT), Dilatometer test (DMT), and pressure meter testing
7	Penetrometer testing
8	Inclinometer tests
9	GPR and NDT techniques
10	Scaled model and centrifuge techniques

2.1 Forensic Geotechnical Investigations

Forensic Geotechnical Engineering involves the analysis of the project, investigations of site conditions, and construction methodology from a geotechnical standpoint. Such analyses may be performed during the design phase of a project (pre facto) to check the calculations and engineering assumptions or during and/or after the construction of a project to provide quality assurance. Analyses may also be performed to address issues that arise during or after construction (ex post facto). Common issues that may arise that forensic geotechnical analysis can help include historic structures, potential problems, failures, man-made disasters, and natural disasters (Table 2).

As can be seen, this type of work is a special niche that requires attention to detail, and engaged, highly qualified professionals—exactly the reason to study it as a separate discipline in higher university education (Table 3).

2.2 Ex Post Facto Geotechnical Investigations

Forensic investigations are often ex post facto Investigations. This is also known as after-the-fact research and is defined as those inquiries and explorations carried out after a failure or disaster has occurred. These often involve the study of things that can't be controlled—ethically or physically. Ex post facto geotechnical study design is a quasi-experimental study examining how an independent variable, present prior to the study, affects a dependent variable. Such a study is a category of research design in which the investigation starts after the fact has occurred without interference from the researcher but which needs analysis and possible solutions and means to prevent further such incidents.

Table 3 Reasons for forensic geotechnical investigations

No.	Reason for forensic investigations
1	Problems caused by Expansive Soils
2	Problems caused by Collapsible Soils
3	Settlement of Shallow and Deep Compacted Fill Soils
4	Transportation, Parking Area Pavement, and Embankment Failures
5	Slope Protection Failures
6	Foundation Failures
7	Excavation Failures
8	Underground Pipeline Failures
9	Underground Tunnel Failures
10	Differing Site Condition Disputes
11	Site Runoff and Drainage
12	Site Quantity Analysis
13	Site Quality Analysis
14	Soil Corrosion
15	Moisture Intrusion Below Slabs
16	Sulfate Exposure
17	Tsunami Related Infrastructure Failures
18	Liquefaction and Sand boiling
19	Seismic and Tectonic Failures
20	Slope Instability, Rockfalls, and Landslides
21	Discover a technique not recorded in history

It is not possible or acceptable to manipulate the characteristics of geotechnical components on which ex post facto research design is based. It is also often applied as a true experimental research to test hypotheses about cause and effect relationships. Such research may be used in situations in which it is not practical or ethically acceptable to apply the full protocol of true experimental design.

The main purpose of using an ex post facto is to determine the cause and effect relationship between the dependent and the independent variables that led to the occurrence of the event.

There are some strategies that have been proposed to ensure the credibility of the research. These tactics are Matching, Selecting homogenous groups, Building extra venous variables into the investigative design, and Partial or full correlations (Table 4). Using these strategies, the geotechnical investigator arrives at a correct interpretation of what caused the effect.

Table 4 Strategies for Ex Post -Facto investigations

No.	Strategy	Investigation criteria
1	Matching	Class similar geotechnical events together
2	The use of Homogeneous groups	Gives the researcher some degree of control over the variable and the ability to get the desired results
3	Building extra venous variables	Selecting variables which specifically fit the type of data that the researcher is studying
4	Correlations	Acquire a degree of control over the variable

2.3 Pre Facto Geotechnical Investigations

Pre facto geotechnical investigations are also called accident or hazard prevention investigation. These are the second most common type of forensic geotechnical investigations. The hazard theory is developed for the geo-structure by applying the principals of modern safety science and accident-causing theory, which must be based on adequate case studies. Learning from past accidents and near accidents can lead to accident prediction and prevention. A considerable progress has been achieved in the area of predictive safety management. Some of the techniques that have been developed for industrial safety and have become routine including risk analysis can also be used for geotechnical analysis. These techniques permit us to study potential geotechnical problems systematically for the identification of probable hazards and to institute suitable prior action to prevent any untoward happenings.

The factors which are of greatest relevance in determining geotechnical risk are risk potential factors, injury incidence factors, and significance of damage factors (Table 5). These should be methodically and meticulously determined.

The attitude of people also influences disasters. When it is known that disaster is probable, people try to avoid it rather than prevent it. When they know that there is a geotechnical device preventing the event, they become less cautious about their safety. When they then are required to intervene, they may not have the necessary competence or ability. Harmful factors will always be present in human surroundings. It is often not possible to isolate all potential hazards using the control measures. Thus, the concept of geotechnical hazards must be properly analyzed and the requisite

Table 5 Pre Facto risk determination factors

No.	Factors	Investigation criteria
1	Risk potential	Factors which determine the presence or absence (or potential) of risks of any sort
2	Injury incidence	Factors which either increase or minimize the probability of these risks resulting in accidents or injuries
3	Significance of damage	Factors affecting the seriousness of accidents associated with these risks

Table 6 Controlling human conduct for Pre Facto risk management

No.	Safety measures	Controls
1	Elimination/substitution safety measures	General controls
2	Technical safety measures	Engineering controls
3	Organizational safety measures	Administrative controls

Table 7 Pre Facto risk analysis

No.	Analyses	Controls
1	Identification of where and which types of accidents occur	The goal is to determine the incidence of the injuries, as associated, for example, with sectors, trade groups, enterprises, work processes and types of technology
2	Monitoring incidence of accidents and calculating frequency and seriousness of accidents	Measuring the effect of preventive initiatives, warning of new risk elements and probabilistic analysis
3	Prioritize initiatives for high degrees of risk measurement	Establish a basis for prioritization of preventive measures
4	How the accidents occurred, to establish both direct and underlying causes	Selection, elaboration, and implementation of concrete corrective action and preventive initiatives
5	Control analyses	Special injury risk or the discovery of a hitherto unrecognized risk

know-how must be transferred to the affected population—namely, the individual persons must have the knowledge, the skills, the opportunity, and the will to act to ensure safety (Table 6) in case of occurrence of a geotechnical risk event.

There are five primary types of analyses of accidents, (Table 7) each having a distinct purpose that includes identifying, monitoring, prioritizing, establishing the cause, and controlling the geotechnical risk.

The research on pre facto geotechnical hazards should be strengthened; especially the research on identification and control of direct hazard, the first triggering hazard, and initial hazard. Full understanding of all types of a geotechnical hazards resulting in accidents is necessary to establish a complete hazard theory in order to enhance the level of safety management and control accidents.

2.4 Historical Geotechnical Investigations

The geotechnical investigations needed for the older structures are called historical geotechnical investigations. These are often carried out before the reconstruction and restoration of old structures (buildings in the old town, bridges, monuments, etc.). Some of the techniques mentioned in pre facto and post facto geotechnical research

Table 8 Geotechnical testing methods for historical investigation

No.	Testing methods
1	Borehole drilling near and under the foundation with disturbed soil sampling for laboratory tests
2	Hole digging for the assessment of foundation quality
3	CPT, SPT, DMT
4	Groundwater and pore water pressure measurement
5	Settlement and Tilt of structure
6	GPR and seismic wave test
7	Soil Classification testing in Laboratory
8	Soil basic properties and Atterberg limits in Laboratory
9	Shear Testing—static and cyclic in Laboratory
10	Computerized modeling

Table 9 Information needed for report of geotechnical historical investigation

No.	Information provided
1	The physical and mechanical properties of soils and rocks determined by laboratory and in situ methods
2	The topography of the area
3	Natural soil and rock lithological structure
4	The structure and quality of the foundation
5	The thickness of the fill
6	Groundwater level depth and Groundwater aggressiveness on concrete
7	Exogenous processes which are taking place in the area
8	Materials and possible construction techniques if identifiable

can be used in historical research. The use field and laboratory methods (Table 8) is commonly adopted as the first stage of such investigations.

After fieldwork, data analysis, and interpretation, the geotechnical report is provided, which contains all information (Table 9) needed for the proper execution of reconstruction and restoration processes.

3 Historical Geotechnical Research

Doing historical geotechnical research isn't as simple as solving an engineering problem. It requires just the right approach, to avoid finding a wrong answer. Any connection and clue must be examined with an open mind. It's a good idea to have a general idea of the time period or location being researched. This helps to inform

the researcher when interesting facts are found and to identify them along the way to help guide the research.

It would be useful to understand some of the basic technical concepts of the other similar structures and substructures of that period including; tools, equipment, material availability, etc. Historical geotechnical research method comprises the techniques and guidelines by which engineers use primary and secondary sources, site investigation, and other evidence, including the evidence of archaeology, to research and then to write about the construction techniques, design philosophy, and materials utilized of the past.

3.1 *Need for Historical Geotechnical Research*

Physical conservation of our monuments is a critical task. We can't just make physical and computerized models of them and then destroy the real item. So much of our culture is associated with the physical reality that we created, that it would be a gigantic mistake, to assume it would be enough to preserve these structures as 3D renderings alone. Much of the technical benefits that could have been derived from historic structures and substructures have not yet fully accrued to us (Table 10). There is therefore a great need and much scope for the full geotechnical study of these structures.

As such these have been minimized in the treatments of modern geotechnical study. There exists a great need for further research of historic and prehistoric geotechnical substructures and superstructures and their building techniques and variability. As they have lasted for a long time (in some cases thousands of years), they are truly sustainable. We must overview these important but oft-ignored historic and prehistoric architectural remains by an engineering interpretation that addresses the need for sustainability. We can learn from their flaws and perfections the necessary techniques for a more lasting future.

Table 10 Technical benefits obtained from historic structures

Structures ^a	a	b	c	d	e	f	g	h	i	j	k	l
Construction technology	Y	N	Y	Y	N	N	Y	Y	N	Y	N	Y
Material technology	Y	Y	Y	Y	Y	N	Y	N	Y	Y	N	Y
Design technology	N	N	N	Y	N	N	Y	N	N	N	N	Y
Technology transfer	N	N	N	Y	N	N	N	N	N	N	N	N
Technology assimilation	N	Y	N	Y	N	N	N	N	N	N	N	N

^a(forts), b (religious), c (ports), d (residential), e (embankments, dams, bunds), f (slope stabilizations and land reclamation), g (foundations), h (tunnels), j (tombs), k (storage) and l (underground habitations)

Y = Yes, N = No

3.2 Sources for Historical Geotechnical Research

Any relict of the past is a valuable source for Historical Geotechnical Research. It could be a document, but it might also be a building, an artwork, a broken tool, a defective container, or even perhaps a pair of shoes. All these are potential sources of information which provide us different clues with information which can add to the sum of our understanding of the past. Such sources only turn out to be historical evidence, when they are correctly interpreted by the geotechnical historian from a forensic geotechnical point of view.

3.3 Primary Sources

Primary sources are preferred sources of geotechnical investigations as they provide direct evidence about a geotechnical structure (Table 11). These sources include tests, written works, and objects.

Primary geotechnical research sources are often empirical studies—research where an experiment was performed or a test was made. The results of such studies are typically found in scholarly articles or papers delivered at conferences. The following types of materials are other examples of primary sources, especially for historic structures: Diaries, journals, speeches, interviews, letters, memos, manuscripts, and other papers that describe historical events that an individual observed or participated in. For prehistoric structures however primary sources are limited to religious texts, legends and myths, and actual site tests and observations.

Table 11 Primary sources of geotechnical historical investigation

No.	Sources
1	Historical and legal documents
2	Eyewitness accounts
3	Results of site investigations, tests and experiments
4	Statistical data
5	Pieces of creative writing, engineering/religious texts
6	Audio and video recordings
7	Speeches, Proclamations, Orders,
8	Interviews, Surveys, Fieldwork
9	Building/Structures/Art Objects

3.4 Secondary Sources

Secondary sources describe, discuss, interpret, comment upon, analyze, evaluate, summarize, and process primary sources. Secondary source materials can be articles in newspapers or popular magazines, book or movie reviews, or articles found in scholarly journals that discuss or evaluate someone else's original research. These are used when primary sources are not sufficiently available. Often secondary and parallel studies have to be carried out to validate secondary sources.

4 Historical Geotechnical Structures

Karl Terzaghi is credited with inventing Soil Mechanics but he is not the first Geotechnical engineer. While addressing the Academy of Science in Paris in 1773, Coulomb who served as the "Engineer of the King of France," presented a modest "*essay on the application of the rules of maxima and minima to certain statics problems relevant to architecture*." This work, which is the earliest published soil mechanics theory, was printed three years later by the academy. It stated the active and passive pressure concepts. He assisted in the design and construction of many important geotechnical structures (Herle 2004). Evidence shows that, under certain cultural and environmental conditions, ancient societies acquired an awareness of sophisticated geotechnical engineering techniques involving the risks linked to the earth phenomena (Carpani 2014). The constantly evolving mud—brick architecture of ancient Mesopotamia demonstrated the development of new building materials, adoption of new building techniques, and designs of buildings modified to suit the changing requirements of the inhabitants (Roaf 1982).

Our ancestors in the olden days used soil for an extensive variety of activities from building and creation of construction materials to irrigation and flood control. There are many ancient structures that deserve a systematic geotechnical study in India and abroad. For instance, the ancient people notably built pad footings, strip-and-raft foundations as well as seismic-resistant foundations during this time. In India, in ancient times Saraswat (commonly called Harappan or Indus Valley Civilization as this was the first place of discovery) Engineers had already incorporated many important geotechnical techniques in embankment building in the lost cities of Harappa and Mohenjo-daro and are still observed in the Bunds seen in Goa. However, the science of soil design was still a non-existing phenomenon, and the rule of thumb was predominant. Below are classed together some of the historical edifices that still need thorough and meticulous geotechnical oriented research. Table 12 below indicates the historic development of Geotechnology.

Historic Geotechnical Edifices can be mainly categorized into superstructures and substructures (Fig. 1).

Table 12 Historic contributions to soil mechanics

Year	Scientist	Contributions
–5000	Saraswat (Harappan)	Embankments, ports, foundations, sewer tunnels, soil stabilization, geo-synthetics
–3000	Egypt, Greece, Mesopotamia	Pyramids, foundations, dams, forts, soil stabilization, geo-synthetics
–100	Vitruvius	Roman Geo-techniques
1103	Sung Code	Improvement of clayey soils
1773	Charles Augustin Coulomb	Active and passive earth pressure concepts
1807	Thomas Young	Elastic constant
1828	A.L. Cauchy	Equations of isotropic linear elasticity
1846	Alexandre Collin	Analysis of landslides in clay
1856	H.P.G. Darcy	Filtration of water through sand
1857	W.J.M. Rankine	Critical states of stress in a mass of soil, planes of rupture
1882	Otto Mohr	stress diagrams
1883	G.H. Darwin	Density-dependent friction angle
1885	Osborne Reynolds	Dilatancy
1885	J. Boussinesq	Stress and deformation of elastic half-space
1911	A. M. Atterberg	Water content associated with changes in state from solid to plastic to liquid
1916	K.E. Petterson	Method of slices
1925	Karl von Terzaghi	Effective stress, consolidation theory
1936	Arthur Casagrande	Plasticity chart, critical void ratio
1936	M.J. Hvorslev	Shear strength of clay as a function of effective normal stress and void ratio
1958	Roscoe et al.	Critical state soil mechanics

Indicates BC

4.1 Historical Geotechnical Superstructures

These are structures basically built using mud and rock as primary constituents. They served various purposes and were built using technologies prevalent at that time. Many are in a state of disrepair due to ignorance of the geotechnical processes that led to their existence and continuance. Some are functional even today they serve various engineering functions sustainably, that need study and replication within the limits of contemporary geotechnical proficiency. There were no specified building trades initially, structures, and construction equipment and trades evolved with the needs of community. Technology was the method, Repetitive technological solutions for similar problems were used. The material used was stone, wood, and earth. Structures were mainly sacral defensive and family (Vidovszky 2009).

Forts. Not many people know the fact that Coulomb's earth pressure theories were developed to determine how much mud should be placed against a fort wall to resist bombardment. But the study of damping capacity/ability of mud against cannon fire (dynamic loads) is pending. There are many mud forts in existence in the world today. Excavations in China have uncovered rammed earth constructions dating from the seventh century BC as parts of The Great Wall of China (2014; Minke 2006), the citadel of Bam in Iran, parts of which are ca. 2500 years old, a fortified city in the Draa valley in Morocco, which is around 250 years old (Minke 2006). The walls of forts of Mesopotamia provided defense against attack and in Southern Mesopotamia protection from flooding (Roaf 1982). The Gulf states are famous for their mud forts, especially Oman, The sixteenth-century Portuguese Forts guarding the harbor of Muscat, The lookout towers which policed the wadi routes, etc., Walls (1977). Most of the Indian forts were stone-faced but had mud backfill. They also had ingenious water structures designed for harvesting and storage, including step-wells, elaborate reservoirs and channels (KTPI), and intricate hidden escape tunnels. The remains of this ancient mud forts and similar structures, surrounded by a moat, now in ruins are found in many parts of north and central India, especially in Chhattisgarh. We must study the static and dynamic stability of these structures for applicability in conservation efforts.

Religious. Earth was used as the building material in all ancient cultures, not only for homes but for religious buildings as well like Temple of Ramses II at Gourn, Egypt, 3200 years ago (Minke 2006). Chinese used open halls with equal span bays and bracketed column beam connections for their temples constructed of mud mounds. They adopted seismic-resistant foundations of columns in hollow stone bases resting on rounded rubble. The eastern part of India comprising of Magadha and Bengal yielded many Buddhist Stupas made from mud and mud bricks with intricately carved stone facing. Large pseudo-fortified mosques are located in Oman (Walls 1977) and many Gulf Countries. modern engineering expertise. As religious structures are meant to last forever, their study can help us incorporate various techniques to make modern structures more sustainable.

Ports. Ancient ports all over the world were constructed of stabilized soil and bricks or stones. There are many ancient Dockyards at Lothal, Dholavira, and other Harappan cities which are remarkable lined structures, with evidence of channels for inlet and outlet of water and mud brick platforms and earthen brick-lined embankment (Pandey 2016). At Sungai Batu in Malasia on the Strait of Malaca, ancient fifth-century upriver brick-lined ports have been discovered used for iron-based trade (Zakaria et al. 2010). Study of such geotechnical structures can help develop infrastructure in remote riverside regions.

Residential. From the earliest times, men built dwellings that were closest at hand: out of fibers, leaves, stone, or unbaked-sundried mud (Sruthi 2013). The use of mud for home construction has recurred independently throughout the diverse climates and regions of the Earth in response to the need for a strong, comfortable, easy to build, affordable shelter (Moquin 1994). In Russian Turkestan houses dating from

8000 to 6000 BC have been discovered (Minke 2006). Earth and reinforced earth has been used traditionally by ancient civilizations for residential and even monumental purposes. Demonstrably different rammed earth construction techniques evolved from China, Indian, Nepal, and Bhutan. Tapering walls in rammed earth buildings are not generally found in Europe and North African but appear to have developed in Eastern Asia (Jaquin 2012). Large pseudo-fortified mansions, gigantic round towers surrounded by settlements, and fortified palaces of the interior's oases exist in Oman (Walls 1977). Shibam, with its 500 multi-story houses is a city in the People's Democratic Republic of Yemen which is made up of towers, seven or eight story high and clustered together, most of which are several centuries old. These towers, built of mud, allow the families to live beneath the same roof, while permitting intimacy of domestic life to be respected (Lewcock 1986). There are many benefits to mud houses that are “green” in nature which we must incorporate in our houses to increase their sustainability.

Pyramids. There are many ancient pyramids built everywhere. Why so many ancient civilizations, many of which had no contact with each other, were constructing pyramids at around the same time remains a bit of a mystery (Holloway 2018) pyramids not only exist in Egypt but also exist in—the Ziggurats of Mesopotamia an Ur, The Pyramid of Cestius-Rome, Gumar-Tenerife—Canary Islands, Cholula-Mexico (the largest pyramid in the world), White Pyramid—Xian-China, Caral-Peru, etc., in fact, the pyramids of Egypt may have actually originated from the little known mud pyramids of Sudan. The core of the Sun Pyramid in Teotihuacan, Mexico, built between the 300 and 900 AD, consists of approximately 2 million tons of rammed earth (Minke 2006). In Egypt pyramids, rock facings had toe restraints and better slope stability (Fig. 2) and straw mats between bricks were used in Mesopotamia as geomembranes (Herle 2004). Pyramids have many geotechnical lessons we can use in sustainable buildings today.

Embankments. Saraswat civilization made extensive use of embankments for transportation, river training, and defensive purposes. Massive mud brick walls enclosed each of the cities with access limited to narrow gates that were only wide enough for

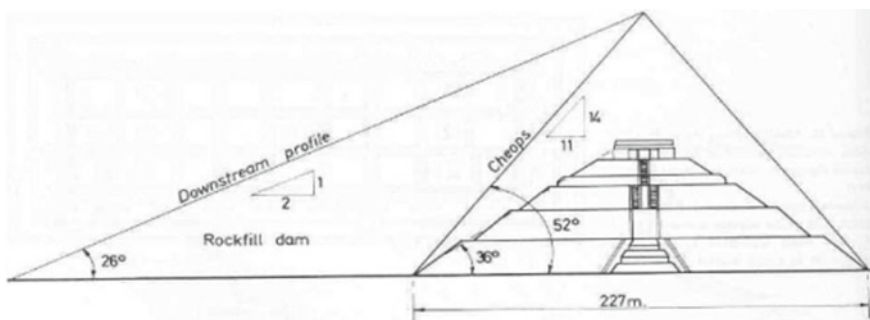


Fig. 2 Comparison of slopes of rockfill dam, Egyptian and Mexican pyramids (Herle 2004)

a single ox cart to enter or leave (Vahia 2011). These mud structures found all over the world can give valuable knowledge in Geo-engineering.

Dams and Reservoirs. There were community water tank (baths), water tunnels, several rock-cut reservoirs, and check dams in Ancient Saraswat Cities, waterproofed by addition gypsum in mud mortar, with a backing of bitumen course for further damp proofing (Pandey 2016). Karafa dam Egypt was a geotechnical structure (Herle 2004). There are still in existence many functional historic dams around the world that can help us develop better and more space-efficient and, economic earthen water storage structures.

Bunds. There are many ancient small bunds built by the Saraswat civilization people to store rainwater for irrigation and drinking in the ancient Saraswati/Indus river Basin (Pandey 2016). These exist in Goa even today (Souza et al. 2016). They used advanced geotechnical methods of soil compaction, stabilization, root reinforcement, etc. These methods are cheap, environment-friendly, and use locally available materials very efficiently. They definitely deserved to be studied.

Slope Stabilization and Land Reclamation Methods. Sung's code of China talks about clayey soil stabilization (Herle 2004). There ancient Saraswat civilization people who settled in Goa used many methods to reclaim and stabilize slopes and land. The most common method was of using bunds and embankments for multiple purposes (Souza et al. 2016). This technique of one solution fits many used by ancient engineers deserves a geotechnical study.

4.2 *Historical Geotechnical Sub-Structures*

These historic architectural remains are hidden from view and seldom get the attention that their overground 'brothers' do. By using a geotechnical engineering interpretation that addresses the need for actions, we must study and preserve these substructures and use what technology we can assimilate from them within the bounds of modern engineering expertise.

Foundations. Rammed earth foundations dating from ca. 5000 BC have been discovered in Assyria (Minke 2006). The Saraswat civilization's essence was a settlement pattern in which cities and towns were particularly prominent. That such urban centers contained monumental structures (Satpathy no date) whose construction required advanced foundation techniques and soil stabilization. South American civilization used basket footings for earthquake resistance. Chinese, Japanese, and Korean temples used hollow stone and column footings. Egyptians used self-sinking caissons (Fig. 3). Greek used iron clamps and "tee" beam-shaped foundation, and wooden reinforced rubble foundation for earthquake protection in Anatolia. Vitruvius an architect and engineer under Julius Caesar wrote a ten-volume account of known technology about city planning, building materials, and acoustics. He also gives the technology of cofferdams, dewatering foundations, piling and compaction,

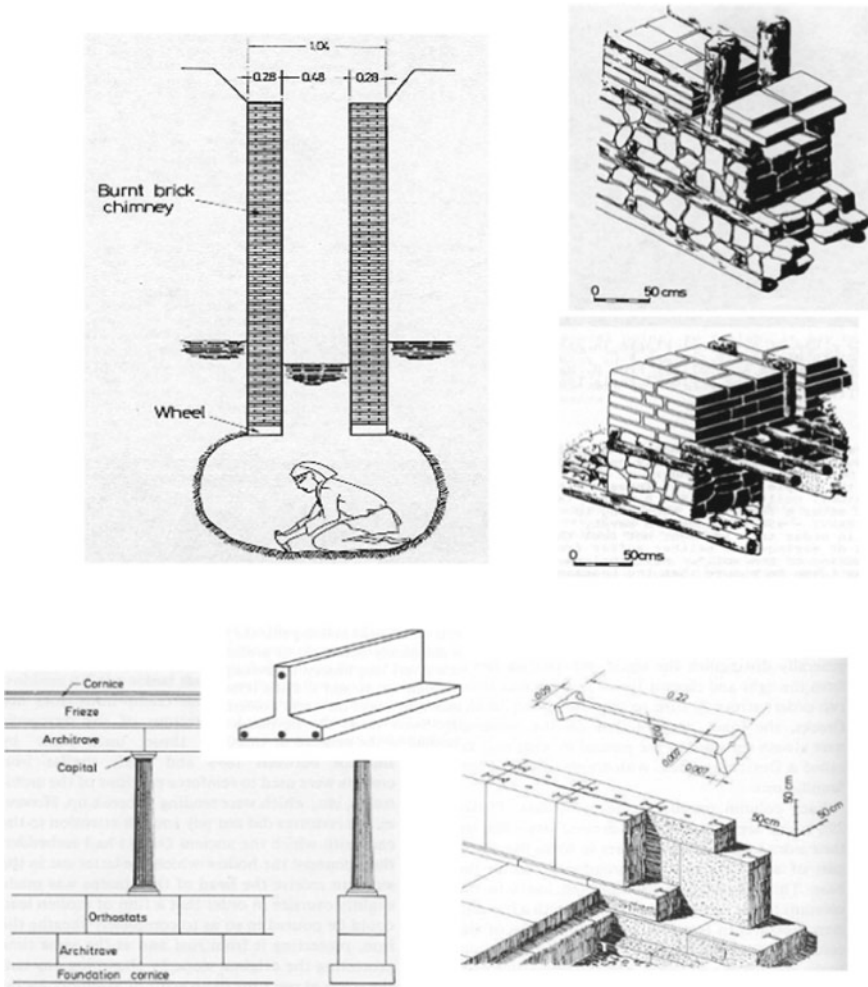


Fig. 3 Foundations (Herle 2004; Carpani 2014)

and teeth-shaped walls for foundations. Concrete raft foundations were used under the Coliseum (Herle 2004).

Seismic base isolation was done in the temples of Greece by using a layer of charcoal under foundation. By the early fourth century BC, Greeks developed a new method for building foundations that consists of alternate layers of soaked and tamped loess and tamped ash and charcoal (Carpani 2014).

Timber Piles were driven under bridges and ancient monuments in Europe (Fig. 4). They were also used as fender piles and for shore protection works. In Goa, there exists the longest ancient causeway in the world built using similar technology at Ribandar-Panjim (Fig. 5).

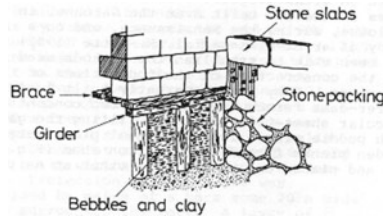


Fig. 4 Pile driving under bridges (Herle 2004)



Fig. 5 Ribandar causeway in 1950 and 2001, Goa

Many techniques used by ancients in foundations are being reinvented today. It is therefore better that we study these techniques thoroughly and reuse them.

Tunnels. In ancient cities, like our modern ones, there is a need for water piping, drainage, and sanitary sewers. These ancient urban infrastructure systems existed for 6000 years (Diamond and Kassel 2018). Qanats are 5000-year-old artificial underground water channels beneath the surface of the earth up to 305 m deep, which bring a continual stream of water to the earth's surface for human agricultural and domestic use. The water emerging from Qanats is not lifted to the surface but flows down the channel away from the point of seepage. They were variously used for water supply, house cooling, and watermills (Jeloudar et al. 2018). A network of corbelled tunnels lay out in ancient Indus/Saraswat cities crisscrossing the citadel area to collect rainwater and sewage (Pandey 2016). One of the greatest marvels of ancient engineering achievements is a 1036-meter-long water tunnel, excavated through a mountain in the sixth century BC on the Greek island of Samos. Two separate teams advancing in a straight line from both ends accurately dug through solid limestone using only picks, hammers, and chisels. Around 700 BC, another famous ancient tunnel, the Tunnel of Hezekiah (also known as the Siloam tunnel), was excavated below Jerusalem. While digging the tunnel, the Greeks used no magnetic compass, no surveying instruments, no topographic maps; they didn't even have the benefit of written mathematics (Apostol 2004). In Afghanistan, the population within Kandahar Province living far from rivers relies upon groundwater delivered from karez (sub-horizontal 1–2 km tunnels) which supply unconfined groundwater recharged largely by snowmelt from the Hindukush mountains (Macpherson et al.

1689). Today's tunneling technology can learn valuable cost-effective lessons from these ancient tunnels.

Tombs. There are many ancient ones. The Mesopotamians made provisions for the afterlife. In general, underground structures were constructed for burial and for burial gifts. These structures were sometimes intramural beneath the floors of houses or palaces (Roaf 1982). Similar burials have also been found in ancient Egypt and Saraswat Cultures.

Storage Facilities. There are many ancient ones. In Egypt, the grain stores of Ramasseum built-in adobe in 1300 BC still exist (Sruthi 2013). Today storage is being moved underground for many dangerous and toxic substances. These ancient structures, their plus and minus points must be studied to better redesign the new underground storage facilities.

Habitations. Many mythical underground living spaces are discovered today. The catacombs of Rome are a famous example of Historic Geotechnical underground residences. These were used by the persecuted populations to live underground and escape death. Today, overhead space gets crowded underground offers vast unexplored space availability free of many legal encumbrances of overhead space. We need to study and develop these geotechnical techniques for living spaces.

5 Historic Geotechnical Studies

There is an urgent and pressing need to study Historic Geotechnical Structures as an important sub-branch of Forensic Geotechnical Engineering Studies. A forensic review of different ancient geotechnical structures helps us gather the essential information needed for such research and studies. Great progress toward a more environmentally conscious, sustainable construction can be achieved, if those who are actively building with adobe, rammed earth, and compressed earth block are included in the discussion and planning of codes and education (Moquin 1994).

The research activities must focus on the understanding and prediction of historic geotechnical structure and sub-structure behavior. The research groups must move from extensive experimental campaigns involving several sites and laboratory tests carried out on models and sites to its applicability in conservation efforts. Within such context, the cause and effects (including post and pre facto studies) of various loading conditions should be currently under investigation. Efforts must be made in order to extend the approaches already developed in Geotechnical Engineering to historic structures.

Computerized models must be developed and studied and these models have must be modified to accommodate other important phenomena such as the soil creep, in order to explore the time-dependent stability of historic structures. A vacuum has been created from one end of Oman to the other by the exodus of the indigenous workers, who in the past maintained the buildings and Falaj systems, and tended the

oases (Walls 1977). A similar lack of trained people exists in Goa as the technology was not passed down and assimilated. This necessitates the proper geotechnical study of such ancient structures.

5.1 Need to Incorporate Historic Geotechnical Structures Studies in University Curriculum

There is, unfortunately, a lack of both awareness and university curricula for pursuing geotechnical conservation studies. The 1997 Master Plan for Moenjodaro states that recent storms and heavy rainfall prove that previous archaeological intervention of storm water drainage on the remaining structures is ineffective, and has in fact accelerated the structural damage (Fodde and Khan 2010). This is because of a lack of proper knowledge and stress on Historical Geotechnical Engineering. Hence, it can be seen that as a separate branch of higher studies Historical Geotechnical Engineering, can play a key role in the development of successful conservation designs by analyzing the foundation behavior and the soil–structure–foundation interaction. Pollution, human activities, and lack of knowledge of traditional techniques and methods have caused great damage to historic structures and sub-structures. While greater attention is placed on what is above the ground there is a lack of sufficient interest in the sub-structural components. We need to incorporate the study of Historic Geotechnical Structures as an important full-fledged sub-branch of Forensic Geotechnical Engineering Studies in University curriculum without a delay for the proper maintenance and management, of our fast disappearing historical heritage.

5.2 Possible Curricular Structure for Historic Geotechnical Structures Studies

There is great scope for conservation studies. A proper syllabus must be developed in consultation with industry and conservation experts.

In the first year, courses could be mainly oriented to attend to basic issues: History of local and international Architecture, the significance of Heritage Conservation from Geotechnical Perspective, Conservation Theory of Historic Buildings, Conservation Services, Diagnostic and Survey techniques for Historic Structures and Sub-structures, Materials and Technologies used in Historic Structures and Sub-structures, Mechanics of Historic Structures and Sub-structures materials, Advanced Geotechnical Mechanics and computerized modeling, production of Historical building components.

The second year can consist of compulsory and elective courses on specialized topics, such as Sub-Structural Diagnostics, Seismic Assessment, Rehabilitation and

Retrofitting, Geotechnical Engineering for the Preservation of Historic Structures and Sub-structures, Geotechnical facility management.

There can be a Design Project in applying the acquired knowledge to a case-study suitably split across both years.

6 Conclusions

The preservation of monuments and Historic Sites has gained an increasing involvement by geotechnical engineers. The recent interest seen in the preservation of historic sites mandates a need for a separate discipline in the study of Historical Geotechnical Engineering. This area is still in nascent stages, even though the requisite technology exists. There are many vital areas for conservation efforts, both in India and abroad. There is, unfortunately, a scarcity of both interest and curricular content for such studies. We need to incorporate the study of Historic Geotechnical Structures as an important full-fledged sub-branch of Forensic Geotechnical Engineering Studies in University curriculum for the maintenance, management, continuation, and perpetuation of our historical heritage.

References

- Apostol TM (2004) The tunnel of samos. *Eng Sci* 1
- Carpani B (2014) A survey of ancient geotechnical engineering techniques in sub-foundation preparation. In: 9th international conference on structural analysis of historical constructions Mexico City, SAHC2014, Mexico, 14–17 October 2014
- Dabaieh M (2014) Building with rammed earth—a practical experience with Martin Rauch. Lund University
- Diamond RS, Kassel BG (2018) A history of the urban underground tunnel. *J Transp Technol* 8:11–43
- Fodde E, Khan MS (2010) Affordable monsoon rain mitigation measures in the world heritage site of Moenjodaro, Pakistan. BRE Centre for Innovative Construction Materials, Department of Architecture and Civil Engineering, University of Bath, Bath BA2 7AY, UK
- Herle I (2004) History of geotechnical engineering. Institute of Geotechnical Engineering, TU Dresden
- Holloway A (2018) 5 Pyramids of the ancient world that you may not have heard about. www.ancient-origins.net/ancient-places
- Jaquin P (2012) Influence of Arabic and Chinese rammed earth techniques in the Himalayan. *Reg Sustain* 4:2650–2660
- Jeloudar MT, Han M, Davoudi M, Kim M (2018) Review of ancient wisdom of Qanat, and suggestions for future water management. *Environ Eng Res* 18(2):57–63
- Lewcock R (1986) Wadi Hadaramawt and the walled city of Shibam. United Nations Educational, Scientific and Cultural Organization 75700 Paris, France
- Macpherson GL, Johnson WC, Liu H (2017) Viability of karezes (ancient water supply systems in Afghanistan) in a changing world. *Appl Water Sci* 7(4):1689–1710
- Maria N (2007) Geotechnical problems on historic buildings consolidation. XVIII EYGEC—Portonovo, Ancona, Italy

- Minke G (2006) *Building with Earth* Birkhäuser. Publishers for Architecture, Kassel
- Moquin M (1994) *Ancient solutions for future sustainability: building with adobe, rammed earth, and mud*. CIB TG 16, Sustainable Construction, Tampa, Florida, USA
- Pandey A (2016) Society and Environment in Ancient India (Study of Hydrology). *Int J Human Soc Sci Invent* 5(2):26–31
- Roaf M (1982) Palaces and temples in ancient Mesopotamia. Book Chapter, 423–441
- Satpathy BB, Politico-social and administrative history of ancient India. DDCE/History (M.A)/SLM/Paper-10
- Shankar B, Uma S (2012) Conservation strategies for Srirangapatna town: evaluation of heritage buildings. *Int J Modern Eng Res (IJMER)* 2(2):160–164
- Souza L, Naik A, Chanekar TP, Savoikar P (2016) Stability of traditional ‘Bundhs’—Earthen Levees—from Goa. In: Indian geotechnical conference IGC-2016
- Sruthi GS (2013) Mud architecture. In: International conference on energy and environment 2013 (ICEE 2013)
- Tringham R (1991) Men and women in prehistoric architecture. TDSR, III
- Vahia MN, Yadav N (2011) Reconstructing the history of Harappan civilization social evolution & history 10(2)
- Vidovszky I (2009) Brief construction history—BUTE Department of Construction Management and Technology
- Walls AG, Preservation of monuments and sites Sultanate Of Oman. Technical Report PPI 1977–78/4.121.8 UNDP/OMA/77/002, (1077)
- Zakaria II, Saidin M, Abdullah J (2010) Ancient Jetty at Sungai Batu Complex, Bujang Valley. Kedah. Centre for Global Archaeological Research

Machine-Induced Vibration Isolation Using Geocell Reinforcement



K. N. Ujjawal and A. Hegde

Abstract The present study aims to investigate the vibration isolation efficacy of the geocell reinforcement through the numerical simulation technique. The explicit finite difference package, FLAC^{3D} was chosen for the dynamic simulations. Initially, the developed numerical models were validated with the results of the vertical mode block resonance test. The behaviour of soil bed and concrete footing was simulated using Mohr–Coulomb and linear elastic models, respectively. The geocell was modelled using two techniques, namely Equivalent Composite Approach (ECA) and Honeycomb-Shaped Approach (HSA). The results revealed that the use of the geocells reduce the resonant displacement amplitude by 56% and increase the natural frequency of the soil–foundation system by 42% as compared to the unreinforced bed. As compared to the experimental results, the ECA modelling technique was found to overestimate the improvement in resonant frequency and the reduction in displacement amplitude by 4% and 10%, respectively, in the presence of geocells.

1 Introduction

The dawn of the twenty-first century has witnessed a tremendous growth rate of population and urbanization. This has resulted in an increase in construction and industrial dynamic sources. These dynamic sources can produce ground-borne vibrations. The emanated vibrations can lead to high dynamic settlements and can be hazardous for the adjacent structures and their inhabitants. Moreover, these vibrations can pose a hurdle to the satisfactory operation of the machine and the nearby sensitive equipment. These adverse effects can be reduced by improving the dynamic properties of the foundation–soil system. The dynamics of the system depends on two key parameters, namely the natural frequency of the system and vibration amplitude at its operating frequency.

K. N. Ujjawal (✉) · A. Hegde

Department of Civil and Environmental Engineering, Indian Institute of Technology Patna, Patna 801106, India

e-mail: nishant.2050.ujjawal@gmail.com

© Springer Nature Singapore Pte Ltd. 2020

M. Latha Gali and P. Raghuvver Rao (eds.), *Construction in Geotechnical Engineering*, Lecture Notes in Civil Engineering 84, https://doi.org/10.1007/978-981-15-6090-3_56

755

The inadequacy of high-quality in situ land has forced mankind to spread to the relatively inferior soil. In such a case, it is very much possible that the in situ soil is unable to control vibrations and provide sufficient natural frequency and stiffness. In addition, the development of higher rating machines with a better tolerance results in significantly higher dynamic loads (Bhatia 2008). All these situations demand enhanced performance and stability of the foundation system. This can be ensured by limiting the excessive resonant amplitude and providing adequate dynamic bearing capacity.

The most common existing remedial technique is the placement of isolation material (rubber pads, spring coils, cork sheets and felt) between the machine and the supporting foundation (Gazetas 1983). The pioneering work of Woods (1968) has drawn the attention of many researchers to investigate the efficiency of wave barriers as a vibration screening technique. A huge wealth of references can be found in the literature regarding the investigation of open (Ahmad et al. 1996; Alzawi and El Naggar 2011; Ju 2004; to name a few) and in-filled (Kumar et al. 2014; Coulier et al. 2015; Thompson et al. 2016; to name a few) trenches. The in-filled trenches are filled with water, concrete, sheet piles, soil bags, geofoam material, etc. Further, based on their locations, they are classified as active and passive mode wave barriers. A huge amount of earth material needs to be excavated and transported to adopt this technique. Moreover, these methods help only in controlling the vibration levels and do not lead to any improvement in the dynamic bearing capacity. This situation has raised a need for an alternative technique which can satisfy both the criteria, i.e., limiting vibrations as well as improving dynamic bearing capacity.

The geocells have emerged as a popular ground improvement technique since last few decades. Several researchers have highlighted the advantageous utilization of geocells in various geotechnical applications such as foundations (Dash et al. 2003; Sitharam and Sireesh 2005; Tafreshi and Dawson 2010), pavements (Yang et al. 2012; Thakur et al. 2012; Tanyu et al. 2013), embankments (Krishnaswamy et al. 2000; Sitharam and Hegde 2013), slope stability (Mehdipour et al. 2013; and Boyle and Robertson 2007) and railroads (Leshchinsky and Ling 2013; Indraratna et al. 2014; Satyal et al. 2018). But unfortunately, only a handful of researchers (Azzam 2015; Venkateswarlu and Hegde 2017) have investigated the possible utilization of geocells under machine foundation. Both the studies were carried out in a two-dimensional framework using a finite element package, PLAXIS 2D. Based on the existing literature, it is evident that there is a lack of field studies as well as comprehensive numerical investigation to understand the efficiency of geocells under machine foundations. Hence, an attempt has been made in the present study to explore the possible benefits of geocell in isolating the machine-induced vibrations. The numerical simulations were carried out using a three-dimensional explicit finite difference package FLAC^{3D}. Further, a comparison has been established between the two different geocell modelling techniques, namely Equivalent Composite Approach (ECA) and Honeycomb-Shaped Approach (HSA) in predicting the dynamic response of the geocell reinforced foundation bed.

2 Numerical Modelling

In the present study, the dynamic simulations were carried out using a three-dimensional finite-difference commercial package, FLAC^{3D}. It was chosen considering its capability of modelling a wide range of geotechnical materials and complex structures. The explicit finite difference formulation is used to solve initial and boundary value problems. It consists of several built-in mechanical constitutive models and structural elements (SEs) for modelling the wide variety of soil behaviour, geomaterials and reinforcements. Further, FLAC^{3D} contains a powerful built-in programming language called FISH (FLACish) for analysing and defining the new variables and functions.

A square footing, having width 0.6 m and depth 0.5 m, was considered as the machine foundation. It was assumed to be cast with M20 grade concrete. The available Standard Penetration Test (SPT) data were utilized to obtain the soil profile for the numerical investigation. The data revealed the existence of three different soil layers, namely silty clay, loose sand and dense sand up to a depth of 10 m. The raw SPT-*N* values reported in the bore log data sheet were corrected to their 60% energy efficiency as suggested by Skempton (1986). The Young's modulus (*E*) for various soil layers was determined using the corrected SPT-*N* values as per the recommendations of Bowles (1996). The different major properties of the individual soil layer were determined through the appropriate laboratory tests. The Poisson's ratio (*ν*) for all the three soil layers was considered as 0.3 (Mandal et al. 2012). The various properties of all the three soil layers have been summarized in Table 1.

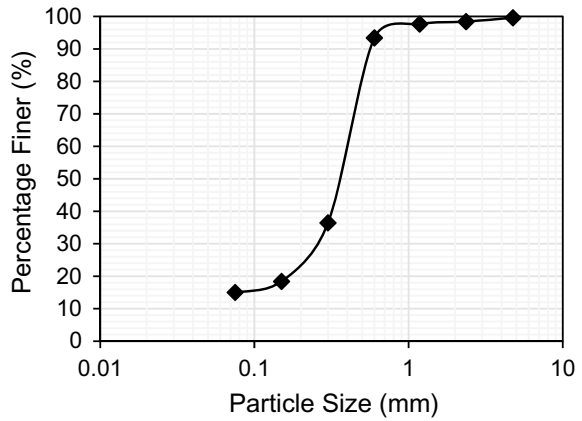
The accuracy of the numerical model also depends on the boundary distances and the mesh density. The preliminary analysis revealed that the optimum location of the boundaries was at a distance of $12B$ (where *B* is the width of the footing) from the footing face such that the dynamic response of the system was not affected. Hence, the dimension of the numerical model was selected as 15 m × 15 m × 10 m. The coarse mesh was selected in the present study as the mesh density had a minimum influence on the results. The brick element was used for the development of the three-dimensional numerical model. A foundation bed with/without geocell reinforcement was simulated centrally over the soil profile. The foundation bed having a dimension 2 m × 2 m × 0.5 m was prepared with the locally borrowed soil material. The material was classified as Silty Sand (SM) based on the Unified Soil Classification System. The Poisson's ratio of the foundation soil was borrowed from Bowles (1996). Figure 1 represents the particle size distribution curve of the foundation soil.

The concrete machine foundation was developed centrally over the prepared foundation bed. The three soil layers and the foundation soil were assigned with the Mohr–Coulomb yield criteria with non-linear failure envelope. A 5% material damping was considered for all the soil layers (Richart et al. 1970). The linear elastic material model was used to simulate the behaviour of the concrete footing. The displacement along the bottom plane of the model was restrained in all the three directions. The four vertical faces of the model were restrained only in the horizontal direction, such that the displacement was permitted in the vertical direction. In addition, the

Table 1 Various properties of the three soil layers

Material	Parameter	Values
Top Soil (Silty clay)	Density, ρ (g/cc)	1.63
	Angle of shearing resistance, φ ($^{\circ}$)	3
	Cohesion, C (kPa)	48
	Young's modulus, E (MPa)	5.1
	Poisson's ratio, ν	0.3
Middle soil (Loose sand)	Density, ρ (g/cc)	1.78
	Angle of shearing resistance, φ ($^{\circ}$)	30
	Cohesion, C (kPa)	1
	Young's modulus, E (MPa)	25.2
	Poisson's ratio, ν	0.3
Bottom soil (Dense sand)	Density, ρ (g/cc)	1.84
	Angle of shearing resistance, φ ($^{\circ}$)	36
	Cohesion, C (kPa)	1
	Young's modulus, E (MPa)	51.0
	Poisson's ratio, ν	0.3

Fig. 1 Particle size distribution of the foundation soil

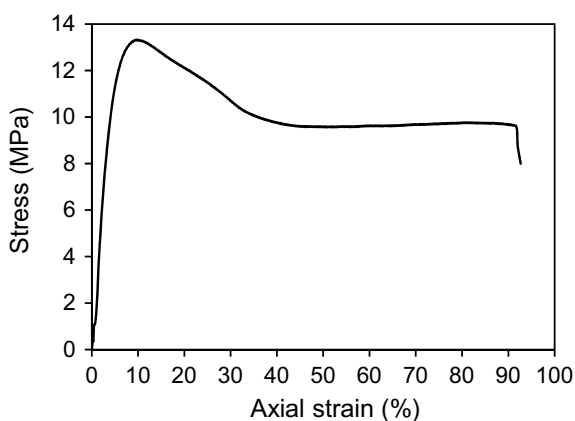


quiet (viscous) boundary conditions were specified at the vertical faces to reduce the wave reflections and energy radiation from the boundaries. Table 2 shows the various properties of the machine foundation and the foundation soil.

Table 2 Properties of concrete machine foundation and foundation soil

Material	Parameter	Values	Test method
Machine foundation	Young's modulus of concrete, E_c (MPa)	2×10^4	IS: 456–2000
	Unit weight of concrete, γ_c (kN/m ³)	24	
	Poisson's ratio of concrete, ν_c	0.15	
Foundation soil	Classification	Silty Sand (SM)	USCS
	Specific Gravity, G	2.64	IS: 2720 (Part III)—1980
	Unit weight, γ_d (kN/m ³)	17.9	IS: 2720 (Part VII)—1980
	Internal friction, ϕ (°)	32	ASTM D3080 (2011)
	Cohesion, C (kPa)	1	
	Young's modulus, E (MPa)	20	ASTM D4767 (2011)
	Poisson's ratio, ν	0.3	N/A

In the present study, the geocell manufactured from Novel Polymeric Alloy (NPA), commonly known as Neoloy was used. The equivalent diameter of the geocell pocket (d_0) was observed as 0.25 m. The height (H) of the geocell mattress was 0.12 m. Figure 2 shows the tensile stress–strain behaviour of the NPA geocell determined in accordance with ASTM D4885 (2018). The geocell reinforcement was simulated by using two modelling techniques, namely ECA and HSA. The depth of placement of the geocell mattress was kept as $0.1B$ (where B is the width of the footing) from the ground surface. The width of the geocell was considered as 2 m (i.e., $3.33B$). The foundation soil (Silty Sand) itself was used as infill material for the geocell pockets.

Fig. 2 Stress–strain behaviour of the geocell reinforcement

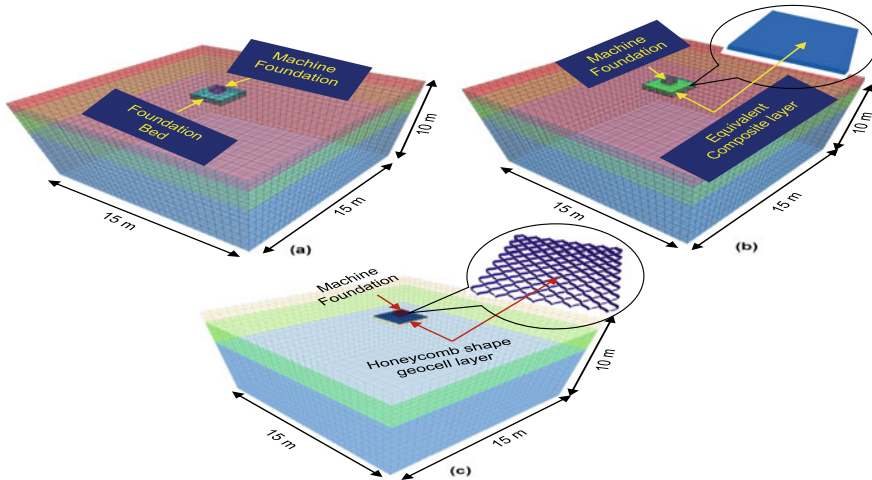


Fig. 3 Three dimensional finite difference models for different conditions: **a** unreinforced; **b** geocell reinforced-ECA; **c** geocell reinforced-HSA

The developed three-dimensional finite-difference models for different reinforced cases have been shown in Fig. 3.

The vertical harmonic excitation with a constant force amplitude was applied over the footing to simulate the vertical mode rotating mass type excitation. It can be given by,

$$F(t) = F_0 \sin(\omega t) \tag{1}$$

$$F_0 = m_e e \omega^2 \tag{2}$$

where $F(t)$ is the vertical component of the total dynamic force in N, F_0 is the total unbalanced dynamic force excited over the footing in N, m_e is the total eccentric mass weight in kg, e is the eccentricity in m, ω is the circular natural frequency in cycles (rotations) per second and t is the dynamic time in sec. The frequency of the dynamic excitation was varied from 5 Hz to 45 Hz with an increment of 5 Hz.

2.1 Equivalent Composite Approach (ECA) of Modelling Geocells

In the ECA, the geocell mattress with infill material is treated as a composite soil layer with improved strength and stiffness parameters. Figure 3b shows the developed equivalent composite layer using the HSA technique. The geocell–soil composite layer was modelled as to follow elastic–perfectly plastic Mohr–Coulomb failure

criterion. A similar approach has been adopted by past researchers (Bathurst and Knight 1998; Madhavi Latha and Rajagopal 2007; Madhavi Latha and Somwanshi 2009; Hegde and Sitharam 2015) for modelling geocell reinforcement. The studies conducted by Bathurst and Karpurapu (1993) and Rajagopal et al. (1999) suggested that the cohesion of the composite layer increases without any change in the angle of internal friction. Rajagopal et al. (1999) proposed Eqs. (3) and (4) to evaluate the increase in the cohesion of the geocell–soil composite layer. The increase in the confining pressure ($\Delta\sigma_3$) on the soil due to geocells can be given by,

$$\Delta\sigma_3 = \frac{2M\xi_c}{d} \frac{1}{1-\xi_a} = \frac{2M}{d_0} \left[\frac{1 - \sqrt{1-\xi_a}}{1-\xi_a} \right] \quad (3)$$

where M is the secant modulus of the geocell material corresponding to the axial strain ξ_a , d_0 is the equivalent diameter of the geocell pocket opening. The increase in the apparent cohesion (C_r) due to the increase in the confining pressure ($\Delta\sigma_3$) is given by,

$$C_r = \frac{\Delta\sigma_3}{2} \sqrt{K_p} \quad (4)$$

$$K_p = \frac{1 + \sin \phi}{1 - \sin \phi} \quad (5)$$

where K_p is the coefficient of passive earth pressure and depends on the internal friction angle (ϕ) of the infill material. The shear and bulk modulus of the equivalent composite layer was determined based on the studies of Latha and Somwanshi (2009) and Hegde and Sitharam (2015a).

2.2 Honeycomb-Shape Approach (HSA) of Modelling Geocells

HSA is a complicated and realistic technique of modelling geocells. In the HSA, the geocells are modelled in the three-dimensional skeleton by considering their actual honeycomb shape. Unlike ECA, the geocell and the infill material were modelled separately so that the geocell–soil composite behaviour can be simulated more accurately. The digitization technique was applied over the photograph of the expanded geocell, to obtain the coordinates of the reinforcement. The obtained coordinates were used to model the 3D honeycomb shape of geocell in FLAC^{3D}. Figure 3c shows the developed actual honeycomb shape of the geocell reinforcement using the HSA technique. A similar technique of modelling geocells was adopted by Yang et al. (2010) and Hegde and Sitharam (2015a and c). The geocell was modelled with the geogrid structural element option available in FLAC^{3D}. The behaviour of geocell and infill material was simulated using the linear elastic and Mohr–Coulomb models,

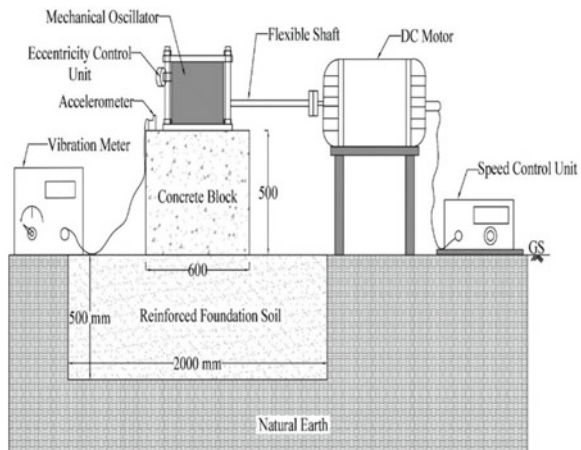
respectively. The interface shear relationship between the geocell and the infill material adopted herein was linear with the Mohr–Coulomb yield criterion. The modified direct shear test was performed in accordance with ASTM D5321 (2017) to determine the interface shear properties between the geocell and infill material. A value of 2.36 MPa/m was considered for interface shear modulus (k_i) for the geocells as suggested by Itasca (2008) and Hegde and Sitharam (2015c). The various parameters used for the two geocell modelling techniques have been summarized in Table 3.

The developed numerical model requires validation before it could be employed for further analysis. Hence, the numerical models were systematically validated with the results of block vibration field tests. The vertical mode vibration test was conducted as per the guidelines of IS: 5249-1992. Figure 4 shows the schematic diagram of a large-scale block resonance field test. The major components of the test

Table 3 Various parameters used for two geocell modelling techniques

Modelling technique	Parameter	Values
Geocell-soil composite layer (ECA)	Cohesion (kPa)	33
	Internal friction (°)	32
	Poisson’s ratio, ν	0.3
	Shear modulus, G (MPa)	25
	Bulk Modulus, K (MPa)	50
Geocell mattress (HSA)	Young’s modulus, E (MPa)	275
	Poisson’s ratio, ν	0.45
	Thickness, t_i (mm)	1.5
	Interface shear modulus, k_i (MPa/m)	2.36
	Interface cohesion, c_i (kPa)	0
	Interface friction angle, ϕ_i (°)	30

Fig. 4 Schematic representation of large-scale block resonance test set-up

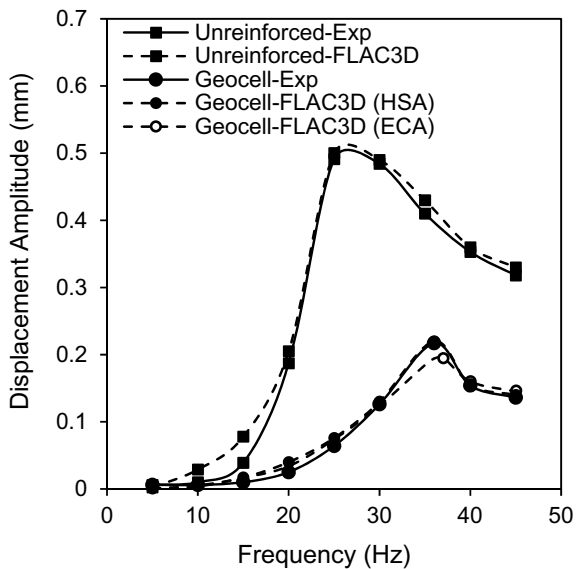


set-up consist of a mechanical oscillator, DC Motor, speed control unit and the vibrationmeter with an accelerometer. The mechanical oscillator was mounted over the top of the machine foundation using bolting assembly. It was used to induce the rotating mass type excitation over the foundation. The oscillator was connected to a DC motor through a flexible shaft. A speed control unit was used to monitor the rotating speed of the motor, which in turn controlled the dynamic force induced from the oscillator. The machine induced vibration was sensed through the accelerometer, and its magnitude was recorded using the digital vibration meter. The experimental results of geocell-reinforced conditions were compared with the two modelling approaches namely ECA and HSA.

3 Results and Discussions

The comparison of the displacement amplitude–frequency behaviour of the foundation bed obtained from the experimental and numerical studies for the different reinforced conditions has been shown in Fig. 5. The performance of the foundation bed was significantly improved with the provision of geocell reinforcement. In the presence of geocell, a 56% reduction in displacement amplitude while 42% increment in resonant frequency was observed. It can be mainly attributed to the all-round confinement provided by the geocell pockets. Overall, an encouraging agreement was found between the findings of the experimental and numerical investigation. Moreover, the adopted technique was also found to play an important role in numerical simulations. From the figure, the ECA technique was found to overestimate the

Fig. 5 Validation of the numerical model using displacement amplitude-frequency data



improvement in resonant frequency and the reduction in displacement amplitude by 4% and 10%, respectively, as compared to the experimental values. On the other hand, the HSA technique provided a realistic estimate of the dynamic response of a reinforced foundation bed.

The vibration levels originated from the machine source was quantified in terms of a parameter called Peak Particle Velocity (PPV). It can be defined as the maximum velocity at which an individual soil particle vibrates/moves when the induced wave passes through the soil medium. Table 4 summarizes the comparison of the peak particle velocity obtained from the experimental and numerical studies for the different reinforced conditions. Irrespective of the condition, it was observed that the PPV was decreased with an increase in distance from the vibration source. In the presence of geocell, the PPV was reduced by around 49% at a distance of 0.5 m from the vibration source. Moreover, the PPV data estimated from the numerical simulations were complimenting the data obtained from the experimental investigation. As compared to the experimental results, the ECA technique overestimated the reduction in PPV by about 12% at 0.5 m distance from the vibration source.

The emanated vibrations from the machine foundations lead to the development of strains in the foundation–soil system. Figure 6 shows the lateral strain increment contours for the various reinforced conditions. The maximum strain values were observed in the case of the unreinforced condition. The lack of shear strength behaviour of the unreinforced foundation bed results in the higher strain values. A significant reduction of about 59% in the lateral strain was observed in the presence of geocell. Further, the contours from the two modelling techniques were also compared. From the figure, it was found that the lateral spreading of contours was less in the ECA technique as compared to the HSA technique. The overestimation of the natural frequency of the foundation–soil system in the ECA technique is the reason for observing lesser strain values.

The various dynamic properties of the foundation bed including the dynamic elastic constants (C_u , C_τ , C_ϕ and C_ψ), elastic modulus (E), shear modulus (G) and the Damping ratio (D_f) were estimated for the unreinforced and geocell-reinforced condition. The ECA and HSA techniques were also compared based on the experimental values. Table 5 summarizes the various dynamic properties evaluated for the different conditions. The improvement in the elasticity of the foundation bed in the presence of geocells was studied in term of the dynamic elastic constants. The coefficient of elastic uniform compression (C_u) can be determined by,

$$C_u = 4\pi^2 f_{nz}^2 \frac{M}{A} \quad (6)$$

where M is the total mass of the concrete block and oscillator assembly, A is the contact area of the block with the soil and f_{nz} is the natural frequency of the foundation–soil system. The coefficient of elastic uniform compression is the ratio of external uniform pressure in a vertical direction to the elastic part of the vertical settlement. The remaining three dynamic elastic constants (C_τ , C_ϕ and C_ψ) were

Table 4 Comparison of peak particle velocity obtained from experimental and numerical studies

Distance from vibration source (m)	Peak Particle Velocity (mm/sec)					
	Unreinforced-Exp.	Unreinforced-FLAC ^{3D}	Geocell-Exp.	Geocell-FLAC ^{3D} (ECA)	Geocell-FLAC ^{3D} (HSA)	
0.5	16.8	17.79	8.6	7.56	8.17	
1	13	11.68	6.3	5.00	5.63	
1.5	9.5	8.41	4.2	3.14	3.94	
2	8.5	6.31	3.8	2.32	3.05	

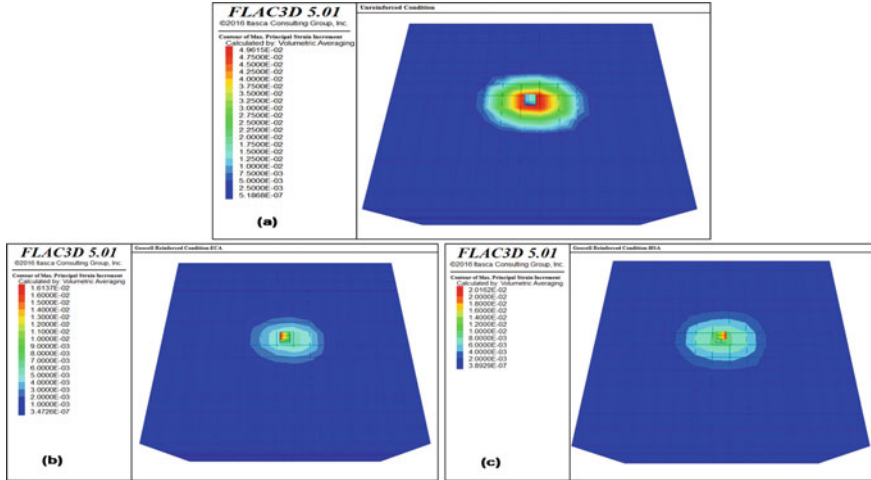


Fig. 6 Lateral strain contours: **a** Unreinforced; **b** ECA technique; **c** HSA technique

Table 5 Dynamic properties for various reinforced conditions

Dynamic properties of the foundation bed	Unreinforced	Geocell (Exp.)	Geocell (ECA)	Geocell (HSA)
Resonant frequency, f_r (Hz)	25	35.5	37	36
Resonant displacement amplitude, X_m (mm)	0.515	0.217	0.195	0.22
Coefficient of elastic uniform compression, C_u (MN/m ³)	39.13	78.89	85.70	81.13
Coefficient of elastic uniform shear, C_τ (MN/m ³) ($C_\tau = 0.5C_u$)	19.56	39.45	42.85	40.56
Coefficient of elastic non-uniform compression, C_ϕ (MN/m ³) ($C_\phi = 2C_u$)	29.34	59.17	64.27	60.85
Coefficient of elastic non-uniform shear, C_ψ (MN/m ³) ($C_\psi = 0.75C_u$)	78.25	157.78	171.40	162.26
Soil stiffness, K (MN/m)	14.09	28.40	30.85	29.21
Shear Modulus, G (MN/m ²)	7.28	14.68	15.95	15.10
Young's Modulus, E (MN/m ²)	18.93	38.17	41.47	39.26
Damping ratio, D_f (%)	2.06	4.9	5.45	4.83

determined based on the value of C_u . The stiffness of the foundation bed was calculated by multiplying the contact area of the block with the soil and the coefficient of elastic uniform compression. The shear modulus of the soil was determined using the following equation as suggested by Lysmer (1965),

$$G = \frac{K(1 - \nu)}{4r_0} \quad (7)$$

$$r_0 = \sqrt{A/\pi} \quad (8)$$

where K is the soil stiffness, ν is the Poisson's ratio of the soil and r_0 is the equivalent radius of the non-circular footing. The damping ratio of the foundation–soil system was obtained by,

$$\frac{X_m M}{m_e e} = \frac{1}{2D_f \sqrt{1 - D_f^2}} \quad (9)$$

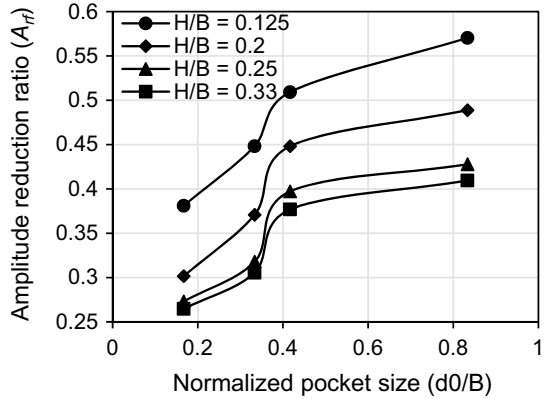
$$m_e e = \frac{W_e e}{g} = \frac{0.7 \sin(\frac{\theta}{2})}{g} \quad (10)$$

where X_m is resonant displacement amplitude, M is the total mass of the concrete block and oscillator assembly, m_e is eccentric rotating mass, e is the eccentricity, g is the acceleration due to gravity and θ is the eccentricity angle.

It is evident from the table that all the dynamic properties improved significantly with the provision of geocells. The elasticity and the damping ratio were found to increase by about 102% and 134%, respectively, in the presence of geocell reinforcement. Further, the ECA technique overestimated the elastic constants and the damping ratio by around 9% and 11%, respectively, as compared to the experimental values. Overall, the HSA technique has been found to provide a realistic estimation of the dynamic response of the geocell-reinforced bed. Hence, the HSA technique is suggested for modelling the geocells and has been used for further analysis.

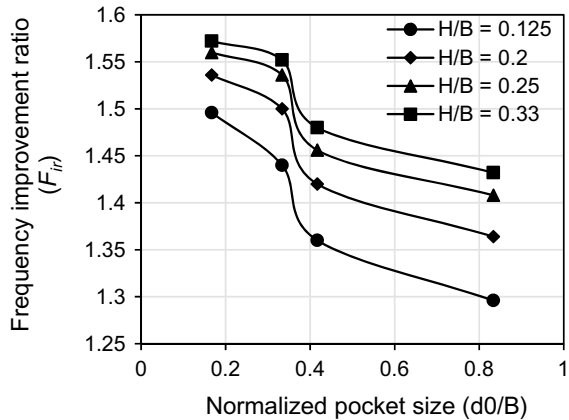
The effect of normalized cell depth (H/B) and normalized pocket diameter (d_0/B) on the isolation efficiency of geocells was investigated. The values of H/B and d_0/B used in the baseline case were 0.2 and 0.42, respectively. Two terms, namely amplitude reduction ratio (A_{rf}) and frequency improvement ratio (F_{ir}) were defined to quantify the efficacy of geocells. A_{rf} is defined as the ratio of the displacement amplitude of the reinforced system to that of the unreinforced system. It should be minimum for better isolation system. The influence of normalized cell depth and diameter on the A_{rf} has been shown in Fig. 7. From the figure, it can be observed that the amplitude reduction ratio increases with an increase in the cell diameter irrespective of the cell depth. Moreover, for a constant value of pocket size, the A_{rf} was found to decrease with an increase in cell depth. The rate of reduction in A_{rf} was observed as minimal beyond the cell depth of $0.25B$. Hence, it was considered as the optimum value of the cell height.

Fig. 7 Influence of normalized pocket size and cell depth on amplitude reduction ratio



The Frequency improvement ratio F_{ir} is defined as the ratio of the resonant frequency of the reinforced soil system to that of the unreinforced system. The influence of normalized cell depth and diameter on the Frequency improvement ratio has been shown in Fig. 8. From the figure, it was observed that the F_{ir} decreases with an increase in pocket size for all the values of the normalized cell depth. Further, the rate of increment in F_{ir} was reduced beyond the cell depth value of $0.25B$. Overall, the geocell mattress having cell depth $0.25B$ and minimum pocket size can prove to be the best for the vibration isolation purpose.

Fig. 8 Influence of normalized pocket size and cell depth on frequency improvement ratio



4 Conclusions

The present study investigates the efficiency of the geocells in isolating the machine-induced vibrations. A square concrete footing resting on unreinforced and geocell reinforced foundation beds was considered. The developed numerical models were initially validated with the results of large-scale block resonance field tests. From the results, 56% reduction in displacement amplitude and 42% improvement in resonant frequency was observed with the provision of geocells as compared to the unreinforced condition. Similarly, the PPV was reduced by 49% in the presence of geocells at 0.5 m distance from the vibration source. The dynamic elastic constants and the damping ratio were increased by more than two times due to geocells. Moreover, a comparison was established between the two different modelling techniques, namely ECA and HSA. Though the ECA technique is simple, it overestimates the vibration isolation efficiency of the geocells. The ECA overestimated the improvement in resonant frequency and the reduction in displacement amplitude by 4% and 10%, respectively. On the contrary, the HSA technique is complex but provides more realistic and accurate results. The present study also suggests an optimum configuration of the geocell mattress under the machine foundation. The results revealed that geocells with $0.25B$ cell depth and minimum pocket size are best for the vibration isolation purpose.

References

- Ahmad S, Al-Hussaini TM, Fishman KL (1996) Investigation on active isolation of machine foundations by open trenches. *J Geotechn Eng* 122(6):454–461
- Alzawi A, El Naggar MH (2011) Full scale experimental study on vibration scattering using open and in-filled (GeoFoam) wave barriers. *Soil Dyn Earthq Eng* 31(3):306–317
- ASTM D3080/D3080M (2011) Standard Test Method for Direct Shear Test of Soils Under Consolidated Drained Conditions, ASTM International, West Conshohocken, PA, USA
- ASTM D4885-01 (2018) Standard Test Method for Determining Performance Strength of Geomembranes by the Wide Strip Tensile Method, ASTM International, West Conshohocken, PA
- ASTM D5321/D5321M-17 (2017) Standard Test Method for Determining the Shear Strength of Soil-Geosynthetic and Geosynthetic-Geosynthetic Interfaces by Direct Shear, ASTM International, West Conshohocken, PA
- Azzam WR (2015) Utilization of the confined cell for improving the machine foundation behavior-numerical study. *J GeoEng* 10(1):17–23
- Bathurst RJ, Karpurapu R (1993) Large-scale triaxial compression testing of geocell-reinforced granular soils. *Geotechn Testing J* 16(3):296–303
- Bathurst RJ, Knight MA (1998) Analysis of geocell reinforced-soil covers over large span conduits. *Comput Geotechn* 22(3–4):205–219
- Bhatia KG (2008) Foundations for industrial machines and earthquake effects. *ISET J Earthq Technol* 45(1–2):13–29
- BIS (1992). IS: 5249 (1992) Determination of dynamic properties of soil-Method of test, Bureau of Indian Standards, Manak Bhawan, 9 Bahadur Shar Zafar Marg, New Delhi-12, India

- BIS (2000). IS: 456 (2000) Plain and Reinforced Concrete—Code of Practice, Bureau of Indian Standards, Manak Bhawan, 9 Bahadur Shar Zafar Marg, New Delhi-12, India
- Bowles LE (1996) Foundation analysis and design. McGraw Hill, New York, USA
- Coulter P, Cuéllar V, Degrande G, Lombaert G (2015) Experimental and numerical evaluation of the effectiveness of a stiff wave barrier in the soil. *Soil Dyn Earthq Eng* 77:238–253
- Dash SK, Sireesh S, Sitharam TG (2003) Model studies on circular footing supported on geocell reinforced sand underlain by soft clay. *Geotextiles Geomembranes* 21(4):197–219
- Gazetas G (1983) Analysis of machine foundation vibrations: state of the art. *Int J Soil Dyn Earthq Eng* 2(1):2–42
- Hegde A, Sitharam TG (2015a) 3-dimensional numerical modelling of geocell reinforced sand beds. *Geotextiles Geomembranes* 43:171–181
- Hegde AM, Sitharam TG (2015b) Effect of infill materials on the performance of geocell reinforced soft clay beds. *Geomech Geoenviron Eng* 10(3):163–173
- Hegde AM, Sitharam TG (2015c) Three-Dimensional numerical analysis of geocell reinforced soft clay beds by considering the actual geometry of geocell pockets. *Canadian Geotechn J* 52:1–12
- Indraratna B, Biabani MM, Nimbalkar S (2014) Behavior of geocell-reinforced subballast subjected to cyclic loading in plane-strain condition. *J Geotechn Geoenviron Eng* 141(1):04014081
- Itasca (2008) Fast Lagrangian analysis of continua (FLAC^{3D} 5.01). Itasca Consulting Group Inc., Minneapolis, Minn
- Ju SH (2004) Three-dimensional analyses of wave barriers for reduction of train-induced vibrations. *J Geotechn Geoenviron Eng* 130(7):740–748
- Krishnaswamy NR, Rajagopal K, Latha GM (2000) Model studies on geocell supported embankments constructed over a soft clay foundation. *Geotechn Testing J* 23(1):45–54
- Kumar P, Sandhu HK, Chakraborty SK (2014) Isolation of plane shear wave using water saturated trench barrier. *Soil Dyn Earthq Eng* 59:42–50
- Latha GM, Somwanshi A (2009) Effect of reinforcement form on the bearing capacity of square footings on sand. *Geotextiles Geomembranes* 27(6):409–422
- Leshchinsky B, Ling H (2013) Effects of geocell confinement on strength and deformation behavior of gravel. *J Geotechn Geoenviron Eng* 139(2):340–352
- Lysmer J (1965) Vertical motions of rigid footings, PhD thesis, University of Michigan, Ann Arbor
- Madhavi Latha G, Rajagopal K (2007) Parametric finite element analyses of geocell-supported embankments. *Canadian Geotechn J* 44(8):917–927
- Mandal A, Baidya DK, Roy D (2012) Dynamic response of the foundations resting on a two-layered soil underlain by a rigid layer. *Geotechn Geol Eng* 30(4):775–786
- Mehdipour I, Ghazavi M, Moayed RZ (2013) Numerical study on stability analysis of geocell reinforced slopes by considering the bending effect. *Geotextiles Geomembranes* 37:23–34
- Rajagopal K, Krishnaswamy NR, Latha GM (1999) Behaviour of sand confined with single and multiple geocells. *Geotextiles Geomembranes* 17(3):171–184
- Richart FE, Hall JR, Woods RD (1970) Vibrations of soils and foundations. *Int Series Theoret Appl Mech*
- Satyaj SR, Leshchinsky B, Han J, Neupane M (2018) Use of cellular confinement for improved railway performance on soft subgrades. *Geotextiles Geomembranes* 46(2):190–205
- Sitharam TG, Sireesh S (2005) Behavior of embedded footings supported on geogrid cell reinforced foundation beds. *Geotechn Testing J* 28(5):452–463
- Sitharam TG, Hegde A (2013) Design and construction of geocell foundation to support the embankment on settled red mud. *Geotextiles Geomembranes* 41:55–63
- Skempton AW (1986) Standard penetration test procedures and the effects in sands of overburden pressure, relative density, particle size, ageing and overconsolidation. *Geotechnique* 36(3):425–447
- Tafreshi SM, Dawson AR (2010) Comparison of bearing capacity of a strip footing on sand with geocell and with planar forms of geotextile reinforcement. *Geotextiles Geomembranes* 28(1):72–84

- Tanyu BF, Aydilek AH, Lau AW, Edil TB, Benson CH (2013) Laboratory evaluation of geocell-reinforced gravel subbase over poor subgrades. *Geosynth Int* 20(2):47–61
- Thakur JK, Han J, Pokharel SK, Parsons RL (2012) Performance of geocell-reinforced recycled asphalt pavement (RAP) bases over weak subgrade under cyclic plate loading. *Geotextiles Geomembranes* 35:14–24
- Thompson DJ, Jiang J, Toward MGR, Hussein MFM, Ntotsios E, Dijkmans A, Coulier D, Lombaert G, Degrande G (2016) Reducing railway-induced ground-borne vibration by using open trenches and soft-filled barriers. *Soil Dyn Earthq Eng* 88:45–59
- Venkateswarlu H, Hegde A (2017) Dynamic response of the machine foundation resting on geocell reinforced soil beds. In: *Proceedings of Indian geotechnical conference-2017*, 14–16 December, Guwahati, Paper ID Th11-559
- Yang X, Han J, Parsons RL, Leshchinsky D (2010) Three-dimensional numerical modeling of single geocell-reinforced sand. *Front Architect Civil Eng China* 4(2):233–240
- Yang X, Han J, Pokharel SK, Manandhar C, Parsons RL, Leshchinsky D, Halahmi I (2012) Accelerated pavement testing of unpaved roads with geocell-reinforced sand bases. *Geotextiles Geomembranes* 32:95–103